

Graph-theoretical analysis of local and latent symmetries in physical systems

Dissertation

zur Erlangung der Würde des Doktors der

Naturwissenschaften (Dr. rer. nat.)

der Fakultät für Mathematik, Informatik und Naturwissenschaften

Fachbereich Physik

der Universität Hamburg

vorgelegt von Malte Röntgen

aus Henstedt-Ulzburg

Hamburg

2021

Gutachter/innen der Dissertation:

Prof. Dr. Peter Schmelcher
Prof. Dr. Henning Moritz

Zusammensetzung der Prüfungskommission:

Prof. Dr. Peter Schmelcher
Prof. Dr. Henning Moritz
Prof. Dr. Daniela Pfannkuche
Prof. Dr. Franz X. Kärtner
Dr. Thore Posske

Vorsitzende der Prüfungskommission:

Prof. Dr. Daniela Pfannkuche

Datum der Disputation:

04.04.2022

Vorsitzender Fach-Promotionsausschusses PHYSIK:

Prof. Dr. Wolfgang Hansen

Leiter des Fachbereichs PHYSIK:

Prof. Dr. Günter H. W. Sigl

Dekan der Fakultät MIN:

Prof. Dr. Heinrich Graener

Elimu haina mwisho
Education never ends.

— Swahili proverb

ABSTRACT

The overarching topic of this thesis is the study of different types of symmetries in physical systems that are described by a discrete model, a prominent example being condensed matter systems in the tight-binding approximation.

In the first chapter of this thesis, we focus on one-dimensional tight-binding chains that feature local symmetries, that is, symmetries of a part of the system. We employ two different pathways for the treatment of such locally symmetric chains. The first pathway is a recently introduced framework which unveils the impact of local symmetries through certain current-like correlators, the so-called non-local currents. The framework is experimentally verified by measuring these non-local currents in a system of so-called evanescently coupled optical waveguides. The second pathway is a framework of locally symmetric resonators, which we develop in the context of binary tight-binding chains. In these chains, the next-neighbor coupling is constant, while the on-site potentials may take two different values. In particular, we investigate the cases where the on-site potential binary values are ordered according to the Fibonacci, Thue-Morse, and Rudin-Shapiro sequence. Among others, our framework explains the finding that, for low coupling strength, the eigenstates of these chains feature locally symmetric localization patterns.

The second chapter deals with the phenomenon of compact localized states (CLSs). Such states are eigenstates of a discrete system, e.g., a tight-binding model, which have compact support. That is, they have non-vanishing elements only on a (usually small) part of the system. This extreme kind of localization is caused by destructive interference, which is in turn allowed for by a suitable interplay of coupling strengths and the geometry of the system. In many cases, the systems supporting compact localization have been found to feature local symmetries, and we investigate the connection between these two phenomena in more detail. By applying insights from graph theory, we find that certain classes of local symmetries can indeed be systematically linked to compact localization. We further use these insights to derive a powerful construction principle to equip tight-binding systems with CLSs. In particular, this principle allows to equip each unit cell of a lattice with a CLS at the same energy. This leads to macroscopic degeneracy and thus a completely flat band. Our principle allows to tune the position of this flat band without changing the remaining bands of the lattice. Apart from developing this construction principle and applying it to tight-binding lattices, we further show that local symmetry induced compact localization is also possible in long range interacting systems of coupled dipole scatterers, which we analyze in terms of the so-called dyadic Green's matrix.

In the third chapter, we investigate different methods of transferring a CLS across a tight-binding system. The first of these methods is optimal control theory, where the Hamiltonian is changed in an optimized, time-dependent manner to allow for the high-fidelity transfer of CLSs. For the second method, we modify the principles of so-called perfect state transfer and pretty good state transfer to enable the transfer of CLSs. These principles have originally been developed for

the faithful transfer of excitations of a single site across a system. In particular, by fine-tuning the underlying static Hamiltonian, these two methods achieve the transfer of the state by pure time-evolution. Unfortunately, direct application of these methods to our aim of transferring CLSs is not possible, since our CLSs are not single-site excitations, but anti-symmetric excitations of a dimer, that is, two-site excitations. However, we show that one can easily modify a Hamiltonian featuring perfect or pretty good state transfer of single-site excitations such that the high-fidelity transfer of CLSs is possible.

In the fourth chapter of this thesis, the focus lies on the concept of latent symmetries. A Hamiltonian features a latent symmetry if a suitable dimensional reduction—the so-called isospectral reduction—of this Hamiltonian features a symmetry. We provide methods for the construction of systems with such latent symmetries. We further link non-abelian latent symmetries to spectral degeneracies of the underlying Hamiltonian. Moreover, we use a special class of latent symmetries for the construction of compact localized states and flat bands. Lastly, we unite the two topics of this thesis by showing that there is a profound connection between local and latent symmetries. Namely, a latent symmetry is nothing else but a local symmetry not only in the original Hamiltonian matrix, but also in all of its matrix powers.

ZUSAMMENFASSUNG

Das übergreifende Thema dieser Arbeit ist die Untersuchung verschiedener Arten von Symmetrien in physikalischen Systemen die durch ein diskretes Modell beschrieben werden, beispielsweise im Rahmen der tight-binding-Approximation.

Im ersten Kapitel dieser Arbeit konzentrieren wir uns auf eindimensionale tight-binding Ketten, welche lokale Symmetrien aufweisen. Unter einer „lokalen Symmetrie“ meinen wir hierbei eine Symmetrie eines Subsystems, das heißt, eine Symmetrie, die üblicherweise nur in einem Teil des Systems gültig ist. Wir verwenden zwei verschiedene Methoden zur Behandlung solcher lokal symmetrischer Ketten: Erstens ein kürzlich eingeführtes Framework, welches die Auswirkungen lokaler Symmetrien durch bestimmte stromähnliche Korrelatoren, die sogenannten nichtlokalen Ströme, aufdeckt. Dieses Framework wird experimentell verifiziert, indem die nichtlokalen Ströme in einem System von sog. evaneszent gekoppelten optischen Wellenleitern gemessen werden. Unsere zweite Methode ist ein Framework von lokal symmetrischen Resonatoren, das wir im Zusammenhang mit binären tight-binding Ketten entwickeln. In diesen Ketten ist die Kopplung der nächsten Nachbarn konstant, während die on-site Potentiale zwei verschiedene Werte annehmen können. Insbesondere untersuchen wir die Fälle, in denen die binären Werte der on-site Potentiale gemäß der Fibonacci-, Thue-Morse- und Rudin-Shapiro-Sequenz angeordnet sind. Unser Framework erklärt unter anderem, dass die Eigenzustände dieser Ketten bei geringer Kopplungsstärke lokal symmetrische Lokalisierungsmuster aufweisen.

Das zweite Kapitel befasst sich mit dem Phänomen der kompakten lokalisierten Zustände (KLZ). Solche Zustände sind Eigenzustände eines diskreten Systems, z. B. eines tight-binding Modells, die einen kompakten Träger haben. Das heißt, sie sind nur in einem (üblicherweise kleinen) Teil des Systems nichtverschwindend. Diese extreme Art der Lokalisierung wird durch destruktive Interferenz verursacht, die wiederum durch ein geeignetes Zusammenspiel von Kopplungsstärken und der Geometrie des Systems ermöglicht wird. In vielen Fällen hat sich gezeigt, dass Systeme, die eine kompakte Lokalisierung unterstützen, lokale Symmetrien aufweisen, und wir untersuchen den Zusammenhang zwischen diesen beiden Phänomenen genauer. Durch die Anwendung von Erkenntnissen aus der Graphentheorie stellen wir fest, dass bestimmte Klassen lokaler Symmetrien tatsächlich systematisch mit kompakter Lokalisierung in Verbindung gebracht werden können. Aus diesen Erkenntnissen leiten wir ein mächtiges Konstruktionsprinzip ab, mit dem sich tight-binding Systeme mit KLZ ausstatten lassen. Dieses Prinzip ermöglicht es insbesondere, jede Einheitszelle eines Kristalls mit einem KLZ mit derselben Energie auszustatten. Dies führt zu makroskopischer Entartung und damit zu einem völlig flachen Band. Unser Prinzip erlaubt es, die Position dieses flachen Bandes zu tunen, ohne die übrigen Bänder des Kristalls zu verändern. Neben der Entwicklung dieses Konstruktionsprinzips und seiner Anwendung auf tight-binding Systeme zeigen wir außerdem, dass eine durch lokale Symmetrie induzierte kompakte Lokalisierung auch in langreichweitig wechselwirkenden Systemen mit gekoppelten

Dipolstreuern möglich ist, welche wir mittels der sog. dyadischen Green-Matrix untersuchen.

Im dritten Kapitel untersuchen wir verschiedene Methoden, um einen KLZ in einem tight-binding System zu transferieren. Die erste dieser Methoden ist die optimale Steuerung, bei der der Hamiltonian in einer optimierten, zeitabhängigen Weise verändert wird, um den perfekten Transfer eines KLZ zu ermöglichen. Bei der zweiten Methode bauen wir auf zwei Techniken des Zustandstransfers auf, namentlich, auf dem perfekten Zustandstransfer (englisch: perfect state transfer) und dem ziemlich guten (englisch: pretty good state transfer) Zustandstransfer. Beide Techniken wurden ursprünglich für den (fast) perfekten Transfer von single-site Anregungen eines tight-binding Systems entwickelt. Durch Tuning des zugrundeliegenden zeitunabhängigen Hamiltonians erreichen diese beiden Techniken insbesondere die Übertragung des Zustands durch reine Zeitentwicklung. Leider ist eine direkte Anwendung dieser Techniken auf unser Ziel des Transfers von KLZs nicht möglich, da unsere KLZs keine single-site Anregungen sind, sondern antisymmetrische Anregungen eines Dimers, d. h. eine Anregung von zwei Sites. Wir zeigen jedoch, dass ein Hamiltonian, der den perfekten oder ziemlich guten Transfer von single-site Anregungen erlaubt, leicht so modifiziert werden kann, dass der Transfer von KLZ mit hoher Fidelität möglich ist.

Der Fokus des vierten Kapitels dieser Arbeit liegt auf sogenannten "latenten Symmetrien". Ein Hamiltonian besitzt eine latente Symmetrie wenn eine bestimmte Art von Dimensionsreduktion, nämlich die sogenannte Isospektralreduktion, dieses Hamiltonians eine Symmetrie besitzt. Wir entwickeln Methoden für die Konstruktion von latent symmetrischen Systemen. Außerdem stellen wir eine Verbindung zwischen nichtabelschen latenten Symmetrien und spektralen Entartungen des zugrundeliegenden Hamiltonians her. Zuletzt vereinigen wir die beiden Themen dieser Arbeit, indem wir zeigen, dass eine latente Symmetrie nichts anderes als eine lokale Symmetrie in jeder Matrix-Power des Hamiltonians ist.

CONTENTS

I INTRODUCTION

1	LOCAL SYMMETRIES IN ONE-DIMENSIONAL SYSTEMS	3
1.1	Local symmetries	3
1.1.1	Analyzing the impact of local symmetries through non-local currents	4
1.2	Outline: Observation of local symmetry in a photonic system	7
1.3	Outline: Local symmetry theory of resonator structures for the real-space control of edge states in binary aperiodic chains	10
2	COMPACT LOCALIZED STATES AND FLAT BANDS	17
2.1	Compact localization	17
2.2	Flat bands	19
2.2.1	Flat band generators	20
2.3	Outline: Compact localized states and flat bands from local symmetry partitioning	20
2.4	Outline: Compact localized states of open scattering media: a graph decomposition approach for an ab initio design	23
3	QUANTUM STATE TRANSFER	27
3.1	Perfect and pretty good transfer	28
3.2	Outline: Quantum network transfer and storage with compact localized states	31
4	GRAPH THEORY AND LATENT SYMMETRIES	37
4.1	Graphs	37
4.2	Cospectrality: The symmetry of walks	41
4.3	Latent symmetries	44
4.4	Outline: Designing systems with pretty good state transfer	46
4.5	Outline: Cospectrality preserving graph modifications	47
4.6	Outline: Flat bands by latent symmetry	48
4.7	Outline: Latent symmetry induced degeneracies	50

II SCIENTIFIC CONTRIBUTIONS AND OUTLOOK

5	SCIENTIFIC CONTRIBUTIONS	55
	Observation of Local Symmetry in a Photonic System	56
	Local symmetry theory of resonator structures for the real-space control of edge states in binary aperiodic chains	65
	Compact localized states and flat bands from local symmetry partitioning	89
	Compact localized states of open scattering media: a graph decomposition approach for an ab initio design	101
	Quantum Network Transfer and Storage with Compact Localized States Induced by Local Symmetries	106
	Designing pretty good state transfer via isospectral reductions	129

	Cospectrality preserving graph modifications and eigenvector properties via walk equivalence of vertices	149
	Flat bands by latent symmetry	183
	Latent symmetry induced degeneracies	198
6	SUMMARY, CONCLUSIONS, AND OUTLOOK	211
6.1	Local symmetries	211
6.1.1	Local symmetries in one-dimensional systems	212
6.1.2	Compact localized states and flat bands through local symmetries	214
6.1.3	Transfer of compact localized states	217
6.2	Latent symmetries	219
6.2.1	Outlook	222

ACRONYMS

CLS	compact localized state.
CRAB	chopped random-basis.
DLL	decorated Lieb lattice.
EPT	equitable partition theorem.
GM	dyadic Green's matrix.
nEPT	non-equitable partition theorem.
NLC	non-local current.
PGST	pretty good state transfer.
PST	perfect state transfer.

PREFACE

LIST OF PUBLICATIONS THIS DISSERTATION IS BASED ON

- MR¹N. Schmitt, S. Weimann, C. V. Morfonios, M. Röntgen, M. Heinrich, P. Schmelcher, and A. Szameit, “Observation of local symmetry in a photonic system,” *Laser Photonics Rev.* **14**, 1900222 (2020).
- MR²M. Röntgen, C. V. Morfonios, R. Wang, L. Dal Negro, and P. Schmelcher, “Local symmetry theory of resonator structures for the real-space control of edge states in binary aperiodic chains,” *Phys. Rev. B* **99**, 214201 (2019).
- MR³M. Röntgen, C. V. Morfonios, and P. Schmelcher, “Compact localized states and flat bands from local symmetry partitioning,” *Phys. Rev. B* **97**, 035161 (2018).
- MR⁴F. Sgrignuoli, M. Röntgen, C. V. Morfonios, P. Schmelcher, and L. Dal Negro, “Compact localized states of open scattering media: a graph decomposition approach for an ab initio design,” *Opt. Lett.* **44**, 375 (2019).
- MR⁵M. Röntgen, C. V. Morfonios, I. Brouzos, F. K. Diakonov, and P. Schmelcher, “Quantum network transfer and storage with compact localized states induced by local symmetries,” *Phys. Rev. Lett.* **123**, 080504 (2019).
- MR⁶M. Röntgen, N. E. Palaiodimopoulos, C. V. Morfonios, I. Brouzos, M. Pyzh, F. K. Diakonov, and P. Schmelcher, “Designing pretty good state transfer via isospectral reductions,” *Phys. Rev. A* **101**, 042304 (2020).
- MR⁷C. V. Morfonios, M. Pyzh, M. Röntgen, and P. Schmelcher, “Cospectrality preserving graph modifications and eigenvector properties via walk equivalence of vertices,” *Linear Algebra Its Appl.* **624**, 53 (2021).
- MR⁸C. V. Morfonios, M. Röntgen, M. Pyzh, and P. Schmelcher, “Flat bands by latent symmetry,” *Phys. Rev. B* **104**, 035105 (2021).
- MR⁹M. Röntgen, M. Pyzh, C. V. Morfonios, N. E. Palaiodimopoulos, F. K. Diakonov, and P. Schmelcher, “Latent symmetry induced degeneracies,” *Phys. Rev. Lett.* **126**, 180601 (2021).

DECLARATION OF PERSONAL CONTRIBUTIONS TO THE PUBLICATIONS [MR¹–MR⁹]

The idea for the project [MR¹] emerged during several meetings with Prof. Dr. Alexander Szameit and his group. Dr. Christian Morfonios and myself provided the theory part for the treatment of non-local currents. This includes, in particular, the results in Appendices C and D of that work. The remaining part and especially the experiments were performed by M.Sc. Nora Schmitt and other members of Professor Alexander Szameit’s group.

[MR²] was done in close collaboration with Dr. Christian Morfonios, who also wrote parts of the manuscript. The idea for this project was developed jointly

with Dr. Ren Wang and Prof. Dr. Luca Dal Negro, with whom we also frequently discussed.

The research of [MR3] was almost entirely conducted and written by myself. I frequently discussed the work with Dr. Christian Morfonios, who further designed figure 3 and provided the corresponding calculations.

The idea of the project [MR4] was provided by myself, and I wrote and conducted the part concerning the application of the equitable partition theorem together with Dr. Christian Morfonios. The remaining part of the work was conducted by Dr. Fabrizio Sgrignuoli, who also wrote all non-graph-theoretical parts of the manuscript. All parts of the work were frequently discussed among all authors.

For [MR5], I did most of the simulations and also wrote large parts of the manuscript. All calculations that involved optimal control were performed by Dr. Ioannis Brouzos, who also wrote parts of the manuscript. I frequently discussed the work with Dr. Christian Morfonios, who wrote parts of the manuscript, double-checked many calculations of the main part of the work and further designed the figures in it.

[MR6] was conducted and written mostly by myself. I frequently discussed the work with Dr. Christian Morfonios and M.Sc. Maxim Pyzh. The search for graphs with cospectral vertices was done in equal parts by all three of us. The optimization of the transfer time was performed by Dr. Ioannis Brouzos and Dr. Nikolaos Palaiodimopoulos.

[MR7] was conducted and written in equal parts by Dr. Christian Morfonios, M.Sc. Maxim Pyzh, and myself.

The work [MR8] emerged during the close collaboration of Dr. Christian Morfonios, M.Sc. Maxim Pyzh and myself in the context of [MR7]. I have performed some of the band structure calculations, checked the example systems provided in the manuscript, and further provided the MATLAB tool that was used to find and test cospectral graphs in an intuitive manner. Together with M.Sc. Maxim Pyzh, I provided routines for detecting the walk-multiplets that are used for the construction of flat band lattices. The three of us also frequently discussed the work and the manuscript.

The work [MR9] has been conducted and written in equal parts by Dr. Christian Morfonios, M.Sc. Maxim Pyzh, and myself. The group-theoretical reasoning and the corresponding calculations were conducted together with Dr. Nikolaos Palaiodimopoulos, Prof. Dr. Fotios Diakonos, and Prof. Dr. Peter Schmelcher.

In all cases, the results were discussed on a regular basis with my supervisor Prof. Dr. Peter Schmelcher.

FURTHER PUBLICATIONS

^{MR10}M. Röntgen, C. Morfonios, F. Diakonos, and P. Schmelcher, “Non-local currents and the structure of eigenstates in planar discrete systems with local symmetries,” *Ann. Phys.* **380**, 135 (2017).

^{MR11}R. Wang, M. Röntgen, C. V. Morfonios, F. A. Pinheiro, P. Schmelcher, and L. Dal Negro, “Edge modes of scattering chains with aperiodic order,” *Opt. Lett.* **43**, 1986 (2018).

- MR¹²C. V. Morfonios, M. Röntgen, F. K. Diakonou, and P. Schmelcher, “Transfer efficiency enhancement and eigenstate properties in locally symmetric disordered finite chains,” *Ann. Phys. (N. Y.)* **418**, 168163 (2020).
- MR¹³M. Röntgen, M. Pyzh, C. V. Morfonios, and P. Schmelcher, *On symmetries of a matrix and its isospectral reduction*, (May 25, 2021) <http://arxiv.org/abs/2105.12579>.

OUTLINE OF THIS THESIS

This thesis is structured as follows.

In Part [i](#) of this thesis, we outline our works [[MR1](#)–[MR9](#)] and embed them into their respective scientific context. This first part is divided into four chapters, each dealing with different aspects of local and latent symmetries. In each chapter, we first give an overview over the corresponding literature, and then outline our contributions.

In Chapter [1](#), we introduce the concept of local symmetries and investigate one-dimensional locally symmetric tight-binding chains. In Chapter [2](#), we turn our attention to higher-dimensional tight-binding networks and investigate the connection of local symmetries to so-called compact localized states. In Chapter [3](#), we investigate means of transferring these compact localized states. In Chapter [4](#), our focus lies on a recently introduced concept from graph theory, namely, so-called “latent symmetries”. We investigate several aspects of this concept and also draw a direct connection to local symmetries.

In Part [ii](#), we present our scientific contributions in Chapter [5](#). We then end this thesis in Chapter [6](#) with a separate summary, conclusions, and an outlook for each of the four topics that were presented in Chapters [1](#) to [4](#).

Part I

INTRODUCTION

IN this first chapter of the thesis, we will first introduce the concept of local symmetries in Section 1.1. Afterwards, in Sections 1.2 and 1.3, we will discuss our works [MR1, MR2] that focus on local symmetries in systems that can be described by a one-dimensional tight-binding model.

1.1 LOCAL SYMMETRIES

Symmetry, that is, the invariance of a system under certain transformations—such as rotations and reflections, for example—, plays a major role in all areas of physics. Noether’s theorem is a prominent example highlighting both the relevance and usefulness of symmetries. Stating that there corresponds a conserved quantity to every¹ continuous symmetry of a physical system [1], Noether’s theorem gives a symmetry-based explanation of fundamental conservation laws of energy as well as linear and angular momentum.

In quantum mechanics, many models feature an abundance of symmetries, thereby significantly simplifying their treatment while simultaneously leading to a better understanding of the underlying physics. The treatment of the hydrogen atom, for example, greatly profits from its spherical symmetry, since it can be used to derive an analytical solution of the three-dimensional Schrödinger equation. But apart from this computational advantage, the spherical symmetry can also be used to derive selection rules for electronic transitions, thereby explaining why only some of those are observed in spectroscopic experiments. Such interplay of symmetry, easier computation and selection rules is not limited to the hydrogen atom, but on the contrary lies at the heart of chemistry, with many molecules being highly symmetric [2–5]. Another example for the power of symmetries to greatly simplify a problem is the field of solid state physics. Here, the translational symmetry of a crystal leads to Bloch waves, that is, plane waves modulated by a function that has the same periodicity as the underlying crystal lattice. Before we continue, we want to mention one last and particularly important aspect of symmetries, namely, its study in terms of group theory [6]. Besides providing a beautiful method for describing symmetries, group theory in particular allows to explain how spectral degeneracies of the underlying operator describing a physical system (such as the Hamiltonian) are linked to its symmetries [6, 7].

An important aspect of the above examples is that their symmetry is *global*, that is, the underlying symmetry is valid everywhere in space. The rotational symmetry of the hydrogen atom, for example, is assumed to hold everywhere, and crystals are assumed to be infinitely extended. But in reality, such idealized symmetries are never met: The hydrogen atom is certainly not isolated, and thus the rotational symmetry of the problem will be broken at some points in space, and any real crystal

¹ To be precise, Noether’s theorem only makes statements about systems that can be described by a Lagrangian.

is necessarily finite. The symmetries are thus *local*, that is, they only hold in certain parts of space. Fortunately, the deviations from global symmetry are in many cases only small, so that the locality of symmetries does not pose so much of a problem. For example, in a finite crystal, an electron within the bulk of this crystal does not ‘feel’ the effects of broken translational symmetry at the crystal’s boundaries, so that many results derived by means of symmetry (such as the band structure) are still approximately valid. Sometimes, however, this perturbative ansatz is not useful any more, be it because the perturbation of global symmetries is too big or simply because there is no identifiable global symmetry to be broken in the first place. Examples for this class range from glasses and partially disordered systems [8] to quasicrystals (which feature a long range order but no translational symmetry) to so-called order-disorder structures where layers of different symmetries are stacked onto each other [9–11]. A system may also be designed to be locally symmetric, with examples ranging from multilayered photonic devices [12–19] over quantum semiconductor superlattices [20] and acoustic waveguides [21] to magnonic systems [22]. Given this broad range of examples, the question arises what effects the local symmetries may have on the properties of the system (such as its eigenstates). This question represents the overarching topic of this dissertation and will be treated in different ways throughout this and the following chapters. Before we continue, let us first give a brief overview of what has been done in this respect so far.

1.1.1 Analyzing the impact of local symmetries through non-local currents

Contrary to their broad occurrence, local symmetries do not seem to have been treated systematically for a long time. There are a few notable exceptions to this. Firstly, local symmetry have been used in the study of molecular vibrations [23, 24], but unfortunately this idea does not seem to have spread further in the chemistry community. Another noteworthy approach, also in the context of chemistry, is the analysis of the electronic structure of molecules in terms of their local symmetries [25, 26]. The last exception comes from the field of X-Ray scattering, where local symmetries of the scatterers were used to make predictions about cross-correlations of scattering intensities [8, 27–29].

To the best of our knowledge, the first systematic approach to study the impact of local symmetries in a general fashion and in a broad range of systems was introduced in 2013 through a framework of so-called non-local currents [30]. Since this framework provides a first insight into the analysis of local symmetries, and also since it was the basis of our work [MR1] further below, we will discuss it now in more detail. In its simplest form, the framework can be developed in terms of the one-dimensional Helmholtz equation²

$$A''(x) + U(x)A(x) = 0. \quad (1.1)$$

This equation describes a number of interesting wave systems. For example, for an electromagnetic wave of frequency ω propagating in a medium with refractive index n , we have $U(x) = \omega^2 n^2(x)/c^2$ (c denoting the speed of light) and $A(x)$

² We note that this general formulation through the Helmholtz equation was only introduced in the third work on non-local currents [31]; the first two works dealt with the special cases of quantum [30] and electromagnetic [32] scattering.

describes the complex amplitude of the electric field. For a matter wave $U(x) = (2m/\hbar^2)(E - V(x))$, and $A(x)$ describes the wavefunction of a particle with mass m and energy E moving in a potential $V(x)$.

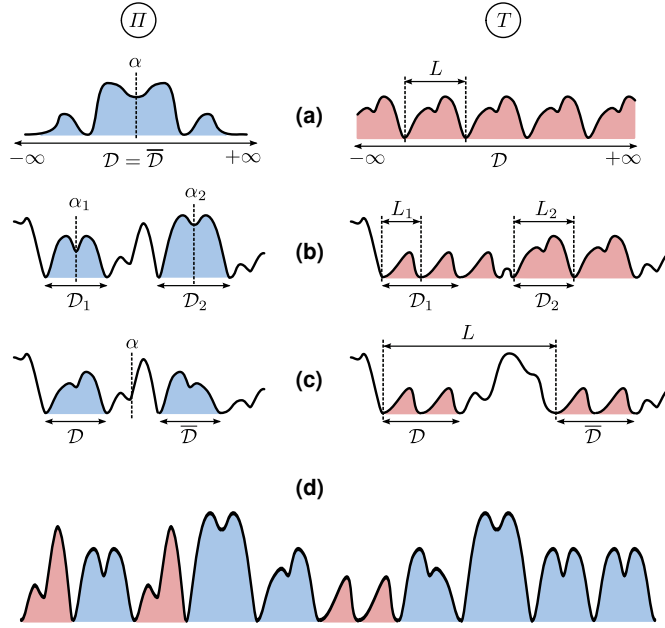


Figure 1.1: Visualization of different symmetry classes of a one-dimensional potential $U(x)$. From top to bottom: (a) Global reflection (Π , left) and translation (T , right) symmetry. (b) Nongapped local symmetries. (c) Gapped local symmetries. (d) Complete local symmetries (see text for details). Reprinted figure with permission from P. A. Kalozoumis et al., “Invariants of broken discrete symmetries,” *Phys. Rev. Lett.* **113**, 050403 (2014). Copyright (2014) by the American Physical Society.

The potential term $U(x)$ may feature reflection and translation symmetries, with the underlying symmetry transformation being described by

$$F : x \rightarrow \bar{x} = F(x) = \sigma x + \rho$$

with a reflection about the point α described by $\sigma = -1$, $\rho = 2\alpha$, and a translation by L described by $\sigma = 1$, $\rho = L$. In Fig. 1.1, we showcase different types of these symmetries. (a) shows the case of global reflection (Π) and translation (T) symmetries, that is, the domain \mathcal{D} of symmetry comprises the whole space. (b) to (d) then show different variations of local symmetries. In (b), these are *nongapped*³, while they are gapped in (c). (d) shows a “completely locally symmetric” system, that is, a system which is entirely composed of locally symmetric units. As can be seen from these very different cases, already in the simple case of one-dimensional systems, the world of local symmetries is a vast one.

Let us now introduce non-local currents by evaluating Eq. (1.1) at points x and \bar{x} and constructing the difference

$$A^*(x)A''(\bar{x}) - A(\bar{x})A''^*(x) = A^*(x)A(\bar{x})\left(U(x) - U(\bar{x})\right) := 2iQ'(x) \quad (1.2)$$

³ To be precise, a local symmetry is nongapped if $\mathcal{D} \cup \bar{\mathcal{D}}$ is connected, where \mathcal{D} denotes the domain of local symmetry, and $\bar{\mathcal{D}} = F(\mathcal{D})$ denotes its image. Thus, a reflection symmetry is nongapped if the center α of reflection lies within the domain \mathcal{D} of local symmetry.

with $*$ denoting the complex conjugate, and where we assumed real-valuedness of the potential $U(x)$. If there is a local symmetry, then $U(x) = U(\bar{x})$ for all x within the corresponding local symmetry domain \mathcal{D} . As a result, we have $Q'(x) = 0$ so that

$$Q = \frac{1}{2i} \left[\sigma A^*(x) A'(\bar{x}) - A(\bar{x}) A'^*(x) \right] \quad (1.3)$$

is constant throughout the domain \mathcal{D} . We note that $A'(\bar{x}) = dA(x)/dx|_{x=\bar{x}}$, and σ distinguishes between the Qs for translation ($\sigma = 1$) and reflection ($\sigma = -1$). The complex quantity Q is called a non-local current (NLC), since (i) it contains wave amplitudes at two points x, \bar{x} and (ii) it becomes the quantum probability current

$$j = \frac{1}{2i} \left[A^*(x) A'(x) - A(x) A'^*(x) \right]$$

when setting $\bar{x} = x$.

After the initial work on NLCs in 2013, the theory has been further developed in a series of papers and, along the way, applied to numerous physical setups. Shortly after their introduction in [30], NLCs were used to classify so-called perfect transmission resonances through the value that an alternating sum of different scaled NLCs takes [32]. NLCs were further used to generalize the classical Bloch and parity theorems—which make statements about waves in globally translational or reflection symmetric systems, respectively—to the case of local translation and reflection symmetries [31]. The results of [31] were generalized even more in [33], where also a central tool in one-dimensional scattering, the transfer matrix, was expressed through NLCs.

While the above works treated NLCs only within the special context of the one-dimensional time-independent Helmholtz Eq. (1.1), the theory has meanwhile been generalized in several regards. In [34], it was applied to scattering off locally symmetric potential landscapes in two dimensions. The generalization of the theory to local symmetries in systems that are driven in time was performed in [35]. In [MR10, 36], NLCs were developed for one- and two-dimensional discrete eigenvalue problems, which arise, for example, in tight-binding models. The theory was further generalized in [37] to interacting particles by harnessing the Bogoliubov-Born-Green-Kirkwood-Yvon (BBGKY) hierarchy [38–43]. Interestingly, non-local currents can be derived from a variational principle that is based on a “super Lagrangian” obtained by combining two separate Lagrangians [44]. Moreover, NLCs were also applied as an order-parameter [45, 46] in so-called \mathcal{PT} -symmetric non-hermitian quantum mechanics which was introduced in two seminal papers by Carl Bender [47, 48] (for more information on \mathcal{PT} -symmetric systems, see, e.g., the recent review articles [49, 50]).

So far, NLCs have been measured experimentally in two different setups [MR1, 51]. In [51], scattering through acoustic waveguides was performed. Local symmetries were here induced by placing scatterers in a locally-symmetric manner into the waveguides. Interestingly, the NLCs can be shown to keep their constancy even in the presence of losses, which is an important factor in acoustical experiments. The second experiment, [MR1], was performed in an optical setup of evanescently coupled waveguides and will be discussed in detail in the next section.

1.2 OUTLINE: OBSERVATION OF LOCAL SYMMETRY IN A PHOTONIC SYSTEM

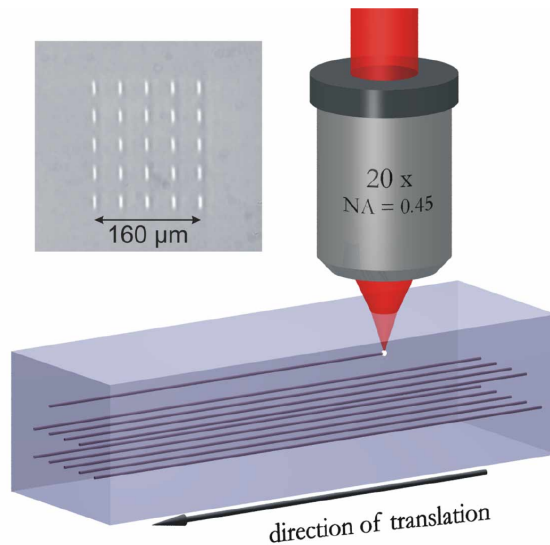


Figure 1.2: The femtosecond laser writing technique and an example waveguide array. Inset: Microscopic image of the end of such an array. Reprinted with permission from [52] © The Optical Society.

In [MR1], NLCs are measured in a photonic system. Before we come to the details of this work, we briefly introduce the experimental platform, namely, so-called optical waveguide arrays, and embed it in a broader context.

An example of an optical waveguide array is depicted in Fig. 1.2. Such arrays can be produced by different methods [53, 54], with examples including etching in semiconductors [55], inducing light in a photorefractive material [56], or using arrays of optical fibers [57], to name just a few. In the experiment performed in [MR1], evanescently coupled waveguide arrays are produced by “writing” them into fused silica glass by means of a femtosecond laser [58]. During this procedure—illustrated in Fig. 1.2—the laser light in the focal region partly destroys the glass. This leads to a local increase in density and the refractive index (more details about this process are given in the tutorial [58]); a waveguide is created by moving the focal region along the desired path. This process can be repeated at different locations of the bulk glass so that arrays of waveguides with a near-arbitrary geometry can be produced.

Optical waveguide arrays are interesting from several perspectives. First and foremost, they may play a role in future all-optical networking and highly miniaturized photonics [59–64] (see also [65] and references therein), and may even be used to implement all-optical logical gates [66]. Besides these obvious applications, optical waveguide arrays are also of fundamental interest since they enable the emulation of quantum mechanical phenomena in a highly controlled manner. This is made possible by the striking similarity between the two-dimensional Schrödinger equation

$$i\hbar \frac{\partial}{\partial t} \Psi(x, y, t) = - \left(\frac{\hbar^2}{2m} \left[\frac{\partial^2}{\partial x^2} + \frac{\partial^2}{\partial y^2} \right] - V(x, y, t) \right) \Psi(x, y, t) \quad (1.4)$$

for a particle with mass m within a potential $V(x, y, t)$, and the optical paraxial Helmholtz equation for light traveling along the z -axis,

$$i\hbar \frac{\partial}{\partial z} E(x, y, z) = - \left(\frac{\lambda^2}{2n_0} \left[\frac{\partial^2}{\partial x^2} + \frac{\partial^2}{\partial y^2} \right] + \Delta n(x, y, z) \right) E(x, y, z) \quad (1.5)$$

where E denotes the electrical field envelope, $\lambda = \lambda / (2\pi)$ the reduced wavelength, $\Delta n = n_0 - n(x, y, z)$ the refractive index change with n_0 being the refractive index of the bulk material [58]. In other words, the role of time in the 2-dimensional Schrödinger Eq. (1.4) is played by the z -axis in Eq. (1.5). In a suitably designed waveguide array, Eq. (1.5) may be converted to a tight-binding equation by applying coupled-mode theory [67], and in the past years this has been used to emulate several phenomena from condensed matter physics. Among these phenomena are Bloch-oscillations [68–70], Anderson localization [71, 72], topological insulators [73–77], and quasicrystals [78, 79]. Optical waveguide arrays were also used to implement concepts such as supersymmetry [80], flat bands [64, 81], artificial gauge fields [82], Dirac dynamics [83] or \mathcal{PT} -symmetric systems [84, 85]. For further information on coupled optical waveguide arrays, we refer the reader to, e.g., the review articles [54, 86, 87].

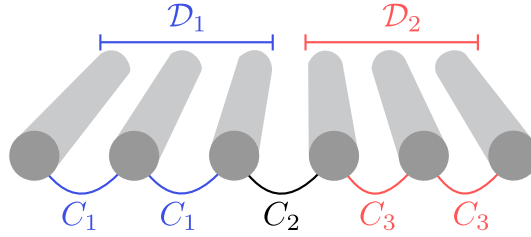


Figure 1.3: An example setup comprised of six waveguides, with C_1, C_2 , and C_3 denoting the next-neighbor couplings, which are assumed to be pairwise different from each other, that is, they fulfill $C_i \neq C_j$ for $i \neq j$. The setup is thus locally symmetric, with two local reflection symmetry domains indicated above the waveguides. Source: Adapted figure from [MR1].

Now that the foundations for our work [MR1] are set, we can describe it in more detail. Its main content is the measurement of NLCs in the context of one-dimensional arrays of coupled waveguides. The propagation of light in this system is described by the discrete Schrödinger equation

$$-i\hbar \frac{\partial \psi_m(z)}{\partial z} = C_{m,m-1} \psi_{m-1}(z) + C_{m,m+1} \psi_{m+1}(z) \quad (1.6)$$

where $\psi_m(z)$ denotes the light field in the m -th waveguide at position z , and $C_{n,m}$ describes the coupling between the adjacent waveguides n, m .

Let us now link Eq. (1.6) to the concept of local symmetries. Since we have so far—as in Fig. 1.1—concentrated on continuous systems, we first need to define what exactly we mean by a local symmetry in the context of a discrete setup. This poses no difficulty:

A local symmetry is a symmetry of a subsystem. That is, when isolating this subsystem from the remainder of the setup, it features a symmetry.

An example for a simple waveguide setup with local symmetries is depicted in Fig. 1.3. Here, the subsystem consisting of the three left waveguides is locally symmetric, since it features a reflection symmetry when one decouples it from the remaining three waveguides. Similarly, the subsystem consisting of the three right waveguides is locally reflection symmetric as well.

We note that Eq. (1.6) is discrete, while the NLCs were originally developed in the context of the one-dimensional Helmholtz equation Eq. (1.1), which is *continuous*. However, the adaptation of the formalism of NLCs to discrete models is possible, and was done in detail in [MR10, 36].

In order to measure the NLCs, both modulus and phase of the light field $\psi_m(z)$ need to be determined. The measurement of the modulus is the easier one; we achieve it by employing a fluorescence method. That is, the waveguides are fabricated such that a small fraction of the light propagating in a waveguide is converted into omnidirectional light. The resulting intensity pattern varies between different waveguides and along the z -direction, and thus allows to measure the modulus $|\psi_m(z)|$ of the light field in each waveguide. This technique, however, is unable to recover the phase of the light field. For the measurement of this phase, we initially (that is, at $z = 0$) excite only a single site, that is, we shine light only in a single waveguide. As a result, at any position z , the phase difference of the light field on two neighboring waveguides is equal to $\pi/2$. Moreover, along a waveguide the phase only changes at points where the light field vanishes, with the phase change at these points being equal to π . Since these zero-crossing points can be obtained from the intensity measurement, we can thus obtain both modulus and phase of the light field $\psi_m(z)$ for arbitrary z and in each waveguide m , and thus also the NLCs.

Besides the measurement of NLCs, a main point of our work [MR1] is to demonstrate their practical value for the distinction between locally symmetric and asymmetric setups. The idea behind this principle is as follows: Given an eigenstate $\vec{\Psi} = (\Psi_1, \dots, \Psi_N)^T$ of an unknown setup with N waveguides, the presence of local symmetries could be easily detected, since the corresponding non-local current is then spatially constant in a local symmetry domain⁴ \mathcal{D} . Unfortunately, this idea cannot directly be employed to the experimental setup in [MR1], since it is difficult to excite an eigenstate of the discrete Schrödinger equation describing the waveguide array. Instead, in the experiment only a single site is excited at $z = 0$, that is, $\vec{\phi}(0) = \sum_i c_i \vec{\Psi}^{(i)}$ is a superposition of eigenstates. For such a superposition the NLCs are in general *not constant* throughout a local symmetry domain. To circumvent this problem, we employ a non-local continuity equation which has been developed in [36], and which allows to distinguish between globally symmetric, locally symmetric, and asymmetric waveguide arrays through measurements of NLCs.

⁴ Of course, one would need to define this domain first. For example, for a local reflection symmetry one would need to define the center of reflection and the size of the domain. It follows that, in order to check whether the setup features *any* local symmetry, one would have to test all possible local symmetry domains and evaluate the NLCs in them.

1.3 OUTLINE: LOCAL SYMMETRY THEORY OF RESONATOR STRUCTURES FOR THE REAL-SPACE CONTROL OF EDGE STATES IN BINARY APERIODIC CHAINS

In the above work [MR1], the focus lied on the experimental measurement of NLCs. In our second work [MR2], we move away from that specific topic of non-local currents, though still focus on local symmetries in one-dimensional systems. In particular, we investigate setups described by the N -site tight-binding Hamiltonian

$$\hat{H} = \sum_{i=1}^N v_i |i\rangle \langle i| + h \sum_{i=1}^{N-1} (|i\rangle \langle i+1| + |i+1\rangle \langle i|) \quad (1.7)$$

where $|n\rangle$ is a single-site excitation of the site n , v_i denotes the on-site potential of the i -th site, and with h denoting the next-neighbor coupling which is constant throughout the system. With the coupling being constant, the choice of on-site potentials clearly determines the character of the system. For example, when these potentials are arranged periodically, Eq. (1.7) describes a finite crystal. In [MR2], however, our focus does not lie at all on periodic systems. Instead, we explore the realm of so-called deterministic aperiodic setups. A prime example of such systems are *quasicrystals*.

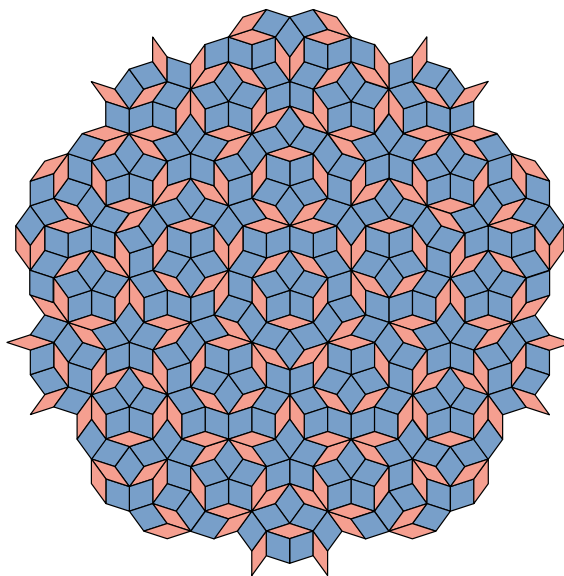


Figure 1.4: The Penrose tiling is a quasicrystalline pattern, as it is aperiodic, but features long range order. Source: Own modification of [88].

A quasicrystal is an aperiodic, but long range ordered arrangement of atoms such that its X-Ray diffraction pattern is—just as for conventional, translational invariant crystals—composed of Bragg peaks [12]. This turns out to be a very peculiar property, and in fact quasicrystals have long been deemed impossible [89]. It was only in 1984 that they were discovered by Shechtman et al. [90], for which he was rewarded with the 2011 Nobel prize in chemistry. An example for a quasicrystalline pattern is shown in Fig. 1.4.

Besides their very existence, which was indeed heavily disputed in the beginning (see, e.g., [89, 91, 92]), quasicrystals are also interesting due to a number of peculiar

properties. For one, many quasicrystalline alloys have a much (sometimes orders of magnitudes) lower electric conductivity than the metals they are composed of [93]. Due to this and other anomalies regarding the electric conductivity [94], it was suggested that quasicrystals fill a gap between metals and superconductors. Quasicrystals may further feature low friction, high hardness, difficult wetting of the surface, and corrosion resistance, most combinations of which are technologically interesting [79, 93]. They may further be brittle, which allows to produce ultra-fine chemically homogeneous powders that can be used in catalysis [93, 95, 96].

So far, more than one hundred quasicrystalline intermetallic systems have been found [97]. Quasicrystalline order, however, is not limited to metals, and indeed was found in fluid substrates and phyllotaxis [98] as well as soft matter (see [99, 100] and references therein). Moreover, quasicrystals were realized with cold atoms [101], and in the last years several more such realizations have been proposed [102–104].

When trying to understand and simulate the properties of quasicrystals (and other aperiodic systems), the absence of translational symmetry poses a serious problem. Namely, the powerful Bloch theorem—which is the standard tool for tight-binding computations of conventional, periodic crystals and which enables band structure calculations—cannot be applied to quasicrystals or other aperiodic systems. The good side of this problem, however, is that the quest for deriving efficient methods for simulating the (electronic) properties of aperiodic systems provides a fruitful playground for interdisciplinary research. This ranges from the application of topological methods such as K -theory and C^* algebras [105, 106] to tools such as spatial point pattern analysis and spectral graph theory [107]. Indeed, especially the latter work [107] acted as a trigger for our own research involving graph theory that we will discuss in Chapter 4.

Perhaps the prime model (sometimes also called the “fruit fly of quasiperiodic studies” [108]) of a one-dimensional quasicrystal is the so-called Fibonacci quasicrystal [93, 109]. It can be described by the tight-binding Hamiltonian of Eq. (1.7) as follows: In a first step, the on-site potential v is constrained to be binary, that is, it may take only two different values, v_A and v_B . Depending on the sequence of A 's and B 's, Eq. (1.7) may then describe different systems. The sequence $ABABABAB\dots$, for example, would correspond to a crystal. For a Fibonacci quasicrystal, the A 's and B 's are arranged according to the Fibonacci word, that is,

$$ABAABABAAB\dots \quad (1.8)$$

This word is constructed by repeatedly applying the inflation rule $A \rightarrow AB, B \rightarrow A$, starting with the first Fibonacci word $S_1 = A$. The first six words are thus

$$\begin{aligned} S_1 &= A \\ S_2 &= AB \\ S_3 &= ABA \\ S_4 &= ABAAB \\ S_5 &= ABAABABA \\ S_6 &= ABAABABAABAAB. \end{aligned}$$

A Fibonacci quasicrystal may be either infinite or finite. The latter case can, for example, be modeled by taking only the N -th generation Fibonacci word. That is, by taking a one-dimensional chain of length l_N , with the on-site potentials arranged according to the N -th Fibonacci word S_N , with l_N denoting the length of this word. For concreteness, a third-generation Fibonacci quasicrystal would thus be modeled by the Hamiltonian

$$\hat{H} = v_A |1\rangle \langle 1| + v_B |2\rangle \langle 2| + v_A |3\rangle \langle 3| + h \sum_{i=1}^2 \left(|i\rangle \langle i+1| + |i+1\rangle \langle i| \right). \quad (1.9)$$

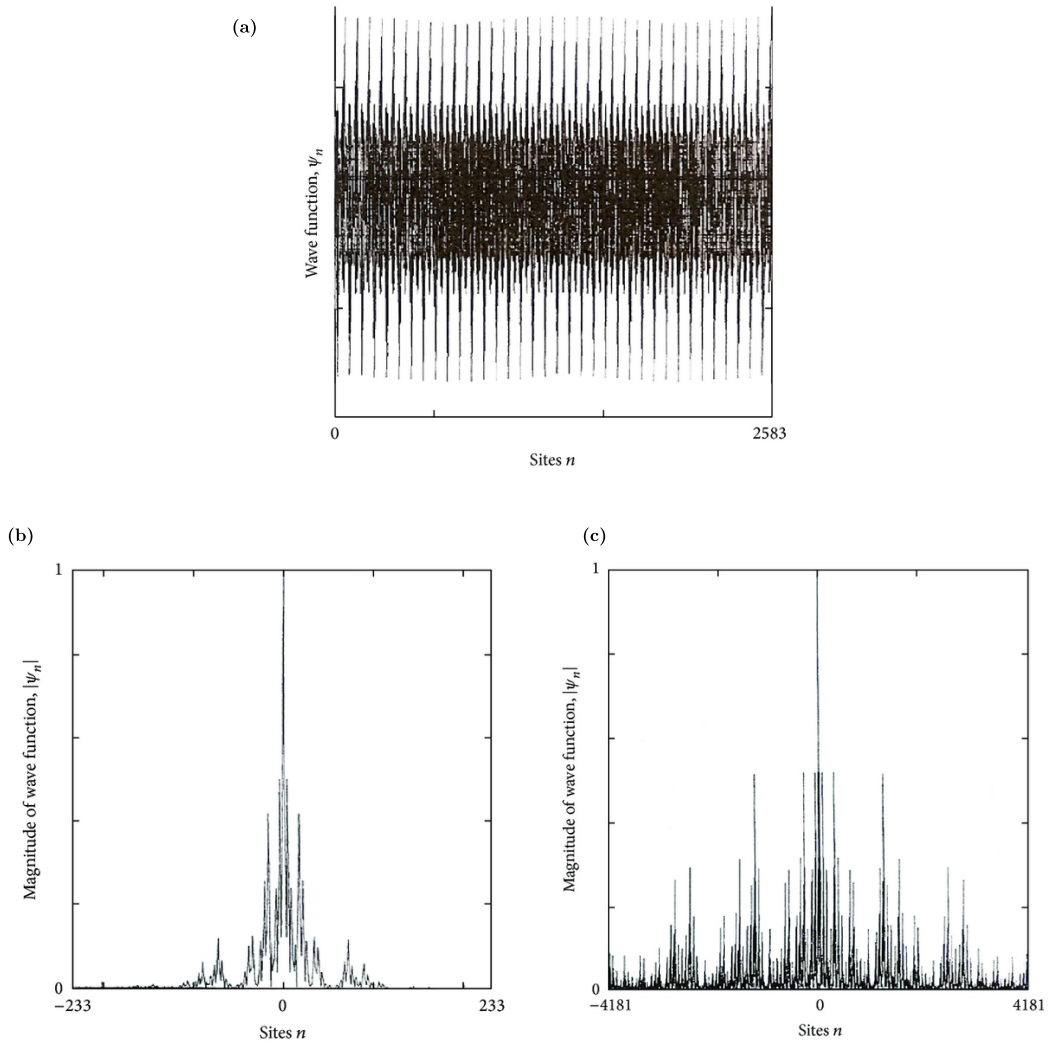


Figure 1.5: Representative images showing the wave function amplitude of **(a)** an extended Bloch state, **(b)** an exponentially localized state, and **(c)** a critical state. Source: [110].

The treatment of the eigenstates of the Hamiltonian Eq. (1.7) with v_A, v_B ordered in a Fibonacci manner, has a long tradition. For weak coupling, this Hamiltonian can be treated perturbatively⁵, and a common method for the investigation of its

⁵ Here, the unperturbed Hamiltonian would refer to one where the sites are not coupled at all to each other.

spectral properties is the so-called renormalization group method. This method was first used for this purpose by Niu and Nori in [111]. By employing perturbation theory up to the first few orders, it achieves a recurrent decimation of the original chain into smaller and smaller chains, each of which are again of Fibonacci nature. This method, which is exact in the limit of weak coupling h , is especially well suited for the treatment of infinite chains, and has been used to show that the eigenvalue spectrum of an infinite Fibonacci chain is self-similar. The eigenstates of a Fibonacci chain also behave in an interesting way: While the Bloch states of a perfect crystal follow its translational symmetry, and are thus completely extended across the crystal, the eigenstates of a sufficiently strongly disordered crystal can be exponentially localized [72]; this is the famous *Anderson localization*⁶. The eigenstates of a Fibonacci chain, however, are neither Bloch-like nor exponentially localized; they are dubbed⁷ *critical* [110]. Figure 1.5 shows a graphical comparison of these three classes of eigenstates.

In a certain sense, the Fibonacci quasicrystal thus resides in-between the two extremes of perfectly periodic systems on the one side, and of completely disordered systems on the other side. It turns out that the space between these two extremes is vast, with the Fibonacci quasicrystal being just one out of many different possibilities. In photonics, this vast world of aperiodic order has been analyzed extensively in the past years; an overview over the field can be found in the book [118] and the review articles [12, 17, 119]. In particular, it was found that aperiodic photonic systems—manufactured, for example, in the form of dielectric multilayers or aperiodic photonic crystals (see [119] and references therein)—may have fascinating and technologically highly relevant properties such as anomalous transport [120] or fractal transmission spectra [121]. Apart from photonics, aperiodically ordered structures may also be implemented—in the form of superlattices manufactured, e.g., by molecular beam epitaxy [122, 123]—in electronics. In this context, aperiodic structures were proposed as devices for electronic filtering [124–126] or as tools for the enhancement of the Seebeck effect [127].

Besides the Fibonacci quasicrystal introduced above, another relevant one-dimensional aperiodic system is the Thue-Morse chain, where the on-site potentials v_A, v_B are ordered by the sequence

$$ABBABAABBAAB\dots \quad (1.10)$$

which can be constructed⁸ by the inflation rule $A \rightarrow AB, B \rightarrow BA$. Compared to the infinite Fibonacci chain, the eigenstates of the infinite Thue-Morse chain have been found to be more extended [128].

A common feature of both the Fibonacci and the Thue-Morse chain is the occurrence of quasi-bands, that is, clusters of eigenvalues [129]. Moreover, when investigating the case of *finite* chains, both of them may feature eigenstates which are spatially localized on one or both edges of the chain, and which energetically

⁶ The exciting field of Anderson localization is not at all the focus of this thesis, but the interested reader may find the reviews and books [112–117] on this topic useful.

⁷ A deeper review of the nature of eigenstates and a discussion of the term “critical” can be found in [110].

⁸ We note that this inflation rule is only slightly different from the inflation rule $A \rightarrow AB, B \rightarrow A$ of the Fibonacci quasicrystal.

lie in-between the quasi-bands; we call these gap-edge⁹ states. The emergence of states that are localized on the edge is a well-known phenomenon in finite periodic systems¹⁰. They are here also known as surface states [130], and their appearance depends on where exactly in the unit cell the edge is placed, that is, where exactly in the unit cell the system is cut off [131]. In an aperiodic system, however, there are no unit cells, and this poses the question of how the emergence of edge states might be explained.

Our work [MR2]—which was further motivated by the fact that binary aperiodic chains are full of local symmetries [132]—takes a first step into answering this question. In this work, we develop a framework which explains, in a unifying way, the emergence of quasi bands and gap-edge states in finite aperiodic chains by introducing the concept of *local resonators*. A local resonator is a—usually symmetric—substructure which can confine a wave for sufficiently low coupling strength h . A very simple example is the symmetric three-site resonator BAB , with A playing the role of the “resonator cavity” while the two outer B -sites play the role of the “resonator walls”. This distinction into the cavity itself and the resonator walls can be emphasized by putting vertical bars between these functional units, yielding $B|A|B$.

When an eigenstate Ψ of the chain is localized on a local resonator¹¹, then it locally (closely) resembles an eigenmode ϕ of this resonator substructure. As a consequence, the energy E of the eigenstate Ψ has to be approximately equal to the energy of ϕ , that is, to the energy of the corresponding eigenmode of this resonator [133]. A common characteristic of the three classes of deterministic aperiodic chains that we investigated is that most resonators occur many times within a chain. A simple example would be the resonator $B|AA|B$, which occurs already three times in the sixth-generation Fibonacci chain $ABAABABAABAAB$. In such a case of a repeated resonator, any eigenstate that localizes on one of these identical resonators is energetically allowed also to localize on the others¹². Moreover, there may be more than one eigenstate that is localized on these resonators. By the above reasoning, the energy of all of these eigenstates lie closely together. As a result, a quasi band emerges.

In the resonator picture, the emergence of gap-edge states can be easily understood, with the line of argument here being as follows. To start, we note that the resonators lying at the edge of the chain are structurally different from those within its bulk, the difference being that one of the two “resonator walls” that a bulk resonator possesses are absent in an edge-resonator. For example, in a Fibonacci chain $ABAABABA\dots$, the left-most resonator is $|A|B$, representing a truncated version of the resonator $B|A|B$ occurring within the bulk of the chain. Now, since they structurally differ from other resonators of the chain, edge resonators usually have an energy spectrum that has no overlap with that of other resonators. Thus,

⁹ We note that these gap-edge states are not necessarily *topologically protected* edge states; the investigation of such topological states by our local resonator method explained below would be an interesting topic of future research.

¹⁰ These can be obtained by cutting a finite piece out of an infinitely extended crystal.

¹¹ In the sense of having a high amplitude on this resonator while having lowing amplitudes in the immediate environment left and right of this resonator.

¹² Moreover, if two non-identical resonators R_1 and R_2 in the chain share some eigenenergies, then an eigenstate of the chain may simultaneously localize on both of them.

an eigenmode of such an edge resonators lies energetically not within a quasi band, but in a gap between two of them¹³. Thus, an eigenstate whose energy matches that of an edge-resonator usually finds no energetically suitable resonators within the bulk of the chain, and thus is localized on the edge. In other words, this eigenstate is a gap-edge state. However, if a subset or even all energy levels of an edge resonator match that of bulk-resonators, the number of gap-edge states is reduced or even vanishes. We demonstrate the validity of this logic in finite Fibonacci and Thue-Morse chains by applying suitable modifications of the edge-resonators that reduce the number of gap-edge states. In particular, we demonstrate the case of an edge-modified Fibonacci chain which does not possess any gap-edge states at all.

On a technical side, we show that the principles behind our local resonator framework can be justified through higher-order degenerate perturbation theory [134]. From this perturbation-theoretical viewpoint, the framework is expected to be applicable for sufficiently small coupling strength h , and the finite Fibonacci and Thue-Morse chains that we investigated confirm this reasoning. Interestingly, for these chains, the predictions of the framework—in particular, the predicted removal of gap-edge states through energy matching—seem to remain correct even in the case of intermediate coupling strength h . To further investigate this observation, we also apply our framework to a chain whose binary on-site potentials are modulated by the so-called Rudin-Shapiro [135] sequence. Compared to the case of Fibonacci and Thue Morse, the Rudin-Shapiro sequence much more resembles a random chain¹⁴. It thus possesses many more different resonator types, and perhaps as the result of this, our framework is applicable to the Rudin-Shapiro chain only at low coupling strength.

As written above, binary chains are imbued by local symmetries, and our developed local resonator framework thus marks an important connection between the locally symmetric structure of these chains and their energy spectra. Apart from this spectral viewpoint, we have also observed that—in the weak coupling regime—most eigenstates of the Fibonacci, Thue-Morse, and Rudin-Shapiro chain are indeed highly locally symmetric in the sense that the amplitude distribution of these eigenstates follows the local symmetries of the underlying potential landscape (that is, the sequence of A 's and B 's). By relying on higher-order degenerate perturbation theory, we give a mathematical justification for this finding. Moreover, by explicitly analyzing the first few orders, we make several statements on the exact nature of this connection between the local symmetries of eigenstates and that of the potential landscape.

¹³ In principle it may also lie above the last or below the first quasi band, but these cases do not appear in the systems that we investigated.

¹⁴ To be precise, the Fourier spectrum of the Rudin-Shapiro is absolutely continuous, and it shares this trait with a completely random sequence. On the other hand, the Fourier spectra of the Fibonacci and Thue-Morse sequence are point-like and singular continuous, respectively. More information on this spectral classification of aperiodic sequences can be found, for example, in [12].

COMPACT LOCALIZED STATES AND FLAT BANDS

At the end of the last chapter, we took a glance at the fascinating interconnection of local symmetries, aperiodic order, and localization properties. This chapter is dedicated to another interesting effect which is tightly connected to both local symmetries and localization, namely, the phenomenon of so-called compact localized states (CLSs).

In the following, we will first introduce the concept of CLSs and review some of their fascinating properties. We will then outline [MR3] that connects local symmetries to CLSs, and [MR4] which investigates CLSs in systems of dipolar nanoparticles.

2.1 COMPACT LOCALIZATION

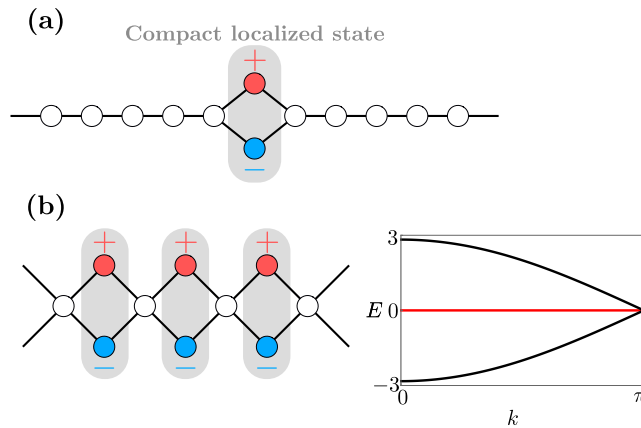


Figure 2.1: Different tight-binding systems, with circles corresponding to sites. All circles have the same on-site potential of zero. The sites are connected by solid lines that correspond to couplings with a strength of unity. (a) A symmetric dimer defect leads to compact localization in an infinitely extended chain, with the compact localized state being an anti-symmetric excitation of the two dimer sites. (b) A one-dimensional lattice built from regularly placed dimers features macroscopic degeneracy, so that a flat band (see the band structure plot of $E(k)$ on the right-hand side, with E and k denoting the energy and crystal momentum, respectively) emerges.

In layman’s terms, a CLS could be best characterized as a “perfectly localized” eigenstate of a physical system (modeled, for instance, by a tight-binding model). Mathematically speaking, a CLS is an eigenstate with a compact support, that is, it vanishes everywhere outside of a (usually small) portion of the system. Although—as we shall see later on—such states can exist in a broad range of systems, it is easiest to introduce them by means of a tight-binding setup described by

$$\hat{H} = \sum_i v_i |i\rangle \langle i| + \sum_{\langle i,j \rangle} h_{ij} |i\rangle \langle j|, \quad (2.1)$$

where the sum goes over neighboring—that is, connected—sites, and with all quantities as in Eq. (1.7). For simplicity, let us now assume that all on-site potentials vanish, $v_i = 0$, and also that all couplings are of identical strength h . In such a very simple model, compact localization is introduced solely through a suitable geometry, and an example for such a geometry is depicted in Fig. 2.1 (a). Here, a defect consisting of two sites—a dimer—is placed within a one-dimensional chain. Since all couplings have the same strength, this dimer is coupled symmetrically to its two adjacent sites. In this setup, a CLS is then simply an anti-symmetric excitation of the two dimer sites, with vanishing amplitude on all other sites. Indeed, this excitation of only two sites has compact support, and it is also an *eigenstate* of the underlying Hamiltonian \hat{H} , thereby fulfilling the conditions for being a CLS. We note that, since it is an eigenstate, up to a phase $\exp(-iE_{CLS}t/\hbar)$ (with E_{CLS} denoting the CLS' energy), this excitation will not change in time. This implies, in particular, that it will stay localized on the very same two sites forever. The reason for this counter intuitive behavior—normally, one would expect an excitation in a small part of a system to “leak out” over time—is caused by destructive interference: The sum of the tunneling/leaking amplitudes of the CLS to either of the two neighboring sites vanishes.

We stress that compact localization is fundamentally different from the disorder-induced Anderson localization mentioned in Chapter 1, since CLSs can exist even in perfectly periodic systems, as we shall discuss in Section 2.2.

Owing to their general nature and since they essentially only depend on destructive interference, CLSs¹ have been realized in a large variety of systems. Among others, these include evanescently coupled waveguides [64, 136, 137], terahertz spoof plasmons [138, 139], tailored atomic structures on substrates [140, 141], or cold atom setups [142–145]. Apart from these experiments, theoretical studies and/or proposals exist for many other platforms, including metamaterials [146], optomechanical systems [147], photonic crystals [148], electrical circuits [149, 150], setups of electromagnetic scatterers [MR4], and Rydberg systems [151, 152].

For several reasons, the completely localized nature of CLSs renders them quite interesting. For one, CLSs may be used for data transmission avoiding crosstalk in highly miniaturized optical waveguide systems, where the light modes of individual fibers couple to each other [61–64]. On another level, a particularly interesting feature of CLSs is their robustness against perturbations: Since they vanish *exactly* outside their localization domain \mathcal{D} , it can be easily shown that they are not affected at all by any changes to the system outside of \mathcal{D} [MR5]. For our introductory example of Fig. 2.1, one could couple an arbitrarily large system to either end of the one-dimensional chain, but the dimer-CLS would not be affected at all. As we shall see in Chapter 3, this robustness renders them ideal candidates for the storage of information, with a qubit being a prime example. Lastly, CLSs may also be used to realize so-called bound states in a scattering continuum [153], as was demonstrated, e.g., with evanescently coupled waveguides [154, 155].

¹ Sometimes in the context of flat bands which we will discuss below.

2.2 FLAT BANDS

Apart from the above mentioned properties, CLSs are also relevant due to a closely related phenomenon, namely, perfectly *flat bands*. That is, energy bands of tight-binding lattices that fulfill $E(\mathbf{k}) = \text{constant}$ for all wave vectors \mathbf{k} . In such a flat band, the group velocity $\nabla_{\mathbf{k}}E(\mathbf{k})$ vanishes, so that transport is strongly suppressed. An intuitive picture of how compact localized states are related to flat bands is shown in Fig. 2.1 (b): When each unit cell of a lattice features a CLS at identical energy E_{CLS} , then the lattice Hamiltonian will have a macroscopic degeneracy at this very energy. Thus, a flat band emerges. On the other hand, if a lattice possesses a flat band at energy E , one could superpose the corresponding highly degenerate Bloch states to obtain a set of CLSs [156]. This means that one can consider a CLS as an “*extreme limit of the Wannier function whose amplitude is finite only in a bounded region in real space, and completely vanishes outside of it*” [156].

Flat bands are interesting for several reasons. Firstly, since the density of states at the flat band energy diverges, any disorder or non-linear effects may qualitatively change the transport properties (see for example [81, 157] and references therein). Other interesting effects can emerge when one includes interactions: Firstly, ferromagnetism can emerge² in several lattices whose single-electron Hamiltonian features a flat band [159] (for reviews on this area, see, e.g., [158, 160]). Secondly, if one considers the case of flat bands formed for non-interacting particles, then even arbitrarily weak interactions between them may act non-perturbatively. This can lead to boson pair formation [161–163] and phases such as the Haldane insulator [164] or Wigner crystals [165]. Interestingly, it has been shown that dispersive (that is, non-flat) bands of a system without interactions can be made completely flat by introducing interactions [166].

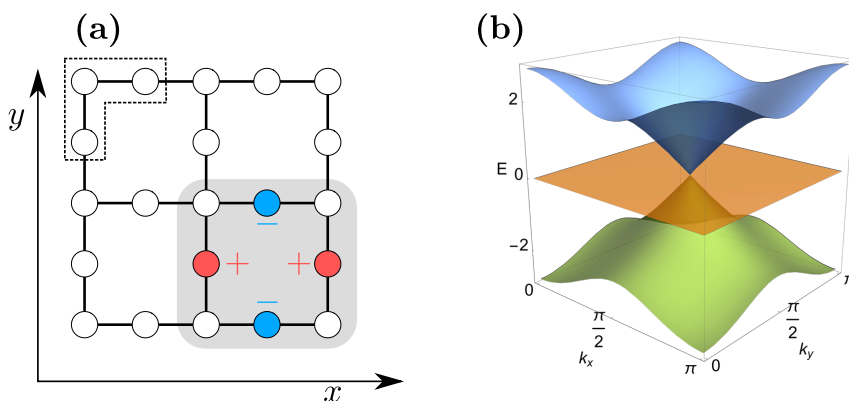


Figure 2.2: (a) The Lieb lattice [with its three-site unit cell marked by a dotted line] hosts CLSs that are localized on a plaquette of four sites. One of these CLSs is depicted. (b) The band structure of the Lieb lattice features a Dirac cone and a flat band.

Historically, perhaps the first notion of flat bands and, as he called the corresponding eigenstates, “strictly localized states” were made by Sutherland in 1986

² A very basic explanation can be given in terms of Stoner’s criterion, which states that the Bose-Hubbard model may feature ferromagnetism when $UD_F > 1$, where U is the interaction strength, and D_F denotes the density of states at the Fermi level [158]. Since a flat band features an infinite density of states, we see that flat band systems may easily fulfill Stoner’s criterion.

for a dice lattice [167]. Further works on systems with flat bands soon followed within the scope of ferromagnetism [159, 168–170]. Among these was also a seminal paper by Lieb in 1989 [171] in which he analyzed the Hubbard model and showed that a certain bipartite lattice features ferromagnetism at half filling. Today, this lattice is simply called the “Lieb lattice”. Due to its simple structure, and probably also due to the fact that its band structure features a Dirac cone [64, 172] [see Fig. 2.2 (b)], it soon became quite popular. In fact, most of the above mentioned experiments on CLSs and flat bands realized a Lieb lattice [64, 139–141, 144, 145, 173]. The Lieb lattice is furthermore also of importance, as the CuO_2 planes in high-temperature cuprate superconductors possess a Lieb lattice structure, and it has been conjectured that flat bands might play a role in their high critical temperature [81, 174–178].

2.2.1 Flat band generators

As indicated above, every flat band is in fact caused by the presence of CLSs [156]. CLSs, in turn, are caused by the generic phenomenon of destructive interference, which can be realized in a large variety of lattices. It should therefore not surprise that, over the years, a number of very different methods for designing tight-binding lattices featuring CLSs and flat bands have been suggested. These include graph-theoretical tools [MR8, 169], the use of symmetry principles such as chirality [179] and local symmetry [MR3], fractal structures [180, 181], repetition of oligomers [182] and of mini-arrays [183], the use of Fano resonances [184], or so-called Origami rules [185]. Each of these construction principles harnesses a particular concept (such as symmetry) for the creation of CLSs and flat bands. While being very intuitive, none of them allows for the construction of all possible flat band lattices. Flat band generators, on the other hand, aim on constructing a very large class of flat band systems by relying on much more general (but less intuitive) overarching principles such as the solution of inverse eigenvalue problems [186]. The development of such generators for arbitrary lattices is still an ongoing topic of research. So far, a universal flat band generator capable of constructing all possible hermitian one-dimensional lattices with a single flat band has been presented [186, 187]. In very recent works, this generator was generalized to two-dimensional lattices [188] and to non-hermitian systems [189].

In the next section, we will continue the treatment of CLS-generating mechanisms by discussing our own contribution to this problem.

2.3 OUTLINE: COMPACT LOCALIZED STATES AND FLAT BANDS FROM LOCAL SYMMETRY PARTITIONING

As written above, compact localization and flat bands are induced by destructive interference, which in turn depends on a suitable interplay between the geometry of the underlying tight-binding system and its coupling parameters. Interestingly, and relating to the topic of this thesis, many flat band lattices feature local symmetries [184]. This observation led us to the question of whether a connection between local symmetries and CLSs (which, in a lattice, induce flat bands) can be made. In [MR3], we treat tight-binding systems and partly answer this question in the

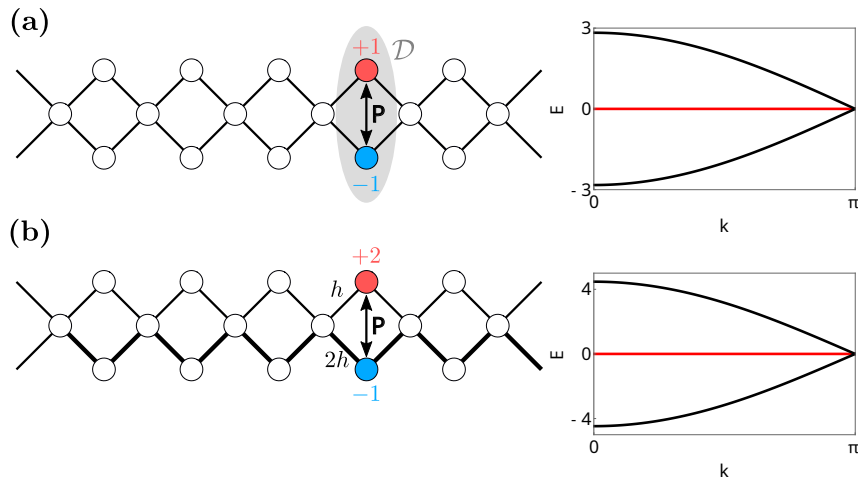


Figure 2.3: Left: Structure of the chain and one of the many CLSs hosted by this chain. Right: band structure of the chain. **(a)** The diamond chain. It is invariant under the operation P that permutes two sites within a dimer. **(b)** A modified diamond chain. It is now no longer invariant under the operation P , but nevertheless features CLSs which can be explained by the non-equitable partition theorem (nEPT).

affirmative by applying and generalizing a recently developed tool from graph theory. This tool is the so-called equitable partition theorem (EPT) [190–192], and it relies on what we call *commuting local symmetries* that we will explain now. To this end, let us look at Fig. 2.3 (a), which shows again the so-called diamond chain we already encountered in Fig. 2.1 (b). As can be easily seen, the dimer-subsystem \mathcal{D} that consists of the blue and red site is locally symmetric: If we isolate it from the remainder of the lattice, it is invariant under the reflection operation P [indicated by arrows in Fig. 2.3 (a)]. What makes this symmetry P special is the following. Even when we do not disconnect the dimer from the remainder of the lattice, the symmetry P remains unbroken. That is, the lattice is invariant under the operation that performs a local reflection on the single dimer \mathcal{D} , while acting as the identity (that is, not doing any operation at all) on the remaining sites. In other words, the Hamiltonian describing the lattice commutes with the local reflection symmetry P . As a result of this *commuting local symmetry*, the eigenstates of the underlying Hamiltonian can be chosen to have definite parity with respect to the local reflection operation P , with the negative parity eigenstate corresponding to the depicted CLS. Now, since each unit cell features such a commuting local symmetry, there exists one such CLS per unit cell, and since all these CLSs have the same eigenenergy, this explains the chain’s flat band.

At this point, we note that the lattice shown in Fig. 2.3 (a) also features a global reflection symmetry, corresponding to the case where P is simultaneously performed in each unit cell. While this symmetry would indeed lead to the emergence of negative parity eigenstates which vanish on the sites lying on the axis of reflection, these states are not necessarily compactly localized. That is, they do not necessarily “live” only on a small number of unit cells. Thus, this global reflection symmetry acting on all unit cells cannot explain the emergence of compact localization, and thus can also not explain the flat band of this lattice.

In summary, we have seen above that the commuting local reflection symmetry P leads to the formation of CLSs in the diamond lattice of Fig. 2.3 (a). The EPT allows to formalize this observation through a simple algorithm for constructing the corresponding CLSs. Importantly, the EPT is not limited to a simple reflection symmetry as in Fig. 2.3 (a), but on the contrary can be applied to any commuting local symmetry that corresponds to a permutation of sites (in the example above, P corresponds to the permutation of the two dimer sites). Thus, the EPT can be applied to cases that are much more complex than the one of Fig. 2.3 (a). An important aspect of the EPT is that it allows to decompose the original Hamiltonian \hat{H} into smaller Hamiltonians \hat{H}_i , whose collective eigenvalue spectrum³ equals the eigenvalue spectrum of H .

Apart from the EPT, which can be used for local symmetries that commute with the underlying Hamiltonian, we further apply recent insights from graph theory [193] to generalize the EPT. We call this generalized version the non-equitable partition theorem (nEPT). The nEPT can be applied when the system features a local *non-commuting* permutation symmetry, provided that this symmetry fulfills two conditions. Namely, the subsystems that are permuted with each other by the symmetry operation must (i) not be coupled to each other and (ii) must be coupled to the remainder of the setup in a certain asymmetric, scaled manner. An example of a non-commuting local symmetry that fulfills the criteria (i) and (ii) is depicted in Fig. 2.3 (b). Here, the same symmetric dimer as in (a) is connected to the remainder of the chain, though now in an asymmetric manner: The upper dimer-site is connected via couplings of strength h , while the lower one is connected via couplings of strength $2h$. As a result of this asymmetry, the local reflection operation P (which permutes the two dimer sites) does not commute with the underlying Hamiltonian⁴. However, the dimer still features a CLS, whose amplitudes $+2$ and -1 are now asymmetric. Again, and just as the EPT does for commuting local symmetries, the nEPT provides a simple algorithm for the construction of such CLSs and also provides a local symmetry induced decomposition of the underlying Hamiltonian. We stress that the examples shown in Fig. 2.3 are just the simplest possible ones, and both the EPT and the nEPT can be applied to much more complex systems as well. On the other hand, we emphasize that not all flat band systems can be related to local symmetries that can be described by the (n)EPT. An example of such a system is the Lieb lattice depicted in Fig. 2.2.

Apart from using the (n)EPT to systematically understand the origin of CLSs in a range of different systems, we also use the underlying (non-)commuting local symmetries to generate systems featuring CLSs and flat bands. In particular, we provide a method to equip a lattice with a single CLS by dimerizing a site in

³ To be precise, if we denote the eigenvalues (including multiplicities) of \hat{H} by the multiset $\sigma(\hat{H})$, then $\sigma(\hat{H}) = \sigma(\hat{H}_1) + \dots + \sigma(\hat{H}_n)$ where $+$ denotes the multiset sum and n denotes the number of smaller Hamiltonians into which \hat{H} is decomposed.

⁴ An intuitive way to see this is as follows: Think of the two sites within the dimer as masses, each of them attached to the remainder of the lattice via two different springs (corresponding to the couplings of strength h and $2h$). The reflection operation P corresponds to exchanging the two masses, but the respective springs stay attached to them during this exchange. Therefore, after the exchange, the upper spring corresponds to a coupling of $2h$ (instead of h before the exchange). In summary, the system looks different before and after the exchange, and thus it is not invariant under the operation P .

only one of the lattice's unit cells. Though this dimerization breaks the lattice's translational invariance, we show that one can fine-tune the coupling and on-site parameter values of the dimer such that (i) one can define a band structure even in this aperiodic lattice and (ii) the dimerization does not alter the band structure of the system. That is, the band structure is the same before and after the dimerization, but the system additionally features a dimer-CLS whose energy can be freely tuned. In particular it may energetically lie within a dispersive band with its spatially extended Bloch states. In this case, the CLS represents a so-called bound state in the continuum. Such states were originally proposed in a seminal paper by von Neumann and Wigner in 1929 in the context of quantum mechanics [153], and since then have been realized in a number of different wave systems. Two excellent reviews which also emphasize the numerous applications of bound states in the continuum are [154, 194].

2.4 OUTLINE: COMPACT LOCALIZED STATES OF OPEN SCATTERING MEDIA: A GRAPH DECOMPOSITION APPROACH FOR AN AB INITIO DESIGN

In the introduction to this chapter, we wrote that compact localization and flat bands can be easily understood in terms of tight-binding systems. Naturally, these feature short-range interactions, that is, a given site is often only coupled to its next-neighbors or next-nearest-neighbors. Destructive interference and CLSs, however, can in principle occur even in systems with long range coupling, as we demonstrate in [MR4]. In this work, we consider electromagnetic scattering of a setup of N identical scatterers. We assume these to be much smaller than the wavelength of the incoming radiation, so that each scatterer can be described by a point-like dipole characterized by a Breit-Wigner resonance at frequency ω_0 and resonant width Γ_0 . To analyze the properties of this open system, we rely on the so-called dyadic Green's matrix (GM). The GM describes the electromagnetic coupling between the dipoles. For N such dipoles, the GM is of dimension $3N$, and its 3×3 blocks G_{ij} are given by

$$G_{ij} = i (\delta_{ij} + \tilde{G}_{ij}) \quad (2.2)$$

with the indices $i, j \in 1, \dots, N$ corresponding to the N scatterers, and with

$$\begin{aligned} \tilde{G}_{ij} = & \frac{3}{2} (1 - \delta_{ij}) \frac{e^{ik_0 r_{ij}}}{ik_0 r_{ij}} \left\{ \left[\mathbf{U} - \hat{\mathbf{r}}_{ij} \otimes \hat{\mathbf{r}}_{ij} \right] \right. \\ & \left. - \left(\mathbf{U} - 3\hat{\mathbf{r}}_{ij} \otimes \hat{\mathbf{r}}_{ij} \right) \left[\frac{1}{(k_0 r_{ij})^2} + \frac{1}{ik_0 r_{ij}} \right] \right\} \end{aligned} \quad (2.3)$$

where $\delta_{i,j}$ is the Kronecker delta and \otimes denotes the dyadic (sometimes called outer) product⁵. k_0 is the wave vector of light, \mathbf{U} is the 3×3 identity matrix, $\hat{\mathbf{r}}_{ij}$ is the

⁵ The dyadic product $\mathbf{a} \otimes \mathbf{b}$ of two 3-dimensional vectors is given by the square 3×3 matrix

$$\mathbf{a} \otimes \mathbf{b} = \begin{pmatrix} a_x b_x & a_x b_y & a_x b_z \\ a_y b_x & a_y b_y & a_y b_z \\ a_z b_x & a_z b_y & a_z b_z \end{pmatrix},$$

with the subscripts x, y, z denoting the components of the two vectors \mathbf{a} and \mathbf{b} .

unit vector pointing from the i -th and j -th scatterer, with r_{ij} denoting the distance between these two scatterers. The eigenvectors of G describe the quasi modes—that is, scattering resonances [195, 196]—of the setup, with their normalized frequency ω_n and decay rate Γ_n , respectively, given by

$$\Re[\Lambda_n] = (\omega_0 - \omega_n)/\Gamma_0 \quad (2.4)$$

$$\Im[\Lambda_n] = \Gamma_n/\Gamma_0 \quad (2.5)$$

where Λ_n is the complex eigenvalue of the n -th quasi mode, and \Re and \Im denoting the real and imaginary part, respectively.

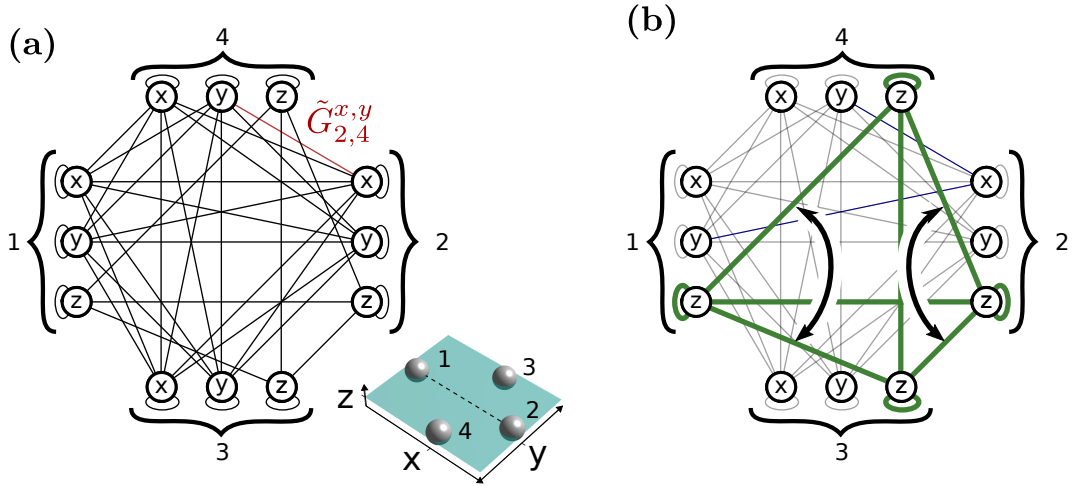


Figure 2.4: **(a)** Bottom right: A planar setup of four scatterers which is reflection symmetric about the dotted line. Due to this symmetry, the setup features a CLS that has zero amplitudes on the scatterers 1 and 2 which lie on the dotted line. Upper left: A graphical depiction of the GM describing the setup. Each line corresponds to a non-vanishing matrix element, with loops (small rings connecting a vertex to itself) representing diagonal matrix elements. Since the GM describes the coupling of dipoles through a *vectorial* electromagnetic field, each scatterer corresponds to three vertices x, y, z . Thus, for N scatterers, the GM has dimension $3N$. **(b)** The reflection symmetry of the setup in the bottom right of (a) leads to a local reflection symmetry (indicated by black arrows) in the GM; see text for details.

To help the reader drawing a connection between the GM and the tight-binding models treated so far, in Fig. 2.4 (a) we graphically depict the structure of the GM of a simple setup of $N = 4$ scatterers. In a tight-binding language, each circle/vertex could be interpreted as one “site”. We note that, since each scatterer has three degrees of freedom (corresponding to field components along the three coordinate axes), the GM is of size $3N \times 3N$, and there are thus three sites for each dipole. Each line in Fig. 2.4 (a) corresponds to a non-vanishing matrix element of the complex-valued symmetric (and thus non-hermitian) matrix G , and as one can see, each scatterer is coupled to all others⁶. This statement holds also for larger systems:

⁶ Though not all degrees of freedom—that is, dipole components—of one scatterer are connected to all degrees of freedom of any other scatterer.

Two dipoles $i \neq j$ are always coupled to each other through the GM, even if they are placed far away from each other. We thus see that the GM describes a discrete, long range coupled system. Since this coupling is of electromagnetic nature, we are dealing with a wave phenomenon which allows for destructive interference. In this respect, we define a CLS as an eigenvector of the GM which “lives” (that is, has non-vanishing entries) *only on some of the dipoles*. In other words, a CLS describes a perfectly localized quasi mode—that is, scattering resonance—of the scatterer array. We note though that, contrary to eigenstates of a closed system, this quasi mode is leaky and thus has a finite life time determined by its decay rate Γ_{CLS} .

Let us now briefly comment more on the GM method. Compared to full electromagnetic computations, which especially in three dimensions can be prohibitively expensive [197], an analysis of the system by diagonalizing the GM is much less demanding in terms of computational effort. On the other hand, and since it takes into account all scattering orders [107], the GM is a very good approximation for scattering from arrays of dielectric or metallic particles whose size is much smaller than the wavelength [198]. Moreover, the fact that the GM does not take into account the specific properties of materials makes it an ideal candidate to investigate the impact of the geometry of the setup on its scattering properties. For this reason, and connecting to Section 1.3, the Green’s matrix method was used to analyze a number of aperiodically ordered scatterer arrangements [MR11, 107, 199–201]. Moreover, the GM is also an excellent tool for the study of random systems such as atomic clouds [202, 203] or disordered photonic crystals formed by ultra cold atoms [204–206]. We note that the GM can also be extended to incorporate the effects of electric [207] or magnetic [208] fields, or to incorporate higher-order multipolar resonances beyond the simple electric dipole framework by means of the so-called electric and magnetic coupled dipole approximation, where each particle is characterized by an electric and a magnetic dipole [209–211]. We refer the reader interested in more details about the GM method to the works [107, 212].

Let us now briefly discuss the realization of a CLS as proposed in our work [MR4]. Here, we arrange the scatterers in a plane [an example of such an arrangement is shown in Fig. 2.4 (a)] such that the setup is reflection symmetric with respect to a line that lies in this plane. For the simplest kind of CLS, we then let all but two scatterers lie on this line, with the remaining two scatterers being symmetrically displaced from it. Figure 2.4 (a) shows such a setup for a total number of $N = 4$ scatterers, with scatterers 3 and 4 being the displaced ones and with the axis of reflection depicted by a dashed line. As can be easily shown, the global reflection symmetry of the scatterer arrangement *corresponds to a local reflection symmetry* in the corresponding Green’s matrix. In Fig. 2.4 (b), this reflection symmetry is indicated by two black arrows. It consists of exchanging the z -degrees of freedom of the dipoles 3 and 4, while acting as the identity on all other degrees of freedom. This local reflection symmetry commutes with the GM, and thus we can apply the equitable partition theorem which we have used previously in [MR3]. In particular, this theorem predicts the presence of a CLS which vanishes on all scatterers lying on the reflection axis. The theorem further allows to derive analytical expressions for the CLS’ eigenvalue which then, by Eqs. (2.4) and (2.5), give the CLS’ resonance frequency ω_{CLS} as well as its decay rate Γ_{CLS} . Importantly, and due to the reflection symmetry of the setup, ω_{CLS} and Γ_{CLS} are completely independent of how (for

example, in a periodic or random manner) the scatterers on the reflection line are placed.

Having demonstrated compact localization in a long range coupling system, we end our work [MR4] with an analysis of the CLS decay rate Γ_{CLS} . In particular, we investigate the impact of changing the separation d between the two displaced scatterers while keeping the reflection symmetry. It is found that Γ_{CLS} becomes smaller for small d . In particular, Γ_{CLS} vanishes for the (unrealistic) case where $d = 0$, that is, where both scatterers are placed onto each other. In this case, the CLS would thus have an infinite lifetime and would resemble a bound state in the scattering continuum.

IN the previous chapter, we have introduced the topic of compact localized states and investigated the role of local symmetries for this phenomenon. CLSs and local symmetries will also be the focus of this chapter, though we will now be interested in harnessing the favorable properties of compact localization. To this end, let us first recapitulate these properties. A defining property of CLSs is their compact (and usually small) domain of localization, which in the extreme case of a dimer CLS comprises only two sites. Compared to other, more extended, states, the preparation of such a CLS is therefore easier in that only a small number of sites have to be excited. Now, since a CLS is an eigenstate of the underlying Hamiltonian \hat{H} , such an excitation will be stable in time, that is, it will stay localized forever provided that \hat{H} does not change in time. But even if \hat{H} is time-dependent, a CLS is most likely not affected: Thanks to the favorable properties of compact localization, a CLS is only affected by changes of the Hamiltonian that take place within its domain of localization.

From the above, it is clear that CLSs are ideal candidates for the stable storage of an excitation pattern within a small part of a given system. This ability is of relevance¹ in the field of quantum information, where the excitation pattern would correspond to a qubit² in a quantum computer. In any quantum-computing application, however, the ability to store information is not sufficient; it also needs to be *transferred* across the device. Although we will not dive into the vast field of quantum computing, we will nevertheless use it as a motivation to explore different mechanisms for the transfer of CLSs. Moreover, we will use this field also as an inspiration by taking several state transfer techniques that were developed in the context of quantum computing and apply them in a slightly modified form to the transfer of CLSs.

In the following, we will first give a brief introduction to the two concepts of so-called perfect and pretty good state transfer. We will then present our first work [MR5] that adapts the concept of perfect state transfer (PST) to CLSs. The second work [MR6] deals with the more realistic scenario of pretty good state transfer (PGST) and relies on the more advanced concept of so-called latent symmetries, which will be the subject of Chapter 4. In order to allow for an easy comprehension of the material, we will outline this second work [MR6] only after the corresponding foundations are laid, and thus postpone its outline to Chapter 4.

¹ There could be other applications of this as well. In a spring-mass system, for example, it could be of interest to store energy in localized excitations (oscillations) of a very small number of masses without exciting the remainder of the system.

² There are different methods for encoding a qubit into CLSs, but the most intuitive would be to use two orthogonal CLSs $|\Psi_1\rangle$ and $|\Psi_2\rangle$ such that a qubit $\alpha|0\rangle + \beta|1\rangle$ could be realized as

$$\alpha|\Psi_1\rangle + \beta|\Psi_2\rangle.$$

3.1 PERFECT AND PRETTY GOOD TRANSFER

In 2003, Sougato Bose proposed to use spin chains as channels for the transfer of qubits [213]. In Fig. 3.1 (a), we visualize such a spin chain for the special case of $N = 4$ chains.

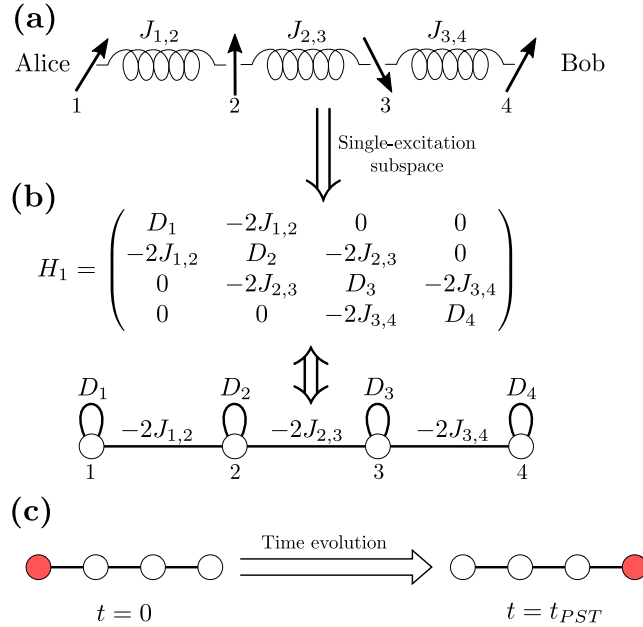


Figure 3.1: **(a)** A spin chain consisting of $N = 4$ spins that connects Alice to Bob (see text for details). The springs represent the couplings between the spins, as expressed in the Hamiltonian Eq. (3.5). **(b)** In the single-excitation subspace, the Heisenberg Hamiltonian describing the spin chain can be written as a tridiagonal, four-dimensional matrix H_1 . This matrix can be represented graphically by a chain of four sites, with loops corresponding to on-site potentials (diagonal matrix elements). **(c)** Perfect transfer of a qubit from Alice to Bob would, in this picture, correspond to the perfect transfer of a single-site excitation from the left end of the chain to the right end.

Each of the two communication parties Alice and Bob are positioned on one end of the chain, and Bose's proposal was as follows. Alice wants to send a qubit

$$\alpha |0\rangle + \beta |1\rangle \quad (3.1)$$

to Bob. To do so, she encodes the qubit into the spin chain connecting the two parties through the following procedure. At the very beginning, the spin chain is prepared in the state $|\downarrow \dots \downarrow\rangle$ where all spins point downwards. By changing the state of the first spin to be

$$\alpha |\downarrow\rangle + \beta |\uparrow\rangle \quad (3.2)$$

Alice then prepares³ the state

$$|\Psi(t=0)\rangle = |I\rangle = \alpha |\downarrow \dots \downarrow\rangle + \beta |\uparrow \downarrow \dots \downarrow\rangle, \quad (3.3)$$

³ For completeness, we note that Bose proposed a slightly different protocol. Namely, instead of changing the state of the first spin of the chain, Alice exchanges it with a suitably prepared spin. The resulting state of the chain is, again, Eq. (3.3).

so that her qubit is effectively encoded in the spin chain. The two parties then wait for a suitable time, during which the state Eq. (3.3) propagates by simple time evolution governed by the time-independent Hamiltonian \hat{H} of the spin chain⁴. Ideally, there exists a time $t = t_{PST}$ at which the state of the chain would read

$$|\Psi(t = t_{PST})\rangle = |F\rangle = \alpha |\downarrow \dots \downarrow\rangle + \beta |\downarrow \downarrow \dots \downarrow \uparrow\rangle. \quad (3.4)$$

In this case the reduced density matrices $\rho(t = 0) = \text{Tr}_{2,\dots,N} |\Psi(0)\rangle \langle \Psi(0)|$ and $\rho(t = t_{PST}) = \text{Tr}_{1,\dots,N-1} |\Psi(t_{PST})\rangle \langle \Psi(t_{PST})|$, obtained from the initial (final) state by tracing out the states of spins $2, \dots, N$ ($1, \dots, N-1$), would be equal. In other words, the qubit would be *perfectly transferred* from Alice to Bob.

Let us assume now that the spin chain is formed by N spins and is described by the Heisenberg Hamiltonian

$$\hat{H} = - \sum_{\langle i,j \rangle} J_{i,j} \vec{\sigma}^i \cdot \vec{\sigma}^j - \sum_{i=1}^N B_i \sigma_z^i, \quad (3.5)$$

where the first sum goes over neighboring spins, with $J_{i,j}$ denoting the coupling between the i -th and j -th spin, and with B_i denoting a local static magnetic field acting on the i -th spin. $\vec{\sigma}^i = (\sigma_x^i, \sigma_y^i, \sigma_z^i)$ denotes the vector formed by the Pauli matrices that act on the i -th spin. As can easily be shown, this Hamiltonian commutes with the operator $\sum_{i=1}^N \sigma_z^i$. Thus, the total spin is a conserved quantity. As a consequence, the state $|\Psi(t)\rangle$ stays in the single-excitation subspace spanned by the states

$$|\uparrow \downarrow \downarrow \dots \downarrow\rangle, |\downarrow \uparrow \downarrow \dots \downarrow\rangle, \dots, |\downarrow \downarrow \downarrow \dots \uparrow \downarrow\rangle, |\downarrow \downarrow \downarrow \dots \downarrow \uparrow\rangle, \quad (3.6)$$

in which exactly one spin points up and all others point down. In this basis, the restriction of the Hamiltonian \hat{H} to the single-excitation subspace can be written as an N -dimensional tridiagonal matrix

$$H_1 = \begin{pmatrix} D_1 & -2J_{1,2} & 0 & \dots & 0 \\ -2J_{1,2} & D_2 & -2J_{2,3} & \ddots & \vdots \\ 0 & -2J_{2,3} & \ddots & \ddots & 0 \\ \vdots & \ddots & \ddots & D_{N-1} & -2J_{N-1,N} \\ 0 & \dots & 0 & -2J_{N-1,N} & D_N \end{pmatrix} \quad (3.7)$$

with the diagonal entries $D_i = -\sum_{j=1}^{N-1} J_{j,j+1} + 2(J_{i,i-1} + J_{i,i+1} - B_i) + \sum_{j=1}^N B_j$ and with $J_{1,0} = J_{N,N+1} = 0$.

Before we continue, let us link the above spin system to the tight-binding models encountered in Chapters 1 and 2. To this end, we note that the tridiagonal matrix of Eq. (3.7) could also correspond to a tight-binding chain consisting of N sites, with the i -th site having an on-site potential D_i , and with neighboring sites i, j coupled by the coupling $-2J_{i,j}$. In Fig. 3.1 (b), we depict this chain for the case of $N = 4$. We note that this relation between spin systems in the single-excitation subspace and tight-binding models is not limited to one dimension, but on the contrary holds for arbitrary geometries and can, in particular, also be generalized to the case where the spin system is modeled by the XX-Hamiltonian [213, 214].

⁴ Such as the Heisenberg Hamiltonian Eq. (3.5) which we will write down below.

In the above tight-binding picture, the perfect transfer of Alice’s qubit corresponds to the perfect transfer of an excitation of the first site of H_1 to the last site of this Hamiltonian; this principle is visualized in Fig. 3.1 (c). The main idea behind our work [MR5] is then to replace the single-site excitations by symmetric dimers and to allow for perfect transfer of the corresponding CLSs living on these dimers. In the following, and in particular when outlining [MR5, MR6], we will use the terms “site” and “spin” interchangeably.

A central finding of Bose was that an unmodulated Heisenberg chain, that is, one where all couplings are equal and with constant magnetic fields $B_i = B$, is—except for very short chains—not suitable for perfect transfer of qubits. Indeed, defining the transfer fidelity as

$$f(t) = |\langle \Psi(t) | F \rangle|^2 = |\langle I | \exp(i\hat{H}t) | F \rangle|^2 \quad (3.8)$$

[setting $\hbar = 1$ and using Eqs. (3.3) to (3.5)], Bose investigated chains of lengths $N \leq 80$ and demonstrated that the maximum value of $f(t)$ in a reasonable time interval is rather small even for intermediate chain lengths, though still outperforming a classical channel. Soon after⁵, however, it was shown that a *modulated* chain—that is, one where the couplings and magnetic fields are fine-tuned—achieves a fidelity of unity, corresponding to PST [214].

There are several points that make PST appealing. The first point is that, in principle, PST works over arbitrarily long distances. The second point is its simplicity: Only a static tuning of couplings and local magnetic fields is necessary, but not a dynamical control. Moreover, PST can in principle be realized on many different platforms [216], such as in spin chains using liquid magnetic resonance [217], systems of superconducting qubits [218], and coupled photonic waveguides [219, 220]. In this respect, we note that PST is not limited to one-dimensional chains, but can indeed also be realized in higher-dimensional spin networks by fine-tuning the network-geometry and/or the couplings and local magnetic fields (see, e.g., [216, 221]).

The proposed use of spin chains for the transmission of qubits, and especially the concept of PST, triggered a large amount of subsequent research, overviews on specific aspects of which can be found in [216, 222–224]. In particular, the impact of imperfections such as noise [225] or next-nearest-neighbor couplings [226–228] have been investigated, and alternative schemes such as the use of homogeneous chains with control only over the couplings to the first and the last site have been proposed [229–231]. In the context of this thesis, we are mainly interested in a particular generalization of PST, namely, the concept of PGST.

The motivation for PGST is the following. Although PST is a powerful concept, it turned out to be highly restrictive⁶ in the sense that the class of Hamiltonians supporting PST is rather small [232]. On the other hand, the defining property

⁵ We note that the concept of PST was also independently developed in the context of coupled harmonic systems [215].

⁶ For example, in order to feature PST from site u to v , all eigenstates of a Hamiltonian must have definite parity with respect to these two sites. While this is easy to achieve, e.g., by making the system reflection symmetric, a further necessary condition for PST is that the eigenvalues $\{\lambda_i\}$ corresponding to positive parity eigenstates must fulfill

$$\frac{\lambda_i - \lambda_j}{\lambda_k - \lambda_l} \in \mathbb{Q} \quad (3.9)$$

of PST, namely, a fidelity of unity, is also unnecessarily strict. Indeed, even in a PST-Hamiltonian, inevitable imperfections of an experimental realization will lead to non-perfect transfer.

PGST, which is sometimes also called “almost perfect state transfer” [233], is defined as follows [234]: Instead of demanding that the fidelity $f(t)$ is equal to unity at a specific time, PGST only demands that it becomes arbitrarily close to unity. Specifically, for every $\epsilon > 0$ there is a time t_ϵ such that $F(t_\epsilon) > 1 - \epsilon$. It is clear that PST is a special case of PGST, and thus the latter is a generalization of the former. In the past years, several construction principles for PGST-Hamiltonians have been proposed, many of which build upon results from number theory [233, 235, 236] or graph theory [236–240]. We remark that this strong connection between quantum state transfer and graph theory was one of the reasons for our closer investigation of the latter; the corresponding results will be the topic of Chapter 4.

In his original work [213], Bose assumed that the first and last spin of the chain could be detached. Thus, the storage of the initial or final state prior to and after the transfer would be done by simply decoupling the corresponding spin from the chain. However, such a decoupling is an idealized scenario, and the question arises whether alternative means of storage could be pursued. Although there are indeed some works proposing such alternative means, for instance storing the qubit within the chain itself [222] or within a defect [230], most research on quantum state transfer concentrates only on the transfer part itself⁷. In light of this, and especially in view of the large body of literature on the two schemes of PST/PGST, we wondered whether they could easily be equipped with storage capabilities in the form of CLSs. This is indeed the case, as we have shown in our works [MR5, MR6]. In the following, we will outline the first of these two, [MR5]. As explained above, we postpone the outline of [MR6] to Chapter 4. In both [MR5] and [MR6], our aim is to explore interesting combinations of the concepts of PST/PGST and CLSs. Thus, we will exclusively concentrate on generic tight-binding models, assuming that a complete control over on-site potential and coupling values is possible. Due to the mapping from the Heisenberg and XX-model in the single-excitation subspace to tight-binding models, our results are readily applicable to these systems as well.

We further note that we have chosen the two techniques of PST and PGST mainly because of their simplicity. For completeness, let us also note that the literature on quantum information offers several alternative schemes that achieve high-fidelity transfer of qubits, including topologically protected edge states [245, 246], flying qubits [247], or optimal control methods [248–250]. An overview over state transfer on spin networks is given in the book [216].

3.2 OUTLINE: QUANTUM NETWORK TRANSFER AND STORAGE WITH COMPACT LOCALIZED STATES INDUCED BY LOCAL SYMMETRIES

In [MR5], we explore different methods for the high-fidelity transfer of CLSs in tight-binding models. In particular, we provide a method of adapting the perfect state transfer technique of single site excitations to the transfer of CLSs. Figure 3.2

for all i, j, k, l and $\lambda_k \neq \lambda_l$ [232]. This condition is rather difficult to fulfill.

⁷ In the greater context of quantum information as a whole, however, there is of course a large body of literature on quantum state storage, see e.g., the reviews [241–243] and the thesis [244].

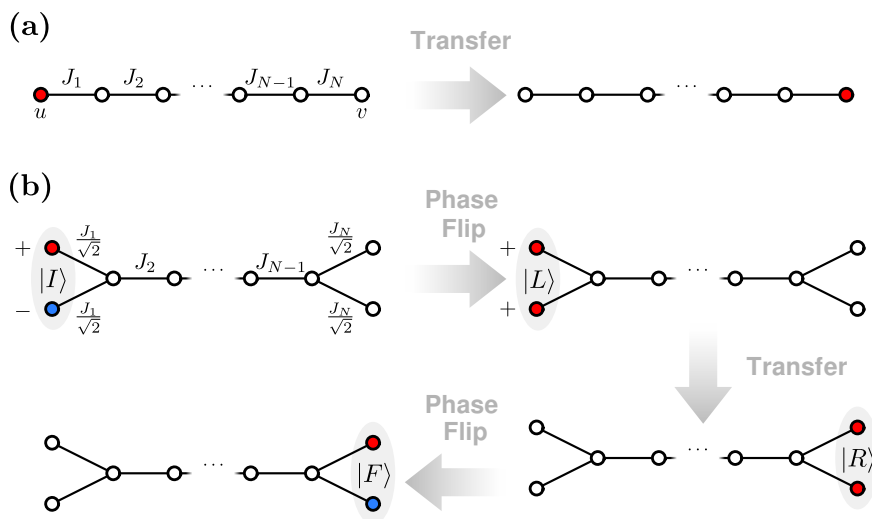


Figure 3.2: A visualization of how to equip a PST Hamiltonian with CLSs. (a) shows the original Hamiltonian that supports PST between two sites u and v . In this specific example, the Hamiltonian is a one-dimensional chain and supports PST between the two outermost sites u and v . (b) By dimerizing these two sites and subsequently rescaling the corresponding couplings by dividing them by $\sqrt{2}$, perfect transfer of CLSs can be achieved (see text for details). Source: A modified figure from [MR5].

graphically depicts this method. The starting point is a Hamiltonian that supports PST of single site excitations between two sites u and v . This Hamiltonian could in principle be quite complicated, but to show the underlying principle, in Fig. 3.2 (a) we depict the simple case of a one-dimensional chain. Here, u and v denote the sites on both ends of the chain. Let us now denote the perfect transfer time of this chain by t_F . In other words, if we perform a single-site excitation on the site u at time $t = 0$, then at time $t = t_F$ this excitation will be completely transferred to the site v .

In order to equip this chain with a CLS, we symmetrically dimerize the two sites u and v and also rescale the couplings connecting u, v to the remainder of the chain; see Fig. 3.2 (b). To initiate the amplitude transfer, we perform a flip of the relative phase between the two dimer sites on which the CLS $|I\rangle$ is localized. As we show, the resulting state $|L\rangle$ is then transferred across the chain with a fidelity of unity. The time at which this fidelity is reached is the same as in the original PST-Hamiltonian. Thus, at time $t = t_F$, the state $|L\rangle$ has been perfectly transferred to the state $|R\rangle$. At this time, another phase flip is performed, thereby transforming the symmetric dimer excitation $|R\rangle$ to the anti-symmetric CLS $|F\rangle$. As we mathematically prove, this scheme can be applied to a broad class of PST-Hamiltonians, and thus allows for the *perfect transfer and storage* of CLSs by minimally modifying the Hamiltonians employed so far for the perfect transfer of single site excitations.

Apart from equipping PST-Hamiltonians with CLSs, another focus of our work [MR5] was the introduction of what we call the decorated Lieb lattice (DLL). This lattice is depicted in Fig. 3.3 (a); it is obtained from the classical Lieb lattice by replacing the two outer sites of each unit cell by a symmetric dimer. Each unit cell is thus locally symmetric and possesses two dimers, each of which can host

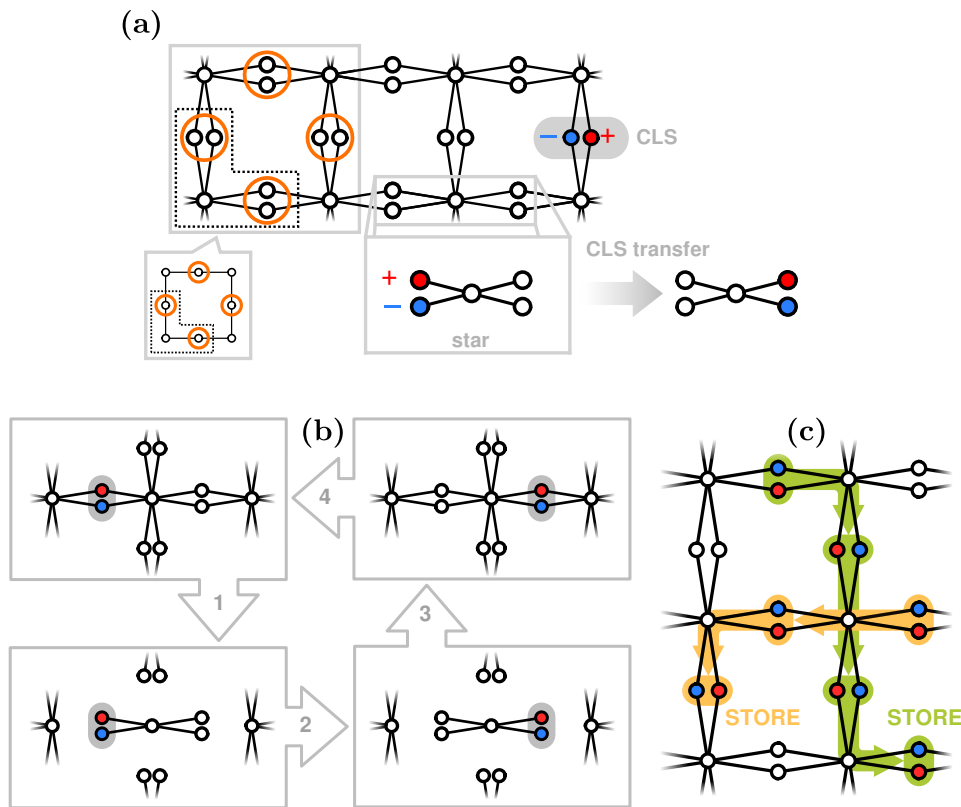


Figure 3.3: **(a)** The DLL, which is obtained from the Lieb lattice (lower left inset) by dimerizing the orange marked sites. Each unit cell (encircled by a dashed line) of the DLL features two dimers, each of which can host a CLS. The transfer of these CLSs is achieved via “dimer jumps”. **(b)** shows the principle behind these dimer jumps (see text for details). **(c)** visualizes the capability of the DLL to simultaneously perform storage and transfer of individual CLSs. Source: Compilation of slightly modified figures from [MR5].

a CLS. The main idea behind the DLL is to harness this large number of dimer CLSs such that this lattice becomes a combined CLS storage/transfer unit. To this end, we divide the process of CLS-transfer into smaller steps, and use these dimers as intermediate storage units for the storage of CLSs between different transfer phases.

The transfer process itself is done in terms of a “dimer jump”, which is schematically visualized in Fig. 3.3 (a). At the beginning of the process, a CLS is stored on one of the dimers and shall be transferred further across the lattice. In a first step, a five-site star-subsystem is decoupled from the remainder of the setup. This subsystem consists of the dimer on which the CLS is currently residing as well as the next dimer along its transfer path. By harnessing one of two different methods that we shall discuss below, the CLS is then transferred within this star to the opposite dimer and stored on it. Afterwards, the star is coupled back to the lattice. The process can then start anew, thus allowing the transfer of CLSs over arbitrarily long distances in the lattice.

Due to the modular character of the CLS transfer in the DLL, the storage of a CLS in one of the dimers is possible at any intermediate step within a transfer process. The lattice may further host more than one CLS at the same time, and these may

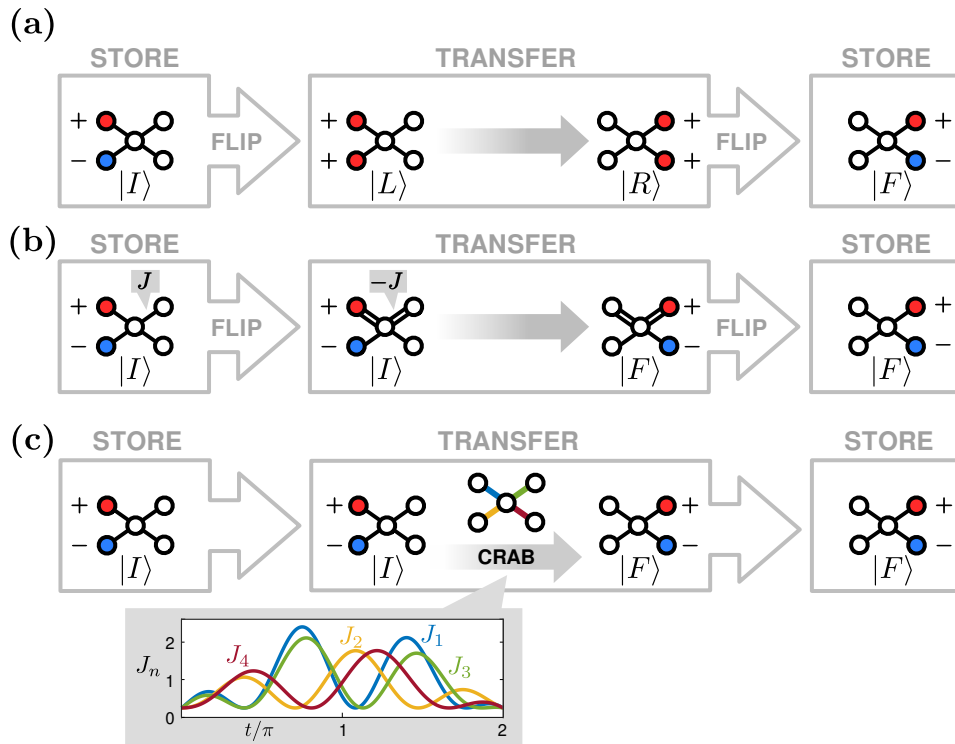


Figure 3.4: Three different routes for the CLS-transfer within the star subsystem of Fig. 3.3. In (a), the transfer is done by flipping the phase on one of the two dimer sites on which the CLS resides. This flip is done at $t = 0$, and as the resulting state is no longer an eigenstate, it propagates. At $t = T_f = 2\pi$, the state has completely tunneled to the other dimer (here, the right one), and by performing another phase flip at this time, the state becomes a CLS again. Instead of applying a phase flip to the states $|I\rangle$ and $|R\rangle$, one could also flip the sign of the two upper couplings in the star subsystem. This principle is shown in (b). Lastly, the CLS can also be transferred through optimal control in form of the CRAB method by continuously modulating the four coupling strengths J_1, \dots, J_4 of the star-subsystem in time. This principle is shown in (c). The inset shows the time-dependence of these four coupling during transfer. Source: Combination of different, slightly modified figures from [MR5].

also be stored and transferred individually, the only requirement being that the paths of two different CLSs do not cross simultaneously both in space *and* in time. Figure 3.3 (c) visualizes this highly parallelized combined CLS storage/transfer capability within the DLL.

On a technical side, we employ two different methods for the CLS-transfer within the isolated star-subsystem. The first method is based on the above scheme of perfect transfer of CLSs, and is visualized in Fig. 3.4 (a). Instead of applying a phase flip to the states $|I\rangle$ and $|R\rangle$, we show that perfect CLS-transfer could also be achieved by instantaneously flipping the sign of two of the couplings in the star-subsystem; see Fig. 3.4 (b). Interestingly, if this flip is not done instantaneously, the transfer fidelity decreases only slightly below unity⁸.

⁸ To be precise, if the flip is realized in terms of a linear ramp, then even if this ramp takes up one quarter of the overall transfer time of 2π , the fidelity is still above 0.998.

Our second method of achieving CLS-transfer within the star-subsystem is to vary some of the system's parameters—in our case, the coupling strengths—in an optimized, time-dependent manner. To this end, we optimize the time-dependent coupling strengths by means of optimal control⁹ in form of the chopped random-basis (CRAB) method [253, 254]. For the transfer of a CLS within the star-subsystem, we yield close to perfect fidelities of approximately $1 - 10^{-12}$. An example of this scheme, together with the time-dependency of the couplings, is shown in Fig. 3.3 (c).

Another central part of our work is an analysis of the performance of the DLL under various perturbations and imperfections. For the static part of storing CLSs, we analyze the impact of disorder of both on-site potentials and coupling strengths on the storage fidelity of the decorated Lieb lattice. For the dynamic part of CLS transfer, we analyze a variety of different perturbations, including static and dynamical disorder and the impact of non-perfect decoupling of the star-subsystem during the dimer-jumps. Overall, we find that our proposed CLS storage and transfer scheme is remarkably robust.

⁹ For an introduction to this field, see, e.g., the reviews [251, 252].

So far, we analyzed the impact of local symmetries in various setups such as tight-binding setups of different geometries and arrays of dipolar nanoparticles. What all of these have in common is their discrete character. In particular, and as we will explicate below, they could be described through the matrix eigenvalue problem $H\vec{\Psi} = E\vec{\Psi}$. Such matrix-eigenvalue problems, however, are also subject of study in the mathematical field of graph theory. And as we shall see in this highly interdisciplinary chapter, graph theory gives us the opportunity to see our physical setups from a completely different viewpoint, leading to interesting insights and new perspectives.

In the following, we will first give a short introduction to the mathematical field of graph and network theory in Section 4.1. We shall explain the dualism between graphs and square matrices, and use this dualism to build a bridge to the field of spectral graph theory that also deals with the matrix eigenvalue problem. Once we entered the realm of spectral graph theory, we will see in Section 4.2 that the powers of a matrix describing a physical system can be a valuable source of knowledge about this system. Specifically, we will show that in certain cases, these matrix powers allow to make detailed predictions about the system's eigenvectors. Moreover, we will further be able to interpret these powers in a very appealing manner through the concept of walks, which are related to quantum interference. Following this, we will explore the recently developed graph-theoretical concept of so-called latent symmetries in Section 4.3, and outline our own contributions to this field in Sections 4.4 to 4.7.

4.1 GRAPHS

Before we come to applications of graph-theoretical concepts to physics, let us quickly give an introduction to graphs and networks. Due to the vastness of the field of graph theory and network analysis, we will focus on some highlights that are important in the context of this thesis; we refer the reader interested in learning more about this field to the reviews [257–259] as well as to the books [260–263].

Mathematically speaking, a graph is a set of vertices interconnected by edges. To fill this rather abstract notion with life, we depict a simple example graph in Fig. 4.1 (a). This graph depicts marriages between 16 wealthy families of 15-th century Florence. Each family corresponds to a vertex, while edges connecting different vertices depict at least one marriage between them. The edges of a graph may also be directed, as shown in Fig. 4.1 (b), where a so-called food web (“who eats whom”) is represented. Moreover, edges may also have a weight, as shown in Fig. 4.1 (c), where the road transportation network of some of the major cities in central and southern Germany is shown, with the edge-weights corresponding to the distance between two cities.

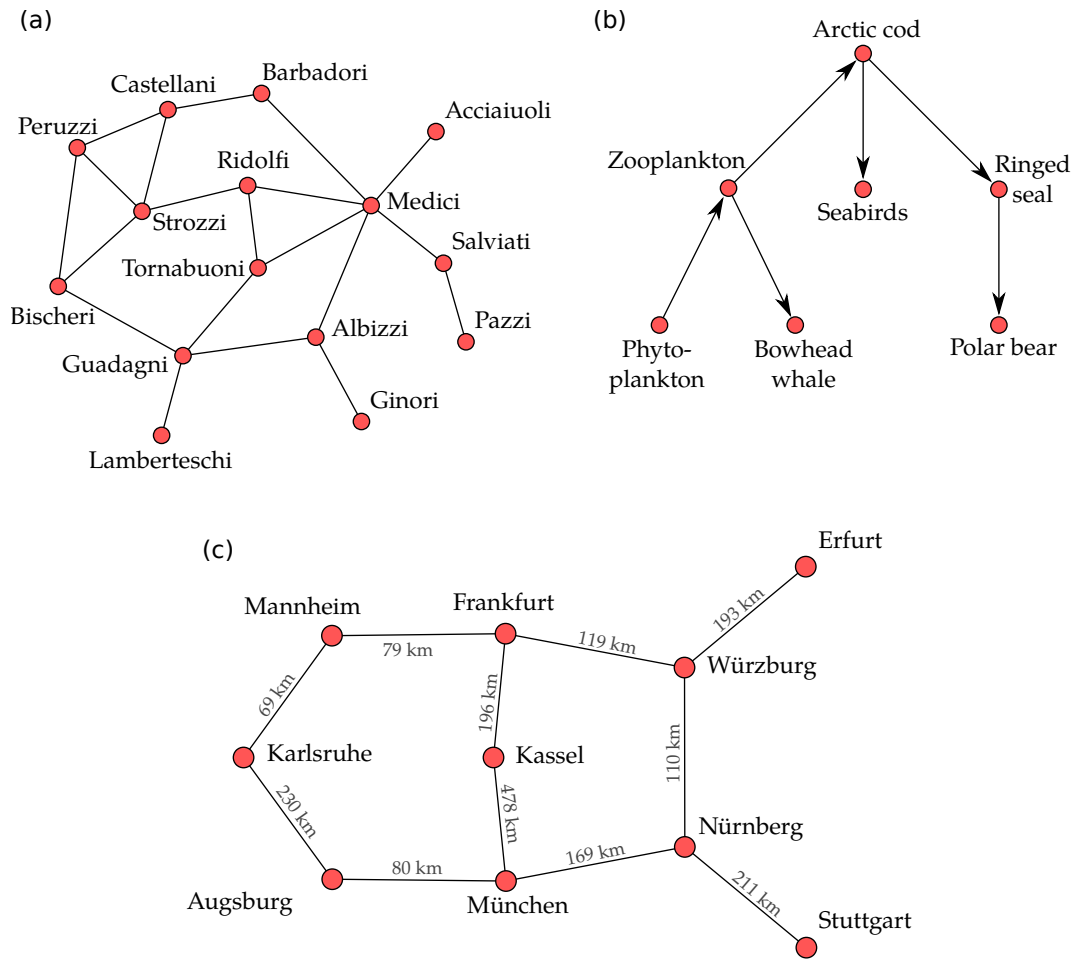


Figure 4.1: Some example graphs. (a) An unweighted graph showing marriage relations between 16 families in Florence of the 15-th century, data from [255]. (b) A directed graph showing a food web, data from [256]. (c) A weighted graph showing the travel distance between several major cities in central and southern Germany.

In a similar manner, graphs can represent a plethora of different structures, such as neural networks, power grids, citation networks, genetic regulatory networks, the internet, and many more [260]. The analysis of these networks, which can be larger than a billion vertices, is a highly interdisciplinary task, with contributions coming from fields as diverse as pure mathematics, sociology [264], chemistry [265], biology [266], computer science [267], or statistical physics [259, 268]. Besides providing an interesting playground for the applications of methods from statistical physics, there is also another important reason for why graph theory is interesting from a physics perspective: Recently, several important *NP*-complete algorithms from graph theory have been shown to be solvable through adiabatic computation with Ising Hamiltonians [269].

There were two major motivating factors for us to dive into graph theory. Firstly, the fact that locally symmetric substructures—an example of a graph containing some of these is shown in Fig. 4.2—are ubiquitous in real-world networks [270–275]. Secondly, the fact that there is a one-to-one correspondence between square matrices and graphs. That is, any square $N \times N$ matrix can be drawn as an N -vertex

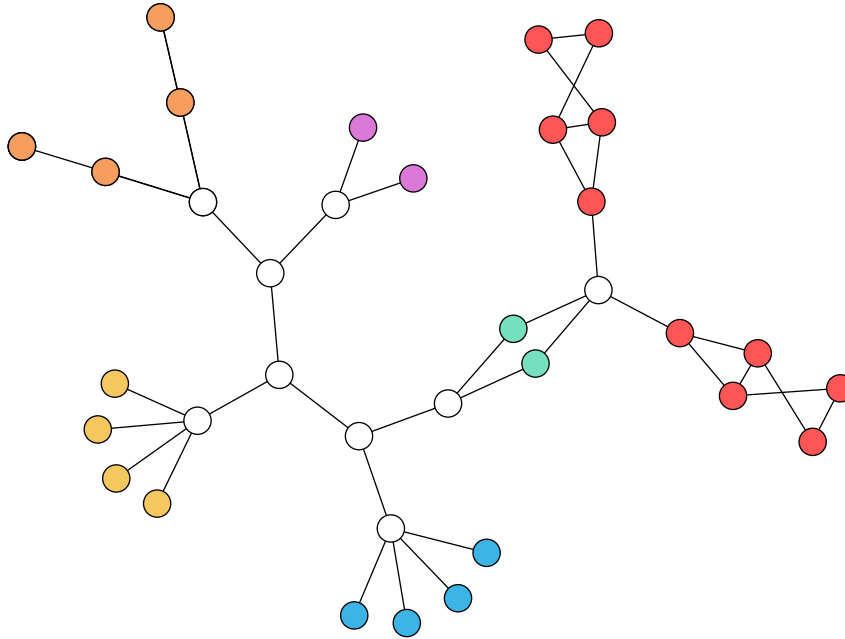


Figure 4.2: An example graph with many local symmetries, indicated by colored vertices.

graph, and vice versa (we will explicate this correspondence in a second). Now, since any linear operator—including, in particular, Hamiltonians—can be written as a matrix by going to a specific basis¹, it follows from the above that they can be drawn as a graph. Thus, graph theory is applicable to a large number of physical systems. Examples of such systems are, of course, the tight-binding networks treated throughout this thesis, but also the dipole-scatterer setups described in Section 2.4, and—for example, by choosing a basis of Fock states—also systems of interacting indistinguishable particles [151, 276].

Let us now demonstrate and explain the correspondence between matrices and graphs in more detail. In Fig. 4.3, an example of this correspondence is shown for the case of $N = 4$, with each non-vanishing matrix element depicted by an edge. We emphasize that in the above correspondence, it does not matter *how* exactly the graph is drawn, that is, the vertices of the graph can be placed arbitrarily. What matters is only the topology, that is, which vertex is connected to which, and how strongly. Thus, the two graphs shown in Fig. 4.3 (a) and (c) both correspond to the same matrix H which is depicted in Fig. 4.3 (b). We note that, since most parts of this thesis are focused on tight-binding models, we will continue to use its terminology, and in particular will continue to call the diagonal elements of the matrix H describing a graph “on-site potentials”. Thus, we see that the three sites (or, in graph-theoretical nomenclature, vertices) 1, 2, and 3 in Fig. 4.3 have vanishing on-site potential, while the fourth site has an on-site potential of v .

¹ For example, if our tight-binding Hamiltonian operator of Eq. (2.1),

$$\hat{H} = \sum_i v_i |i\rangle \langle i| + \sum_{\langle i,j \rangle} h_{i,j} |i\rangle \langle j|, \quad (4.1)$$

describes a setup of N sites, then we can write it as the $N \times N$ matrix H by choosing the basis of single site-excitations. In this basis, the matrix element $H_{i,j}$ of H is given by v_i if $i = j$, $h_{i,j}$ if $i \neq j$ and i, j are coupled, and zero otherwise.

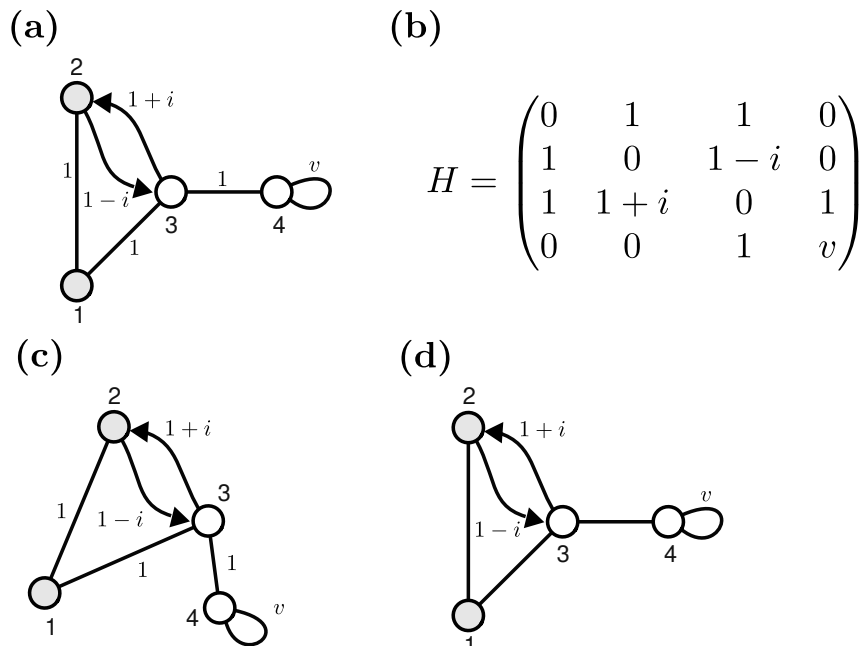


Figure 4.3: **(a)** A weighted, directed four-vertex graph and **(b)** the corresponding 4×4 matrix. Each non-vanishing element H_{ij} of this matrix is depicted in (a) by a line connecting the two vertices (or, in a physical language, *sites*) i, j . **(c)** The same graph as in (a), but with a different placement of vertices. **(d)** To not overload a graph, the usual convention is that all lines without an explicitly printed weight have a weight of unity. Thus, the depicted graph is equal to that in (a) and (c).

The correspondence between graphs and matrices is very powerful, as it represents a bridge between physics and graph theory. This bridge is made even more obvious through the field of “spectral graph theory”, which analyzes graphs in terms of their eigenvalues and eigenvectors². Specifically, spectral graph theory analyzes graphs through their corresponding eigenvalue problem

$$H \vec{\Psi} = E \vec{\Psi}, \quad (4.2)$$

with the matrix H describing the underlying graph and with $\vec{\Psi}$ denoting an eigenvector with eigenvalue E . In many cases, H is hermitian, and we thus see that Eq. (4.2) treated in spectral graph theory is nothing else but the eigenvalue problem that occurs when solving the discrete time-independent Schrödinger equation. Now, since the viewpoints of physics and mathematics usually differ, the common grounds of Eq. (4.2) represent a big chance for fruitful interdisciplinary work.

Before we dive into the exciting world of spectral graph theory, let us make some important remarks. In the following, we will make extensive use of the correspondence between matrices and graphs. In particular, in all figures shown in the following Sections 4.2 and 4.3, we will implicitly link each depicted graph to a

² A relevant question in that field is, for example, under which circumstances a graph is uniquely characterized by its eigenvalue spectrum [277]. Another important question in spectral graph theory is how eigenvalues and eigenvectors can be used as spectral measures to classify a graph [260]. Well-known examples of such measures are the so-called eigenvector centrality [264], the Katz centrality [278], as well as the Google PageRank algorithm [279, 280]. For an introduction to the field of spectral graph theory, see, for example, [260, 281, 282].

matrix H in the exact same way as was shown in Fig. 4.3. In order to not overload these graphs, we will use the convention that, unless explicitly stated, each line has a weight of unity; see Fig. 4.3 (d). Moreover, we will use the terms “graph”, “discrete model”, “matrix”, and “Hamiltonian” interchangeably, and we will also not differentiate between a “site” or a “vertex”. In particular, when speaking of a graph-theoretical result, we imply that it can also be applied to discrete models such as tight-binding Hamiltonians. We also note that, unless otherwise mentioned, all results in the following are valid for real-symmetric matrices.

4.2 COSPECTRALITY: THE SYMMETRY OF WALKS

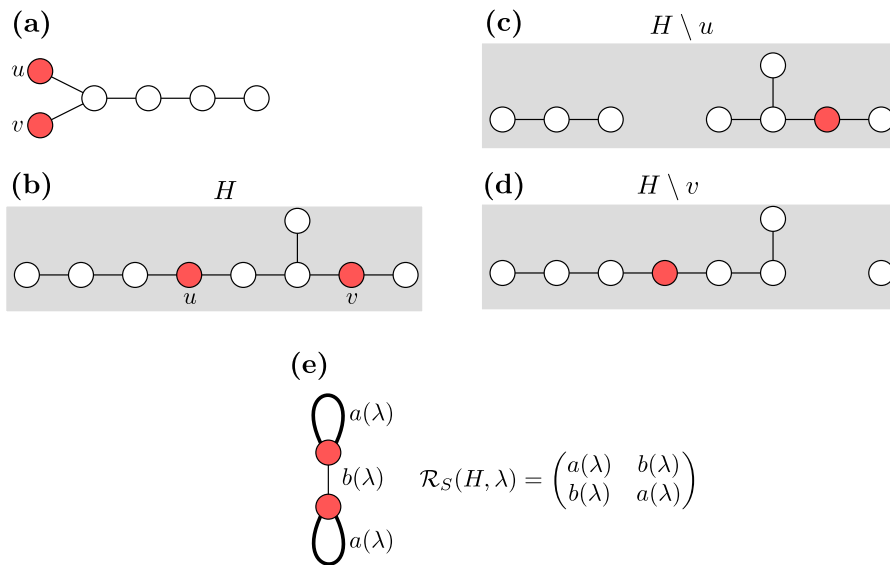


Figure 4.4: A collection of different graphs. As in Fig. 4.3 (d), all sites without a loop have vanishing on-site potential, and all lines without a printed edge weight have a weight of unity. **(a)** A graph that features a reflection symmetry. Due to this reflection symmetry, all eigenvectors have definite parity on the two red sites u and v . **(b)** A graph H without any reflection symmetry. However, irrespective of this lack of symmetry, since the two red sites u and v are cospectral, all eigenvectors have definite parity on them (see text for details). **(c)** and **(d)** show the Hamiltonians $H \setminus u$ and $H \setminus v$, respectively, with H denoting the Hamiltonian describing (b). **(e)** The result of performing the isospectral reduction over the graph H of (b) for the choice of $S = \{u, v\}$. As this isospectral reduction is reflection symmetric, u and v are *latently (reflection) symmetric*.

Having mentioned some aspects of graph theory and its applications, let us now dive deeper by introducing the intriguing concept of *cospectral vertices* [283–285] which also represents the main subject of our works [MR6–MR8]. Vertex cospectrality can be related to a number of different properties of a graph, but perhaps the most interesting one is that of parity. That is, for a graph described by a real-symmetric matrix H that has no degenerate eigenvalues³, two of its vertices u and v are cospectral if and only if all eigenvectors have definite parity on u and v [285].

³ The statement can also be generalized to the case of degenerate eigenvalues; see [285, 286].

What makes cospectrality interesting is that it comes in different flavors, namely, obvious and non-obvious ones. In Fig. 4.4 (a), an example for the former class is depicted. The system shown here consists of six sites and features a reflection symmetry. Due to this reflection symmetry, it is clear that the eigenvectors of this system will have definite parity on the two red sites u and v . Thus, u and v are cospectral. While this case is trivial, the situation is completely different for the system shown in Fig. 4.4 (b). Once again, all eigenvectors of the system have definite parity on the two red sites u and v , and these two sites are thus cospectral. However, now there is no reflection symmetry explaining this parity.

Examples like that of Fig. 4.4 (b) formed our core motivation for diving into the world of cospectral vertices, and before we explore this phenomenon in more detail, let us first comment on the origin of the term “cospectrality”. To this end, we will need the so-called vertex deleted subgraphs $H \setminus u$ and $H \setminus v$, obtained from the graph H by removing the site u or v , respectively. For convenience, and to demonstrate the principle, we depict these two graphs in Fig. 4.4 (c) and (d), respectively, with H describing the system shown in Fig. 4.4 (b). Equipped with this terminology, we can now define cospectrality. Namely, two vertices u, v are said to be cospectral when the corresponding vertex deleted subgraphs $H \setminus u$ and $H \setminus v$ have the same eigenvalue spectrum [285]. In other words, $H \setminus u$ and $H \setminus v$ are *cospectral*, and this is the reason for calling u and v “cospectral vertices”. At this point, let us emphasize that vertex cospectrality includes the conventional case of reflection-symmetric sites. That is, when two sites u, v are mapped onto each other by a reflection symmetry of the underlying graph H , then they are also cospectral. This is especially clear in Fig. 4.4 (a), as in this case the two subgraphs $H \setminus u$ and $H \setminus v$ are identical.

Historically, the study of cospectral vertices was started by Schwenk in 1973 in his study of graphs that share the same eigenvalue spectrum [283]. In that work, Schwenk also provided a method for the construction of a specific class of cospectral graphs. Other methods for the construction of cospectral graphs include graph products [287] or the so-called Godsil-McKay switching [284]; an overview over these and other methods is given in [288]. Cospectral vertices are also used in chemical graph theory, where they are known as “isospectral vertices” [289–291]. Moreover, they have been used in control theory [292–294] and in quantum state transfer. Indeed, and connecting to Chapter 3, it was found that cospectrality of two sites u, v is in fact a necessary condition for perfect or pretty good state transfer between them [285].

A central finding that emerged during the above systematic studies of cospectrality is that it can be connected to relations in the matrix powers of the underlying Hamiltonian [285]. Namely, the cospectrality of two vertices u and v is equivalent to

$$\left(H^k\right)_{u,u} = \left(H^k\right)_{v,v} \quad \forall k \geq 1. \quad (4.3)$$

traversed edges—2 from vertex 1 to vertex 3 would be $(V_1, e_{1,2}, V_2, e_{2,3}, V_3)$, where V_i denotes the i -th vertex and $e_{k,l}$ denotes the edge between vertices V_k and V_l . Now, in order to connect the matrix powers of H to walks, we need to assign a weight to each walk by multiplying the weights of the individual edges used by this walk. For the example walk above the edges used are $e_{1,2}$ and $e_{2,3}$, and since the weight of the edge $e_{k,l}$ is given by the matrix element $H_{k,l}$, the walk $(V_1, e_{1,2}, V_2, e_{2,3}, V_3)$ thus has a weight of $2 \cdot 1 = 2$. Walks can then be connected to matrix powers by noting that the matrix element $(H^k)_{i,j}$ is given by taking all walks of lengths k from vertex i to vertex j and adding up their respective weights; examples for this statement are shown in Fig. 4.5. Before we continue, we note that walks are highly related to the concept of quantum interference, as has recently been elaborated in the review [297]. Personally, we are convinced that the walk-interpretation will lead to many new perspectives on physical systems.

With the above, and after several steps, we have derived a first insight to cospectral vertices. Namely, by applying the above interpretation to Eq. (4.3), we see that u and v are cospectral if and only if the cumulative weight of closed walks from u to itself is the same as those of closed walks from v to itself. In the following, we will relate cospectrality to yet another graph theoretical concept, namely, that of “latent symmetries”.

4.3 LATENT SYMMETRIES

Before we introduce latent symmetries, let us say a few words regarding the environment of complex network analysis in which these symmetries have been first discovered. Such networks may be enormously large, with the graphs representing these networks having vertex numbers exceeding a billion, which naturally makes their analysis difficult. To face this difficulty, in 2011 Webb and Bunimovich developed the so-called isospectral reduction [298, 299]. Roughly speaking, the isospectral reduction reduces the dimension of a graph while keeping its eigenvalue spectrum. This allows to get rid of some unnecessary details, thereby allowing an easier recognition of some key properties of the graph, while at the same time keeping precious information about its eigenvalue spectrum. So far, the isospectral reduction has proven to be a versatile tool for different problems, including eigenvalue approximations [300], the creation of stability preserving transformations of networks [298, 301, 302], the study of pseudo-spectra of graphs and matrices [303], and the study of the survival probabilities in open dynamical systems [304].

The isospectral reduction is equivalent to an effective Hamiltonian obtained through subsystem partitioning [MR9, 305], and is defined as

$$\mathcal{R}_S(E) = H_{SS} + H_{S\bar{S}} (E - H_{\bar{S}\bar{S}})^{-1} H_{\bar{S}S}. \quad (4.4)$$

In this equation, the two sets of sites S and its complement (that is, all other sites) \bar{S} denote a decomposition of the system/graph. The matrices H_{SS} and $H_{\bar{S}\bar{S}}$ then denote the sub-Hamiltonians which describe the corresponding *isolated* subsystems comprised only of S or \bar{S} , respectively. $H_{S\bar{S}}$ and $H_{\bar{S}S}$ describe the coupling between these two subsystems.

We note that the isospectral reduction is a function of the energy parameter E , which can be used to define a generalized eigenvalue problem

$$\text{Det}(\mathcal{R}_S(E) - EI) = 0 \quad (4.5)$$

with Det denoting the determinant, and I denoting the identity matrix. The solutions to this equation are the generalized eigenvalues of $\mathcal{R}_S(E)$. As perhaps can be expected from the statement that the isospectral reduction is equivalent to an effective Hamiltonian, each of these generalized eigenvalues of $\mathcal{R}_S(E)$ is also an eigenvalue of the original Hamiltonian H . In many cases, the eigenvalue spectra of H and $\mathcal{R}_S(E)$ coincide, and this motivates calling $\mathcal{R}_S(E)$ an “isospectral” reduction.

We are now equipped with the necessary ingredients for the introduction of latent symmetries. Formally, *a latent symmetry is defined as a symmetry of the isospectral reduction of a graph* [306]. This being said, let us now bring life into this definition by applying it to a simple example. In Fig. 4.4 (e), we perform the isospectral reduction of the graph H shown in Fig. 4.4 (b) over the two red sites $S = \{u, v\}$. As one can see, the reduction over these two sites is reflection symmetric, and the original Hamiltonian H thus features a latent (reflection) symmetry.

In the above example, the two latently symmetric sites u and v were exactly the ones that are cospectral, and this is no coincidence. Indeed, as was proven in [307], for a real-symmetric matrix H , two sites are latently symmetric if and only if they are cospectral. Thus, we have now yet another explanation for cospectrality by relating it to a symmetry of the isospectral reduction of a Hamiltonian.

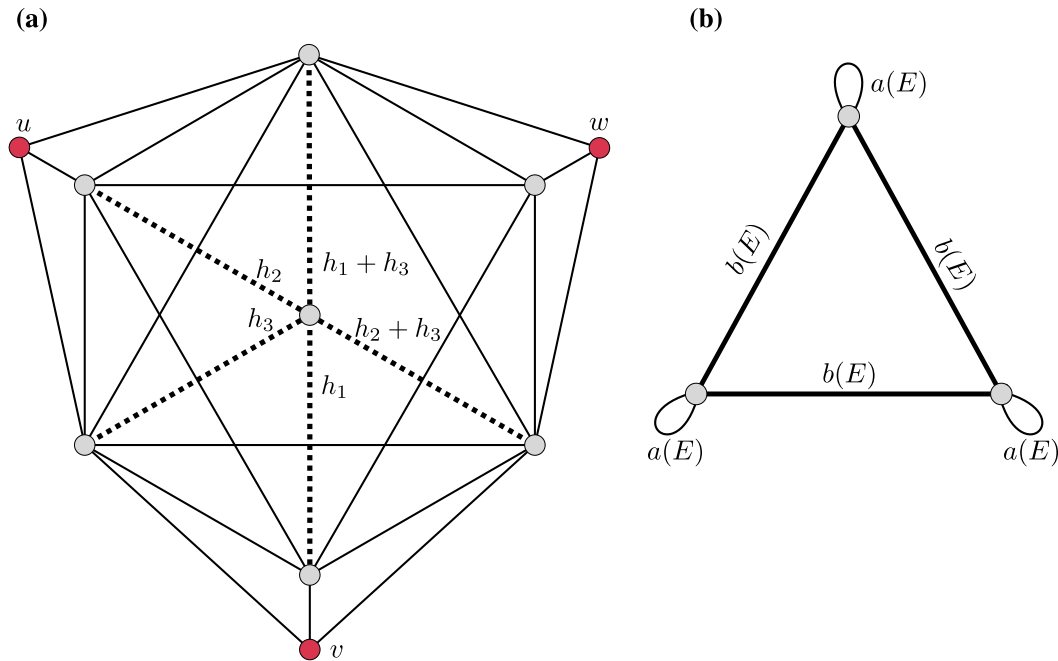


Figure 4.6: **(a)** A ten-site Hamiltonian H . All solid lines correspond to couplings of strength 1, while the dashed lines correspond to couplings whose strength depend on the parameters h_1 , h_2 , and h_3 . Since there are no loops connecting any site to itself, all ten on-site potentials are set to zero. **(b)** Shows the isospectral reduction of H over $S = \{u, v, w\}$. For any choice of the h_i , this reduction is highly symmetric.

We note that the concept of latent symmetries is, by no means, limited to reductions over only two sites or to reflection symmetries. An example for this statement

is shown in Fig. 4.6. In (a), a simple ten-site Hamiltonian is depicted. Here, the isospectral reduction of this Hamiltonian over the three red sites $S = \{u, v, w\}$ features a threefold rotational symmetry as well as three reflection symmetries⁶. These six symmetries—three rotations and three reflections—form the dihedral group D_3 . Thus, the Hamiltonian features a *latent D_3 symmetry*.

Overall, and especially since the study of latent symmetries and cospectral sites is a relatively young field, there are still many open questions and problems. In the following, we will discuss our own research on this topic, which is driven by the desire to understand the interplay of symmetries of a system and the behavior of its eigenstates and eigenvalues.

4.4 OUTLINE: DESIGNING PRETTY GOOD STATE TRANSFER VIA ISOSPECTRAL REDUCTIONS

Our work [MR6] connects the two topics of state transfer and cospectrality, and was our starting point for a further exploration of the latter topic. Here, we achieve two things. Our first achievement is the generalization of some of the results of our work [MR5] on PST to PGST. Namely, we show that also PGST-Hamiltonians can be equipped with CLSs, and that these can also be pretty well transferred. The underlying principle is completely analogous to the scheme presented in [MR5]. That is, starting from a tight-binding Hamiltonian that supports PGST of single-site excitations of sites u and v , we first dimerize these two sites. Then, by applying two control pulses before and after the transfer, pretty good transfer of dimer-CLSs is possible. Our second achievement is the employment of latent symmetries for the design of Hamiltonians that feature PGST.

In order to feature PGST, a Hamiltonian needs to fulfill two conditions. Firstly, all eigenstates must have definite parity on the two sites u and v between which the transfer should take place, and thus these must be cospectral. As we have seen above, such a parity can be trivially induced by a reflection symmetry of the system, but also by a latent symmetry of u and v . Secondly, the eigenvalues of the Hamiltonian need to fulfill certain conditions⁷. Although these conditions are not as demanding as that of PST-Hamiltonians—see, for instance, Eq. (3.9)—they are also of number-theoretical nature. As a result, if one would want to fulfill these conditions by tuning the eigenvalues of the setup, one would need knowledge about the *exact*—that is, with an infinite precision—eigenvalue spectrum. In our work, we build upon recent results from graph theory [286] which show that these conditions can be fulfilled through an alternative pathway for which such knowledge of the exact eigenvalues is not necessary. Instead, a PGST-Hamiltonian can be designed by starting from a Hamiltonian with cospectral sites u and v , and subsequently tuning different properties of the polynomials⁸ P_{\pm} that are related

⁶ The three axes of reflection are obtained by drawing a line from any of the three vertices to the center of the corresponding opposite edge.

⁷ Although not complicated, these conditions are rather technical, and stating them here would give no deeper insights. They can be found, e.g., in Theorem 2 of [308].

⁸ For example, these polynomials need to fulfill

$$\frac{\text{Tr}(P_+)}{\text{deg}(P_+)} \neq \frac{\text{Tr}(P_-)}{\text{deg}(P_-)}$$

to the eigenstates having negative and positive parity on these two sites. More specifically, if $\{\lambda_i^+\}$, $\{\lambda_j^-\}$ are the eigenvalues corresponding to eigenstates with positive or negative parity on u and v , respectively, then these polynomials are equal to

$$P_+(x) = \prod_i (x - \lambda_i^+) = \sum_{i=0}^{n_+} a_i x^i \quad (4.6)$$

$$P_-(x) = \prod_j (x - \lambda_j^-) = \sum_{i=0}^{n_-} b_i x^i, \quad (4.7)$$

where n_{\pm} denote the respective degree of the polynomials.

In our work, we first generate a database comprising millions of tight-binding network geometries where (i) all on-site potentials vanish, (ii) all non-vanishing couplings have an identical strength of unity, and (iii) there is at least one pair of cospectral sites u and v . Out of this database, one may pick an arbitrary Hamiltonian to start with. We then use the fact that, whenever two sites u and v are cospectral, they are also latently symmetric. The isospectral reduction over these two sites is thus reflection symmetric. As we show, this symmetry allows to harness the equitable partition theorem⁹ that we discussed in Section 2.3 to extract the polynomials P_{\pm} . We then devise an algorithm for the construction of setups featuring PGST. The algorithm is based on the fact that, once the polynomials P_{\pm} are known, the properties relevant for PGST can be controlled by tuning the coupling strengths and on-site potentials of the underlying tight-binding network. Importantly, this tuning needs to be done such that the cospectrality of u and v is kept. While we indeed identify a class of such modifications, this class is rather small. The quest for more such modifications then led to our next work [MR7] that we will discuss next.

4.5 OUTLINE: COSPECTRALITY PRESERVING GRAPH MODIFICATIONS AND EIGENVECTOR PROPERTIES VIA WALK EQUIVALENCE OF VERTICES

As we have seen in Section 4.2, the equivalence of cospectrality to relations of diagonal elements of H^k gives a new viewpoint on matrix powers and their analysis. In our work [MR7], we further extend this viewpoint by showing that also the off-diagonal matrix elements of H^k can be an important source of knowledge.

Our work is motivated by the following question: Given a Hamiltonian H with cospectral sites u and v , which changes can be made to H without breaking the cospectrality? An important example of a change is to couple the graph to an additional site c . We find that one can give both necessary and sufficient conditions for when such an addition preserves the cospectrality of u and v by means of what we call *walk multiplets*. In the simplest case, a multiplet \mathcal{M} is a set of sites such that

$$\sum_{i \in \mathcal{M}} (H^k)_{u,i} = \sum_{i \in \mathcal{M}} (H^k)_{v,i} \quad \forall k \geq 1. \quad (4.8)$$

where $\text{Tr}(P)$ and $\text{deg}(P)$ denote the sum of roots and the degree of the polynomial P , respectively.

⁹ We note that the equitable partition theorem can also be applied to other types of latent symmetries, as was recently shown in [309].

As we argued in Section 4.2, the matrix powers of H can be interpreted in terms of walks. Thus, we see from Eq. (4.8) that the cumulative sums of weights of walks from the multiplet to u and to v are equal; we say that u and v are “walk equivalent” for the multiplet \mathcal{M} .

Given a multiplet \mathcal{M} and a Hamiltonian H with cospectral sites u, v , we prove that one can connect a new site c homogeneously to all sites of \mathcal{M} without breaking the cospectrality of u and v . We then further generalize the concept of multiplets by augmenting the sums in Eq. (4.8) with more degrees of freedom (such as individual weights γ_i for each summand on both sides of Eq. (4.8)), and use this generalization to prove two central results: Firstly, that the addition of a single site c preserves the cospectrality of u, v if and only if c is connected to a multiplet. Secondly, that two multiplets can be interconnected without breaking cospectrality. For both of these statements, the interconnection needs to be done in a certain way—that is, the coupling strengths need to fulfill certain relations—that can be derived, again, from the matrix powers of the underlying Hamiltonian. We use these findings to present a novel method for the construction of cospectral graphs, which represents an important topic in spectral graph theory.

Apart from their relevance in finding cospectrality-preserving modifications, we find that multiplets are also a very valuable source of knowledge about the system’s eigenvectors. In the simplest case—the sites u and v are cospectral in a Hamiltonian H which has only non-degenerate eigenvalues, and we have a multiplet as defined in Eq. (4.8)—we find that each negative-parity eigenstate¹⁰ ϕ fulfills

$$\sum_{i \in \mathcal{M}} \phi_i = 0. \quad (4.9)$$

That is, the sum of its components on the multiplet-sites vanishes. This statement can be extended to the case of degenerate eigenvalues and also to the case where the sums in Eq. (4.8) are equipped with more degrees of freedom [such as individual weights γ_i for each summand]. Moreover, depending on the multiplet, also statements about the eigenstates having *positive parity* on u and v can be made.

4.6 OUTLINE: FLAT BANDS BY LATENT SYMMETRY

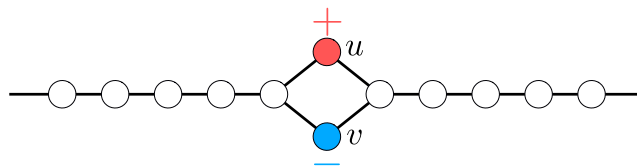


Figure 4.7: The system of Fig. 2.1 (a), now with the two dimer sites marked by u and v .

In [MR8], we employ the results of [MR7] for the construction of compact localized states and flat bands. The core idea of this work is to use a close connection between destructive interference and matrix powers. To demonstrate this connection, let us again look at the example system of Fig. 2.1 (a) which we have replicated for convenience in Fig. 4.7. In Chapter 2, we found that the depicted state is an

¹⁰ That is, each eigenstate having negative parity on u and v .

eigenstate of the underlying Hamiltonian H , and that the tunneling amplitudes to nearby sites cancel each other. Let us now view this problem from another angle and evaluate the time-evolution of this state $|\Psi_{CLS}\rangle = |u\rangle - |v\rangle$, with $|u\rangle, |v\rangle$ denoting the single-site excitations u and v , respectively. With the Hamiltonian being time-independent, we obtain (setting $\hbar = 1$)

$$|\Psi_{CLS}(t)\rangle = e^{-iHt}(|u\rangle - |v\rangle) = \sum_{k=0}^{\infty} \frac{(-it)^k H^k}{k!} (|u\rangle - |v\rangle). \quad (4.10)$$

If we then analyze the overlap $\langle w|\Psi_{CLS}(t)\rangle$ of this state with any white site w of the system [see Fig. 4.7], we know from the above argument of destructive interference¹¹ that this overlap vanishes. Thus

$$\langle w|\Psi_{CLS}(t)\rangle = \sum_{k=0}^{\infty} \frac{(-it)^k}{k!} \left(\langle w|H^k|u\rangle - \langle w|H^k|v\rangle \right) = 0. \quad (4.11)$$

As can easily be seen by multiplying these expressions out,

$$\begin{aligned} \langle w|H^k|u\rangle &= \left(H^k \right)_{w,u} \\ \langle w|H^k|v\rangle &= \left(H^k \right)_{w,v} \end{aligned}$$

denote matrix elements of H^k . Now, since $\langle w|\Psi_{CLS}(t)\rangle = 0$ for all t , and since the power series in Eq. (4.11) is convergent, it follows that

$$\left(H^k \right)_{w,u} = \left(H^k \right)_{w,v} \quad \forall k \geq 1. \quad (4.12)$$

In other words, we have derived an expression that connects the compact support of our CLS $|u\rangle - |v\rangle$ to relations between matrix elements of H^k for all $k \geq 1$. Comparing Eq. (4.12) to the definition of multiplets, Eq. (4.8), we see that w represents a multiplet consisting of a single site, that is, a singlet.

The above two observations— w is a singlet, and the negative parity eigenstate vanishes on it—are directly related to each other. Indeed, if we have a Hamiltonian in which the sites u and v are cospectral—as is the case¹² in our simple example of Fig. 4.7—we see from Eq. (4.9) that each eigenstate $|\phi\rangle$ with negative parity on u, v vanishes on a singlet w , that is,

$$\langle w|\phi\rangle = 0. \quad (4.13)$$

In [MR8], we use Eq. (4.13) to construct CLSs and flat bands. More precisely, we start by designing a single unit cell whose Hamiltonian H features two cospectral sites u and v . We then form a lattice by periodically replicating this unit cell and interconnecting neighboring cells. Using theorems from [MR7], these connections are done in a “singlet”-manner. That is, they are done such that for each unit cell, the cospectrality of its sites u and v is kept, and also such that the sites in *all* other unit cells become singlets. From the above, each unit cell then features at least one CLS, and thus one or more flat bands emerge.

¹¹ Or, alternatively, from the statement that $|\Psi_{CLS}\rangle$ is an eigenstate of the Hamiltonian.

¹² We remind the reader that if two sites are reflection symmetric, then they are automatically latently symmetric and thus also cospectral.

4.7 OUTLINE: LATENT SYMMETRY INDUCED DEGENERACIES

The symmetries of a Hamiltonian can be conveniently described by the mathematical instrument of group theory [6]. A central result of this treatment is that a Hamiltonian which features a non-abelian symmetry group necessarily has degenerate eigenvalues. Given the importance of this result, it was an interesting question whether it can be applied to non-abelian *latent* symmetries as well. In [MR9], we answer this question in the affirmative by generalizing the group-theoretical methods to the treatment of latent symmetries. We then use this result for the treatment of a real-symmetric Hamiltonian with an abelian n -fold rotational symmetry. Since it is real-symmetric, the Hamiltonian also features a time-reversal symmetry, and it is a classical result that the combination of this symmetry with the abelian rotational symmetry leads to degenerate eigenvalues when $n > 2$ [310]. By proving that such a real Hamiltonian with an n -fold rotation symmetry always features a *latent dihedral symmetry* D_n of order n , we give another explanation for this classical result: Since D_n is non-abelian for $n > 2$, this group necessarily leads to degenerate eigenvalues.

We continue by presenting a construction method for Hamiltonians that feature non-abelian latent symmetries while not featuring any geometrical¹³ symmetry. An example of such a Hamiltonian is depicted in Fig. 4.6 (a): For any choice of h_i , this graph features a non-abelian latent symmetry—which becomes visible when reducing over the three sites $S = \{u, v, w\}$ —, but it features no geometrical symmetry when $h_1 h_2 \neq 0$ and $h_1 \neq h_2$.

The fact that latent symmetries are usually hidden from direct observation but nevertheless can induce degeneracies leads to an interesting question: Could it be that—in systems in which either there is no obvious symmetry or the symmetry group is not sufficiently large to explain the degeneracies—several degeneracies which until now are believed to be “accidental” [7, 311] are, in fact, caused by latent symmetries? The exploration of this question will pose an exciting challenge in the near future.

We conclude the description of our work [MR9] by stating what I personally consider its most important result. Namely, the relation between the two concepts of local and latent symmetries, which is expressed by

$$[\mathcal{R}_S(H, E), M] = 0 \quad \Leftrightarrow \quad \left[\left(H^k \right)_{SS}, M \right] = 0 \quad \forall k. \quad (4.14)$$

Here, M is a matrix describing the symmetry of the isospectral reduction; in the simplest case, it would be a 2×2 matrix describing a reflection symmetry of two sites u, v . Now, since a symmetry M of the isospectral reduction is equivalent to a *latent symmetry* M of the original Hamiltonian, we see that the above equation states the following: *A latent symmetry M of a set of sites S is equivalent to a local symmetry M of the Hamiltonian in all matrix powers*¹⁴.

¹³ By “geometrical symmetry” we here mean the invariance of a graph under geometric operations such as (local) reflections, inversions, rotations, and combinations thereof. More specifically, we mean a permutation symmetry of the underlying matrix H , that is, the commutation of H with a permutation matrix.

¹⁴ We remark that, to see whether a Hamiltonian features a latent symmetry, one might thus either (i) look for local symmetries in H itself and in all matrix powers H^k , or (ii) investigate the isospectral

With respect to this result, there are two things that we would like to note. Firstly, it shows once again that the matrix powers of a Hamiltonian are a very valuable source of information. Secondly, we started this thesis with the topic of local symmetries, and with Eq. (4.14) we also end with it. The viewpoints on the problem, however, have changed completely. In Chapter 6, we shall comment more on the significance of Eq. (4.14) and the many possible routes for future research that it opens.

reduction of H . In both cases, whether a given Hamiltonian H features a latent symmetry or not is usually not clear when investigating only H .

Part II

SCIENTIFIC CONTRIBUTIONS AND OUTLOOK

Observation of Local Symmetry in a Photonic System

Nora Schmitt, Steffen Weimann, Christian V. Morfonios, Malte Röntgen,
Matthias Heinrich, Peter Schmelcher, and Alexander Szameit*

The concept of local symmetry has been shown to be a powerful tool in predicting and designing complex transport phenomena in stationary scattering off aperiodic media, in terms of symmetry-adapted nonlocal currents. For time-evolving wavepackets, the spatiotemporal correlations caused by local symmetries are more challenging to reveal. A recent formalism-based nonlocal continuity equation shows how local symmetries are encoded into the dynamics of light propagation in discrete waveguide arrays governed by a Schrödinger equation. However, the experimental demonstration is elusive so far. Representative examples of locally symmetric, globally symmetric, and fully nonsymmetric configurations are fabricated in fs laser-written photonic arrays and their dynamics are probed. The approach allows to distinguish all three types of structures.

than quasicrystals,^[4,5] which can always be seen as the projection of a periodic lattice in higher dimensions, whereas the only condition for local symmetry is the existence of at least one spatial domain equipped with symmetry.^[1] Prominent examples include not only quasicrystals but also macromolecules^[6–8] and additionally systems where the global symmetry is broken because of defects or (partial) disorder.^[9,10] Moreover, local symmetries appear in artificial structures, for example, acoustic waveguides^[11,12] or tailored photonic multilayer systems,^[13,14] where they may lead to the occurrence of perfect transmission resonances.^[15]

Invariance with respect to a symmetry transformation is a fundamental concept

1. Introduction


Symmetry forms one of the cornerstones of describing and studying any physical system. This originates in the connection of symmetry operations to associated conserved quantities (see below), which simplify the theoretical treatment of the system. However, whereas the scenario of perfect global symmetries is only valid in an idealized, special class of systems without any imperfection or symmetry breaking and thus notoriously elusive, local symmetries^[1]—sometimes also referred to as hidden^[2] or internal^[3] symmetries—abound in nature. These configurations are characterized by internal spatial limitation as illustrated in **Figure 1**. The resulting new class of systems is more general

in physics, which is closely related to the formulation of conservation laws. For continuous transformations, E. Noether stated already in 1918 that, to every differentiable symmetry of the action of a physical system, there is a corresponding conservation law.^[16] Famous examples are momentum conservation due to the invariance of physical systems with respect to spatial translation, or energy conservation due to invariance with respect to time translation. Symmetry-induced conservation laws of discrete transformations can usually be described by means of the commutation of the corresponding operators with the Hamiltonian. As a consequence, reflection symmetry imposes definite parity, finite translation symmetry imposes Bloch momentum on the eigenstates of the Hamiltonian, characterizing the overall dynamics.

The Hamiltonian of a locally symmetric scenario does, in general, not commute with the local symmetry operation, even though the potential remains invariant under the respective transformation. Thus, the usual rules of symmetry-induced eigenvalues (e.g., parity and Bloch momenta) of common eigenstates do not apply. Therefore, tracking the influence of local symmetry on a system's behavior becomes challenging. A promising approach to decode the presence of underlying local symmetries from a system's state is given within a recently developed framework of symmetry-adapted, “nonlocal currents.”^[1,10,17–19] In the case of stationary states, these currents are constant within any local symmetry domain and provide an amplitude mapping between symmetry-related points.^[10,18] This generalizes the usual Bloch and parity theorems to local symmetry. Local symmetry domains are in general not unambiguously defined but may be chosen freely from a multitude of different accurate descriptions of the same system. For a general wavepacket, the nonlocal currents vary in space and time. Their translational invariance in 1D stationary states, however, indicate that their

N. Schmitt, Dr. S. Weimann, Dr. M. Heinrich, Prof. A. Szameit
Institute of Physics, University of Rostock
Albert-Einstein-Str. 23, 18059 Rostock, Germany
E-mail: alexander.szameit@uni-rostock.de

Dr. C. V. Morfonios, M. Röntgen, Prof. P. Schmelcher
Centre for Optical Quantum Technologies
University of Hamburg
Luruper Chaussee 149, 22761 Hamburg, Germany
Prof. P. Schmelcher
Hamburg Centre for Ultrafast Imaging
University of Hamburg
Luruper Chaussee 149, 22761 Hamburg, Germany

 The ORCID identification number(s) for the author(s) of this article can be found under <https://doi.org/10.1002/lpor.201900222>

© 2020 The Authors. Published by WILEY-VCH Verlag GmbH & Co. KGaA, Weinheim. This is an open access article under the terms of the Creative Commons Attribution License, which permits use, distribution and reproduction in any medium, provided the original work is properly cited.

DOI: 10.1002/lpor.201900222

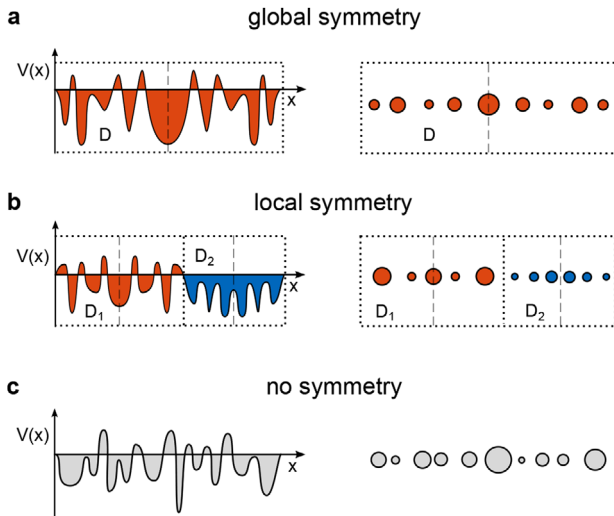


Figure 1. Possible gradations of symmetry of a continuous potential (left) and discrete sites (right). The positions of the symmetry axes are indicated by dashed lines. a) Global inversion symmetry with a single overall symmetry domain D (red). b) Locally symmetric system covered by two symmetry domains D_1 (red) and D_2 (blue). c) Fully nonsymmetric configuration.

general, time-dependent form may originate from a type of current-density continuity, in similarity to the case of the usual quantum probability current. The additional ingredient is here the local symmetry transformation in space, combined with the derivation of a conserved current. Indeed, the nonlocal currents have been shown to obey a generalized, (local) symmetry-adapted continuity equation,^[19] readily applicable to discrete models governed by a Schrödinger equation. However, the fact that this approach requires access to the full spatiotemporal information of the complex-valued wave function has thus far prevented any experimental demonstration. Given the extraordinary success of evanescently coupled photonic waveguide arrays in emulating dynamical discrete quantum systems of various kinds in recent years, they represent an ideal experimental platform to tackle the challenge of uncovering the spatiotemporal correlations caused by local symmetries.

2. Experimental Section

In this work, we distinguish locally symmetric structures with respect to a certain symmetry from both fully nonsymmetric systems and globally symmetric structures by means of the nonlocal continuity formalism. To address this challenge experimentally, we employ the femtosecond laser direct writing technique^[20] to fabricate representative examples of locally symmetric, globally symmetric, and fully nonsymmetric photonic lattices in fused silica glass wafers. For a first experimental demonstration and a proof of principle, a minimal system size of six to seven sites is chosen to decode underlying local symmetries from the generic state evolution in simple configurations. The symmetries were incorporated in the structures by appropriately tuning the waveguide separations and thus the coupling between adjacent sites in line with the desired distribution (see Figure 2 [insets top left] and Appendix). The refractive index increase was chosen to be

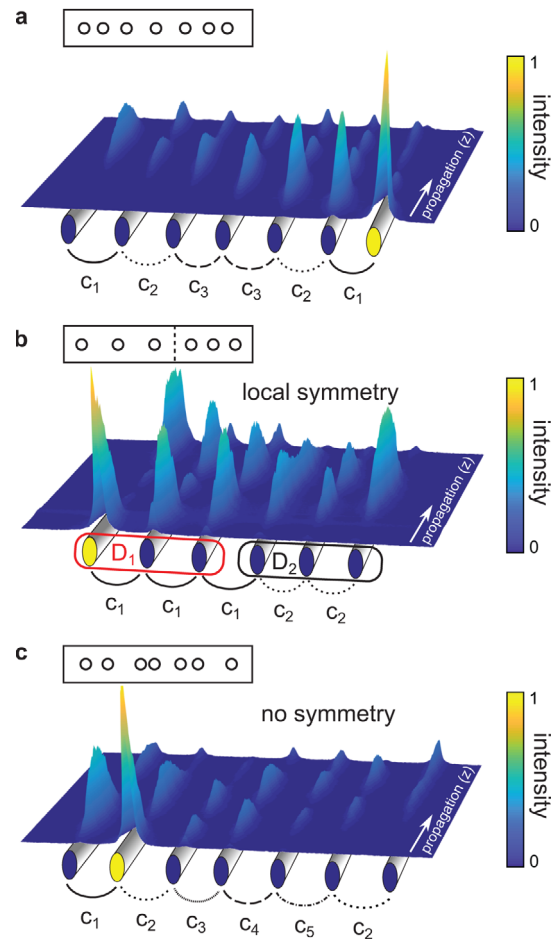


Figure 2. Measured fluorescence intensity patterns after single-waveguide excitation. a) Globally symmetric array, probed via single-site excitation of the seventh waveguide (marked yellow). The waveguide separations and couplings c_1, c_2, c_3 exhibit inversion symmetry. b) Locally symmetric array, probed via single-site excitation of the first waveguide. It can be divided into two domains D_1 and D_2 with inversion-symmetric configurations of the couplings c_1 and c_2 . c) Nonsymmetric array containing five different couplings c_1, c_2, c_3, c_4, c_5 , probed via single site excitation of the second waveguide. In each case, the inset on the top left illustrates the lattice geometries with highly exaggerated differences in spacings.

the same for all waveguides to achieve a system with equal on-site potential in order to preserve the phase relation of $\pi/2$ between adjacent waveguides (see Appendix), which is crucial for retrieving the full wave function from intensity-only fluorescence measurements of the light propagation in our waveguide arrays. The corresponding system dynamics over a propagation length of 70 mm was probed via coherent single-site excitation at 633 nm. As we see in Figure 2, the intensity patterns of the generic light propagation show no direct evidence for the presence or absence of local symmetries in the underlying array. In the following, we will show how a formalism of nonlocal currents can be used to decode the presence of symmetries from the propagating wave.

The complex wave function was extracted from the experimentally observed intensity pattern in accordance with the $\pi/2$ phase jump between adjacent sites and inferring zero crossings at every minimum close to zero (see Appendix). The assumption was

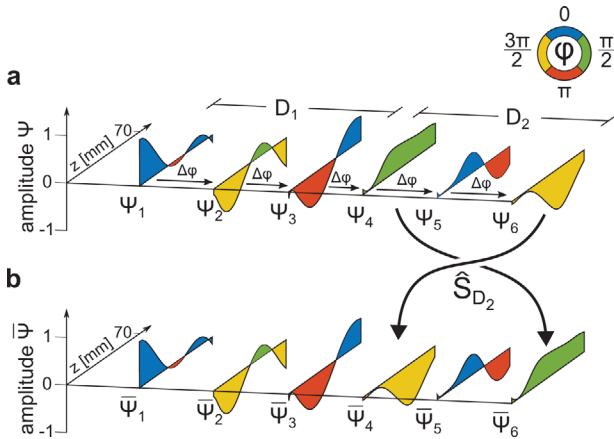


Figure 3. Relation between fit wave function ψ , local symmetry transformation \hat{S}_D and transformed wave function $\bar{\psi}$ of domain D_2 of the locally symmetric configuration. a) Evolution of the fit wave function in the entire system, with the phase φ encoded using the given colors. It consists of components ψ_{1-6} with a characteristic phase difference of $\Delta\varphi = -\pi/2$ between adjacent sites. b) Symmetry transformed wave function $\bar{\psi}$, obtained by the local symmetry transformation \hat{S}_{D_2} acting on the wave function in domain D_2 —naturally, \hat{S}_{D_2} acts trivially on the sites 1–3 in domain D_1 .

justified by tight-binding simulations of the state evolution in our waveguide arrays with the experimentally determined couplings. Thereafter, the wave function was fitted with a high-order polynomial in order to allow the calculation of meaningful derivatives. The resulting evolution of the wave function ψ in the locally symmetric system is exemplarily shown in **Figure 3a**.

3. Theory

To reveal the encoding of local symmetries in the state evolution, the discrete local current-density continuity^[21] for an arbitrary state $|\psi\rangle$ is generalized, taking a local symmetry transformation into account.^[19] Applying a transformation \hat{S}_D on any quantity—sites or states—is denoted by a bar above the symbol, for example, $\hat{S}_D|\psi\rangle = |\bar{\psi}\rangle$, which is illustrated in **Figure 3b**. The transformations may be represented by matrices (see insets in **Figure 4**) that interchange the amplitudes of symmetry related sites when they act on a quantity represented by a vector.

The local overall discrete probability density ρ_D distributed over the sites n in domain D is given by the expectation value of the local density operator $\hat{\rho}_n = |n\rangle\langle n|$.

$$\rho_D = \sum_{n \in D} \langle \psi | n \rangle \langle n | \psi \rangle = \sum_{n \in D} \psi_n^* \psi_n = \langle \psi_D | \psi_D \rangle \quad (1)$$

In the symmetry-adapted formulation, the local density operator $\hat{\rho}_n = |n\rangle\langle n|$ at each site n is replaced by $|n\rangle\langle \bar{n}|$. The total nonlocal charge Σ_D is calculated by taking the scalar product of the wave function and the symmetry-transformed wave function in the respective domain.^[19]

$$\Sigma_D := \sum_{n \in D} \langle \psi | n \rangle \langle \bar{n} | \psi \rangle = \sum_{n \in D} \psi_n^* \bar{\psi}_{\bar{n}} = \langle \psi_D | \bar{\psi}_D \rangle \quad (2)$$

“Nonlocal” refers to the influence of nonadjacent but symmetry-related sites on the respective quantity. Note that the only difference between Equations (1) and (2) is given by the symmetry transformation, denoted by a bar above the symbols. **Figure 3** illustrates how the local symmetry transformation \hat{S}_{D_2} acts on the wave function in domain D_2 of the locally symmetric system.

The discrete local probability current $j_{n,m}$ between sites n and m is given by [21]

$$j_{n,m} = -i(\psi_n^* c_{n,m} \psi_m - \psi_m^* c_{n,m}^* \psi_n) \quad (3)$$

where $c_{n,m}$ is the coupling between the adjacent sites n and $m = n \pm 1$. In the generalized case, the local current $j_{n,m}$ is replaced by the nonlocal (symmetry adapted) current $q_{n,m}$ ^[19]:

$$q_{n,m} = -i(\psi_n^* c_{\bar{n},\bar{m}} \bar{\psi}_{\bar{m}} - \bar{\psi}_{\bar{m}}^* c_{\bar{n},\bar{m}}^* \psi_n) \quad (4)$$

Again, the only modification from Equations (3) to (4) are the symmetry transformed sites \bar{n} and \bar{m} . For arrangements without on-site asymmetry in the refractive index distribution, a simple continuity equation relates the nonlocal charge Σ_D to the nonlocal boundary current $q_{\partial D}$, which is “flowing out of” each symmetry domain^[19] ($[a, \dots, b] \in D$):

$$\partial_z \Sigma_D = q_{a,a-1} + q_{b,b+1} = q_{\partial D} \quad (5)$$

where ∂_z is the derivative in propagation direction. Note that, in forming the boundary current elements of D , $q_{a,a-1}$ and $q_{b,b+1}$, the neighboring outer sites $a-1$ and $b+1$ are by convention also mapped by the local mirror operation corresponding to D , that is, $\bar{a-1} = b+1$ and $\bar{b+1} = a-1$. Also, the term “flows out of” should not obscure the fact that q does not describe a real flow of density between sites like in the usual current j , but rather a quantity adapted to local symmetry, with the breaking of symmetry (here at the boundary of D) acting as a source or sink for the symmetry-adapted current q . We will now use the above nonlocal continuity equation to distinguish local from global or no symmetry in the waveguide array.

The nonlocal boundary current vanishes identically for an even number of sites in one domain of our specific tight-binding Schrödinger system with equal on-site potential and single-site excitation (see Appendix). However, equal on-site potential and initial single-site excitation lead to a well defined phase relation of $\pi/2$ between adjacent sites, which is a necessary condition to retrieve the full wave function from intensity-only fluorescence measurements. Thus, we investigate only domains with an odd number of sites (indices from a to b) to allow for a distinction between global and local symmetry. For global and local symmetry, the boundary currents $q_{\partial D}$ are given by (see Appendix):

$$q_{\partial D} = \pm 2(c_{b,b+1} |\psi_a| |\psi_{b+1}| \mp c_{a,a-1} |\psi_b| |\psi_{a-1}|) \quad (6)$$

Due to the fact that the symmetry domain extends over the entire system for all globally inversion symmetric systems, there is inherently no coupling across domain boundaries. Since then $c_{b,b+1} = c_{a,a-1} = 0$ by definition, the nonlocal boundary current vanishes identically for global symmetry. Nevertheless, the

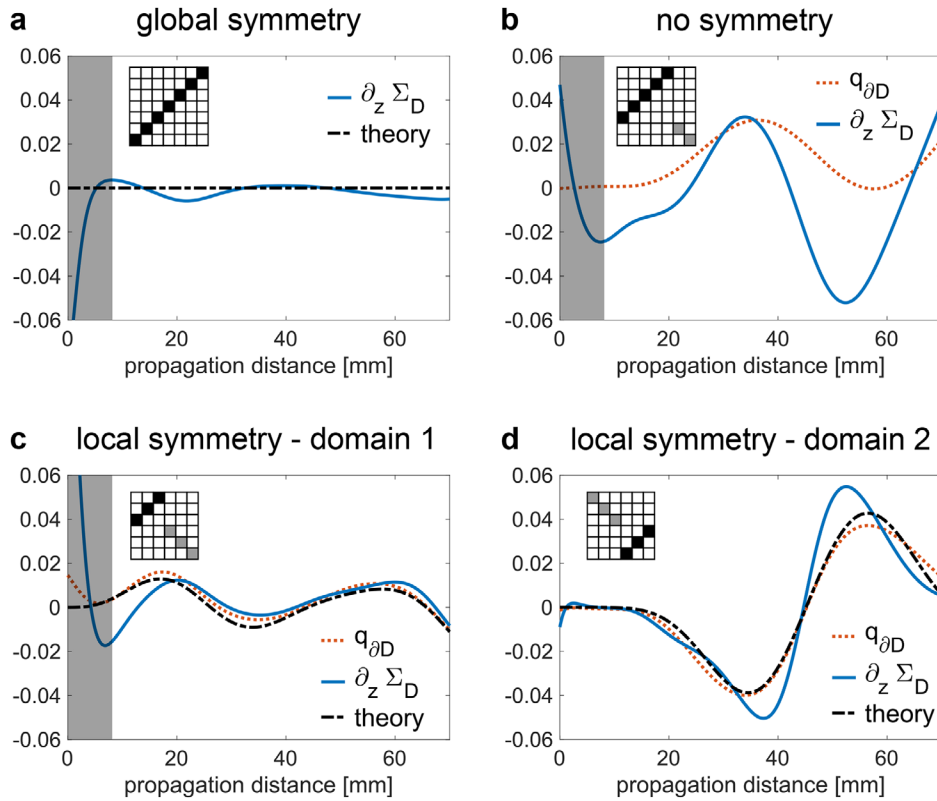


Figure 4. Measurement-based nonlocal continuity equations. a) Global inversion symmetry. The assumed symmetry transformation is given by an anti-diagonal matrix (top left). As the nonlocal boundary currents are vanishing, the derivative of the nonlocal charge $\partial_z \Sigma_D$ along the propagation (solid blue) is compared to the expected value of zero (dashed black). b) In case of no symmetry, there are no valid symmetry transformations. Any transformation can be chosen and shown to violate the continuity equation because $\partial_z \Sigma_D$ (solid blue) and the nonlocal boundary current $q_{\partial D}$ (dotted orange) deviate. c) Local symmetry: $q_{\partial D}$ (dotted orange) is nearly equal to $\partial_z \Sigma_D$ (solid blue), as predicted (dashed black) by the continuity equation. The results shown are taken from the measurements in domain D_1 of the locally symmetric structure. d) Same as (c), but for domain D_2 of our locally symmetric arrangement. Because of measurement-induced deviations, the first few millimeters of propagation, where light is coupled into the structure, are shaded in gray in (a)–(c). In (d), light is coupled into the other domain of the structure; thus there is no shaded part.

continuity equation is still fulfilled, leading to a vanishing derivative of the nonlocal charge.

In contrast to the locally and globally symmetric configurations, the fully nonsymmetric system by definition is entirely devoid of symmetry domains. Any arbitrary transformation can be chosen and proven not to be a (local) symmetry transformation by showing a violation of the continuity equation. As a result, globally symmetric, locally symmetric, and fully nonsymmetric configurations may be distinguished by means of the different forms of their corresponding nonlocal continuity equation:

$$\text{Global symmetry: } \partial_z \Sigma_D = q_{\partial D} = 0$$

$$\text{Local symmetry: } \partial_z \Sigma_D = q_{\partial D} \quad (7)$$

$$\text{No symmetry: } \partial_z \Sigma_D \neq q_{\partial D}$$

4. Results

To evaluate the continuity equation in the three different experimental configurations, the nonlocal charges, their derivatives and the nonlocal currents were subsequently calculated from the fit wave function, symmetry transformation and couplings.

In case of global symmetry, the symmetry operation may be described by the anti-diagonal matrix shown on the top left of Figure 4a. Because $q_{\partial D}$ is identically zero, it is sufficient to calculate the derivative of the nonlocal charge $\partial_z \Sigma_D$ from the experimental data and compare the result to the expected value of zero. Our experiments and calculations show that the nonlocal continuity equation is fulfilled and indeed vanishing for the globally symmetric configuration (Figure 4a). In fact, the deviation of $\partial_z \Sigma_D$ from zero for global symmetry may serve as a measure of the validity of our method to retrieve the wave function. Note that the substantial deviations during the first few millimeters of propagation are an artefact of the measurement method. In order to observe the intensity propagation pattern, we employed a fluorescence method that converts a small fraction of the propagating light into omnidirectional light. Although light was injected into the respective waveguide by focusing a laser beam down to an appropriate spot size, the nonunity overlap between focal spot and mode field results in the presence of stray background light that propagates through the sample and may likewise excite fluorescence whenever it traverses a waveguide, and thereby distort the observed pattern. Since this systematic perturbation rapidly dissipates, the subsequent evolution and the $\partial_z \Sigma_D$ extracted from it coincides remarkably well with the expected behavior. In the

further evolution, $\partial_z \Sigma_D$ is remarkably close to the expected value of zero.

The locally symmetric system is divided into two inversion symmetric domains—each containing three sites (see Figure 2b). In Figure 4, the nonlocal current and derivative of the nonlocal charge extracted from the experiment are shown for domain D_1 (c) and D_2 (d), with corresponding antidiagonal blocks in the used transformation matrix $S_{D_{1,2}}$ (see top left insets). Apart from the first few millimeters, the components of the nonlocal continuity equation for the locally symmetric system are in good agreement with the theoretical value as well as with each other. In the second symmetry domain of the locally symmetric system, the extrema of the experimentally determined derivative of the nonlocal charge $\partial_z \Sigma_D$ appear slightly displaced and exaggerated compared to the extracted nonlocal boundary current $q_{\partial D}$ and the theoretical value. We attribute this feature to the method of flipping the extracted wave function amplitude around zero, which may exaggerate the slope of the zero transitions, as well as to the naturally much higher sensitivity of the derivative to small perturbations. Considering the overall evolution measured, though, our results provide clear evidence that the nonlocal continuity equation is fulfilled in both local symmetry domains.

To demonstrate the violation of the nonlocal continuity equation in the fully nonsymmetric system, an exemplary inversion operation of the first five sites (Figure 4b, top left) is used. The experimentally observed evolution of the nonlocal boundary current $q_{\partial D}$ deviates drastically overall from the evolution of the derivative of the nonlocal charge $\partial_z \Sigma_D$. To explicitly prove that the system is fully nonsymmetric, one would need to show a violation of the continuity equation for all possible transformations. This was done for all possible inversion symmetries with an odd number of sites (see Appendix).

5. Conclusions

In conclusion, we investigated three arrangements with different gradations of symmetry—global, local, and fully nonsymmetric—in laser-written waveguide arrays, employing the nonlocal continuity approach. We thereby decoded the presence of local symmetries in the Hamiltonian from the generic dynamics of wavepackets in a discrete system. We were able to verify the nonlocal continuity equation and to distinguish the three different classes of symmetry by means of their characteristic version of the nonlocal continuity equation.

More generally, based on a novel generalized framework of nonlocal continuity equations, in the present manuscript, we provide the very first experimental evidence of how local symmetries are encoded into the dynamical evolution of a generic wavefunction—although they are hidden from “direct” observa-

tion. Already this is an unprecedented achievement in approaching the fundamental problem of local symmetries and, while not providing a direct technological application at this early stage, it represents the first step in a completely new direction of future research: Namely, to harness the knowledge of the hidden encoding of local symmetries in the dynamical evolution in order to understand and in turn manipulate it within a large variety of (discrete or, as an extension, continuous) wave-mechanical systems. As an example, an interesting setup where local symmetries are inherently present is the random dimer model and its extended versions.^[22] A combination of the nonlocal continuity framework and the spatiotemporal correlations revealed in the wavepacket evolution with, for example, localization measures in (partially) disordered systems yields an exciting direction of future research beyond the fundamental demonstration of the present work.

Finally, while here demonstrated for the case of inversion symmetry in 1D, the same formalism can be readily applied to other symmetry transformations and extended to higher dimensions. The subject offers various possibilities for further experiments, for example, the engineering of perfect transmission resonances^[15] or Floquet states in periodically driven setups,^[19,23] as well as locally symmetric non-Hermitian systems.^[19,24] Our results constitute the first step in investigating local symmetries in photonic systems and harnessing them to shape the flow of light.

Appendix A: System Geometries

The globally inversion symmetric system consists of seven waveguides (see Figure A1) that are symmetric about the fourth waveguide. Three different separations d_{1-3} and thus three different couplings c_{1-3} are present in the array. The geometry chosen for the locally inversion symmetric system is shown in Figure A2. The configuration consists of six waveguides (sites), which can be divided into two symmetry domains both containing three waveguides. The nonsymmetric system is designed such that it cannot be divided into connected symmetry domains at all, except for trivial domains containing only two sites (i.e., a single coupling), which can always be defined in any system. The geometry of the arrangement is presented in Figure A3. Overall, it contains seven waveguides separated by five different distances between 17 and 21 μm , constructed to maximize the difference in separation between three neighboring sites.

The three experimental setups have been fabricated, adjusting the separation between the waveguides to the desired symmetry. To avoid the phase modulations that go along with detuning in the systems, the writing speed was kept constant during the inscription within each array. For characterization purposes, directional couplers with the same separations were written directly next to the arrays. As the laser parameters may be assumed to stay constant during the inscription of the entire system, the couplers

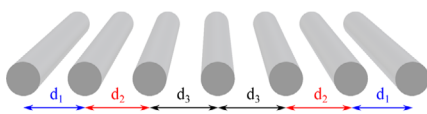
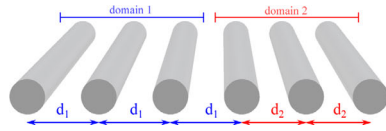


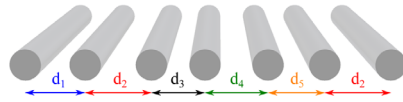
Figure A1. Sketch of the globally inversion symmetric waveguide array. It consists of seven identical waveguides with three different distances d_{1-3} between them. In the center, the separation is larger than on both outer parts. The different distances lead to different couplings c_{1-3} , which are weak in the center and stronger at the edges.

$$\begin{aligned} d_1 &= 18 \mu\text{m} & c_1 &= 0.074 \text{ mm}^{-1} \\ d_2 &= 19 \mu\text{m} & c_2 &= 0.058 \text{ mm}^{-1} \\ d_3 &= 20 \mu\text{m} & c_3 &= 0.050 \text{ mm}^{-1} \end{aligned}$$



$$\begin{aligned} d_1 &= 20 \mu\text{m} & c_1 &= 0.073 \text{ mm}^{-1} \\ d_2 &= 18 \mu\text{m} & c_2 &= 0.099 \text{ mm}^{-1} \end{aligned}$$

Figure A2. Sketch of the locally inversion symmetric waveguide array. It consists of two symmetry domains, each containing three waveguides. In the entire system, there are only two different separations (couplings) $d_{1,2}$ ($c_{1,2}$). Within each domain, the waveguide separation is constant.



$$\begin{aligned} d_1 &= 19 \mu\text{m} & c_1 &= 0.058 \text{ mm}^{-1} \\ d_2 &= 21 \mu\text{m} & c_2 &= 0.041 \text{ mm}^{-1} \\ d_3 &= 17 \mu\text{m} & c_3 &= 0.088 \text{ mm}^{-1} \\ d_4 &= 20 \mu\text{m} & c_4 &= 0.050 \text{ mm}^{-1} \\ d_5 &= 18 \mu\text{m} & c_5 &= 0.074 \text{ mm}^{-1} \end{aligned}$$

Figure A3. Sketch of the nonsymmetric waveguide array. It consists of seven waveguides and cannot be divided into nontrivial symmetry domains. Five different separations between adjacent waveguides lead to five different couplings.

directly exhibit the couplings present in the array under investigation.

Appendix B: Wave Function Evolution for Constant Onsite Potential upon Single-Site Excitation

We here provide a proof of the $\pi/2$ phase difference between the time-dependent wavefunction amplitude on adjacent sites for a tight-binding chain with constant onsite potential and arbitrary couplings, upon excitation of a single site. It is well known that this system possesses the so-called chiral (also referred to as particle-hole) symmetry.^[25] In particular, for zero onsite potential, the energy spectrum is symmetric around $E = 0$, that is, for each eigenenergy E_ν , $-E_\nu$ is also an eigenenergy. Further, the amplitudes of the corresponding (real) eigenfunctions ϕ^ν at site $n = 1, \dots, N$ are related as $\phi_n^{-\nu} = (-1)^n \phi_n^\nu$, where the eigenstates are labeled by $\nu = -N/2, \dots, -1, 1, \dots, N/2$ $\{\nu = -(N-1)/2, \dots, -1, 0, 1, \dots, (N-1)/2\}$ for even $\{\text{odd}\}$ number of sites N . Note that, for odd N , there is a “zero” mode with $E_0 = 0$ and eigenstate amplitude vanishing on even sites, $\phi_{2m}^0 = 0$ with $m = 1, \dots, (N-1)/2$.

Upon a unit excitation $|s\rangle$ on site s , so that $\langle n|s\rangle = \delta_{ns}$, the time-dependent wavefunction at site n is expanded over the eigenmodes as

$$\psi_n(t) = \langle n|\psi(t)\rangle = \langle n|e^{-iHt}|s\rangle \quad (\text{B1})$$

$$= \sum_{\pm\nu=1}^M \langle n|e^{-iE_\nu t}|\phi^\nu\rangle \langle \phi^\nu|s\rangle \{+\langle n|e^{-iE_0 t}|\phi^0\rangle \langle \phi^0|s\rangle\} \quad (\text{B2})$$

$$= \sum_{\nu=1}^M [e^{-iE_\nu t} + (-1)^{n+s} e^{iE_\nu t}] \phi_n^\nu \phi_s^\nu \{+\phi_n^0 \phi_s^0\} \quad (\text{B3})$$

where $M = \frac{N}{2} \{\frac{N-1}{2}\}$ for even $\{\text{odd}\}$ N and the term $\{+\dots\}$ is added only for odd N . In the last step, the properties of the amplitudes due to chiral symmetry, stated above, are taken into account (for zero onsite potential). This yields a real amplitude

$$\psi_n(t) = \sum_{\nu=1}^M 2 \cos(E_\nu t) \phi_n^\nu \phi_s^\nu \{+\phi_n^0 \phi_s^0\} \in \mathbb{R} \quad (\text{B4})$$

for even $n+s$ (that is, n and s both even or both odd), and an imaginary amplitude

$$\psi_n(t) = -\sum_{\nu=1}^M 2i \sin(E_\nu t) \phi_n^\nu \phi_s^\nu \in i\mathbb{R} \quad (\text{B5})$$

for odd $n+s$ (that is, n or s even and the other odd). Thus, for a given input site s , the amplitudes on any adjacent sites $n, n+1$ will have phase difference $\pi/2$,

$$\frac{\psi_{n+1}(t)}{\psi_n(t)} = \pm i \frac{|\psi_{n+1}(t)|}{|\psi_n(t)|} = e^{\pm \frac{\pi}{2}} \frac{|\psi_{n+1}(t)|}{|\psi_n(t)|} \quad (\text{B6})$$

Clearly, this remains true also for a nonzero constant onsite potential V , for which the above wavefunction $\psi_n(t)$ is simply multiplied by an overall dynamical phase e^{-iVt} .

Naturally, in the experiment, slight deviations from the assumed tight-binding model with constant onsite potential are present and affect the amplitudes as well as the phases of the wave function. However, due to the high precision and reproducibility of the waveguide fabrication process,^[20] these detunings between the propagation constants of the individual sites are so small that they are hardly recognizable in the overall experimental evolution.

Appendix C: Wave Function Retrieval from Intensity Distribution

In order to extract the generally complex amplitudes from the intensity distribution along the propagation, one can use the fact that the phase difference between adjacent sites is given by $-\pi/2$ for an initial single-site excitation, as long as the assumed theoretical model with the applied approximations is valid. Along the propagation, the phase at any site is only changing by π , which corresponds to a change from positive to negative values or vice versa. This zero crossing along the propagation only occurs at zero intensity. In the investigated systems, every zero in intensity is assumed to be zero crossing in amplitude, which is justified by tight binding simulations. They confirm that in the particular systems, the amplitudes do not only touch but indeed cross zero. In

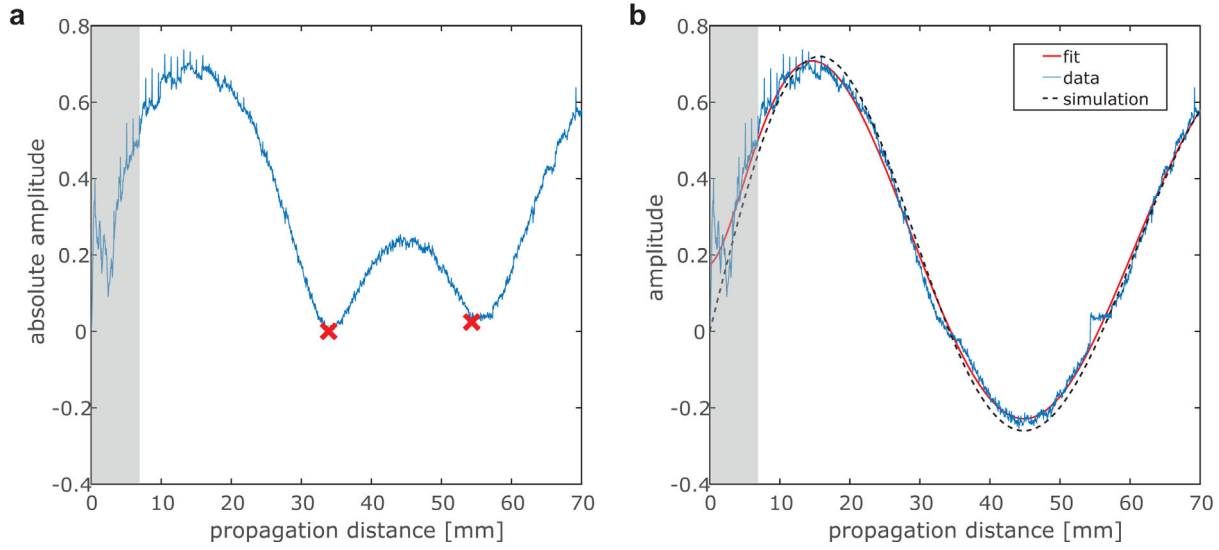


Figure C1. Example of the retrieval of the full fit wave function from the absolute amplitude at site two of the locally symmetric system. a) The minima close to zero of the absolute value of the amplitude along the propagation are found. They are indicated by a red cross. b) The amplitude is flipped at these minima and fit with an eighth-order polynomial. A comparison to a tight binding simulation of the system using the MATLAB ode45 solver is given.

the experiment, there is an offset to the intensity. To extract the zero crossings, all minima close to zero are taken into account.

The amplitudes are flipped at every minimum close to zero (exemplarily shown in Figure C1). Then the data is fit with a high-order polynomial, because the derivative, which is needed for the continuity equations, can be more easily obtained from a smooth function than from the raw data. Finally, the known initial condition in phase is applied to the fit function at one centimeter of propagation, where there is already a significant amplitude value in each waveguide but still no zero crossing expected to happen. The resulting fit wave function for all sites of the locally symmetric system can be seen in Figure 3a.

Appendix D: Nonlocal Boundary Current

In a domain that exhibits inversion symmetry in our 1D tight-binding Schrödinger system with equal on-site potential that consists of N sites (indices from a to b in any larger array), the boundary currents are given by

$$\begin{aligned}
 q_{\partial D} &= q_{a,a-1} + q_{b,b+1} = -i \left(\psi_a^* c_{a,a-1}^- \psi_{a-1} - \psi_{a-1}^* c_{a,a-1}^* \psi_a \right) \\
 &\quad - i \left(\psi_b^* c_{b,b+1}^- \psi_{b+1} - \psi_{b+1}^* c_{b,b+1}^* \psi_b \right) \\
 &= -i \left(\psi_a^* c_{b,b+1} \psi_{b+1} - \psi_{b+1}^* c_{a,a-1} \psi_a \right) \\
 &\quad - i \left(\psi_b^* c_{a,a-1} \psi_{a-1} - \psi_{a-1}^* c_{b,b+1} \psi_b \right)
 \end{aligned} \tag{D1}$$

Assuming real couplings $c_{n,m} = c_{n,m}^*$:

$$q_{\partial D} = -i \left(c_{b,b+1} (\psi_a^* \psi_{b+1} - \psi_{b+1}^* \psi_a) - c_{a,a-1} (\psi_{a-1}^* \psi_b - \psi_b^* \psi_{a-1}) \right) \tag{D2}$$

Depending on the phase difference between the site amplitudes (that is always $\frac{\pi}{2}$ between neighboring sites), there are two different possibilities as follows.

D.1. Odd Number of Sites

For an odd number of sites in one symmetry domain, the phase difference between ψ_{a-1} and ψ_b and also the phase difference between ψ_a and ψ_{b+1} is always an odd multiple of $\frac{\pi}{2}$, leading to

$$\psi_{a-1}^* \psi_b = |\psi_b| |\psi_{a-1}| e^{i \frac{2z-1}{2} \pi} \quad z \in \mathbb{Z} \tag{D3}$$

$$\psi_{a-1} \psi_b^* = (\psi_{a-1}^* \psi_b)^* = |\psi_b| |\psi_{a-1}| e^{-i \frac{2z-1}{2} \pi} \tag{D4}$$

As a result, equation D2 reduces to

$$\begin{aligned}
 q_{\partial D} &= -i c_{b,b+1} (|\psi_a| |\psi_{b+1}| (e^{i \frac{2z-1}{2} \pi} - e^{-i \frac{2z-1}{2} \pi})) \\
 &\quad - i c_{a,a-1} (|\psi_b| |\psi_{a-1}| (e^{i \frac{2y-1}{2} \pi} - e^{-i \frac{2y-1}{2} \pi})) \\
 &= 2c_{b,b+1} \left(|\psi_a| |\psi_{b+1}| \sin \left(\frac{2z-1}{2} \pi \right) \right) \\
 &\quad - 2c_{a,a-1} \left(|\psi_b| |\psi_{a-1}| \left(\sin \left(\frac{2y-1}{2} \pi \right) \right) \right) \\
 &= \pm 2 \left(c_{b,b+1} (|\psi_a| |\psi_{b+1}|) \mp c_{a,a-1} (|\psi_b| |\psi_{a-1}|) \right) \\
 &\quad \text{with sign}(s) \text{ depending on } z, y \in \mathbb{Z}
 \end{aligned} \tag{D5}$$

D.2. Even Number of Sites

For an even number of sites in one symmetry domain, the phase difference between ψ_{a-1} and ψ_b and also the phase difference between ψ_a and ψ_{b+1} is always an even multiple of $\frac{\pi}{2}$, leading to

$$\psi_{a-1}^* \psi_b = |\psi_b| |\psi_{a-1}| e^{iz\pi} \quad z \in \mathbb{Z} \quad (D6)$$

$$= 2 \left(c_{b,b+1} (|\psi_a| |\psi_{b+1}| \sin(z\pi)) \right)$$

$$\psi_{a-1} \psi_b^* = (\psi_{a-1}^* \psi_b)^* = |\psi_b| |\psi_{a-1}| e^{-iz\pi} \quad (D7)$$

$$-c_{a,a-1} (|\psi_b| |\psi_{a-1}| (\sin(\gamma\pi))) = 0, z, \dots \gamma \in \mathbb{Z} \quad (D8)$$

As a result, equation D2 reduces to

$$q_{\partial D} = -ic_{b,b+1} (|\psi_a| |\psi_{b+1}| (e^{iz\pi} - e^{-iz\pi})) - ic_{a,a-1} (|\psi_b| |\psi_{a-1}| (e^{i\gamma\pi} - e^{-i\gamma\pi}))$$

Appendix E: Nonsymmetric System

To explicitly prove that the system is fully nonsymmetric, we show in Figure E1 the violation of the continuity equation for all

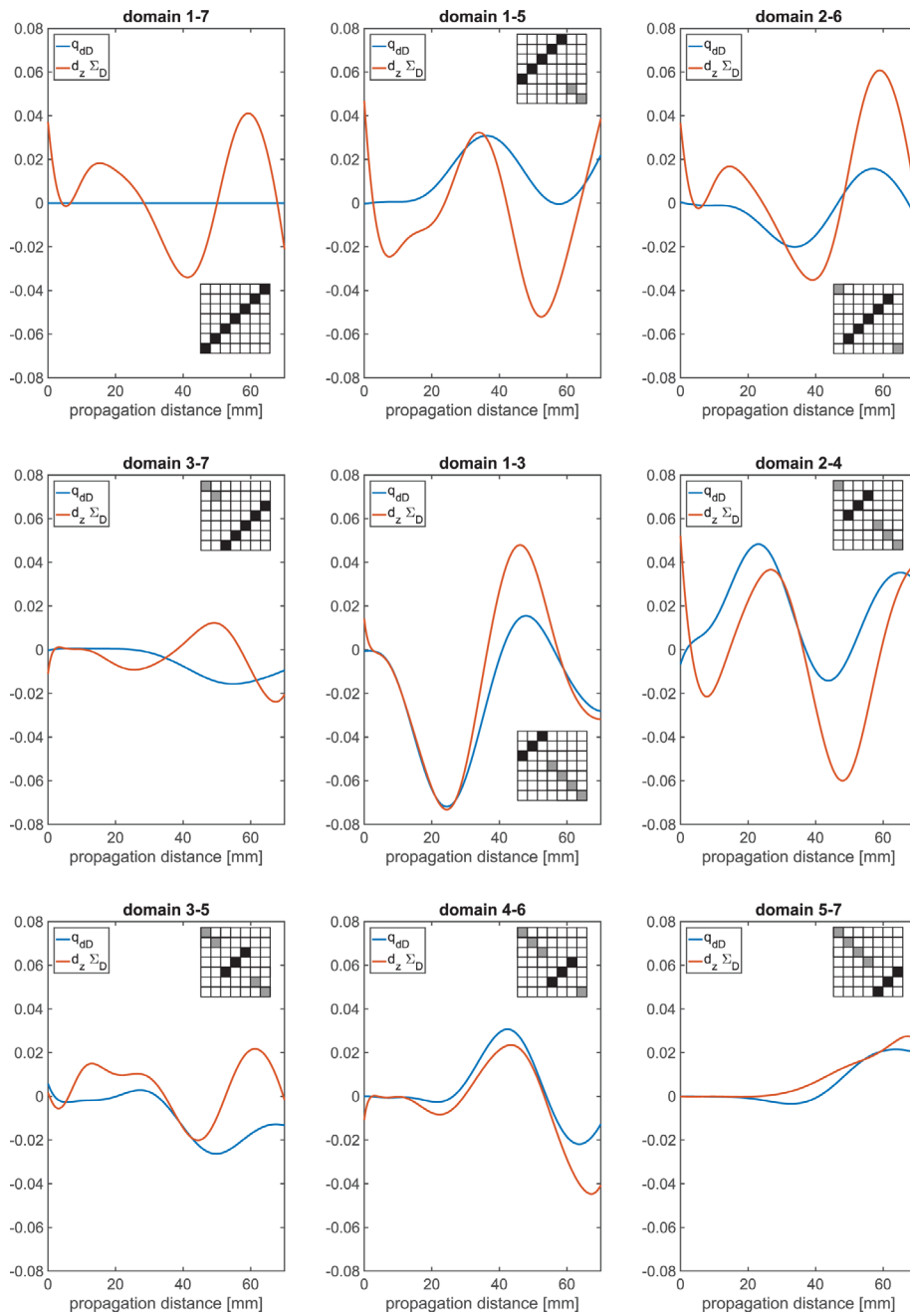


Figure E1. Measurement-based $q_{\partial D}$ and $\partial_z \Sigma_D$ for an assumed inversion symmetry of the nine possible different domains with an odd number of sites. Applied transformations given by inset matrices.

domains with an odd number of sites by comparing the measurement based quantities $q_{\partial D}$ and $\partial_z \Sigma_D$ for an assumed inversion symmetry.

Acknowledgements

The authors gratefully acknowledge financial support from the Deutsche Forschungsgemeinschaft (grants Schm 885/29-1, SZ 276/9-1, SZ 276/12-1, BL 574/13-1, SZ 276/15-1, SZ 276/19-1, and SZ 276/20-1) and the Alfried Krupp von Bohlen und Halbach Foundation. M.R. thanks the “Stiftung der deutschen Wirtschaft” for financial support in the framework of a scholarship. The authors would also like to thank C. Otto for preparing the high-quality fused silica samples used in all experiments presented here.

Conflict of Interest

The authors declare no conflict of interest.

Keywords

integrated optics, quantum optics, waveguides

Received: July 3, 2019

Revised: October 11, 2019

Published online: March 16, 2020

-
- [1] P. A. Kalozoumis, C. Morfonios, F. K. Diakonon, P. Schmelcher, *Phys. Rev. A* **2013**, *87*, 032113.
 [2] R. Nava, J. Tagüeña-Martínez, J. del Río, G. Naumis, *J. Phys.: Condens. Matter* **2009**, *21*, 155901.
 [3] X. Huang, S. Jiang, R. Peng, A. Hu, *Phys. Rev. B* **2001**, *63*, 245104.

- [4] D. Shechtman, I. Blech, D. Gratias, J. Cahn, *Phys. Rev. Lett.* **1984**, *53*, 1951.
 [5] D. Levine, P. Steinhardt, *Phys. Rev. Lett.* **1984**, *53*, 2477.
 [6] S. Domagała, C. Jelsch, *J. Appl. Crystallogr.* **2008**, *41*, 1140.
 [7] R. Pascal, *J. Phys. Chem. A* **2001**, *105*, 9040.
 [8] J. Echeverría, A. Carreras, D. Casanova, P. Alemany, S. Alvarez, *Chem. - Eur. J.* **2010**, *17*, 359.
 [9] P. Wochner, C. Gutt, T. Autenrieth, T. Demmer, V. Bugaev, A. Ortiz, A. Duri, F. Zontone, G. Grübel, H. Dosch, *Proc. Natl. Acad. Sci. USA* **2009**, *106*, 11511.
 [10] P. A. Kalozoumis, C. Morfonios, F. K. Diakonon, P. Schmelcher, *Phys. Rev. Lett.* **2014**, *113*, 050403.
 [11] P. A. Kalozoumis, O. Richoux, F. K. Diakonon, G. Theocharis, P. Schmelcher, *Phys. Rev. B* **2015a**, *92*, 014303.
 [12] A. C. Hladky-Hennion, J. O. Vasseur, S. Degraeve, C. Granger, M. de Billy, *J. Appl. Phys.* **2013**, *113*, 154901.
 [13] S. Zhukovsky, *Phys. Rev. A* **2010**, *81*, 053808.
 [14] R. Peng, X. Huang, F. Qiu, M. Wang, A. Hu, S. Jiang, M. Mazzer, *Appl. Phys. Lett.* **2002**, *80*, 3063.
 [15] P. A. Kalozoumis, C. Morfonios, N. Palaiodimopoulos, F. K. Diakonon, P. Schmelcher, *Phys. Rev. A* **2013b**, *88*, 033857.
 [16] E. Noether, *Mathematisch-Physikalische Klasse.* **1918**, *1918*, 235. <https://eudml.org/doc/59024>.
 [17] P. A. Kalozoumis, C. V. Morfonios, F. K. Diakonon, P. Schmelcher, *Ann. Phys.* **2015b**, *362*, 684.
 [18] M. Röntgen, C. V. Morfonios, F. K. Diakonon, P. Schmelcher, *Ann. Phys.* **2017**, *380*, 135.
 [19] C. V. Morfonios, P. A. Kalozoumis, F. K. Diakonon, P. Schmelcher, *Ann. Phys.* **2017**, *385*, 623.
 [20] A. Szameit, S. Nolte, *J. Phys. B: At., Mol. Opt. Phys.* **2010**, *43*, 163001.
 [21] T. B. Boykin, M. Luisier, G. Klimeck, *Eur. J. Phys.* **2010**, *31*, 1077.
 [22] D. López-González, M. I. Molina, *Phys. Rev. E* **2016**, *93*, 032205.
 [23] T. Wulf, C. V. Morfonios, F. K. Diakonon, P. Schmelcher, *Phys. Rev. E* **2016**, *93*, 052215.
 [24] P. A. Kalozoumis, C. V. Morfonios, F. K. Diakonon, P. Schmelcher, *Phys. Rev. A* **2016**, *93*, 063831.
 [25] H. E. Kondakci, A. F. Abouraddy, B. E. A. Saleh, *Nat. Phys.* **2015**, *11*, 930.

Local symmetry theory of resonator structures for the real-space control of edge states in binary aperiodic chains

M. Röntgen,^{1,*} C. V. Morfonios,¹ R. Wang,² L. Dal Negro,^{2,3,4} and P. Schmelcher^{1,5}

¹Zentrum für optische Quantentechnologien, Universität Hamburg, Luruper Chaussee 149, 22761 Hamburg, Germany

²Department of Electrical and Computer Engineering and Photonics Center, Boston University, Boston, Massachusetts 02215, USA

³Department of Physics, Boston University, Boston, Massachusetts 02215, USA

⁴Department of Material Science and Engineering, Boston University, Boston, Massachusetts 02215, USA

⁵The Hamburg Centre for Ultrafast Imaging, Universität Hamburg, Luruper Chaussee 149, 22761 Hamburg, Germany



(Received 18 July 2018; revised manuscript received 26 October 2018; published 3 June 2019)

We propose a real-space approach explaining and controlling the occurrence of edge-localized gap states between the spectral quasibands of binary tight binding chains with deterministic aperiodic long-range order. The framework is applied to the Fibonacci, Thue-Morse, and Rudin-Shapiro chains, representing different structural classes. Our approach is based on an analysis of the eigenstates at weak intersite coupling, where they are shown to generically localize on locally reflection-symmetric substructures, which we call local resonators. A perturbation theoretical treatment demonstrates the local symmetries of the eigenstates. Depending on the degree of spatial complexity of the chain, the proposed local resonator picture can be used to predict the occurrence of gap-edge states even for stronger couplings. Moreover, we connect the localization behavior of a given eigenstate to its energy, thus providing a quantitative connection between the real-space structure of the chain and its eigenvalue spectrum. This allows for a deeper understanding, based on local symmetries, of how the energy spectra of binary chains are formed. The insights gained allow for a systematic analysis of aperiodic binary chains and offers a pathway to control structurally induced edge states.

DOI: [10.1103/PhysRevB.99.214201](https://doi.org/10.1103/PhysRevB.99.214201)

I. INTRODUCTION

Aperiodic systems with deterministic long-range order have long been a subject of intense study, in the endeavor to systematically bridge the gap between crystalline periodicity and complete disorder [1]. While providing a powerful concept in theoretically modeling the transition to disorder, aperiodic order has become an established property of matter as well. A cornerstone of this was the actual observation of “quasicrystals”—nonperiodic but space-filling structures surpassing the crystallographic restriction theorem—by Shechtman [2]. In nature quasiperiodicity occurs, e.g., in macroscopic constellations such as phyllotaxis [1,3]. Aperiodically ordered systems even play an important role in material science and technology [1,4]. Owing to their long-range order, they can display interesting physical properties such as a low electrical and thermal conductance [1,5], low friction [5,6], and high hardness [6]. Specific quasicrystalline systems have been shown to enhance solar cells [7], serve as a catalyst [8] and could allow for superconductivity [9,10].

A general characteristic of aperiodic lattices is the clustering of Hamiltonian eigenvalues into so-called “quasibands” resembling Bloch bands of periodic systems [11]. The corresponding eigenstates generally neither extend homogeneously across the system like Bloch states in regular crystals, nor do they decay exponentially like in disordered systems, and are therefore dubbed “critical” [1,12–15]. In specific cases,

quasibands have been shown to originate from the localization of different eigenstates on similar repeated substructures in the system, yielding similar eigenenergies [16–20]. The formation of quasibands typically becomes less distinct with increasing spatial complexity, which in turn can be classified by the structure’s spatial Fourier transform—accordingly altering from pointlike to singular continuous to absolutely continuous [1,21–23]. The Fourier spectrum can further be connected to the system’s integrated density of states by the “gap labeling theorem” [24–28], which assigns characteristic integers to the gaps between quasibands.

As ordered lattice systems are truncated in space into finite setups, they may support the occurrence of eigenstates localized along their edges, energetically lying within spectral gaps. In periodic systems, such *edge states* (or “surface states” [29]) may or may not appear depending on how the underlying translation symmetry is broken by the lattice truncation, that is, where in the unit cell the system is cut off [30]. In various types of periodic setups, edge states can also be given a topological origin in terms of nontrivially valued invariants (winding numbers) assigned to the neighboring Bloch bands [31]. This has boosted an intensive research activity in the field of topological insulators [32–34] and the quest for interesting novel materials and applications [35], including, e.g., robust lasing via topological edge states in periodic photonic lattices [36].

Edge states may also be present between quasibands in aperiodic systems, as has been shown for binary 1D systems [37–41] and recently demonstrated for 2D photonic quasiperiodic tilings [18]. Notably, also here a topological

*mroentge@physnet.uni-hamburg.de

character can be assigned to the edge states in correspondence to the system's bulk properties. Indeed, a position-space based topological invariant, the so-called Bott index [42], can be applied to aperiodically structured [18] or even amorphous systems [43]. Moreover, for 1D quasiperiodic systems, the winding of edge state eigenvalues across spectral gaps coincide with the gap labels mentioned above [24,44–46], which have recently also been measured in scattering [47] and diffraction [48] experiments. Remarkably, edge modes occur also as scattering resonances in open systems with different types of deterministic aperiodic order incorporating long-range couplings between lattice constituents, as demonstrated very recently in terms of the eigenmodes of full vectorial Green matrices [49].

The ubiquitous presence of edge states in aperiodic systems indicates that it derives primarily from the underlying geometrical structure and not from model-specific assumptions. Departing from periodicity, however, there is no translation symmetry whose breaking (at the boundary) would provide a mechanism for edge state formation. On the other hand, aperiodic systems are imbued with *local* symmetries, that is, different spatially symmetric substructures are simultaneously present in the composite system which possesses many different domains of local symmetries. Indeed, local “patterns” are known to occur repeatedly in deterministic aperiodic systems, as expressed by Conway's theorem [50]. In the specific case of 1D binary lattices, *local reflection symmetry* is abundantly present and follows, at each scale, a spatial distribution closely linked to the underlying aperiodic potential sequence [51]. The encoding of such local symmetries into generic wave excitations have recently been described within a theoretical framework of symmetry-adapted nonlocal currents [52], which obey generalized continuity equations [52–55] and whose stationary form allows for a generalization of the parity and Bloch theorems to locally restricted symmetries [56] as well as a classification of perfect transmission [57]. In the context of finite, aperiodically ordered setups, an appealing question is whether a real-space picture for the formation—and thereby control—of edge states can be brought into connection with local symmetries.

In the present work, we propose an intuitive real-space picture of the formation of quasibands and edge states in binary aperiodic tight-binding chains. The approach is based on the analysis of eigenstate profiles in the limit of weak intersite coupling. In this regime, eigenstates generically fragment, i.e., have non-negligible amplitudes only on a small number of sites, as we show by means of a perturbation theoretical treatment. The amplitudes on these fragments are in almost all cases locally symmetric and can be identified as *local resonator modes* (LRM), i.e., eigenmodes of local resonators embedded into the full chain. Here, a resonator denotes a substructure that can confine, at certain energies, the wave function within its interior. The LRMs can be used to classify states, and those belonging to quasibands are composed of repeated LRMs hosted by resonators within the bulk, while edge states are composed of unique LRMs occurring on the edge. We further investigate the reasons for the formation of quasibands by linking the energy ϵ of a state to that of its constituting LRMs, where the energy of an LRM is defined as its energy in the corresponding *isolated* resonator. From

this finding, we see that the multiple occurrence of identical resonator structures automatically leads to the formation of quasibands by their capability of hosting identical (and thus degenerate) LRMs. We further use this energetical insight to move a given edge state into a quasiband by performing tailored changes to the corresponding resonators on the edge. The inference of those properties to moderate intersite coupling depends on the type of aperiodic order used in the model. We here apply the approach to the prominent representatives of three main classes of structural complexity: Fibonacci, Thue-Morse, and Rudin-Shapiro chains, featuring pointlike, singular continuous, and purely singular spatial Fourier spectra, respectively.

The paper is organized as follows. In Sec. II, we introduce our setup and show examples of quasibands and edge states in Fibonacci chains. We then develop our approach to edge states based on locally symmetric resonators and apply it to Fibonacci chains in Sec. III, to Thue-Morse chains in Sec. IV A and to Rudin-Shapiro chains in Sec. IV B. In Sec. V, we comment on the generality of our framework and on the connection to related work. We conclude our paper and give an outlook in Sec. VI. A perturbative treatment demonstrating the localization onto reflection-symmetric resonators is provided in the Appendix, together with further technical details including proofs of major statements, complementary explanations, and further comments.

II. PROTOTYPE QUASIPERIODIC ORDER: THE TIGHT-BINDING FIBONACCI CHAIN

We consider a finite one-dimensional chain of N sites with real next-neighbor hoppings $h_{m,n}$ described by the Hamiltonian

$$H = \sum_n v_n |n\rangle\langle n| + \sum_{|m-n|=1} h_{m,n} |m\rangle\langle n|, \quad (1)$$

where v_n is the onsite potential of site n . In the basis of single-site excitations $|n\rangle$, the above Hamiltonian H can be written as a tridiagonal matrix

$$H = \begin{pmatrix} v_1 & h_{1,2} & 0 & \dots & 0 \\ h_{1,2} & v_2 & h_{2,3} & \ddots & \vdots \\ 0 & h_{2,3} & \ddots & \ddots & 0 \\ \vdots & \ddots & \ddots & \ddots & h_{N-1,N} \\ 0 & \dots & 0 & h_{N-1,N} & v_N \end{pmatrix}. \quad (2)$$

Such a tight-binding chain is used in a plethora of interesting model systems, examples including the Aubry-Andre [58] model relevant in the study of localization [59] and the Su-Schrieffer-Heeger model, a simple prototypical chain supporting a topological phase [60]. It also effectively describes one-dimensional arrays of evanescently coupled waveguides [61,62]. We here fix the hoppings to a uniform value h and restrict the onsite elements to be “binary,” that is, the sites are of two possible types A and B , and the v_n take on corresponding values v_A and v_B , with the *contrast* defined as

$$c = \left| \frac{v_A - v_B}{h} \right|. \quad (3)$$

Without loss of generality we will set $v_A \equiv 0$ and $v_B \equiv v$ throughout, having a single control parameter $c = |v/h|$ for a given chain.

In the following, we will investigate the spatial profiles of the eigenvectors $|\phi^v\rangle = \sum_n \phi_n^v |n\rangle$ of H in relation to their eigenvalues ϵ_v , given by

$$H|\phi^v\rangle = \epsilon_v|\phi^v\rangle, \quad (4)$$

for chains with aperiodic order. Note that H represents a generic finite tight-binding chain; the choice $h < 0$ corresponds, e.g., to the kinetic energy of electrons on a lattice with onsite potential v_n , while $h > 0$ (made here) can be used to model the coupling of photonic waveguides [61,62] with propagation constants v_n . Our analysis remains qualitatively unaffected by this choice.

We start by presenting the eigenstates and spectral properties of a finite binary chain following the Fibonacci sequence [22], a prototypical case of quasiperiodic order. This will serve as an initial point motivating the development of a local resonator approach at high contrast in the next section. Starting with A , the sequence is constructed by repeatedly applying the inflation rule $A \rightarrow AB, B \rightarrow A$, resulting in $F = ABAABABAAB \dots$. This sequence is then mapped onto the onsite elements v_n of the tight-binding chain. The spectrum and eigenvectors of this chain are shown in Fig. 1 for a moderate contrast of $c = 1.5$ and $N = 144$ sites. Despite the lack of periodicity, the eigenvalues cluster into so-called quasibands, owing to the long-range order present in the Fibonacci chain [63], and the spectrum attains a self-similar structure of quasibands and gaps in the $N \rightarrow \infty$ limit. For presentation reasons, we have here chosen N large enough to anticipate this spectral feature, though small enough to visually discern the spatial characteristics of the eigenmodes.

The quasibands are occupied by bulk eigenmodes that extend along the interior of the chain. Those are known as “critical states,” with a spatial profile lying between the exponential decay of modes in a randomly disordered chain and uniformly extending Bloch eigenmodes in periodic chains [13–15]. Such modes have recently been shown to consist of locally resonating patterns (i.e., characteristic sequences of amplitudes) which occur on repeating segments of a quasiperiodic structures and are characteristic for a given quasiband [17,19,64]. This is particularly visible for the bulk modes of the uppermost quasiband in Fig. 1. A close inspection reveals that the bulk mode profiles tend to localize into locally reflection-symmetric peaks (see black subregions of high amplitude for a given mode). Those in turn follow the distribution of local symmetry axes (or centers of “palindromes” [65]) which are hierarchically present in the Fibonacci chain [51], as seen by comparison with the bar plot on the top. Each bar shows the maximal size S_n of a continuous domain of reflection symmetry centered at position n , where n can refer here to sites ($n = 1, 2, \dots$) or to links between sites ($n = 1.5, 2.5, \dots$). For instance, as the first few characters of F are

$$\overbrace{ABAABA}^{6 \text{ sites}} \underbrace{BAAB}_{3 \text{ sites}},$$

we have $S_{3.5} = 6$ and $S_5 = 3$.

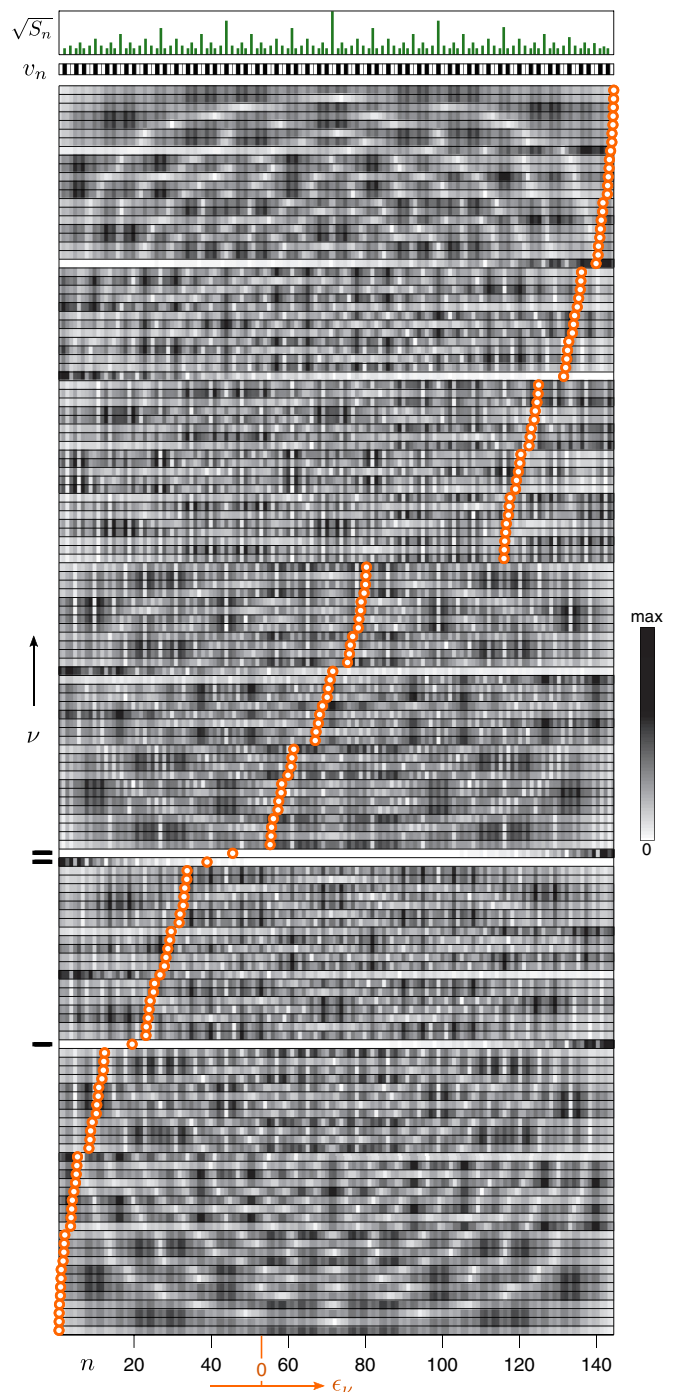


FIG. 1. (Bottom) Eigenstate map of a $N = 144$ -site Fibonacci chain at contrast $c = |v/h| = 1.5$ (hopping $h = 0.1$): each horizontal stripe shows $\sqrt{|\phi_n^v|}$ at sites n for an eigenstate ϕ^v ($v = 1, 2, \dots, N$). The greyscale map is chosen such that it is possible to simultaneously observe the spatial features of edge as well as those of bulk states. Superimposed are the eigenvalues ϵ_v (orange circles) in arbitrary units, with indicated origin $\epsilon = 0$. Edge modes are distinguishable as partially white stripes, with the most pronounced ones indicated by black horizontal bars on the left. (Middle) Potential v_n represented by a stripe with white (black) boxes for $v_n = v_A = 0$ ($v_n = v_B = v$). (Top) Distribution of local reflection symmetry domains, represented by maximal domain size S_n centered at position n , as explained in the text.

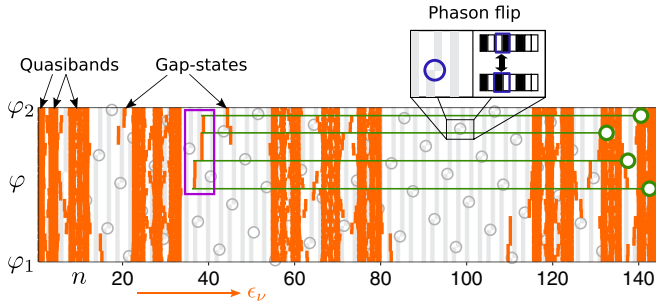


FIG. 2. Spectrum in arbitrary units (orange) of a $N = 144$ -site Fibonacci chain for varying phason φ in Eq. (5) between the values (chosen for presentation reasons) $\varphi_1 = 2.4097$ and $\varphi_2 = 5.5513$ for contrast $c = 1.5$, superimposed on the variation of the onsite potential v_n (v_A : white, v_B : light gray). Dark gray circles indicate local flips $AB \leftrightarrow BA$ in the chain. The inset shows a magnified view on one representative flip. All together, there are 71 such flips between φ_1 and φ_2 . The flips indicated by green circles create/annihilate (when close to the edge) or energetically shift (when further from the edge) the gap state in the purple box.

Within the gaps between quasibands there may appear spectrally isolated modes, reminiscent of gap modes localized on defects within a periodic lattice [66,67]. For the example given in Fig. 1, i.e., an unperturbed but finite Fibonacci chain, the gap modes are known [37,68,69] to be localized at the edges, decaying exponentially into the bulk.

The control of edge states by local changes in the underlying potential sequence is a central aspect of this work. Our approach is that, due to their localization, the occurrence and spectral position of edge states can be influenced by local modifications on the corresponding edge of the aperiodic lattice. We demonstrate the feasibility of this approach in Fig. 2 by using the following representation [47] of the Fibonacci potential sequence:

$$v_n = \frac{v_A + v_B}{2} + \frac{v_A - v_B}{2} \text{sign} \chi_n = \frac{v}{2} (1 - \text{sign} \chi_n), \quad (5)$$

$$\chi_n(\varphi) = \cos(2\pi\tau n + \varphi + \pi\tau) - \cos(\pi\tau), \quad (6)$$

where $\tau = 2/(1 + \sqrt{5})$ is the inverse golden mean and the integer site index n runs from 1 to N . By continuously varying the so-called “phason” φ , localized flips $AB \leftrightarrow BA$ are induced at discrete values of φ , forming a two-dimensional pattern in the (n, φ) plane, see Fig. 2. The finite chain of length N constitutes a different segment (or “factor”) of the infinite Fibonacci sequence after each flip [47]. This allows to investigate different Fibonacci-like configurations while maintaining a constant length N . In Fig. 2, we visualize the effect of these flips on the energy spectrum, shown in orange. As one can see, the gap states in the purple rectangle, which are localized on the right edge (not shown here), are influenced only by flips acting on this edge, marked by green circles. From bottom to top, the green flips (i) create the edge state (ii) and (iii) modify its energy and (iv) finally annihilate it. Note that in general for processes of type (ii) and (iii), the energetical change accompanying the change of the edge is stronger for a flip near the edge than for a flip more distant to the edge.

The occurrence of such edge-localized gap states in a finite 1D quasiperiodic potential was recently very elegantly described within a scattering setting [47,48] in a continuous system as a consequence of a resonance condition when varying the phason φ . At the same time, the connection of the winding of φ to invariant integers labeling the spectral gaps of the quasiperiodic structure through the so-called “gap labeling” theorem [70], renders the nature of the 1D edge states topological [46]. On the other hand, the flip-induced edge state creation/annihilation demonstrated in Fig. 2 suggests that their origin could also be explained by viewing chain edges as a generalized type of “defects” to the quasiperiodic long-range order. In the following, we will develop this idea in terms of the prototype Fibonacci chain. Our aim is to provide a simple and unifying real-space picture for the appearance of edge states in the energy gaps of nonperiodic structures. Contrary to topological methods, as employed for one-dimensional systems in general e.g., in Refs. [24,44–48,71–75], our approach does not rely on topology, but aims at connecting the real-space structure of deterministic aperiodic binary chains and their local symmetries to their quasibands and edge states.

III. EDGE MODES FROM TRUNCATED LOCAL RESONATORS

The analysis of eigenstates at high contrast c [see Eq. (3)] is at the heart of our approach, revealing structural information that would remain hidden at lower contrast. Once this information is retrieved, we leverage it to develop a generic framework for the understanding and manipulation of quasibands and edge states in binary tight-binding chains.

In the following, we will focus on a Fibonacci chain, choosing a relatively small size for easier treatment and visualization. The slight modifications needed for the treatment of longer chains are commented on in Appendix E. We split the presentation into three subsections, covering the concept of fragmentation (Sec. III A), local resonator modes (Sec. III B), the structural control of edge states (Sec. III C), and the behavior at low contrast (Sec. III D).

A. Eigenstate fragmentation from degenerate perturbation theory

Our starting point is an analysis of eigenstates at high contrast. Those are shown in Fig. 3(a) for a 9th generation Fibonacci chain ($N = 55$ sites) with relatively high contrast $c = 6$. We see that each eigenstate is pinned to a small number of sites where it has non-negligible amplitude, practically vanishing on the remaining sites. This is quite different from the states at low contrast (like in Fig. 1) which are smeared out along the whole chain. An impression of how the transition between those two regimes takes place is given in Fig. 3(b), showing the amplitudes of a bulk (ϕ^{55}) and edge (ϕ^{21}) state for varying contrast. When increasing the contrast, the spatial profile of the bulk state becomes gradually *fragmented*: the amplitudes on A sites become suppressed, and a characteristic remnant of the initial distribution appears on a subset of B sites. Fragmentation with increasing contrast c also occurs for the edge state, with the difference that here the amplitudes on B sites become suppressed, and that there is only a *single*

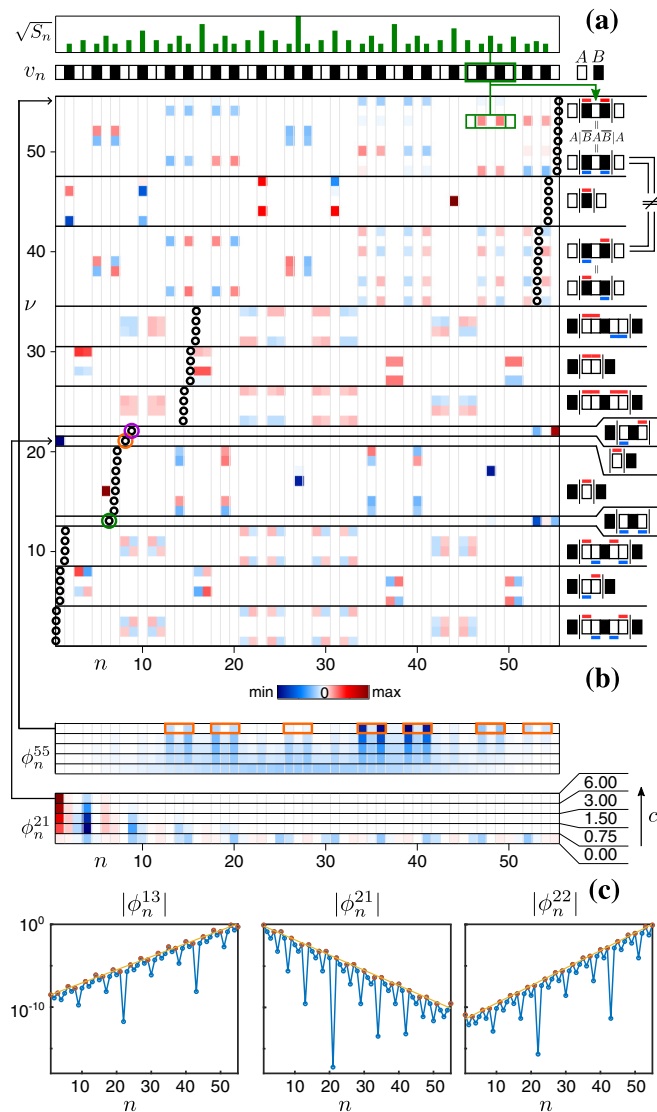


FIG. 3. (a) Eigenstate map, potential, and local symmetry distribution (bottom to top) like in Fig. 1 but for an $N = 55$ -site Fibonacci chain of contrast $c = 6$, and with density $|\phi_n^v|^2$ color-coded by the signs of ϕ_n^v shown in the eigenstate map. Horizontal lines separate the eigenstates into groups according to quasibands and gap states, with corresponding characteristic local resonator modes (LRMs) visualized on the right. The green box indicates the correspondence of the state ϕ^{53} to the LRM $A|\bar{B}A\bar{B}|A$ (see text). The three edge modes of the setup are marked by colored circles. (b) Amplitudes of states ϕ^{55} (extended in the bulk) and ϕ^{21} (localized at the left edge) for different contrast values. (c) Absolute values of amplitudes of the three edge states ϕ^{13} , ϕ^{21} , and ϕ^{22} with corresponding localization lengths 0.37, 0.43, and 0.49, obtained by fitting a line (orange) to local maxima (orange dots) on a logarithmic scale.

fragment remaining; in the present case the A site on the left edge.

The fragmentation at high contrast can be understood by means of a quantitative perturbation-theoretical treatment provided in Appendix C, applying to generic binary tight-binding chains. In the following, we outline the main steps of this analysis. In order to apply perturbation theory, the Hamiltonian is written as $H_0 + h \cdot H_I$, where H_0 solely contains

the diagonal part of H , i.e., isolated sites, while H_I has 1's only on the first sub- and superdiagonal. For convenience, we then rescale $H' = H/v = H'_0 + 1/c \cdot H_I$, changing only the energies $\epsilon^v \rightarrow \epsilon^v/v$, but leaving all eigenstates unaffected. For large contrast c , H_I then acts as perturbation to H_0 , and we can expand an eigenstate $|\phi^{(i)}\rangle$ ($1 \leq i \leq N$) of $H \in \mathbb{R}^{N \times N}$ as well as its energy $\epsilon^{(i)}$ as

$$|\phi^{(i)}\rangle = |\phi^{(i)}\rangle_0 + \lambda|\phi^{(i)}\rangle_1 + \lambda^2|\phi^{(i)}\rangle_2 + \dots, \quad (7)$$

$$\epsilon^{(i)} = \epsilon_0^{(i)} + \lambda\epsilon_1^{(i)} + \lambda^2\epsilon_2^{(i)} + \dots, \quad (8)$$

which, inserted into the Schrödinger equation, yields the perturbation series. Due to the binary nature of H_0 , the only two eigenvalues of H_0 , 0 and 1, are highly degenerate. In particular, before any higher-order state correction can be computed, the so-called “correct zeroth-order states” [76,77]

$$|\phi^{(i)}\rangle_0 = \lim_{\lambda \rightarrow 0} |\phi^{(i)}\rangle \quad (9)$$

must be found. Although these are superpositions of the known eigenstates of H_0 , the corresponding expansion coefficients are in general unknown at the beginning of the treatment [76,77]. In degenerate perturbation theory [76,77], the correct zeroth-order states can be found by diagonalizing a series of recursively [77] defined matrices $\mathcal{H}_1, \mathcal{H}_2, \dots$. More precisely, the matrices \mathcal{H}_n are constructed from the perturbation series up to n th order by demanding that the correct zeroth-order states fulfill certain consistency requirements. One then has to solve

$$0 \langle \phi^{(i)} | \mathcal{H}_n | \phi^{(j)} \rangle_0 = \delta_{i,j} \epsilon_n^{(i)}, \quad \forall i, j \in g_n \quad (10)$$

up to the order n in which all degeneracies are lifted, where $|\phi^{(g_n)}\rangle$ is the set of states which are degenerate up to n th order. Now, contrary to simple examples where the degeneracy is resolved in first order (where \mathcal{H}_1 is simply given by H_I), the degeneracies of binary chains are usually completely resolved only in higher orders. As a result, the procedure of obtaining the correct zeroth-order states is rather complex [76,77].

In Appendix C, we explicitly follow this procedure of finding the correct zeroth-order states up to third order and investigate the first-order state corrections as well. This procedure provides a high degree of understanding of how binary chains, their local symmetries, the fragmentation of eigenstates as well as their symmetries are connected. In particular, it is shown that each $|\phi^{(i)}\rangle_0$ ($1 \leq i \leq N$), with N being the length of the chain, has nonvanishing amplitudes either only on either A -sites or only on B sites (see statement 2 of Appendix C). Thus we can assign each $|\phi^{(i)}\rangle_0$ a type $T \in \{A, B\}$, depending on the sites on which it has nonvanishing amplitudes. The spatial distribution of the nonvanishing amplitudes can be further specified by introducing the concept of *maximally extended blocks of potentials of the same kind* (MEBPS). An example for such MEBPS are

$$\begin{array}{cccc} 1 & 2 & 1 & 3 \\ \overline{A} \overline{B} \overline{AA} \overline{B} \overline{A} \overline{B} \overline{AAA} \\ 1 & 1 & 1 \end{array}$$

where MEBPS of type A (B) are marked by over (under) brackets, with respective length denoted by integers. An important conclusion of the analysis is that a given correct

zeroth-order state $|\phi^{(i)}\rangle_0$ of type T can have nonvanishing amplitude on MEBPS of type T and of individual length l_1, l_2, \dots, l_n only if there exist integers $1 \leq k_j \leq l_j$, $1 \leq j \leq n$ such that (see statement 2 of Appendix C)

$$\frac{k_1}{l_1 + 1} = \frac{k_2}{l_2 + 1} = \dots = \frac{k_n}{l_n + 1}.$$

As one can easily show, for $l_j \leq 6$, this is possible only if all l_j are identical or if all l_j are odd. As a consequence, for the Fibonacci setup, where $l_j \leq 2$, any $|\phi^{(i)}\rangle_0$ can simultaneously have nonvanishing amplitudes only on MEBPS of length 1 or of length 2, but not on both. As a result, any state $|\phi^{(i)}\rangle_0$ has vanishing amplitudes on a large number of sites, ultimately leading to its fragmentation. A closer evaluation reveals that this fragmentation usually persists under inclusion of the first-order state corrections $|\phi^{(i)}\rangle_1$: if $|\phi^{(i)}\rangle_0$ has nonvanishing amplitudes only on A (B) sites, then $|\phi^{(i)}\rangle_1$ will have nonvanishing amplitudes only on a small number of B (A) sites. As, at high contrast, $|\phi^{(i)}\rangle \approx |\phi^{(i)}\rangle_0 + |\phi^{(i)}\rangle_1$, our perturbation theoretical treatment thus explains the origin of the fragmentation of eigenstates in binary tight-binding chains in a rigorous quantitative way. Compared to the renormalization group approach which has been used [68,78–81] to explain the fractal nature of the spectrum of the Fibonacci chain and which needs to be tailored to the system of interest, we stress that our perturbation theoretical approach is much broader and can be used to treat all binary chains where fragmentation occurs. We demonstrate this generality by further analyzing the spatial details of those fragmented states and connecting them to the local symmetries of the chain and their environment (neighboring sites) in Appendix C (see statements 3 and 4 as well as following text).

B. Local resonator modes and local symmetry

Relying on the above perturbation theoretical results, we now promote an intuitive picture for the cause of fragmentation, where a chain is viewed as a collection of *local resonators*. The eigenvalues of this chain are then approximately given by the union of the eigenvalues of the individual resonators. As a consequence, each eigenvector of the full chain with energy ϵ then has very small amplitude on resonators whose energy differs strongly from ϵ . A local resonator is here a discrete substructure which, at high contrast, confines the wavefunction within its interior for a certain eigenenergy. The simplest case consists of a three-site structure $B|A|B$, where the vertical lines demarcate the resonator “cavity” (the inner part A) from its “walls” (the outer parts B). The resonator character of this particular substructure is analyzed in more detail in Appendix A. Two such resonators can be combined to form a *double resonator* $B|ABA|B$, formed by overlapping one wall of each $B|A|B$. Note that, for a substructure to function as a local resonator, either (i) the resonator wall and its next-neighboring site in the cavity must be of different type or (ii) the resonator wall must coincide with one of the edges of the chain ($|X$ or $X|$, with $X = A, B$).

We now link the resonator concept to the eigenstate fragmentation seen in Fig. 3(a). As an example, each fragment of ϕ^{55} [indicated by orange rectangles in Fig. 3(b)] is localized on the B 's of the local resonator $A|BAB|A$. We denote this fact

as $A|\overline{BAB}|A$, which represents an eigenmode of the isolated resonator $A|BAB|A$ and which we will call a *local resonator mode* (LRM). The overlines here indicate sites with equally signed and relatively much higher amplitude than nonoverlined sites; see Appendix A. At high contrast, the state ϕ^{55} can thus be seen as a collection of identical, nonoverlapping LRMs $A|\overline{BAB}|A$ (one on each fragment) with negligible amplitudes on the parts in between. In the same manner, each eigenstate shown in Fig. 3(a) is composed of identical LRMs. In particular, we notice that *all states in a given quasiband are characterized by the same resonator mode*, different from that of other quasibands. This is shown on the right side of the figure, where LRMs are depicted schematically. Here, overlines and underlines in an LRM such as $A|\overline{BAB}|A$ denote amplitudes of opposite sign. Contrary to the bulk states of quasibands, *edge states feature unique resonator modes* which are not repeated elsewhere in the chain, with the underlying resonators located at (one of) the chain edges. We thereby distinguish these two types of LRMs as bulk and edge LRMs (*b*-LRMs and *e*-LRMs, respectively).

The fact that each quasiband is characterized by a single resonator mode can be understood as follows. If a given eigenstate $|\phi\rangle$ of energy ϵ is composed of K nonoverlapping LRMs such that $|\phi\rangle$ has very low amplitude on the next-neighboring sites of the corresponding resonators, then each of the energies $\epsilon_{k=1,2,\dots,K}$ of those LRMs (that is, their eigenenergies in the *isolated* underlying local resonator) must fulfill $\epsilon_k \approx \epsilon$. This statement is proven rigorously in Appendix D. Now, applying the perturbative treatment of Appendix C to the chain of Fig. 3 shows that for any two LRMs to be energetically nearly degenerate they must be identical. Thus each quasiband—having quasidegenerate modes at high contrast—is characterized by a single LRM.

A similar reasoning explains why bulk states of quasibands are more spatially extended compared to edge states lying in spectral gaps. Indeed, due to the quasiperiodicity of the Fibonacci chain, any local resonator (that is, a binary substructure) in the bulk occurs *repeatedly* (though not periodically) along the chain—specifically, at spacings smaller than double its size. This is a general result known as Conway’s theorem [50]. Thus a *b*-LRM hosted by a given local resonator will also be correspondingly repeated along the chain. If the *b*-LRM has energy ϵ_k , then a state with energy $\epsilon \approx \epsilon_k$ is allowed to simultaneously occupy all copies of this *b*-LRM, and is accordingly spatially extended. Edge states, on the other hand, consisting of *e*-LRMs at high contrast, correspond to local resonators induced by the presence of an edge, which *breaks the quasiperiodicity*. Due to this truncation at the edge [e.g., of the type $\dots|\dots X|$ with $X = A, B$ at the right edge, compare Fig. 3(a)], the *e*-LRM generally does not match the energy of any *b*-LRM, and therefore cannot occupy multiple local resonators in the bulk: The eigenstate is confined to the edge, lying energetically isolated in a gap. This is visualized by the marked edge states in Fig. 3(a).

A remarkable observation in Fig. 3(a) is that each local resonator hosting a *b*-LRM is reflection symmetric, such that all isolated *b*-LRMs have definite parity; see schematic on the right. This means that, at high contrast, the fragments (occupied local resonators) of quasiband eigenstates feature, to a very good approximation, local parity with respect to

local reflection symmetries of the chain. The positions and sizes of all such local symmetries are shown in the top panel of Fig. 3(a). An example is given by the state ϕ^{53} which is locally symmetric around, e. g., the position $n = 48$, and corresponds to the *b*-LRM $A|\bar{B}A\bar{B}|A$, as indicated by the green boxes. This behavior is predicted by the degenerate-perturbative treatment of Appendix C. There, we rigorously show that each $|\phi^{(i)}\rangle_0$ is locally parity symmetric individually on each MEBPS (see statement 1 of Appendix C), which itself is by definition a locally symmetric structure. While an MEBPS usually comprises only a few sites, we explicitly give examples for cases where $|\phi^{(i)}\rangle_0$ is locally symmetric also in larger domains. One of this examples explains the local symmetry of LRMs such as $A|\bar{B}A\bar{B}|A$ (see statement 3 of Appendix C). Overall, the perturbation theoretical treatment demonstrates the crucial role of local reflection symmetries in the eigenstate localization profiles of binary aperiodic chains. A promising direction of research would thus be to treat this class of systems within the recently developed theoretical framework of local symmetries [52,53,56].

C. Structural control of edge states

Having understood the real-space mechanism for the formation of edge-localized gap states in Fibonacci chains, we can now utilize this insight to systematically manipulate these states. In particular, let us show how structural modifications at the edges of a Fibonacci chain can selectively “annihilate” a given edge mode. Note that whether or not one considers a particular state localized (near or on) the edge to lie in an energetical gap is obviously a question of the scale under consideration. This is due to the fact that any finite chain naturally has a discrete spectrum, for which, strictly speaking, no continuous energy-bands are defined. In the remainder of this work, we will solely consider states as gap-edge ones provided that, at a contrast of $c = 6$, they lie in a clearly visible energetical gap. This simplifies our treatment, and in Appendix E, we comment on the extensions of this simplification.

For definiteness, we consider the edge state ϕ^{21} (orange circle) of the chain in Fig. 4(a) which simply focuses on states $\nu = 13$ to 22 of Fig. 3(a). This state corresponds to the *e*-LRM $|\bar{A}|B$ [see the right side of Fig. 3(a)] and is exponentially localized, as shown in Fig. 3(c). The underlying resonator $|A|B$ is a left-truncated version of the resonator $B|A|B$, which hosts the *b*-LRM $B|\bar{A}|B$ characterizing the quasiband below (states 14 to 20). Now, as shown in Fig. 4(b), if we *complete* the resonator $|A|B$ into $B|A|B$ by attaching a *B* site to the left end of the chain, then the edge can accommodate the *b*-LRM $B|\bar{A}|B$ instead of the *e*-LRM $|\bar{A}|B$. Consequently, the edge mode is replaced by a bulk mode of the quasiband. In other words, the edge state is “absorbed” into a quasiband by converting the *e*-LRM of the former to the *b*-LRM of the latter through a structural modification at the edge. This intuitive procedure can be applied similarly for the other two pronounced edge states (green and purple circles) in Fig. 4(a), by completing the corresponding edge local resonator into a bulk one. Thus, the selective control of a specific edge state is possible.

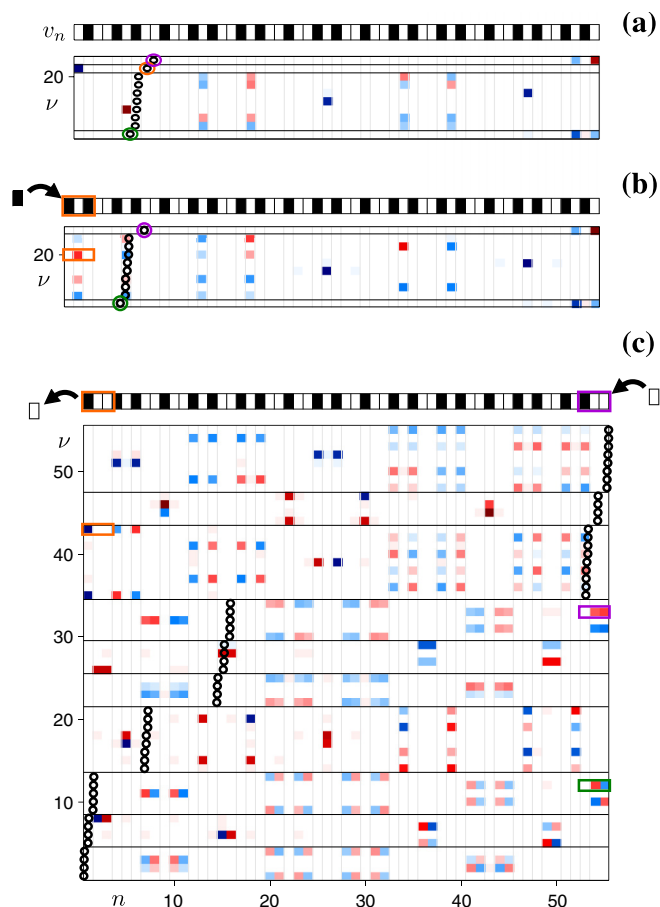


FIG. 4. Selective annihilation of edge states of the Fibonacci chain in Fig. 3(a); see text for details. (a) Original chain and excerpt of the state map (states 13–22), with edge states marked by colored circles. (b) Annihilation of left edge state (orange) by attaching a *B* site to the left of the chain. (c) Complete annihilation of edge states by removing (adding) an *A* (*B*) site on the left (right) end of the chain. Color coding of each subfigure is as in Fig. 3.

Let us note, however, that in most cases such a selective annihilation of one edge state leads to the creation of one (or more) other edge state(s) located elsewhere in the spectrum, as a result of the edge modification. For example, the left edge of the modified chain in Fig. 4(b) features the resonator $|BAB|A$, which is a truncated version of $A|BAB|A$ hosting the *b*-LRM $A|\bar{B}A\bar{B}|A$, thus yielding a new gap-edge state (not shown).

Interestingly, in special cases this issue can be overcome by *exploiting the local symmetry of bulk resonators*, as we now explain using the example shown in Fig. 4(c). Here, an *A* site is attached to the right edge, which formerly hosted the *e*-LRMs $B|\bar{A}\bar{B}A|$ and $B|\bar{A}B\bar{A}|$ [cf. Fig. 4(a)], corresponding to the edge states ϕ^{13} (green) and ϕ^{22} (purple), respectively. In the modified chain, the right edge features a local resonator $B|AA|$. The key point now is that this resonator supports two LRMs, $B|\bar{A}\bar{A}|$ and $B|\bar{A}A|$, which are degenerate to the *b*-LRMs $B|\bar{A}\bar{A}\bar{A}|B$ and $B|\bar{A}A\bar{A}|B$, respectively, due to the reflection symmetry of the underlying resonator $B|\bar{A}B\bar{A}|B$. This symmetry-induced degeneracy is shown rigorously in Appendix B. As a result of their degeneracy, the respective *e*- and *b*-LRMs can combine linearly to compose quasiband states, as

seen in Fig. 4(c); see states in first and third quasiband from bottom with marked edge resonators. The same procedure can be performed on the left edge by removing an A site from it, leaving the edge resonator $|B|A$ hosting $|\bar{B}|A$ which is degenerate to $A|\bar{B}A\bar{B}|A$ [see state in top quasiband with orange marked left edge resonator in Fig. 4(c)]. Note that both (right and left) edge modifications above are consistent with the Fibonacci order: The resulting chain is simply obtained from the former one by a single-site shift to the right along the infinite Fibonacci chain. We thus have a case of finite Fibonacci chain with *no edge-localized gap states*.

From the above it is clear that edge states in binary quasiperiodic chains can now be rigorously understood and manipulated within the framework of local resonators. Structural creation and annihilation represents a first fundamental step in edge state control. Indeed, once an edge state is established, its energetic position within a gap can further be tuned by allowing for nonbinary (freely varying) potentials at the edges, while leaving the quasibands intact.

D. Behavior at low contrast

The local understanding and controllability of edge states at high contrast levels raises the question if these properties are retained also at lower contrast. To address this, in Fig. 5(a), we show the eigenvalue spectrum of the original Fibonacci chain studied previously [Fig. 3(a)] for varying contrast c . As we see, gap states (localization on edges not shown here) are clearly distinguished for all contrast levels. Figure 5(b) shows the spectrum of the modified Fibonacci chain of Fig. 4(c)—where all edge states were annihilated at high contrast—for the same contrast values. Also here the structure of the spectrum is retained with varying c . In particular, a real-space analysis (not shown here) confirms that all quasiband states in the modified chain remain extended in the bulk for varying c . The effect of lowering the contrast is merely a reduction in the fragmentation of the eigenstate profiles which become more smeared out into regions between the LRMs defined at high contrast.

This finding indicates that the mechanism of edge state formation via truncated local resonators based on an analysis at high contrast remains valid also for lower contrast, though “hidden” due to the spatial smearing of the states. In other words, the contrast parameter can be used as an intermediate tool to manipulate edge states in binary aperiodic model chains: It is first ramped up to reveal the eigenstate structure in terms of LRMs subject to modifications, and then ramped down again with the bulk/edge state separation retained.

IV. APPLICATION TO NONQUASIPERIODIC CHAINS

Featuring a pointlike spatial Fourier spectrum (rendering it, by definition, a quasicrystal [1,21]), the Fibonacci chain studied above represents the class of lowest structural complexity when departing from periodicity towards disorder, as mentioned in Sec. I. The question naturally arises whether the local resonator framework developed in Sec. III, distinguishing edge from bulk states via LRMs, applies also to other classes of aperiodic chains. In the following, we will demonstrate the generality of our approach by applying it to

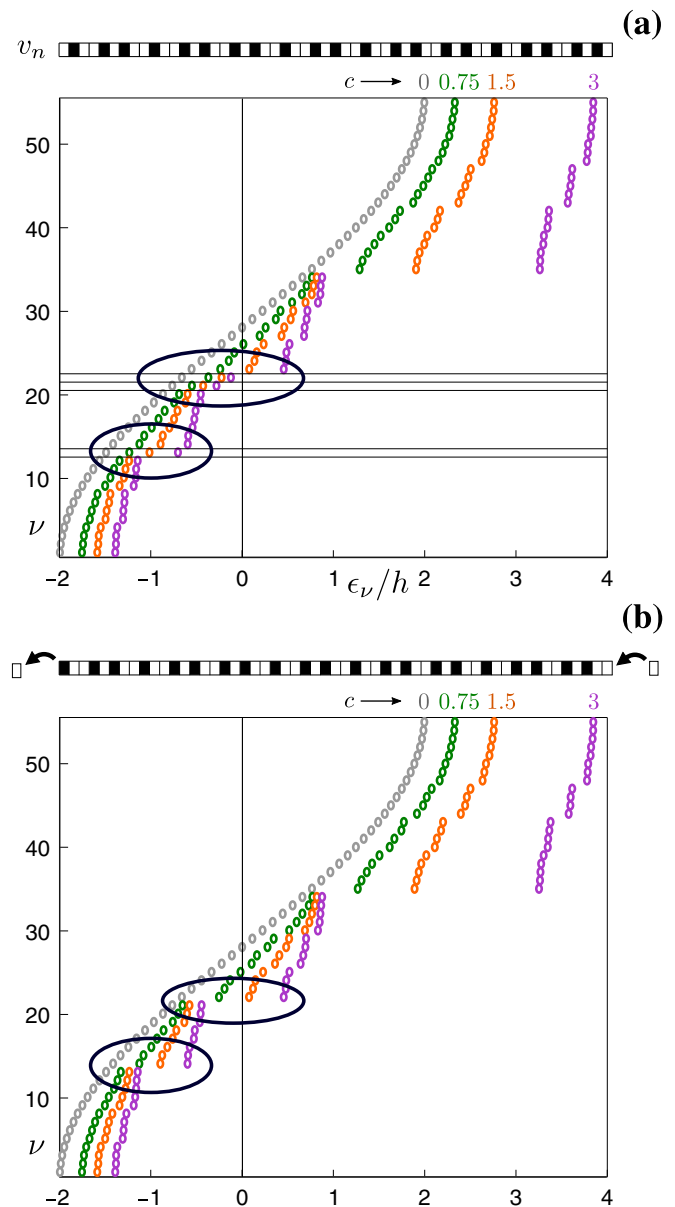


FIG. 5. Eigenvalue spectrum for different values of the contrast c (a) for the original Fibonacci chain of Fig. 3(a), with the three gap modes indicated by horizontal stripes, and (b) for the modified chain of Fig. 4(c). The ellipses highlight the removal of gap modes by the modification, for all contrast levels.

cases of qualitatively different structural character, the Thue-Morse and Rudin-Shapiro chains. We thereby essentially go through the same analysis steps as in Sec. III—identification of LRMs, edge state control, and low contrast behavior—and assess the particularities of each structural case.

A. Singular continuous Fourier spectrum: Thue-Morse chain

A well-studied case of aperiodic order which is not quasiperiodic is the Thue-Morse sequence [1], produced by the inflation rule $A \rightarrow AB, B \rightarrow BA$ yielding $T = ABBABAABBAAB \dots$. Its Fourier spectrum is singular continuous, and from this viewpoint it is considered [82] closer to

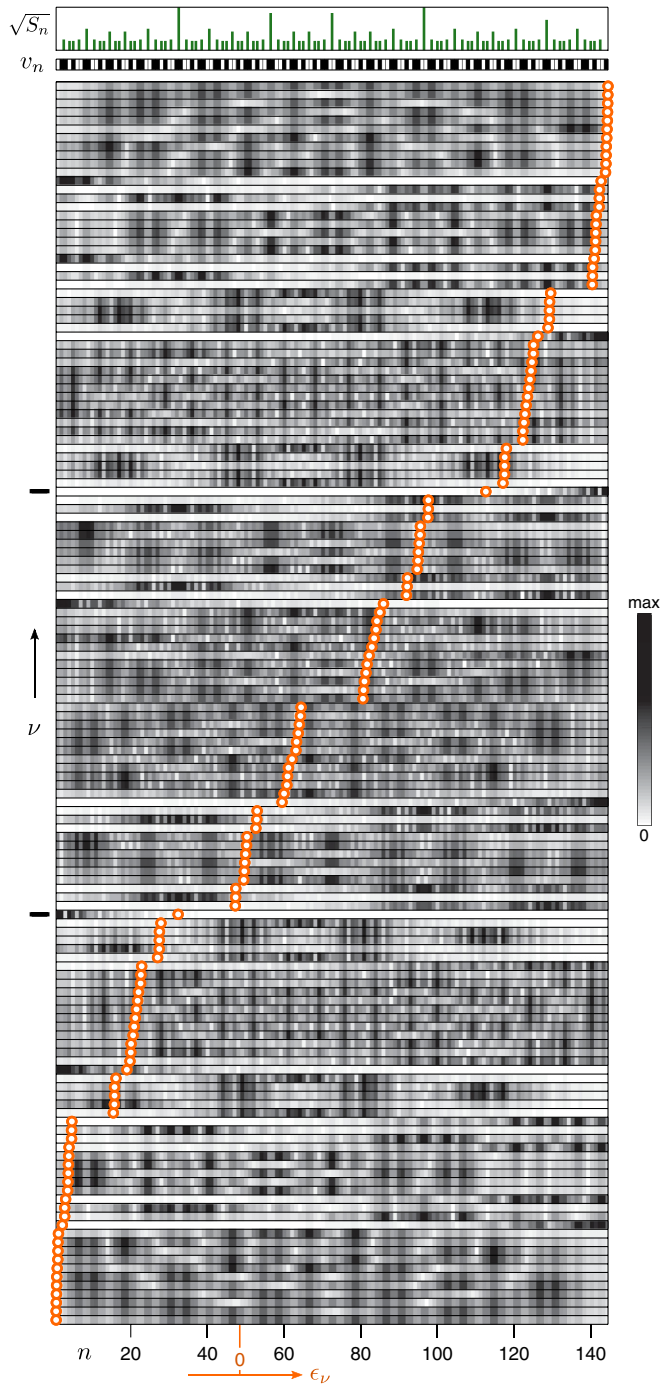


FIG. 6. Like in Fig. 1 but for a $N = 144$ -site Thue-Morse chain.

the disorder limit (with absolutely continuous spectrum [83]) than quasiperiodic order (with pointlike spectrum). On the other hand, a subset of eigenstates of the Thue-Morse chain strongly resemble those of periodic chains [84]. The eigenstates of a $N = 144$ -site Thue-Morse chain [85] are shown in Fig. 6. Indeed, while some bulk states are more strongly localized into subdomains than in the Fibonacci chain for equal contrast $c = 1.5$ (compare to Fig. 1), others are more extended along the chain. As we see in Fig. 6, in spite of the quasiband structure being more fragmented, there occur well

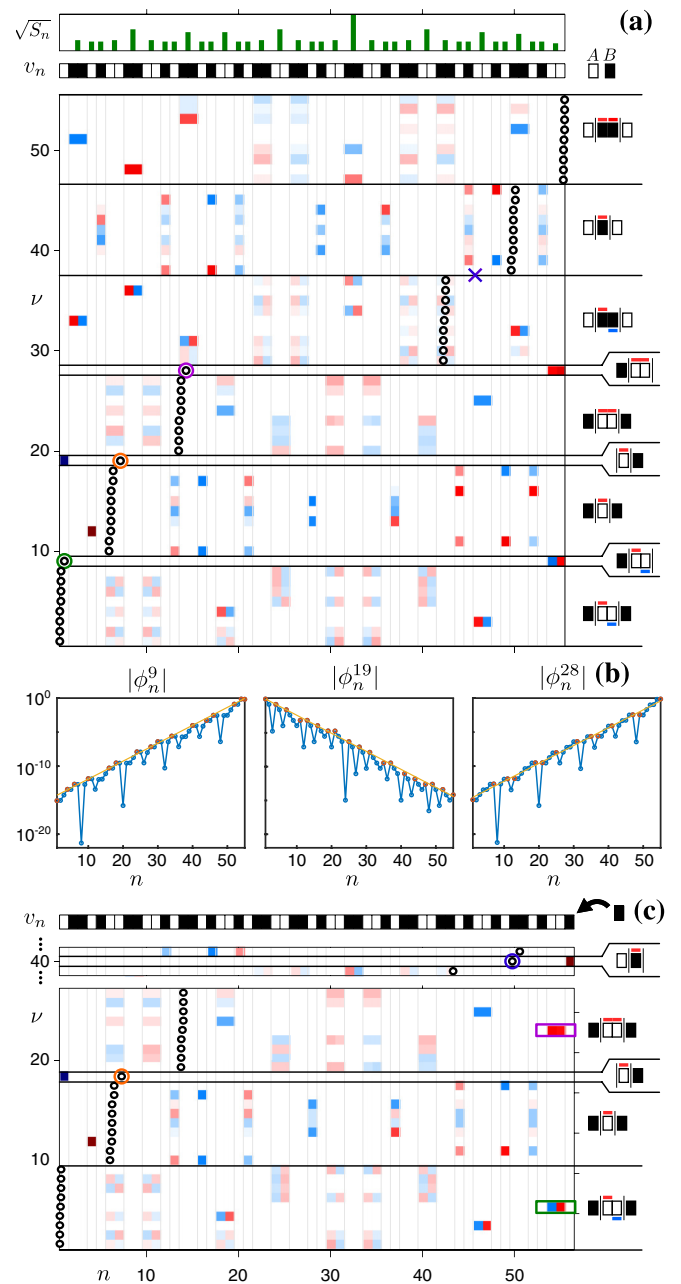


FIG. 7. (a) Like in Fig. 3 (a) but for a $N = 55$ -site Thue-Morse chain, with three edge states marked by colored circles. (b) Absolute values of amplitudes of the three edge states ϕ^9 , ϕ^{19} , and ϕ^{28} with localization lengths 0.61, 0.61, and 0.6, obtained by fitting a line (orange) to local maxima (orange dots) on a logarithmic scale. (c) Absorption of the two right edge states into quasibands (green and purple rectangles) and creation of a new right edge state (blue circle, lying between quasibands as indicated by \times in (a)) by attaching a B site to the right chain end, as explained in the text. Color coding of subfigures (a) and (c) is as in Fig. 3.

distinguishable states within gaps which are localized on one of the chain edges.

Local resonator modes. Like in Sec. III, we consider a smaller chain of $N = 55$ sites to visually facilitate the detailed spatial analysis. Its eigenstates are shown in Fig. 7(a) for contrast $c = 6$, together with the distribution of local

reflection symmetries in the chain (top). As we see, the bulk state profiles are fragmented in a well-defined manner for different quasibands: Like in the Fibonacci case, each bulk state is composed of copies of a b -LRM characterizing the corresponding quasiband, as indicated schematically on the right of the figure. In contrast, the three occurring prominent edge states (marked by colored circles) consist of nonrepeated e -LRMs at one of the chain ends. Like before, the local resonators underlying the e -LRMs can be identified as truncated local resonators underlying the b -LRMs. This demonstrates that our LRM-based framework for the formation of edge states applies also for this class of aperiodic order. Notably, also here the b -LRMs have definite local parity under reflection, and are present in the eigenstates following the local symmetry axes shown in the bar plot [top of Fig. 7(a)]. This is indeed predicted by the perturbation theory of Appendix C. We thus see that also for the Thue-Morse chain its local symmetries essentially provide the regions of localization of the eigenstate fragments at high contrast.

Edge state control. The original Thue-Morse chain contained three edge states, which were exponentially localized [86] as shown in Fig. 7(b). Edge states in Thue-Morse chains were also demonstrated very recently in terms of the eigenmodes of full vectorial Green matrices [49], albeit localized according to a power-law. Now, following the same principle as in the Fibonacci case, Fig. 7(c) shows how two edge states [marked by green and orange circles in Fig. 7(a)] are annihilated by attaching a B site to the right end of the original chain. Indeed, those edge states were localized on the truncated resonator $B|AA|$ which is completed to $B|AA|B$ and can thus host the b -LRMs $B|\overline{AA}|B$ and $B|\overline{A\overline{A}}|B$, so that the edge states are “absorbed” into the corresponding quasibands. However, the right edge of the modified chain now features a new edge state (marked by blue circle) with resonator mode $A|\overline{B}$ [its previous absence is indicated by a \times in Fig. 7(a)]. It lies, energetically, in the gap just below the quasiband with b -LRM $A|\overline{B}|A$. Note that, as expected from our real-space local resonator picture, the left edge state (orange circle) remains unaffected by the present modification on the right edge of the chain, since it is localized on the opposite edge.

Contrast variation. Finally, we investigate how edge states and quasibands behave for lower contrast in the Thue-Morse chain. Figure 8(a) shows the spectrum of the chain of Fig. 7(a) for varying contrast, starting from $c = 3$. As we see, the three edge modes in the spectral gaps are clearly visible also at lower contrast levels. The spectrum of the modified chain (with right-attached B site) for varying c is shown in Fig. 8(b). As is highlighted by the black circle and the ellipse, the two former edge states are absorbed into the neighboring quasibands [as shown in Fig. 7(a)] for all considered contrast levels. Also, the left edge state as well as the modification-induced right edge state [orange and blue in Fig. 7(c), respectively] remain in their gaps as the contrast is varied. Overall therefore, the impact of the modifications persists at lower contrast levels.

B. Absolutely continuous Fourier spectrum: Rudin-Shapiro chain

Taking a step towards higher structural complexity, we finally investigate the case of a Rudin-Shapiro chain in

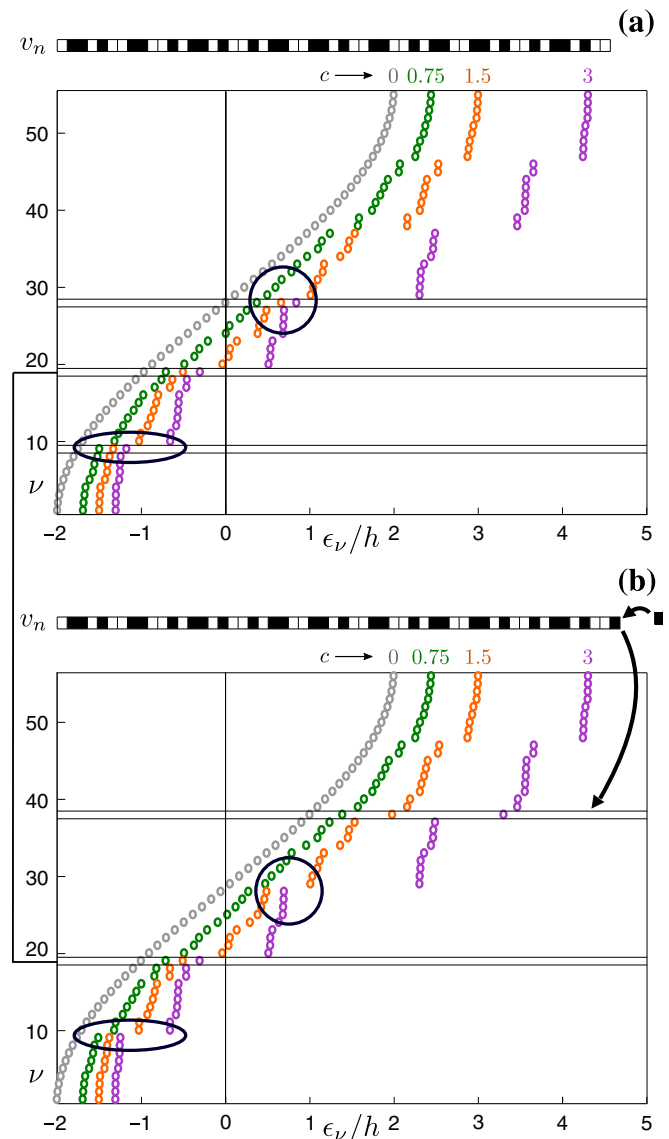


FIG. 8. Eigenvalue spectrum for different values of the contrast c (a) for the original Thue-Morse chain of Fig. 7(a), with gap modes indicated by horizontal stripes, and (b) for the modified chain of Fig. 7(c). The black circle and the ellipse highlight the removal of selected gap modes by the modification, for all contrast levels.

terms of our local resonator framework. The Rudin-Shapiro sequence [87] R is obtained by the inflation rule $AA \rightarrow AAAB$, $AB \rightarrow AABA$, $BA \rightarrow BBAB$, $BB \rightarrow BBBA$, yielding $R = AAABAABAAAABBBAB \dots$ for an initial seed AA . Its Fourier spectrum is absolutely continuous, a property shared with completely disordered chains [83]. Further, there are indications that the tight-binding Rudin-Shapiro chain has both exponentially and weaker-than-exponentially localized eigenstates [13, 88–90], while even extended ones have been shown to exist at low contrast. The different character of the Rudin-Shapiro states compared to the Fibonacci or Thue-Morse chain can be anticipated from the eigenstate map shown in Fig. 9. As we see, at this low contrast ($c = 1.5$), there is now no clear distinction between bulk and edge states. Moreover, no clear energetic clustering into well-defined quasibands is

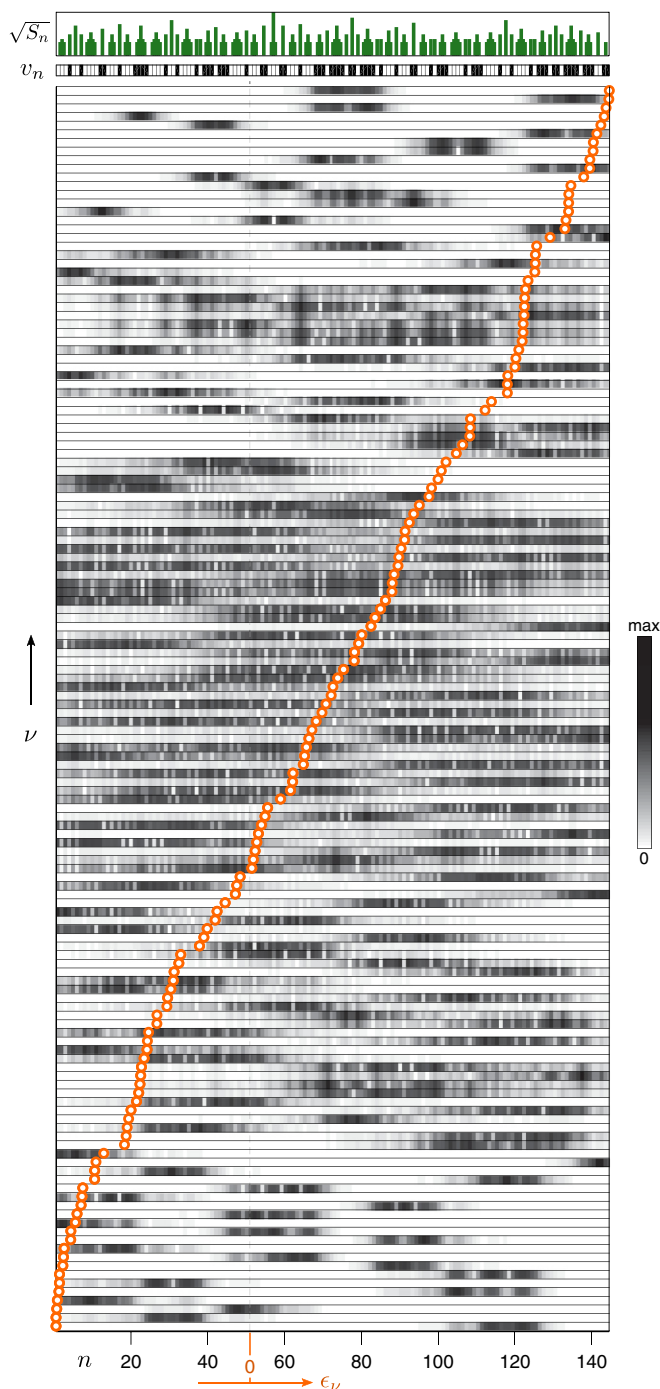


FIG. 9. Like in Fig. 1 but for a $N = 144$ -site Rudin-Shapiro chain.

present. Note also that the distribution of local reflection symmetries along the chain (see top of figure) is much less structured than in the Fibonacci or Thue-Morse chains (cf. top of Figs. 1 and 6), with overall smaller symmetry domains present. At the same time, there is clustering of symmetry axes with gaps in between, caused by the occurrence of larger contiguous blocks of single type (up to four A or B sites in a row) along the sequence. In the following, we show that there is still a strong link of the eigenstates and spectral features of the Rudin-Shapiro to the presence of locally symmetric resonators.

Local resonator modes. For the high-contrast analysis, we consider a Rudin-Shapiro chain of $N = 87$ sites. The size is now chosen slightly larger in order to better reflect the structural properties of the Rudin-Shapiro sequence. Indeed, in accordance with its higher complexity, a given substructure will here repeat at relatively larger distances along the sequence. It may thus occur only once in a too short chain, thereby obscuring its long-range order. Figure 10(a) shows the eigenstate map of the considered chain at contrast $c = 6$. We see that also here the eigenstates fragment onto locally symmetric substructures, and are again composed of b -LRMs corresponding to clustered eigenvalue quasibands, as shown on the right. The difference is now that there are many more different identified b -LRMs compared to the Fibonacci and Thue-Morse chains. This is because the increased number of contiguous block sizes allows for a *higher diversity of local resonator substructures*, with larger resonators additionally hosting a larger number of different LRMs each. In turn, there is a higher possibility that different b -LRMs have (nearly) the same energy, since the different resonators may have partially overlapping individual eigenspectra. Therefore, it may now more easily occur that *different* LRMs participate in the *same* eigenstate (to which they are quasidegenerate; see Appendix D). An example of this are the states indicated by the green ellipse in Fig. 10(a): each of them consists of a $A|B|A$ on the left and two $A|BBB|A$ on the right, consecutively overlapping by one A site. The emergence of such modes is explained in detail by means of perturbation theory in Appendix C. Further, edge states appear which localize on corresponding e -LRMs. Those are now, however, energetically not as clearly distinct from the clustered eigenvalues of quasibands as in the Fibonacci and Thue-Morse cases. For example, the states marked by blue circles are localized on the left edge, but are composed of the e -LRMs (from top to bottom) $|AAA|B$, $|\overline{AAA}|B$, $|\overline{AAA}|B$, which are nearly degenerate to the b -LRMs of the corresponding quasibands (see the right side of figure). Nevertheless, there are also well-distinguished edge states lying in gaps (though close to gap edges) marked by purple circles.

Edge state control. Contrary to the Fibonacci and Thue-Morse cases, the edge states are not exactly exponentially localized, but have different localization lengths in different sections, as shown [86] in Fig. 10(c). The amplitude of state ϕ^{31} , though overall decaying, even rises again at around $n \approx 20$ and ≈ 70 . Unaffected by this different localization behavior compared to the previously treated examples, we now manipulate the two states marked by purple color which are localized on the right edge. These localize on the truncated resonator $B|AA|$, and their energy is different from the energy of states localized on the complete resonator $B|AA|B$ which occurs twice in the bulk. In (b), we add a B on the right edge of the chain, completing this resonator. Due to this completion, the two former gap-edge states move into the respective energy cluster (or quasiband).

Contrast variation. In Fig. 11(a), we investigate the eigenvalues of the Rudin-Shapiro chain of Fig. 10(a) for varying contrast. Compared to the case of the Fibonacci chain presented in Fig. 5 or the Thue-Morse chain presented in Fig. 8, the energetic clusters form only at high contrast values. This already indicates that modifications to the chain done at high

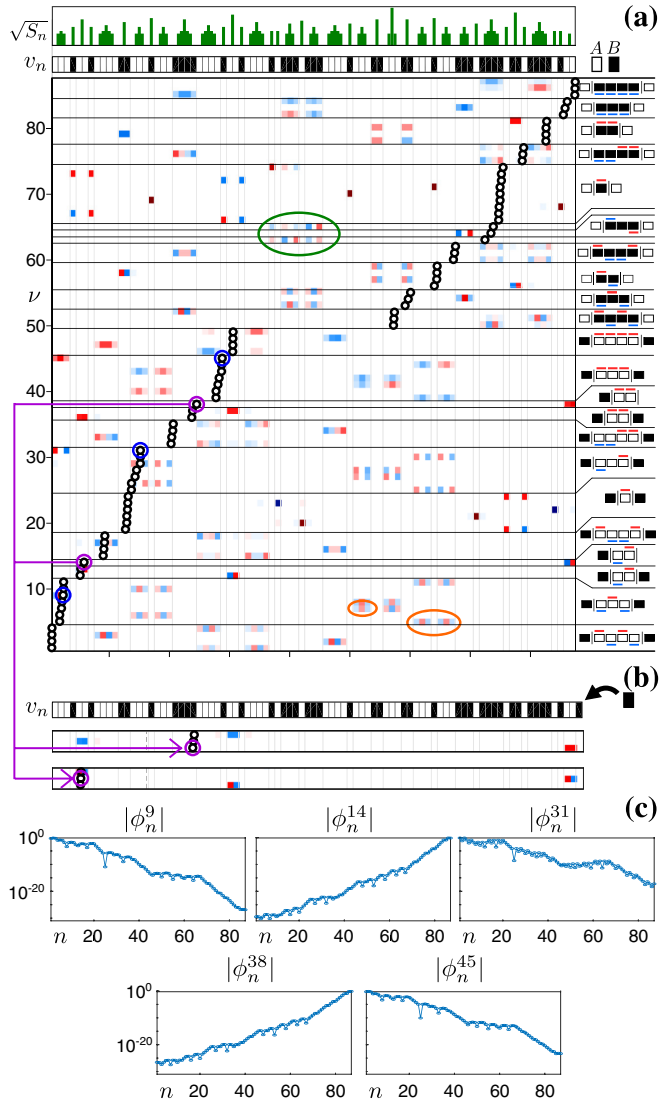


FIG. 10. (a) $N = 87$ site binary chain corresponding to a truncated Rudin-Shapiro sequence at contrast $c = |v/h| = 6$ (hopping $h = 0.1$). To the right, the grouping of eigenstates into resonator modes as explained in the text is shown. To simplify the figure, resonator modes are only shown explicitly if they are shared by at least two states. The two states marked by a green ellipse localize on nonlocally symmetric structures. The two states marked by orange ellipses are examples for states with different resonator modes but nearly equal energy, as explained in the text. (b) The result of an extension of the chain by adding a B to the right. Due to this modification, the resonator $A|BB|$ on the right edge is completed, and the purple marked states in (a) are energetically shifted towards the corresponding states localizing on the $A|BB|A$ resonator located near the right edge. Color coding of subfigures (a) and (b) is as in Fig. 3. (c) Absolute values of amplitudes of the edge states ϕ^9 , ϕ^{14} , ϕ^{31} , ϕ^{38} , and ϕ^{45} .

contrast can not directly be traced to energetic changes at low contrast as was the case for the Fibonacci and Thue-Morse chain. This can also be seen for the two edge states marked by horizontal lines in Fig. 11(a). At high contrast, these are caused by a truncated resonator $B|AA|$ on the right edge. In Fig. 10(b), we have completed this resonator, causing the two

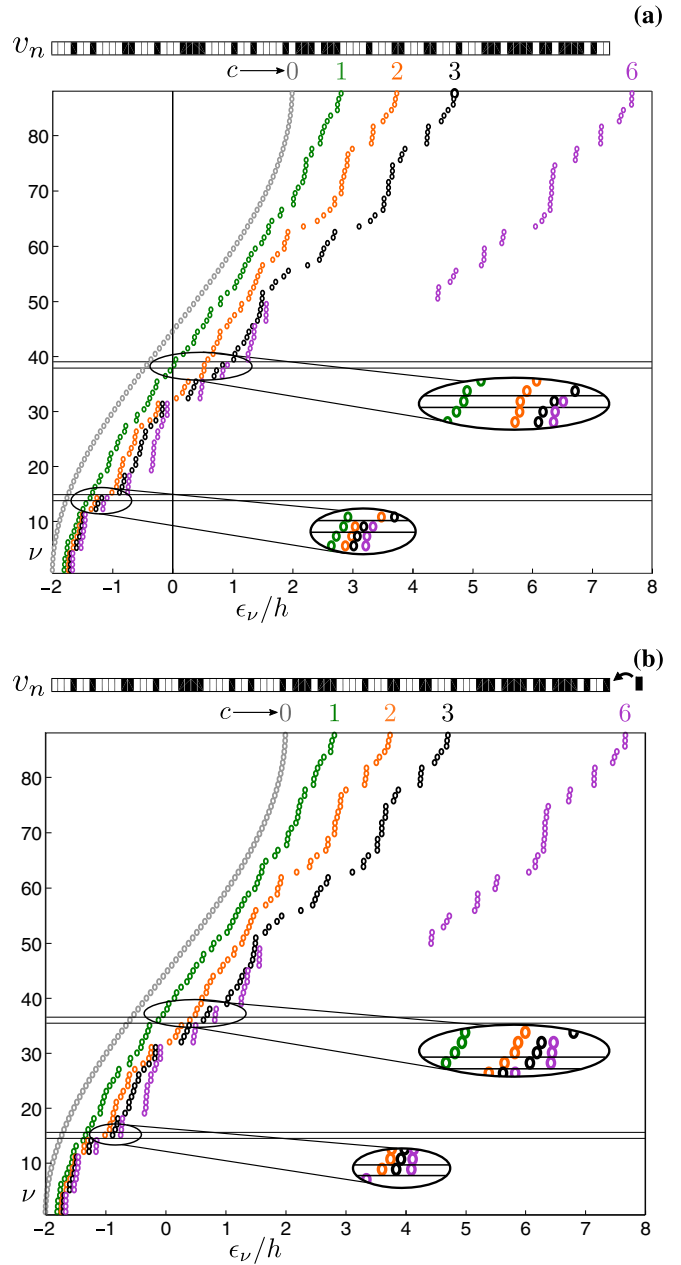


FIG. 11. (a) Evolution of the eigenvalue spectrum of the Rudin-Shapiro chain shown in Fig. 10(a) for various values of the contrast c . The two gap states $\phi^{14,38}$ are denoted by horizontal lines. (b) Same as (a), but now for the modified Rudin-Shapiro chain shown in Fig. 10(b). For high contrast of $c = 6$, the two gap states are removed. However, they reappear, though at slightly different positions, already at a contrast $c = 3$, as shown in the insets.

edge states to move (at high contrast) closer to the nearest eigenvalue cluster. As can be seen in Fig. 11(b), this manipulation is only effective at high contrast. For low contrast, the eigenvalue structure is nearly unchanged compared to the original chain shown in Fig. 11(a).

In conclusion, we have applied our local-symmetry based resonator strategy to the Thue-Morse and the Rudin-Shapiro chain. The results show that our approach can be used to explain and control gap-edge states of the Thue-Morse chain.

At high contrast, the gap-edge states of the Rudin-Shapiro chain are likewise explained. However, our approach can not be used to make qualitative predictions at low contrast.

V. APPLICABILITY AND RELATION TO OTHER APPROACHES

Let us briefly comment on the limitations of applicability of the developed framework and its connection to similar approaches in the literature. The presented methodology essentially relies on the fragmentation of eigenstates at high contrast and can thus only be applied onto chains featuring such a behavior of eigenstates. A perturbation theoretical treatment of binary tight-binding chains which serves as basis for our methodology, see Appendix C, indicates that at high contrast the fragmentation of eigenstates is indeed the generic case. However, the necessary conditions for this behavior still need to be determined in order to clarify the range of applicability.

The connection between local resonators and quasibands in quasiperiodic setups has been commented on in Refs. [18,20,37]. For the Thue-Morse sequence, a similar analysis has been achieved in Ref. [84]. However, to the best of our knowledge, there is no systematic framework bringing together the three concepts of LRMs, quasibands and edge states into a unified context. An approach related to ours is the renormalization group flow analysis. For the tight-binding chains, this method aims at understanding the energetic behavior of a chain through a series of size reductions [68]. At each step, the size of the system is decreased, and the behavior of the decreased one is linked to the bigger one by a renormalization procedure, usually done in terms of perturbation theory. The renormalization group flow is a powerful method, and has been successfully used to explain the fractal nature of the Fibonacci spectrum [68,78–81]. However, it needs to be tailored to the system of interest, and as stated in Ref. [81], finding an appropriate renormalization group flow for a general quasiperiodic chain is not easy. This stands in contrast to the very general method proposed in this work, which was shown to be applicable to a broad range of different setups.

VI. CONCLUSIONS AND OUTLOOK

We have presented a systematic approach to the analysis of aperiodic binary tight-binding chains regarded as a combination of different resonatorlike subsystems rather than a single bulk unit. For low intersite coupling, each eigenstate is seen to be composed of spatially nonoverlapping local resonator modes of these resonator structures. This viewpoint, supported by a rigorous perturbation theoretical treatment, allows for an intuitive explanation of the emergence of both quasibands and gap-edge states in such chains. We demonstrate the power of our approach by applying it to Fibonacci, Thue-Morse, and Rudin-Shapiro chains and show how gap-edge states occurring in these chains can be manipulated.

A repeating motif in our analysis of eigenstates at high contrast is the fact that most resonator modes share the local symmetries of the underlying systems. This strong impact of local symmetries is remarkable, especially as it is hidden at lower

contrast levels by a substantial background in the eigenstate profiles. In this work, we have given an explanation for this finding at high contrast, and we believe that the study of local symmetries in complex setups is a very promising field with rich perspectives and potential applications. The recently established framework of local symmetries [52,53,56,57,91,92] provides dedicated tools for this purpose, and extensions of it are of immediate relevance. In this line, our work may enable the local-symmetry assisted design of novel optical devices that support desired quasiband structures and strongly localized edge states at prescribed energies, offering exciting opportunities to control light-matter coupling in complex aperiodic environments.

ACKNOWLEDGMENTS

M.R. gratefully acknowledges financial support by the “Stiftung der deutschen Wirtschaft” in the framework of a scholarship. L.D.N. gratefully acknowledges the sponsorship of the Army Research Laboratory under Cooperative Agreement No. W911NF-12-2-0023. The views and conclusions contained in this document are those of the authors and should not be interpreted as representing the official policies, either expressed or implied, of the Army Research Laboratory or the U.S. Government. The U.S. Government is authorized to reproduce and distribute reprints for Government purposes notwithstanding any copyright notation herein.

APPENDIX A: DISCRETE RESONATORS

The aim of this Appendix is to justify viewing substructures embedded in a larger binary aperiodic lattice as local resonators. To this end, we investigate the behavior of the simplest case of such a structure, BAB , in more detail. Its Hamiltonian is

$$H = \begin{pmatrix} v_B & h & 0 \\ h & v_A & h \\ 0 & h & v_B \end{pmatrix}, \quad (\text{A1})$$

with the (unnormalized) eigenstates

$$\phi^1 = \begin{pmatrix} -1 \\ 0 \\ 1 \end{pmatrix}, \quad \phi^{2,3} = \begin{pmatrix} 1 \\ \frac{-\delta \pm \sqrt{8 + \delta^2}}{2} \\ 1 \end{pmatrix}. \quad (\text{A2})$$

where $\delta = (v_A - v_B)/h$, with $c = |\delta|$. For high contrast c , $\phi^3 \approx (1, -\delta, 1)^T$ localizes on the central site. The idea now is to view BAB at high contrast as a resonator, where the site A effectively plays the role of a cavity, while the outer sites B play the role of cavity walls. The resemblance to a resonator becomes clearer for a larger structure with more modes between the resonator walls, like the structure in Fig. 12. As one can see, all but two eigenstates extend nearly exclusively on the internal A sites, and the wavelike character of these states is well recognizable. Two states exclusively localize on the outer two B sites. The setup thus acts as an extended cavity consisting of 14 A sites, with two B sites playing the role of the cavity walls. The smaller structure BAB is of the same nature, albeit with a cavity of only a single site A . Notationally, we will divide the actual cavity and the cavity walls of a resonator by a vertical line, writing, e.g., $B|A \dots A|B$. Similarly, we

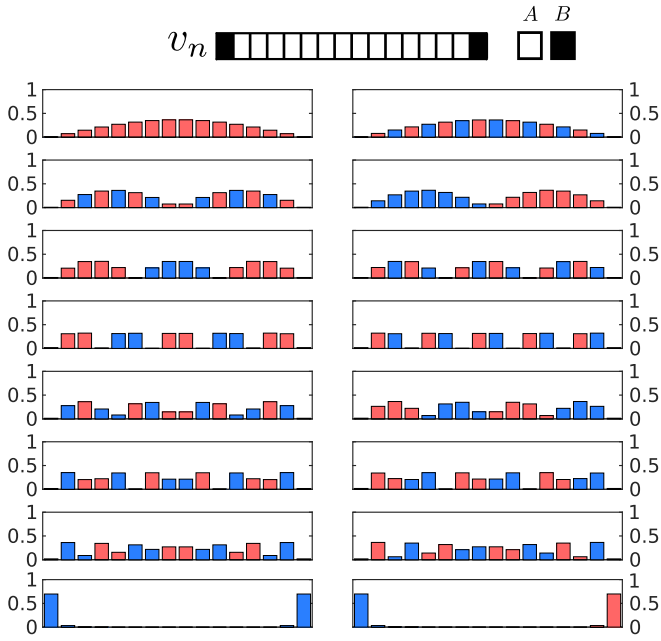


FIG. 12. All 16 eigenstates of the chain (depicted above) $BA \dots B$ with 14 A sites at a contrast of $c = 20$. All but the eigenstates in the last row localize on the A sites.

also view the “inverse” structure $A|B \dots B|A$ as a resonator with resonator modes of higher energy, assuming $v_B \gg v_A$. Moreover, closely neighboring resonators of the form

$$B|A|B|A|B, B|AA|B|AA|B, \dots \quad (\text{A3})$$

can be seen as coupled resonators. To indicate the composite character of such resonators, we omit the inner vertical lines, i.e., $B|ABA|B, B|AABAA|B, \dots$

APPENDIX B: SYMMETRY ARGUMENT FOR THE ABSENCE OF EDGE STATES

Here we explain the absence of edge states in Fig. 4(c) using the concept of local symmetry. The underlying symmetry concept is very general and not limited to the Fibonacci chain, as we demonstrate in the last paragraph of this Appendix. Let us denote an arbitrary sequence of A’s and B’s by X , its reverse ordered counterpart by X^{-1} , and by Y a single site A or B. Then

$$\sigma([X]) \subset \sigma([X^{-1}YX]), \quad (\text{B1})$$

where σ denotes the eigenvalue spectrum and $[X]$ the tridiagonal Hamiltonian representing X . In words, the eigenvalue spectrum of a resonator $[X]$ is completely contained in that of the reflection-symmetric resonator $[X^{-1}YX]$. For example, if $X = AB$ and $Y = B$, then $X^{-1} = BA$ and $\sigma([AB]) \subset \sigma([BABAB])$.

To prove the above statement, we note that the Hamiltonian $[X^{-1}YX]$ reads

$$H = \begin{pmatrix} [X^{-1}] & C & 0 \\ C^T & [Y] & D \\ 0 & D^T & [X] \end{pmatrix}, \quad (\text{B2})$$

where $[X^{-1}], [X] \in \mathbb{R}^{m \times m}$. The matrices $C = (0, \dots, 0, h)^T \in \mathbb{R}^{m \times 1}$ and $D = (h, 0, \dots, 0) \in \mathbb{R}^{1 \times m}$ connect the central site $[Y]$ to $[X]$ and $[X^{-1}]$, respectively. Now, using the “equitable partition theorem” from Ref. [93], we can transform H by a similarity transform into a block-diagonal form

$$H' = \begin{pmatrix} [X^{-1}] & \sqrt{2}C & 0 \\ \sqrt{2}C^T & [Y] & 0 \\ 0 & 0 & [X] \end{pmatrix}. \quad (\text{B3})$$

The similarity transform conserves σ , and since H' is block-diagonal, we have

$$\sigma(H) = \sigma(H') \Rightarrow \sigma([X]) \subset \sigma(H) = \sigma([X^{-1}YX]) \quad (\text{B4})$$

which proves Eq. (B1). Moreover, again using the equitable partition theorem, one can show that the eigenvalues of $[X]$ belong to eigenstates of $[X^{-1}YX]$ with negative parity with respect to the central site Y .

Let us now apply the above statement to Fig. 4(c). Here, for each resonator mode at the edge, there exists one resonator mode within the bulk possessing a similar energy:

$$\epsilon(|\bar{B}|A) \approx \epsilon(A|\bar{B}A\bar{B}|A), \quad (\text{B5})$$

$$\epsilon(A|\bar{B}\bar{B}|) \approx \epsilon(A|\bar{B}\bar{B}A\bar{B}\bar{B}|A), \quad (\text{B6})$$

$$\epsilon(A|\bar{B}\bar{B}|) \approx \epsilon(A|\bar{B}\bar{B}A\bar{B}\bar{B}|A), \quad (\text{B7})$$

where $\epsilon(R)$ denotes the energy of the resonator mode R . In the limit of high contrast, where the resonators present in Eqs. (B5) to (B7) are disconnected from the remainder of the system, the approximations become equalities, and the edge state eigenenergies are thus “absorbed” into the corresponding quasiband.

In a similar manner, the energetic near-equivalence of resonator modes

$$\epsilon(|\bar{A}\bar{A}\bar{A}|B) \approx \epsilon(B|\bar{A}\bar{A}\bar{A}B\bar{A}\bar{A}|B),$$

$$\epsilon(|\bar{A}\bar{A}\bar{A}|B) \approx \epsilon(B|\bar{A}\bar{A}\bar{A}B\bar{A}\bar{A}|B),$$

$$\epsilon(|\bar{A}\bar{A}\bar{A}|B) \approx \epsilon(B|\bar{A}\bar{A}\bar{A}B\bar{A}\bar{A}|B)$$

at high contrast as occurring in Fig. 10(a) can be explained.

APPENDIX C: PERTURBATION THEORETICAL TREATMENT

In this section, we give an explanation for the fragmentation of eigenstates at high contrast in terms of a perturbation theoretical analysis. This will also show why the dominant entries of the eigenstates are in almost all cases obeying local symmetries. Before we start, we note that a degenerate perturbation theoretical treatment of binary chains has been done in the past to retrieve its eigenenergies [94]. The main focus in the following, however, lies on the behavior of eigenstates.

To apply perturbation theory, we write the Hamiltonian Eq. (2) as

$$H = H_0 + \lambda H_I \in \mathbb{R}^{N \times N}, \quad (\text{C1})$$

where H_0 solely contains the diagonal part of H , i.e., isolated sites, while H_I connects them, i.e., contains the off-diagonal elements of H . By means of λ , an eigenstate $|\phi\rangle^{(i)}$, $1 \leq i \leq N$ of H as well as its energy $\epsilon^{(i)}$ are expanded as

$$|\phi^{(i)}\rangle = |\phi^{(i)}\rangle_0 + \lambda|\phi^{(i)}\rangle_1 + \lambda^2|\phi^{(i)}\rangle_2 + \dots \quad (\text{C2})$$

$$\epsilon^{(i)} = \epsilon_0^{(i)} + \lambda\epsilon_1^{(i)} + \lambda^2\epsilon_2^{(i)} + \dots \quad (\text{C3})$$

Inserting Eqs. (C2) and (C3) into the Schrödinger equation $H|\phi^{(i)}\rangle = \epsilon^{(i)}|\phi^{(i)}\rangle$ yields the perturbation series which is assumed to converge and thus solved order by order in λ .

At zeroth order, the perturbation series reduces to the eigenvalue equation for the unperturbed H_0 . Since it is binary, the N eigenstates of H_0 are highly degenerate and form two groups, satisfying

$$H_0|\psi^{(\alpha)}\rangle = v_A|\psi^{(\alpha)}\rangle, \quad 1 \leq \alpha \leq g_A$$

$$H_0|\psi^{(\beta)}\rangle = v_B|\psi^{(\beta)}\rangle, \quad g_A + 1 \leq \beta \leq g_A + g_B = N$$

where $g_{A,B}$ denote the number of sites with potential A, B , respectively. The so-called ‘‘correct’’ zeroth-order states which fulfill

$$|\phi^{(g)}\rangle_0 = \lim_{\lambda \rightarrow 0} |\phi^{(g)}\rangle, \quad g = \{\alpha, \beta\} \quad (\text{C4})$$

and which occur in Eq. (C2) and thus also in the perturbation series are linear superpositions of the $|\psi^{(g)}\rangle$. In the following, we will always denote the two sets $\{\alpha, \beta\}$ by g and simple call the $|\phi^{(g)}\rangle_0$ the zeroth-order states.

At the start of the perturbation theoretical treatment, the $|\psi^{(i)}\rangle$, $1 \leq i \leq N$ are known, but the $|\phi^{(i)}\rangle_0$ are usually not, and the $|\phi^{(i)}\rangle_{1,2,\dots}$ can not be directly be determined. However, it can be shown [76] that already the knowledge of the $|\psi^{(i)}\rangle$ is sufficient to obtain a series of particular solutions to the $1, 2, \dots, n$ th order perturbation equation, yielding the energy corrections $\epsilon_1^{(i)}, \dots, \epsilon_n^{(i)}$ as a byproduct. Provided that the degeneracy of a given state $|\phi^{(j)}\rangle$, $1 \leq j \leq N$ is lifted at k th order, then the corresponding correct-zeroth order state $|\phi^{(j)}\rangle_0$ can be obtained by diagonalizing a $\mathbb{R}^{|j'| \times |j'|}$ matrix which can be derived from the $(k-1)$ th order perturbation equation [76]. Here, $|j'|$ is the number of states $|\phi^{(j')}\rangle$ which are degenerate with $|\phi^{(j)}\rangle$ up to order $k-1$. Then, at order $k+1, \dots, k+l$, the state correction $|\phi^{(j)}\rangle_1, \dots, |\phi^{(j)}\rangle_l$ can be obtained. Note that for the problem at hand, all degeneracies are guaranteed to be lifted at a finite order, since the eigenvalues of tridiagonal matrices with strictly nonvanishing sub- and superdiagonals (such as the one here) are distinct [95] (i.e., nondegenerate). Though all degeneracies will eventually be lifted, the order at which this happens is in general different for different states. In many textbooks, all degeneracies are resolved already at first order, and the zeroth-order states $|\phi^{(i)}\rangle_0$ are the ones that diagonalize the matrix $\langle \psi^{(i)} | H_I | \psi^{(i)} \rangle$ in the corresponding degenerate subspace. This results in simple expressions for the higher-order corrections for both the states and the energy. For our binary H_0 , however, degeneracies are usually resolved only at very high order, and the process becomes complex. For Fibonacci chains, all degeneracies are resolved at fourth order for generation $g=7$, at fifth order for $g=8$, at sixth order for $g=10$ but only in eighth order for $g=12$.

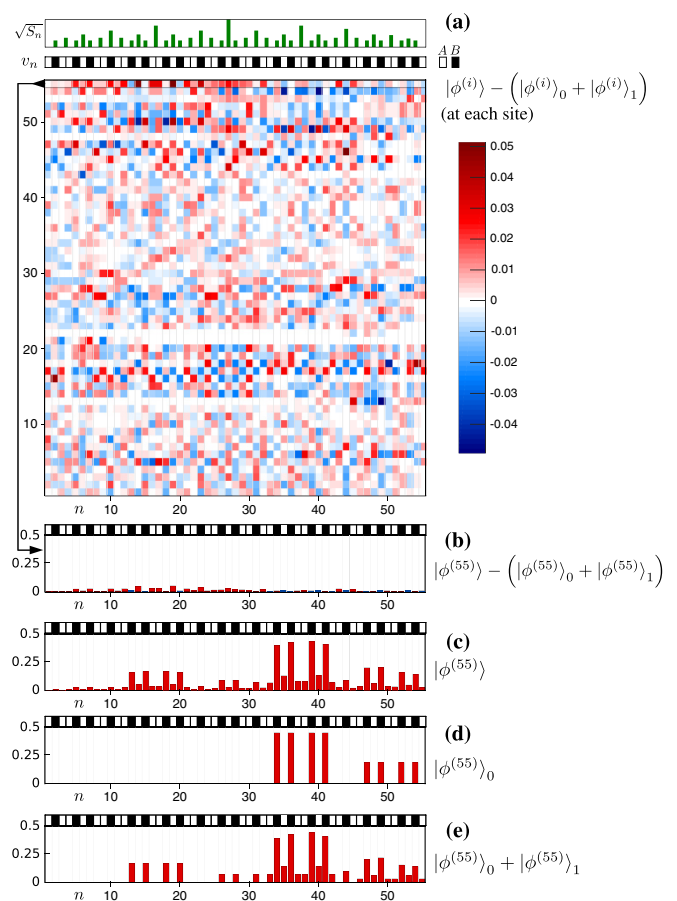


FIG. 13. (a) (Top) Distribution of axes of local symmetry domains and potential sequence, which is identical to that in Fig. 3(a), i.e., corresponds to a ninth generation Fibonacci chain. (Bottom) At each site, the map shows the difference between the full eigenstate $|\phi^{(i)}\rangle$ and the sum of the zeroth-order state and the first-order correction at a contrast of $c=6$. (b) Detailed view on these differences for the uppermost state. The sign of amplitudes is color coded, red for positive and blue for negative values. (c) The amplitudes of the eigenstate $|\phi^{(55)}\rangle$. Note that this particular state does not contain any negative amplitudes. (d) The amplitudes of the zeroth-order state $|\phi^{(55)}\rangle_0$. (e) The amplitudes of the zeroth-order state $|\phi^{(55)}\rangle_0$ plus that of the first-order state correction $|\phi^{(55)}\rangle_1$ (not normalized).

In the following, we will first show the feasibility of degenerate perturbation theory by means of the Fibonacci chain, showing that for high contrast already the zeroth-order states are sufficient to explain the fragmentation of states. Next, we will show the process of determining the zeroth-order states in the first three orders, allowing for an intuitive picture of the emergence of fragmentation and locally symmetric amplitudes. We have numerically observed convergence of the perturbation series if the contrast is larger than roughly 5, depending on the exact chain.

1. Application onto the Fibonacci chain

Figure 13 demonstrates the applicability of degenerate perturbation theory to a ninth generation Fibonacci chain [the same as shown in Fig. 3(a)] at a contrast $c=6$. In subfigure (a),

at each site the difference

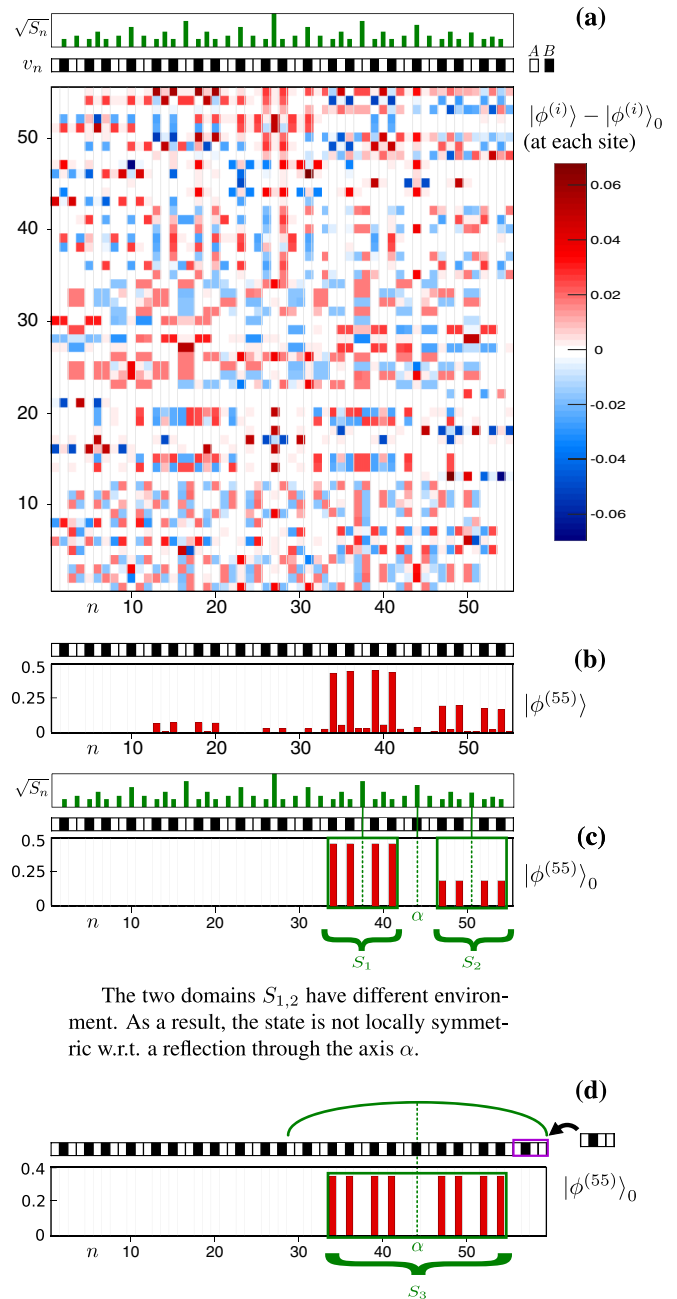
$$\delta^{(i)} = |\phi^{(i)}\rangle - (|\phi^{(i)}\rangle_0 + |\phi^{(i)}\rangle_1), \quad 1 \leq i \leq N = 55$$

is shown. Note that the differences $\delta^{(i)}$ are rather small, and in Fig. 13(b), a detailed picture is given for the uppermost state $|\phi^{(55)}\rangle$. In Figs. 13(c) and 13(d), the full state $|\phi^{(55)}\rangle$ and $|\phi^{(55)}\rangle_0 + |\phi^{(55)}\rangle_1$ are shown, respectively. As one can see, already the zeroth-order state matches the fragmentation behavior of the full state quite well, up to the two double resonator modes $A|\bar{B}A\bar{B}|A$ on the left half of the chain. In Fig. 13(e), we include the first-order correction $|\phi^{(55)}\rangle_1$. As one can see, the resulting state $|\phi^{(55)}\rangle_0 + |\phi^{(55)}\rangle_1$ is very close to the full state $|\phi^{(55)}\rangle$ shown in Fig. 13(c). Although we have here only shown the 55-th state (i.e., uppermost) state in detail, the behavior for all other states is similar. This shows that already the first-order state corrections yield very good results.

If one goes to even higher contrast, already the zeroth-order states $|\phi^{(i)}\rangle_0$ are sufficient to get a full picture of the fragmentation of a given state. This is demonstrated in Fig. 14 for a comparatively very high contrast of $c = 20$. Subfigure (a) shows the difference $|\phi^{(i)}\rangle - |\phi^{(i)}\rangle_0$ at each site. The subfigures (b) and (c) show the complete state $|\phi^{(55)}\rangle$ and the zeroth-order state $|\phi^{(55)}\rangle_0$, for which the main features (the resonator modes) are visible very well. Again, this behavior is the same for all other states, indicating that already the zeroth-order states give a good representation of the localization patterns occurring in the full state. Before we explicitly show the computations for the first three orders in degenerate perturbation theory, let us comment on the connection between the symmetry of the underlying potential sequence and that of the non-negligible amplitudes of a given eigenstate by means of Fig. 14(c). As can be seen, the zeroth-order state is locally parity symmetric individually within the two domains $S_{1,2}$. However, as a whole this state $|\phi^{(55)}\rangle_0$ is not locally reflection symmetric with respect to an axis denoted by α . As we will outline in the following, the reason for this is that the *environment* of the two domains $S_{1,2}$ is different, where environment includes not only next-neighboring sites but also the ones located further away (we will explain the notion of “further away” in more detail below). In Fig. 14(d), we change the environment of the right domain such that it matches that of the first domain up to the first five neighbors. As a result, the zeroth-order state is now symmetric with respect to a reflection through the axis α . In the following, we will investigate the connection between local symmetries of the underlying chain and that of the zeroth-order states in more detail. Finally, we will investigate the first-order state corrections and their relation to the fragmentation of eigenstates.

2. Emergence of localization patterns and their locally symmetric character

We will now show the procedure of finding the zeroth-order states, as can be found e.g. in Refs. [76,96]. Since this procedure is quite technical, to help the reader we have visualized the process in a concise form in Fig. 15 for the easily traceable case of $H_0 = \text{diag}(B, B, A, A, B, A, A)$.



The two domains $S_{1,2}$ have different environment. As a result, the state is not locally symmetric w.r.t. a reflection through the axis α .

Now the environment of the two domains is the same in a sufficiently high range (curvy green line above). This causes the state to be locally symmetric in the domain S_3 .

FIG. 14. (a) Same as in Fig. 13(a), but now at a contrast $c = 15$ and without the first-order correction $|\phi^{(i)}\rangle_1$. (b) The uppermost eigenstate $|\phi^{(55)}\rangle$. (c) The zeroth-order state $|\phi^{(55)}\rangle_0$. Within $S_{1,2}$ the state is locally symmetric with respect to a reflection at the respective centers of these domains (indicated by dotted lines). However, the state is asymmetric with respect to a reflection through the axis α . (d) The environment of $S_{1,2}$ has been made symmetric by adding the sites $ABAA$ on the right-hand side. As a result, the zeroth-order state $|\phi^{(55)}\rangle_0$ (and also, albeit only approximately, the corresponding complete state, though not shown here) is locally symmetric with respect to a reflection through α .

Zeroth-order	0.a The unperturbed Hamiltonian	0.b The states $ \phi^{(g)}\rangle_{0,0}$	
	$H_0 = \text{diag}(BB AA B AA)$	The eigenstates $ \psi^{(g)}\rangle$ of H_0 form the states $ \phi^{(g)}\rangle_0$.	$ \phi^{(\alpha)}\rangle_{0,0} = \left\{ \begin{pmatrix} 0 \\ 0 \\ 1 \\ 0 \\ 0 \\ 0 \\ 0 \end{pmatrix}, \begin{pmatrix} 0 \\ 0 \\ 0 \\ 1 \\ 0 \\ 0 \\ 0 \end{pmatrix}, \begin{pmatrix} 0 \\ 0 \\ 0 \\ 0 \\ 1 \\ 0 \\ 0 \end{pmatrix}, \begin{pmatrix} 0 \\ 0 \\ 0 \\ 0 \\ 0 \\ 1 \\ 0 \end{pmatrix} \right\}$ $ \phi^{(\beta)}\rangle_{0,0} = \left\{ \begin{pmatrix} 1 \\ 0 \\ 0 \\ 0 \\ 0 \\ 0 \\ 0 \end{pmatrix}, \begin{pmatrix} 0 \\ 1 \\ 0 \\ 0 \\ 0 \\ 0 \\ 0 \end{pmatrix}, \begin{pmatrix} 0 \\ 0 \\ 0 \\ 0 \\ 0 \\ 0 \\ 1 \end{pmatrix} \right\}$
First-order	1. At zeroth order, the states are highly degenerate. Thus, we need to go the first order of degenerate perturbation theory and try to resolve the degeneracies here.		
	1.a General structure of the first-order coupling matrices.	1.b Diagonalizing the first-order coupling matrices. Their eigenvalues give the first-order energy corrections $\epsilon_1^{(\alpha)}$ and $\epsilon_1^{(\beta)}$	
	<p style="text-align: center;">$(V_1^{(G)})_{k,j} = {}_{0,0}\langle\phi^{(g[k])} H_I \phi^{(g[j])}\rangle_{0,0}$</p> <p>Due to the tight-binding nature of the perturbation matrix H_I, the first-order coupling matrices are block-diagonal. For each maximally extended contiguous block of potential of the same kind, there is exactly one block in the corresponding coupling matrix.</p> <div style="text-align: center;"> $H_0 = \text{diag}(\overbrace{BB}^{\text{red}} \overbrace{AA}^{\text{blue}} \overbrace{B}^{\text{red}} \overbrace{AA}^{\text{blue}})$ </div> <div style="display: flex; justify-content: space-around;"> <div style="text-align: center;"> $V_1^{(B)} = \begin{pmatrix} D_1^{(B)} \\ D_2^{(B)} \end{pmatrix}$ </div> <div style="text-align: center;"> $V_1^{(A)} = \begin{pmatrix} D_1^{(A)} \\ D_2^{(A)} \end{pmatrix}$ </div> </div> <p>Each block has the structure shown on the right. It is symmetric both around the main and the anti-diagonal, thus <i>bisymmetric</i>.</p> $D_i^{(G)} = \begin{pmatrix} 0 & h & & & & & \\ h & & \ddots & & & & \\ & & & \ddots & & & \\ & & & & h & & \\ & & & & & \ddots & \\ & & & & & & h \\ & & & & & & & 0 \end{pmatrix}$	<p>The Eigenvectors $b^{(G)(k)}\rangle$ of $V_1^{(G)}$ are locally symmetric due to the <i>bisymmetry</i> of $D_i^{(G)}$.</p> <div style="display: flex; justify-content: space-around;"> <div style="text-align: center;"> $b^{(A)(k)}\rangle = \left\{ \begin{pmatrix} \frac{1}{\sqrt{2}} \\ \frac{1}{\sqrt{2}} \\ 0 \\ 0 \end{pmatrix}, \begin{pmatrix} 0 \\ 0 \\ \frac{1}{\sqrt{2}} \\ \frac{1}{\sqrt{2}} \end{pmatrix}, \begin{pmatrix} -\frac{1}{\sqrt{2}} \\ \frac{1}{\sqrt{2}} \\ 0 \\ 0 \end{pmatrix}, \begin{pmatrix} 0 \\ 0 \\ 0 \\ -\frac{1}{\sqrt{2}} \end{pmatrix} \right\}$ $\epsilon_1^{(\alpha)} = \{+2h, +2h, -2h, -2h\}$ </div> <div style="text-align: center;"> $b^{(B)(k)}\rangle = \left\{ \begin{pmatrix} \frac{1}{\sqrt{2}} \\ \frac{1}{\sqrt{2}} \\ 0 \\ 0 \end{pmatrix}, \begin{pmatrix} -\frac{1}{\sqrt{2}} \\ \frac{1}{\sqrt{2}} \\ 0 \\ 0 \end{pmatrix}, \begin{pmatrix} 0 \\ 0 \\ 0 \\ 1 \end{pmatrix} \right\}$ $\epsilon_1^{(\beta)} = \{+2h, -2h, 0\}$ </div> </div> <p>Since $D_1^{(A)} = D_2^{(A)}$, the eigenvalues of $V_1^{(A)}$ are two-fold degenerate.</p> <p>In the next step, the states $\phi^{(g)}\rangle_{0,0}$ are superposed (with coefficients given by the corresponding vectors $b^{(G)(k)}\rangle$). The result of this superposition are the states $\phi^{(g)}\rangle_{0,1}$.</p>	
	1.c Computation of the $ \phi^{(g)}\rangle_{0,1}$		
$V_1^{(G)} b^{(G)(k)}\rangle = \epsilon_1^{(g[k])} b^{(G)(k)}\rangle$ $ \phi^{(g[k])}\rangle_{0,1} = \sum_{1 \leq l \leq g } b_l^{(G)(k)} \phi^{(g[l])}\rangle_{0,0}$ <p>Due to the local parity of $b^{(G)(k)}\rangle$, the states $\phi^{(g)}\rangle_{0,1}$ are locally symmetric as well.</p>	$ \phi^{(\alpha)}\rangle_{0,1} = \left\{ \begin{pmatrix} 0 \\ 1/\sqrt{2} \\ 1/\sqrt{2} \\ 0 \\ 0 \\ 0 \\ 0 \end{pmatrix}, \begin{pmatrix} 0 \\ 0 \\ 0 \\ 1/\sqrt{2} \\ 1/\sqrt{2} \\ 0 \\ 0 \end{pmatrix}, \begin{pmatrix} 0 \\ 0 \\ -1/\sqrt{2} \\ 1/\sqrt{2} \\ 0 \\ 0 \\ 0 \end{pmatrix}, \begin{pmatrix} 0 \\ 0 \\ 0 \\ -1/\sqrt{2} \\ 1/\sqrt{2} \\ 0 \\ 0 \end{pmatrix} \right\}$ <p style="text-align: center;"> $\rightarrow \phi^{(\alpha_1)}\rangle_{0,1}$ $\phi^{(\alpha_2)}\rangle_{0,1} \leftarrow$ </p> <p>Still pairwise degenerate with $\epsilon_1^{(\alpha_1)} = +2h$ and $\epsilon_1^{(\alpha_2)} = -2h$.</p>	$ \phi^{(\beta)}\rangle_{0,1} = \left\{ \begin{pmatrix} 1/\sqrt{2} \\ 1/\sqrt{2} \\ 0 \\ 0 \\ 0 \\ 0 \\ 0 \end{pmatrix}, \begin{pmatrix} 1/\sqrt{2} \\ -1/\sqrt{2} \\ 0 \\ 0 \\ 0 \\ 0 \\ 0 \end{pmatrix}, \begin{pmatrix} 0 \\ 0 \\ 0 \\ 0 \\ 1 \\ 0 \\ 0 \end{pmatrix} \right\}$ <p>Since $\epsilon_1^{(\beta)} = \{+2h, -2h, 0\}$, the degeneracy is completely solved at first order. Thus, $\phi^{(\beta)}\rangle_0 = \phi^{(\beta)}\rangle_{0,1}$.</p>	
Second-order	2. At first order, the states $ \phi^{(\alpha'_1)}\rangle$ and $ \phi^{(\alpha'_2)}\rangle$ are still degenerate. Thus, we need to go to the second order of degenerate perturbation theory and resolve the degeneracies here.		
	2. a Diagonalizing the second order coupling matrices	2. b Computation of the states $ \phi^{(\alpha_1)}\rangle_{0,2}$ and $ \phi^{(\alpha_2)}\rangle_{0,2}$	
	$V_2^{(A_1)} = \frac{h^2}{2v} \begin{pmatrix} 2 & 1 \\ 1 & 1 \end{pmatrix}$ $V_2^{(A_2)} = \frac{h^2}{2v} \begin{pmatrix} 2 & -1 \\ -1 & 1 \end{pmatrix}$ <p>No bisymmetry here due to the <i>asymmetric</i> environment of the two vv-blocks!</p> $ b^{(A_1)(k)}\rangle = \left\{ \begin{pmatrix} \frac{1+\sqrt{5}}{2} \\ 1 \end{pmatrix}, \begin{pmatrix} \frac{1-\sqrt{5}}{2} \\ 1 \end{pmatrix} \right\}$ $ b^{(A_2)(k)}\rangle = \left\{ \begin{pmatrix} \frac{-1-\sqrt{5}}{2} \\ 1 \end{pmatrix}, \begin{pmatrix} \frac{-1+\sqrt{5}}{2} \\ 1 \end{pmatrix} \right\}$ <p>These eigenvectors of $V_2^{(A_1)}$ and $V_2^{(A_2)}$ are <i>not</i> parity symmetric! However, they would if $V_2^{(A_1)}$ and $V_2^{(A_2)}$ would be bisymmetric.</p>	$ \phi^{(g_i[k])}\rangle_{0,2} = \sum_{1 \leq l \leq g_i } b_l^{(G_i)(k)} \phi^{(g_i[l])}\rangle_{0,1}$ $ \phi^{(\alpha_1)}\rangle_{0,2} = \left\{ \begin{pmatrix} 0 \\ 0 \\ \frac{1+\sqrt{5}}{2\sqrt{2}} \\ \frac{1+\sqrt{5}}{2\sqrt{2}} \\ 0 \\ \frac{1}{\sqrt{2}} \end{pmatrix}, \begin{pmatrix} 0 \\ 0 \\ \frac{1-\sqrt{5}}{2\sqrt{2}} \\ \frac{1-\sqrt{5}}{2\sqrt{2}} \\ 0 \\ \frac{1}{\sqrt{2}} \end{pmatrix} \right\}$ $ \phi^{(\alpha_2)}\rangle_{0,2} = \left\{ \begin{pmatrix} 0 \\ 0 \\ \frac{1+\sqrt{5}}{2\sqrt{2}} \\ -\frac{1+\sqrt{5}}{2\sqrt{2}} \\ 0 \\ -\frac{1}{\sqrt{2}} \end{pmatrix}, \begin{pmatrix} 0 \\ 0 \\ \frac{1-\sqrt{5}}{2\sqrt{2}} \\ -\frac{1-\sqrt{5}}{2\sqrt{2}} \\ 0 \\ -\frac{1}{\sqrt{2}} \end{pmatrix} \right\}$ <p>Due to the asymmetry of $b^{(A_j)(k)}\rangle$, $1 \leq j \leq 2$, the states $\phi^{(\alpha_j)}\rangle_{0,2}$ are not locally symmetric on the vv structure. However, they are individually locally symmetric on each vv structure due to the local symmetry of the states $\phi^{(\alpha_j)}\rangle_{0,1}$. The eigenvalues of $V_2^{(A_j)}$ are non-degenerate, thus $\phi^{(\alpha_j)}\rangle_0 = \phi^{(\alpha_j)}\rangle_{0,2}$.</p>	

 FIG. 15. Visualization of the process of finding the zeroth-order states for $H_0 = \text{diag}(B, B, A, A, B, A, A)$.

As stated above, $|\phi^{(g)}\rangle_0$ can in general not be determined before its degeneracy is not completely lifted. At higher orders, the states $|\phi^{(g)}\rangle$ degenerate at zeroth order may split into subsets $|\phi^{(g_1)}\rangle, |\phi^{(g_2)}\rangle, \dots$ which are degenerate up to first order, each of which can subsequently split into subsets of states $|\phi^{(g_{1.1})}\rangle, |\phi^{(g_{1.2})}\rangle, \dots, |\phi^{(g_{2.1})}\rangle, |\phi^{(g_{2.2})}\rangle, \dots$, which are degenerate up to second order, and so on. The determination of the zeroth-order states can be done by means of recursively defined auxiliary states [76,96]

$$|\phi^{(g)}\rangle_{0,0} = |\psi^{(g)}\rangle, \quad (\text{C5})$$

$$|\phi^{(g[k])}\rangle_{0,1} = \sum_{1 \leq l \leq |g|} b_l^{(G)(k)} |\phi^{(g[l])}\rangle_{0,0}, \quad (\text{C6})$$

$$|\phi^{(g_i[k])}\rangle_{0,2} = \sum_{1 \leq l \leq |g_i|} b_l^{(G_i)(k)} |\phi^{(g_i[l])}\rangle_{0,1}, \quad (\text{C7})$$

$$|\phi^{(g_{i,j}[k])}\rangle_{0,3} = \sum_{1 \leq l \leq |g_{i,j}|} b_l^{(G_{i,j})(k)} |\phi^{(g_{i,j}[l])}\rangle_{0,2} \quad (\text{C8})$$

$$\vdots \quad (\text{C9})$$

appearing on the left-hand side of the above equations, where $g[k]$ denotes the k th element of the set g and k can run from 1 to the number of elements $|g|$ within the set. The index G is equal to A if $g \in \alpha$ and equal to B if $g \in \beta$. Each expansion coefficient $b_l^{(S)(k)}$ is the l th component of the vector $|b^{(S)(k)}\rangle, S \in \{G, G_i, G_{i,j}, \dots\}$ defined as

$$V_1^{(G)} |b^{(G)(k)}\rangle = \epsilon_1^{(g[k])} |b^{(G)(k)}\rangle,$$

$$V_2^{(G_i)} |b^{(G_i)(k)}\rangle = \epsilon_2^{(g_i[k])} |b^{(G_i)(k)}\rangle,$$

$$V_3^{(G_{i,j})} |b^{(G_{i,j})(k)}\rangle = \epsilon_3^{(g_{i,j}[k])} |b^{(G_{i,j})(k)}\rangle,$$

\vdots

where the matrices $V_1^{(G)}, V_2^{(G_i)}, \dots$ are obtained by a recursive process [76,96]. Explicitly, for the first three orders they are

$$(V_1^{(G)})_{k,j} = {}_{0,0} \langle \phi^{(g[k])} | H_I | \phi^{(g[j])} \rangle_{0,0},$$

$$(V_2^{(G_i)})_{k,j} = {}_{0,1} \langle \phi^{(g_i[k])} | H_I R^{(g)} H_I | \phi^{(g_i[j])} \rangle_{0,1},$$

$$(V_3^{(G_{i,j})})_{k,l} = {}_{0,2} \langle \phi^{(g_{i,j}[k])} | U^{(g_i)} | \phi^{(g_{i,j}[l])} \rangle_{0,2},$$

where

$$U^{(g_i)} = H_I R^{(g)} \overline{H_I} R^{(g)} H_I + H_I R^{(g)} H_I R^{(g_i)} H_I R^{(g)} H_I$$

with $\overline{H_I} = H_I - \epsilon_1^{(g_i)}$ and

$$R^{(g)} = \sum_{k \neq g} \frac{|\psi^{(k)}\rangle \langle \psi^{(k)}|}{\epsilon_0^{(g)} - \epsilon_0^{(k)}},$$

$$R^{(g_i)} = \sum_{\substack{k \in g_j \\ j \neq i}} \frac{|\phi^{(k)}\rangle_{0,1} {}_{0,1} \langle \phi^{(k)}|}{\epsilon_1^{(g_i)} - \epsilon_1^{(k)}}.$$

The above recursive process does the following: At the start, we have $|\phi^{(g)}\rangle_{0,0} = |\psi^{(g)}\rangle$. These are then superposed according to Eq. (C6), obtaining $|\phi^{(g)}\rangle_{0,1}$. Within each degenerate subspace g_i , these are again superposed according to Eq. (C7), obtaining $|\phi^{(g_i)}\rangle_{0,2}$. Again, within each degenerate subspace $g_{i,j}$, these are superposed according to Eq. (C8), obtaining $|\phi^{(g_{i,j})}\rangle_{0,3}$, and so on. Provided that the degeneracy

of a given state $|\phi^{(k)}\rangle, 1 \leq k \leq N$ is solved at n th order, the degenerate subspace for this state at orders $l > n$ contains only one state, so that naturally $|\phi^{(k)}\rangle_{0,l} = |\phi^{(k)}\rangle_{0,n}$ and [76] $|\phi^{(k)}\rangle_0 = |\phi^{(k)}\rangle_{0,n}$.

In the following, we will prove that the $|\phi^{(i)}\rangle_0, 1 \leq i \leq N$ simultaneously localize on one or more maximally extended blocks of potentials of the same kind (MEBPS) (statement 1) and determine on which such blocks a given state can simultaneously localize (statement 2). Each MEBPS is the cavity of a resonator, thus giving reason for the localization of states on resonators. Statement 1 also shows that the $|\phi^{(i)}\rangle_0$ are locally parity symmetric individually on each MEBPS, and statements 3 and 4 further deal with longer-range symmetries of the zeroth-order states. Out of the many possible choices of $|\psi^{(i)}\rangle$ (due to its high degeneracy), in the following, we chose them such that $|\psi^{(\alpha[k])}\rangle [|\psi^{(\beta[k])}\rangle]$ is solely localized on the k th site with potential $A [B]$ (counted from the left).

Statement 1. Each state $|\phi^{(i)}\rangle_0, 1 \leq i \leq N$ simultaneously localizes on one or more maximally extended blocks $A \dots A$ or $B \dots B$ of potentials of the same kind (MEBPS) and is locally parity symmetric on each of these blocks.

Proof. The proof is done in three steps. Firstly, we show that $V_1^{(G)}, G \in \{A, B\}$ is block-diagonal, where each block is related to exactly one MEBPS. Secondly, we show that the eigenvectors $|b^{(G)(k)}\rangle, 1 \leq k \leq |g|$ of $V_1^{(G)}$ are locally parity symmetric and subsequently the $|\phi^{(g)}\rangle_{0,1}$ are locally symmetric on each MEBPS. Thirdly, we show that any higher-order states $|\phi^{(g)}\rangle_{0,n}$ with $n > 1$ show this local symmetry as well, and thus the zeroth-order states $|\phi^{(g)}\rangle_0$ are locally symmetric as well.

We start by proving the following. For the case that H_I contains only next-neighbor couplings (as is the case here) the $V_1^{(G)}$ become block-diagonal, i.e., can be written as

$$V_1^{(G)} = \begin{pmatrix} D_1^{(G)} & & \\ & \ddots & \\ & & D_{n_G}^{(G)} \end{pmatrix}, \quad (\text{C10})$$

where n_G denote the number of blocks occurring in $V_1^{(G)}$ and each block

$$D_i^{(G)} = \begin{pmatrix} 0 & h & & \\ h & \ddots & \ddots & \\ & \ddots & \ddots & h \\ & & h & 0 \end{pmatrix}, \quad 1 \leq i \leq n_G \quad (\text{C11})$$

is a tridiagonal Toeplitz matrix. To prove that $V_1^{(G)}$ is of the above form, we note that by the definition of $V_1^{(G)}$ and H_I , two states $|\psi^{(j)}\rangle, |\psi^{(k)}\rangle, 1 \leq j, k \leq N$ are coupled to each other by any of the two matrices $V_1^{(G)}$ provided that (i) the single sites on which they localize are direct neighbors and (ii) they have the same zeroth-order energy, i.e., they must be localized on states with identical on-site potential. If (i) and (ii) are fulfilled for $|\psi^{(j)}\rangle, |\psi^{(k)}\rangle, j \neq k$ with $j, k \in g$ and $g[l] = j_1, g[m] = j_2$, then the corresponding matrix element $(V_1^{(G)})_{l,m} = h$ due to the definition of these states. As a result, for each MEBPS $A \dots A [B \dots B]$ containing n sites, there is one tridiagonal $n \times n$ block of the form Eq. (C11) present in $V^{(A)} [V^{(B)}]$.

We now show that the $|\phi^{(g)}\rangle_{0,1}$ are locally parity symmetric on each MEBPS. To this end, we use the fact that the eigenvectors of the block-diagonal matrix $V^{(G)}$ are

$$|b^{(G)(k)}\rangle = \left\{ \begin{pmatrix} \{\mathbf{w}_{1,G}\} \\ \mathbf{0}_{d_{2,G}} \\ \mathbf{0}_{d_{3,G}} \\ \vdots \\ \mathbf{0}_{d_{n_G,G}} \end{pmatrix}, \begin{pmatrix} \mathbf{0}_{d_{1,G}} \\ \{\mathbf{w}_{2,G}\} \\ \mathbf{0}_{d_{3,G}} \\ \vdots \\ \mathbf{0}_{d_{n_G,G}} \end{pmatrix}, \dots, \begin{pmatrix} \mathbf{0}_{d_{1,G}} \\ \mathbf{0}_{d_{2,G}} \\ \mathbf{0}_{d_{3,G}} \\ \vdots \\ \{\mathbf{w}_{n_G,G}\} \end{pmatrix} \right\}$$

with $1 \leq k \leq |g|$ and where $\mathbf{0}_{d_{i,G}}$ is the $d_{i,G} \times 1$ vector with identical zero entries and $\{\mathbf{w}_{i,G}\}$ denotes the set of $d_{i,G}$ eigenvectors of $D_i^{(G)} \in \mathbb{R}^{d_{i,G} \times d_{i,G}}$. All vectors in a given set $\{\mathbf{w}_{i,G}\}$ have nonvanishing components only on one maximally extended block of potentials of the same kind and are parity-symmetric with respect to a reflection through the center of this block. The latter is due to the fact that the $D_i^{(G)}$ are real and bisymmetric, and the eigenstates of such matrices have definite parity [97] (in the case of degeneracies, the eigenvectors can be chosen accordingly). A matrix is bisymmetric if it is symmetric both around the main and the antidiagonal. Since we have ordered the state $|\psi^{(g|k)}\rangle$, $1 \leq k \leq |g|$ such that it has nonvanishing amplitude on the k -th site with potential G , one can easily show that each of the $|\phi^{(g)}\rangle_{0,1}$ has definite parity on each MEBPS.

For second-order degenerate perturbation theory, the states $|\phi^{(g_i)}\rangle_{0,1}$, which are degenerate up to first order, are superposed to obtain $|\phi^{(g_i)}\rangle_{0,2}$. Now, since all states in a given set $\{\mathbf{w}_{j,g}\}$, $1 \leq j \leq n_G$ have distinct eigenvalues, the states $|\phi^{(g_i)}\rangle_{0,1}$ are constructed such that for each set g_i there is at most one state possessing nonvanishing amplitudes on any given MEBPS. Thus, $|\phi^{(g_i)}\rangle_{0,2}, \dots$ will keep the local parity symmetry, and it is trivial to show that the zeroth-order states $|\phi^{(g)}\rangle_0$ are locally parity symmetric on each MEBPS as well. ■

Due to its maximal extension, each MEBPS is directly neighbored either by potentials of the other kind on one or on both sides, with the former being the case if the MEBPS forms one edge of the chain. Thus the $|\phi^{(g)}\rangle_0$ are seen to localize on *resonators*. We now show that a given state $|\phi^{(i)}\rangle_0$, $1 \leq i \leq N$ can only simultaneously localize on resonators fulfilling certain conditions.

Statement 2. A given zeroth-order state $|\phi^{(i)}\rangle_0$, $1 \leq i \leq N$ can simultaneously localize on a set of MEBPS with individual lengths l_1, l_2, \dots, l_n only if the following conditions are met. (i) All the MEBPS must have potentials of the same kind. (ii) There exist integers $1 \leq k_j \leq l_j$, $1 \leq j \leq n$ such that

$$\frac{k_1}{l_1 + 1} = \frac{k_2}{l_2 + 1} = \dots = \frac{k_n}{l_n + 1}. \quad (\text{C12})$$

Proof. By definition, the zeroth-order state $|\phi^{(i)}\rangle_0$ is formed by superpositions of a subset of the states $|\phi^{(g_j)}\rangle_{0,1}$, with $i \in g_j$. Thus, a necessary condition to allow for the localization on multiple MEBPS $\{M_i\}$ is that among $|\phi^{(g_j)}\rangle_{0,1}$, for each M_i there is one state localized on it. By definition, the set $|\phi^{(g_j)}\rangle_{0,1}$ contains states with pairwise identical zeroth-order $\epsilon_0^{(g_j)}$ and pairwise identical first-order energy corrections $\epsilon_1^{(g_j)}$. The zeroth-order energies are identical if all the MEBPS have the same potential. To see when there is an equality of the

first-order energies, we use the fact that the first-order energy corrections $\epsilon_1^{(g)}$ can be given analytically. The block matrix $D_i^{(G)} \in \mathbb{R}^{l_i \times l_i}$ occurring in $V_1^{(G)}$ is of tridiagonal Toeplitz form, and its eigenvalues are thus [98] given by

$$\lambda_k^{D_i^{(G)}} = 2|h| \cos\left(\frac{\pi k}{l_i + 1}\right), \quad k = 1, \dots, l_i. \quad (\text{C13})$$

Thus two blocks $D_1^{(G)}, D_2^{(G)}$ with size l_1, l_2 only share common eigenvalues provided that the integer-equation

$$\frac{k_1}{l_1 + 1} = \frac{k_2}{l_2 + 1} \quad (\text{C14})$$

is fulfilled for some $1 \leq k_1 \leq l_1$ and $1 \leq k_2 \leq l_2$. Generalizing the above to the case of n blocks with corresponding length l_1, \dots, l_n directly yields Eq. (C12). ■

For many combinations of $l_1 \neq l_2$ (especially for small $l_{1,2}$), Eq. (C14) can not be fulfilled, with the prominent exception of $l_{1,2}$ both being odd numbers. In this case, there exist states $|\phi^{(i)}\rangle_{0,1}$ which localize on two resonators of *different* kind, and usually this behavior is kept also for $|\phi^{(i)}\rangle_0$ as well as the corresponding complete states $|\phi^{(i)}\rangle$. This is the explanation for the emergence of the two states in Fig. 10(a), which are marked by green ellipse.

We now show how the local symmetries of the zeroth-order states can be explained by means of that of the underlying potential sequence. Due to the complexity of binary tight-binding chains, we only show two explicit cases, but stress that the process can easily be applied to any given chain.

Statement 3. If H_0 contains one or more of the substructures

$$[\dots] \text{AA} \underset{s_1}{\text{BAB}} \text{AA} [\dots] \quad (\text{C15})$$

or

$$[\dots] \text{AA} \underset{s_1}{\text{BABA}} \quad (\text{C16})$$

(where $[\dots]$ denotes a possibly larger extension of the chain) then all zeroth-order states $|\phi^{(\beta)}\rangle_0$ respect the local symmetry S_1 on each of these structures.

Proof. We label the sites of the substructure AABABAA from left [s_1] to right [s_7] for Eq. (C15) and s_6 for Eq. (C16), where the small s indicates a possible embedding of the corresponding substructure into a greater system. Among the N states $|\phi^{(i)}\rangle_{0,1}$, $1 \leq i \leq N$ of this system, all but the two states $|\phi^{(j_k)}\rangle_{0,1}$, $1 \leq k \leq 2$ with $1 \leq j_k \leq N$, $j_1 \neq j_2$ have vanishing amplitudes on both of the sites s_3 and s_5 . Moreover, $|\phi^{(j_1)}\rangle_{0,1}$ has nonvanishing amplitude only on site s_3 , while $|\phi^{(j_2)}\rangle_{0,1}$ has nonvanishing amplitude only on site s_5 . We denote the set $|\phi^{(g_1)}\rangle$ to contain all states which are degenerate with $|\phi^{(j_k)}\rangle$ up to first order. As can be shown, $V_2^{(G_1)}$ (just as $V_1^{(G)}$) is block-diagonal, and only states that are degenerate up to first order and which are localized on MEBPS which are separated by exactly one site are coupled to each other. Thus, the two states $|\phi^{(j_1)}\rangle_{0,1}, |\phi^{(j_2)}\rangle_{0,1}$, $j_1, j_2 \in g_1$ are *not* coupled to the other $|\phi^{(g_1)}\rangle_{0,1}$ by means of $V_2^{(G_1)}$, but only to each other. If $g_1[1] = j_1$ and $g_1[2] = j_2$, then the submatrix

$$(V_2^{(G_1)})_{l,m} = \frac{h^2}{v_B - v_A} \begin{pmatrix} 2 & 1 \\ 1 & 2 \end{pmatrix}, \quad 1 \leq l, m \leq 2 \quad (\text{C17})$$

which is real-valued and bisymmetric. Its eigenvectors are thus parity-symmetric. As can be easily shown, thus $|\phi^{(j_k)}\rangle_{0,2}$ are parity symmetric within S_1 , i.e., respect this domain of local symmetry. The matrix in Eq. (C17) has nondegenerate eigenvalues referring to $\epsilon_2^{(j_k)}$, and thus the two states $|\phi^{(j_k)}\rangle$ are no longer degenerate to each other at second order. Since $|\phi^{(j_k)}\rangle_{0,1}$ are the only ones out of the $|\phi^{(\beta)}\rangle_{0,1}$ with nonvanishing amplitudes within S_1 , one can easily show that *all* zeroth-order states $|\phi^{(\beta)}\rangle_0$ must respect S_1 . ■

The above is of relevance for the first and third quasiband from top in Fig. 3(a). By means of another example, we indicate the importance of the environment of a domain S such that the zeroth-order states respect it.

Statement 4. If the right edge of H_0 is given by

$$[\dots]BAAB \underbrace{ABA}_{S_1} \quad (\text{C18})$$

(where $[\dots]$ denotes a possibly larger extension of the chain) then the zeroth-order states $|\phi^{(\alpha)}\rangle_0$ do not respect the local symmetry S_1 . However, if the right edge of H_0 is given by

$$[\dots]BAAB \underbrace{ABA}_B \quad (\text{C19})$$

then all zeroth-order states $|\phi^{(\alpha)}\rangle_0$ respect the local symmetry S_1 .

Proof. We label the sites of the substructure $BAABABA$ from left (s_1) to right [s_7 for the first and s_8 for the second statement]. Among the N states $|\phi^{(i)}\rangle_{0,1}$, $1 \leq i \leq N$ of there system, all but the two states $|\phi^{(j_k)}\rangle_{0,1}$, $1 \leq k \leq 2$ with $1 \leq j_k \leq N$, $j_1 \neq j_2$ have vanishing amplitudes on both of the sites s_5 and s_7 . Moreover, $|\phi^{(j_1)}\rangle_{0,1}$ has nonvanishing amplitude only on site s_5 , while $|\phi^{(j_2)}\rangle_{0,1}$ has nonvanishing amplitude only on site s_7 . We denote the set $|\phi^{(g_1)}\rangle$ to contain all states which are degenerate with $|\phi^{(j_k)}\rangle$ up to first order. Again, due to the block-diagonal character of $V_2^{(g_1)}$, the two states $|\phi^{(j_1)}\rangle_{0,1}$, $|\phi^{(j_2)}\rangle_{0,1}$, $j_1, j_2 \in g_1$ are *not* coupled to the other $|\phi^{(g_1)}\rangle_{0,1}$ by means of $V_2^{(G_1)}$, but only to each other. If $g_1[1] = j_1$ and $g_1[2] = j_2$, then the submatrices

$$\left(V_2^{(G_1)}\right)_{l,m} = \frac{h^2}{v_B - v_A} \begin{pmatrix} 2 & 1 \\ 1 & 1 \end{pmatrix}, \quad 1 \leq l, m \leq 2 \quad (\text{C20})$$

for $[\dots]BAABABA$ and

$$\left(V_2^{(G_1)}\right)_{l,m} = \frac{h^2}{v_B - v_A} \begin{pmatrix} 2 & 1 \\ 1 & 2 \end{pmatrix}, \quad 1 \leq l, m \leq 2 \quad (\text{C21})$$

for $[\dots]BAABABAB$. Both Eqs. (C20) and (C21) are real-valued, but the former is not bisymmetric, while the latter is. As can be easily shown, for the first case, the $|\phi^{(j_k)}\rangle_{0,2}$ are also not parity symmetric within S_1 , i.e., do not respect this domain of local symmetry. The matrix in Eq. (C20) has nondegenerate eigenvalues referring to $\epsilon_2^{(j_k)}$, and thus the two states $|\phi^{(j_k)}\rangle$ are no longer degenerate to each other at second order. Since $|\phi^{(j_k)}\rangle_{0,1}$ are the only ones out of the $|\phi^{(\alpha)}\rangle_{0,1}$ with nonvanishing amplitudes within S_1 , one can easily show that no zeroth-order state $|\phi^{(\alpha)}\rangle_0$ respects S_1 . For the second case, the line of argumentation essentially is the same with the difference that, due to the bisymmetry of Eq. (C21), the $|\phi^{(j_k)}\rangle_{0,2}$ are parity symmetric within S_1 , and thus all $|\phi^{(\alpha)}\rangle_0$ respect S_1 . ■

The reason for the nonbisymmetry of Eq. (C20) is the different *environment* of s_5 and s_7 . In this particular case, the environment is made up by the next-neighboring sites, but for higher orders it comprises many more sites left and right to the given domain. The fact that $|\phi^{(55)}\rangle_0$ in Fig. 14(c) is not locally symmetric with respect to a reflection through α is due to the fact that the environment of $S_{1,2}$ is not symmetric with respect to a reflection through α in a sufficiently large radius, while in Fig. 14(d) it is, so that $|\phi^{(55)}\rangle_0$ is locally symmetric with respect to a reflection through α .

3. First-order state corrections and eigenstate fragmentation

In the above, we have seen how the correct zeroth-order states are related to the local symmetries of the underlying potential. In particular, we have argued that each of the $|\phi^{(i)}\rangle_0$ is fragmented, since it has nonvanishing amplitudes only on one kind of site. We have further seen that, already at contrast $c = 6$, $|\phi^{(i)}\rangle_0 + |\phi^{(i)}\rangle_1 \approx |\phi^{(i)}\rangle$. In the following, we show that, in general, the $|\phi^{(i)}\rangle_0 + |\phi^{(i)}\rangle_1$ are fragmented as well.

Contrary to the nondegenerate case, where the first-order state corrections are given by

$$|\phi^{(i)}\rangle_1 = \sum_{j \neq i} \frac{|\phi^{(j)}\rangle_0 \langle \phi^{(j)} | H_I | \phi^{(i)} \rangle_0}{\epsilon_0^{(i)} - \epsilon_0^{(j)}}$$

the corresponding expression in degenerate perturbation theory depends on the order in which the degeneracy of $|\phi^{(i)}\rangle$ is completely resolved. A full, recursive expression for $|\phi^{(i)}\rangle_1$ can be found in Ref. [77]. In this context, we only need the easily provable fact that

$$\langle \psi^{(\bar{g}[j])} | \phi^{(g[k])} \rangle_1 = \frac{\langle \psi^{(\bar{g}[j])} | H_I | \phi^{(g[k])} \rangle_0}{\epsilon_0^{(g[k])} - \epsilon_0^{(\bar{g}[j])}}, \quad (\text{C22})$$

where \bar{g} denotes the set of sites which are not elements of g . In other words, if $|\phi^{(i)}\rangle_0$ “lives” on, say, sites with potential A , then $|\phi^{(i)}\rangle_1$ will have nonvanishing amplitudes only on directly *neighboring* B sites, but not on those further away. As a result, if $|\phi^{(i)}\rangle_0$ has nonvanishing amplitudes on a small number of sites (which we have observed for Fibonacci, Thue-Morse, and Rudin-Shapiro chains), then $|\phi^{(i)}\rangle_0 + |\phi^{(i)}\rangle_1$ is fragmented.

APPENDIX D: DISCRETE ENERGY-LOCALIZATION THEOREM AND APPROXIMATION OF EIGENVALUES BY SUB-HAMILTONIANS

We here extend a theorem of Ref. [99], connecting the localization of a state to its eigenenergy, to discrete Hamiltonians.

Theorem. The following equation holds

$$\frac{\|\phi\|_{\partial\bar{D}}}{\|\phi\|_D} \geq \min_{\epsilon_k} \frac{|\epsilon - \epsilon_k|}{|h|}, \quad (\text{D1})$$

where $|\phi\rangle$ is an eigenvector of H with energy ϵ and ϵ_k are eigenvalues of H restricted to the domain D which is a simply connected subdomain of the whole system. $\|\phi\|_D$ is the norm of $|\phi\rangle$ on D and $\|\phi\|_{\partial\bar{D}}$ the norm of $|\phi\rangle$ on next-neighbors of D .

Proof. If D contains N_D sites, define the $N_D \times N_D$ matrix H_D constructed from the corresponding matrix elements of the

complete Hamiltonian H . In other words, H_D is the restriction of H onto D . Similarly, we further define $|i\rangle$ as the $N_D \times 1$ vector constructed from the full eigenvector $|\phi\rangle$ by taking the interior elements of D . If we now let H_D act on $|i\rangle$, one can easily show that

$$H_D|i\rangle = \epsilon|i\rangle - h|\partial\phi\rangle, \quad (\text{D2})$$

where ϵ is the eigenvalue of the complete state $|\phi\rangle$. Here, h denotes the next-neighboring hopping of H [as defined in Eq. (2)] and $|\partial\phi\rangle$ denotes a $N_D \times 1$ vector with zeros everywhere but on the first and last entry. These two nonvanishing entries are constructed by taking the corresponding two elements of $|\phi\rangle$ within ∂D . If $N_D = 1$, then we define the only entry of $|\partial\phi\rangle$ as the sum of the two amplitudes of $|\phi\rangle$ within ∂D .

To make the notation introduced above more explicit, let us assume that

$$H = \begin{pmatrix} v_1 & h & 0 & 0 \\ h & v_2 & h & 0 \\ 0 & h & v_3 & h \\ 0 & 0 & h & v_4 \end{pmatrix}, \quad |\phi\rangle = \begin{pmatrix} a \\ b \\ c \\ d \end{pmatrix}. \quad (\text{D3})$$

If D would denote the central two sites, then $|i\rangle = (b, c)^T$ and $|\partial\phi\rangle = (a, d)^T$.

Equation (D2) can be interpreted as follows: Provided that $|\phi\rangle$ is identically zero on the next-neighboring sites of D , $|i\rangle$ would be an eigenstate to H_D . However, $|\phi\rangle$ usually has *nonvanishing* amplitudes on sites neighboring to D , and thus $|\partial\phi\rangle \neq 0$. Thus this correction must be included in Eq. (D2).

We now proceed with our proof of Eq. (D1). Multiplying from the left with $\langle\phi_k|$, i.e., the k th eigenstate of H_D , we get

$$h \cdot \langle\phi_k|\partial\phi\rangle = (\epsilon - \epsilon_k) \cdot \langle\phi_k|i\rangle. \quad (\text{D4})$$

Multiplying this expression by its complex conjugate, summing over k and taking the square root of the result, we get

$$|h| \left(\sum_k |\langle\phi_k|\partial\phi\rangle|^2 \right)^{1/2} = \left(\sum_k (\epsilon - \epsilon_k)^2 \cdot |\langle\phi_k|i\rangle|^2 \right)^{1/2}. \quad (\text{D5})$$

Since the $|\phi_k\rangle$ are a complete orthonormal basis set, the left-hand side can be simplified by using the definition of the norm, getting

$$|h| \left(\sum_k |\langle\phi_k|\partial\phi\rangle|^2 \right)^{1/2} = |h| \| |\phi\rangle \|_{\partial D}. \quad (\text{D6})$$

The sum on the right-hand side can be estimated as

$$\sum_k (\epsilon - \epsilon_k)^2 \cdot \| |\phi_k\rangle \|_{\partial D}^2 \geq \min_{\epsilon_k} (\epsilon - \epsilon_k)^2 \cdot \sum_{k'} \| |\phi_{k'}\rangle \|_{\partial D}^2. \quad (\text{D7})$$

Again, due to the definition of the norm, we can thus write Eq. (D5) as

$$|h| \| |\phi\rangle \|_{\partial D} \geq \min_{\epsilon_k} |\epsilon - \epsilon_k| \| |\phi\rangle \|_D \quad (\text{D8})$$

which directly yields Eq. (D1). ■

Roughly speaking, the theorem states the following. Assume that an eigenstate $|\phi\rangle$ has a high integrated density on

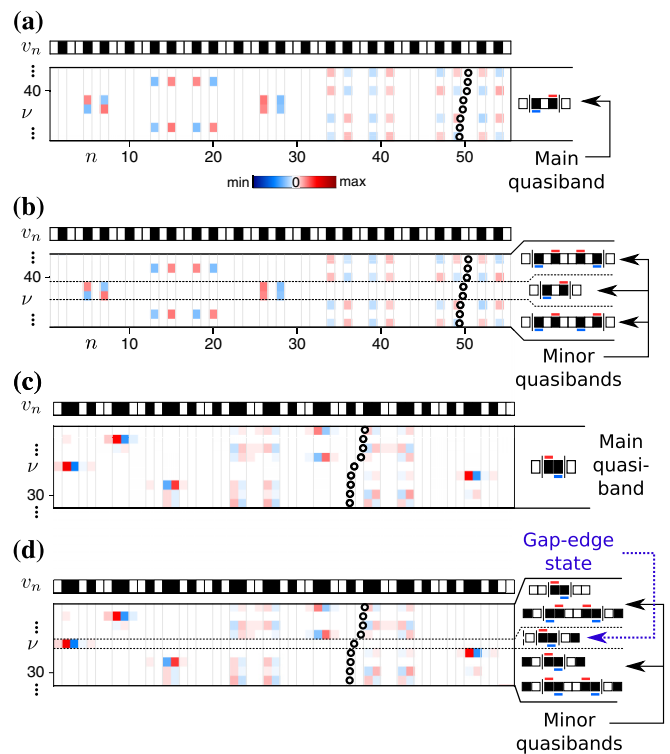


FIG. 16. (a) Shown is the third quasiband from top for the ninth generation Fibonacci chain at contrast $c = 3$. (b) The three minor quasibands and their respective LRMs. (c) The third quasiband from top for a $L = 55$ sites truncated Thue-Morse chain at contrast $c = 3$. (d) The two minor quasibands as well as the gap-edge state and their respective LRMs.

some domain D , with low amplitudes on the next-neighboring sites left and right of the domain. Then, the energy ϵ of this eigenstate is approximately equal to the energy of one of the eigenstates $|\phi_k\rangle$ of the local Hamiltonian H_D . If D is a resonator and $|\phi\rangle$ represents an LRM of H_D within D and suitably small amplitudes on next-neighboring sites of D , then $\epsilon \approx \epsilon_i$, where ϵ_i is the energy of the LRM.

APPENDIX E: COMMENTS ON THE APPLICATION TO LONGER CHAINS

We now comment on how the treatment of longer chains or the investigation of the subband structure can be pursued. To this end, the core element of our approach, the analysis of states in terms of their constituting LRMs needs to be slightly changed by extending the class of resonators taken into account. The process of finding the constituting LRMs of a given state $|\phi\rangle$ with energy ϵ is then as follows. Starting from a domain D exclusively containing sites with very high amplitudes, one forms a simply connected domain D' by the union of D and its surrounding sites (not limited to next-neighbors) such that $|\phi\rangle$ has very low amplitude on next-neighbors of D' . Then [guaranteed by Eq. (D1)], one eigenstate of the Hamiltonian $H_{D'}$ has nearly the same energy $\epsilon \approx \epsilon^i$ and is (up to normalization), within D' , nearly equal to $|\phi\rangle$ and thus forms an LRM. As the maximum deviation between ϵ^i and ϵ is bounded by means of Eq. (D1) and generally becomes

smaller for larger D' , its size should thus be chosen large enough to achieve the accuracy needed for an explanation of the subquasibands and gap-edge states present but as small as possible in order not to lose the local character of the treatment. If the LRM obtained by the above process does not explain all fragments of $|\phi\rangle$, then one needs to repeat it for each of the remaining fragments until all constituting LRMs of $|\phi\rangle$ are found.

We now exemplify in Fig. 16 some possible results of such a deeper analysis. Subfigure (a) shows the third quasiband from top of the ninth generation Fibonacci chain [the one shown in Fig. 3(a)], but now at a lower contrast of $c = 3$. At this contrast, the energetical substructure of the band becomes apparent, denoted by the two dashed lines in Fig. 16(b). There

are three minor quasibands, comprising the three uppermost, the two central and the three lowermost eigenstates within this quasiband. The above process then yields the LRMs shown on the right-hand side of this subfigure. Another example is demonstrated in Figs. 16(c) and 16(d), showing the third quasiband from top for a truncated $L = 55$ site Thue-Morse chain [as shown in Fig. 7(a)] at contrast $c = 3$. Here, the main quasiband features the resonator mode $A|\overline{BB}|A$, but again features a substructure as shown in subfigure (d). Each minor quasibands is made up of two nearly degenerate LRMs, with the underlying resonators having resonator walls each consisting of *two* sites. The state in-between these minor bands consists of the edge-LRM $\downarrow A|\overline{BB}|AB$, where the \downarrow indicates the edge of the chain.

-
- [1] E. Maciá, The role of aperiodic order in science and technology, *Rep. Prog. Phys.* **69**, 397 (2006).
- [2] D. Shechtman, I. Blech, D. Gratias, and J. W. Cahn, Metallic Phase with Long-Range Orientational Order and No Translational Symmetry, *Phys. Rev. Lett.* **53**, 1951 (1984).
- [3] M. Pennybacker and A. C. Newell, Phyllotaxis, Pushed Pattern-Forming Fronts, and Optimal Packing, *Phys. Rev. Lett.* **110**, 248104 (2013).
- [4] E. Maciá, Exploiting aperiodic designs in nanophotonic devices, *Rep. Prog. Phys.* **75**, 036502 (2012).
- [5] J.-M. Dubois, Properties- and applications of quasicrystals and complex metallic alloys, *Chem. Soc. Rev.* **41**, 6760 (2012).
- [6] C. Mancinelli, C. J. Jenks, P. A. Thiel, and A. J. Gellman, Tribological properties of a B2-type Al-Pd-Mn quasicrystal approximant, *J. Mater. Res.* **18**, 1447 (2003).
- [7] C. Bauer and H. Giessen, Light harvesting enhancement in solar cells with quasicrystalline plasmonic structures, *Opt. Express* **21**, A363 (2013).
- [8] M. Yoshimura and A. P. Tsai, Quasicrystal application on catalyst, *J. Alloy. Comp.* **342**, 451 (2002).
- [9] A. Koga, First observation of superconductivity in new alloys with Tsai-Type clusters, *JPSJ News Comments* **12**, 02 (2015).
- [10] K. Kamiya, T. Takeuchi, N. Kabeya, N. Wada, T. Ishimasa, A. Ochiai, K. Deguchi, K. Imura, and N. K. Sato, Discovery of superconductivity in quasicrystal, *Nat. Commun.* **9**, 154 (2018).
- [11] L. Dal Negro, R. Wang, and F. Pinheiro, Structural and spectral properties of deterministic aperiodic optical structures, *Crystals* **6**, 161 (2016).
- [12] S. Ostlund and R. Pandit, Renormalization-group analysis of the discrete quasiperiodic Schrödinger equation, *Phys. Rev. B* **29**, 1394 (1984).
- [13] E. Maciá, On the nature of electronic wave functions in one-dimensional self-similar and quasiperiodic systems, *ISRN Condens. Matter Phys.* **2014**, 165943 (2014).
- [14] M. Kohmoto, B. Sutherland, and C. Tang, Critical wave functions and a Cantor-set spectrum of a one-dimensional quasicrystal model, *Phys. Rev. B* **35**, 1020 (1987).
- [15] T. Fujiwara, M. Kohmoto, and T. Tokihiro, Multifractal wave functions on a Fibonacci lattice, *Phys. Rev. B* **40**, 7413 (1989).
- [16] E. de Prunelé and X. Bouju, Fibonacci, koch, and penrose structures: Spectrum of finite subsystems in three-dimensional space, *Phys. Status Solidi (b)* **225**, 95 (2001).
- [17] E. de Prunelé, Penrose structures: Gap labeling and geometry, *Phys. Rev. B* **66**, 094202 (2002).
- [18] M. A. Bandres, M. C. Rechtsman, and M. Segev, Topological Photonic Quasicrystals: Fractal Topological Spectrum and Protected Transport, *Phys. Rev. X* **6**, 011016 (2016).
- [19] P. Vignolo, M. Bellec, J. Böhm, A. Camara, J.-M. Gambaudo, U. Kuhl, and F. Mortessagne, Energy landscape in a Penrose tiling, *Phys. Rev. B* **93**, 075141 (2016).
- [20] E. Maciá, Clustering resonance effects in the electronic energy spectrum of tridiagonal Fibonacci quasicrystals, *Phys. Status Solidi B* **254**, 1700078 (2017).
- [21] L. Dal Negro and S. V. Boriskina, Deterministic aperiodic nanostructures for photonics and plasmonics applications, *Laser Photonics Rev.* **6**, 178 (2012).
- [22] L. Dal Negro, *Optics of Aperiodic Structures: Fundamentals and Device Applications* (Pan Stanford, Singapore, 2013).
- [23] E. Maciá, Spectral classification of one-dimensional binary aperiodic crystals: An algebraic approach, *Ann. Phys. (Berl.)* **529**, 1700079 (2017).
- [24] R. Johnson and J. Moser, The rotation number for almost periodic potentials, *Commun. Math. Phys.* **84**, 403 (1982).
- [25] F. Delyon and B. Souillard, The rotation number for finite difference operators and its properties, *Commun. Math. Phys.* **89**, 415 (1983).
- [26] J. M. Luck, Cantor spectra and scaling of gap widths in deterministic aperiodic systems, *Phys. Rev. B* **39**, 5834 (1989).
- [27] J. Bellissard, A. Bovier, and J.-M. Ghez, Gap labeling theorems for one dimensional discrete schrödinger operators, *Rev. Math. Phys.* **04**, 1 (1992).
- [28] M. Baake, U. Grimm, and D. Joseph, Trace maps, invariants, and some of their applications, *Int. J. Mod. Phys. B* **07**, 1527 (1993).
- [29] S. G. Davison and M. Steslicka, *Basic Theory of Surface States*, Monographs on the Physics and Chemistry of Materials (Oxford University Press, Oxford, New York, 1996).
- [30] J. Zak, Symmetry criterion for surface states in solids, *Phys. Rev. B* **32**, 2218 (1985).
- [31] B. A. Bernevig, *Topological Insulators and Topological Superconductors* (Princeton University Press, Princeton, NJ, 2013).
- [32] C. L. Kane and E. J. Mele, Z_2 Topological Order and the Quantum Spin Hall Effect, *Phys. Rev. Lett.* **95**, 146802 (2005).

- [33] M. Z. Hasan and C. L. Kane, Colloquium: Topological insulators, *Rev. Mod. Phys.* **82**, 3045 (2010).
- [34] X.-L. Qi and S.-C. Zhang, Topological insulators and superconductors, *Rev. Mod. Phys.* **83**, 1057 (2011).
- [35] W. Tian, W. Yu, J. Shi, and Y. Wang, The property, preparation and application of topological insulators: A review, *Materials* **10**, 814 (2017).
- [36] P. St-Jean, V. Goblot, E. Galopin, A. Lemaître, T. Ozawa, L. Le Gratiet, I. Sagnes, J. Bloch, and A. Amo, Lasing in topological edge states of a one-dimensional lattice, *Nat. Photon.* **11**, 651 (2017).
- [37] E. S. Zijlstra, A. Fasolino, and T. Janssen, Existence and localization of surface states on Fibonacci quasicrystals: A tight-binding study, *Phys. Rev. B* **59**, 302 (1999).
- [38] Y. El Hassouani, H. Aynaou, E. H. El Boudouti, B. Djafari-Rouhani, A. Akjouj, and V. R. Velasco, Surface electromagnetic waves in Fibonacci superlattices: Theoretical and experimental results, *Phys. Rev. B* **74**, 035314 (2006).
- [39] H. Lei, J. Chen, G. Nouet, S. Feng, Q. Gong, and X. Jiang, Photonic band gap structures in the Thue-Morse lattice, *Phys. Rev. B* **75**, 205109 (2007).
- [40] X.-N. Pang, J.-W. Dong, and H.-Z. Wang, Photonic localization of interface modes at the boundary between metal and Fibonacci quasiperiodic structure, *J. Opt. Soc. Am. B* **27**, 2009 (2010).
- [41] A. J. Martínez and M. I. Molina, Surface solitons in quasiperiodic nonlinear photonic lattices, *Phys. Rev. A* **85**, 013807 (2012).
- [42] T. A. Loring and M. B. Hastings, Disordered topological insulators via C^* -algebras, *Europhys. Lett.* **92**, 67004 (2010).
- [43] A. Agarwala and V. B. Shenoy, Topological Insulators in Amorphous Systems, *Phys. Rev. Lett.* **118**, 236402 (2017).
- [44] S. S. Negi and R. Ramaswamy, Critical states and fractal attractors in fractal tongues: Localization in the Harper map, *Phys. Rev. E* **64**, 045204(R) (2001).
- [45] J. Kellendonk and I. Zois, Rotation numbers, boundary forces and gap labelling, *J. Phys. A: Math. Gen.* **38**, 3937 (2005).
- [46] Y. E. Kraus and O. Zeitlinger, Topological Equivalence between the Fibonacci Quasicrystal and the Harper Model, *Phys. Rev. Lett.* **109**, 116404 (2012).
- [47] F. Baboux, E. Levy, A. Lemaître, C. Gómez, E. Galopin, L. Le Gratiet, I. Sagnes, A. Amo, J. Bloch, and E. Akkermans, Measuring topological invariants from generalized edge states in polaritonic quasicrystals, *Phys. Rev. B* **95**, 161114(R) (2017).
- [48] A. Dureau, E. Levy, M. B. Aguilera, R. Bouganne, E. Akkermans, F. Gerbier, and J. Beugnon, Revealing the Topology of Quasicrystals with a Diffraction Experiment, *Phys. Rev. Lett.* **119**, 215304 (2017).
- [49] R. Wang, M. Röntgen, C. V. Morfonios, F. A. Pinheiro, P. Schmelcher, and L. Dal Negro, Edge modes of scattering chains with aperiodic order, *Opt. Lett.* **43**, 1986 (2018).
- [50] M. Gardner, Mathematical games, *Sci. Am.* **236**, 110 (1977).
- [51] C. Morfonios, P. Schmelcher, P. A. Kalozoumis, and F. K. Diakonou, Local symmetry dynamics in one-dimensional aperiodic lattices: A numerical study, *Nonlinear Dyn.* **78**, 71 (2014).
- [52] C. V. Morfonios, P. A. Kalozoumis, F. K. Diakonou, and P. Schmelcher, Nonlocal discrete continuity and invariant currents in locally symmetric effective Schrödinger arrays, *Ann. Phys.* **385**, 623 (2017).
- [53] M. Röntgen, C. Morfonios, F. Diakonou, and P. Schmelcher, Non-local currents and the structure of eigenstates in planar discrete systems with local symmetries, *Ann. Phys.* **380**, 135 (2017).
- [54] A. G. B. Spourdalakis, G. Pappas, C. V. Morfonios, P. A. Kalozoumis, F. K. Diakonou, and P. Schmelcher, Generalized continuity equations from two-field Schrödinger Lagrangians, *Phys. Rev. A* **94**, 052122 (2016).
- [55] T. Wulf, C. V. Morfonios, F. K. Diakonou, and P. Schmelcher, Exposing local symmetries in distorted driven lattices via time-averaged invariants, *Phys. Rev. E* **93**, 052215 (2016).
- [56] P. A. Kalozoumis, C. Morfonios, F. K. Diakonou, and P. Schmelcher, Invariants of Broken Discrete Symmetries, *Phys. Rev. Lett.* **113**, 050403 (2014).
- [57] P. A. Kalozoumis, C. Morfonios, N. Palaiodimopoulos, F. K. Diakonou, and P. Schmelcher, Local symmetries and perfect transmission in aperiodic photonic multilayers, *Phys. Rev. A* **88**, 033857 (2013).
- [58] S. Aubry and G. André, Analyticity breaking and Anderson localization in incommensurate lattices, *Ann. Israel Phys. Soc.* (1980).
- [59] G. Roati, C. D'Errico, L. Fallani, M. Fattori, C. Fort, M. Zaccanti, G. Modugno, M. Modugno, and M. Inguscio, Anderson localization of a non-interacting Bose-Einstein condensate, *Nature* **453**, 895 (2008).
- [60] J. K. Asbóth, L. Oroszlány, and A. Pályi, *A Short Course on Topological Insulators: Band Structure and Edge States in One and Two Dimensions*, Lecture Notes in Physics (Springer International, Cham, Switzerland, 2016).
- [61] A. Szameit, F. Dreisow, and S. Nolte, *Discrete Optics in Femtosecond Laser Written Waveguide Arrays*, Topics in Applied Physics (Springer, Berlin, Heidelberg, 2012).
- [62] N. K. Efremidis, P. Zhang, Z. Chen, D. N. Christodoulides, C. E. Rüter, and D. Kip, Wave propagation in waveguide arrays with alternating positive and negative couplings, *Phys. Rev. A* **81**, 053817 (2010).
- [63] E. Maciá Barber, *Aperiodic Structures in Condensed Matter: Fundamentals and Applications*, 1st ed. (Taylor & Francis Inc, Boca Raton, 2008).
- [64] N. Macé, A. Jagannathan, and F. Piéchon, Fractal dimensions of wave functions and local spectral measures on the Fibonacci chain, *Phys. Rev. B* **93**, 205153 (2016).
- [65] X. Droubay, Palindromes in the Fibonacci word, *Inf. Process. Lett.* **55**, 217 (1995).
- [66] M. Grundmann, *The Physics of Semiconductors: An Introduction Including Nanophysics and Applications*, 3rd ed., Graduate Texts in Physics (Springer International, Cham, Switzerland, 2016).
- [67] M. L. Povinelli, S. G. Johnson, S. Fan, and J. D. Joannopoulos, Emulation of two-dimensional photonic crystal defect modes in a photonic crystal with a three-dimensional photonic band gap, *Phys. Rev. B* **64**, 075313 (2001).
- [68] Q. Niu and F. Nori, Spectral splitting and wave-function scaling in quasicrystalline and hierarchical structures, *Phys. Rev. B* **42**, 10329 (1990).
- [69] F. Nori and J. P. Rodriguez, Acoustic and electronic properties of one-dimensional quasicrystals, *Phys. Rev. B* **34**, 2207 (1986).

- [70] X. Fu, Y. Liu, P. Zhou, and W. Sritrakool, Perfect self-similarity of energy spectra and gap-labeling properties in one-dimensional Fibonacci-class quasilattices, *Phys. Rev. B* **55**, 2882 (1997).
- [71] E. Levy, A. Barak, A. Fisher, and E. Akkermans, Topological properties of Fibonacci quasicrystals : A scattering analysis of Chern numbers, [arXiv:1509.04028](https://arxiv.org/abs/1509.04028).
- [72] M. Verbin, O. Zilberberg, Y. Lahini, Y. E. Kraus, and Y. Silberberg, Topological pumping over a photonic Fibonacci quasicrystal, *Phys. Rev. B* **91**, 064201 (2015).
- [73] M. Baake, F. Gähler, and U. Grimm, Spectral and topological properties of a family of generalised Thue-Morse sequences, *J. Math. Phys.* **53**, 032701 (2012).
- [74] M. Parto, S. Wittek, H. Hodaie, G. Harari, M. A. Bandres, J. Ren, M. C. Rechtsman, M. Segev, D. N. Christodoulides, and M. Khajavikhan, Edge-Mode Lasing in 1D Topological Active Arrays, *Phys. Rev. Lett.* **120**, 113901 (2018).
- [75] A. Blanco-Redondo, I. Andonegui, M. J. Collins, G. Harari, Y. Lumer, M. C. Rechtsman, B. J. Eggleton, and M. Segev, Topological Optical Waveguiding in Silicon and the Transition between Topological and Trivial Defect States, *Phys. Rev. Lett.* **116**, 163901 (2016).
- [76] J. O. Hirschfelder and P. R. Certain, Degenerate RS perturbation theory, *J. Chem. Phys.* **60**, 1118 (1974).
- [77] H. J. Silverstone and R. K. Moats, Practical recursive solution of degenerate Rayleigh-Schrödinger perturbation theory and application to high-order calculations of the Zeeman effect in hydrogen, *Phys. Rev. A* **23**, 1645 (1981).
- [78] P. A. Kalugin, A. Y. Kitaev, and L. S. Levitov, Electron spectrum of a one-dimensional quasicrystal, *Zh. Eksp. Teor. Fiz.* **91**, 692 (1986).
- [79] F. Piéchon, M. Benakli, and A. Jagannathan, Analytical Results for Scaling Properties of the Spectrum of the Fibonacci Chain, *Phys. Rev. Lett.* **74**, 5248 (1995).
- [80] Y. Liu and W. Sritrakool, Branching rules of the energy spectrum of one-dimensional quasicrystals, *Phys. Rev. B* **43**, 1110 (1991).
- [81] Q. Niu and F. Nori, Renormalization-Group Study of One-Dimensional Quasiperiodic Systems, *Phys. Rev. Lett.* **57**, 2057 (1986).
- [82] M. Kolář, M. K. Ali, and F. Nori, Generalized Thue-Morse chains and their physical properties, *Phys. Rev. B* **43**, 1034 (1991).
- [83] L. Kroon and R. Riklund, Absence of localization in a model with correlation measure as a random lattice, *Phys. Rev. B* **69**, 094204 (2004).
- [84] R. Riklund, M. Severin, and Y. Liu, The thue-morse aperiodic crystal, a link between the fibonacci quasicrystal and the periodic crystal, *Int. J. Mod. Phys. B* **01**, 121 (1987).
- [85] Note that we have not used here a generation of the Thue-Morse sequence (of length [63] 2^8 for the g -th generation), but the same length $N = 144$ as for the Fibonacci chain. This is done for the sake of comparison but also to avoid certain symmetries [100] of the Thue-Morse sequence generations (spatial mirror symmetry for odd g and spectral mirror symmetry around $E = 0$ for even g), in favor of the generality of the analysis.
- [86] To give precise results also for smallest amplitudes of around 10^{-20} , the corresponding eigenstates have been obtained by diagonalizing H with 64 decimal digits of precision by using the variable precision tools from the MATLAB[®] Symbolic Math Toolbox[™].
- [87] L. Kroon, E. Lennholm, and R. Riklund, Localization-delocalization in aperiodic systems, *Phys. Rev. B* **66**, 094204 (2002).
- [88] M. Dulea, M. Johansson, and R. Riklund, Unusual scaling of the spectrum in a deterministic aperiodic tight-binding model, *Phys. Rev. B* **47**, 8547 (1993).
- [89] M. Dulea, M. Johansson, and R. Riklund, Trace-map invariant and zero-energy states of the tight-binding Rudin-Shapiro model, *Phys. Rev. B* **46**, 3296 (1992).
- [90] M. Dulea, M. Johansson, and R. Riklund, Localization of electrons and electromagnetic waves in a deterministic aperiodic system, *Phys. Rev. B* **45**, 105 (1992).
- [91] P. A. Kalozoumis, C. V. Morfonios, F. K. Diakonou, and P. Schmelcher, Invariant currents and scattering off locally symmetric potential landscapes, *Ann. Phys.* **362**, 684 (2015).
- [92] V. E. Zampetakis, M. K. Diakonou, C. V. Morfonios, P. A. Kalozoumis, F. K. Diakonou, and P. Schmelcher, Invariant current approach to wave propagation in locally symmetric structures, *J. Phys. A* **49**, 195304 (2016).
- [93] M. Röntgen, C. V. Morfonios, and P. Schmelcher, Compact localized states and flat bands from local symmetry partitioning, *Phys. Rev. B* **97**, 035161 (2018).
- [94] D. Barache and J. M. Luck, Electronic spectra of strongly modulated aperiodic structures, *Phys. Rev. B* **49**, 15004 (1994).
- [95] B. Parlett, *The Symmetric Eigenvalue Problem*, Classics in Applied Mathematics (Society for Industrial and Applied Mathematics, Philadelphia, PA, 1998).
- [96] H. J. Silverstone, Explicit solution for the wavefunction and energy in degenerate Rayleigh-Schrödinger perturbation theory, *J. Chem. Phys.* **54**, 2325 (1971).
- [97] A. R. Collar, On centrosymmetric and centroskew matrices, *Quart. J. Mech. Appl. Math.* **15**, 265 (1962).
- [98] S. Noschese, L. Pasquini, and L. Reichel, Tridiagonal Toeplitz matrices: Properties and novel applications, *Numer. Linear Algebra Appl.* **20**, 302 (2013).
- [99] M. Filoche and S. Mayboroda, Universal mechanism for Anderson and weak localization, *Proc. Natl. Acad. Sci. USA* **109**, 14761 (2012).
- [100] M. Noguez and R. A. Barrio, Properties of the Thue-Morse Chain, in *Physics of Low Dimensional Systems* (Springer, Boston, MA, 2001), pp. 223–232.

Compact localized states and flat bands from local symmetry partitioning

M. Röntgen,¹ C. V. Morfonios,¹ and P. Schmelcher^{1,2}

¹Zentrum für Optische Quantentechnologien, Universität Hamburg, Luruper Chaussee 149, 22761 Hamburg, Germany

²The Hamburg Centre for Ultrafast Imaging, Universität Hamburg, Luruper Chaussee 149, 22761 Hamburg, Germany



(Received 22 September 2017; revised manuscript received 6 January 2018; published 30 January 2018)

We propose a framework for the connection between local symmetries of discrete Hamiltonians and the design of compact localized states. Such compact localized states are used for the creation of tunable, local symmetry-induced bound states in an energy continuum and flat energy bands for periodically repeated local symmetries in one- and two-dimensional lattices. The framework is based on very recent theorems in graph theory which are here employed to obtain a block partitioning of the Hamiltonian induced by the symmetry of a given system under local site permutations. The diagonalization of the Hamiltonian is thereby reduced to finding the eigenspectra of smaller matrices, with eigenvectors automatically divided into compact localized and extended states. We distinguish between local symmetry operations which commute with the Hamiltonian, and those which do not commute due to an asymmetric coupling to the surrounding sites. While valuable as a computational tool for versatile discrete systems with locally symmetric structures, the approach provides in particular a unified, intuitive, and efficient route to the flexible design of compact localized states at desired energies.

DOI: [10.1103/PhysRevB.97.035161](https://doi.org/10.1103/PhysRevB.97.035161)

I. INTRODUCTION

Compact localized states [1,2], i.e., wave excitations that strictly vanish outside a finite subpart of a system, are caused by destructive interference in the presence of local spatial symmetries [1]. Contrary to the case of Anderson localization [3], where exponentially localized states are caused by disorder, compact localized states (CLSs) typically occur in perfectly ordered systems [1]. They were early deduced from symmetry principles in bipartite lattices [4], and studied more recently in, e.g., frustrated hopping models [5] as well as magnonic [6] and interacting [7] systems. A possible application of CLSs lies in information transmission [8–10] and directly stems from their compactness: Being an eigenstate of the Hamiltonian, a CLS does not spread out spatially during evolution, while it is much less challenging to excite than a regular extended eigenstate. For example, CLSs are ideal candidates for the transmission of information along photonic waveguide arrays avoiding “crosstalk” between waveguides [11]. Further, CLSs essentially enable the appearance of isolated bound states within a scattering continuum [12–14]. Such states were, e.g., realized recently as a symmetry-induced topological eigenstate subspace of coupled-chain setups [15]. On a computational level, CLSs induced by symmetries may also be used as a symmetry-adapted basis for numerical computations [16]. In periodic lattice systems, macroscopically degenerate CLSs lead to the occurrence of flat, i.e., dispersionless, energy bands [17]. Flat bands are studied in different contexts, including the quantum Hall effect in topologically nontrivial lattices [18–21], induced metal-insulator transitions [22,23], and non-Hermitian quantum mechanics [24,25].

Different approaches have been suggested to *design* systems featuring CLSs and flat bands. They are based on strategies such as so-called origami rules [26], the repetition of mini-arrays [27], working on bipartite Hamiltonians [28],

detangling the lattice into Fano lattices [1], or even more general approaches, such as band engineering [29] or generator principles [2]. Most of these works are based on the presence of different kinds of *local symmetries*, i.e., on the invariance of a subset of matrix elements under a site permutation. In general, local symmetries of the underlying Hamiltonian are indirectly encoded into its eigenstates, as has been demonstrated recently in various contexts [30–38]. However, not every locally symmetric system features CLSs, and a systematic framework linking a theory of local symmetries to the formation and control of both CLSs and the resulting flat bands is still missing.

In the present work, we take a step in this direction by applying very recent graph theoretical results to generic single-particle discrete Hamiltonians. The resulting unifying framework connects two types of local symmetries to the occurrence of CLSs, flat bands, and bound states in the continuum. Complementing many of the above CLS design strategies, this framework uniquely pairs a high degree of control with an in-depth understanding of the impact of local symmetries. Technically, we apply and generalize two recently published theorems [16,39–41] to general Hamiltonian matrices. These theorems, which we refer to as the equitable and nonequitable partition theorems, quantify the effect of certain local symmetries of the Hamiltonian matrix H underlying a given discrete system. Specifically, the equitable partition theorem (EPT) applies to locally acting symmetry transformations which commute with H , while the nonequitable partition theorem (nEPT) applies to a subclass of transformations that do not commute with H . In essence, the theorems assert a symmetry-induced decomposition of H into a direct sum (i.e., block-diagonal form) of smaller matrices, whose spectrum and eigenvectors thereby determine those of H . In particular, the eigenvectors of submatrices corresponding to symmetric subsystems of the complete setup uniquely provide all existing CLSs of H together with their eigenenergies. The remaining

submatrix is analogously connected to extended eigenstates (non-CLSs) of H .

In the context of periodic lattices, the presence of local symmetries is thus shown to *automatically* enforce the presence of flat bands, while the (n)EPT can be used to control both the flat *and* dispersive bands of the system. The approach can be seen as complementary to the general and powerful design principle of Refs. [1,2] based on elementwise conditions on the underlying eigenvalue equation, in that it solely relies on generalized symmetry concepts. Moreover, the methodology can be used to reduce the computational effort of diagonalisation by exploiting local symmetries present in the Hamiltonian.

We apply the framework to the design of both flat bands and symmetry-induced bound states in the continuum. It should be emphasized that the approach allows for the design of symmetry-induced flat bands at prescribed energies in *arbitrary* dimensions. Moreover, since it is solely based on the symmetries of a complex-valued square matrix, the framework is applicable to a broad range of physical problems, treated by, e.g., multichannel scattering theory or dyadic Green functions [42–44]. We thus believe that this work may inspire the exploration of the effect of local symmetries in the broader research community.

The paper is structured as follows. Sec. II introduces the concept and description of local symmetries and subsequently states the EPT and nEPT in terms of simple example setups. In Sec. III we demonstrate the methodology in the design of bound states in the continuum and flat band lattices. Sec. IV contains our conclusions.

II. LOCAL SYMMETRIES AND EQUITABLE PARTITIONS

The setting we will operate on is the eigenvalue problem

$$H\phi = E\phi \quad (1)$$

of a Hamiltonian matrix H modeling a (lattice) system of sites n with elements

$$H_{mn} = \begin{cases} v_n, & m = n, \\ h_{m,n} \neq 0, & n \in \mathcal{N}(m), \\ 0 & \text{else,} \end{cases} \quad (2)$$

where $\mathcal{N}(n)$ denotes a set of neighboring sites connected to site n via a nonvanishing hopping. H is graphically represented by a (weighted) graph with vertices connected by edges for corresponding nonzero hoppings, as in Fig. 1. Throughout, we will use different vertex sizes and coloring to indicate different values of the onsite potential of the represented Hamiltonian. The considered model can be seen as a generalized tight-binding network, with more than just next-neighbor hopping being allowed. Such a model is extensively used to describe single-electron phenomena, such as localization in lattice systems [5,45]. It also effectively describes, for instance, arrays of evanescently coupled photonic waveguides, in terms of which both flat bands [11,46,47] and bound states in the continuum [48,49] have been studied.

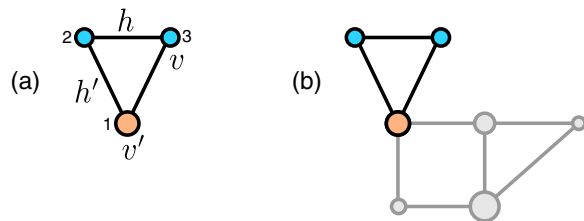


FIG. 1. (a) The Hamiltonian of a three-site system is represented by a graph with connected vertices, with vertex sizes (and colors) indicating different onsite potential values. The system is symmetric under the permutation of sites 2 and 3, or globally symmetric under a left-right flip. In (b) the system is extended by attaching an arbitrary subsystem (grey) to site 1 (which is fixed under the permutation), so that the original global symmetry becomes a commutative local symmetry. Independently of the parameters of the attached subsystem, the eigenvalue $v - h$ corresponding to a compact localized eigenstate on the two sites 2, 3 is always present in the Hamiltonian spectrum.

A. Commutative local symmetries

To introduce the concept of local symmetry, let us first consider the three-site system depicted in Fig. 1(a). Its Hamiltonian H is invariant under permutation of sites 2 and 3, which represents a global left-right flip of the system. Since the corresponding permutation matrix Π squares to unity ($\Pi^2 = I$) and commutes with H , their common eigenvectors will have definite parity under this permutation. The spectrum $\sigma(H) = \{E_1, E_2, E_3\}$ of H is given by $E_1 = v - h$ and $E_{2,3} = \frac{1}{2}[v + v' + h \pm \sqrt{8h^2 + (h + v - v')^2}]$. The corresponding (unnormalized) eigenvectors are $\phi^1 = [0, 1, -1]^T$ and $\phi^{2,3} = [a_{\pm}, 1, 1]^T$ (with a_{\pm} depending on all system parameters), which indeed are of odd and even parity under Π , respectively.

Let us now connect an arbitrary subsystem to site 1, still leaving the resulting composite system symmetric under the site permutation $2 \leftrightarrow 3$, as shown in the example of Fig. 1(b). The corresponding permutation matrix Π now has the dimension of the enlarged system, but performs the left-right flip only *locally* on subsystem $\{1, 2, 3\}$, leaving site 1 and the added subsystem identical, or *fixed* under Π . Since this local permutation commutes with the Hamiltonian, $\Pi H = H \Pi$, we say that the system possesses a *commutative local symmetry*.

With $\Pi^2 = I$, the composite system eigenvectors again possess a definite parity under Π . In particular, any eigenvector with odd parity will have zero amplitude on all sites fixed under Π (since $\phi_n = -\phi_n$ for those sites), that is, the state is compactly localized on the symmetric subsystem. Consequently, also the eigenvalues of these odd parity states are left unaltered by variations of the parameters (onsite and hopping elements) in the fixed subsystem. In the example of Fig. 1, the same eigenvalue $E_1 = v - h$ (of the odd parity eigenstate) will always be present in $\sigma(H)$, irrespectively of the fixed subsystem connected to site 1. The corresponding eigenstate is localized only on sites 2 and 3 with opposite sign.

The above symmetry considerations, explaining the persistence of compact localized eigenstates of odd parity in the presence of commutative local symmetries, are formalized within graph theory by the so-called *equitable partition theorem* (EPT) [50], which also provides the eigenvalues of associated even parity eigenvectors. The term “equitable”

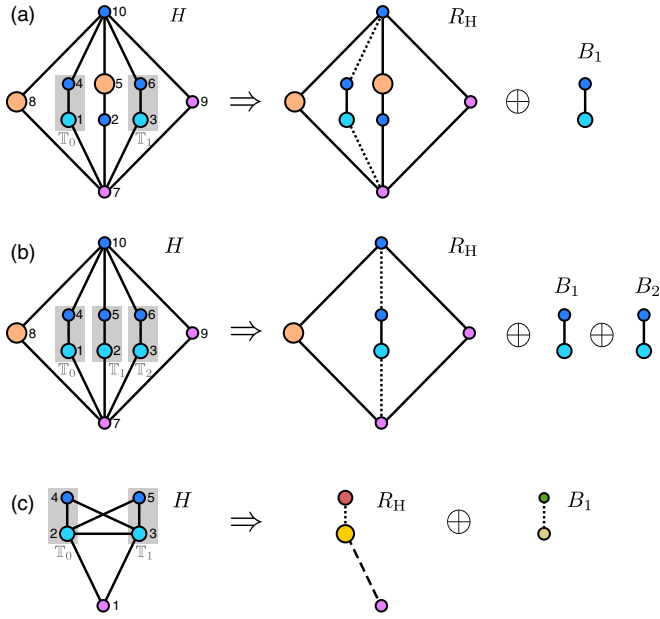


FIG. 2. Left: Graphically represented Hamiltonian H (with uniform hoppings h and onsite elements indicated by different vertex sizes and coloring) of a system with local symmetry under mutual exchange of (a) two subparts $\mathbb{T}_0, \mathbb{T}_1$, (b) three subparts $\mathbb{T}_0, \mathbb{T}_1, \mathbb{T}_2$, and (c) two interconnected subparts $\mathbb{T}_0, \mathbb{T}_1$ (indicated by gray background). Right: Using the equitable partition theorem (EPT), the Hamiltonian matrix H is transformed (\Rightarrow) into a direct sum (\oplus) of the graphically represented matrices R_H and B_j ; Eqs. (16) and (21). In (a) and (b) there is no connection between the \mathbb{T}_i , and only the divisor matrix R_H has altered hoppings [dotted lines; $\sqrt{2}h$ in (a) and $\sqrt{3}h$ in (b)] compared to H . In (c), the intraconnections between \mathbb{T}_0 and \mathbb{T}_1 lead to altered onsite and hopping elements in both R_H and B_j .

denotes a partitioning of the vertices of a graph into nonoverlapping classes such that for *distinct* classes A_i, A_j all vertices belonging to A_i have the same number of adjacent vertices belonging to class A_j . Although this concept is limited to unweighted graphs, which can be represented by very specific matrices such as the adjacency or Laplacian matrix, the above definition of equitable partitions has recently been extended to general complex square matrices [39,51] including the model Hamiltonians considered here. In this generalization, a matrix is “equitably partitionable” if it can be partitioned into blocks of constant row sum. For instance, in Fig. 1(a) this is the case as

$$H = \left[\begin{array}{c|cc} v' & h' & h' \\ \hline h' & v & h \\ h' & h & v \end{array} \right] \quad (3)$$

with row sums $v', 2h', h', v + h$.

Before stating the EPT, let us introduce the employed nomenclature through a suitable example. Consider the Hamiltonian graphically represented on the left-hand side of Fig. 2(a). The structure possesses a commutative local symmetry which can be visualized as a local flip of the sites $\{1,3\}$ and $\{4,6\}$ around the axis running through the sites $7-2-5-10$. By “local” we mean that only the sites $\{1,3,4,6\}$ are flipped, while all other sites are unaffected. This commutative local symmetry

can be expressed by the commutation of the Hamiltonian with the permutation matrix

$$\Pi_S = \begin{bmatrix} J_3 & 0 & 0 \\ 0 & J_3 & 0 \\ 0 & 0 & I_3 \end{bmatrix} \equiv J_3 \oplus J_3 \oplus I_3, \quad (4)$$

I_N and J_N being the N -dimensional identity and exchange (antidiagonal, reverse identity) matrix, where \oplus denotes direct sum (i.e., block-diagonal concatenation). This symmetry operation on H , or *automorphism* of its graph, can be described as a simultaneous permutation

$$S : 1 \mapsto 3, 3 \mapsto 1, 4 \mapsto 6, 6 \mapsto 4, \quad (5)$$

with all other sites being unaffected. This permutation $S : \{1, \dots, 10\} \rightarrow \{1, \dots, 10\}$ is commonly written in the so-called cyclic notation

$$S = (2)(5)(7)(8)(9)(10)(1,3)(4,6). \quad (6)$$

Each tuple within parentheses in Eq. (6) is called an *orbit*. Orbits are classified by their size, i.e., by the number of sites they comprise. Orbits of size 1 are called *trivial*. Note that since permutations are bijective, orbits are always nonoverlapping.

In accordance with the above, we will call a permutation $S : \{1, \dots, N\} \rightarrow \{1, \dots, N\}$ satisfying

$$H_{i,j} = H_{S(i),S(j)} \quad \forall i, j \Leftrightarrow [H, \Pi_S] = 0 \quad (7)$$

a commutative local symmetry of H , with S acting nontrivially on a subset of the system’s sites, and Π_S being the matrix representation of S . If S is a commutative local symmetry and all of its nontrivial orbits are of uniform size k , then we call it a *basic commutative local symmetry of order k* . In the present example, S given in Eq. (6) is a basic commutative local symmetry of H of order 2 with two nontrivial and six trivial orbits. It is clear from Eq. (7) that, in order to be a commutative local symmetry, a given permutation must leave the connections between sites invariant. For example, for H in Fig. 2(a), the permutation

$$S = (1)(2)(3)(4)(6)(7)(9)(10)(5,8) \quad (8)$$

is not a commutative local symmetry: While indeed $v_8 = v_5$, S breaks the connection, e.g., between sites 7 (which is fixed under S) and 8, $h_{S(8),S(7)} = 0 \neq h_{8,7}$, thus violating Eq. (7).

If H is represented graphically, commutative local symmetries of order 2 can be seen as the invariance of the Hamiltonian under a local flip of a subsystem about an axis (which depends on how H is depicted graphically), represented by a corresponding local permutation matrix Π_S . While this procedure aids in the graphical identification of commutative local symmetries, the notion of orbits is more powerful as it makes the description more compact in the case of increased local symmetry. For example, in Fig. 2(b) all of the following are commutative local symmetries of H of order 2:

$$\begin{aligned} \mathcal{S}_a &= (7)(8)(9)(10)(2)(5)(4,6)(1,3), \\ \mathcal{S}_b &= (7)(8)(9)(10)(3)(6)(4,5)(1,2), \\ \mathcal{S}_c &= (7)(8)(9)(10)(1)(4)(5,6)(2,3), \end{aligned} \quad (9)$$

each one corresponding to a local flip of a symmetric subsystem. Those different local symmetries of order 2 can now be

unified into a single one of order 3,

$$S = (7)(8)(9)(10)(4,5,6)(1,2,3), \quad (10)$$

i.e., by the simultaneous *cyclic* permutations $1 \mapsto 2 \mapsto 3 \mapsto 1$ and $4 \mapsto 5 \mapsto 6 \mapsto 4$, exploiting the full local symmetry of the system at once. For the purpose of the EPT, S is preferably chosen to be of highest possible order.

There is a fundamental connection between a basic commutative local symmetry S of order k and the structure of H : If it exists, then the sites of the system can be reordered [40] by a suitable permutation P such that H is transformed into

$$\tilde{H} = P^{-1}HP = \begin{bmatrix} F & G & G & \dots & G \\ G^\dagger & C_0 & C_1 & \dots & C_{k-1} \\ G^\dagger & C_{k-1} & C_0 & \ddots & \vdots \\ \vdots & \vdots & \ddots & \ddots & C_1 \\ G^\dagger & C_1 & \dots & C_{k-1} & C_0 \end{bmatrix} \quad (11)$$

with k copies of the block C_0 on its diagonal and $C_i \in \mathbb{C}^{l \times l}$, where l is the number of nontrivial orbits of S . For a Hermitian Hamiltonian $H = H^\dagger$ the relation $C_i = C_{k-i}^\dagger$ holds. A general procedure to transform H to \tilde{H} for a given basic commutative local symmetry S of order k , with f trivial and l nontrivial orbits, is as follows:

- (i) Collect all f sites fixed by S into the subset \mathbb{F} of the set \mathbb{N} of all sites.
- (ii) Construct a set \mathbb{T}_0 of size l by picking one arbitrary site from each one of the l nontrivial orbits of S .
- (iii) Construct the sets $\mathbb{T}_i = S^i \mathbb{T}_0$, $i = 1, \dots, k-1$, by the i -fold application of S onto \mathbb{T}_0 (noting that $\mathbb{T}_k = S^k \mathbb{T}_0 = \mathbb{T}_0$).
- (iv) Construct \tilde{H} in the form of Eq. (11) using

$$F = H_{\mathbb{F},\mathbb{F}}, \quad G = H_{\mathbb{F},\mathbb{T}_0}, \quad C_i = H_{\mathbb{T}_0,\mathbb{T}_i}, \quad (12)$$

where $H_{\mathbb{A},\mathbb{B}}$ denotes all elements H_{mn} with $m \in \mathbb{A}$, $n \in \mathbb{B}$.

As an example, for the system in Fig. 2(a) we could choose $\mathbb{T}_0 = \{1,4\}$, so that $\mathbb{T}_1 = \{3,6\}$, and get

$$C_0 = \begin{bmatrix} v_1 & h_{1,4} \\ h_{4,1} & v_4 \end{bmatrix}, \quad C_1 = \begin{bmatrix} 0 & 0 \\ 0 & 0 \end{bmatrix}, \quad (13)$$

where C_1 vanishes since there are no interconnections between \mathbb{T}_0 and \mathbb{T}_1 . The other matrices are given as

$$F = \begin{bmatrix} v_2 & h_{2,5} & 0 & h_{2,8} & 0 & 0 \\ h_{5,2} & v_5 & h_{5,7} & 0 & 0 & 0 \\ 0 & h_{7,5} & v_7 & 0 & h_{7,9} & h_{7,10} \\ h_{8,2} & 0 & 0 & v_8 & h_{8,9} & h_{8,10} \\ 0 & 0 & h_{9,7} & h_{9,8} & v_9 & 0 \\ 0 & 0 & h_{10,7} & h_{10,8} & 0 & v_{10} \end{bmatrix}, \quad (14)$$

$$G = \begin{bmatrix} 0 & 0 \\ 0 & 0 \\ h_{7,1} & 0 \\ 0 & 0 \\ 0 & 0 \\ 0 & h_{10,4} \end{bmatrix}.$$

Note that F constitutes the Hamiltonian of the isolated fixed subsystem \mathbb{F} , the matrix ($k = 2$)

$$C = \begin{bmatrix} C_0 & C_1 & \dots & C_{k-1} \\ C_{k-1} & C_0 & \ddots & \vdots \\ \vdots & \ddots & \ddots & C_1 \\ C_1 & \dots & C_{k-1} & C_0 \end{bmatrix} = \begin{bmatrix} v_1 & h_{1,4} & 0 & 0 \\ h_{4,1} & v_4 & 0 & 0 \\ 0 & 0 & v_1 & h_{1,4} \\ 0 & 0 & h_{4,1} & v_4 \end{bmatrix} \quad (15)$$

represents the isolated symmetric subsystem $\mathbb{S} = \mathbb{N} \setminus \mathbb{F}$ (which in this case are two uncoupled symmetric blocks), while G couples the subsystems \mathbb{F} and \mathbb{S} . Thus, \tilde{H} in Eq. (11) can be seen as a symmetry-adapted restructuring of the Hamiltonian.

We can now, following Refs. [39,40], state the following: *Equitable partition theorem*. Let $H \in \mathbb{C}^{N \times N}$ have a commutative local symmetry S of order k with l nontrivial and f trivial orbits. Then the following properties hold:

P1 There exists an invertible, nonunitary matrix M such that

$$H' = M^{-1}HM = R \oplus \bigoplus_{j=1}^{k-1} B_j = \begin{bmatrix} R & 0 & \dots & 0 \\ 0 & B_1 & \ddots & \vdots \\ \vdots & \ddots & \ddots & 0 \\ 0 & \dots & 0 & B_{k-1} \end{bmatrix} \quad (16)$$

where

$$R = \begin{bmatrix} F & k \cdot G \\ G^\dagger & B_0 \end{bmatrix}, \quad B_j = \sum_{m=0}^{k-1} \omega^{jm} C_m, \quad (17)$$

with $\omega = e^{2\pi i/k}$ and the matrices F, G, C_m as defined in Eq. (12).

P2 The spectrum $\sigma(H)$ is given by

$$\sigma(H) = \sigma(H') = \sigma(R) \cup \sigma(B_1) \cup \dots \cup \sigma(B_{k-1}) \quad (18)$$

(regarding the hermiticity of R , see the remark below).

P3 The $N = f + kl$ eigenstates of the index-reordered matrix \tilde{H} defined in Eq. (11) are given by

$$\phi^v = \begin{bmatrix} \mathbf{w}_v \\ \mathbf{v}_v \\ \mathbf{v}_v \\ \vdots \\ \mathbf{v}_v \end{bmatrix}, \quad \phi^{f+ml+r} = \begin{bmatrix} \mathbf{0}_f \\ \mathbf{u}_{m,r} \\ \omega^m \mathbf{u}_{m,r} \\ \vdots \\ \omega^{(k-1)m} \mathbf{u}_{m,r} \end{bmatrix} \quad (19)$$

for $v \in [1, f + l]$ and $m \in [1, k - 1], r \in [1, l]$, where $R[\mathbf{w}_v] = \lambda_v [\mathbf{w}_v]$ with $\mathbf{w}_v \in \mathbb{C}^{f \times 1}$, $\mathbf{v}_v \in \mathbb{C}^{l \times 1}$, and $B_m \mathbf{u}_{m,r} = \lambda_{m,r} \mathbf{u}_{m,r}$.

The vectors ϕ^{f+ml+r} are thereby compact localized on \mathbb{S} .

P4 The first $f + l$ eigenvectors of H are symmetric under S , while the remaining $(k - 1)l$ eigenvectors are both compact localized and not symmetric under S . Specifically, defining the index-reordered permutation matrix $\tilde{\Pi}_S = P^{-1} \Pi_S P$ with P defined from Eq. (11), we have $\tilde{\Pi}_S \phi^v = \phi^v$ for $v \in [1, f + l]$,

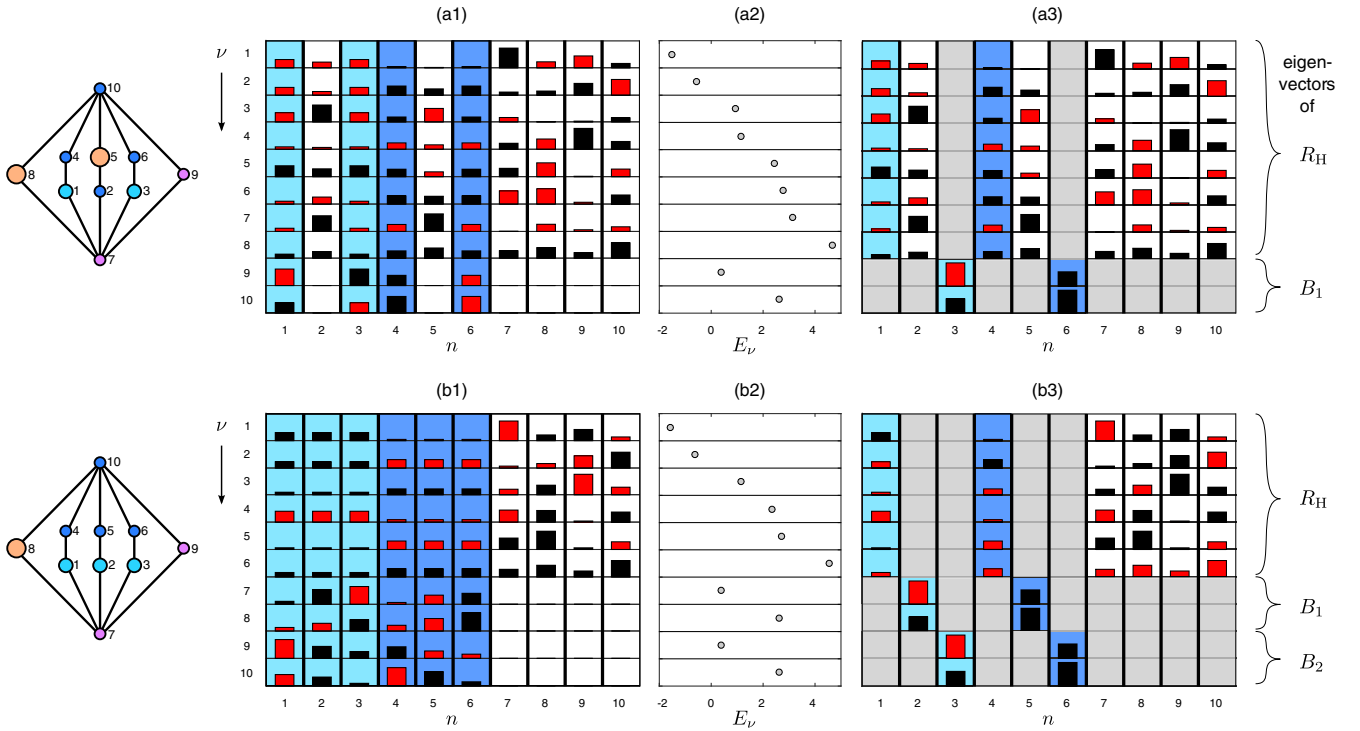


FIG. 3. (a1) Eigenvectors ϕ^ν of the Hamiltonian matrix H , with index ν ordered according to Eq. (19) in the EPT, (a2) their corresponding eigenvalues $\{E_\nu\}$, and (a3) eigenvectors of the matrices R_H and B_j ($j = 1, 2$), for the system of Fig. 2(a), depicted on the left, with indicated onsite elements and homogeneous hoppings $h_{mn} = 1$. (b1)–(b3) Similarly, but for the system of Fig. 2(b). The norm $|\phi_n^\nu|$ of each real eigenstate at each site n is plotted in black (red) for $\phi_n^\nu > 0$ ($\phi_n^\nu < 0$). The sites comprising the locally symmetric part of H are indicated by corresponding light and dark blue background. The eigenvectors of R_H and B_j , which share eigenvalues E_ν with H , are spatially plotted following the site-indexing of H with gray background for sites they are not defined on. Note that the CLSs [$\nu = 9, 10$ in (a1) and $\nu = 7, 8, 9, 10$ in (b1)] are constructed from the components of B_j eigenvectors at the same energy [with pairwise degeneracy for $\nu = 7, 9$ and $8, 10$ in (b1)], and that the remaining eigenstates are symmetric within the locally symmetric part.

while the remaining compact \mathbb{S} -localized eigenvectors transform as

$$\tilde{\Pi}_S \begin{bmatrix} \mathbf{0}_f \\ \mathbf{u}_{m,r} \\ \omega^m \mathbf{u}_{m,r} \\ \vdots \\ \omega^{(k-1)m} \mathbf{u}_{m,r} \end{bmatrix} = \begin{bmatrix} \mathbf{0}_f \\ \omega^{(k-1)m} \mathbf{u}_{m,r} \\ \mathbf{u}_{m,r} \\ \vdots \\ \omega^{(k-2)m} \mathbf{u}_{m,r} \end{bmatrix}. \quad (20)$$

Remark. The generally non-Hermitian “divisor” matrix R defined in Eq. (17) is isospectral to the similar Hermitian matrix

$$R_H = \begin{bmatrix} F & \sqrt{k} \cdot G \\ \sqrt{k} \cdot G^\dagger & B_0 \end{bmatrix} = K R K^{-1} \quad (21)$$

with eigenvectors $[\frac{w_\nu}{v_\nu/\sqrt{k}}]$, where $K = I_f \oplus \sqrt{k} \cdot I_l$. Thus, properties **P2** and **P3** of the EPT hold if we replace R by R_H and v_ν by v_ν/\sqrt{k} ; we shall do so in the remainder of this work.

We see that, in essence, the EPT uses the symmetries described by S to acquire partial information from H , namely its spectral composition and corresponding eigenvector localization, without diagonalizing it. This information could indeed alternatively be obtained by considering the system’s symmetry under local flip operations (represented by involutory matrices Π), as explained above. In particular, however, the EPT provides *all* eigenvalues and eigenvectors of H in terms of those of the symmetry-adapted matrices R and B_j ,

i.e., not only those of the “decoupled” CLSs. Since R and B_j are of reduced dimension, the EPT may additionally offer a computational advantage in diagonalizing Hamiltonians of extended systems with commutative local symmetries.

To give a concrete impression of the EPT, we consider again the Hamiltonian H in Fig. 2(a), which is transformed to the direct sum of matrices R_H and B_1 according to Eq. (16). Recall that the similarity transformation involved preserves the spectrum of H , while the final block-diagonal form ensures property **P2** in the EPT. The eigenvectors of H , R_H , and B_1 of Fig. 2(a) are shown in Figs. 3(a1)–3(a3) together with their eigenvalues. As predicted by the EPT (here with $f = 6$, $k = 2$, and $l = 2$), there are two (antisymmetric) CLSs of H (states $\nu = 9, 10$) localized on the sites $\{1, 3, 4, 6\}$ that form a commutative local symmetry under the permutation S of Eq. (6), while all other eigenstates are extended and symmetric under S . In particular, the CLSs are constructed from the components of the eigenvectors of B_1 in Fig. 3(a3).

The matrices C_0, C_1 and F, G , used in this example to construct the matrices R and B_j of the transformed Hamiltonian H' in Eq. (16), are given in Eqs. (13) and (14), respectively, for the choice $\mathbb{T}_0 = \{1, 4\}$ as initial orbit sites. Note that the choice of \mathbb{T}_0 generally affects the matrices G, B_1, \dots, B_{k-1} (but not B_0), though does not change the resulting decomposition of the spectrum and the eigenvectors of the Hamiltonian. In the present example, the sites in each orbit are disconnected, so

that C_1 vanishes and

$$B_0 = B_1 = C_0 = \begin{bmatrix} v_1 & h_{1,4} \\ h_{4,1} & v_4 \end{bmatrix} \quad (22)$$

from Eq. (17) becomes the single submatrix corresponding to the two CLSs.

The EPT works in a completely similar form for the example in fig. 2(b): There are now 2 orbits of size $k = 3$, leading to $(k - 1)l = 4$ (pairwise degenerate) CLSs, as seen in Figs. 3(b1)–3(b2). Note that any two degenerate real CLS eigenvectors can be linearly combined to either be antisymmetric under one of the (partial) local symmetry transformations in Eq. (9), or to be of the complex form in Eq. (19). Also in this example there are no intra-orbit connections, and so we have $B_0 = B_1 = B_2 = C_0$.

In contrast, the system shown in Fig. 2(c) is invariant under the permutation $\mathcal{S} = (1)(2,3)(4,5)$ but has intraconnected orbits (or interconnected local symmetry units \mathbb{T}_0 and \mathbb{T}_1), since $h_{2,3}, h_{2,5}, h_{4,3} \neq 0$. In such a case the matrices B_j differ; here we have (with the choice $\mathbb{T}_0 = \{2,4\}$)

$$R = [v_1], \quad B_0 = \begin{bmatrix} v_2 & h_{2,4} \\ h_{4,2} & v_4 \end{bmatrix} \pm \begin{bmatrix} h_{2,3} & h_{2,5} \\ h_{4,3} & h_{4,5} \end{bmatrix}. \quad (23)$$

Notably, the B_0 and B_1 here are given by adding and subtracting the intra-orbit connection, respectively. In Sec. III A we will use this property to tailor periodic systems featuring bound states in the continuum.

B. Noncommutative local symmetries

So far we have considered the case of local symmetries which, although localized within a part of a composite system, are represented by a permutation matrix $\Pi_{\mathcal{S}}$ that commutes with the system Hamiltonian H . We now show, partially following the procedure in Ref. [41], how the merits of the EPT can be extended to cases where a symmetric subsystem is *asymmetrically* coupled to the rest of the system under the given site permutation. Since $\Pi_{\mathcal{S}}$ then does not commute with H , we call the underlying permutation \mathcal{S} a *noncommutative local symmetry*. In the following, we will impose two further restrictions on \mathcal{S} .

Specifically, consider a Hamiltonian H which can be index-reordered, in analogy to Eq. (11), into the form

$$\tilde{H} = \begin{bmatrix} F & \gamma_1^* G & \gamma_2^* G & \dots & \gamma_k^* G \\ \gamma_1 G^\dagger & C_0 & 0 & \dots & 0 \\ \gamma_2 G^\dagger & 0 & C_0 & \ddots & \vdots \\ \vdots & \vdots & \ddots & \ddots & 0 \\ \gamma_k G^\dagger & 0 & \dots & 0 & C_0 \end{bmatrix} \quad (24)$$

with generally complex parameters $\gamma_1, \dots, \gamma_k$. As in Eq. (11), the k copies of $C_0 \in \mathbb{C}^{l \times l}$ correspond to the same local symmetry units under permutation \mathcal{S} , the matrix $F \in \mathbb{C}^{n \times n}$ corresponds to sites fixed by \mathcal{S} , while $G \in \mathbb{C}^{n \times l}$ connects fixed to local symmetry sites. Now, however, (i) the local symmetry units are not interconnected (i.e., $C_{j>0} = 0$), and (ii) while each of them is geometrically coupled to the fixed part \mathbb{F} in the same manner, the coupling strength for each unit is weighted by a factor γ_i . Thus, if $\gamma_i \neq \gamma_j$ for some $i \neq j$, the coupling of \mathbb{S} (denoting the locally symmetric subsystems as a whole)

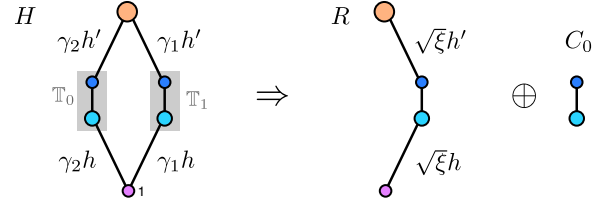


FIG. 4. Graphically represented example Hamiltonian H of the form in Eq. (24) with a restricted noncommutative (local) symmetry under the exchange of subparts \mathbb{T}_0 and \mathbb{T}_1 , and its partitioning into matrices R and C_0 according to the nEPT with $\xi = \gamma_1^2 + \gamma_2^2$.

to \mathbb{F} (denoting the fixed subsystem) is asymmetric, and \mathcal{S} is no longer a commutative local symmetry of H . A simple example is given by the system in Fig. 4; also by Fig. 2(a) if, e.g., only $h_{1,7}$ and $h_{4,10}$ were multiplied by a factor γ , or similarly in Fig. 2(b)—though not in Fig. 2(c), where there is local symmetry unit interconnection.

In the following, we will call noncommutative local symmetries fulfilling the above restrictions (i) and (ii) *restricted noncommutative* ones. For such local symmetries the EPT can be modified, along the lines of Ref. [41], to the following:

Nonequitable partition theorem. Let $\tilde{H} \in \mathbb{C}^{N \times N}$ be of the form in Eq. (24), with $F \in \mathbb{C}^{f \times f}$, k copies of $C_0 \in \mathbb{C}^{l \times l}$, and $\tilde{\mathcal{S}}$ a restricted noncommutative local symmetry of \tilde{H} . Then the following properties hold:

P1 The eigenvalue spectrum of \tilde{H} is given by $\sigma(\tilde{H}) = \sigma(H') = \sigma(R) \cup \sigma_{k-1}(C_0)$, where H' is a similarity transform of \tilde{H} and is given by

$$H' = R \oplus \bigoplus_{m=1}^{k-1} C_0, \quad R = \begin{bmatrix} F & \sqrt{\xi} \cdot G \\ \sqrt{\xi} \cdot G^\dagger & C_0 \end{bmatrix} \quad (25)$$

with $\xi = \sum_{j=1}^k \gamma_j^2$ and $\sigma_i(R)$ denoting i copies of $\sigma(R)$ (i.e., i -fold degeneracy of those eigenvalues).

P2 The $N = f + kl$ eigenstates of \tilde{H} are given by

$$\phi^v = \begin{bmatrix} \mathbf{w}_v \\ \frac{\gamma_1}{\sqrt{\xi}} \mathbf{v}_v \\ \frac{\gamma_2}{\sqrt{\xi}} \mathbf{v}_v \\ \vdots \\ \frac{\gamma_k}{\sqrt{\xi}} \mathbf{v}_v \end{bmatrix}, \quad \phi^{f+ml+r} = \left. \begin{array}{c} \mathbf{0}_f \\ \frac{\gamma_1}{\gamma_1} \mathbf{u}_{0,r} \\ \frac{\gamma_2}{\gamma_1} \mathbf{u}_{0,r} \\ \vdots \\ \frac{\gamma_m}{\gamma_1} \mathbf{u}_{0,r} \\ -\frac{\sum_{i=1}^m \gamma_i^2}{\gamma_1 \gamma_{m+1}} \mathbf{u}_{0,r} \\ \mathbf{0}_l \\ \vdots \\ \mathbf{0}_l \end{array} \right\} (k-1) - m \quad (26)$$

for $v \in [1, f + l]$, $m \in [1, k - 1]$, and $r \in [1, l]$, where $R[\frac{\mathbf{w}_v}{\mathbf{v}_v}] = \lambda_v[\frac{\mathbf{w}_v}{\mathbf{v}_v}]$ with $\mathbf{w}_v \in \mathbb{C}^{f \times 1}$, $\mathbf{v}_v \in \mathbb{C}^{l \times 1}$, and $C_0 \mathbf{u}_{m,r} = \lambda_{0,r} \mathbf{u}_{m,r}$.

The naming of the theorem was chosen to reflect the fact that, for unequal γ_i , the matrix (24) cannot generally be

partitioned into blocks with blockwise constant row sum; that is, the matrix is “nonequitably” partitionable according to the definition above in Sec. II A. The theorem is proven in Ref. [41] for real \tilde{H} , but is generalized here in a straightforward manner to complex \tilde{H} and γ_j ; see the Appendix. This may allow for the possibility to include appropriately applied external magnetic fields in the present symmetry-adapted construction of CLSs (via Peierls phase factors in the hopping elements [28]), or to include parametric gain and loss (via complex onsite elements [24]).

It should here be mentioned that there exists a large class of local symmetries which are neither commutative nor restricted noncommutative. Also, the restrictions for the nonequitable partition theorem (nEPT) to apply are indeed relatively strong. However, the nEPT may still provide larger flexibility than the EPT (requiring exact commutative local symmetry) in designing CLSs for systems with non-intraconnected symmetric subparts.

Comparing the nEPT with the EPT, some similarities but also subtle differences become evident. Both the nEPT and the EPT block-diagonalize the Hamiltonian, and in both cases the eigenstates are decomposed into two classes: extended states generally occupying all sites of the system, and CLSs localized on \mathbb{S} (the sites of the symmetric subsystems, non-trivially affected by the permutation \mathcal{S}). However, the detailed properties of eigenstates in each class are different for the EPT and nEPT. Extended eigenstates [the $\phi^{v \in [1, f+l]}$ in Eqs. (19) and (26)] are symmetric under the action of \mathcal{S} for the EPT, while this holds only for equal γ_i for the nEPT (in which case \mathcal{S} becomes commutative and the EPT applies). Also, CLSs [the ϕ^{f+ml+r} in Eqs. (19) and (26)] determined by the nEPT are more compactly localized, on only a subset of \mathbb{S} , as the $k-1-m$ vectors $\mathbf{0}_l$ in Eq. (26) indicate.

III. COMPACT LOCALIZED EIGENSTATES IN LATTICE SYSTEMS

Having presented and analyzed the (n)EPT and its implications for the eigenspectra and eigenstates of discrete models with (restricted non)commutative local symmetries, in the following we demonstrate concrete applications to compact state design in extended lattice systems.

A. Engineering bound states in the continuum

The band structure of a periodic lattice provides energetic continua for extended (Bloch) eigenstates respecting the underlying discrete translational symmetry. In this section we will demonstrate how certain perturbations, which destroy the periodic character of the lattice, may nevertheless leave the band structure of the system unchanged. Key to this are tailored local perturbations of one or more unit cells, which can be described by local symmetries and thereby induce the occurrence of CLSs.

Let us consider the system depicted in Fig. 5(a): a tight-binding periodic chain (with $v_n = v$ and $h_{n,n+1} = h$) perturbed locally by replacing a lattice site with a dimer of onsite energy v_1 and intrahopping h_2 , in turn connected to the chain by hoppings h_1 . For generic defect parameters, the Bloch states of the unperturbed chain are no longer eigenstates of the system,

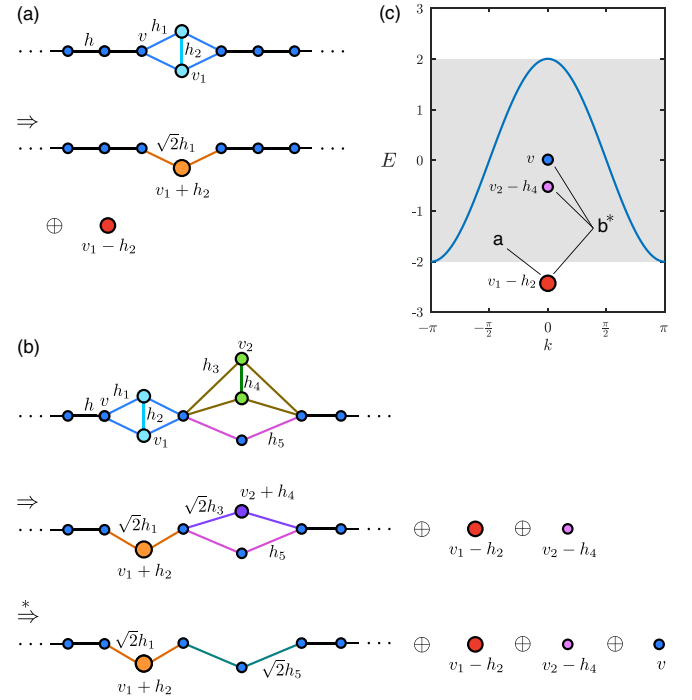


FIG. 5. (a) Periodic lattice system locally perturbed by a symmetric dimer defect with indicated onsite and hopping elements (top). The corresponding Hamiltonian can be transformed (bottom) via the EPT into the direct product of the divisor matrix R , corresponding to a generally perturbed linear chain, and the 1×1 matrix B_1 corresponding to a CLS on the defect with energy $E_{\text{CLS}} = v_1 - h_2$. For the special case of $h_1 = h/\sqrt{2}$ and $h_2 = v - v_1$, the spectrum $\sigma(H)$ consists of the unperturbed chain band structure with an additional tunable bound state energy E_{CLS} . (b) The same chain with an additional, different, locally symmetric perturbation next to the first one, which can be treated by an iterative decomposition. The first decomposition (\Rightarrow) reveals the occurrence of two CLEs at energies $v_1 - h_2, v_2 - h_4$. The second decomposition ($\stackrel{*}{\Rightarrow}$) applies if $v_2 + h_4 = v$, $\sqrt{2}h_3 = h_5$. For parameters tuned so that $\sqrt{2}h_1 = h$, $v_1 + h_2 = v$, $\sqrt{2}h_5 = h$, the spectrum of the perturbed system again consists of the unperturbed chain band structure and three CLS energies $v_1 - h_2, v_2 - h_4, v$. (c) Band structure of the unperturbed chain (blue line), present in the spectra of the tuned locally symmetric systems of (a) and (b), together with indicated corresponding CLS eigenenergies. Different onsite and hopping elements are depicted with different sizes and colors.

and defect modes with exponential decay into the left and right semi-infinite chains arise. This may change, however, if the defect forms a commutative local symmetry, as we now demonstrate. In this case, the EPT provides a symmetry-adapted partitioning of the Hamiltonian into the matrices R and B_1 , as shown graphically in Fig. 5(a). The divisor matrix R corresponds to a linear chain with a single-site defect of energy $v_1 + h_2$, connected by hoppings $\sqrt{2}h_1$, while B_1 corresponds to a single CLS, localized only on the dimer, with energy $E_{\text{CLS}} = v_1 - h_2$, as indicated in Fig. 5(c) [52]. Following this partitioning, the spectrum is given by $\sigma(H) = \sigma(R) \cup \sigma(B_1)$.

As we see, also in the partitioned representation a defect is generally retained in the chain, which would lead to, e.g., backscattering of incident waves lying energetically in the unperturbed continuum. Note, however, that the defect

parameters can be tuned so as to effectively recover those of the unperturbed chain: Setting $h_1 = h/\sqrt{2}$ and $h_2 = v - v_1$ indeed makes R coincide with the unperturbed Hamiltonian. Thus, despite the presence of the defect, the spectrum in this case consists of the band structure of the unperturbed chain, augmented by the energy of the CLS. Moreover, by simultaneously tuning v_1 and h_2 such that $h_2 = v - v_1$, the CLS can be moved in energy into the band of the chain, so that it becomes “bound state in the continuum” [12,13]. In the present case, this state does not interact with the extended continuum states due to eigenvector orthogonality, and thus the defect is effectively invisible for an incident wave (i.e., causes no backscattering).

Such a “renormalization” of defects into unperturbed chain sites was recently shown to explain the absence of localization [53], though for the special case of one dimension and zero intradimer coupling h_2 . Following the above paradigm, the EPT can be used to easily generalize the approach to perturbations of various complexity and connectivity as well as to higher dimensions. The key for such a generalization is to have a perturbation that renders the divisor matrix R identical to the unperturbed Hamiltonian. Note that this can be done even for different kinds of perturbations, as shown in Fig. 5(b). Here, an iterative decomposition is possible, provided that $v_2 + h_4 = v$, $\sqrt{2}h_3 = h_5$. If, additionally, $\sqrt{2}h_1 = h$, $v_1 + h_2 = v$, $\sqrt{2}h_5 = h$ [indicated by an asterisk in Fig. 5(b)], then the original band structure of the unperturbed chain is recovered, together with three additional bound states at energies $v_1 - h_2, v_2 - h_4, v$, as shown in Fig. 5(c).

CLSs tailored as above to be “invisible” to a host lattice can clearly be inserted in multiple positions in the lattice without affecting the unperturbed band structure. Notably, the same could be done for restricted noncommutative local symmetry defects using the nEPT, as long as its conditions are met. This concept of tailoring R is thereby neither limited by the number of dimensions nor by the number of perturbed unit cells, and thus applies to quite generic extended lattice models. As an application, CLSs could be distributed along a given aperiodic or even random sequence, to then study their interaction with continuum states by gradually breaking the local symmetry of the defects.

B. Using symmetries to design flat bands

The above engineering of bound states in an unperturbed continuum via the (n)EPT relies on making the divisor matrix R coincide with the unperturbed lattice Hamiltonian by tuning the defect parameters. To obtain a band structure for generic defect parameters, however, the defects need to be placed periodically as well. Then, since the corresponding CLSs vanish on the sites (fixed under the local symmetry S) connected to adjacent lattice cells, their energy will also be independent of the Bloch momentum. Consequently, a flat band will form at each CLS eigenenergy. An example for this is the well-known one-dimensional diamond ladder lattice [1] which can be constructed by periodically repeating the perturbed unit cell in Fig. 5(a) and which features global chiral symmetry [28]; similarly, cross-stitch and one-dimensional pyrochlore lattices [1] can be treated with the present local symmetry approach.

We now show how the (n)EPT can be used to design lattices in arbitrary dimensions hosting a prescribed number

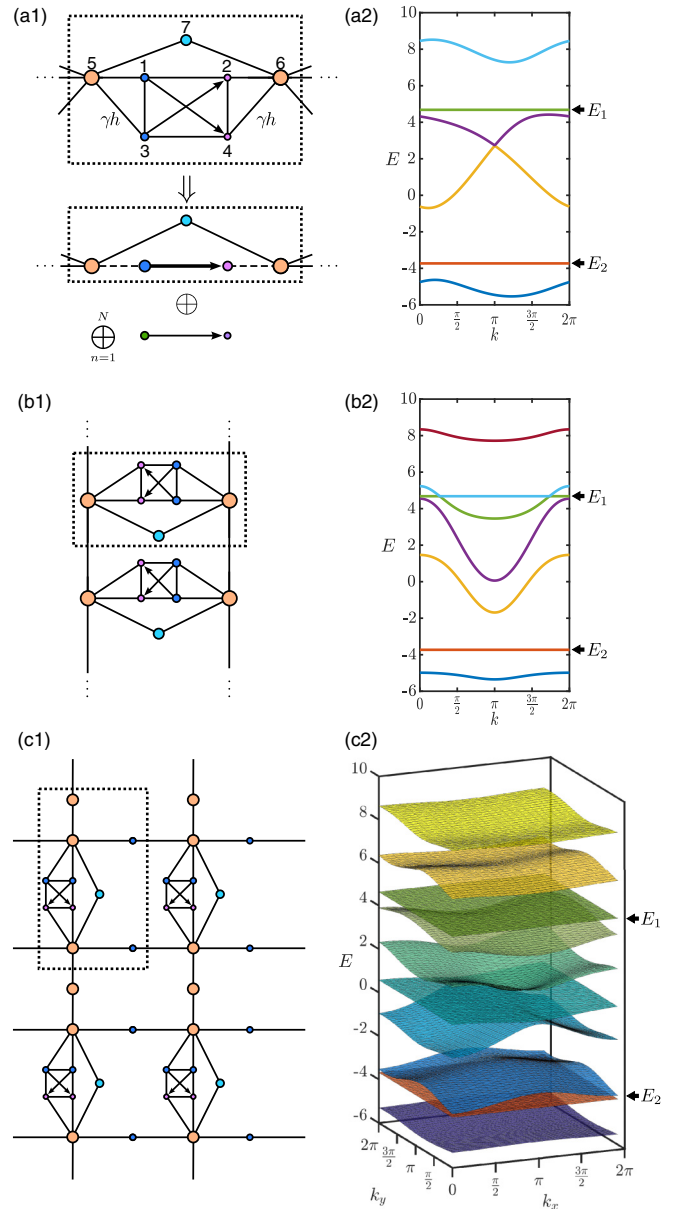


FIG. 6. (a1) Unit cell (indicated by dotted rectangle) of a periodic setup, with a local symmetry under the permutation $S: 1 \leftrightarrow 3, 2 \leftrightarrow 4$ leading to CLSs at two energies E_1, E_2 , and (a2) corresponding band structure with flat bands at E_1, E_2 . (b1)–(b2) As in (a1)–(a2) but with the same unit cell connected in parallel via two sites to each neighboring cell. (c1)–(c2) As in (a1)–(a2) but with the same unit cell augmented by three sites and connected into a 2D lattice. While the dispersive bands are different in each case, the flat bands remain at $E_{1,2}$ since the symmetric subsystem remains unchanged. In the lower part of (a1), the EPT decomposition (\Rightarrow) of the system’s Hamiltonian into that of a modified lattice and $(\oplus) N \rightarrow \infty$ copies of isolated dimers (with eigenenergies $E_{1,2}$) is visualized. Arrowed lines indicate complex-valued hoppings and dashed lines modified real hoppings. For an asymmetry parameter $\gamma \neq 1$ [indicated in (a1)] and vanishing intraconnections ($h_{mn} = 0; m, n = 1, 2, 3, 4$), the nEPT applies (see text).

of flat bands at desired energies. Consider a lattice like the one in Fig. 6(a1), featuring a commutative local symmetry for $\gamma = 1$ in each unit cell under the permutation $S: 1 \leftrightarrow 3, 2 \leftrightarrow 4$

(leaving all other sites fixed). Then, by the EPT there are $(k-1)l = 2$ CLSs localized on the sites $\mathbb{S} = \{1, 2, 3, 4\}$ within the unit cell, with k and l being the uniform size and number of nontrivial orbits of \mathcal{S} , respectively. Two flat bands thus form at the CLS energies $E_{1,2}$, as shown in Fig. 6(a2) [52]. Specifically, $E_{1,2}$ are the eigenvalues of the matrix

$$B_1 = \begin{bmatrix} v_1 & h_{1,2} \\ h_{2,1} & v_2 \end{bmatrix} - \begin{bmatrix} h_{1,3} & h_{1,4} \\ h_{2,3} & h_{2,4} \end{bmatrix}, \quad (27)$$

of Eq. (17), and thus depend only on the elements within the subpart \mathbb{S} of the unit cell. Note here that, for H to be Hermitian and \mathcal{S} -symmetric, $h_{1,3}$ and $h_{2,4}$ need to be real, while $h_{2,3} = h_{4,1}$ may as well be complex (indicated by arrows).

In complete analogy, flat bands form in the presence of restricted noncommutative local symmetries in the unit cell following the conditions of the nEPT. Specifically, for $\gamma \neq 1$ in Fig. 6(a1), but with vanishing local symmetry intraconnection ($h_{1,3}, h_{2,4}, h_{2,3}, h_{4,1} = 0$), we obtain two flat bands (not shown) at the CLS eigenvalues of the matrix

$$C_0 = \begin{bmatrix} v_1 & h_{1,2} \\ h_{2,1} & v_2 \end{bmatrix} \quad (28)$$

defined in Eq. (12). Note that those are *independent* of the asymmetry factor γ .

Figure 6(b1) shows a lattice where the same unit cell as before is connected “in parallel” (via two connections) to each neighboring unit cell, instead of “serially” as in Fig. 6(a1). Again, the unit cell’s CLSs lead to two tunable flat bands at energies given by the eigenvalues of Eq. (27), as shown in Fig. 6(b2).

In the two-dimensional (2D) example of Fig. 6(c1), the unit cell differs from that of Fig. 6(a1) in that it contains three additional sites, though still containing the same locally symmetric unit. The CLS eigenenergies are also here independent of the Bloch momentum, now in both directions of translational invariance, and 2D corresponding bands thus arise. Note that their position is the same as in Figs. 6(a) and 6(b), since the underlying symmetric substructure is not changed.

Concluding the above, we have shown that a lattice automatically features one or more symmetry-induced flat bands if (i) the unit cell possesses a commutative or restricted noncommutative local symmetry and (ii) this symmetry is unbroken when isolated unit cells are connected to form the lattice. Note that this approach to flat bands can be related to the common description of symmetry via the point group of the unit cell, whose action leaves at least one point fixed. Indeed, the discreteness of the considered model Hamiltonian maps each point group element to a site permutation. This constitutes then a global symmetry of the isolated unit cell, and thus a special case of condition (i) above. In turn, condition (ii) is fulfilled provided that the unit cells are connected through sites located at the point group’s fixed points. This link of the proposed approach to point groups may aid the description and design of symmetry-induced flat bands in more complex lattice systems.

Having seen how local symmetries lead to $(k-1)l$ flat bands [k being the number of copies of $C_0 \in C^{l \times l}$ defined in Eqs. (11) and (24)], let us now look at the remaining bands. Note that these are usually completely dispersive, but could

contain flat bands as well that are induced by other means than the above (restricted non)commutative local symmetries. In any case, all of these remaining bands are entirely determined by the divisor matrix R which is explicitly represented graphically in Fig. 6(a1) (between \Downarrow and \oplus). Thus, these remaining bands can be directly obtained by diagonalizing the matrix R which represents a strictly periodic system. Note that the partition into matrices R and B_j (by the EPT) or C_0 (by the nEPT) allows for an effective design process in which the symmetry-induced flat bands and the remaining band structure can be designed *separately*.

It is clear that the present approach to design flat bands using the EPT or nEPT applies to the class of lattices containing commutative or restricted noncommutative local symmetries. Thus, it does not cover other cases of lattices with other classes of local symmetries, which may also host flat bands generated by the very general method developed in Ref. [2]. The essence of the present approach is that, instead of generating flat bands from conditions imposed on the site-resolved eigenvalue problem (1), it is based on unified and intuitive symmetry principles forcing the occurrence of CLSs. We thus view it as a complementary method which lends an insightful understanding to already existing methods.

IV. CONCLUSIONS

We have shown how two very recent results from graph theory can be used to analyze discrete Hamiltonians with local symmetries. The resulting framework demonstrates the impact of two types of local symmetries on the eigenstates of a Hamiltonian H , including the formation of so-called compact localized states (CLSs). These two types of local symmetries are described by site permutations which either leave all (commutative local symmetries) or some (restricted noncommutative local symmetries) matrix elements of H invariant. More specifically, the restricted noncommutative local symmetries are such that the symmetric subsystems are (i) not interconnected and (ii) asymmetrically coupled to the remaining part of the system.

The essence of the framework is a symmetry-adapted partition of H into smaller matrices R and B_i whose collective eigenvalue spectrum is equal to that of the original H . Depending on the exact character of the local symmetry, H is assured to have one or more compact localized eigenstates which are localized on the symmetric subsystem \mathbb{S} . Their energies are given by the spectra of the matrices B_i . All other eigenstates of H are not localized on \mathbb{S} , with their energy given by the spectrum of R . In short, the framework provides the total eigenvalue spectrum as well as eigenvectors of the Hamiltonian in terms of symmetry-adapted submatrices, which are in turn more efficiently computed and better controllable by parametric tuning.

We apply this novel framework to tight binding systems and explicitly design flat bands at tailored energies in lattices of one and two dimensions, with the generalization to arbitrary dimensions being straightforward. Moreover, we use the methodology to demonstrate the occurrence of bound states in the energy continuum of a periodic chain perturbed by one or

more symmetric defects. For both flat bands and bound states in the continuum, our results give an intuitive understanding of the impact of local symmetries, paired with a high degree of control over the respective energies. We believe that the present framework may serve as a complement to existing methods in the design of CLSs and flat bands, by offering a unifying, intuitive, and efficient way to connect them to local symmetries.

ACKNOWLEDGMENTS

Financial support by the Deutsche Forschungsgemeinschaft under grant DFG Schm 885/29-1 is gratefully acknowledged. M.R. gratefully acknowledges financial support by the ‘Stiftung der deutschen Wirtschaft’ in the framework of a scholarship. We thank C. Fey for discussions on the proof of the nonequitable partition theorem.

APPENDIX: PROOF OF THE nEPT

We here prove property **P2** of the nEPT. To this end, we need to show that the vectors

$$\mathbf{x}_j = \begin{bmatrix} \mathbf{w}_j \\ \frac{\gamma_1}{\sqrt{\xi}} \mathbf{v}_j \\ \frac{\gamma_2}{\sqrt{\xi}} \mathbf{v}_j \\ \vdots \\ \frac{\gamma_k}{\sqrt{\xi}} \mathbf{v}_j \end{bmatrix}, \quad \mathbf{y}_{m,r} = \begin{bmatrix} \mathbf{0}_f \\ \frac{\gamma_1}{\gamma_1} \mathbf{u}_{0,r} \\ \frac{\gamma_2}{\gamma_1} \mathbf{u}_{0,r} \\ \vdots \\ \frac{\gamma_m}{\gamma_1} \mathbf{u}_{0,r} \\ -\frac{\sum_{i=1}^m \gamma_i^2}{\gamma_1 \gamma_{m+1}} \mathbf{u}_{0,r} \\ \mathbf{0}_l \\ \vdots \\ \mathbf{0}_l \end{bmatrix}, \quad (\text{A1})$$

with $j \in [1, f+l], m \in [1, k-1], r \in [1, l]$, are linearly independent eigenvectors of the Hamiltonian H' given in Eq. (25).

Since $[\mathbf{v}_j^w]$ is the j th eigenvector of the divisor matrix R [given in Eq. (25)] with eigenvalue λ_j , i.e.,

$$\begin{bmatrix} F & \sqrt{\xi} \cdot G \\ \sqrt{\xi} \cdot G^\dagger & C_0 \end{bmatrix} \begin{bmatrix} \mathbf{w}_j \\ \mathbf{v}_j \end{bmatrix} = \begin{bmatrix} F \mathbf{w}_j + \sqrt{\xi} \cdot G \mathbf{v}_j \\ \sqrt{\xi} \cdot G^\dagger \mathbf{w}_j + C_0 \mathbf{v}_j \end{bmatrix} = \lambda_j \begin{bmatrix} \mathbf{w}_j \\ \mathbf{v}_j \end{bmatrix},$$

applying H' on \mathbf{x}_j yields

$$H' \mathbf{x}_j = H \begin{bmatrix} \mathbf{w}_j \\ \frac{\gamma_1}{\sqrt{\xi}} \mathbf{v}_j \\ \vdots \\ \frac{\gamma_k}{\sqrt{\xi}} \mathbf{v}_j \end{bmatrix} = \begin{bmatrix} F \mathbf{w}_j + \frac{\sum_{i=1}^k |\gamma_i|^2}{\sqrt{\xi}} G \mathbf{v}_j \\ \gamma_1 G^\dagger \mathbf{w}_j + \frac{\gamma_1}{\sqrt{\xi}} C_0 \mathbf{v}_j \\ \vdots \\ \gamma_k G^\dagger \mathbf{w}_j + \frac{\gamma_k}{\sqrt{\xi}} C_0 \mathbf{v}_j \end{bmatrix} = \begin{bmatrix} F \mathbf{w}_j + \sqrt{\xi} \cdot G \mathbf{v}_j \\ \gamma_1 G^\dagger \mathbf{w}_j + \frac{\gamma_1}{\sqrt{\xi}} C_0 \mathbf{v}_j \\ \vdots \\ \gamma_k G^\dagger \mathbf{w}_j + \frac{\gamma_k}{\sqrt{\xi}} C_0 \mathbf{v}_j \end{bmatrix} = \lambda_j \begin{bmatrix} \mathbf{w}_j \\ \frac{\gamma_1}{\sqrt{\xi}} \mathbf{v}_j \\ \vdots \\ \frac{\gamma_k}{\sqrt{\xi}} \mathbf{v}_j \end{bmatrix} = \lambda_j \mathbf{x}_j. \quad (\text{A2})$$

Thus, $\{\mathbf{x}_j\}$ are eigenvectors of H' . If we choose the set of eigenvectors $\{[\mathbf{v}_j^w]\}$ such that they are pairwise linearly independent (which can always be done), then this is also the case for the set $\{\mathbf{x}_j\}$. To see this, let us assume that there exists an \mathbf{x}_i and constants $\{\alpha_j\}$ such that \mathbf{x}_i is given by a superposition of $\{\mathbf{x}_j\}$ with $j \neq i$, i.e.,

$$\mathbf{x}_i = \sum_{j \neq i} \alpha_j \mathbf{x}_j. \quad (\text{A3})$$

Then, from the definition of \mathbf{x}_i , it would hold that

$$\begin{bmatrix} \mathbf{w}_i \\ \frac{\gamma_1}{\sqrt{\xi}} \mathbf{v}_i \end{bmatrix} = \sum_{j \neq i} \alpha_j \begin{bmatrix} \mathbf{w}_j \\ \frac{\gamma_1}{\sqrt{\xi}} \mathbf{v}_j \end{bmatrix} \Rightarrow \begin{bmatrix} \mathbf{w}_i \\ \mathbf{v}_i \end{bmatrix} = \sum_{j \neq i} \alpha_j \begin{bmatrix} \mathbf{w}_j \\ \mathbf{v}_j \end{bmatrix}, \quad (\text{A4})$$

which is not true since the $[\mathbf{v}_j^w]$ are pairwise linearly independent. Thus, the \mathbf{x}_j are pairwise linearly independent eigenvectors of H' .

Further, since $C_0 \mathbf{u}_{0,r} = \lambda_{0,r} \mathbf{u}_{0,r}$ by definition, application of H' on $\mathbf{y}_{m,r}$ yields

$$H' \begin{bmatrix} \mathbf{0}_f \\ a_1 \mathbf{u}_{0,r} \\ \vdots \\ a_k \mathbf{u}_{0,r} \end{bmatrix} = \begin{bmatrix} C_0 \mathbf{0}_f \\ a_1 C_0 \mathbf{u}_{0,r} \\ \vdots \\ a_k C_0 \mathbf{u}_{0,r} \end{bmatrix} = \lambda_{0,r} \begin{bmatrix} \mathbf{0}_f \\ a_1 \mathbf{u}_{0,r} \\ \vdots \\ a_k \mathbf{u}_{0,r} \end{bmatrix} \quad (\text{A5})$$

for any $a_1, \dots, a_k \in \mathbb{C}$. Thus, the $\mathbf{y}_{m,r}$ are eigenvectors of H' . As is easily shown, they are also pairwise orthogonal, both for the same and for different $\mathbf{u}_{0,r}$.

Having shown that both sets $\{\mathbf{y}_{m,r}\}, \{\mathbf{x}_j\}$ are eigenvectors of H' , we need to show that they form a linearly independent set. Evaluating the scalar product of \mathbf{x}_j and $\mathbf{y}_{m=i,r}$ for arbitrary i and r gives

$$\mathbf{x}_j \cdot \mathbf{y}_{i,r} = \left(\frac{\sum_{p=1}^i \gamma_p^2}{\gamma_1 \sqrt{\xi}} - \frac{\gamma_{i+1}}{\sqrt{\xi}} \frac{\sum_{p=1}^i \gamma_p^2}{\gamma_1 \gamma_{i+1}} \right) \mathbf{v}_j \cdot \mathbf{u}_{0,r} = 0, \quad (\text{A6})$$

where the last equality stems from the cancellation of the two summands in parentheses. Note that $H' \in \mathbb{C}^{N \times N}$ has $N = f + kl$ linearly independent eigenstates. Since $R \in \mathbb{C}^{n+l}$ and since $\{\mathbf{y}_{m,r}\}$ contains $(k-1)l$ orthogonal eigenstates, we have thus proved that the eigenstates of H' are given by $\{\mathbf{x}_j\}, \{\mathbf{y}_{m,r}\}$.

-
- [1] S. Flach, D. Leykam, J. D. Bodyfelt, P. Matthies, and A. S. Desyatnikov, *Europhys. Lett.* **105**, 30001 (2014).
- [2] W. Maimaiti, A. Andrianov, H. C. Park, O. Gendelman, and S. Flach, *Phys. Rev. B* **95**, 115135 (2017).
- [3] P. W. Anderson, *Phys. Rev.* **109**, 1492 (1958).
- [4] B. Sutherland, *Phys. Rev. B* **34**, 5208 (1986).
- [5] D. L. Bergman, C. Wu, and L. Balents, *Phys. Rev. B* **78**, 125104 (2008).
- [6] O. Derzhko and J. Richter, *Eur. Phys. J. B* **52**, 23 (2006).
- [7] O. Derzhko, J. Richter, A. Honecker, M. Maksymenko, and R. Moessner, *Phys. Rev. B* **81**, 014421 (2010).
- [8] R. A. Vicencio and C. Mejía-Cortés, *J. Opt.* **16**, 015706 (2014).
- [9] S. Rojas-Rojas, L. Morales-Inostroza, R. A. Vicencio, and A. Delgado, *Phys. Rev. A* **96**, 043803 (2017).
- [10] S. Xia, Y. Hu, D. Song, Y. Zong, L. Tang, and Z. Chen, *Opt. Lett.* **41**, 1435 (2016).
- [11] R. A. Vicencio, C. Cantillano, L. Morales-Inostroza, B. Real, C. Mejía-Cortés, S. Weimann, A. Szameit, and M. I. Molina, *Phys. Rev. Lett.* **114**, 245503 (2015).
- [12] J. von Neuman and E. Wigner, *Phys. Z.* **30**, 465 (1929).
- [13] F. H. Stillinger and D. R. Herrick, *Phys. Rev. A* **11**, 446 (1975).
- [14] C. W. Hsu, B. Zhen, A. D. Stone, J. D. Joannopoulos, and M. Soljačić, *Nat. Rev. Mater.* **1**, 16048 (2016).
- [15] Y.-X. Xiao, G. Ma, Z.-Q. Zhang, and C. T. Chan, *Phys. Rev. Lett.* **118**, 166803 (2017).
- [16] D. J. Klein and B. Mandal, *MATCH Commun. Math. Comput. Chem.* **74**, 247 (2015).
- [17] J. D. Bodyfelt, D. Leykam, C. Danieli, X. Yu, and S. Flach, *Phys. Rev. Lett.* **113**, 236403 (2014).
- [18] S. A. Parameswaran, R. Roy, and S. L. Sondhi, *C. R. Phys.* **14**, 816 (2013).
- [19] S. Yang, Z. C. Gu, K. Sun, and S. Das Sarma, *Phys. Rev. B* **86**, 241112 (2012).
- [20] T. Neupert, L. Santos, C. Chamon, and C. Mudry, *Phys. Rev. Lett.* **106**, 236804 (2011).
- [21] E. Tang, J. W. Mei, and X. G. Wen, *Phys. Rev. Lett.* **106**, 236802 (2011).
- [22] A. M. C. Souza and H. J. Herrmann, *Phys. Rev. B* **79**, 153104 (2009).
- [23] C. Danieli, J. D. Bodyfelt, and S. Flach, *Phys. Rev. B* **91**, 235134 (2015).
- [24] D. Leykam, S. Flach, and Y. D. Chong, *Phys. Rev. B* **96**, 064305 (2017).
- [25] H. Ramezani, *Phys. Rev. A* **96**, 011802 (2017).
- [26] R. G. Dias and J. D. Gouveia, *Sci. Rep.* **5**, 16852 (2015).
- [27] L. Morales-Inostroza and R. A. Vicencio, *Phys. Rev. A* **94**, 043831 (2016).
- [28] A. Ramachandran, A. Andrianov, and S. Flach, *Phys. Rev. B* **96**, 161104 (2017).
- [29] C. Xu, G. Wang, Z. H. Hang, J. Luo, C. T. Chan, and Y. Lai, *Sci. Rep.* **5**, 18181 (2015).
- [30] P. A. Kalozoumis, C. Morfonios, F. K. Diakonou, and P. Schmelcher, *Phys. Rev. A* **87**, 032113 (2013).
- [31] P. A. Kalozoumis, C. Morfonios, N. Palaiodimopoulos, F. K. Diakonou, and P. Schmelcher, *Phys. Rev. A* **88**, 033857 (2013).
- [32] P. A. Kalozoumis, C. Morfonios, F. K. Diakonou, and P. Schmelcher, *Phys. Rev. Lett.* **113**, 050403 (2014).
- [33] P. A. Kalozoumis, C. V. Morfonios, F. K. Diakonou, and P. Schmelcher, *Ann. Phys. (N.Y.)* **362**, 684 (2015).
- [34] V. E. Zampetakis, M. K. Diakonou, C. V. Morfonios, P. A. Kalozoumis, F. K. Diakonou, and P. Schmelcher, *J. Phys. A: Math. Theor.* **49**, 195304 (2016).
- [35] C. V. Morfonios, P. A. Kalozoumis, F. K. Diakonou, and P. Schmelcher, *Ann. Phys.* **385**, 623 (2017).
- [36] M. Röntgen, C. V. Morfonios, F. K. Diakonou, and P. Schmelcher, *Ann. Phys. (N.Y.)* **380**, 135 (2017).
- [37] P. Schmelcher, S. Krönke, and F. K. Diakonou, *J. Chem. Phys.* **146**, 044116 (2017).
- [38] T. Wulf, C. V. Morfonios, F. K. Diakonou, and P. Schmelcher, *Phys. Rev. E* **93**, 052215 (2016).
- [39] W. Barrett, A. Francis, and B. Webb, *Linear Algebra Appl.* **513**, 409 (2017).
- [40] A. Francis, D. Smith, D. Sorensen, and B. Webb, *Linear Algebra Appl.* **532**, 432 (2017).
- [41] E. Fritscher and V. Trevisan, *SIAM J. Matrix Anal. Appl.* **37**, 260 (2016).
- [42] M. Rusek, J. Mostowski, and A. Orłowski, *Phys. Rev. A* **61**, 022704 (2000).
- [43] F. A. Pinheiro, M. Rusek, A. Orłowski, and B. A. van Tiggelen, *Phys. Rev. E* **69**, 026605 (2004).
- [44] A. Christofi, F. A. Pinheiro, and L. Dal Negro, *Opt. Lett.* **41**, 1933 (2016).
- [45] J. T. Chalker, T. S. Pickles, and P. Shukla, *Phys. Rev. B* **82**, 104209 (2010).
- [46] S. Mukherjee, A. Spracklen, D. Choudhury, N. Goldman, P. Öhberg, E. Andersson, and R. R. Thomson, *Phys. Rev. Lett.* **114**, 245504 (2015).

- [47] R. L. Doretto and M. O. Goerbig, *Phys. Rev. B* **92**, 245124 (2015).
- [48] Y. Plotnik, O. Peleg, F. Dreisow, M. Heinrich, S. Nolte, A. Szameit, and M. Segev, *Phys. Rev. Lett.* **107**, 183901 (2011).
- [49] J. M. Zhang, D. Braak, and M. Kollar, *Phys. Rev. A* **87**, 023613 (2013).
- [50] R. J. Trudeau, *Introduction to Graph Theory*, 2nd ed. (Dover, Mineola, NY, 1994).
- [51] M. Thüne, [arXiv:1605.05924](https://arxiv.org/abs/1605.05924).
- [52] Band structure calculations were performed using the software package PythTB (<http://www.physics.rutgers.edu/pythtb/>).
- [53] B. Pal, S. K.Maiti, and A. Chakrabarti, *Europhys. Lett.* **102**, 17004 (2013).

Compact localized states of open scattering media: a graph decomposition approach for ab initio design

FABRIZIO SGRIGNUOLI^{*1}, MALTE RÖNTGEN^{*2}, CHRISTIAN V. MORFONIOS², PETER SCHMELCHER^{2,3}, AND LUCA DAL NEGRO^{**1,4,5}

¹Department of Electrical and Computer Engineering, Boston University, Boston, Massachusetts, 02215, USA.

²Zentrum für optische Quantentechnologien, Universität Hamburg, Luruper Chaussee 149, 22761 Hamburg, Germany

³The Hamburg Centre for Ultrafast Imaging, Universität Hamburg, Luruper Chaussee 149, 22761 Hamburg, Germany

⁴Division of Material Science and Engineering, Boston University, Boston, Massachusetts, 02215, USA.

⁵Department of Physics, Boston University, Boston, Massachusetts, 02215, USA

*Authors with equal contribution

**Corresponding author: dalnegro@bu.edu

Note: This is the final accepted version of the manuscript. Unfortunately, a permission for a reprint of the published version was not given by the Optical Society of America. This article has been published in *Opt. Lett.* **44**, 375-378 (2019).

We study the compact localized scattering resonances of periodic and aperiodic chains of dipolar nanoparticles by combining the powerful Equitable Partition Theorem (EPT) of graph theory with the spectral dyadic Green's matrix formalism for the engineering of embedded quasi-modes in non-Hermitian open scattering systems in three spatial dimensions. We provide analytical and numerical design of the spectral properties of compact localized states in electromagnetically coupled chains and establish a connection with the distinctive behavior of Bound States in the Continuum. Our results extend the concept of compact localization to the scattering resonances of open systems with arbitrary aperiodic order beyond tight-binding models, and are relevant for the efficient design of novel photonic and plasmonic metamaterial architectures for enhanced light-matter interaction. © 2018 Optical Society of America

<http://dx.doi.org/10.1364/OL.44.000375>

The engineering of spatially localized wave excitations in complex scattering media is a fundamental problem that arises in many different contexts of optics and quantum mechanics. In particular, careful design of the symmetry properties of scattering potentials enables the creation of Compact Localized States (CLS), which are resonant electronic or photonic modes spatially localized over a compact subset of lattice sites [1–7]. These peculiar modes have received significant attention due to their importance for the design of dispersion-less flat bands (FB) in the spectrum of periodic lattices within the tight-binding model [1–7]. Moreover, symmetry arguments also play a key role in the manipulation of embedded eigenstates, which are eigenmodes of open large-scale structures with infinite lifetime and diverging quality factors appearing in the radiation continuum [8–17]. In fact, the symmetries of periodic structures, traditionally described by their space groups properties, determine the behavior of such peculiar eigenstates, also referred to as Bound

States in the Continuum (BIC) [8–17]. Symmetry-induced photonic eigenstates have recently attracted a significant attention in the nano-optics and metamaterials communities due to the many potential applications to ultra-compact and efficient solid-state lasers [18], optical sensors [19], and narrowband filters [20]. However, the predictive design of photonic CLS and BICs is currently limited to either the approximate tight-binding approximation or the use of intensive full-vector numerical simulations of large-scale photonic structures [3, 4].

In this letter, we propose a more general framework that captures in three-spatial dimensions the effects of local symmetries in the electromagnetic response of large chains of dipolar scattering nanoparticles with arbitrary geometry, enabling the efficient design of CLS and embedded eigenstates in photonic systems. Such local symmetries have been treated within a theory of non-local currents and were recently shown to induce a class of CLS in tight-binding networks [6, 21–24]. The proposed approach is based on the combination of the rigorous Green's matrix multiple scattering technique and recently established theorems in graph theory here employed to obtain a block partitioning of the dyadic Green's matrix induced by the symmetry properties of a given system under local site permutations. The diagonalization of the Green's matrix is reduced to finding the eigenspectra of smaller matrices, with eigenvectors naturally divided into compact localized and extended states. While valuable as a computational tool for arbitrary symmetric discrete open-scattering media, the proposed approach provides a unified, intuitive, and efficient method for the design of the energy spectra of CLS in both periodic and non-periodic arrays of nanostructures.

Our work applies the powerful Equitable Partition Theorem (EPT) of graph theory to the analysis of the dyadic Green's matrix formalism for the spectral engineering of embedded quasi-modes in non-Hermitian open scattering systems in three spatial dimensions. Moreover, by analyzing the spectral properties of the dyadic Green's matrix we discover a fundamental similarity between CLS quasi-modes (vanishing waves outside a finite subset of the system due to destructive interference [1–4, 6]) and the distinctive behavior of photonic BICs, which is achieved in the

limit of photonic systems of infinite optical density. Indeed, for infinite optical density, the analyzed structures support distinctive resonances with diverging normalized quality factors Q/Q_0 when bound states are gradually decoupled from the continuum. Remarkably, we demonstrate that the vertical mirror symmetry (y-axis mirror) of our system is responsible for the formation of embedded eigenstates regardless of the translational invariance (periodicity) of the system. Indeed, we show that exactly the same Q/Q_0 behavior can be obtained by randomly modulating the inter-particle positions along the horizontal x-axis by introducing a white noise structural perturbation in the system. Our work demonstrates that the EPT can be successfully applied to the Green's matrix formalism providing a novel and powerful theoretical tool for the analytical investigation of the spectra of embedded quasi-modes based only on local symmetry arguments, beyond the conventional tight-binding approach [6]. Our findings are relevant for the efficient design of novel photonic and metamaterials architectures that support scattering resonances with engineered compact localization and BIC behavior leading to enhanced light-matter interactions.

The Green's matrix method is a major theoretical tool that accounts for all the scattering orders, such that multiple scattering processes are treated exactly as long as the particles are much smaller than the wavelength. In this limit, each scatterer is characterized by a Breit-Wigner resonance at frequency ω_0 and a resonant width Γ_0 . The quasi-modes of arbitrary open-scattering systems are provided by the eigenvectors of the Green's matrix \overleftrightarrow{G} which, for N vector dipoles, is a $3N \times 3N$ matrix with components [25]:

$$G_{nm} = i (\delta_{nm} + \tilde{G}_{nm}) \quad (1)$$

\tilde{G}_{nm} has the form:

$$\tilde{G}_{nm} = \frac{3}{2} (1 - \delta_{nm}) \frac{e^{ik_0 r_{nm}}}{ik_0 r_{nm}} \left\{ \left[\mathbf{U} - \hat{\mathbf{r}}_{nm} \hat{\mathbf{r}}_{nm} \right] - \left(\mathbf{U} - 3\hat{\mathbf{r}}_{nm} \hat{\mathbf{r}}_{nm} \right) \left[\frac{1}{(k_0 r_{nm})^2} + \frac{1}{ik_0 r_{nm}} \right] \right\} \quad (2)$$

where k_0 is the wavevector of light, the integer indexes $n, m \in (1, \dots, N)$ refer to different particles, \mathbf{U} is the 3×3 identity matrix, $\hat{\mathbf{r}}_{nm}$ is the unit vector position from the n -th and m -th scatterer while r_{nm} identifies its magnitude. This formalism has been extensively used for the study of wave transport and localization phenomena in open multiple scattering media [25–30]. Because the matrix (1) is non-Hermitian, its $3N$ eigenvalues Λ_p are complex and they completely describe the scattering resonances of the system under study [26]. Specifically, the real and the imaginary parts of Λ_p are related to the normalized scattering frequency and normalized decay rates, respectively [25, 26]:

$$\Re[\Lambda_p] = (\omega_0 - \omega_p)/\Gamma_0 \quad (3)$$

$$\Im[\Lambda_p] = \Gamma_p/\Gamma_0 \quad (4)$$

The Green's matrix formalism is particularly suitable to study embedded eigenstates whenever each scattering particle is coupled to every other particle due to long-range electromagnetic interactions. Therefore, it is suitable to extend the traditional concept of embedded states [8, 9] to the multiple scattering regime. While the method is limited to vector scattering dipoles, it very well captures the fundamental multiple scattering physics of large-scale coupled systems without the prohibitive costs associated to traditional numerical techniques that are typically

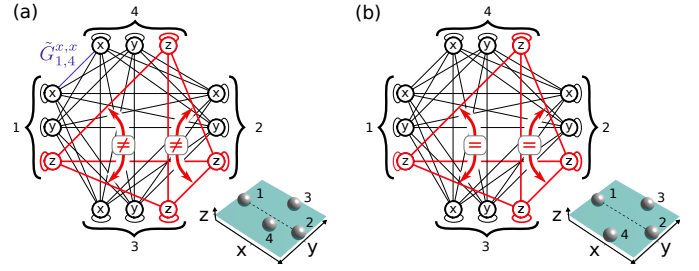


Fig. 1. (a) Graph representation of G for a four-scatterer planar configuration in the xy -plane (see inset). Each line represents a non-vanishing matrix element of G . Due to Eq.(5), the graph splits into two disconnected subgraphs (black and red lines) for planar arrangements of scatterers. If, as in (b), the scatterers are placed symmetrically about the x -axis (dotted line), the graph features the local symmetry $G_{m,A}^{z,z} = G_{\bar{m},\bar{A}}^{z,z}$ ($m = 1, 2$). For generic planar configurations, as in (a), there is no local symmetry within the red subgraph.

employed for the design of similar electromagnetic structures [11–14, 31].

Originally developed in graph theory [32], the EPT exploits a permutation symmetry ϕ of a square matrix M to decompose it into smaller matrices B_i , the eigenvalues of which collectively give those of M . The corresponding eigenvectors of M can likewise be constructed from the eigenvectors of B_i and can be shown to share the symmetries of M . Interestingly, if $\sigma: \{1, \dots, k\} \rightarrow \{1, \dots, k\}$ acts as the identity operator on a subset $\mathcal{S} \subset \{1, \dots, k\}$, then $M \in \mathbb{C}^{k \times k}$ is guaranteed to host at least one CLS whose amplitudes vanish on \mathcal{S} [33]. We now apply the EPT to planar configurations that are symmetric with respect to the x -axis (see Fig.1 (c)). For generic planar configuration,

$$G_{nm}^{a,z} = G_{\bar{n}\bar{m}}^{a,z} = 0 \quad \forall n, m; a \in \{x, y\} \quad (5)$$

where $G_{nm}^{a,b}$, with $a, b \in \{x, y, z\}$, describes the b -component of the electric field at the position of the scatterer n due to a dipole m oscillating along the a -axis. If, additionally, the scatterers are placed symmetrically with respect to the x -axis,

$$G_{nm}^{z,z} = G_{\bar{m}\bar{n}}^{z,z} = G_{\bar{n}\bar{m}}^{z,z} = G_{\bar{m}\bar{n}}^{z,z} \quad \forall n \in \mathcal{S}, m \notin \mathcal{S} \quad (6)$$

where \bar{m} denotes the symmetry-mapped counterpart of m and \mathcal{S} identifies the scatterers which are positioned on the symmetry axis. Eq.(6) is equivalent to a local permutation symmetry σ of G which pairwise permutes the matrix elements $G_{nm}^{z,z} \leftrightarrow G_{\bar{n}\bar{m}}^{z,z}, G_{\bar{m}\bar{n}}^{z,z} \leftrightarrow G_{nm}^{z,z}, \forall n \in \mathcal{S}, m \notin \mathcal{S}$ and acts as the identity on all others. This allows to apply the EPT, which predicts that G hosts $C = (N - |\mathcal{S}|)/2$ CLS, where $|\mathcal{S}|$ denotes the number of scatterers on the symmetry axis. The corresponding eigenvalues $\{\Lambda_{CLS}\}$ are obtained by diagonalizing a small matrix $B_1 \in \mathbb{C}^{C \times C}$. For $C = 1$

$$\Lambda_{CLS} = G_{nm}^{z,z} - G_{\bar{m}\bar{n}}^{z,z} = \left[i - \frac{3}{2} \frac{e^{ik_0 R}}{k_0 R} \left(1 - \frac{1}{ik_0 R} - \frac{1}{(k_0 R)^2} \right) \right] \quad (7)$$

with m being either of the two scatterers not lying on the symmetry axis and $R = r_{m\bar{m}}$ being the distance to its mirrored counterpart. In terms of the optical density $\rho\lambda$ (keeping $R = 2/\rho$), where ρ is the linear density across the x -axis and λ is the optical wavelength, the normalized decay rate $\Gamma_{CLS}/\Gamma_0 = \Im[\Lambda_{CLS}] \rightarrow 0$ for $\rho\lambda \rightarrow \infty$, corresponding to the case of embedded bound states in the scattering continuum.

In the following, we apply our theory to the simplest possible structure that supports compact localization due to y -mirror symmetry. Indeed, it is also very well-known that symmetry-protected BICs can be formed in a system with reflection or rotational symmetry and that their coupling with the extended states is forbidden as long as the symmetry is preserved [13]. Our test geometry, sketched in Fig. 2 (a), closely resembles the one analyzed in Ref.[15] and it is characterized by a periodic array of 500 scattering nanoparticles distributed along the x -direction with two additional scatterers located symmetrically above and below the array. Although we present results on a system composed by $N = 502$ scatterers, the proposed ab-initio design method is valid for any value of N provided that the symmetry with respect to the x -axis is preserved. Fig. 2 highlights the main concept behind this work, *i.e.* the possibility to analytically predict the spectrum of CLS quasi-modes by using the EPT on the dyadic Green's matrix (1). In order to immediately identify the CLS resonance in the complex scattering plane of the Green's matrix we computed the Mode Spatial Extent (MSE) parameter for all the modes in the spectrum. This parameter characterizes the spatial extent of a photonic mode Ψ_p and it is defined as $MSE_p = \left[\sum_{t=1}^N |\Psi_p(\mathbf{r}_t)|^2 \right]^2 / \left[\sum_{t=1}^N |\Psi_p(\mathbf{r}_t)|^4 \right]$ [25, 34]. Panels (b-d) show the CLS spectrum from Eq. (7) (see black-dotted lines) obtained via the EPT Green's matrix decomposition. We also show the CLS spectrum obtained by numerical diagonalization of the Green's matrix, perfectly matching the analytical result. Moreover, panels (b-c) show the detuned normalized frequency

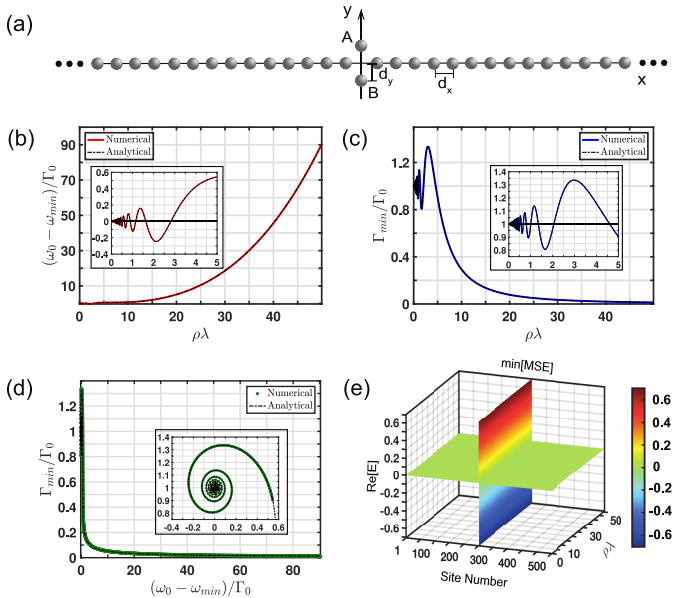


Fig. 2. The simple benchmark structure, composed by 502 vector electric dipoles, is shown in panel (a). Panels (b-c) show the detuned normalized frequency and the normalized decay rates as function of $\rho\lambda$ corresponding to the Green's matrix eigenvalue with the lowest MSE value (named *min*), respectively. Panel (d) shows how the *min* complex eigenvalue organizes itself for each considered optical density value. Insets: enlarged view of these trends for low optical density values. The black horizontal lines in the inset of Fig. 2 (b-c) identify the $\omega_{min}=\omega_0$ and $\Gamma_{min}=\Gamma_0$ point, respectively. Panel (e) displays the real part of the quasi-mode corresponding to the *min* eigenvalue as a function of the scatterer site number and $\rho\lambda$.

and the normalized decay rates corresponding to the Green's matrix eigenvalue with the lowest MSE (referred to as "the *min* eigenvalue") as function of the parameter $\rho\lambda$, which corresponds to the optical density of the system (*i.e.*, the number of scattering particles per unit wavelength). The insets display an enlarged view of these trends that feature a fast oscillatory behavior for small values of the optical density ($\rho\lambda < 2$). These oscillations of the *min* eigenvalue around the Breit-Wigner resonance are typical of proximity resonances. Indeed, exactly the same behavior can be observed in a system composed of only two scatterers separated by a distance d [26]. The complex scattering plane associated to two electric point dipoles for different distances d is also characterized by two spiral arms associated to the excitation of p-wave and s-wave scattering resonances, respectively. In the limit $d \rightarrow \infty$ they meet at the isolated point characterized by $\omega=\omega_0$, $\Gamma=\Gamma_0$ [26]. To completely clarify the nature of these oscillations we report in panel (d) the normalized decay rate of the *min* eigenvalue as a function of its normalized detuned frequency. The typical spiral features of proximity resonances are clearly visible in the inset of Fig. 2(d), demonstrating that in the limit of very low optical density CLS quasi-modes appear as isolated single scattering resonances in the Green's matrix spectrum. In order to confirm that the *min* eigenvalue corresponds to a CLS quasi-mode, we have evaluated the spatial distribution of its corresponding eigenvector as a function of $\rho\lambda$. Its real part is reported in panel (e). As expected, this eigenvector is non-zero only on the sites of the chain corresponding to the position of the scatterers A and B, as shown in Fig. 2. This mode is therefore a CLS supported only on the two particles at the center of the chain, with reference to Fig. 2 (a). Our analysis demonstrates that the eigenvalue of the Green's matrix with the lowest MSE corresponds to a CLS quasi-mode.

In order to investigate the link between CL quasi-modes and BIC states, we have also analyzed the behavior of the normalized quality factor $Q/Q_0 = 1/\Im[\Lambda_n]$ of the *min* eigenvalue as a function of the vertical relative position of the scatterers A and B normalized with respect to the optical wavelength (\hat{d}_y). The results of this analysis are reported in Fig. 3 (a-b) for a periodic and a randomly perturbed alignment of scatterers on the x -axis, respectively. The results of Fig. 3 are obtained by fixing the optical density equal to 50 and they demonstrate a rapid decrease of the leakage radiation of the minimally extended mode when the y -mirror symmetry of the system is progressively restored. This symmetric condition is identified by the black-dotted lines of Fig. 3 (a-b) while the positive and negative values of \hat{d}_y refer to the position of the scatterers A and B, respectively. Specifically, the quantity Q/Q_0 shows a monotonically increasing behavior when the state is gradually decoupled from the continuum, and it diverges in the limit of infinite optical density similarly to what is reported in Ref. [12] for BICs in a photonic crystal slab. In order to demonstrate that this behavior is produced only from the symmetry about the x -axis, we perturbed the particle positions along the x -axis by adding white-noise positional fluctuations[35]. The inter-particle separation fluctuates around the unperturbed distance with relative amplitude 0.5. Interestingly, we obtained exactly the same Q/Q_0 behavior also in the disorder configuration (as reported in Fig. 3(b) for 50 different realizations of the disordered chains), thus demonstrating that the symmetry about the x -axis is solely responsible for the formation of the CLS states with distinctive BIC behavior. Representative spatial distributions of the Green's matrix eigenvectors corresponding to the lowest MSE values are also reported on the right side of Fig. 3(a-b). The typical CLS spatial profile is

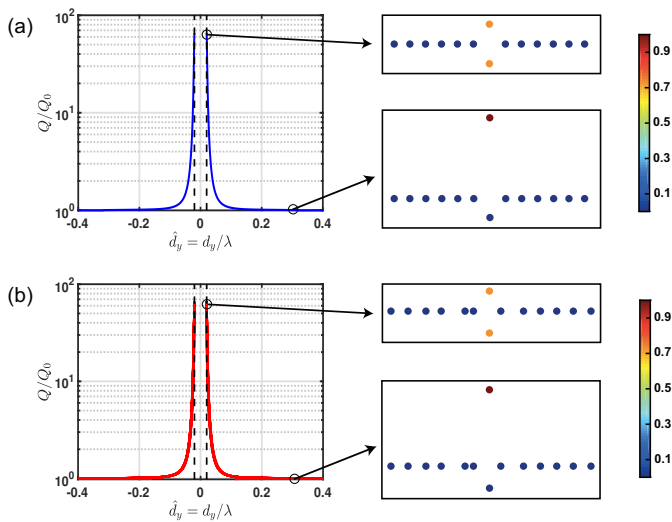


Fig. 3. Panel (a-b) display the normalized Q-factor as a function of position of the scatterers A and B normalized with respect to the optical wavelength, for the periodic and disorder configuration, respectively. These data are obtained by fixing $\rho\lambda=50$. The trend of panel (b) is characterized by 50 different disorder realizations. Representative spatial distribution of the Green's matrix eigenvector, corresponding to the lowest MSE value, are shown for different \hat{d}_y values for both configurations.

supported only by the central two sites only when the mirror symmetry condition is reached in both configurations. Progressively breaking the symmetry about the x -axis in our system produces a gradual coupling of the CLS to the continuum states, resulting in radiative losses.

Our work extends the concept of compact localized states to open electromagnetic scattering systems and fully demonstrates the potential of the EPT graph decomposition theorem applied to the dyadic Green's matrix method for the study of the localization properties and the spectra of symmetric collectively coupled electromagnetic structures. While valuable as a computational framework for arbitrary discrete open-scattering media, the proposed approach provides a unified, intuitive, and efficient method for designing the spectra of CLS and BICs in both periodic and non-periodic arrays of resonant nanostructures.

FUNDING INFORMATION

Army Research Laboratory (ARL) through the Collaborative Research Alliance (CRA) for MultiScale Multidisciplinary Modeling of Electronic Materials (MSME) under Cooperative Agreement (W911NF-12-2-0023). L.D.N also acknowledges the partial support from the NSF-ECCS EAGER Award 1643118. M.R. gratefully acknowledges financial support by the 'Stiftung der deutschen Wirtschaft' in the framework of a scholarship.

REFERENCES

1. S. Flach, D. Leykam, J. D. Bodyfelt, P. Matthies, and A. S. Desyatnikov, *EPL* **105**, 30001 (2014).
2. W. Maimaiti, A. Andreanov, H. C. Park, O. Gendelman, and S. Flach, *Phys. Rev. B* **95**, 115135 (2017).
3. D. Leykam, A. Andreanov, and S. Flach, *Adv. Physics: X* **3**, 1473052 (2018).

4. D. Leykam and S. Flach, *APL Photonics* **3**, 070901 (2018).
5. O. Derzhko, J. Richter, and M. Maksymenko, *Int. J. Mod. Phys. B* **29**, 1530007 (2015).
6. M. Röntgen, C. Morfonios, and P. Schmelcher, *Phys. Rev. B* **97**, 035161 (2018).
7. B. Real, C. Cantillano, D. López-González, A. Szameit, M. Aono, M. Naruse, S. J. Kim, K. Wang, and R. A. Vicencio, *Sci. Rep.* **7**, 15085 (2017).
8. J. von Neumann and E. P. Wigner, "Über merkwürdige diskrete eigenwerte," in *The Collected Works of Eugene Paul Wigner*, (Springer, 1993), pp. 291–293.
9. F. H. Stillinger and D. R. Herrick, *Phys. Rev. A* **11**, 446 (1975).
10. F. Capasso, C. Sirtori, J. Faist, D. L. Sivco, S.-N. G. Chu, and A. Y. Cho, *Nature* **358**, 565 (1992).
11. D. Marinica, A. Borisov, and S. Shabanov, *Phys. Rev. Lett.* **100**, 183902 (2008).
12. C. W. Hsu, B. Zhen, J. Lee, S.-L. Chua, S. G. Johnson, J. D. Joannopoulos, and M. Soljačić, *Nature* **499**, 188 (2013).
13. C. W. Hsu, B. Zhen, A. D. Stone, J. D. Joannopoulos, and M. Soljačić, *Nat. Rev. Mater.* **1**, 16048 (2016).
14. S. Weimann, Y. Xu, R. Keil, A. E. Miroshnichenko, A. Tünnermann, S. Nolte, A. A. Sukhorukov, A. Szameit, and Y. S. Kivshar, *Phys. Rev. Lett.* **111**, 240403 (2013).
15. Y. Plotnik, O. Peleg, F. Dreisow, M. Heinrich, S. Nolte, A. Szameit, and M. Segev, *Phys. Rev. Lett.* **107**, 183901 (2011).
16. N. Rivera, C. W. Hsu, B. Zhen, H. Buljan, J. D. Joannopoulos, and M. Soljačić, *Sci. Rep.* **6**, 33394 (2016).
17. H. M. Döeleman, F. Monticone, W. Hollander, A. Alù, and A. F. Koenderink, *Nat. Photon.* p. 1 (2018).
18. A. Kodigala, T. Lepetit, Q. Gu, B. Bahari, Y. Fainman, and B. Kanté, *Nature* **541**, 196 (2017).
19. A. A. Yanik, A. E. Cetin, M. Huang, A. Artar, S. H. Mousavi, A. Khanikaev, J. H. Connor, G. Shvets, and H. Altug, *Proc. Natl. Acad. Sci. U.S.A.* **108**, 11784 (2011).
20. J. M. Foley, S. M. Young, and J. D. Phillips, *Phys. Rev. B* **89**, 165111 (2014).
21. P. Kalozoumis, C. Morfonios, F. Diakonov, and P. Schmelcher, *Phys. Rev. Lett.* **113**, 050403 (2014).
22. M. Röntgen, C. Morfonios, F. Diakonov, and P. Schmelcher, *Ann. Phys.* **380**, 135 (2017).
23. C. Morfonios, P. Kalozoumis, F. Diakonov, and P. Schmelcher, *Ann. Phys.* **385**, 623 (2017).
24. P. Kalozoumis, O. Richoux, F. Diakonov, G. Theocharis, and P. Schmelcher, *Phys. Rev. B* **92**, 014303 (2015).
25. S. E. Skipetrov and I. M. Sokolov, *Phys. Rev. Lett.* **112**, 023905 (2014).
26. M. Rusek, J. Mostowski, and A. Orłowski, *Phys. Rev. A* **61**, 022704 (2000).
27. A. Lagendijk and B. A. Van Tiggelen, *Phys. Reports* **270**, 143 (1996).
28. F. Sgrignuoli, R. Wang, F. A. Pinheiro, and L. Dal Negro, *arXiv preprint arXiv:1810.01909* (2018).
29. R. Wang, F. A. Pinheiro, and L. Dal Negro, *Phys. Rev. B* **97**, 024202 (2018).
30. R. Wang, M. Röntgen, C. V. Morfonios, F. A. Pinheiro, P. Schmelcher, and L. Dal Negro, *Opt. Lett.* **43**, 1986 (2018).
31. Y. Yang, C. Peng, Y. Liang, Z. Li, and S. Noda, *Phys. Rev. Lett.* **113**, 037401 (2014).
32. W. Barrett, A. Francis, and B. Webb, *Linear Algebr. its Appl.* **513**, 409 (2017).
33. D. J. Klein and B. Mandal, *MATCH Commun. Math. Comput. Chem* **74**, 247 (2015).
34. F. Sgrignuoli, G. Mazzamuto, N. Caselli, F. Intonti, F. S. Cataliotti, M. Gurioli, and C. Toninelli, *ACS Photonics* **2**, 1636 (2015).
35. G. J. Lord, C. E. Powell, and T. Shardlow, *An introduction to computational stochastic PDEs* (Cambridge University Press, 2014).

FULL REFERENCES

1. S. Flach, D. Leykam, J. D. Bodyfelt, P. Matthies, and A. S. Desyatnikov, "Detangling flat bands into fano lattices," *EPL* **105**, 30001 (2014).
2. W. Maimaiti, A. Andreanov, H. C. Park, O. Gendelman, and S. Flach, "Compact localized states and flat-band generators in one dimension," *Phys. Rev. B* **95**, 115135 (2017).
3. D. Leykam, A. Andreanov, and S. Flach, "Artificial flat band systems: from lattice models to experiments," *Adv. Physics: X* **3**, 1473052 (2018).
4. D. Leykam and S. Flach, "Perspective: Photonic flatbands," *APL Photonics* **3**, 070901 (2018).
5. O. Derzhko, J. Richter, and M. Maksymenko, "Strongly correlated flat-band systems: The route from heisenberg spins to hubbard electrons," *Int. J. Mod. Phys. B* **29**, 1530007 (2015).
6. M. Röntgen, C. Morfonios, and P. Schmelcher, "Compact localized states and flat bands from local symmetry partitioning," *Phys. Rev. B* **97**, 035161 (2018).
7. B. Real, C. Cantillano, D. López-González, A. Szameit, M. Aono, M. Naruse, S. J. Kim, K. Wang, and R. A. Vicencio, "Flat-band light dynamics in stub photonic lattices," *Sci. Rep.* **7**, 15085 (2017).
8. J. von Neumann and E. P. Wigner, "Über merkwürdige diskrete eigenwerte," in *The Collected Works of Eugene Paul Wigner*, (Springer, 1993), pp. 291–293.
9. F. H. Stillinger and D. R. Herrick, "Bound states in the continuum," *Phys. Rev. A* **11**, 446 (1975).
10. F. Capasso, C. Sirtori, J. Faist, D. L. Sivco, S.-N. G. Chu, and A. Y. Cho, "Observation of an electronic bound state above a potential well," *Nature* **358**, 565 (1992).
11. D. Marinica, A. Borisov, and S. Shabanov, "Bound states in the continuum in photonics," *Phys. Rev. Lett.* **100**, 183902 (2008).
12. C. W. Hsu, B. Zhen, J. Lee, S.-L. Chua, S. G. Johnson, J. D. Joannopoulos, and M. Soljačić, "Observation of trapped light within the radiation continuum," *Nature*. **499**, 188 (2013).
13. C. W. Hsu, B. Zhen, A. D. Stone, J. D. Joannopoulos, and M. Soljačić, "Bound states in the continuum," *Nat. Rev. Mater.* **1**, 16048 (2016).
14. S. Weimann, Y. Xu, R. Keil, A. E. Miroshnichenko, A. Tünnermann, S. Nolte, A. A. Sukhorukov, A. Szameit, and Y. S. Kivshar, "Compact surface fano states embedded in the continuum of waveguide arrays," *Phys. Rev. Lett.* **111**, 240403 (2013).
15. Y. Plotnik, O. Peleg, F. Dreisow, M. Heinrich, S. Nolte, A. Szameit, and M. Segev, "Experimental observation of optical bound states in the continuum," *Phys. Rev. Lett.* **107**, 183901 (2011).
16. N. Rivera, C. W. Hsu, B. Zhen, H. Buljan, J. D. Joannopoulos, and M. Soljačić, "Controlling directionality and dimensionality of radiation by perturbing separable bound states in the continuum," *Sci. Rep.* **6**, 33394 (2016).
17. H. M. Doeleman, F. Monticone, W. Hollander, A. Alù, and A. F. Koenderink, "Experimental observation of a polarization vortex at an optical bound state in the continuum," *Nat. Photon.* p. 1 (2018).
18. A. Kodigala, T. Lepetit, Q. Gu, B. Bahari, Y. Fainman, and B. Kanté, "Lasing action from photonic bound states in continuum," *Nature*. **541**, 196 (2017).
19. A. A. Yanik, A. E. Cetin, M. Huang, A. Artar, S. H. Mousavi, A. Khanikaev, J. H. Connor, G. Shvets, and H. Altug, "Seeing protein monolayers with naked eye through plasmonic fano resonances," *Proc. Natl. Acad. Sci. U.S.A.* **108**, 11784–11789 (2011).
20. J. M. Foley, S. M. Young, and J. D. Phillips, "Symmetry-protected mode coupling near normal incidence for narrow-band transmission filtering in a dielectric grating," *Phys. Rev. B* **89**, 165111 (2014).
21. P. Kalozoumis, C. Morfonios, F. Diakonov, and P. Schmelcher, "Invariants of broken discrete symmetries," *Phys. Rev. Lett.* **113**, 050403 (2014).
22. M. Röntgen, C. Morfonios, F. Diakonov, and P. Schmelcher, "Non-local currents and the structure of eigenstates in planar discrete systems with local symmetries," *Ann. Phys.* **380**, 135–153 (2017).
23. C. Morfonios, P. Kalozoumis, F. Diakonov, and P. Schmelcher, "Nonlocal discrete continuity and invariant currents in locally symmetric effective schrödinger arrays," *Ann. Phys.* **385**, 623–649 (2017).
24. P. Kalozoumis, O. Richoux, F. Diakonov, G. Theocharis, and P. Schmelcher, "Invariant currents in lossy acoustic waveguides with complete local symmetry," *Phys. Rev. B* **92**, 014303 (2015).
25. S. E. Skipetrov and I. M. Sokolov, "Absence of anderson localization of light in a random ensemble of point scatterers," *Phys. Rev. Lett.* **112**, 023905 (2014).
26. M. Rusek, J. Mostowski, and A. Orłowski, "Random green matrices: From proximity resonances to anderson localization," *Phys. Rev. A* **61**, 022704 (2000).
27. A. Lagendijk and B. A. Van Tiggelen, "Resonant multiple scattering of light," *Phys. Reports* **270**, 143–215 (1996).
28. F. Sgrignuoli, R. Wang, F. A. Pinheiro, and L. Dal Negro, "Light localization and cooperative effects in aperiodic vogel spirals," *arXiv preprint arXiv:1810.01909* (2018).
29. R. Wang, F. A. Pinheiro, and L. Dal Negro, "Spectral statistics and scattering resonances of complex primes arrays," *Phys. Rev. B* **97**, 024202 (2018).
30. R. Wang, M. Röntgen, C. V. Morfonios, F. A. Pinheiro, P. Schmelcher, and L. Dal Negro, "Edge modes of scattering chains with aperiodic order," *Opt. Lett.* **43**, 1986–1989 (2018).
31. Y. Yang, C. Peng, Y. Liang, Z. Li, and S. Noda, "Analytical perspective for bound states in the continuum in photonic crystal slabs," *Phys. Rev. Lett.* **113**, 037401 (2014).
32. W. Barrett, A. Francis, and B. Webb, "Equitable decompositions of graphs with symmetries," *Linear Algebr. its Appl.* **513**, 409–434 (2017).
33. D. J. Klein and B. Mandal, "Local symmetries for molecular graphs," *MATCH Commun. Math. Comput. Chem* **74**, 247–58 (2015).
34. F. Sgrignuoli, G. Mazzamuto, N. Caselli, F. Intonti, F. S. Cataliotti, M. Gurioli, and C. Toninelli, "Necklace state hallmark in disordered 2d photonic systems," *ACS Photonics* **2**, 1636–1643 (2015).
35. G. J. Lord, C. E. Powell, and T. Shardlow, *An introduction to computational stochastic PDEs* (Cambridge University Press, 2014).

Quantum Network Transfer and Storage with Compact Localized States Induced by Local Symmetries

M. Röntgen,¹ C. V. Morfonios,¹ I. Brouzos,² F. K. Diakonou,² and P. Schmelcher^{1,3}

¹Zentrum für optische Quantentechnologien, Universität Hamburg, Luruper Chaussee 149, 22761 Hamburg, Germany

²Department of Physics, University of Athens, 15771 Athens, Greece

³The Hamburg Centre for Ultrafast Imaging, Universität Hamburg, Luruper Chaussee 149, 22761 Hamburg, Germany



(Received 7 November 2018; published 23 August 2019)

We propose modulation protocols designed to generate, store, and transfer compact localized states in a quantum network. Induced by parameter tuning or local reflection symmetries, such states vanish outside selected domains of the complete system and are therefore ideal for information storage. Their creation and transfer is here achieved either via amplitude phase flips or via optimal temporal control of intersite couplings. We apply the concept to a decorated, locally symmetric Lieb lattice where one sublattice is dimerized, and also demonstrate it for more complex setups. The approach allows for a flexible storage and transfer of states along independent paths in lattices supporting flat energetic bands. We further demonstrate a method to equip *any* network featuring static perfect state transfer of single-site excitations with compact localized states, thus increasing the storage ability of these networks. We show that these compact localized states can likewise be perfectly transferred through the corresponding network by suitable, time-dependent modifications. The generic network and protocols proposed can be utilized in various physical setups such as atomic or molecular spin lattices, photonic waveguide arrays, and acoustic setups.

DOI: [10.1103/PhysRevLett.123.080504](https://doi.org/10.1103/PhysRevLett.123.080504)

Introduction.—The storage and transfer of information in quantum systems is a task of great importance for the realization of quantum computers and simulators. Storage of a quantum state implies that it is effectively decoupled from surrounding building blocks of a system and, thus, is not affected by its environment. In contrast, transfer of a state requires a successive interaction with its environment leading to its directed propagation. We here propose a quantum state that can be easily prepared and robustly stored and present protocols that transfer it through a quantum network. We thereby merge key ingredients of three different fields of research: (i) compact localized states in flatband lattices [1–14], (ii) perfect state transfer (PST) [15–23], and (iii) optimal control theory [24–28].

A compact localized state (CLS) is a Hamiltonian eigenstate defined by its strictly vanishing amplitudes outside a spatial subdomain of the system. This compact localization originates from destructive interference caused by the right combination of lattice geometry and Hamiltonian matrix elements. Such a combination is possible in a broad range of physical systems [2], and CLSs have been realized in, e.g., photonic waveguide arrays [3,6,8,13], ultracold atomic ensembles [4,5], and optomechanical setups [11]. Though typically residing in “flat” energy bands of periodic lattices with macroscopic degeneracy [3–6,8,12–14], CLSs can exist in nonperiodic setups just as well.

By their defining property, CLSs are ideally suited for storage: Because of their compactness, they can be stored

using only a very small number of physical sites and, being Hamiltonian eigenstates, they can in principle be stored for an infinite amount of time. Moreover, their compactness protects CLSs against a wide range of imperfections. In particular, CLSs remain unaffected by changes of the Hamiltonian outside their localization domain. Furthermore, there is a class of CLSs which are protected by spatial *local symmetry* of the Hamiltonian against *any* perturbations preserving this local symmetry and the geometry within their localization domain [10]. As a side note, the more general study of local symmetries has recently been put on new grounds by introducing a framework of nonlocal currents [29–34] by means of which the parity and Bloch theorem are generalized to locally symmetric systems [35]. Recently, it has been shown that CLSs may result from particular local symmetries which commute with the Hamiltonian in discrete systems [10].

While favoring their storage, the compactness and consequent decoupling of CLSs from their surroundings poses the challenge of how to *transfer* them controllably across a lattice. We here demonstrate how transfer of local-symmetry-induced CLSs can be achieved using two different approaches, based on free and driven time evolution. The first approach utilizes the common perfect (i.e., with unit fidelity) quantum state transfer scenario, where static intersite couplings are tailored such that a selected state evolves freely from one location to another. Quantum

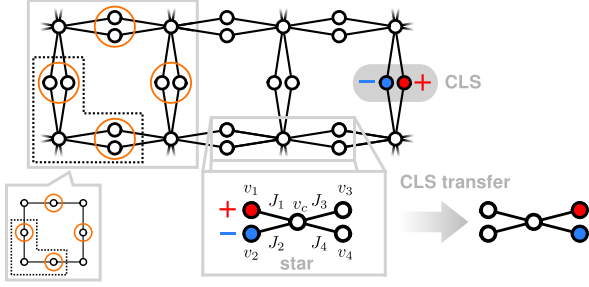


FIG. 1. Decorated Lieb lattice (DLL), constructed from the original Lieb lattice (whose plaquette is shown in the lower left-hand inset) by replacing the encircled sites with dimers. Each such dimer can host one CLS with opposite amplitudes on the two dimer sites. The lower right-hand inset shows the isolated “star” subsystem functioning as a unit for the CLS transfer.

state transfer techniques are especially explored in connection with entanglement transfer [17,18], while engineered coupling conditions for perfect transfer are also applied to network setups [15,16]. As we show here, a CLS can be perfectly transferred under free evolution after a suitable local phase flip in its amplitude or in selected intersite hoppings. The second approach uses optimal control theory [24–28], where the system is dynamically driven to the target state. For the tight-binding systems treated here, it aims at maximizing the fidelity of the transfer of a CLS across the system by designing smooth time-dependent modulations of the couplings. The main advantage is its applicability in cases where instantaneous changes, like the phase flips above, are not feasible in practice. A special representative of optimal control is, e.g., the celebrated stimulated adiabatic Raman passage (STIRAP) [36] in three level systems. Recently [37], CLSs in Lieb lattices have been used, in the form of “dark states” [38], as a transfer channel between two local states during a spatial STIRAP process. We here take an orthogonal viewpoint, since our aim is to transfer the dark state (CLS) itself to other dark states through the network.

For definiteness, we shall apply the proposed concept of storage and transfer of CLSs to a decorated Lieb lattice (DLL); see Fig. 1. It is derived from the original Lieb lattice [39] by replacing the sites of one sublattice with dimers. The resulting network can be extended to more complex geometries and to higher dimensions, and different CLSs can be routed independently across the network.

Star subsystem.—The basic building block for CLS transfer in the DLL is its isolated unit cell. It represents a five-point star graph and is shown in the lower inset of Fig. 1. It is governed by the Hamiltonian

$$H = v_c |c\rangle\langle c| + \sum_{n=1}^4 v_n |n\rangle\langle n| + J_n (|n\rangle\langle c| + |c\rangle\langle n|), \quad (1)$$

with on-site potentials v_n and outer nodes $n = \{1, \dots, 4\}$ coupled to the central node c by real hoppings J_n .

The above Hamiltonian can be physically realized in various contexts. One possibility is a coupled waveguide array [40,41], with each node representing a waveguide cross section and neighboring waveguides evanescently coupled through the overlap of their fundamental modes. By tuning the distance between neighboring waveguides, their coupling can be individually controlled [42,43] and also made negative [44]. The system is then effectively described by a discrete Schrödinger equation in terms of single-site excitations $|n\rangle$, with time t replaced by the coordinate along the waveguide axis [41]. Another possible physical realization of H is in terms of spins, with each node representing a spin-1/2 qubit (measured up or down). The Heisenberg XX interaction Hamiltonian reduces to this simple description within the subspace of one excitation (1 spin up and all others down) [17].

In the presence of local symmetry under permutation only of sites 1 and 2, that is, $J_1 = J_2 \equiv J$ and $v_1 = v_2 \equiv v$, the star Hamiltonian H hosts the eigenstate $|I\rangle = [(|1\rangle - |2\rangle)/\sqrt{2}]$. This is a CLS with opposite amplitudes on sites 1 and 2 and vanishing amplitudes on all others. Its hopping rate $J_1 I_1 + J_2 I_2 = J_1 - J_2$ (with $I_n = \langle n|I\rangle$) to the central site vanishes. It is thus decoupled by local symmetry from the rest of the star system, and, being an eigenstate, “stored” for an arbitrary time interval until the local symmetry condition is violated. Crucially, this local-symmetry-induced decoupling persists even if $J(t)$ and $v(t)$ are time dependent, allowing for a gradual modulation without perturbing the CLS [up to a global phase, $|I(t)\rangle = e^{-i\phi(t)/\hbar}|I\rangle$ with $\phi(t) = \int_{t_0}^t v(t')dt'$]. Moreover, $|I\rangle$ is unaffected by any change of the remainder of the Hamiltonian, i.e., of v_c , v_3 , v_4 , J_3 , or J_4 . In complete similarity, for $J_3 = J_4$ and $v_3 = v_4$ the star hosts a second compact localized eigenstate $|F\rangle = [(|3\rangle - |4\rangle)/\sqrt{2}]$. Both $|I\rangle$ and $|F\rangle$ are also dark states since they are the only eigenstates of the Hamiltonian Eq. (1) which have nonzero coefficients only in two sites. An important fact is that $|I\rangle$ and $|F\rangle$ are also eigenstates of the full Hamiltonian when the star subsystem is repeatedly connected to form the DLL (see Fig. 1). In fact, *different* locally symmetric star subsystems, each with its own parameters v_n , J_n , can be connected in a suitable way to form a network hosting multiple independent CLSs, each stored on only two sites with opposite amplitude.

In the following, we first present different protocols transferring a CLS in the star subsystem. These can easily be extended to the full DLL, as we will show afterwards. In the Supplemental Material (SM) [45], we demonstrate the robustness of the considered protocols to perturbations. For the state transfer within the time T , the two CLSs $|I\rangle$ and $|F\rangle$ will serve as the initial and final state. Throughout the rest of this work, we set $v_n = v$, but J_n are not necessarily equal to each other and may also be time dependent during the pulse. However, we impose the symmetry condition $J_3 = J_4$ at the end of the transfer to ensure that $|F\rangle$ is an energy eigenstate. The initially stored CLS is thus transferred to the target

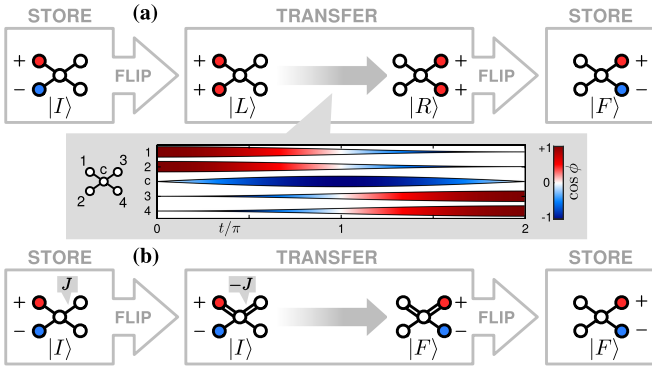


FIG. 2. Transfer of a stored dimer-localized CLS $|I\rangle$ to a final CLS $|F\rangle$ within a star subsystem via free time evolution between sign flips of (a) one component of the initial and final states and (b) one of the couplings (double line) of the central site to each of the initial and final CLS dimers. The inset in (a) shows the evolution of the state $|\psi\rangle$ over time $T = 2\pi$ with $|\psi(0)\rangle = |L\rangle$ and $|\psi(T)\rangle = |R\rangle$ for $v_n = 2J_n = 1/4 \forall n$. The phase of $\psi_n(t) = \langle n|\psi(t)\rangle$ at site n is color coded and its amplitude is indicated by the width of the corresponding stripe. The evolution for (b) is identical except for opposite signs on $\psi_2(t)$, $\psi_c(t)$, and $\psi_4(t)$.

location and can be stored again indefinitely. In a spin network setting, the initial state $|I\rangle$ is a maximally entangled state between the spins at sites 1 and 2 of a dimer.

Transfer by phase flips.—For the transfer protocol visualized in Fig. 2(a), we set $J_n = J$ and consider the possibility to instantaneously imprint a phase flip by π (that is, a sign change) on one of the components of $|I\rangle$ at $t = 0$, turning it into $|L\rangle \equiv [(|1\rangle + |2\rangle)/\sqrt{2}]$. This new state $|L\rangle$ is no longer an eigenstate of H , and will evolve freely and with unit fidelity within time T to the state $|R\rangle \equiv [(|3\rangle + |4\rangle)/\sqrt{2}]$ for suitable chosen on-site potentials and couplings. Exactly at $t = T$ another sign flip is applied to one of the components of $|R\rangle$ in order to turn it into the desired target CLS $|F\rangle$. For the choice $J = 1/4$ energy units and $v = 2J$, the transfer time is $T = (\hbar\pi/2J) = 2\pi$ (setting $\hbar = 1$). General analytical derivations for the evolution $|\psi(t)\rangle = e^{-iHt}|I\rangle$ are given in the SM [45], exploiting the so-called “equitable partition theorem” [10,50,51]. As an alternative version of this transfer protocol, we can apply the instantaneous sign flips at $t = 0$ and T to the hoppings J_1, J_3 (or J_2, J_4) instead, as depicted in Fig. 2(b). The free time evolution is then essentially equivalent to the previous one in Fig. 2(a).

Transfer by optimal control.—Now we turn to optimal control solutions in order to design smooth pulses to avoid instantaneous operations. Taking into account that the initial state $|I\rangle$ is an eigenstate of $H(t = 0)$, we need to smoothly drive it out of stationarity in order to end up with the final state $|F\rangle$ as an eigenstate of the final Hamiltonian $H(t = T)$. To find smooth optimal driving pulses for the couplings J_n , we apply the chopped random-basis (CRAB) [52,53] optimal control method to the functional form:

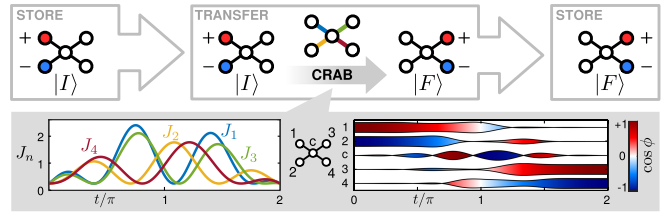


FIG. 3. CLS transfer via optimal control using the CRAB method for the couplings J_n of the form in Eq. (2). At the end of the procedure, all couplings $J_n = J$ again. The inset shows the temporal profile of the $J_n(t)$ and the evolution of the state over time $T = 2\pi$.

$$J_n(t) = J \left(1 + \sin\left(\frac{t}{2}\right) [x_n \sin(\omega_n t) + x'_n \cos(\omega_n t)] \right). \quad (2)$$

This determines the optimal parameters x_n, x'_n, ω_n ($n = 1, 2, 3, 4$) for transferring $|I\rangle$ to $|F\rangle$ in time T , with the same initial and final conditions as previously (that is, $J_n = J$). More information on the CRAB procedure and the specific optimizations performed here can be found in the SM [45]. For this particular case, we further impose $J_n(t) \geq J = 1/4$, so that sign changes in the J_n are avoided. The resulting optimal J_n -driving pulses are presented in Fig. 3 together with the state evolution. The infidelity $1 - |\langle F|\Psi(T_f)\rangle|^2$ of these pulses is approximately 10^{-12} .

Transfer across a network.—By exploiting the robustness of CLSs, the state transfer schemes established above can now be used in the full DLL, as shown in Fig. 4(a). Starting from the upper left, the transfer process consists of (1) separating the star subsystem hosting the initial CLS $|I\rangle$ from the remainder of the lattice, (2) performing the transfer to the final CLS $|F\rangle$ within the star, and

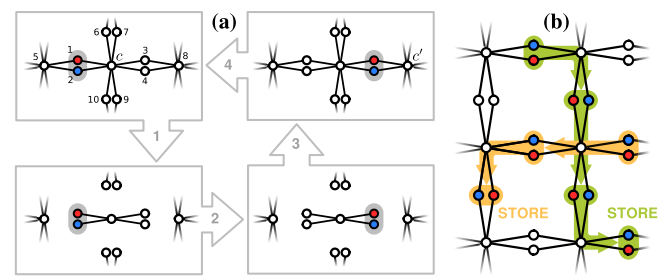


FIG. 4. (a) The “dimer-jump” process reducing state transfer within the decorated Lieb lattice to a star subsystem. It transfers a CLS on sites 1,2 to another CLS on sites 3,4 by (1) decoupling the corresponding star from the remainder of the system, (2) performing the transfer, and subsequently (3) recoupling the star, whence the process can (4) start anew, as indicated by $c \rightarrow c'$. (b) The robustness of CLSs with respect to perturbations outside their localization domain allows for the transfer of multiple CLSs along different routes in the network (orange and green directed paths), as long as these routes do not simultaneously use the same star subsystem.

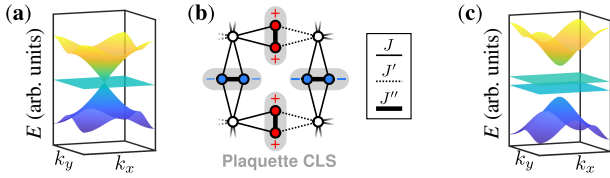


FIG. 5. (a) Band structure of the DLL. (b) Plaquette CLS in the modified DLL. (c) Band structure of the modified lattice for $0 < |J''| < |J - J'|$. See text for details.

(3) reconnecting the star to the remainder. The process can then start anew (4) to transport the state over longer distances.

To separate the star while keeping $|I\rangle$ unaffected, we ramp-down its outer couplings to surrounding sites to zero within time δt such that the local symmetry protecting $|I\rangle$ is *preserved*. With the site indexing in Fig. 4(a), starting at $t = 0$ this means that $J_{1,5}(t) = J_{2,5}(t)$ for $0 \leq t \leq \delta t$ with $J_{1,5}(\delta t) = 0$. This modulation does not perturb $|I\rangle$, even for $\delta t \rightarrow 0$. The other couplings of the star to its surroundings ($J_{3,8}$, $J_{4,8}$ and $J_{n,c}$ with $n = 6, 7, 9, 10$) can be ramped down in an *arbitrary* way, since they do not connect to the localization domain of $|I\rangle$. Within the separated star, the actual state transfer can be performed according to one of the above protocols over time T . Afterwards, we ramp-up the outer couplings again, now preserving the local symmetry which protects $|F\rangle$, that is, increasing $J_{3,8}$ and $J_{4,8}$ symmetrically, and the other couplings arbitrarily, from zero to their final values.

Transferring a CLS to a distant dimer in another star subsystem is achieved via consecutive “dimer jumps” like the one just described, as depicted in Fig. 4(b). This procedure can be employed simultaneously along different paths in the network. These may also intersect in space, as long as in each instant in time the different paths use different star subsystems; see orange and green paths in Fig. 4(b). Once a CLS has reached its final destination, it is stored for arbitrary time. In this sense, the proposed network becomes a simple model for a hybrid setup functioning simultaneously as a directional transfer device and as a multiple quantum memory unit. Crucially, this functionality is retained with high fidelity in the presence of various perturbations [45], even when the transfer paths remain connected to the surrounding lattice during the dimer jumps.

In practice, an actual realization of an equivalent network will depend on the limitations of the underlying physical platform. We emphasize that the DLL operated on here is a very basic lattice geometry enabling the proposed CLS transfer concept, but can be generalized to other geometries in a straightforward way. For instance, if intradimer coupling is non-negligible due to the small spatial separation, an alternative CLS transfer unit can be used, with essentially the same procedure applied [45].

Robustness.—As we demonstrate in the SM [45], the proposed protocols are quite robust against imperfections.

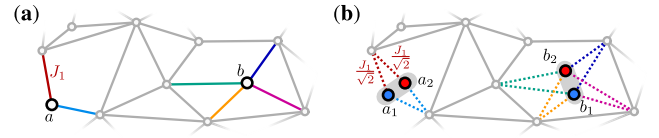


FIG. 6. Equipping a network capable of PST between sites a, b with CLS storage. (a) Original network. (b) Modified network, along with CLSs (see text).

For example, when considering finite-time linear ramps of duration δt instead of instantaneous hopping flips, a single dimer jump can still be performed with a fidelity above 0.998 even for slow ramps of $\delta t = T/4$. One can easily increase the robustness of the protocols further, as we now show by optimizing the storage fidelity of the DLL. In this network, the dimer CLSs correspond to two flatbands, which are degenerate to an additional flatband related to so-called “plaquette” CLSs [shown in Fig. 5(b)]. Additionally, two Dirac cones touch these three flatbands, as shown in Fig. 5(a). Under (small) perturbations, the dimer CLSs mix—due to their small energy separation—with other states. As a result, they spread across the lattice, which decreases the storage fidelity. However, this issue can be solved [45] by modifying the DLL as shown in Fig. 5(b). For $0 < |J''| < |J - J'|$, the two degenerate dimer CLS flatbands are gapped from all others, as demonstrated in Fig. 5(c), thus increasing the storage performance. In this modified DLL, dimer jumps are achieved by (i) decoupling the corresponding star subsystem, (ii) modifying the couplings within the star so as to recover the values of the original DLL, (iii) transferring the CLS, and (iv) reestablishing the coupling values of the modified DLL before recoupling the star.

Equipping static transfer protocols with storage.—Lastly, we demonstrate the versatility of our approach by showing how to equip *any* static (i.e., relying on simple time evolution) PST network with CLSs, thus greatly enhancing its storage capabilities. Figure 6 sketches the procedure. One replaces each of the sites a, b by dimers $a_{1,2}, b_{1,2}$, and all couplings between a, b and the remainder of the network by symmetric, renormalized couplings to these dimers. The modified network then features one CLS per dimer, which can be perfectly transferred by a procedure similar to the hopping flip presented above [45]. Interestingly, the transfer fidelity of the modified network can *exceed* that of the original network, as we demonstrate for a one-dimensional chain in the SM [45].

Conclusion.—We have demonstrated how local symmetries in a decorated Lieb lattice can be exploited to store and transfer compact localized states via different, easily realizable, modulation protocols. This provides a powerful prototype for a quantum device which simultaneously performs flexible transfer and robust storage of information within the same physical platform. We also have demonstrated how *any* network capable of static perfect state

transfer of single-site excitations can be equipped with CLSs, such that these can be both perfectly transferred and stored. The transfer protocols utilize either instantaneous phase flips (with unit fidelity) or optimal temporal control of intersite couplings with near-unit fidelity. They can thus be adapted to the needs of different potential realizations in, e.g., electronics, atom optics, photonics, or acoustics. Under the very weak requirement of local symmetries protecting the CLSs, extension of the proposed concept to alternative network geometries and different dimensionality is straightforward. Based on multiple intersecting CLS transfer paths as proposed here, a future vision would be the design of a dynamical network with switchable quantum gates and embedded quantum memories.

M. R. gratefully acknowledges financial support by the “Stiftung der deutschen Wirtschaft” in the framework of a scholarship. I. B. acknowledges financial support by Greece and the European Union (European Social Fund–ESF) through the Operational Programme “Human Resources Development, Education and Lifelong Learning” in the context of the project “Reinforcement of Postdoctoral Researchers” (MIS-5001552), implemented by the State Scholarships Foundation (IKY).

-
- [1] W. Maimaiti, A. Andreanov, H. C. Park, O. Gendelman, and S. Flach, Compact localized states and flat-band generators in one dimension, *Phys. Rev. B* **95**, 115135 (2017).
- [2] D. Leykam, A. Andreanov, and S. Flach, Artificial flat band systems: From lattice models to experiments, *Adv. Phys.* **3**, 1473052 (2018).
- [3] S. Mukherjee, A. Spracklen, D. Choudhury, N. Goldman, P. Öhberg, E. Andersson, and R. R. Thomson, Observation of a Localized Flat-Band State in a Photonic Lieb Lattice, *Phys. Rev. Lett.* **114**, 245504 (2015).
- [4] S. Taie, H. Ozawa, T. Ichinose, T. Nishio, S. Nakajima, and Y. Takahashi, Coherent driving and freezing of bosonic matter wave in an optical Lieb lattice, *Sci. Adv.* **1**, e1500854 (2015).
- [5] V. Apaja, M. Hyrkäs, and M. Manninen, Flat bands, Dirac cones, and atom dynamics in an optical lattice, *Phys. Rev. A* **82**, 041402(R) (2010).
- [6] S. Mukherjee and R. R. Thomson, Observation of localized flat-band modes in a quasi-one-dimensional photonic rhombic lattice, *Opt. Lett.* **40**, 5443 (2015).
- [7] O. Derzhko, J. Richter, and M. Maksymenko, Strongly correlated flat-band systems: The route from Heisenberg spins to Hubbard electrons, *Int. J. Mod. Phys. B* **29**, 1530007 (2015).
- [8] R. A. Vicencio, C. Cantillano, L. Morales-Inostroza, B. Real, C. Mejía-Cortés, S. Weimann, A. Szameit, and M. I. Molina, Observation of Localized States in Lieb Photonic Lattices, *Phys. Rev. Lett.* **114**, 245503 (2015).
- [9] L. Morales-Inostroza and R. A. Vicencio, Simple method to construct flat-band lattices, *Phys. Rev. A* **94**, 043831 (2016).
- [10] M. Röntgen, C. V. Morfonios, and P. Schmelcher, Compact localized states and flat bands from local symmetry partitioning, *Phys. Rev. B* **97**, 035161 (2018).
- [11] L.-L. Wan, X.-Y. Lü, J.-H. Gao, and Y. Wu, Hybrid interference induced flat band localization in bipartite optomechanical lattices, *Sci. Rep.* **7**, 15188 (2017).
- [12] R. Shen, L. B. Shao, B. Wang, and D. Y. Xing, Single Dirac cone with a flat band touching on line-centered-square optical lattices, *Phys. Rev. B* **81**, 041410(R) (2010).
- [13] B. Real, C. Cantillano, D. López-González, A. Szameit, M. Aono, M. Naruse, S.-J. Kim, K. Wang, and R. A. Vicencio, Flat-band light dynamics in Stub photonic lattices, *Sci. Rep.* **7**, 15085 (2017).
- [14] S. Rojas-Rojas, L. Morales-Inostroza, R. A. Vicencio, and A. Delgado, Quantum localized states in photonic flat-band lattices, *Phys. Rev. A* **96**, 043803 (2017).
- [15] M. Christandl, N. Datta, A. Ekert, and A. J. Landahl, Perfect State Transfer in Quantum Spin Networks, *Phys. Rev. Lett.* **92**, 187902 (2004).
- [16] M. Christandl, N. Datta, T. C. Dorlas, A. Ekert, A. Kay, and A. J. Landahl, Perfect transfer of arbitrary states in quantum spin networks, *Phys. Rev. A* **71**, 032312 (2005).
- [17] S. Bose, Quantum communication through spin chain dynamics: An introductory overview, *Contemp. Phys.* **48**, 13 (2007).
- [18] A. Kay, Perfect, efficient, state transfer and its application as a constructive tool, *Int. J. Quantum. Inform.* **08**, 641 (2010).
- [19] J. I. Cirac, P. Zoller, H. J. Kimble, and H. Mabuchi, Quantum State Transfer and Entanglement Distribution among Distant Nodes in a Quantum Network, *Phys. Rev. Lett.* **78**, 3221 (1997).
- [20] M.-H. Yung and S. Bose, Perfect state transfer, effective gates, and entanglement generation in engineered bosonic and fermionic networks, *Phys. Rev. A* **71**, 032310 (2005).
- [21] A. Wójcik, T. Łuczak, P. Kurzyński, A. Grudka, T. Gdala, and M. Bednarska, Unmodulated spin chains as universal quantum wires, *Phys. Rev. A* **72**, 034303 (2005).
- [22] T. J. Osborne and N. Linden, Propagation of quantum information through a spin system, *Phys. Rev. A* **69**, 052315 (2004).
- [23] R. J. Chapman, M. Santandrea, Z. Huang, G. Corrielli, A. Crespi, M.-H. Yung, R. Osellame, and A. Peruzzo, Experimental perfect state transfer of an entangled photonic qubit, *Nat. Commun.* **7**, 11339 (2016).
- [24] C. Brif, R. Chakrabarti, and H. Rabitz, Control of quantum phenomena: Past, present and future, *New J. Phys.* **12**, 075008 (2010).
- [25] S. J. Glaser, U. Boscain, T. Calarco, C. P. Koch, W. Köckenberger, R. Kosloff, I. Kuprov, B. Luy, S. Schirmer, T. Schulte-Herbrüggen, D. Sugny, and F. K. Wilhelm, Training Schrödinger’s cat: Quantum optimal control, *Eur. Phys. J. D* **69**, 279 (2015).
- [26] M. Murphy, S. Montangero, V. Giovannetti, and T. Calarco, Communication at the quantum speed limit along a spin chain, *Phys. Rev. A* **82**, 022318 (2010).
- [27] X.-P. Zhang, B. Shao, S. Hu, J. Zou, and L.-A. Wu, Optimal control of fast and high-fidelity quantum state transfer in spin-1/2 chains, *Ann. Phys. (Amsterdam)* **375**, 435 (2016).

- [28] H. Nakao and N. Yamamoto, Optimal control for perfect state transfer in linear quantum memory, *J. Phys. B* **50**, 065501 (2017).
- [29] P. A. Kalozoumis, C. Morfonios, F. K. Diakonou, and P. Schmelcher, Local symmetries in one-dimensional quantum scattering, *Phys. Rev. A* **87**, 032113 (2013).
- [30] P. A. Kalozoumis, C. V. Morfonios, F. K. Diakonou, and P. Schmelcher, Invariant currents and scattering off locally symmetric potential landscapes, *Ann. Phys. (Amsterdam)* **362**, 684 (2015).
- [31] A. G. B. Spourdalakis, G. Pappas, C. V. Morfonios, P. A. Kalozoumis, F. K. Diakonou, and P. Schmelcher, Generalized continuity equations from two-field Schrödinger Lagrangians, *Phys. Rev. A* **94**, 052122 (2016).
- [32] C. V. Morfonios, P. A. Kalozoumis, F. K. Diakonou, and P. Schmelcher, Nonlocal discrete continuity and invariant currents in locally symmetric effective Schrödinger arrays, *Ann. Phys. (Amsterdam)* **385**, 623 (2017).
- [33] M. Röntgen, C. Morfonios, F. Diakonou, and P. Schmelcher, Non-local currents and the structure of eigenstates in planar discrete systems with local symmetries, *Ann. Phys. (Amsterdam)* **380**, 135 (2017).
- [34] V. E. Zampetakis, M. K. Diakonou, C. V. Morfonios, P. A. Kalozoumis, F. K. Diakonou, and P. Schmelcher, Invariant current approach to wave propagation in locally symmetric structures, *J. Phys. A* **49**, 195304 (2016).
- [35] P. A. Kalozoumis, C. Morfonios, F. K. Diakonou, and P. Schmelcher, Invariants of Broken Discrete Symmetries, *Phys. Rev. Lett.* **113**, 050403 (2014).
- [36] N. V. Vitanov, A. A. Rangelov, B. W. Shore, and K. Bergmann, Stimulated Raman adiabatic passage in physics, chemistry, and beyond, *Rev. Mod. Phys.* **89**, 015006 (2017).
- [37] S. Taie, T. Ichinose, H. Ozawa, and Y. Takahashi, Spatial adiabatic passage of massive quantum particles, [arXiv:1708.01100](https://arxiv.org/abs/1708.01100).
- [38] M. O. Scully, *Quantum Optics* (Cambridge University Press, Cambridge, England, 1997).
- [39] E. H. Lieb, Two Theorems on the Hubbard Model, *Phys. Rev. Lett.* **62**, 1201 (1989).
- [40] I. L. Garanovich, S. Longhi, A. A. Sukhorukov, and Y. S. Kivshar, Light propagation and localization in modulated photonic lattices and waveguides, *Phys. Rep.* **518**, 1 (2012).
- [41] A. Szameit, F. Dreisow, and S. Nolte, *Discrete Optics in Femtosecond Laser Written Waveguide Arrays*, Topics in Applied Physics (Springer, Berlin, 2012).
- [42] A. Perez-Leija, R. Keil, A. Kay, H. Moya-Cessa, S. Nolte, L.-C. Kwek, B. M. Rodríguez-Lara, A. Szameit, and D. N. Christodoulides, Coherent quantum transport in photonic lattices, *Phys. Rev. A* **87**, 012309 (2013).
- [43] L. J. Maczewsky, J. M. Zeuner, S. Nolte, and A. Szameit, Observation of photonic anomalous Floquet topological insulators, *Nat. Commun.* **8**, 13756 (2017).
- [44] R. Keil, C. Poli, M. Heinrich, J. Arkininstall, G. Weihs, H. Schomerus, and A. Szameit, Universal Sign Control of Coupling in Tight-Binding Lattices, *Phys. Rev. Lett.* **116**, 213901 (2016).
- [45] See Supplemental Material at <http://link.aps.org/supplemental/10.1103/PhysRevLett.123.080504> for calculations regarding the state transfer protocols, a method to generate CLS, the treatment of a modified DLL for evanescently coupled waveguides, an exhaustive analysis of the behavior of the proposed protocols under perturbations providing several improvements increasing their robustness, as well as technical details for equipping any static network with CLSs, and Refs. [46–49].
- [46] E. Fritscher and V. Trevisan, Exploring symmetries to decompose matrices and graphs preserving the spectrum, *SIAM J. Matrix Anal. Appl.* **37**, 260 (2016).
- [47] S. Yang, A. Bayat, and S. Bose, Spin-state transfer in laterally coupled quantum-dot chains with disorders, *Phys. Rev. A* **82**, 022336 (2010).
- [48] S. Xia, A. Ramachandran, S. Xia, D. Li, X. Liu, L. Tang, Y. Hu, D. Song, J. Xu, D. Leykam, S. Flach, and Z. Chen, Unconventional Flatband Line States in Photonic Lieb Lattices, *Phys. Rev. Lett.* **121**, 263902 (2018).
- [49] D. Moldovan, M. Anđelković, and F. Peeters, PYBINDING v0.9.4: A PYTHON package for tight-binding calculations, [Zenodo](https://zenodo.org/record/1000000) (2017).
- [50] W. Barrett, A. Francis, and B. Webb, Equitable decompositions of graphs with symmetries, *Linear Algebra Appl.* **513**, 409 (2017).
- [51] A. Francis, D. Smith, D. Sorensen, and B. Webb, Extensions and applications of equitable decompositions for graphs with symmetries, *Linear Algebra Appl.* **532**, 432 (2017).
- [52] P. Doria, T. Calarco, and S. Montangero, Optimal Control Technique for Many-Body Quantum Dynamics, *Phys. Rev. Lett.* **106**, 190501 (2011).
- [53] T. Caneva, T. Calarco, and S. Montangero, Chopped random-basis quantum optimization, *Phys. Rev. A* **84**, 022326 (2011).

Supplemental Material

I. STATE TRANSFER PROTOCOLS NOT RELYING ON OPTIMAL CONTROL

A. State transfer with amplitude flip

For $v_n = v, n \in \{1, 2, 3, 4, c\}$ and $J_n = J, n \in \{1, 2, 3, 4\}$, the Hamiltonian

$$H = \begin{pmatrix} v_1 & 0 & J_1 & 0 & 0 \\ 0 & v_2 & J_2 & 0 & 0 \\ J_1 & J_2 & v_c & J_3 & J_4 \\ 0 & 0 & J_3 & v_3 & 0 \\ 0 & 0 & J_4 & 0 & v_4 \end{pmatrix} \quad (1)$$

can be analyzed analytically by means of the so-called equitable partition theorem [1–3]. This theorem gives a block-partitioning of a locally symmetric Hamiltonian, allowing for a simpler computation of both eigenvectors and eigenvalues. The underlying local symmetry is restricted to be a permutation that commutes with the Hamiltonian and which acts non-trivially only on a subset of sites. For the Hamiltonian treated here, the underlying symmetry is described by the operator S performing the cyclic permutation $1 \rightarrow 2 \rightarrow 3 \rightarrow 4 \rightarrow 1$ and mapping c to itself. Then, $[H, S] = 0$, and by the equitable partition theorem, the eigenvectors are

$$|\phi^{(i)}\rangle = \left\{ \begin{pmatrix} -1/\sqrt{2} \\ 1/\sqrt{2} \\ 0 \\ 0 \\ 0 \end{pmatrix}, \begin{pmatrix} 0 \\ 0 \\ 0 \\ -1/\sqrt{2} \\ 1/\sqrt{2} \end{pmatrix}, \begin{pmatrix} 1/2 \\ 1/2 \\ 0 \\ -1/2 \\ -1/2 \end{pmatrix}, \begin{pmatrix} 1/(2\sqrt{2}) \\ 1/(2\sqrt{2}) \\ -1/\sqrt{2} \\ 1/(2\sqrt{2}) \\ 1/(2\sqrt{2}) \end{pmatrix}, \begin{pmatrix} 1/(2\sqrt{2}) \\ 1/(2\sqrt{2}) \\ 1/\sqrt{2} \\ 1/(2\sqrt{2}) \\ 1/(2\sqrt{2}) \end{pmatrix} \right\}$$

with corresponding eigenvalues $E^{(i)} = \{v, v, v, v - 2J, v + 2J\}$. In terms of these eigenvectors, the two states $|L\rangle = (1/\sqrt{2}, 1/\sqrt{2}, 0, 0, 0)^T$ and $|R\rangle = (0, 0, 0, 1/\sqrt{2}, 1/\sqrt{2})^T$ are expanded as

$$\begin{aligned} |L\rangle &= \sum_i a_L^{(i)} |\phi^{(i)}\rangle = \frac{1}{\sqrt{2}} |\phi^{(3)}\rangle + \frac{1}{2} |\phi^{(4)}\rangle + \frac{1}{2} |\phi^{(5)}\rangle \\ |R\rangle &= \sum_i a_R^{(i)} |\phi^{(i)}\rangle = -\frac{1}{\sqrt{2}} |\phi^{(3)}\rangle + \frac{1}{2} |\phi^{(4)}\rangle + \frac{1}{2} |\phi^{(5)}\rangle \end{aligned}$$

with coefficients $a_{L,R}^{(i)} = \langle \phi^{(i)} | L, R \rangle$. To achieve a unitary time-evolution of state $|L\rangle$ at $t = 0$ to $|R\rangle$ at $t = T_f$, the conditions $a_L^{(i)} e^{-iE^{(i)}T_f} = a_R^{(i)}$ (here and in the following, we set $\hbar = 1$) must hold, leading to

$$e^{-iE^{(3)}T_f} = -1, \quad e^{-iE^{(4)}T_f} = 1, \quad e^{-iE^{(5)}T_f} = 1 \quad (2)$$

which is fulfilled for

$$v = J \left(\frac{4k_1}{1+2k_2} - 2 \right), \quad T_f = \frac{\pi(1+2k_2)}{2J}, \quad k_{1,2} \in \mathbb{Z}. \quad (3)$$

For $k_1 = 1, k_2 = 0$, one finds $v = 2J, T_f = \frac{\pi}{2J}$ which was given in the main text. We note that if $v = J \left(\frac{4k_1}{1+2k_2} - 2 \right) + \delta v = v_{opt} + \delta v$ deviates from the optimal value, then

$$\langle L | e^{iHT_f} | R \rangle = e^{i\delta v T_f},$$

so that v could be chosen arbitrarily if the global phase of $|R\rangle$ (and therefore of $|F\rangle$) is not of importance. A similar version of this statement holds for all protocols of this work that do not rely on optimal control.

B. State transfer with hopping flip

For v_n as above and $J_1 = J_3 = J$ and $J_2 = J_4 = -J$, the eigenvectors of H are

$$|\phi^{(i)}\rangle = \left\{ \begin{pmatrix} 1/\sqrt{2} \\ 1/\sqrt{2} \\ 0 \\ 0 \\ 0 \end{pmatrix}, \begin{pmatrix} 0 \\ 0 \\ 0 \\ 1/\sqrt{2} \\ 1/\sqrt{2} \end{pmatrix}, \begin{pmatrix} 1/2 \\ -1/2 \\ 0 \\ -1/2 \\ 1/2 \end{pmatrix}, \begin{pmatrix} 1/(2\sqrt{2}) \\ -1/(2\sqrt{2}) \\ -1/\sqrt{2} \\ 1/(2\sqrt{2}) \\ -1/(2\sqrt{2}) \end{pmatrix}, \begin{pmatrix} 1/(2\sqrt{2}) \\ -1/(2\sqrt{2}) \\ 1/\sqrt{2} \\ 1/(2\sqrt{2}) \\ -1/(2\sqrt{2}) \end{pmatrix} \right\}$$

with corresponding eigenvalues $E^{(i)} = \{v, v, v, v - 2J, v + 2J\}$. In order to enable a unitary time-evolution of state $|I\rangle = (1/\sqrt{2}, -1/\sqrt{2}, 0, 0, 0)^T$ at $t = 0$ to $|F\rangle = (0, 0, 0, 1/\sqrt{2}, -1/\sqrt{2})^T$ at $t = T_f$, one must solve $a_I^{(i)} e^{-iE^{(i)}T_f} = a_F^{(i)}$. This system of equations is equal to Eq. (2), and the parameters needed to achieve perfect transfer are thus identical to that of the phase flip protocol. Similarly, one can show that for $J_1 = J_3 = -J$, the same parameters are needed to perfectly transfer the state $|I\rangle$ to $|F\rangle$.

II. METHODS AND CALCULATIONS FOR OPTIMAL CONTROL PROTOCOLS

The optimal control method Chopped Random-Basis quantum optimization (CRAB) [4, 5] is based on expressing the time-dependent driving functions/pulses for the control fields (here the couplings J) on a truncated randomized basis. This recasts the problem of a functional minimization (of the infidelity function) to a multi-variable function minimization that can be performed, for example, via a direct-search method. Here we use Nelder-Mead optimization for the parameters of the function. To achieve state transfer within the star-subsystem, we assume an initial and final $J_0 = 1/4$ which is also the minimum threshold for all couplings, and we have chosen the following (CRAB-inspired) expressions for the driving functions:

$$J_n(t) = J_0 \left\{ 1 + \sin\left(\frac{t}{2}\right) [x_n \sin(\omega_n t) + x'_n \cos(\omega_n t)]^2 \right\} \quad (4)$$

The method essentially starts with a random set of frequencies ω_i ($i = 1, \dots, 4$) which is different in every iteration and optimizes 8 amplitude parameters x_i, x'_i . The set $\{\omega_i, x_i, x'_i\}$ which minimizes the infidelity is defining the optimal pulses. For the pulses presented in Fig. 3 of the main text, we have $x_n = \{0.584995, 2.40152, 2.503224, 0.219905\}$, $x'_n = \{2.999709, 0.595406, 0.455494, 2.810278\}$ and $\omega_n = \{1.445214, 1.306884, 1.168016, 1.351003\}$.

III. GENERATION OF CLS

In the transfer protocols presented in the main text, we assumed that the initial CLS $|I\rangle$ already exists at $t = 0$. Depending on the system realization, however, it may be easier to imprint a local excitation only on *one* lattice site rather than to excite the dimer CLS directly. Therefore, we now propose protocols that start with state $|c\rangle$ (occupying only the central site in the star) at $t = 0$ and end with $|I\rangle$ at a desired generation time T_g . To this aim, we initially decouple all outer sites from $|c\rangle$ by setting $J_n(t = 0) = 0$ and turn on only J_1 and J_2 . The on-site potentials are $v_n = 2J = 1/2$ as in the main text.

Analogously to the transfer protocols shown there, the CLS generation can be done either by instantaneous phase or hopping flips, or by continuous modulation via optimal control. In the first case, $J_1 = J_2$ are switched on at $t = 0$ to the value $J' = 3\sqrt{2}$, for which the system evolves freely from $|c\rangle$ to $|L\rangle$ in time $T_g = T/2 = \pi$ (analytical details are given in the next section below). Then, at $t = T_g$ a phase flip is applied to obtain $|I\rangle$. In the second case we use optimal control to evolve the system from $|c\rangle$ directly to $|I\rangle$ by gradually turning on J_1, J_2 (from 0 to J') according to a temporal profile produced via the CRAB method (with an infidelity of approximately 10^{-13}), graphically depicted in Fig. 1. Here, a linear rise has been chosen for J_2 , while J_1 oscillates and necessarily also becomes negative, as shown below. With these conditions we prepare and store (due to the equal final couplings) the CLS $|I\rangle$.

As easily anticipated, these CLS generation protocols can also be used in order to perform the state transfer from $|I\rangle$ to $|F\rangle$, now in two steps. In the first step $|I\rangle$ is evolved to $|c\rangle$ within time $T/2$ using one of the generation protocols *time-reversed*. In the second step $|F\rangle$ is generated from $|c\rangle$ within time $T/2$, just like $|I\rangle$ was above.

A. Preparation, storage and piecewise transfer with phase flip

Let us now show how one can yield $|L\rangle$ from initially exciting the state $|c\rangle = (0, 0, 1, 0, 0)^T$ for $J_3 = J_4 = 0$ and $J_1 = J_2 = J'$. After obtaining $|L\rangle$, a phase flip can be applied to yield $|I\rangle$. For the above choice of couplings, the Hamiltonian Eq. (1)

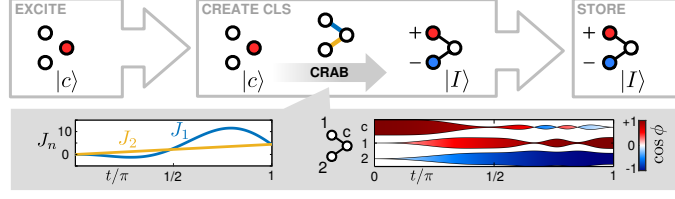


Figure 1. Creation of the CLS by an initial excitation of the central site c and subsequent optimal control using the CRAB method for the couplings J_1 and J_2 . The inset shows the temporal profile of the $J_n(t)$ and the evolution of the state over time $T_g = \pi$.

becomes block-diagonal, and the eigenvectors split into two groups, each of which having nonvanishing amplitudes only on sites of one of the two blocks. The eigenvectors relevant for the expansion of $|L\rangle$ and $|c\rangle$ are

$$|\phi^{(i)}\rangle = \left\{ \begin{pmatrix} 1/\sqrt{2} \\ -1/\sqrt{2} \\ 0 \\ 0 \\ 0 \end{pmatrix}, \begin{pmatrix} -1/2 \\ -1/2 \\ 1/\sqrt{2} \\ 0 \\ 0 \end{pmatrix}, \begin{pmatrix} 1/2 \\ 1/2 \\ 1/\sqrt{2} \\ 0 \\ 0 \end{pmatrix} \right\}$$

with eigenvalues $E^{(i)} = \{v, v - \sqrt{2}J', v + \sqrt{2}J'\}$. By expanding $|c\rangle$ and $|L\rangle$ into the eigenvectors of the Hamiltonian, one can show that

$$e^{-iE^{(2)}T_f} = -1, \quad e^{-iE^{(3)}T_f} = 1$$

must be fulfilled in order to have

$$\langle c|e^{iHT_f}|L\rangle = 1.$$

This is the case for

$$v = -\frac{\sqrt{2}J'(4k'_1 - 1)}{4k'_2 - 1}, T_f = \frac{\pi(4k'_1 - 1)}{2v} \quad \text{or} \quad v = -\frac{\sqrt{2}J'(4k'_1 + 1)}{1 + 4k'_2}, T_f = \frac{\pi(4k'_1 + 1)}{2v} \quad (5)$$

where in both equations $k'_{1,2} \in \mathbb{Z}$. The special form $v = \frac{\sqrt{2}J'}{3}, t = \frac{\pi}{2v}$ given above is obtained by taking the second solution as well as setting $k'_1 = 0, k'_2 = 1$ and $J' = 3\sqrt{2}J$.

B. Preparation, storage and piecewise transfer with hopping flip

The CLS $|I\rangle$ can likewise be obtained from $|c\rangle$ by performing instantaneous hopping flips. We therefore switch H to H' at $t = 0$, for which $J_2 = -J' = -J_1$, and at T_f we switch H' back to H . As the final state is now $|I\rangle = (1/\sqrt{2}, -1/\sqrt{2}, 0, 0, 0)^T$, we need to expand $|c\rangle$ and $|I\rangle$ in terms of the eigenvectors of H' . The eigenvectors relevant for the expansion of $|I\rangle$ and $|c\rangle$ are then

$$|\phi^{(i)}\rangle = \left\{ \begin{pmatrix} 1/\sqrt{2} \\ 1/\sqrt{2} \\ 0 \\ 0 \\ 0 \end{pmatrix}, \begin{pmatrix} -1/2 \\ 1/2 \\ 1/\sqrt{2} \\ 0 \\ 0 \end{pmatrix}, \begin{pmatrix} 1/2 \\ -1/2 \\ 1/\sqrt{2} \\ 0 \\ 0 \end{pmatrix} \right\}$$

with eigenvalues $v, v - \sqrt{2}J', v + \sqrt{2}J'$. The expansion of $|c\rangle$ and $|I\rangle$ is equal to that of the phase flip protocol, with identical parameters needed to achieve $\langle c|e^{iHT_f}|I\rangle = 1$.

C. Preparation, storage and piecewise transfer with optimal control

For the preparation storage and piecewise transfer protocol with optimal control, shown in Fig. 1, we use

$$\begin{aligned} J_1 &= \left\{ 1 + x \sin(\omega t) + x' \sin(\omega' t) \right\} 3\sqrt{2}(1 - t/\pi) \\ J_2 &= 3\sqrt{2}(1 - t/\pi). \end{aligned} \quad (6)$$

Here we have a set of 4 parameters to optimize (both frequencies and amplitudes) and we allow the J_n to take also negative values. For Fig. 1, the optimal parameter values are $x = 0.829226$, $x' = 1.524626$, $\omega = 1.7638$, $\omega' = 1.943375$. The necessity of negative values for J_n becomes apparent if we see the system of differential equations governing the dynamics, which simplifies to:

$$\begin{aligned}\dot{\psi}_1 &= i(J_1\psi_c + v_1\psi_1) \\ \dot{\psi}_2 &= i(J_2\psi_c + v_2\psi_2) \\ \dot{\psi}_c &= i(J_1\psi_1 + J_2\psi_2 + v_c\psi_c)\end{aligned}$$

With $|\psi(t=0)\rangle = |c\rangle$ and $v_1 = v_2 = v_c = 1/2$, the amplitude ψ_1 or ψ_2 can acquire the desired negative value $-1/\sqrt{2}$ only if J_1 or J_2 becomes negative (for some t -intervals) as well, respectively.

IV. MODIFIED NETWORK FOR EVANESCENTLY COUPLED WAVEGUIDE ARRAYS

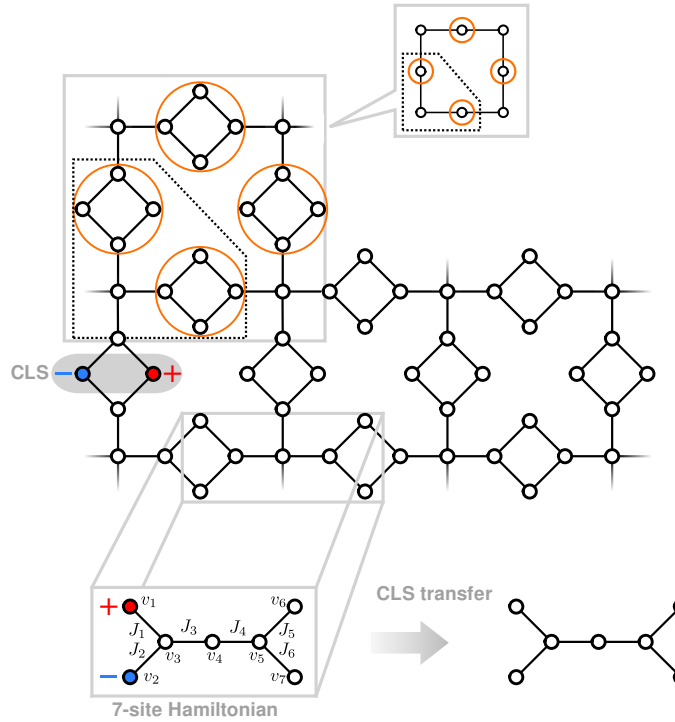


Figure 2. Modified network for evanescently coupled waveguide arrays.

We here provide a modified network, along with some transfer protocols, for cases where the five-point Hamiltonian Eq. (1) is not suitable for a physical realization. The basis for these protocols is the seven-point graph, described by the Hamiltonian

$$H_7 = \begin{pmatrix} v_1 & 0 & J_1 & 0 & 0 & 0 & 0 \\ 0 & v_2 & J_2 & 0 & 0 & 0 & 0 \\ J_1 & J_2 & v_3 & J_3 & 0 & 0 & 0 \\ 0 & 0 & J_3 & v_4 & J_4 & 0 & 0 \\ 0 & 0 & 0 & J_4 & v_5 & J_5 & J_6 \\ 0 & 0 & 0 & 0 & J_5 & v_6 & 0 \\ 0 & 0 & 0 & 0 & J_6 & 0 & v_7 \end{pmatrix}. \quad (7)$$

For $v_1 = v_2$, $J_1 = J_2$ and $v_3 = v_4$, $J_3 = J_4$, this Hamiltonian hosts two compact localized states, $|I\rangle = (1/\sqrt{2}, -1/\sqrt{2}, 0, 0, 0, 0, 0)^T$ and $|F\rangle = (0, 0, 0, 0, 0, 1/\sqrt{2}, -1/\sqrt{2})^T$. We assume that at $t = 0$, the state $|I\rangle$ is excited and one wants to transfer it to the CLS $|F\rangle$ at $t = T_f$.

A. Phase flip protocol

Similar to protocol 1 for the five-point Hamiltonian, we assume that at $t = 0$, a phase flip is applied, changing the state $|I\rangle$ into $|L\rangle = (1/\sqrt{2}, 1/\sqrt{2}, 0, 0, 0, 0, 0)^T$. Our aim is to transfer this into $|R\rangle = (0, 0, 0, 0, 0, 1/\sqrt{2}, 1/\sqrt{2})^T$ at $t = T_f$, where we apply another phase flip, turning $|R\rangle$ into $|F\rangle$. In the following, we will choose $v_i = 0$, $i = \{1, \dots, 7\}$, $J_1 = J_2 = J_5 = J_6 = J$. With this choice of parameters, H_7 is globally symmetric w.r.t. to a left-right flip with site 4 as a center for $J_3 = J_4$, but only locally symmetric for $J_3 \neq J_4$. In both cases, the so-called ‘nonequitable partition theorem’ [1, 6] allows to obtain analytical expressions for both the eigenvalues and eigenvectors of H_7 . This theorem is similar to the equitable partition theorem, but allows for the treatment of a greater class of local symmetries. For the current example, the eigenvalues of H_7 are the union of the eigenvalues of

$$R = \begin{pmatrix} v & \sqrt{\xi} & 0 & 0 \\ \sqrt{\xi} & v & J & J \\ 0 & J & v & 0 \\ 0 & J & 0 & v \end{pmatrix}, \quad C_0 = \begin{pmatrix} v & J & J \\ J & v & 0 \\ J & 0 & v \end{pmatrix}$$

with $\xi = J_3^2 + J_4^2$. If we denote the eigenvectors x^ν , $\nu \in \{1, \dots, 4\}$ of R as $(x_1^\nu, \dots, x_4^\nu)^T$ and those of C_0 as $(w_1^\mu, w_2^\mu, w_3^\mu)^T$, $\mu \in \{1, 2, 3\}$, with T denoting the transpose, then the (unnormalized) eigenvectors of H_7 are

$$\begin{pmatrix} \frac{J_3}{\sqrt{\xi}} x_4^\nu \\ \frac{J_3}{\sqrt{\xi}} x_3^\nu \\ \frac{J_3}{\sqrt{\xi}} x_2^\nu \\ x_1^\nu \\ \frac{J_4}{\sqrt{\xi}} x_2^\nu \\ \frac{J_4}{\sqrt{\xi}} x_3^\nu \\ \frac{J_4}{\sqrt{\xi}} x_4^\nu \end{pmatrix}, \quad \begin{pmatrix} w_3^\mu \\ w_2^\mu \\ w_1^\mu \\ 0 \\ -\frac{J_3}{J_4} w_1^\mu \\ -\frac{J_3}{J_4} w_2^\mu \\ -\frac{J_3}{J_4} w_3^\mu \end{pmatrix}. \quad (8)$$

For $J_3 = J_4 = J' = \sqrt{3}$, $J = 1$, we find that

$$|\phi^{(i)}\rangle = \left\{ \begin{pmatrix} 1/\sqrt{2} \\ -1/\sqrt{2} \\ 0 \\ 0 \\ 0 \\ 0 \\ 0 \end{pmatrix}, \begin{pmatrix} 0 \\ 0 \\ 0 \\ 0 \\ 1/\sqrt{2} \\ -1/\sqrt{2} \\ 0 \end{pmatrix}, \begin{pmatrix} -\sqrt{3}/4 \\ -\sqrt{3}/4 \\ 0 \\ 1/2 \\ 0 \\ -\sqrt{3}/4 \\ -\sqrt{3}/4 \end{pmatrix}, \begin{pmatrix} -1/(2\sqrt{2}) \\ -1/(2\sqrt{2}) \\ 1/2 \\ 0 \\ -1/2 \\ 1/(2\sqrt{2}) \\ 1/(2\sqrt{2}) \end{pmatrix}, \begin{pmatrix} -1/(2\sqrt{2}) \\ -1/(2\sqrt{2}) \\ -1/2 \\ 0 \\ 1/2 \\ 1/(2\sqrt{2}) \\ 1/(2\sqrt{2}) \end{pmatrix}, \begin{pmatrix} 1/(4\sqrt{2}) \\ 1/(4\sqrt{2}) \\ -1/2 \\ \sqrt{3}/8 \\ -1/2 \\ 1/(4\sqrt{2}) \\ 1/(4\sqrt{2}) \end{pmatrix}, \begin{pmatrix} 1/(4\sqrt{2}) \\ 1/(4\sqrt{2}) \\ 1/2 \\ \sqrt{3}/8 \\ 1/2 \\ 1/(4\sqrt{2}) \\ 1/(4\sqrt{2}) \end{pmatrix} \right\}$$

are normalized eigenvectors of Eq. (7) with corresponding eigenvalues $E^{(i)} = \{0, 0, 0, -\sqrt{2}, \sqrt{2}, -2\sqrt{2}, 2\sqrt{2}\}$. In terms of $|\phi^{(i)}\rangle$, the initial and final state $|L, R\rangle$ are written as

$$|L\rangle = \sum_i a_L^{(i)} |\phi^{(i)}\rangle = -\sqrt{\frac{3}{8}} |\phi^{(3)}\rangle - \frac{1}{2} |\phi^{(4)}\rangle - \frac{1}{2} |\phi^{(5)}\rangle + \frac{1}{4} |\phi^{(6)}\rangle + \frac{1}{4} |\phi^{(7)}\rangle$$

$$|R\rangle = \sum_i a_R^{(i)} |\phi^{(i)}\rangle = -\sqrt{\frac{3}{8}} |\phi^{(3)}\rangle + \frac{1}{2} |\phi^{(4)}\rangle + \frac{1}{2} |\phi^{(5)}\rangle + \frac{1}{4} |\phi^{(6)}\rangle + \frac{1}{4} |\phi^{(7)}\rangle$$

where $a_{L,R}^{(i)} = \langle \phi^{(i)} | L, R \rangle$. Then, for $T_f = \frac{\pi}{\sqrt{2}}$, the state $|L\rangle$ has evolved into $|R\rangle$. We then apply another instantaneous phase flip, turning $|R\rangle$ into the CLS $|F\rangle$.

B. Hopping flip protocol

This protocol is similar to the hopping flip protocol presented in the main part of this work for the five-point Hamiltonian. We initially set $v_i = 0$, $i = \{1, \dots, 7\}$, $J_1 = J_2 = J_5 = J_6 = J$ and $J_3 = J_4 = J'$ as for the protocol of Section III A. Then, at

$t = 0$, the couplings J_2 and J_6 are instantaneously changed to $-J$. After this change, the new eigenvectors of Eq. (7) are

$$|\phi^{(i)}\rangle = \left\{ \begin{pmatrix} 1/\sqrt{2} \\ 1/\sqrt{2} \\ 0 \\ 0 \\ 0 \\ 0 \\ 0 \end{pmatrix}, \begin{pmatrix} 0 \\ 0 \\ 0 \\ 0 \\ 1/\sqrt{2} \\ 1/\sqrt{2} \\ 0 \end{pmatrix}, \begin{pmatrix} -\sqrt{3}/4 \\ \sqrt{3}/4 \\ 0 \\ 1/2 \\ 0 \\ -\sqrt{3}/4 \\ \sqrt{3}/4 \end{pmatrix}, \begin{pmatrix} 1/(2\sqrt{2}) \\ -1/(2\sqrt{2}) \\ -1/2 \\ 0 \\ 1/2 \\ -1/(2\sqrt{2}) \\ 1/(2\sqrt{2}) \end{pmatrix}, \begin{pmatrix} 1/(2\sqrt{2}) \\ -1/(2\sqrt{2}) \\ 1/2 \\ 0 \\ -1/2 \\ -1/(2\sqrt{2}) \\ 1/(2\sqrt{2}) \end{pmatrix}, \begin{pmatrix} -1/(4\sqrt{2}) \\ 1/(4\sqrt{2}) \\ 1/2 \\ -\sqrt{3}/8 \\ 1/2 \\ -1/(4\sqrt{2}) \\ 1/(4\sqrt{2}) \end{pmatrix}, \begin{pmatrix} -1/(4\sqrt{2}) \\ 1/(4\sqrt{2}) \\ -1/2 \\ -\sqrt{3}/8 \\ -1/2 \\ -1/(4\sqrt{2}) \\ 1/(4\sqrt{2}) \end{pmatrix} \right\}$$

with corresponding eigenvalues $E^{(i)} = \{0, 0, 0, -\sqrt{2}, \sqrt{2}, -2\sqrt{2}, 2\sqrt{2}\}$. In terms of these eigenvectors, the initial and final states $|I, F\rangle$ are expanded as

$$|I\rangle = \sum_i a_I^{(i)} |\phi^{(i)}\rangle = -\sqrt{\frac{3}{8}} |\phi^{(3)}\rangle + \frac{1}{2} |\phi^{(4)}\rangle + \frac{1}{2} |\phi^{(5)}\rangle - \frac{1}{4} |\phi^{(6)}\rangle - \frac{1}{4} |\phi^{(7)}\rangle$$

$$|F\rangle = \sum_i a_F^{(i)} |\phi^{(i)}\rangle = -\sqrt{\frac{3}{8}} |\phi^{(3)}\rangle - \frac{1}{2} |\phi^{(4)}\rangle - \frac{1}{2} |\phi^{(5)}\rangle - \frac{1}{4} |\phi^{(6)}\rangle - \frac{1}{4} |\phi^{(7)}\rangle$$

where $a_{I,F}^{(i)} = \langle \phi^{(i)} | I, F \rangle$. Then, for $T_f = \frac{\pi}{\sqrt{2}}$, the state $|I\rangle$ has evolved into $|F\rangle$. We then perform another flip such that the couplings $J_2 = J_6 = J$, and $|F\rangle$ becomes a CLS again.

C. State transfer with CRAB

This protocol is similar to the five-site optimal control protocol presented in the main part of this work. It is graphically depicted in Fig. 3. We start with an initial CLS $|I\rangle$, with Hamiltonian parameters $v_i = 1/2$ and $J_1 = J_2 = J_5 = J_6 = \frac{1}{4\sqrt{2}} = J$ as well as $J_3 = J_4 = 3$. We then vary $J_n, n = \{1, 2, 5, 6\}$ in time according to

$$J_n = J \left\{ 1 + \sin\left(\frac{t}{4}\right) \left[x_n \sin(\omega_n t) + x'_n \cos(\omega_n t) \right]^2 \right\}. \quad (9)$$

The optimal parameters are $x_n = \{4.1435, 3.2435, 2.5509, 4.7169\}$, $x'_n = \{2.2124, 3.3942, 3.3221, 1.9491\}$ and $\omega_n = \{1.9171, 0.9476, 0.4496, 0.9671\}$, and the infidelity $1 - |\langle F | \Psi(T_f) \rangle|^2$ of these pulses is approximately 10^{-8} .

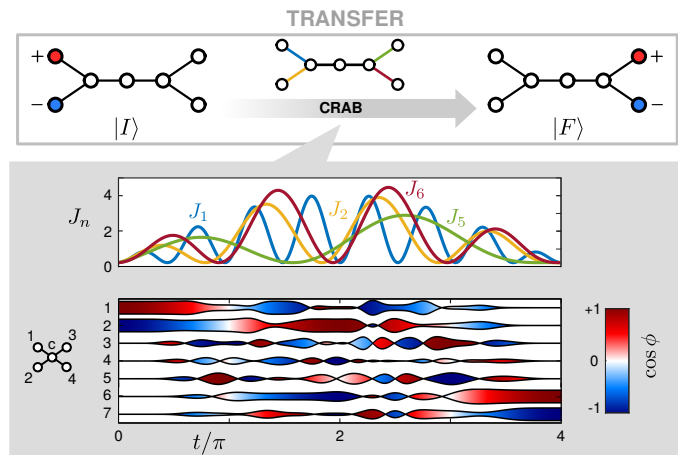


Figure 3. CLS transfer within the seven-point graph of Fig. 2 via optimal control using the CRAB method for the couplings J_1, J_2, J_5 and J_6 of the form in Eq. (9). $J_3 = J_4 = 3$ are constant throughout the process. The inset shows the temporal profile of the varied $J_n(t)$ and the evolution of the state over time $T = 4\pi$.

D. Piecewise transfer and CLS creation with CRAB

This protocol is similar to the three-site optimal control protocol presented above which prepares a CLS, as was shown in Fig. 1. It is graphically depicted in Fig. 4, with an infidelity of approximately 10^{-8} . We start with an excitation of site $4 \equiv c$, which is decoupled from the remainder of the graph. The coupling $J_3 = t/(2\pi)$ to the left half of the graph is then linearly ramped up, and the couplings $J_{1,2}(t)$ are varied as well. At time $T_g = 2\pi$, the CLS $|I\rangle$ is created. The on-site potentials $v_i = 1/2$ are constant throughout the process, and the ansatz for $J_{1,2}(t)$ is

$$J_n = J \left\{ 1 + \sin\left(\frac{t}{2}\right) \left[(x_n \sin(\omega_n t) + x'_n \cos(\omega_n t)) \right] \right\}, \quad n \in \{1, 2\} \quad (10)$$

with $J = \frac{1}{4\sqrt{2}}$ as above and final parameters $x_n = \{6.9763, 4.1098\}$, $x'_n = \{2.1072, 6.4490\}$ and $\omega_n = \{1.7465, 0.7946\}$. Again, as for the CLS-generation protocol presented above, one could use this protocol also to transfer $|I\rangle$ to $|F\rangle$ by first transferring $|I\rangle$ to $|c\rangle$ by means of a time-reversed reversal of the protocol shown, and then transfer $|c\rangle$ to $|F\rangle$ via its forward version.

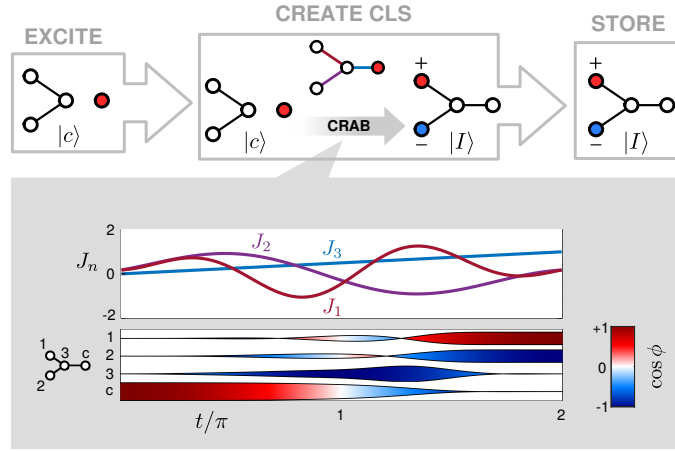


Figure 4. Creation of the CLS by an initial excitation of the central site c and subsequent optimal control using the CRAB method for the couplings J_1 , J_2 and J_3 . The inset shows the temporal profile of the $J_n(t)$ and the evolution of the state over time $T_g = 2\pi$.

V. ROBUSTNESS OF THE HOPPING FLIP PROTOCOL

We now investigate the robustness of the two hopping flip protocols, as described in Sections IB and IV B of this Supplemental Material.

A. Impact of disorder

To investigate the impact of disorder on the hopping flip protocol, we perform the protocol for the two cases that (a) only the couplings and (b) both couplings and on-site potentials deviate from their optimal value. The deviation is modeled as

$$v_i \rightarrow v_i \cdot (1 + \delta_i), \quad i = 1, \dots, 5 \quad (11)$$

$$J_i \rightarrow J_i \cdot (1 + \delta'_i), \quad i = 1, \dots, 4 \quad (12)$$

for the five-site protocol presented in the main text, where $v_i = 0.5 \forall i$ and $J_{1,3} = -J$, $J_{2,4} = J = .25$, and

$$v_i \rightarrow \delta_i, \quad i = 1, \dots, 7 \quad (13)$$

$$J_i \rightarrow J_i \cdot (1 + \delta'_i), \quad i = 1, \dots, 6 \quad (14)$$

for the seven-site protocol presented above, where $J_1 = J_5 = J = 1$, $J_2 = J_6 = -J$, and $J_3 = J_4 = \sqrt{3}$.

In both cases, the δ_i, δ'_i are normally distributed random numbers with zero mean and variance σ^2 . For both protocols, we evaluate the mean value $\langle F \rangle$ of the fidelity $F = |\langle I_{CLS} | U(t_{final}) | F_{CLS} \rangle|^2$, with $U(t)$ being the time-evolution operator for

$H(t)$. We note that $H(t)$ describes the situation where an instantaneous hopping flip is performed at $t = 0$ and t_{final} . The two states $|I_{CLS}, F_{CLS}\rangle$ are the CLS “living” on the left or right dimer, respectively. For the five-site protocol, $t_{final} = 2\pi$, while for the seven-site protocol $t_{final} = \pi/\sqrt{2}$. As can be seen in Fig. 5, the instantaneous hopping flip protocol is, both for five and seven sites, quite robust against disorder.

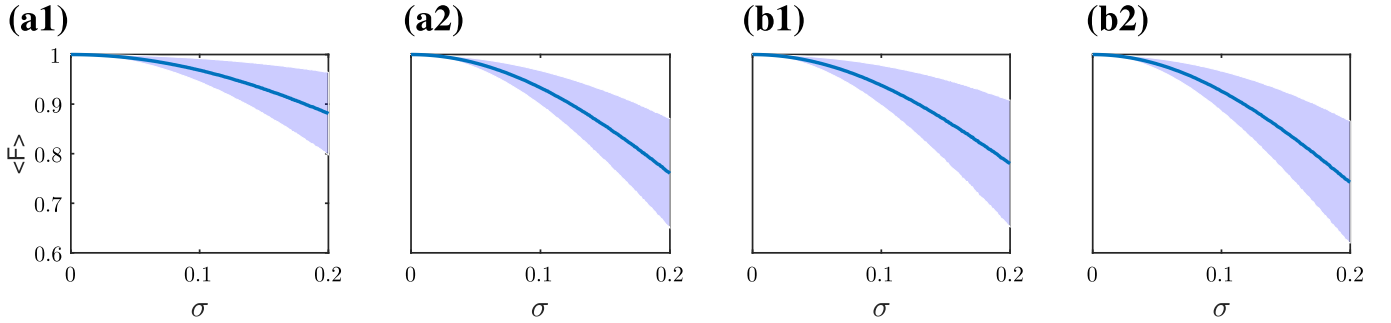


Figure 5. Performance of the two hopping flip protocols as a function of the standard deviation σ of the noise δ . Subfigures (a1 – a2) and (b1 – b2) correspond to the performance of the five and seven-site site protocols, respectively. The subfigures (a1) and (b1) show the case where only the couplings are perturbed, while subfigures (a2) and (b2) show the case where both couplings and on-site potentials are perturbed. The blue line shows the mean value $\langle F \rangle = \mu$ of the fidelity, with the shaded blue area denoting μ plus/minus one standard deviation of the fidelity. For each data point, 50000 realizations have been simulated.

B. Finite duration hopping flip

So far, we assumed that the hopping flips (both in the five- and seven-site protocol) could be performed *instantaneously*, which, in the absence of disorder, led to unit fidelity. In both protocols, two of the couplings were flipped to $-J$ at $t = 0$ and flipped back to J at $t = t_{final}$. We now investigate the impact of a finite-duration ramp instead of an instantaneous flip. As we show in Fig. 6 for different durations of the linear ramp, the fidelity decreases only slightly. Even for extraordinary slow pulses with a duration of $\pi/2$, the fidelity $F(t) = |\langle I|U(t)|F \rangle|^2$ [with $U(t)$ being the time-evolution operator for $H(t)$] for $t = t_{final} + \delta t$ is still above 0.998 for the five-site protocol.

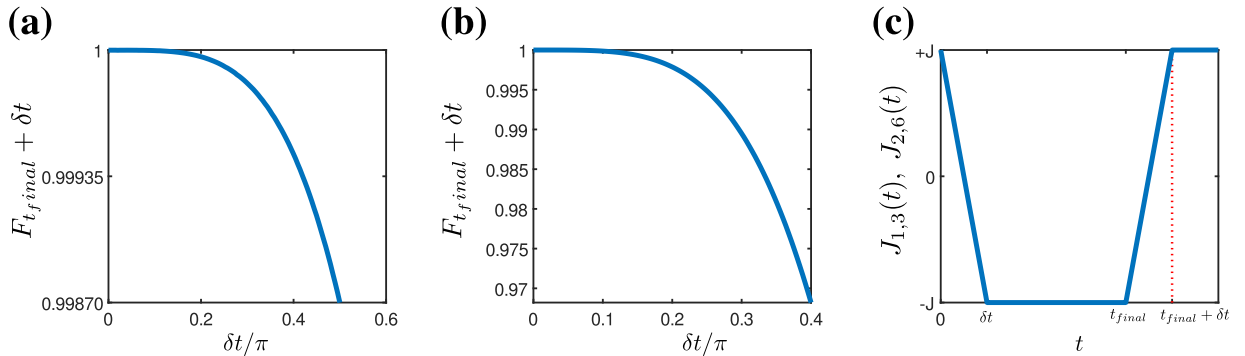


Figure 6. Performance of the five-site (a) and seven-site (b) hopping flip for the case of a linear ramp of duration δt . The parameter $t_{final} = 2\pi$ for the five-site protocol and $t_{final} = \pi/\sqrt{2}$ for the seven-site protocol, respectively. An example pulse is shown in (c).

C. Non-perfect decoupling

Throughout the main part of the manuscript, we assumed that it is possible to *completely* decouple the five-point star graph from the remainder of the system. In practice, however, a complete decoupling is usually quite challenging. In Fig. 7, we therefore investigate the impact of a non-vanishing coupling of the five-point star graph to its surroundings during state transfer (the “dimer-jump”). Here, d and d' control the coupling strengths of the immediate neighbors of the five-star graph, and the coupling of these neighbors to their other neighbors, respectively. Throughout the main part of the manuscript, during state

transfer we set $d = 0$ and ramp it up to 1 afterwards, while $d' = 1$ for all times. In the modified protocol demonstrated here, before the transfer $d = d' = 1$. One then ramps them up (or down) to their respective values (see Fig. 7 (b)), performs the transfer and ramps them back to $d = d' = 1$ after the transfer has been done. As Fig. 7 clearly demonstrates, our method is quite robust against imperfect decouplings, and can be made to function even in the case of $d = 1$ by increasing the value of d' . Indeed, when setting d' to a high value such as 3, a high fidelity above 0.9 is obtained even for $d = 1$.

The reason behind this remarkable robustness against finite coupling strengths lies in the compactness of the CLS. For example, during propagating from $|I\rangle$ to $|F\rangle$ by means of a flip pulse of finite duration $\delta t > 0$, the amplitudes of the propagating state $|\Psi(t)\rangle$ at sites 1 and 2 are, in good approximation, equal in absolute value and have a phase-difference of π . There is thus nearly no tunneling from these two sites to site 7. The same applies for the amplitudes at sites 4 and 5 and their tunneling to site 6, which is likewise suppressed.

Lastly, we would like to note that setting the on-site potentials $v_i = v' > v$ for $i = \{1, \dots, 6\}$ is also a practical way to decouple the star-subsystem from the remainder of the network and can further increase the transfer fidelity in cases where $d' \neq 0$ can not be achieved. We would like to thank the referee for pointing this out.

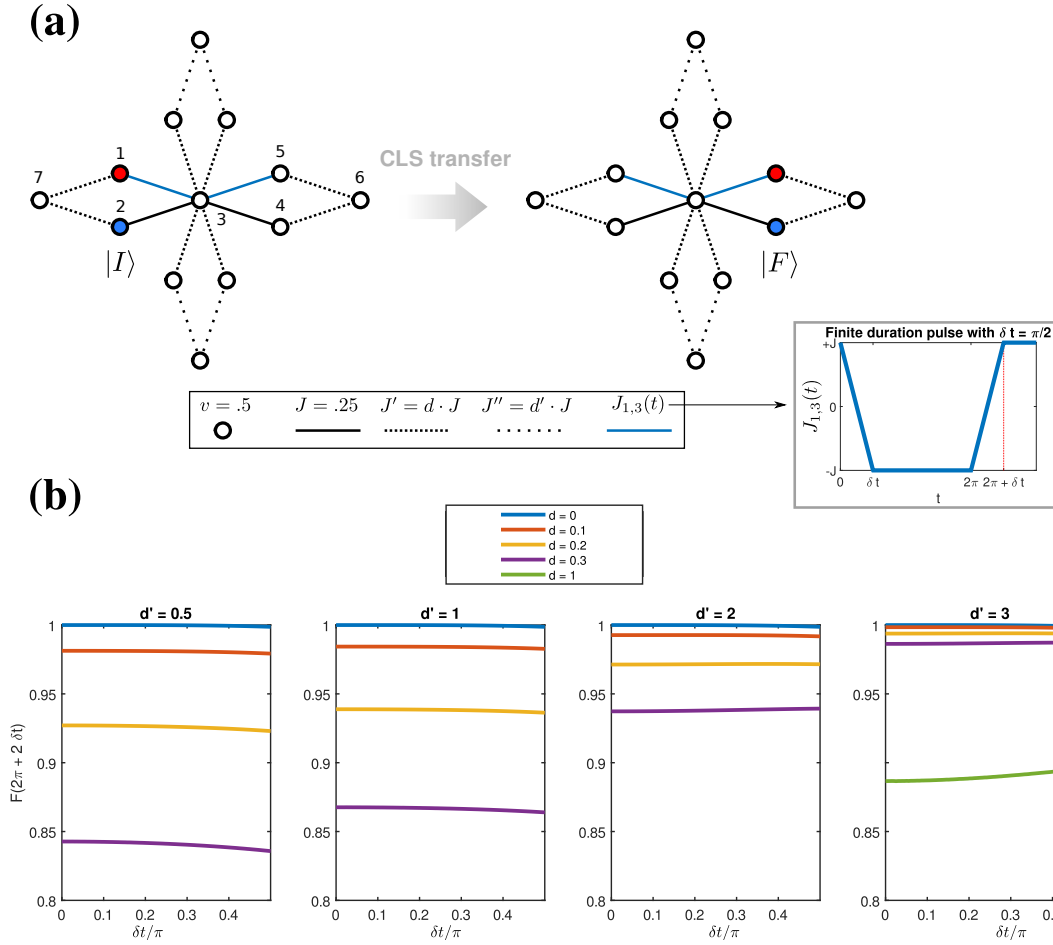


Figure 7. (a) Physical setup: Transfer of a CLS within a five-point star graph (central five sites 1 to 5 connected by black and blue solid lines) which is *not* decoupled from the remainder of the system, here simplified to consist of 8 other sites. (b) Fidelity $F(t) = |\langle F|U(t)|I\rangle|^2$ at $t = 2(\pi + \delta t)$ [with $U(t)$ being the time-evolution operator for $H(t)$] of the finite-duration hopping flip protocol [$J_{1,3}(t) = J_{3,5}(t)$ shown in the lower right of subfigure (a)] for varying values of the hopping flip pulse duration δt and d, d' . For $d = 0$, the five-star graph is completely decoupled from the remainder of the system.

VI. PERTURBATIONS OF THE OPTIMAL CONTROL PROTOCOLS

In order to investigate the effect of perturbations on the optimal control protocols for five sites [described in Eqs. (4) and (6)] and seven sites [described in Eqs. (9) and (10)], we now analyze different scenarios.

A. Static disorder

We first disturb only the *amplitudes* x_n and x'_n of the corresponding Eqs. (4), (6), (9) and (10) and assume that the frequencies ω_n do not suffer from disorder. We disturb the amplitudes as

$$x_n \rightarrow x_n \cdot (1 + \delta_n) \quad (15)$$

$$x'_n \rightarrow x'_n \cdot (1 + \delta'_n) \quad (16)$$

where δ_n and δ'_n are zero mean uniformly distributed random numbers between $-d/100$ and $d/100$, so $d = 5$ would describe a disorder strength of 5 percent. The result of this perturbation is shown in the first column of Fig. 8.

Next, we disturb only the frequencies ω_n so that

$$\omega_n \rightarrow \omega_n \cdot (1 + \delta_n) \quad (17)$$

where δ_n are zero mean uniformly distributed random numbers between $-d/100$ and $d/100$. The result of this perturbation is shown in the second column of Fig. 8.

Lastly, we disturb both the amplitudes x_n, x'_n as well as the frequencies ω_n so that

$$x_n \rightarrow x_n \cdot (1 + \delta_n) \quad (18)$$

$$x'_n \rightarrow x'_n \cdot (1 + \delta'_n) \quad (19)$$

$$\omega_n \rightarrow \omega_n \cdot (1 + \delta''_n) \quad (20)$$

where $\delta_n, \delta'_n, \delta''_n$ are zero mean uniformly distributed random numbers between $-d/100$ and $d/100$. The result of this perturbation is shown in the third column of Fig. 8.

In conclusion, the optimal control protocols are very robust against perturbations of the amplitudes of the pulses, while being prone to frequency deviations. However, this does not pose a problem if the pulses are realized by superposing different lasers, as their frequency bandwidth is usually extremely small, so that frequency deviations can therefore be neglected for this case.

B. Additive noise

Lastly, we investigate the effect of additive noise on the optimal control pulses, which we model as

$$J_n(t) \rightarrow J_n(t) + \delta_n(t, \alpha, f_{max}, \sigma). \quad (21)$$

Here, $\delta_n(t, \alpha, f_{max}, \sigma)$ describes colored noise of zero mean and with variance σ , with frequencies between 0 and f_{max} and a spectrum $S(f) \propto 1/f^\alpha$. Similarly to Ref. 7, we individually generate each differentiable noise sequence as

$$\delta_n(t, \alpha, f_{max}, \sigma) = \sigma \frac{N(f_{max}, \alpha)}{M} \sum_{k=0}^{M-1} \sqrt{S(f_k)} \cos\left(2\pi(f_k t + \eta_k^{(n)})\right) + \Delta_n \quad (22)$$

where the $\eta_k^{(n)}$ are normally distributed random variables with zero mean and unit variance, $f_k = \frac{k}{M} f_{max}$, $S(f_k) = f_k^{-\alpha}$, and $S(0) = 0$. Here and in the following, we set $M = 2^{14}$. The frequency and α -dependent normalization factor $N(f_{max}, \alpha)$ is set to 181 for $f_{max} = \{10, 1\}$ and to 185 for $f_{max} = 0.1$, with $\alpha = 0$. The offset Δ_n is chosen for each realization $\eta_k^{(n)}$ such that

$$\int_0^{t_{max}} \delta_n(t, \alpha, f_{max}, \sigma) dt = 0. \quad (23)$$

Figure 9 shows the impact of white ($\alpha = 0$) additive noise of different frequencies f_{max} [for a subset of frequencies f_{max} , we have also done the computations for pink noise with $\alpha = 1$ and achieved similar results, though not shown here]. As can be seen, all protocols maintain an average fidelity above 0.9 for $\sigma \leq 0.1$, demonstrating their robustness. For $f_{max} = 10$, the impact of the noise strongly decreases. This is simply due to the fact that for large f_{max} , the Hamiltonian is disturbed on much smaller timescales than that of the actual transport, so that the wavepacket cannot follow the perturbation, but only “sees” a time-averaged version instead. As all noise sequences are of zero mean, this time-average vanishes in the limit of infinite f_{max} , so the fidelity naturally increases with increasing f_{max} .

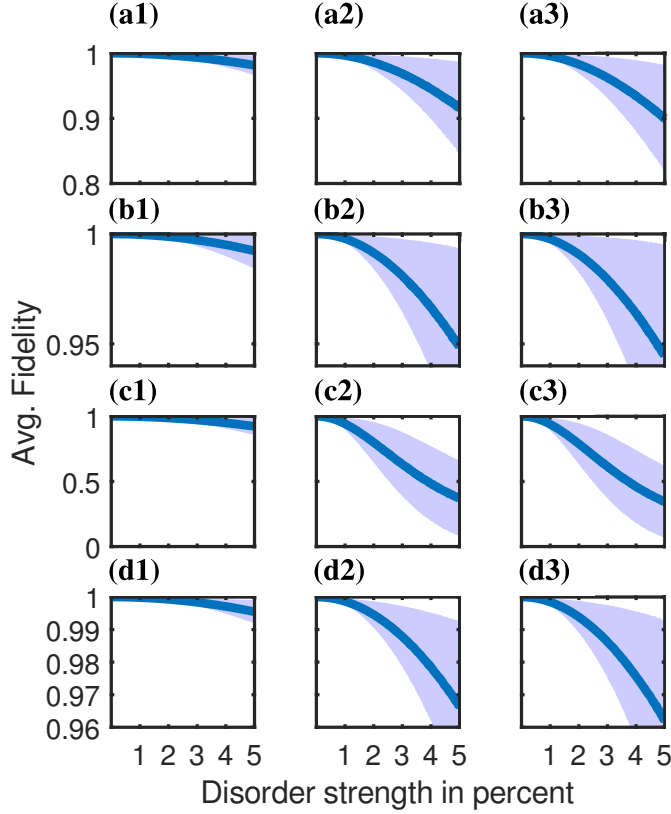


Figure 8. Performance of the optimal control protocols by disturbances in the parameters. From top to bottom: Five-site transfer [subfigures (a1 – a3)], five-site CLS creation [subfigures (b1 – b3)], seven-site transfer [subfigures (c1 – c3)], seven-site CLS creation protocols [subfigures (d1 – d3)], described by Eqs. (4), (6), (9) and (10), respectively. From left to right: Parameter distortions in the amplitudes x_n, x'_n [subfigures (a1 – d1)], in the frequencies ω_n [subfigures (a2 – d2)], and in both amplitudes and frequencies [subfigures (a3 – d3)]. For each data point, 50000 realizations have been computed. For the CLS-creation protocols, the fidelity has been computed for a full transfer between two CLS by performing the protocol twice (from the initial CLS to the central site, and then from the central site to the final CLS).

VII. INCREASING THE ROBUSTNESS OF THE STORAGE PROTOCOL

To investigate the impact of perturbations on the storage protocol for realistic cases, we create a two-dimensional network consisting of 7×7 unit cells as the one shown in Fig. 5 (b) of the main part. For clarity, the basic geometry and numerical values of on-site potentials and couplings are shown in Fig. 10 (a1). To emulate a macroscopically large network, we impose periodic boundary conditions on the network. We then disturb every single on-site potential and coupling of this network as

$$v_i \rightarrow v_i \cdot (1 + \delta_i) \quad (24)$$

$$J_i \rightarrow J_i \cdot (1 + \delta'_i) \quad (25)$$

where δ_i, δ'_i are normally distributed random variables with zero mean and variance σ^2 . Due to these perturbations, an initially excited CLS $|\Psi(0)\rangle$ on any of the dimers will no longer be stationary, but spread out across the network. In Fig. 10 (b1), we show the ensemble average of the time-dependent fidelity

$$F(t) = |\langle \Psi(0) | \Psi(t) \rangle|^2 \quad (26)$$

with $|\Psi(t)\rangle = \exp(-iHt) |\Psi(0)\rangle$. Although the network is prone to errors, its robustness against them can be greatly enhanced by suitable modifications. Two such modifications are shown in Fig. 10 (a2) and (a3), with the respective ensemble averaged fidelities shown in Fig. 10 (b2) and (b3) for different values of the standard deviation σ of the perturbation. Especially the rightmost modification is extremely robust. To understand the reason for these different degrees of robustness, we have shown the corresponding band structures [8] of the (unperturbed) periodic networks in Fig. 10 (c1 – c3). Each network features three flat bands (FBs), labeled I to III, with corresponding eigenstates shown in Fig. 10 (d). FBs I and II are degenerate for all three networks and in case of the first and second network, they are also degenerate to FB III. Moreover, the dispersive bands feature a Dirac cone for the first network, with the touching point lying exactly at the energetical position of the three FBs.

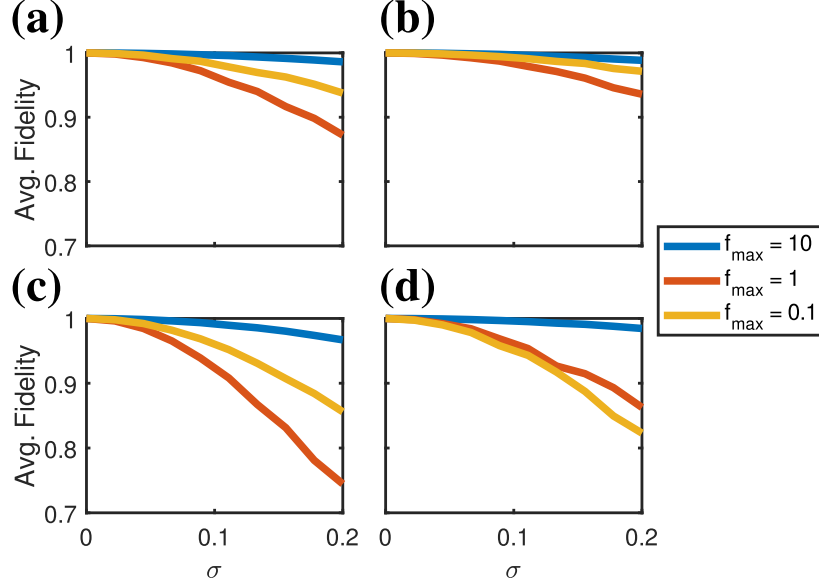


Figure 9. Performance of the optimal control protocols by adding white noise ($\alpha = 0$). (a) Five-site transfer, (b) five-site CLS creation, (c) seven-site transfer, (d) seven-site CLS creation protocols, described by Eqs. (4), (6), (9) and (10), respectively. For each data point, approximately 1400 realizations have been computed. For the CLS-creation protocols, the fidelity has been computed for a full transfer between two CLS by performing the protocol twice (from the initial CLS to the central site, and then from the central site to the final CLS).

In an unperturbed network, any single-dimer CLS as the two shown in Fig. 10 (d), is an eigenstate of the underlying Hamiltonian. We stress that if this network is perturbed such that the local symmetry protecting the particular CLS is *not violated*, this CLS remains an eigenstate, independent of the strength of the perturbation. However, if the perturbation – like the one we introduced above – does not preserve the local symmetry, then the CLS is no longer an eigenstate. For weak perturbations, it will then couple mostly to states which are energetically close in the unperturbed system, which are many for the case of the first and second network due to the simultaneous degeneracy of three flat bands, and additionally due to the Dirac-cone for the first network. This explains the small storage robustness of the first and second network. In the third network, the two flat bands I and II are still degenerate, though their eigenstates have no spatial overlap, which might explain the high robustness of this network even for strong perturbations with $\sigma = 0.2$.

We now derive the conditions under which the FBs I and II separate from the other bands. Importantly, the band structure of the networks shown in Fig. 10 (a3) can be computed analytically for arbitrary values of v, J, J' and J'' . In order to do this, we once more rely on the powerful EPT, which can be used to decompose a locally symmetric system into block-diagonal form by means of a similarity transform, so that the union of the eigenvalues of the individual blocks are equal to that of the original system. In order to make the reader familiar with the EPT, we apply it on a simple locally symmetric three-site system in Fig. 10 (e). For clarity, the Hamiltonian is depicted both in matrix form (top) and in graphical form (bottom). In Fig. 10 (f), we then apply the EPT to the full network from Fig. 10 (a3). The result of this decomposition is a set of disconnected sites with on-site potential $v - J''$, which correspond to the degenerate two flat bands I and II at $E_{CLS}^{(I)} = E_{CLS}^{(II)} = v - J''$. The connected part is equal to a modified Lieb-lattice, whose Hamiltonian reads in momentum space

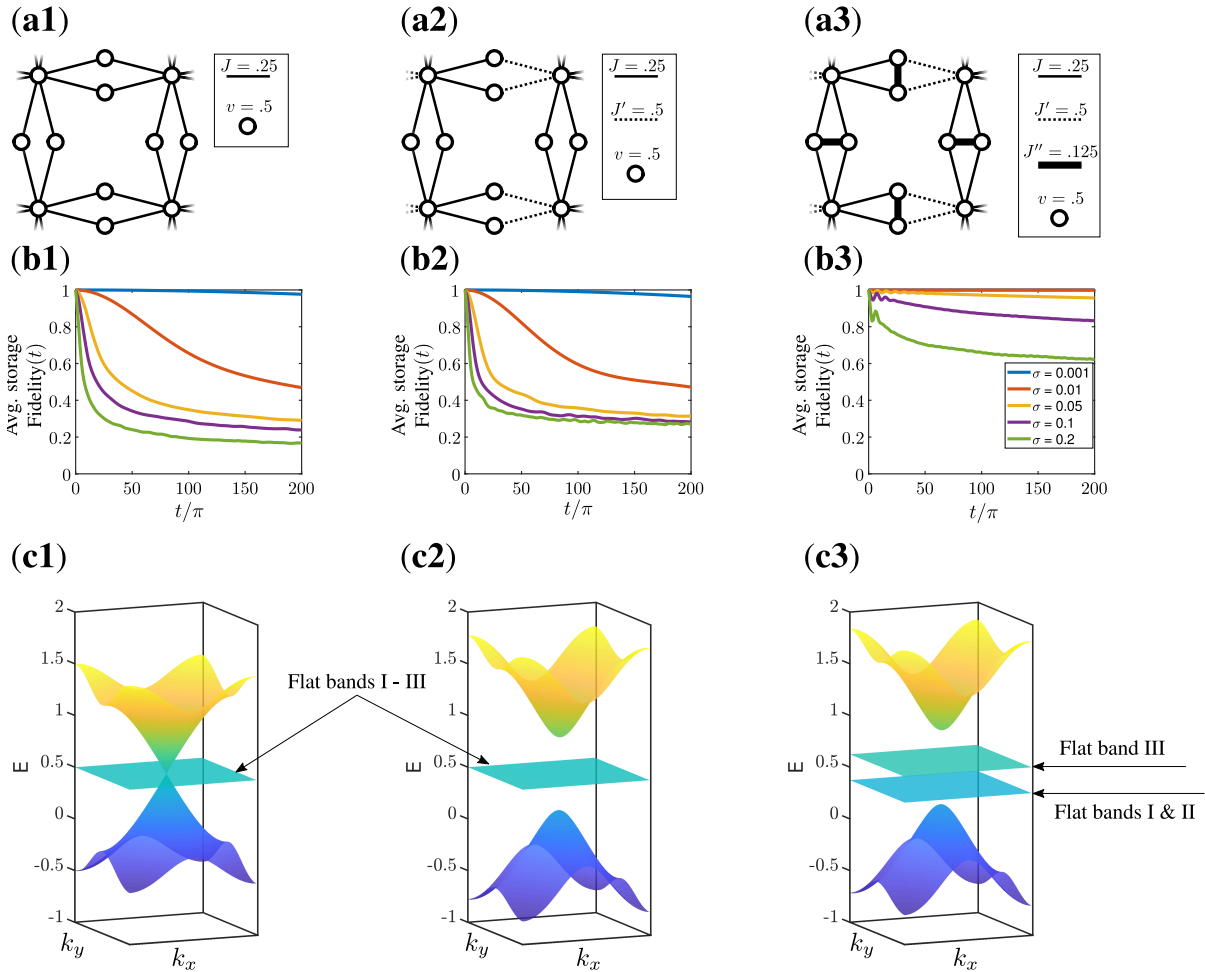
$$H(\mathbf{k}) = \begin{pmatrix} v & \sqrt{2}e^{-\frac{ik_x}{2}} (J + J'e^{ik_x}) & 2\sqrt{2}J \cos\left(\frac{k_y}{2}\right) \\ \sqrt{2}e^{-\frac{ik_x}{2}} (J' + J'e^{ik_x}) & v + J'' & 0 \\ 2\sqrt{2}J \cos\left(\frac{k_y}{2}\right) & 0 & v + J'' \end{pmatrix}.$$

Since $H(\mathbf{k}) \in \mathbb{C}^{3 \times 3}$ it can be diagonalized analytically, and its bands are given as

$$E_{CLS}^{(II)} = v + J''$$

$$E_{1,2} = v + \frac{1}{2} \left(J'' \pm \sqrt{24J^2 + 16J(J \cos(k_y) + J' \cos(k_x)) + 8J'^2 + J''^2} \right).$$

Since $E_{CLS}^{(I)} = E_{CLS}^{(II)} = v - J''$, these two flat bands separate from the others provided that $0 < |J''| < |J - J'|$.



(d) Eigenstates of flat bands

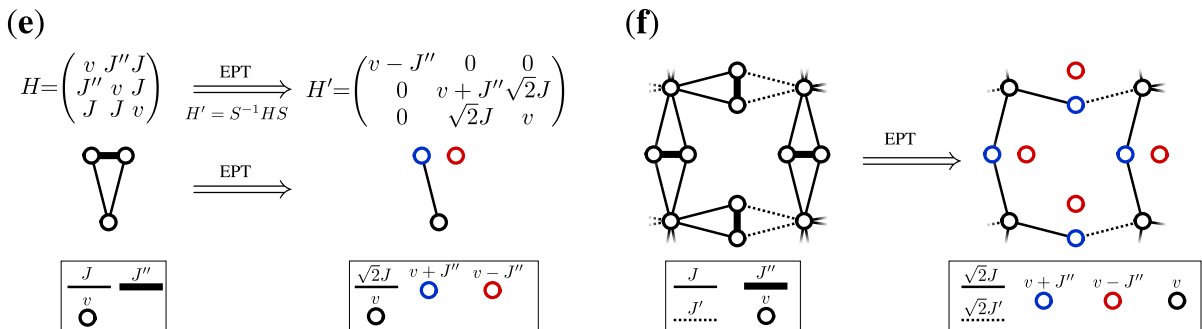
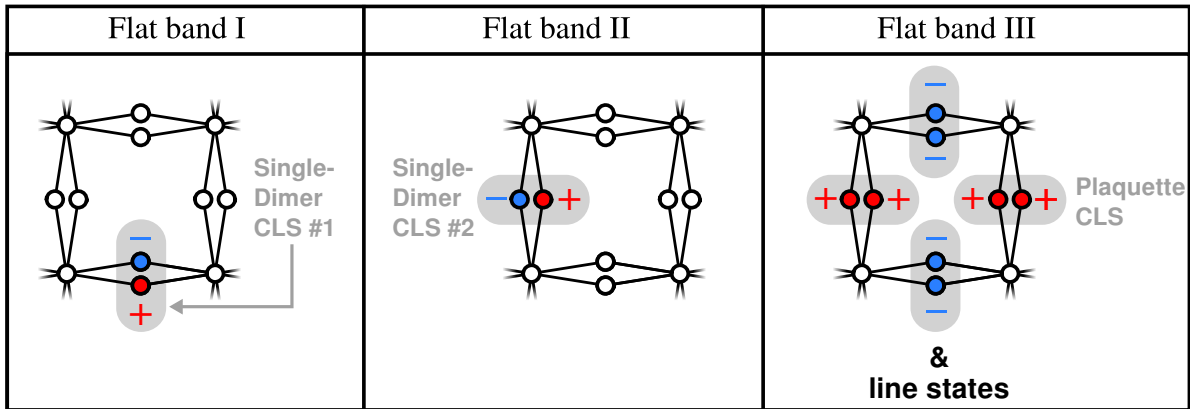


Figure 10. Increasing the robustness of storage. (a1 – a3) real-space setups, (b1 – b3) performance of the average storage fidelity of these networks under perturbations, (c1 – c3) the corresponding band structures for the unperturbed networks. (d) shows the eigenstates of the three flat bands appearing in (c1 – c3). Under some conditions, the plaquette CLS may become linearly dependent, and so-called line-states emerge, which are investigated in more detail in Ref. 9. Subfigures (e) and (f) demonstrate the application of the equitable partition theorem (EPT).

VIII. ROBUSTNESS OF THE PROTOCOLS FOR COMBINED DISTORTIONS

In this Supplemental Material, we provide three video files demonstrating the robustness of the combined transfer and storage network. These videos show the results for the following key parameters:

- A 7×7 -grid of five-point star graphs has been used as a basis, whose unperturbed parameters are equal to the system shown in Fig. 10 (a3). To emulate the effect of very large networks, periodic boundary conditions are enforced on the network.
- Every coupling and on-site potential is multiplied by an individual random number $1 + \delta$, where δ are normally distributed numbers with zero mean and variance σ^2 . The parameter σ is given in the top of the corresponding video.
- The hopping flips are done in a finite time $\delta t = 2\pi/10$.

In the videos, the radius of each circle is proportional to the absolute value of the amplitude on the corresponding site. In order to increase the visibility, circles below a certain size are plotted in white. The coupling strength is both encoded in the color (red for positive, blue for negative values) and thickness (proportional to the coupling's absolute value). The dotted couplings connect the outermost unit cells, so that periodic boundary conditions are enforced.

IX. EQUIPPING EXISTING PERFECT STATE TRANSFER NETWORKS WITH COMPACT LOCALIZED STATES

In the past, different methods for transferring a state across a static network, especially for one-dimensional chains, have been proposed[10–12]. For long chains and under the impact of perturbations, the transfer fidelity of these methods is usually better than our method. This is due to the fact that we would rely on a series of sequential dimer-jumps, instead of transferring the state through the chain in a single step, as is done in static transfer protocols. While the transfer fidelity of our method is usually lower, it allows for a faithful storage by means of compact localized states. This is a key advantage over commonly used protocols, which – after the transfer process – store the state in a single site by decoupling it from its environment. In reality, a complete decoupling to neighboring sites is usually not feasible, and the state to be saved will tunnel to these neighbors. If, on the other hand, the state is stored by means of a compact localized state, the two sites hosting it do not need to be decoupled at all. The only requirement to allow for faithful storage is that they are coupled *symmetrically* to their environment, so that the CLS is protected by destructive interference, preventing any tunneling. In particular, for a strictly symmetric coupling to the environment, the strength of this coupling can be arbitrary.

When faced with scenarios where states need to be transferred across large distances *and* stored before and after transfer, it would thus be ideal to equip existing transfer methods, which are robust against imperfections during transfer, with compact localized states, which allow for robust storage. Indeed, such a combination of both approaches can be achieved for *any* static routing network supporting perfect state transfer of single excitations, with only minimal changes in this network. The procedure is shown in detail in Fig. 12 (a – c) for one-dimensional chains and is elaborated below for arbitrary networks. In Fig. 12 (d), we benchmark the original and the modified protocols for the case of $J_n = \sqrt{n(N-n)}$. Importantly, the modified CLS protocol is always as good as the original one in terms of the transfer fidelity under perturbed conditions, and for $N \leq 11$ even *outperforms* it.

We now explicate and prove the method for arbitrary networks. To this end, let us assume that the original network is described by a Hamiltonian H and supports perfect state transfer between sites a, b within time T_f . A sketch of the network is shown in Fig. 11 (a). We now renumber the sites, so that a refers to the second-last site $N-1$ and b to the last site N , and \mathbf{H} (here and in the following, vectors and matrices – but not brackets – are written bold-faced for clarity) is then written as

$$\mathbf{H} = \begin{pmatrix} \mathbf{R} & \mathbf{G} \\ \mathbf{G}^\dagger & \mathbf{C}_0 \end{pmatrix}. \quad (27)$$

Here

$$\mathbf{C}_0 = \begin{pmatrix} v_a & h_{a,b} \\ h_{a,b}^* & v_b \end{pmatrix}$$

describes the *subsystem* of sites a, b only, $\mathbf{R} \in \mathbb{C}^{(N-2) \times (N-2)}$ describes the subsystem without sites a, b , and $\mathbf{G} \in \mathbb{C}^{(N-2) \times 2}$ describes the coupling between \mathbf{R} and \mathbf{C}_0 . The eigenvectors of \mathbf{H} can then be written as

$$|x^\nu\rangle = \begin{pmatrix} \mathbf{w}^\nu \\ u_a^\nu \\ u_b^\nu \end{pmatrix}$$

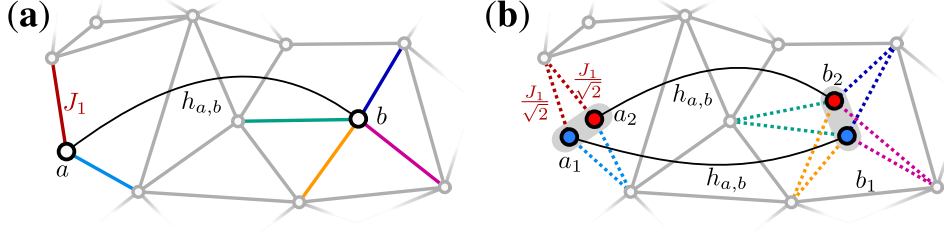


Figure 11. Equipping a network capable of perfect state transfer between sites a, b with CLSs. (a) Original network, described by \mathbf{H} . (b) Modified network described by \mathbf{H}' , along with the CLSs $|I'\rangle, |F'\rangle$. By a combination of hopping flips and time-evolution (not shown here, see text for details) $|I'\rangle$ can be perfectly transferred to $|F'\rangle$.

with $\mathbf{w}^\nu \in \mathbb{C}^{(N-2) \times 1}$ and $\nu = 1, \dots, N$. Since \mathbf{H} supports perfect state transfer between sites a and b at time T_f , we have

$$\langle I | e^{i\mathbf{H}T_f} | F \rangle = \langle N-1 | e^{i\mathbf{H}T_f} | N \rangle = \sum_{\nu} u_a^\nu (u_b^\nu)^* e^{iE_\nu T_f} = e^{i\phi}$$

with ϕ a phase and $|I\rangle = |N-1\rangle, |F\rangle = |N\rangle$, where $|n\rangle$ denotes the vectors whose n th entry is equal to one and vanishes otherwise.

We now modify the system as shown in Fig. 11 (b), so that its Hamiltonian becomes

$$\mathbf{H}' = \begin{pmatrix} \mathbf{R} & \frac{1}{\sqrt{2}}\mathbf{G} & \frac{1}{\sqrt{2}}\mathbf{G} \\ \frac{1}{\sqrt{2}}\mathbf{G}^\dagger & \mathbf{C}_0 & \mathbf{0}_{2 \times 2} \\ -\frac{1}{\sqrt{2}}\mathbf{G}^\dagger & \mathbf{0}_{2 \times 2} & \mathbf{C}_0 \end{pmatrix}$$

and it is straightforward to show that the two CLS $|I'\rangle = \frac{|N-1\rangle - |N+1\rangle}{\sqrt{2}}$ (localized on sites a_1 and a_2) and $|F'\rangle = \frac{|N\rangle - |N+2\rangle}{\sqrt{2}}$ (localized on sites b_1 and b_2) are eigenstates of \mathbf{H}' . To transfer $|I'\rangle$ to $|F'\rangle$, we perform an instantaneous flip of couplings, so that

$$\mathbf{H}' \rightarrow \mathbf{H}'' = \begin{pmatrix} \mathbf{R} & \frac{1}{\sqrt{2}}\mathbf{G} & -\frac{1}{\sqrt{2}}\mathbf{G} \\ \frac{1}{\sqrt{2}}\mathbf{G}^\dagger & \mathbf{C}_0 & \mathbf{0}_{2 \times 2} \\ -\frac{1}{\sqrt{2}}\mathbf{G}^\dagger & \mathbf{0}_{2 \times 2} & \mathbf{C}_0 \end{pmatrix}$$

and $|I'\rangle, |F'\rangle$ are no longer eigenstates of \mathbf{H}'' . By means of the so-called ‘*nonequitable partition theorem*’ [1] its $N+2$ eigenstates can then be shown to be

$$|x^\nu\rangle = \begin{pmatrix} \mathbf{w}^\nu \\ \frac{1}{\sqrt{2}}u_a^\nu \\ \frac{1}{\sqrt{2}}u_b^\nu \\ -\frac{1}{\sqrt{2}}u_a^\nu \\ -\frac{1}{\sqrt{2}}u_b^\nu \end{pmatrix}, |x^{N+r}\rangle = \begin{pmatrix} \mathbf{0}_{N \times 1} \\ \mathbf{z}^r \\ \mathbf{z}^r \end{pmatrix}$$

with $\nu = 1, \dots, N$ and $r = 1, 2$. The $\mathbf{z}^r \in \mathbb{C}^{2 \times 1}$ are the eigenvectors of the *isolated* \mathbf{C}_0 . For the modified system, we then have

$$\langle I' | e^{i\mathbf{H}''T_f} | F' \rangle = \sum_{\nu=1}^N e^{iE_\nu T_f} \langle I' | x^\nu \rangle \langle x^\nu | F' \rangle = \frac{1}{2} \sum_{\nu=1}^N \frac{2u_a^\nu}{\sqrt{2}} \cdot \frac{2(u_b^\nu)^*}{\sqrt{2}} \cdot e^{iE_\nu T_f} = e^{i\phi},$$

since the overlap of $|x^{N+1}\rangle, |x^{N+2}\rangle$ with $|I'\rangle, |F'\rangle$ vanishes. Thus, at time T_f , we have successfully transferred $|I'\rangle$ to $|F'\rangle$. By performing another instantaneous hopping flip, so that $\mathbf{H}'' \rightarrow \mathbf{H}'$, the state $|F'\rangle$ becomes again an eigenstate of the system and can thus be stored. We note that the time to perfectly transfer the CLS $|I'\rangle$ within the modified system \mathbf{H}'' is the same as that to transfer the single-site excitation $|I\rangle$ in the original system \mathbf{H} .

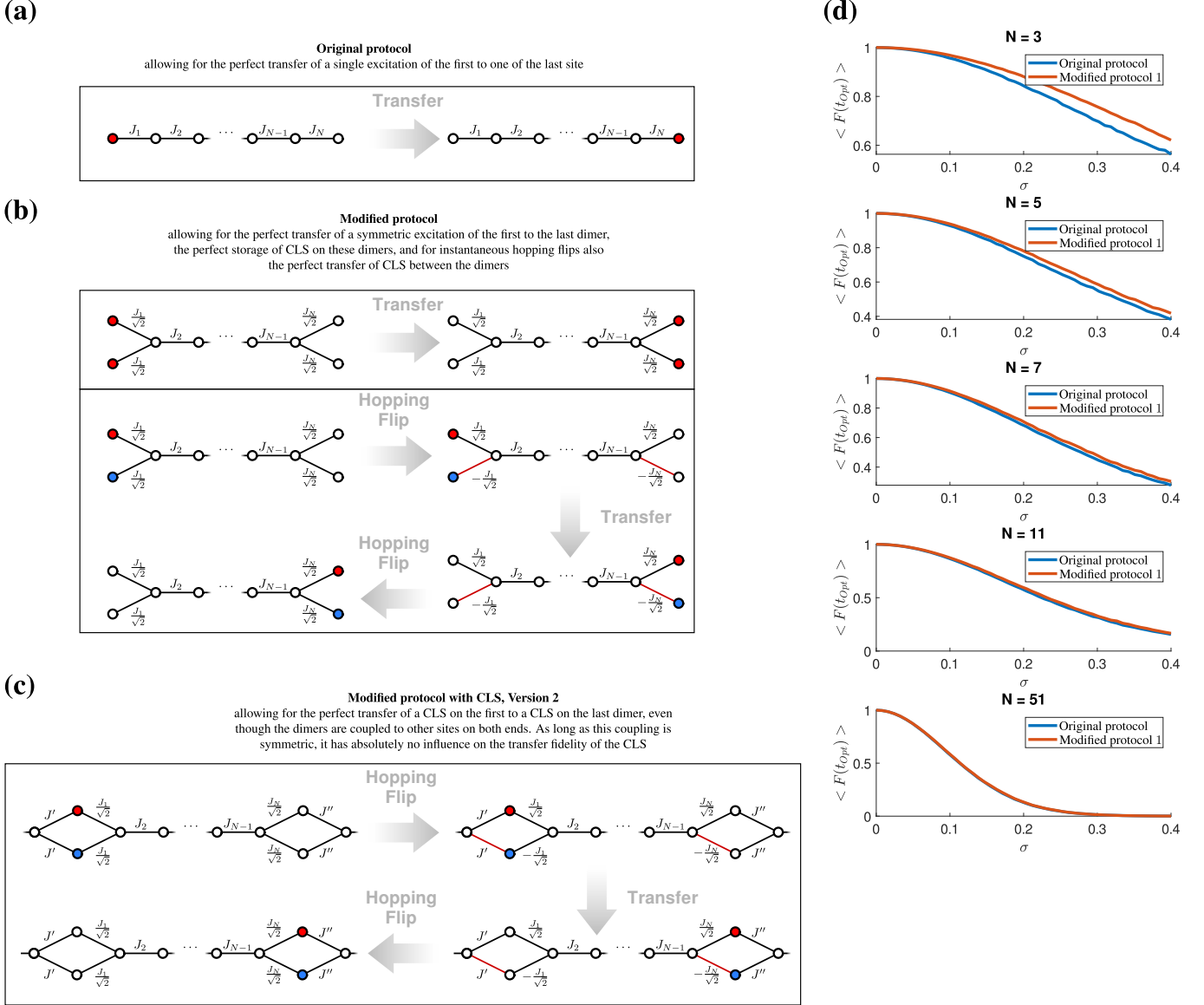


Figure 12. (a – c) Demonstration of a general method to equip chains supporting perfect state transfer with CLSs. (d) Benchmark on the performance of protocols (a) and (b) for different chain lengths. For both protocols, *every* coupling (thus in particular breaking the local symmetry of the dimer couplings) is individually multiplied by $(1 + \delta)$, where δ is a normally distributed random number with zero mean and variance σ^2 . The fidelity is defined as $|\langle I_l | \exp(iHt_{Opt}) | F_r \rangle|^2$, where $|I_l, F_r\rangle$ denote the states at the left and right end. For the original protocol, these are single excitations of the first and last site, respectively. For the modified CLS-protocol, these are compact localized states on the first and last dimer, respectively. The time t_{Opt} is the one for which, in the unperturbed case, optimal transfer with unit fidelity is achieved. We have here chosen $v_n = 0$ and $J_n = \sqrt{n(N - n)}$, for which it is well-known that perfect transfer is possible in time $t_{Opt} = \pi/2$.

-
- [1] M. Röntgen, C. V. Morfonios, and P. Schmelcher, Compact localized states and flat bands from local symmetry partitioning, *Phys. Rev. B* **97**, 035161 (2018).
- [2] W. Barrett, A. Francis, and B. Webb, Equitable decompositions of graphs with symmetries, *Linear Algebra Its Appl.* **513**, 409 (2017).
- [3] A. Francis, D. Smith, D. Sorensen, and B. Webb, Extensions and applications of equitable decompositions for graphs with symmetries, *Linear Algebra Its Appl.* **532**, 432 (2017).
- [4] P. Doria, T. Calarco, and S. Montangero, Optimal Control Technique for Many-Body Quantum Dynamics, *Phys. Rev. Lett.* **106**, 190501 (2011).
- [5] T. Caneva, T. Calarco, and S. Montangero, Chopped random-basis quantum optimization, *Phys. Rev. A* **84**, 022326 (2011).
- [6] E. Fritscher and V. Trevisan, Exploring Symmetries to Decompose Matrices and Graphs Preserving the Spectrum, *SIAM J. Matrix Anal. Appl.* **37**, 260 (2016).
- [7] S. Yang, A. Bayat, and S. Bose, Spin-state transfer in laterally coupled quantum-dot chains with disorders, *Phys. Rev. A* **82**, 10.1103/PhysRevA.82.022336 (2010).
- [8] The band structures shown in this work have been obtained by means of the pybinding [13] package.
- [9] S. Xia, A. Ramachandran, S. Xia, D. Li, X. Liu, L. Tang, Y. Hu, D. Song, J. Xu, D. Leykam, S. Flach, and Z. Chen, Unconventional Flatband Line States in Photonic Lieb Lattices, *Phys. Rev. Lett.* **121**, 263902 (2018).
- [10] M. Christandl, N. Datta, T. C. Dorlas, A. Ekert, A. Kay, and A. J. Landahl, Perfect transfer of arbitrary states in quantum spin networks, *Phys. Rev. A* **71**, 032312 (2005).
- [11] M. Christandl, N. Datta, A. Ekert, and A. J. Landahl, Perfect State Transfer in Quantum Spin Networks, *Phys. Rev. Lett.* **92**, 187902 (2004).
- [12] A. Kay, Perfect, efficient, state transfer and its application as a constructive tool, *Int. J. Quantum Inform.* **08**, 641 (2010).
- [13] D. Moldovan, M. Anđelković, and F. Peeters, *Pybinding v0.9.4: A Python package for tight-binding calculations*, Zenodo (2017).

Designing pretty good state transfer via isospectral reductions

M. Röntgen¹, N. E. Palaiodimopoulos², C. V. Morfonios¹, I. Brouzos^{2,3}, M. Pyzh¹, F. K. Diakonou², and P. Schmelcher^{1,4}

¹Zentrum für optische Quantentechnologien, Universität Hamburg, Luruper Chaussee 149, 22761 Hamburg, Germany

²Department of Physics, University of Athens, 15771 Athens, Greece

³Le Mans University, LAUM UMR CNRS 6613, Av. O. Messiaen, 72085, Le Mans, France

⁴The Hamburg Centre for Ultrafast Imaging, Universität Hamburg, Luruper Chaussee 149, 22761 Hamburg, Germany



(Received 6 August 2019; revised manuscript received 18 December 2019; accepted 25 February 2020; published 1 April 2020)

We present an algorithm to design networks that feature pretty good state transfer (PGST), which is of interest for high-fidelity transfer of information in quantum computing. Realizations of PGST networks have so far mostly relied either on very special network geometries or imposed conditions such as transcendental on-site potentials. However, it was recently shown that PGST generally arises when a network's eigenvectors and the factors P_{\pm} of its characteristic polynomial P fulfill certain conditions, where P_{\pm} correspond to eigenvectors which have ± 1 parity on the input and target sites. We combine this result with the so-called isospectral reduction of a network to obtain P_{\pm} from a dimensionally reduced form of the Hamiltonian. Equipped with the knowledge of the factors P_{\pm} , we show how a variety of setups can be equipped with PGST by proper tuning of P_{\pm} . Having demonstrated a method of designing networks featuring pretty good state transfer of single site excitations, we further show how the obtained networks can be manipulated such that they allow for robust storage of qubits. We hereby rely on the concept of compact localized states, which are eigenstates of a Hamiltonian localized on a small subdomain, and whose amplitudes completely vanish outside of this domain. Such states are natural candidates for the storage of quantum information, and we show how certain Hamiltonians featuring pretty good state transfer of single site excitation can be equipped with compact localized states such that their transfer is made possible.

DOI: [10.1103/PhysRevA.101.042304](https://doi.org/10.1103/PhysRevA.101.042304)

I. INTRODUCTION

The ability to reliably transfer information through a quantum system is of key importance in the quest towards quantum computers. One particularly appealing approach is that of *perfect state transfer* (PST) [1–4] of a given state—usually a single site excitation of an XY Hamiltonian—from an input to a target site. What makes PST appealing is that it achieves perfect transfer fidelity (the portion of the final state at the desired site) $F = 1$ by simple time evolution of the input excitation with the time-independent Hamiltonian. On the other hand, the demand of strictly unity fidelity for PST is very restrictive for designing quantum networks for state transfer. For practical applications it is anyway never met since imperfections and noise eventually lead to nonperfect transfer. Therefore, given that in any practical case the transfer fidelity will be lower than unity, a less restrictive alternative (in terms of conditions to be applied when designing different configurations of networks for state transfer) is *pretty good* [5] (also called almost perfect [6]) *state transfer* (PGST), where F gets arbitrarily close to unity at a corresponding time: Specifically, for every $\epsilon > 0$ there is a time t_{ϵ} such that $F(t_{\epsilon}) > 1 - \epsilon$, where $F(t) = |\langle \psi_I | e^{i\mathbf{H}t} | \psi_F \rangle|^2$ (setting $\hbar = 1$) for a transfer from state $|\psi_I\rangle$ to state $|\psi_F\rangle$ at time t , with \mathbf{H} denoting the Hamiltonian. Since PGST includes the case of PST, it is a broader concept, and it can be realized in a broader range of setups. As a consequence, the—compared to PST—enlarged parameter space of Hamiltonians supporting

PGST could be explored to find configurations that are less prone against both imperfections and noise than others.

On a practical level, however, PGST suffers from two problems. First, the design of PGST Hamiltonians is challenging, since it usually requires information about the *exact* eigenvalue spectrum. So far, many approaches to PGST are therefore based on special Hamiltonian designs such as certain graph products [7–11]. A general and intuitive design mechanism of PGST Hamiltonians is thus lacking. The need for such a mechanism becomes even more apparent in view of the difficulty of designing a PGST Hamiltonian that achieves reasonable fidelities in sufficiently short transfer time. From the investigation of different Hamiltonians, it is known that these transfer times can be prohibitively large for certain systems [12,13], while classes of chains are known as well where these times can be sufficiently low [6]. Overall, further research is needed in order to make practical use of the concept of PGST, and to this end the ability of generating huge families of PGST Hamiltonians is of high importance.

Recently, progress in the design of PGST has been made in Ref. [14]. There, an approach is presented that achieves PGST between two sites u and v *without* direct tuning of the eigenvalue spectrum. The approach is based on Hamiltonians \mathbf{H} which feature so-called cospectral sites u and v for a range of parameters. In Hamiltonians with such cospectral sites u and v , all eigenvectors can be chosen to have parity ± 1 on u and v . Eisenberg *et al.* then show that PGST between u and v automatically arises if the factors P_{\pm} , which are related to

eigenvectors which have nonvanishing amplitudes on u and v and additionally have ± 1 parity on them, respectively, of the characteristic polynomial of \mathbf{H} fulfill certain conditions. The task of achieving PGST therefore boils down to proper tuning of the factors P_{\pm} . In practice, though, obtaining these factors from the underlying Hamiltonian is not easy. In Ref. [14], P_{\pm} are (up to special cases involving symmetries or very small setups) not obtained, but indirect methods, which manipulate \mathbf{H} such that P_{\pm} are enforced to meet the desired properties, are presented. An example of such a method is the addition of transcendental numbers to the values of certain on-site potentials of the Hamiltonian. While elegant, this method is restricted in the sense that it requires the ability to manipulate on-site potentials. The question thus arises whether other, more general methods of designing PGST Hamiltonians exist.

In this work we present such a method by pursuing an alternative road to PGST. Namely, by directly obtaining the polynomials P_{\pm} from an underlying symmetric Hamiltonian that features cospectral sites u and v . To this end, we combine the mathematical relations underlying the works in Refs. [14,15] with the theory of isospectral reductions [16–22]. Isospectral reduction is a method to reduce the size of a given Hamiltonian while keeping a large amount of information on its eigenvalues and eigenvectors. We utilize the isospectral reduction to “compress” only the relevant spectral information for the problem at hand by building upon the very recent results of Ref. [22]. These results put strong constraints on the structure of the isospectral reduction of a Hamiltonian that features cospectral sites. We use these structural constraints to extract the P_{\pm} from the isospectral reduction of \mathbf{H} . Equipped with P_{\pm} , we show how this allows for a convenient and powerful algorithm for designing Hamiltonians featuring PGST by properly tuning P_{\pm} while maintaining the cospectrality of u and v . In order to be self-contained, we also collect known facts from the literature and condense them into a detailed method to generate Hamiltonians that feature cospectral sites u and v .

Interestingly, this cospectrality is often accounted for by *spatial local symmetries*, i.e., symmetries, which are only valid in spatial subdomains of the whole system. Usually the signatures of such local symmetries are only indirectly encoded into so-called nonlocal currents, as has been shown in Refs. [23–28]. On the contrary, the impact of the underlying local symmetries is directly visible in setups featuring cospectral vertices u and v , where all eigenvectors are (in the case of degeneracies, can be chosen to be) locally parity symmetric on these sites. It would thus be interesting to analyze cospectral Hamiltonians within the framework developed in those works.

Having demonstrated how to design networks capable of PGST of single site excitations, we show how these networks can be modified to allow for robust storage of qubits. To this end, we slightly modify these networks, thereby equipping them with so-called *compact localized states*. Such states are eigenstates of the underlying Hamiltonian [29,30], and are perfectly localized on a finite number of sites. They are thus ideally suited for the storage of qubits, and we show how, after equipping networks with compact localized states, these can also be pretty well transferred.

This work is structured as follows. We first define the necessary and sufficient conditions for the realization of PGST in Sec. II A. We then investigate the necessary condition, namely strong cospectrality, which is a stronger version of cospectrality, in more detail in Sec. II B, and the connection of this property to symmetries in Sec. II C. Our treatment of strong cospectrality is completed in Sec. II D, where we show how Hamiltonians with this property can be designed. In Sec. II E we introduce isospectral reductions, and show how they can be harnessed to extract the polynomials P_{\pm} . In Sec. III we use this method to construct an algorithm for the design of graphs featuring PGST. This algorithm represents one of the two highlights of this work. We apply the algorithm to three examples in Secs. III B and III C. In Sec. IV we present the necessary modifications needed for PGST of compact localized states. Finally, we conclude our work in Sec. V.

II. THEORY: PRETTY GOOD STATE TRANSFER OF SINGLE-SITE EXCITATIONS

Throughout this work we will consider setups described by symmetric Hamiltonians of the form

$$\mathbf{H} = \sum_i E_i |i\rangle\langle i| + \sum_{(i,j)} h_{i,j} |i\rangle\langle j|, \quad (1)$$

with real on-site potentials E_i and couplings $h_{i,j} = h_{j,i}$, where the sum in Eq. (1) runs over all interconnected sites i and j . We use boldface for both vectors and matrices. The Hamiltonian given by Eq. (1) can be represented, for example, by coupled waveguide arrays [31,32]. However, in the context of quantum computers, a natural choice are spin networks, where each site represents a spin-1/2 qubit (measured up or down). The Heisenberg XX interaction Hamiltonian then reduces to the simple description Eq. (1) within the subspace of one excitation (1 spin up and all others down) [33].

In the course of this work, we will often depict \mathbf{H} as a graph, i.e., as a collection of vertices and edges connecting them. The weighted adjacency matrix of the graph then equals \mathbf{H} . As this establishes a one-to-one relation between graphs and the underlying \mathbf{H} , we will use these two terms interchangeably. Likewise, we will use the terms “site” and “vertex” interchangeably throughout this work.

In the following we will comment on the conditions for PGST, and show how it can be achieved. In order to help the reader in comprehending the different aspects involved, we visualize in Fig. 1 the main mathematical background of our method to achieve PGST. The overview Fig. 1 contains all core mathematical theorems used in this work in compact form. We stress that the style of presentation at this point aims at being self-contained, thereby transferring insights from graph theory to a broader physics community in Secs. II B to II D. Sections II E and III contain, along with the results provided in Sec. IV, the highlights and main novelties of this work.

A. Necessary and sufficient conditions

In order to support PGST between two sites u and v , a Hamiltonian \mathbf{H} has to fulfill the following two conditions,

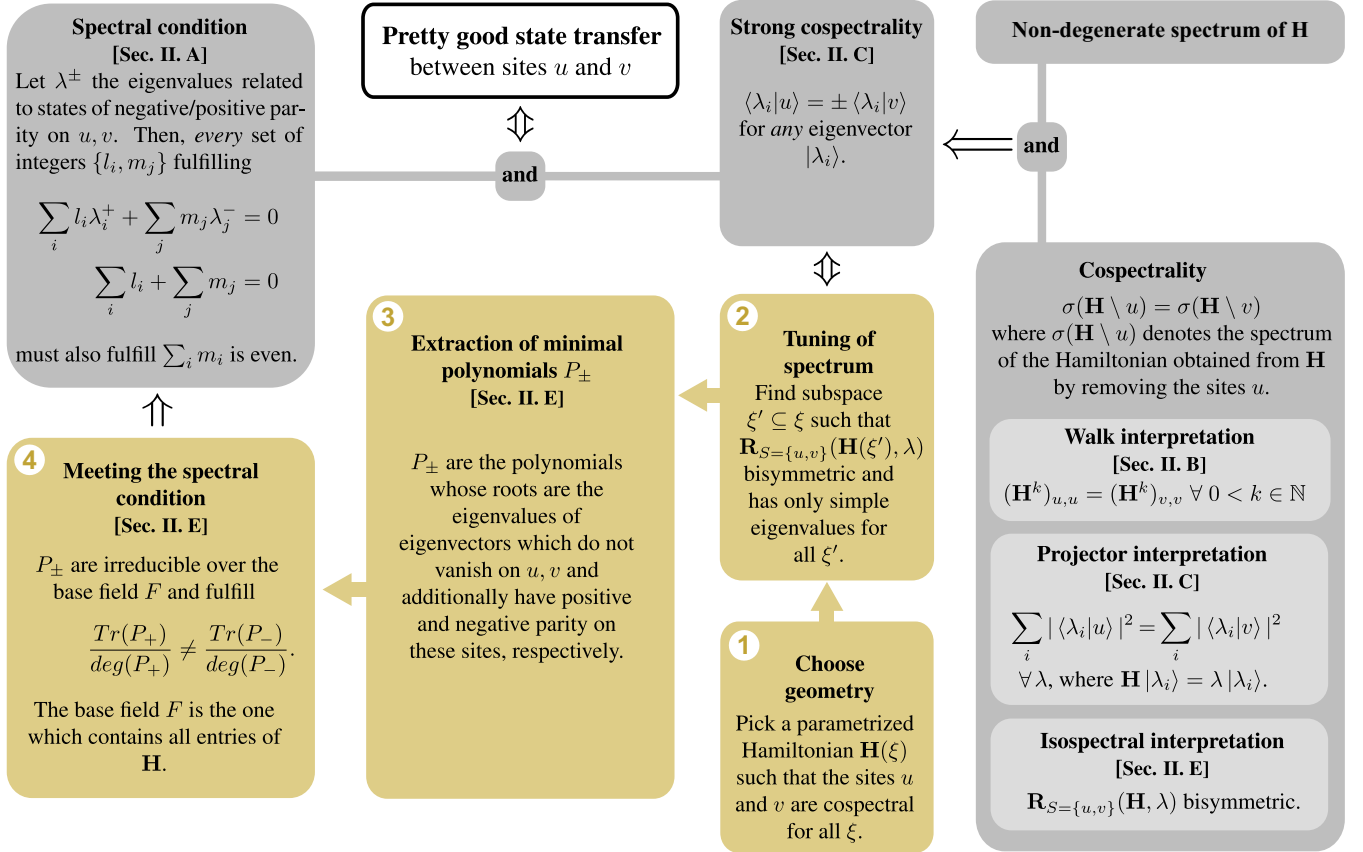


FIG. 1. Gray part: The connection between main theorems that lead to realizations of PGST. Double lines with arrows denote mathematical relations $\Leftarrow, \Rightarrow, \Leftrightarrow$. Yellow/golden part: Essential steps (enumerated 1 to 4) of the algorithm for the design of PGST Hamiltonians (presented in Sec. III). The isospectral reduction $\mathbf{R}_S(\mathbf{H}, \lambda)$ is defined in Eq. (14).

whose combination is necessary and sufficient: (i) The two sites u and v must be *strongly cospectral* (see the following subsection) and (ii) its spectrum must fulfill the following condition [34]: Every set of integers $\{l_i, m_j\}$ which fulfills

$$\sum_i l_i \lambda_i^+ + \sum_j m_j \lambda_j^- = 0, \quad (2)$$

$$\sum_i l_i + \sum_j m_j = 0, \quad (3)$$

must also fulfill

$$\sum_i m_i \text{ is even.} \quad (4)$$

Here λ_i^+, λ_j^- are the eigenvalues associated with eigenvectors $|\psi_i^+\rangle, |\psi_j^-\rangle$ of \mathbf{H} that fulfill

$$\langle \psi_i^+ | u \rangle = +\langle \psi_i^+ | v \rangle \neq 0, \quad \langle \psi_j^- | u \rangle = -\langle \psi_j^- | v \rangle \neq 0,$$

where $|u\rangle, |v\rangle$ describe single-site excitations of sites u and v , respectively. We note that the above condition is stated in Ref. [34] in slightly different form. We connect the two variants in Appendix A.

Note that there is always at least one set of integers $\{l_i, m_j\}$ fulfilling Eqs. (2) and (3), namely, the trivial choice $l_i = m_j = 0 \forall i, j$, which also fulfills Eq. (4). In certain cases, this trivial choice is also the *only one* fulfilling Eqs. (2) and (3). An example is the case where there are only two eigenvalues,

$\lambda^+ = \sqrt{2}, \lambda^- = \sqrt{3}$. Then

$$l\sqrt{2} + m\sqrt{3} = 0,$$

for integers l, m can only be fulfilled when $l = m = 0$. Provided that the two sites u and v are also strongly cospectral, the setup would thus feature PGST between them.

B. Geometric interpretation of cospectrality

A necessary condition for PGST is that u and v are *strongly cospectral* [34]. As strongly cospectral vertices are also cospectral [35] (see Fig. 1), we will first investigate and understand this weaker property before turning to its stronger version. Two vertices u, v are said to be cospectral if $\sigma(\mathbf{H} \setminus u) = \sigma(\mathbf{H} \setminus v)$, where $\sigma(\mathbf{H})$ denotes the eigenvalue spectrum of \mathbf{H} , and $\mathbf{H} \setminus u$ denotes the Hamiltonian obtained from \mathbf{H} by deleting the u th row and column. For our purpose, it is easier to rely on an equivalent condition [35] in terms of the diagonal entries of powers of \mathbf{H} . Namely, u and v are cospectral if and only if

$$(\mathbf{H}^k)_{u,u} = (\mathbf{H}^k)_{v,v} \quad (5)$$

for all non-negative integers $k < N$, where $\mathbf{H} \in \mathbb{R}^{N \times N}$. As a side remark, we note that Eq. (5) automatically holds for all $k > 0$ provided that it holds for $0 < k < N$. This is due to the Cayley-Hamilton theorem, which states that every matrix power $\mathbf{H}^{k \geq N}$ can be expanded in terms of smaller powers

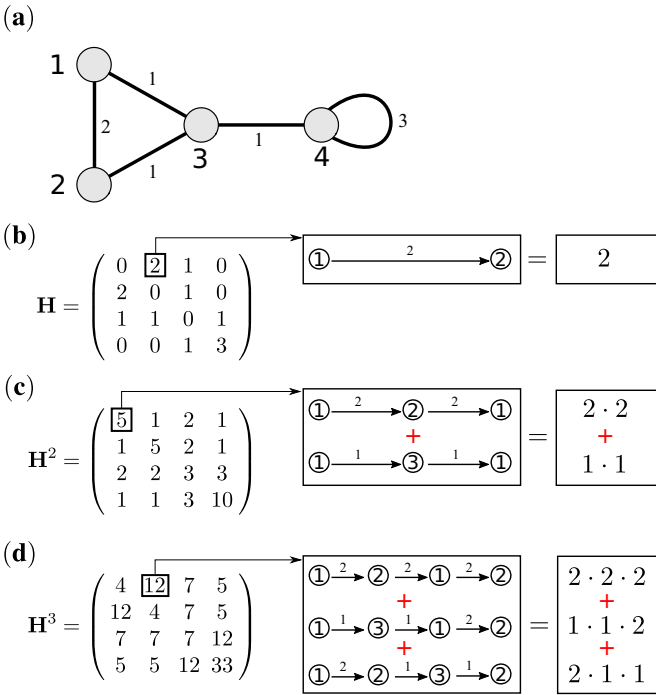


FIG. 2. The entries of matrix powers of any matrix can be interpreted in terms of walks. (a) A graph, described by the matrix \mathbf{H} denoted in (b). We have here used the convention from graph theory that diagonal elements $\mathbf{H}_{i,i}$ are plotted as links from i to itself. (b)–(d) Help on how to interpret the entries of powers \mathbf{H}^k (see text for details).

$\mathbf{H}^{k < N}$, i.e.,

$$\mathbf{H}^{k \geq N} = \sum_{i=0}^{N-1} a_i^{(k)} \mathbf{H}^i,$$

with $a_i^{(k)}$ being the expansion coefficients. These coefficients are scalars, and therefore Eq. (5) must hold for all non-negative integers k , provided that it holds for $0 \leq k < N$.

While well known in graph theory, it is perhaps surprising to many physicists that the entries of \mathbf{H}^k (for integer $k > 0$) possess a convenient interpretation. To this end, we interpret the Hamiltonian matrix as a graph, i.e., as a network of vertices V_i connected to each other by weighted edges $e_{i,j} = \{V_i, V_j\}$, with weight $w(e_{i,j}) = \mathbf{H}_{i,j}$. This is exemplarily done in Fig. 2(a) for the Hamiltonian given in Fig. 2(b). In this picture of representing \mathbf{H} as a graph, every matrix element $\mathbf{H}_{i,j} \neq 0$ is connected to an edge between vertices i and j ; and in particular, nonvanishing diagonal elements $\mathbf{H}_{i,i} \neq 0$ refer to a link from site i to itself, with weight given by $w(e_{i,i}) = \mathbf{H}_{i,i}$.

Now that we have interpreted the entries of \mathbf{H} in terms of edges, we show how entries of higher-order powers $\mathbf{H}^{k > 1}$ can be interpreted in terms of walks. A walk can be thought of as a route through the graph from one vertex to another by walking along the edges connecting neighboring vertices. Mathematically, it is defined as an alternating sequence of vertices and edges, where each edge must connect its precursor vertex to its successor. For example, in Fig. 2(a) a walk of length 2 from vertex 1 to 4 would be the sequence $p = \{V_1, e_{1,3}, V_3, e_{3,4}, V_4\}$. In order to interpret the entries

of \mathbf{H}^k , we note that, just as each edge $e_{i,j}$ can be given a weight $w(e_{i,j})$, we can also give each walk a weight by multiplying the weights of all edges occurring within this walk. Thus, the weight of the walk $p = \{V_1, e_{1,3}, V_3, e_{3,4}, V_4\}$ would be $w(p) = w(e_{1,3})w(e_{3,4}) = 1 \cdot 1$. Equipped with these definitions, one can show that (a proof is provided in Appendix B)

$$(\mathbf{H}^{k > 0})_{a,b} = \sum_p w(p_{a,b}^{(k)}), \quad (6)$$

where $p_{a,b}^{(k)}$ denotes one possible walk of length k between vertices a and b , and the sum is over all such walks. In other words, the value of the matrix element $(\mathbf{H}^k)_{i,j}$ is equal to the sum of weights of all walks of length k between vertices i and j . In Figs. 2(b)–2(d) we have visualized this interpretation of walks, and have also explicitly given the integer powers $\mathbf{H}^{k < N}$.

We now connect the interpretation of matrix elements of \mathbf{H}^k in terms of walks to the cospectrality of two vertices u and v . As we have seen above, these are cospectral if and only if Eq. (5) is fulfilled for all integer $k < N$, with N being the number of sites contained in \mathbf{H} . Now, by interpreting the entries of \mathbf{H}^k in terms of walks, the cospectrality of u and v can therefore be determined in a simple and straightforward manner. Namely, by evaluating all walks of length k that go from u onto itself, and those that go from v onto itself, and comparing the respective sum of weights, order by order in $k < N$. Thus, in Fig. 2, $(\mathbf{H}^k)_{1,1} = (\mathbf{H}^k)_{2,2}$ for $k < 4$ (and, by the Cayley-Hamilton theorem, also for all integer $k > 0$), which makes the sites $u = 1$ and $v = 2$ cospectral. Alternatively, one can also rely on the statement that two sites u and v are cospectral if and only if $\sigma(\mathbf{H} \setminus u) = \sigma(\mathbf{H} \setminus v)$. As the graph of $\mathbf{H} \setminus 1$ is identical to that of $\mathbf{H} \setminus 2$, their spectra $\sigma(\mathbf{H} \setminus 1) = \sigma(\mathbf{H} \setminus 2)$ are trivially identical, and the sites $u = 1$ and $v = 2$ are therefore cospectral.

We show a collection of cospectral graphs in Fig. 3. In every graph, the two red vertices (labeled u and v) are cospectral, provided that (i) any two couplings denoted by the same line style are identical, (ii) the two red sites u, v have identical on-site potential, and (iii) all light-gray vertices have identical on-site potential. Let us now investigate these graphs in more detail. By comparing different variations, it can be seen that certain changes do not break the cospectrality of two vertices. For example, in Fig. 3(a2) we have modified the graph from Fig. 3(a1) by identically coupling each red vertex u and v to an additional vertex. In Fig. 3(a3) we have modified the graph of Fig. 3(a1) by inserting the “central” vertex m . We term this vertex central since it can be reached from sites 1 and 5 by a walk comprising two steps, and the corresponding weights of these two walks are identical. To understand why inserting this vertex does not break the cospectrality, one only needs to investigate the influence of this change by comparing the diagonal matrix elements $(\mathbf{H}_B^k)_{S,S}$ and $(\mathbf{H}^k)_{S,S}$. Here \mathbf{H}_B and \mathbf{H} describe the setup of Figs. 3(a1) and 3(a3), respectively, and $S = \{u, v\}$ label the two red sites. Before the change, u and v were cospectral, so that $(\mathbf{H}_B^k)_{u,u} = (\mathbf{H}_B^k)_{v,v} \forall k$. Thus, to understand why the cospectrality is kept, we only need to look at the differences $(\Delta \mathbf{H}^k)_{S,S} = (\mathbf{H}^k)_{S,S} - (\mathbf{H}_B^k)_{S,S}$ caused by inserting the new vertex. Though tedious, it is a straightforward task to show that $(\Delta \mathbf{H}^k)_{1,1} = (\Delta \mathbf{H}^k)_{5,5}$ for $k < 9$,

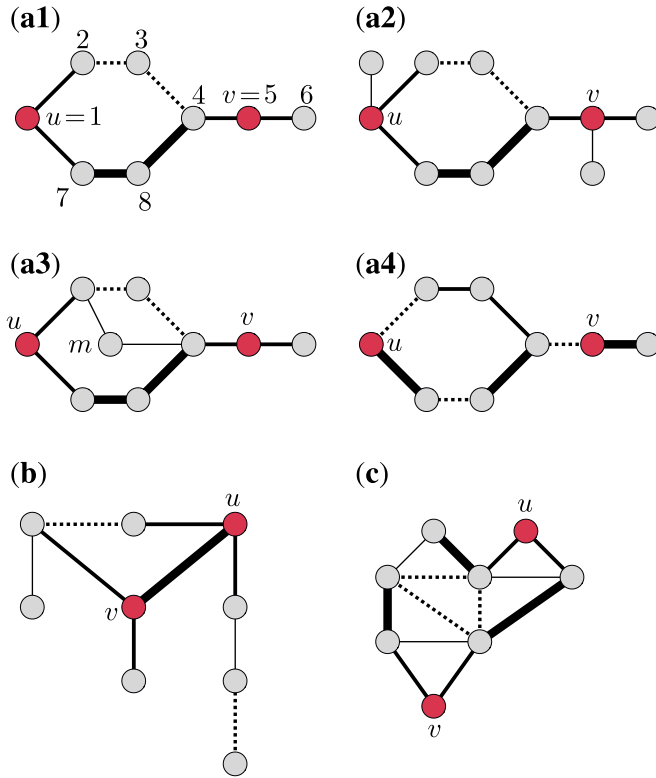


FIG. 3. A collection of graphs featuring cospectral vertices. In every graph, the two red vertices (labeled u and v) are cospectral, provided that (i) any two couplings denoted by the same line style are identical, (ii) the two red sites u , v have identical on-site potential, and (iii) all light-gray vertices have identical on-site potential.

and, by the Cayley-Hamilton theorem, therefore for all k . The addition of vertex m does thus, at each order k , add an equally valued sum of weights of walks from site 1 to itself compared to those from site 5 to itself. For this reason, its addition does not change the cospectrality of $u = 1$ and $v = 5$.

C. Strong cospectrality and the impact of symmetries

As we have seen above, cospectrality is linked to the geometric and spectral properties of a graph. It is likewise linked to properties of the graph's eigenstates. Indeed, it can be shown that two sites u , v are cospectral if and only if [35], for $\mathbf{H}|\lambda_i\rangle = \lambda|\lambda_i\rangle$,

$$\sum_i |\langle \lambda_i | u \rangle|^2 = \sum_i |\langle \lambda_i | v \rangle|^2 \quad (7)$$

is fulfilled for all λ . In words, u and v are cospectral if and only if, within each degenerate subspace, the sum of squares of absolute values of projections on sites u is equal to that of projections on site v .

If u and v are cospectral and additionally [14]

$$\langle \tilde{\lambda}_i | u \rangle = \pm \langle \tilde{\lambda}_i | v \rangle \quad (8)$$

for any superposition $|\tilde{\lambda}_i\rangle = \sum_j c_j |\lambda_j\rangle$ of degenerate states $|\lambda_j\rangle$, then u and v are said to be *strongly cospectral*. Therefore, strong cospectrality implies cospectrality, but the reverse

is not necessarily true. Unlike cospectrality, which can be readily interpreted and tested for in terms of walks, we are not aware of an easy, i.e., without computing the determinant or the eigenstates of the graph, method to test whether a given general graph is strongly cospectral or not. As the field of cospectral vertices is quite young, there is hope that this may change in the future, and we refer the interested reader to Ref. [35] for further information on the fascinating field of strongly cospectral vertices.

With the above statements in mind, let us now investigate the symmetries of cospectral graphs. To this end, we compare the graphs shown in Fig. 3 to the one shown in Fig. 2(a). The latter graph has the special property that the underlying Hamiltonian is invariant under the permutation of vertices 1 and 2 and therefore commutes with the corresponding permutation operator. As is well known, such a symmetry has a drastic impact: The eigenstates are (or, in case of degeneracies, can be chosen to have) parity ± 1 with respect to a flip of sites u and v . Thus, they fulfill Eq. (7), so that u and v are cospectral. Provided that states of negative and positive parity are nondegenerate to each other, they additionally fulfill Eq. (8), so that u and v are even strongly cospectral. While the fact that a permutation symmetry of u and v leads to their (strong) cospectrality should be no surprise, things change when inspecting the graphs shown in Fig. 3. While they indeed all have cospectral vertices u and v , none of them is invariant under any nontrivial permutation of vertices. In other words, the underlying Hamiltonian does not commute with the corresponding permutation matrices. However, due to cospectrality their eigenstates fulfill *the same equation* Eq. (7) [and, depending on degeneracies, also Eq. (8)] as they would do in the presence of a permutation symmetry. For this reason, graphs (or, just as well, matrices) whose eigenstates fulfill Eqs. (7) and (8) (and which need not have any permutation symmetries) were recently termed *latently symmetric* [21,22]. However, although these symmetries may indeed seem hidden, we would like to mention here that all the graphs shown in Fig. 3 *indeed* feature *local symmetries*, i.e., symmetries within subdomains of the system, such that the underlying symmetry operations commute with the Hamiltonian of the subsystem, but not with that of the complete one. An example is the subsystem of sites 2, 3, 4 in Fig. 3(a1), which is invariant under the permutation of sites 2 and 4. Given the high number of local symmetries in latently symmetric setups, it would be interesting to investigate such systems under the recently established framework of local symmetries [23–28], which provides dedicated tools for the analysis of such setups.

As a concluding remark, we note that there are still many open questions regarding the connection between local symmetries of a Hamiltonian \mathbf{H} and the cospectrality of two sites u and v of \mathbf{H} . Given such a Hamiltonian, it is clear that the subsystem $\mathbf{H}_{SS} \in \mathbb{R}^{2 \times 2}$ with $S = \{u, v\}$ is invariant under the exchange of u and v , since \mathbf{H} is symmetric and cospectrality of u and v implies that $\mathbf{H}_{u,u} = \mathbf{H}_{v,v}$. However, it is yet unknown whether and to which amount \mathbf{H} must *necessarily* feature more (i.e., apart from that of \mathbf{H}_{SS}) local symmetries in order to allow for the cospectrality of u and v . Although the question about the necessity of local symmetries for cospectrality is thus still open, local symmetries often naturally appear during

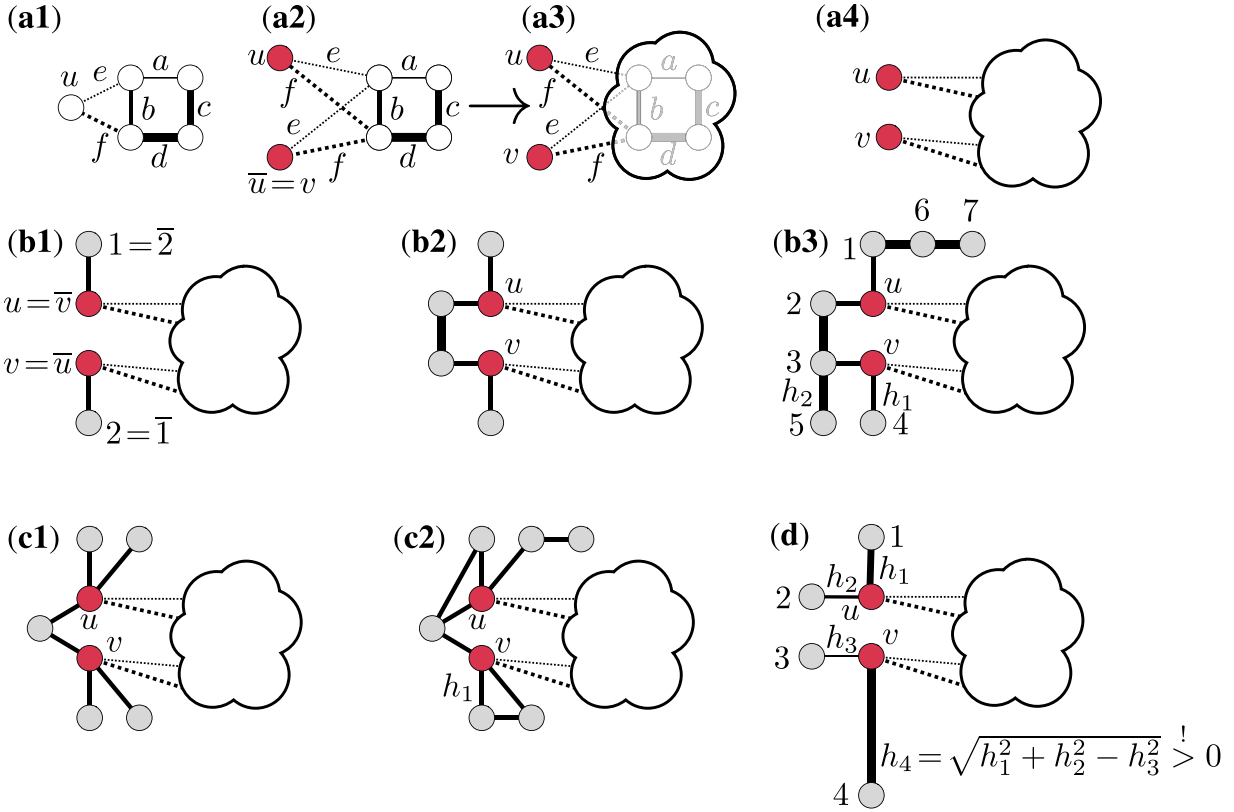


FIG. 4. Different procedures of generating graphs featuring cospectral vertices u and v . (a1) and (a2) Creation of a graph [as the one shown in (a2)] featuring cospectral vertices from an arbitrary graph [as the one shown in (a1)] by symmetrization of the site u . In (a3) we divide the given graph featuring cospectral sites u and v into two parts: The two red sites denoting u , v , and the remainder of the graph, denoted by a cloud. In the remainder of this figure, the combination of the two red sites u , v with a cloud denotes an arbitrary subsystem featuring cospectral vertices u and v . In (a4)–(d) we present a number of operations on such a general graph which preserve the cospectrality. The validity of these operations is proven in Appendix C. Notably, if one removes the cloud which depicts a larger subgraph from (b3), one gains the iconic graph that is shown in the first paper on cospectral vertices by Schwenk [36] and is also depicted in many publications related to cospectrality, for example in Refs. [14,22,35].

the process of designing networks with cospectral vertices, as we will see in the following section.

D. Designing graphs featuring strongly cospectral vertices

Let us now briefly recapitulate the above. We have seen that a necessary condition for PGST from u to v is strong cospectrality of these two vertices. This implies that u and v are cospectral, and we demonstrated that whether u and v are cospectral can be easily determined by testing whether $(\mathbf{H}^k)_{u,u} = (\mathbf{H}^k)_{v,v} \forall k < N$. We then showed how these matrix entries can in turn be determined by summing up the respective weights of all possible walks of length k from sites u and v to themselves. In the following we will show how one can *design* graphs featuring strongly cospectral vertices u and v . We will start with a simpler problem, namely, the design of graphs with cospectral vertices u and v , and then show how strong cospectrality can be achieved.

A convenient way to create a graph with cospectral vertices is to take any graph, and replicate and symmetrize one of its sites u , as shown in Figs. 4(a1)–4(a4). This symmetrization then automatically yields the cospectrality of site u and its symmetry partner $\bar{u} = v$ (see Fig. 4). This is due to the fact that the underlying Hamiltonian is invariant under an

exchange of u and v , which can easily be shown to imply cospectrality of these vertices.

Having seen how a graph can be changed to feature cospectral vertices u and v , let us now show some modifications of this graph which *keep the cospectrality*. The procedure is shown in Figs. 4(b1)–4(d), but let us elaborate more on Figs. 4(a1)–4(a3) first. Figures 4(a1) and 4(a2) show the above symmetrization procedure for a simple example setup of five sites. In Fig. 4(a3), the logic underlying Figs. 4(b1)–4(d) is shown. Namely, the cloud incorporates a subgraph which must be chosen such that the composite graph, consisting of this subgraph and the two red vertices, features cospectrality of these two red vertices. This subgraph can consist of the four vertices as shown in Fig. 4(a3), but can likewise be an arbitrarily complicated structure as long as the two red vertices u , v are cospectral in the composite structure. In Fig. 4(a4) we show a first composite structure. We then change it by a series of modifications in Figs. 4(b1)–4(b3), Figs. 4(c1) and 4(c2), and Fig. 4(d). Each of these modifications keeps the cospectrality of the two red vertices u , v , as we prove in Appendix C.

These modifications can be divided into two classes: Those where the subsystem \mathbf{H}_{RG} consisting of the two red sites u , v and the light gray sites is reflection symmetric about the

TABLE I. The results of an exhaustive search, where all $M_{\text{tot}}(N)$ graphs with unity-valued weights and with N vertices have been generated and further analyzed. Out of these $M_{\text{tot}}(N)$ graphs, the ones featuring permutation symmetries, have been excluded, and the remaining $M_{\text{na}}(N)$ graphs have been individually checked whether they contain at least two cospectral vertices. The total number $M_{\text{LS}}(N)$ of these graphs is then counted for every N . The generation and counting of the $M_{\text{tot}}(N)$ and $M_{\text{na}}(N)$ have been done by using the “nauty” suite [37], while we counted the graphs $M_{\text{LS}}(N)$ by means of a custom Mathematica routine. Technically, for each of the $M_{\text{na}}(N)$ graphs, we computed the matrix powers up to order $N - 1$, and by analyzing the diagonal entries of these powers checked if there are at least two cospectral vertices.

N	$M_{\text{tot}}(N)$	$M_{\text{na}}(N)$	$M_{\text{LS}}(N)$
8	11 117	3 552	78
9	261 080	131 452	2 247
10	11 716 571	7 840 396	78 489
11	1 006 700 565	797 524 380	3 714 397

horizontal axis, so that its sites i are transformed as $i \leftrightarrow \bar{i}$ [see Fig. 4(b1)] and those where there is no such symmetry. The graphs shown in Figs. 4(b1), 4(b2), and 4(c1) belong to the first class. The principle underlying this class of modifications is that, under the symmetry operation of a reflection of \mathbf{H}_{RG} about the horizontal axis, the two sites u and v are mapped onto each other. Due to this symmetry, they are trivially cospectral within \mathbf{H}_{RG} . As we show in Appendix C, their cospectrality is preserved also in the full system, where \mathbf{H}_{RG} is connected to the cloud. The graphs shown in Figs. 4(b3), 4(c2), and 4(d) belong to the second class. In these setups, the corresponding subgraph \mathbf{H}_{RG} is no longer symmetric at all. Nevertheless, the sites u and v are cospectral, and their cospectrality can readily be understood by evaluating the powers of \mathbf{H}_{RG} , as was done in Sec. II B.

While it is straightforward to show that two vertices u and v are cospectral in any given graph \mathbf{H} (such as the subgraphs \mathbf{H}_{RG} above), finding a systematic way to create graphs which (i) do not feature any permutation symmetries and (ii) nevertheless feature two cospectral vertices u and v is not easy. For this work, we have obtained such asymmetric cospectral graphs by systematically perturbing symmetric cospectral graphs (by adding nodes and/or modifying couplings), such that their permutation symmetries are broken while the cospectrality is kept. An alternative and more systematic way is to create databases of graphs with cospectral vertices. We have done so by systematically generating all $M_{\text{LS}}(N)$ unweighted (i.e., with all couplings being unity) graphs of N vertices that feature two cospectral vertices u, v , but no permutation symmetry. The obtained numbers are rather large and are given in Table I. This suggests that graphs with cospectral vertices are, by no means, a rare phenomenon. As the study of these graphs is still an emerging field, we expect that more construction principles for such graphs will be found in the near future. To help the reader and to spread the understanding of graphs with cospectral vertices, we developed a graphical MATLAB tool that allows us to design graphs and check for cospectrality of vertices in

an intuitive and fast way. This tool is available upon request from the authors.

Let us now come back to a statement about local symmetries, made in the last paragraph of Sec. II C. There we stated that local symmetries often occur naturally during the process of designing Hamiltonians featuring cospectral sites. We can now support this statement by looking at the graphs depicted in Figs. 4(b3) and 4(c2), both of which feature local symmetries. In Fig. 4(b3) the subgraph consisting of the sites $u, v, 1, 2, 3, 4$ is invariant under the permutation $1 \leftrightarrow 4, 2 \leftrightarrow 3, u \leftrightarrow v$. This local symmetry is caused by the way Fig. 4(b3) was constructed. Namely, by first making symmetric changes [performed in Figs. 4(b1) and 4(b2)] to the initial setup of Fig. 4(a4), and breaking them afterwards by performing another change, as done in Fig. 4(b3). The underlying symmetries present in Figs. 4(b1) and 4(b2) are then rendered to be local symmetries in Fig. 4(b3). A similar reasoning can be done for the setup depicted in Fig. 4(c2). Local symmetries can also occur accidentally, as we now show. To this end, we note that the graph in Fig. 4(d) was designed on purpose such that u and v are cospectral for arbitrary $h_1, h_2, h_3, h_4 > 0$. In particular, the h_i can be chosen asymmetrically, i.e., such that no any two couplings are identical. Yet, as a byproduct of this construction that aims at an asymmetric graph, the on-site potentials of the sites 1 to 4 must all have the same value in order to maintain cospectrality of u and v for arbitrary h_1, h_2, h_3, h_4 . As a result, the subgraph of sites 1,2,3,4 is invariant under the cyclic permutation $1 \rightarrow 2 \rightarrow 3 \rightarrow 4 \rightarrow 1$, representing an accidental local symmetry caused by cospectrality.

Having shown a method to create graphs featuring cospectral vertices, let us now comment on how these can be modified to achieve strong cospectrality. To this end, let us analyze Eqs. (7) and (8) which describe the conditions for cospectrality and strong cospectrality, respectively. From these two equations, it follows that whenever a Hamiltonian \mathbf{H} features two sites u and v which are cospectral but *not* strongly cospectral, \mathbf{H} must have degenerate eigenvalues. One can thus achieve strong cospectrality of u and v by suitably modifying \mathbf{H} such that (i) the cospectrality of u and v is kept and (ii) the spectrum of \mathbf{H} becomes nondegenerate. In other words, if we let $\mathbf{H}(\xi)$ denote a Hamiltonian with cospectral sites u and v for a set of N parameters $\xi \subseteq \mathbb{R}^N$ describing couplings and on-site potentials occurring in $\mathbf{H}(\xi)$, we look for subspaces $\xi' \subseteq \xi$ in which $\mathbf{H}(\xi')$ is nondegenerate. For the graph shown in Fig. 3(c), we have a six-dimensional parameter space

$$\xi = \{(h_1, h_2, h_3, h_4, E_{\text{red}}, E_{\text{gray}}) \in \mathbb{R}\},$$

where $E_{\text{red}}, E_{\text{gray}}$ denote the on-site potentials of the red (denoted by u and v) and light gray sites, respectively, and h_1 to h_4 label the four different couplings, which are denoted by four different line styles in Fig. 3(c). For a setup designed using the procedure demonstrated in this section, the parameter space ξ can be obtained as follows:

(1) Parametrize the couplings and on-site potentials occurring in $\mathbf{H}_{\text{cl}} = \mathbf{H}_{\text{cl}}(\xi_{\text{cl}})$, where \mathbf{H}_{cl} denotes the Hamiltonian describing the isolated cloud. For the graph depicted in Fig. 4(a3), we have

$$\xi_{\text{cl}} = \{(a, b, c, d, E_{\text{white}}) \in \mathbb{R}\}, \quad (9)$$

where E_{white} denotes the on-site potential of the white sites.

(2) Denote by ξ_{coupl} the parameter space for the symmetrized couplings from \mathbf{H}_{cl} to the sites u and v . For Fig. 4(a3) we have

$$\xi_{\text{coupl}} = \{(e, f) \in \mathbb{R}\}. \quad (10)$$

(3) Constrain the couplings and on-site potentials occurring in $\mathbf{H}_{\text{cl}} = \mathbf{H}_{\text{cl}}(\xi_{\text{cl}})$ such that u and v are cospectral within $\mathbf{H}_{\text{cl}}(\xi_{\text{cl}})$. Here \mathbf{H}_{cl} denotes the Hamiltonian describing the setup *without* the cloud. For graphs designed using Fig. 4, we explicitly have

$$\xi_{\text{cl}} = \begin{cases} \{E_r \in \mathbb{R}\} & \text{Fig. 4(a3),} \\ \{(E_r, E_g, h_1, h_2) \in \mathbb{R}\} & \text{Fig. 4(b3),} \\ \{(E_r, E_g, h_1) \in \mathbb{R}\} & \text{Fig. 4(c2),} \\ \{(E_r, E_g, h_1, h_2, h_3) \in \mathbb{R} : h_4 > 0\} & \text{Fig. 4(d),} \end{cases}$$

where E_r, E_g denote the on-site potentials of the red (denoted by u, v) and light gray sites, respectively.

(4) Construct ξ from $\xi_{\text{cl}}, \xi_{\text{coupl}}$, and ξ_{cl} as

$$\xi = \xi_{\text{cl}} \cup \xi_{\text{coupl}} \cup \xi_{\text{cl}} \quad (11)$$

so that the dimension of ξ is equal to the sum of dimensions of $\xi_{\text{cl}}, \xi_{\text{coupl}}$, and ξ_{cl} . For Fig. 4(a3) we yield

$$\xi = \{(a, b, c, d, e, f, E_{\text{white}}, E_r) \in \mathbb{R}\}.$$

E. Relating the spectral condition to minimal polynomials

As explained in Sec. II A, PGST between u and v happens if and only if u and v are strongly cospectral and the spectrum meets the conditions Eqs. (2) to (4). In the previous section we showed that designing a strongly cospectral graph is straightforward. On the other hand, meeting the spectral requirements remains a difficult task. Nevertheless, in a recent paper [14] by Eisenberg *et al.*, this task has been rendered simpler. They showed that Eqs. (2) to (4) are *automatically* fulfilled, provided that the polynomials P_{\pm} (defined below) are irreducible over the base field F (which contains all the entries of \mathbf{H}) and fulfill

$$\frac{\text{Tr}(P_+)}{\deg(P_+)} \neq \frac{\text{Tr}(P_-)}{\deg(P_-)}, \quad (12)$$

where $\text{Tr}(P_{\pm})$ denote the sum of roots of P_{\pm} , and $\deg(P_{\pm})$ denote their respective degree. The polynomials P_{\pm} stem from a decomposition of the characteristic polynomial of \mathbf{H} . More specifically, given a Hamiltonian \mathbf{H} with two strongly cospectral sites u and v , its characteristic polynomial P can be decomposed [14] as

$$P = P_0 P_+ P_-, \quad (13)$$

such that P_+ and P_- have no multiple roots, do not share any roots, and where the polynomials P_{\pm} are related to eigenvectors of \mathbf{H} which are (i) nonvanishing on sites u and v and (ii) are of positive/negative parity on these sites, respectively. Each root of P_0 with multiplicity k is related to exactly k eigenvectors of \mathbf{H} , all of which have vanishing amplitudes on u and v . The problem of fulfilling the spectral condition for PGST thus boils down to tuning the polynomials P_{\pm} accordingly. There are two possible routes to achieve this, an indirect and a direct one. In the indirect route, the properties of the polynomials P_{\pm} are controlled by applying certain changes to the underlying Hamiltonian that cause P_{\pm} to be irreducible

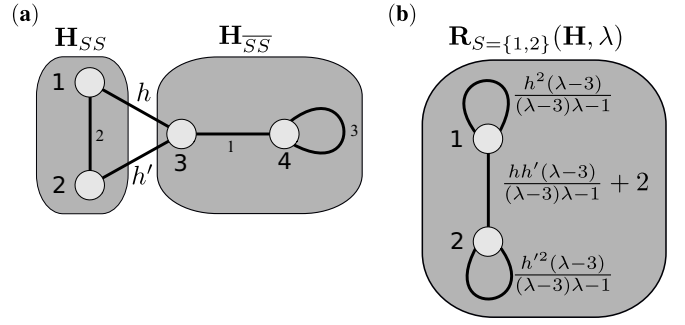


FIG. 5. (a) Original graph \mathbf{H} , and its decomposition into \mathbf{H}_{SS} and $\mathbf{H}_{\overline{S}\overline{S}}$, where $S = \{1, 2\}$. (b) The isospectral reduction $\mathbf{R}_S(\mathbf{H}, \lambda)$ of the graph \mathbf{H} over S .

over F and meet Eq. (12), but P_{\pm} are not directly known. Such a method has been presented in Ref. [14], where several such mechanisms have been shown. In particular, the method shown there starts from a graph with cospectral vertices and selectively adds transcendental numbers to some diagonal entries of \mathbf{H} , such that the modified setup features PGST. While elegant and powerful, indirect methods do not provide explicit forms of the polynomials P_{\pm} . This limits the ability to understand under which circumstances the underlying setup might feature PGST.

In cases where \mathbf{H} features an involutory permutation symmetry σ , i.e., $[H, \sigma] = 0$ with $\sigma^2 = I$, the Hamiltonian can be block diagonalized [15] to obtain P_{\pm} . An example for such an involutory symmetry is any permutation that does only pairwise permutations of two indices, such as $\mathbb{S} : 1 \leftrightarrow 2$ (acting as the identity on indices 3 and 4) for the graph in Fig. 2. Unfortunately, this approach is not applicable to setups that do not invoke such permutation symmetries, such as all graphs in Fig. 3.

In the following we will present a method to create PGST that relies on the recently introduced isospectral reduction of \mathbf{H} . This method and the transfer of compact localized states, as presented in Sec. IV, are the two highlights of our work. Once the polynomials are obtained, proper tuning of parameters allows us to meet the requirements for PGST.

1. Isospectral reductions

We first provide some key aspects of isospectral reductions [16–20,22], introduced first by Bunimovich and Webb [16]. This concept will allow us to extract the polynomials P_{\pm} . Our explanations will be accompanied by the illustration in Fig. 5.

The basic idea of isospectral reductions is to reduce the dimension of a given matrix Hamiltonian \mathbf{H} by certain transformations specified by a set of sites S , yielding a smaller matrix $\mathbf{R}_S(\mathbf{H}, \lambda)$ dependent on a parameter λ , which carries the same or almost the same spectral information as the original matrix \mathbf{H} . Among others, the benefit of such a reduction lies in a reduction of complexity. For this reason, the isospectral reduction has been invented in the context of network analysis, where the sheer size of the investigated networks often complicates their treatment. Let us now define the isospectral reduction of a given matrix \mathbf{H} . This reduction

$\mathbf{R}_S(\mathbf{H}, \lambda)$ is done over the set of sites S , so that

$$\mathbf{R}_S(\mathbf{H}, \lambda) = \mathbf{H}_{SS} - \mathbf{H}_{S\bar{S}}(\mathbf{H}_{\bar{S}\bar{S}} - \mathbf{I}\lambda)^{-1}\mathbf{H}_{\bar{S}S} \quad (14)$$

and is defined for all values of λ that are not eigenvalues of $\mathbf{H}_{\bar{S}\bar{S}}$, where \bar{S} denotes the complement of the set of vertices S . \mathbf{H}_{SS} and $\mathbf{H}_{\bar{S}\bar{S}}$ denote two subsystems of \mathbf{H} , obtained from \mathbf{H} by deleting all sites in \bar{S} or S , respectively. $\mathbf{H}_{S\bar{S}} = (\mathbf{H}_{\bar{S}S})^T$ are the submatrices which couple \mathbf{H}_{SS} to $\mathbf{H}_{\bar{S}\bar{S}}$ and $\mathbf{H}_{\bar{S}\bar{S}}$ to \mathbf{H}_{SS} , respectively. The dimension of $\mathbf{R}_S(\mathbf{H}, \lambda)$ is given by $|S|$, i.e., the number of sites over which \mathbf{H} is isospectrally reduced. Such a decomposition is shown in Fig. 5(a). In Fig. 5(b) we then show the isospectral reduction of the graph in Fig. 5(a) over the sites $S = \{1, 2\}$.

A major goal of the isospectral reduction is to reduce the size of the problem, while maintaining (almost) all of its spectral features. It may seem that such a reduction is impossible, since, by the fundamental theorem of algebra, a Hermitian matrix $\mathbf{H} \in \mathbb{C}^{N \times N}$ has exactly N eigenvalues. A reduced version $\mathbf{H}' \in \mathbb{C}^{|S| \times |S|}$, $|S| < N$ would, therefore, inevitably have $N - |S|$ less eigenvalues. However, the above is not necessarily true anymore if the entries of \mathbf{H}' are not just constant real or complex numbers, but functions of a parameter λ , i.e., $\mathbf{H}' = \mathbf{H}'(\lambda)$. The so-called nonlinear eigenvalues of \mathbf{H}' are then given by solving the nonlinear eigenvalue equation

$$\mathbf{H}'(\lambda)\mathbf{x} = \lambda\mathbf{x} \quad (15)$$

for λ , where \mathbf{x} is called the nonlinear eigenvector. For the isospectral reduction, we have $\mathbf{H}'(\lambda) = \mathbf{R}_S(\mathbf{H}, \lambda)$, and the nonlinear eigenvalues of $\mathbf{R}_S(\mathbf{H}, \lambda)$ are thus found by solving

$$\det[\mathbf{R}_S(\mathbf{H}, \lambda) - \mathbf{I}\lambda] = 0. \quad (16)$$

It can be shown that the set of nonlinear eigenvalues of $\mathbf{R}_S(\mathbf{H}, \lambda)$ is equal to the set of all eigenvalues of \mathbf{H} , except those which are also eigenvalues of $\mathbf{H}_{\bar{S}\bar{S}}$. Thus, if \mathbf{H} and $\mathbf{H}_{\bar{S}\bar{S}}$ do not share any eigenvalues, the spectrum $\sigma[\mathbf{R}_S(\mathbf{H}, \lambda)]$ is identical with that of \mathbf{H} , i.e., $\sigma[\mathbf{R}_S(\mathbf{H}, \lambda)] = \sigma(\mathbf{H})$, as desired.

From Eq. (15) we get that the nonlinear eigenvectors $\{\mathbf{v}_1, \dots, \mathbf{v}_n\}$ of $\mathbf{R}_S(\mathbf{H}, \lambda)$, where n is the number of nonlinear eigenvalues of $\mathbf{R}_S(\mathbf{H}, \lambda)$, fulfill

$$\mathbf{H}'(\lambda_i)\mathbf{x}_i = \mathbf{R}_S(\mathbf{H}, \lambda_i)\mathbf{v}_i = \lambda_i\mathbf{v}_i.$$

Importantly, the set of nonlinear eigenvectors $\{\mathbf{v}_i\}$ does not need to be pairwise orthogonal, and could even be linearly dependent or pairwise identical. In the context of isospectral reductions, the importance of these nonlinear eigenvectors stems from the fact that they can be linked [20,38] to the eigenvectors of \mathbf{H} . Namely, every nonlinear eigenvector $\mathbf{v}_i \in \mathbb{R}^{|S| \times 1}$ of $\mathbf{R}_S(\mathbf{H}, \lambda)$ with nonlinear eigenvalue λ_i is, up to normalization, the *projection* of the corresponding eigenvector $\mathbf{V}_i \in \mathbb{R}^{N \times 1}$ of $\mathbf{H} \in \mathbb{R}^{N \times N}$ onto the sites S . In other words,

$$\mathbf{v}_i = k_i(\mathbf{V}_i)_S \in \mathbb{R}^{|S| \times 1}, \quad (17)$$

where k_i is a normalization constant, $\mathbf{H}\mathbf{V}_i = \lambda_i\mathbf{V}_i$, and $|S|$ denotes the number of elements in S .

2. Extracting the polynomials P_{\pm} through isospectral reductions

In order to use the isospectral reduction to extract the polynomials P_{\pm} , we will rely on a recently proven theorem from Ref. [22]. This theorem states that for symmetric matrices \mathbf{H} ,

the isospectral reduction $\mathbf{R}_S(\mathbf{H}, \lambda)$ over two sites $\{u, v\} = S$ is bisymmetric if and only if u and v are cospectral in \mathbf{H} . Moreover, u and v are strongly cospectral if and only if they are cospectral and all nonlinear eigenvalues of $\mathbf{R}_S(\mathbf{H}, \lambda)$ are simple. This theorem is remarkable, as it connects the two seemingly unrelated concepts of cospectrality and isospectral reductions.

To give an intuitive argument for why this theorem makes sense, we show how cospectrality of u and v follows from bisymmetry of $\mathbf{R}_{S=\{u,v\}}(\mathbf{H}, \lambda)$ for the simple case when $\sigma(\mathbf{H}) = \sigma[\mathbf{R}_S(\mathbf{H}, \lambda)]$. In this case, each nonlinear eigenvector \mathbf{v}_i of $\mathbf{R}_S(\mathbf{H}, \lambda)$ is the projection of the corresponding eigenvector \mathbf{V}_i of \mathbf{H} on the sites S . Now, as can be easily shown, the nonlinear eigenvectors of $\mathbf{R}_S(\mathbf{H}, \lambda)$ have (in the case of degeneracies, can be chosen to have) parity ± 1 on u and v if and only if $\mathbf{R}_S(\mathbf{H}, \lambda)$ is bisymmetric. Therefore, the eigenvectors $\{\mathbf{V}_i\}$ of \mathbf{H} fulfill Eq. (7), i.e., sites u, v are cospectral due to the bisymmetry of $\mathbf{R}_S(\mathbf{H}, \lambda)$. If, additionally, all nonlinear eigenvalues of $\mathbf{R}_S(\mathbf{H}, \lambda)$ are simple, the $\{\mathbf{V}_i\}$ also fulfill Eq. (8), i.e., $(\mathbf{V}_i)_u = \pm(\mathbf{V}_i)_v$.

We now use the connection between cospectrality and bisymmetry of $\mathbf{R}_{S=\{u,v\}}(\mathbf{H}, \lambda)$ to extract P_{\pm} . To this end, we assume that u and v are strongly cospectral. By Theorem 3.8. from Ref. [22], $\mathbf{R}_S(\mathbf{H}, \lambda)$ is then bisymmetric, and all its nonlinear eigenvalues are simple. Due to its bisymmetry, we can parametrize

$$\mathbf{R}_S(\mathbf{H}, \lambda) = \begin{pmatrix} A(\lambda) & B(\lambda) \\ B(\lambda) & A(\lambda) \end{pmatrix}, \quad (18)$$

with $A(\lambda), B(\lambda)$ being rational functions of λ . As we have explained above, all nonlinear eigenvectors of $\mathbf{R}_S(\mathbf{H}, \lambda)$ are (in the case of degeneracies, can be chosen to be) of definite parity on u and v . Therefore, the characteristic polynomial $P_{\mathbf{R}}(\lambda)$ of $\mathbf{R}_S(\mathbf{H}, \lambda)$ can be factored into two parts, $P_{\mathbf{R}} = P_{\mathbf{R}}^+(\lambda)P_{\mathbf{R}}^-(\lambda)$, such that the roots of the polynomials $P_{\pm}(\lambda)$ are the nonlinear eigenvalues of nonlinear eigenvectors of $\mathbf{R}_S(\mathbf{H}, \lambda)$ with positive and negative parity, respectively. As we show in Appendix D, $P_{\mathbf{R}}^{\pm} = A(\lambda) \pm B(\lambda) - \lambda$. They obey the relation

$$P_{\mathbf{R}}^+(\lambda)P_{\mathbf{R}}^-(\lambda) = \det(\mathbf{R}_S(\mathbf{H}, \lambda) - \mathbf{I}\lambda) = \frac{\det(\mathbf{H} - \mathbf{I}\lambda)}{\det(\mathbf{H}_{\bar{S}\bar{S}} - \mathbf{I}\lambda)},$$

where the first equality is proven in Appendix D, and the second on p. 7 in Ref. [18].

There are now two possible scenarios for which the polynomials $P_{\pm}(\lambda)$ can be obtained. In the first scenario, \mathbf{H} and $\mathbf{H}_{\bar{S}\bar{S}}$ must not share any eigenvalues. In that case, all eigenvalues of \mathbf{H} are given by the union of roots of $P_{\mathbf{R}}^{\pm}(\lambda)$, and by the above assumption of strong cospectrality of u and v , all these eigenvalues are nondegenerate. Combining these properties, we see that *all* eigenvectors of \mathbf{H} do not vanish [39] on the sites u and v , and the corresponding amplitudes on these two sites are of definite parity with respect to exchanging u and v . Thus, $P_0(\lambda) = 1$ [from the decomposition of the characteristic polynomial of \mathbf{H} , as done in Eq. (13)], and we get

$$P(\lambda) = P_+(\lambda)P_-(\lambda),$$

where $P(\lambda) = \det(\mathbf{H} - \mathbf{I}\lambda)$ is the characteristic polynomial of \mathbf{H} . The $P_{\mathbf{R}}^{\pm} \equiv p_{\pm}/q_{\pm}$ are rational functions in λ , so that

$$P_{\mathbf{R}}^+(\lambda)P_{\mathbf{R}}^-(\lambda) = \frac{p_+(\lambda)}{q_+(\lambda)} \frac{p_-(\lambda)}{q_-(\lambda)} = \frac{\det(\mathbf{H} - \mathbf{I}\lambda)}{\det(\mathbf{H}_{\overline{SS}} - \mathbf{I}\lambda)}, \quad (19)$$

where $p_{\pm}(\lambda)$, $q_{\pm}(\lambda)$ and both determinants are polynomials in λ . Since

$$\det(\mathbf{H} - \mathbf{I}\lambda) = P(\lambda) = P_+(\lambda)P_-(\lambda),$$

it would be ideal if the numerators in Eq. (19) match, so that $p_{\pm}(\lambda) = P_{\pm}(\lambda)$. However, since Eq. (19) remains invariant under the transformation

$$p_{\pm}(\lambda) \rightarrow c_{\pm}(\lambda)p_{\pm}(\lambda), \quad (20)$$

$$q_{\pm}(\lambda) \rightarrow c_{\pm}(\lambda)q_{\pm}(\lambda), \quad (21)$$

with $c_{\pm}(\lambda)$ functions of λ , the $p_{\pm}(\lambda)$ are not uniquely determined by Eq. (19) alone. To uniquely determine $P_{\pm}(\lambda)$, one needs to properly reduce the fractions $p_{\pm}(\lambda)/q_{\pm}(\lambda)$ [i.e., performing the transformations of Eqs. (20) and (21) with suitable $c_{\pm}(\lambda)$] such that the following conditions are fulfilled. First, the leading-order coefficients $a_{n_{\pm}}^{(\pm)}$ of the polynomials

$$p_+(\lambda) = \sum_{n=0}^{n_+} a_n^{(+)} \lambda^n, \quad p_-(\lambda) = \sum_{n=0}^{n_-} a_n^{(-)} \lambda^n,$$

where n_{\pm} are the respective degrees of $p_{\pm}(\lambda)$, must be chosen such that

$$a_{n_+}^{(+)} = 1, \quad a_{n_-}^{(-)} = (-1)^N,$$

where N is the dimension of $\mathbf{H} \in \mathbb{R}^{N \times N}$. This ensures that the product of $p_+(\lambda)p_-(\lambda)$ has a leading order coefficient of $(-1)^N$, which matches the leading order coefficient of $\det(\mathbf{H} - \mathbf{I}\lambda)$. Second, the fractions $p_{\pm}(\lambda)/q_{\pm}(\lambda)$ must be *irreducible*. The latter property means that $p_+(\lambda)$, $q_+(\lambda)$ [and also $p_-(\lambda)$, $q_-(\lambda)$] are coprime, i.e., their only common factor is unity. If the above two conditions are fulfilled, we obtain

$$P_{\pm}(\lambda) = p_{\pm}(\lambda)$$

as desired.

The second scenario where $P_{\pm}(\lambda)$ can be obtained is when all eigenvectors \mathbf{x}'_i of \mathbf{H} which are related to common eigenvalues λ'_i of both \mathbf{H} and $\mathbf{H}_{\overline{SS}}$ vanish on S . The polynomial $P_0(\lambda)$ from Eq. (13) then becomes

$$P_0(\lambda) = \prod_i (\lambda'_i - \lambda) \quad (22)$$

and we can factorize

$$\begin{aligned} \det(\mathbf{H} - \mathbf{I}\lambda) &= \left(\prod_i (\lambda_i - \lambda) \right) \left(\prod_i (\lambda'_i - \lambda) \right), \\ \det(\mathbf{H}_{\overline{SS}} - \mathbf{I}\lambda) &= \left(\prod_i (\lambda'_i - \lambda) \right) \left(\prod_i (\lambda''_i - \lambda) \right), \end{aligned} \quad (23)$$

where λ''_i are the eigenvalues of $\mathbf{H}_{\overline{SS}}$ which are not simultaneously eigenvalues of \mathbf{H} . As a result of Eqs. (13), (22),

and (23),

$$\prod_i (\lambda_i - \lambda) = P_+(\lambda)P_-(\lambda)$$

and similarly to Eq. (19) we obtain

$$P_{\mathbf{R}}^+(\lambda)P_{\mathbf{R}}^-(\lambda) = \frac{p_+(\lambda)}{q_+(\lambda)} \frac{p_-(\lambda)}{q_-(\lambda)} = \frac{\prod_i (\lambda_i - \lambda)}{\prod_i (\lambda''_i - \lambda)}.$$

If the fractions $p_{\pm}(\lambda)/q_{\pm}(\lambda)$ are properly reduced as above, we again have that

$$P_{\pm}(\lambda) = p_{\pm}(\lambda).$$

The isospectral reduction can thus be used to extract the polynomials P_{\pm} provided that (i) \mathbf{H} and $\mathbf{H}_{\overline{SS}}$ do not share a common root, or (ii) all common roots of \mathbf{H} and $\mathbf{H}_{\overline{SS}}$ are related to eigenvectors of \mathbf{H} which vanish on S . In the next section we show how this knowledge can be harnessed to design Hamiltonians featuring PGST.

III. APPLICATION: DESIGNING GRAPHS WITH PRETTY GOOD STATE TRANSFER

In Sec. II we have introduced the concept of cospectrality and have shown how, based on the isospectral reduction, the polynomials P_{\pm} can be extracted. With this theoretical background, one can derive the following algorithm for the design of graphs with PGST.

(1) Achieving cospectrality

Design/take a graph $\mathbf{H}(\xi)$ with cospectral vertices u and v , e.g., by means of the procedure demonstrated in Sec. II D. Here ξ denotes the parameter space of couplings and on-site potentials occurring in \mathbf{H} for which u and v are cospectral and for which there exists at least one possible walk from u to v .

(2) Achieving strong cospectrality

Due to cospectrality of u and v for all $\mathbf{H}(\xi)$, the isospectral reduction

$$\mathbf{R}_{S=\{u,v\}}(\mathbf{H}(\xi), \lambda) = \begin{pmatrix} A(\xi, \lambda) & B(\xi, \lambda) \\ B(\xi, \lambda) & A(\xi, \lambda) \end{pmatrix}$$

of $\mathbf{H}(\xi)$ over $S = \{u, v\}$ [with rational functions $A(\xi, \lambda)$, $B(\xi, \lambda)$] is, by Theorem 3.3 from Ref. [22], guaranteed to be bisymmetric. Compute

$$P_{\mathbf{R}}^{\pm}(\xi, \lambda) = A(\xi, \lambda) \pm B(\xi, \lambda) - \lambda \equiv \frac{p_{\pm}(\xi, \lambda)}{q_{\pm}(\xi, \lambda)},$$

and, by suitable algorithms (see Sec. III A), find a subspace $\xi' \subseteq \xi$ for which $P_{\mathbf{R}}^{\pm}(\xi', \lambda)$ individually have only simple roots, and additionally have no common roots. By Theorem 3.8 from Ref. [22], u and v are then strongly cospectral.

(3) Extraction of P_{\pm}

By suitable algorithms (see Sec. III A), either

(a) further restrict ξ' such that $\mathbf{H}(\xi')$ and $\mathbf{H}_{\overline{SS}}(\xi')$ do not share any eigenvalues,

(b) or, alternatively, restrict ξ' such that all eigenvalues λ'_i shared by $\mathbf{H}(\xi')$ and $\mathbf{H}_{\overline{SS}}(\xi')$ are related to eigenvectors of $\mathbf{H}(\xi')$ which vanish on S .

In both cases, properly reduce (or expand) the fractions occurring in $P_{\mathbf{R}}^{\pm}(\xi', \lambda)$ such that

(a) the leading order coefficients of $p_{\pm}(\xi', \lambda)$ (which are polynomials in λ) are $+1$ and $(-1)^N$, respectively, where N is the dimension of $\mathbf{H} \in \mathbb{R}^{N \times N}$,

(b) $p_{\pm}(\xi', \lambda)/q_{\pm}(\xi', \lambda)$ are irreducible.

As a result $P_{\pm}(\xi', \lambda) = p_{\pm}(\xi', \lambda)$.

(4) **Enforcing pretty good state transfer**

Within the subspace ξ' , search (see Sec. III A) for realizations $\xi'' \subseteq \xi'$ such that

(a) $P_{\pm}(\xi'', \lambda)$ are irreducible over the base field F which contains all entries of $\mathbf{H}(\xi'')$.

(b) $\frac{\text{Tr}[P_{\pm}(\xi'', \lambda)]}{\text{deg}[P_{\pm}(\xi'', \lambda)]} \neq \frac{\text{Tr}[P_{\pm}(\xi', \lambda)]}{\text{deg}[P_{\pm}(\xi', \lambda)]}$.

$\mathbf{H}(\xi'')$ then features PGST from u to v . We note that $\text{Tr}[P_{\pm}(\xi'', \lambda)]$ can be computed without finding the roots of these polynomials, since $\text{Tr}[f(x)] = -a_{n-1}/a_n$ for a polynomial $f(x) = \sum_{i=0}^n a_i x^i$ of degree n .

(5) **Repetition (if necessary)**

Since not every graph may support PGST, the above procedure is not guaranteed to work in all cases (see Sec. III A for details). Thus, if step 4 is not successful, i.e., no parameters ξ'' exist such that $P_{\pm}(\xi'', \lambda)$ fulfill steps 4(a) and 4(b), go back to step 3 and try its alternative route. If this, again, is not successful, go back to step 1, modify the graph by adding/removing vertices, and start anew.

A. Annotations

Let us now make two comments regarding the above algorithm. First, steps 2 to 4 require the search for suitable subspaces, which in general must be performed by means of suitable trial-and-error algorithms. However, the subspace $\xi' \subseteq \xi$ (the search for which is the subject of steps 2 and 3 of the algorithm) can in some cases be given by explicit expressions, as we demonstrate in Sec. III B. Second, not all setups may support PGST, and the above algorithm is therefore not guaranteed to work in all cases. However, we have successfully tested the algorithm with a variety of setups, and among others, all six graphs depicted in Fig. 3 were successfully tuned to support PGST between the two red sites.

Overall, we stress that the main advantage of our algorithm, compared to existing methods for the design of PGST, is the ability to derive *explicit* forms for the polynomials P_{\pm} . We hope that the insights gained on how to extract the polynomials P_{\pm} will lead to a better understanding on the classes of setups which support PGST. This understanding is facilitated by the fact that the core method of our approach, the isospectral reduction $\mathbf{R}_{S=\{u,v\}}(\mathbf{H}(\xi), \lambda)$, can be performed symbolically. As we will see in the next section, in some cases, nearly all steps of the algorithm can be done without numerical evaluations at all.

B. Example

We now apply the algorithm presented above to a simple example, depicted in Fig. 6(a), and will go separately through each of the steps 1 to 4.

1. Achieving cospectrality

We start the algorithm with the graph shown in Fig. 6(a), which represents a very simple graph featuring cospectral

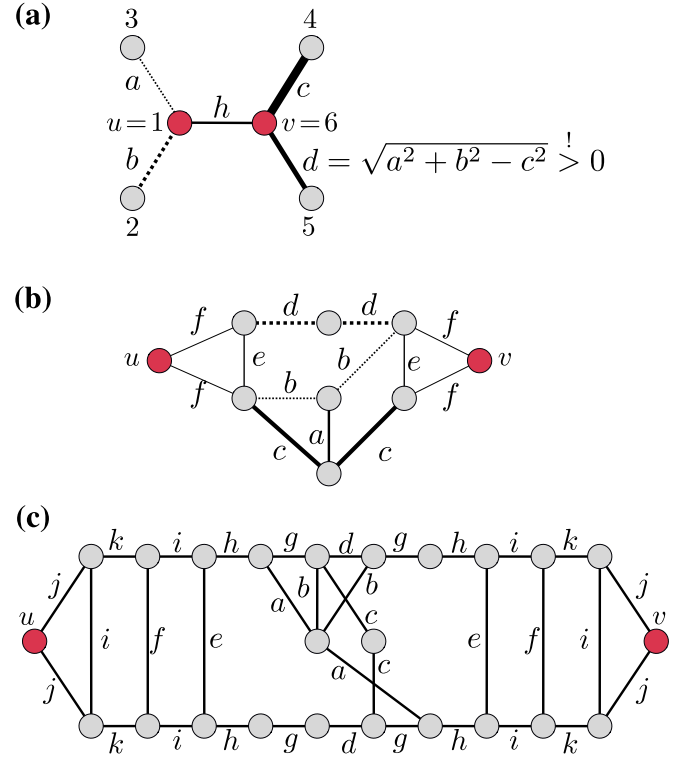


FIG. 6. (a)–(c) Three setups which can, by means of our algorithm, be tuned to feature PGST between the two red vertices labeled u and v . In all figures, u and v are cospectral for any choice of on-site potentials and couplings, as long as (i) u and v have identical on-site potential, (ii) all light gray vertices have identical on-site potential, and (iii) all couplings denoted by the same letter [and in (a) and (b) also share the same line style] have the same value. Details on the application of our algorithm to these three setups are given in Sec. III B and Sec. III C.

vertices u and v . The graph is described by

$$\mathbf{H}(\xi) = \begin{pmatrix} E_r & b & a & 0 & 0 & h \\ b & E_g & 0 & 0 & 0 & 0 \\ a & 0 & E_g & 0 & 0 & 0 \\ 0 & 0 & 0 & E_g & 0 & c \\ 0 & 0 & 0 & 0 & E_g & d \\ h & 0 & 0 & c & d & E_r \end{pmatrix}, \quad (24)$$

where $d = \sqrt{a^2 + b^2 - c^2}$,

$$\xi = \{(a, b, c, h, E_r, E_g) \in \mathbb{R} : d > 0 \text{ and } (a, b, c, h) \neq 0\},$$

and E_r, E_g denote the on-site potentials of the red (denoted by u, v) and light gray sites, respectively. The red sites $u = 1$ and $v = 6$ are then guaranteed to be cospectral for the Hamiltonian $\mathbf{H}(\xi)$.

The form of $d = \sqrt{a^2 + b^2 - c^2}$ is chosen such as to ensure cospectrality of u and v within a large parameter space. For example, for $a = b = c$, \mathbf{H} would be invariant under the exchange $3 \leftrightarrow 4, 2 \leftrightarrow 5, 1 \leftrightarrow 6$, so that $u = 1$ and $v = 6$ would trivially be cospectral. However, our choice of $d = \sqrt{a^2 + b^2 - c^2} > 0$ ensures this cospectrality even for asymmetric cases such as $a = 2b = 4c$, where \mathbf{H} is not invariant under any nontrivial permutation of sites.

2. Achieving strong cospectrality

The isospectral reduction of $\mathbf{H}(\xi)$ over $S = \{u, v\}$ then gives

$$\mathbf{R}_{S=\{u,v\}}[\mathbf{H}(\xi), \lambda] = \begin{pmatrix} \frac{\delta}{\lambda - E_g} + E_r & h \\ h & \frac{\delta}{\lambda - E_g} + E_r \end{pmatrix},$$

where $\delta = a^2 + b^2$, so that

$$P_{\mathbf{R}}^+(\xi, \lambda) = \frac{\delta}{\lambda - E_g} + h - \lambda + E_r,$$

$$P_{\mathbf{R}}^-(\xi, \lambda) = \frac{\delta}{\lambda - E_g} - h - \lambda + E_r.$$

Following the procedure of the algorithm, we now have to investigate (i) under which circumstances all roots of $P_{\mathbf{R}}^{\pm}(\xi, \lambda)$ are simple and (ii) under which conditions $P_{\mathbf{R}}^+(\xi, \lambda)$ and $P_{\mathbf{R}}^-(\xi, \lambda)$ do not share any roots. Since

$$P_{\mathbf{R}}^+(\xi, \lambda) = \frac{-E_g(h - \lambda + E_r) + \lambda(h - \lambda) + \delta + \lambda E_r}{\lambda - E_g}, \quad (25)$$

$$P_{\mathbf{R}}^-(\xi, \lambda) = \frac{E_g(h + \lambda - E_r) - \lambda(h + \lambda) + \delta + \lambda E_r}{\lambda - E_g} \quad (26)$$

are rational functions in λ , we define the corresponding numerators and denominators as $p_{\pm}(\xi, \lambda)$ and $q_{\pm}(\xi, \lambda)$. Since the $p_+(\xi, \lambda)$, $q_+(\xi, \lambda)$ and $p_-(\xi, \lambda)$, $q_-(\xi, \lambda)$ could in principle share roots, we need to evaluate when this can happen. To this end, we can use the so-called *resultant* [40]. Two given polynomials $f(x)$ and $g(x)$ share at least one root if and only if their resultant $R(f, g)$ is zero. The resultant, defined in terms of the so-called Sylvester matrix, can be computed symbolically and is implemented in common computer algebra systems. For the problem at hand, we yield

$$R[p_+(\xi, \lambda), q_+(\xi, \lambda)] = R[p_-(\xi, \lambda), q_-(\xi, \lambda)] = \delta, \quad (27)$$

which can obviously never vanish, since $\delta = a^2 + b^2$ and we demanded that $a, b \in \mathbb{R}$ and $a, b \neq 0$. Thus, we can evaluate the roots of $P_{\mathbf{R}}^{\pm}(\xi, \lambda)$ by evaluating only their numerators $p_{\pm}(\xi, \lambda)$.

To check whether $p_+(\xi, \lambda)$ and $p_-(\xi, \lambda)$ share any roots, we again rely on the resultant, which gives

$$R[p_+(\xi, \lambda), p_-(\xi, \lambda)] = 4h^2\delta > 0.$$

Thus, $p_+(\xi, \lambda)$ and $p_-(\xi, \lambda)$ will not share any roots. We then need to check when $p_+(\xi, \lambda)$ and $p_-(\xi, \lambda)$ individually have multiple roots. To this end, we compute their so-called *discriminant* [41]. The discriminant $D(f(x))$ of a polynomial $f(x)$ is zero if and only if $f(x)$ has at least one multiple root. Like the resultant, the discriminant can be computed analytically and is implemented in many computer algebra systems. We then get

$$D(p_{\pm}(\xi, \lambda)) = (E_g - E_r)(E_g \mp 2h - E_r) + h^2 + 4\delta.$$

$D(p_{\pm}(\xi, \lambda))$ can only vanish if $\delta = -\frac{1}{4}(E_g - E_r \mp h)^2 < 0$, which is again forbidden by our assumptions that $a, b \in \mathbb{R}$ and $a, b \neq 0$.

Let us now recapitulate the above. We have investigated under which conditions all roots of $\mathbf{R}_{S=\{u,v\}}[\mathbf{H}(\xi), \lambda]$ are simple. The motivation for this study is the fact that, whenever

this is the case, the sites u and v are not only cospectral, but also *strongly cospectral*. For the Hamiltonian given by Eq. (24), we have found that both of the above conditions are fulfilled for all elements in the parameter space ξ , so that $\xi' = \xi$, and u, v are always strongly cospectral in this Hamiltonian $\mathbf{H}(\xi)$. We can thus move on to the third step of our algorithm.

3. Extraction of P_{\pm}

Following the procedure of the algorithm, we now have to investigate under which circumstances $\mathbf{H}(\xi')$ and $\mathbf{H}_{\overline{SS}}(\xi')$ share eigenvalues. We therefore compute their resultant

$$R(\det[\mathbf{H}(\xi') - \mathbf{I}\lambda], \det[\mathbf{H}_{\overline{SS}}(\xi') - \mathbf{I}\lambda]) = 0. \quad (28)$$

Thus, $\mathbf{H}(\xi')$ and $\mathbf{H}_{\overline{SS}}(\xi')$ always share at least one eigenvalue. Indeed, closer evaluation shows that, irrespective of how ξ' is chosen, $\mathbf{H}(\xi')$ and $\mathbf{H}_{\overline{SS}}(\xi')$ share a twofold degenerate eigenvalue $\lambda = E_g$, with corresponding (unnormalized) eigenvectors $\mathbf{x}_1 = (0, 1, -b/a, 0, 0, 0)^T/\sqrt{4}$ and $\mathbf{x}_2 = (0, 0, 0, 1, -c/d, 0)^T/\sqrt{4}$. Both eigenvectors have zero amplitude on the sites $S = \{1, 6\}$, and by the reasoning in Sec. II E 2, the corresponding doubly degenerate eigenvalue E_g of $\mathbf{H}(\xi')$ is not of relevance to us. To see whether there are any other common eigenvalues of $\mathbf{H}(\xi')$ and $\mathbf{H}_{\overline{SS}}(\xi')$, we investigate the resultant

$$R\left(\frac{\det[\mathbf{H}(\xi') - \mathbf{I}\lambda]}{(\lambda - E_g)^2}, \frac{\det[\mathbf{H}_{\overline{SS}}(\xi') - \mathbf{I}\lambda]}{(\lambda - E_g)^2}\right) = \delta^4. \quad (29)$$

Since $\delta = a^2 + b^2 > 0$, $\mathbf{H}(\xi')$, $\mathbf{H}_{\overline{SS}}(\xi')$ do not share any other roots.

To extract $P_{\pm}(\xi', \lambda)$, we test whether $p_{\pm}(\xi', \lambda)$, given by the respective numerators of Eqs. (26) and (25), have leading order coefficients $+1$ and that $p_{\pm}(\xi', \lambda)/q_{\pm}(\xi', \lambda)$ are irreducible fractions. The latter is indeed the case, but the leading order coefficients are -1 . Thus, we have $P_{\pm}(\xi', \lambda) = -p_{\pm}(\xi', \lambda)$, and explicitly

$$P_+(\xi', \lambda) = E_g(h - \lambda + E_r) - \lambda(h - \lambda) - \delta - \lambda E_r,$$

$$P_-(\xi', \lambda) = -E_g(h + \lambda - E_r) + \lambda(h + \lambda) - \delta - \lambda E_r.$$

4. Enforcing pretty good state transfer

Inserting $P_{\pm}(\xi', \lambda)$ into Eq. (12) and simplifying the resulting inequality yields

$$\frac{2}{E_g - h + E_r} \neq \frac{2}{E_g + h + E_r}, \quad (30)$$

which is obviously fulfilled whenever $h \neq 0$. The only task left is to search for realizations $\xi'' \in \xi$ which render both $P_{\pm}(\xi'', \lambda)$ to be irreducible over the base field F which contains all entries of $\mathbf{H}(\xi'')$. If we choose (ξ'') such that $\mathbf{H}(\xi'') \in \mathbb{Q}^{6 \times 6}$, we have $F = \mathbb{Q}$, and one realization leading to PGST is

$$a = 1, \quad b = 2, \quad c = 1/4, \quad h = 1, \quad E_g = E_r = 0. \quad (31)$$

5. Comparison with an alternative treatment

As an alternative to applying our algorithm onto the simple setup of Fig. 6(a), one could also find exact conditions for the occurrence of both perfect and pretty good state transfer

by directly computing the eigenvalue spectrum and the corresponding eigenvectors. We will now do so for the case that $E_g = E_r = 0$.

For this case, one can obtain analytical expressions for the eigenvalues $\lambda_0 \cup \lambda_- \cup \lambda_+$ with

$$\lambda_0 = \{0, 0\}, \quad (32)$$

$$\lambda_- = \{-h \pm \sqrt{h^2 + 4\delta}\}, \quad (33)$$

$$\lambda_+ = \{h \pm \sqrt{h^2 + 4\delta}\}, \quad (34)$$

where δ as above and where the eigenvectors belonging to λ_0 identically vanish on u and v , and the eigenvectors belonging to λ_- (λ_+) are of negative (positive) parity on u and v . Evaluating the transfer amplitude

$$\langle u | e^{i\mathbf{H}t} | v \rangle = \sum_i [\langle u | \phi_i \rangle \langle \phi_i | v \rangle e^{i\lambda_i t}], \quad (35)$$

with $|\phi_i\rangle$, λ_i being the eigenvectors and eigenvalues of \mathbf{H} , then yields

$$\langle u | e^{i\mathbf{H}t} | v \rangle = 2i\alpha \sin\left(\frac{h+\beta}{2}t\right) + (1-2\alpha)i \sin\left(\frac{h-\beta}{2}t\right), \quad (36)$$

where

$$\alpha = \frac{1}{4} \left(\frac{h}{\sqrt{\delta+h^2}} + 1 \right), \quad \beta = \sqrt{h^2 + 4\delta}. \quad (37)$$

If

$$\frac{h}{\beta} = \frac{1+4c_1}{1+4c_2}, \quad (38)$$

with c_1, c_2 being integers, the setup features PST between u and v . If

$$\frac{h}{\beta} \in \mathbb{R} \setminus \mathbb{Q} \quad (39)$$

is irrational, the setup features pretty good state transfer between u and v . The latter statement follows from the fact that, if expression Eq. (39) holds, the only set of integers $\{l_i, m_j\}$ fulfilling Eqs. (2) and (3) is the trivial one where $l_i = 0, m_j = 0$ for all i, j , which also fulfills Eq. (2).

For comparison with the outcome of our algorithm, we insert the parameters of (31) into (39), yielding the irrational number

$$\frac{1}{\sqrt{21}} \quad (40)$$

as expected.

C. Application of the algorithm to larger systems

The graph treated in the previous subsection has been deliberately chosen to be rather simple, so that the reader can comprehend the essential steps of our algorithm. The algorithm itself is not limited to such simple examples, and indeed can be applied to rather complicated networks. In Figs. 6(b) and 6(c) we show two such networks. The first such network has been taken from our collection of 2247 unweighted (i.e., where all couplings are unity) graphs with nine

vertices (see Table I) which have no permutation symmetries, but cospectral vertices. In a second step, we systematically checked which edge weights and on-site potentials of this particular graph can be changed while preserving the cospectrality. One out of several different choices is then depicted in Fig. 6(b). The graph depicted in Fig. 6(c) has been obtained by starting from a highly symmetric graph with 22 vertices (namely, the graph shown without the two central vertices) in which, among other pairs of sites, the two sites u and v are cospectral. We then added the two central sites and systematically checked in which ways these two sites and the highly symmetric prototype graph can be connected such that the symmetry is broken, but the cospectrality of u and v is preserved.

We now give the results of the application of our algorithm onto these two examples. For the graph of Fig. 6(b) the algorithm yields that, among many other possible choices of parameters, PGST between the sites u and v is achieved for

$$a = b = c = d = e = 1, \quad f = 2 \quad (41)$$

and with all on-site potentials being equal to zero. For this set of parameters, all eigenvalues of H are nondegenerate, and u and v are thus strongly cospectral. Furthermore, for this specific choice of parameters, the algorithm yields the polynomials

$$P_+(\lambda) = \lambda^7 + \lambda^6 - 16\lambda^5 - 26\lambda^4 + 33\lambda^3 + 51\lambda^2 - 16\lambda - 8, \quad (42)$$

$$P_-(\lambda) = -\lambda^2 + \lambda + 8, \quad (43)$$

and it can easily be shown that these two polynomials are irreducible over the base field of the Hamiltonian H (namely, over the rational numbers), and also fulfill Eq. (12), so that the setup supports PGST between u and v .

For the graph of Fig. 6(c) the application of our algorithm yields that one possible choice for obtaining PGST between the sites u and v is to set all on-site potentials equal to zero, and all couplings equal to unity. The polynomials P_{\pm} are then obtained as

$$\begin{aligned} P_+(\lambda) &= \lambda^{18} + 2\lambda^{17} - 24\lambda^{16} - 52\lambda^{15} + 211\lambda^{14} \\ &\quad + 501\lambda^{13} - 841\lambda^{12} - 2282\lambda^{11} + 1520\lambda^{10} \\ &\quad + 5271\lambda^9 - 960\lambda^8 - 6129\lambda^7 - 158\lambda^6 + 3392\lambda^5 \\ &\quad + 172\lambda^4 - 792\lambda^3 + 34\lambda^2 + 42\lambda - 4, \end{aligned} \quad (44)$$

$$P_-(\lambda) = \lambda^6 - 2\lambda^5 - 6\lambda^4 + 8\lambda^3 + 10\lambda^2 - 5\lambda - 2. \quad (45)$$

IV. STORAGE AND PRETTY GOOD TRANSFER OF COMPACT LOCALIZED STATES

So far we investigated the transfer of single-site excitations, and showed how networks supporting pretty good transfer of these states can be designed. In the following we will demonstrate how such networks can be modified to allow for robust *storage* of qubits. The need for such modifications arises since, although relatively easy to transfer, single site excitations are difficult to store. To achieve storage, the underlying sites would need to be completely decoupled from

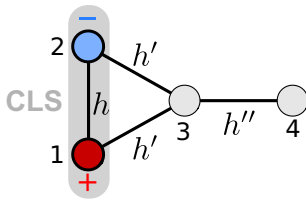


FIG. 7. The graph shown features a compact localized state (CLS) $|\Psi_{\text{CLS}}\rangle = \frac{|1\rangle - |2\rangle}{\sqrt{2}}$ on sites 1 and 2.

the remainder of the Hamiltonian right after state transfer, which is usually not achievable. As a consequence, the single site excitation would tunnel to adjacent (weakly) coupled sites, drastically degrading the storage performance. Recently, a solution to this problem has been proposed in Ref. [42]. There, qubits were not encoded into excitations of single sites, but into excitations of dimers, which are schematically shown in Fig. 7, where the dimer consisting of the two sites 1 and 2 is excited. Storage in these dimers does not rely on decoupling, but rather on destructive interference. To achieve such interference, the couplings of the two constituents of the dimer to the remainder of the system (in Fig. 7, these are identically given by h') are chosen symmetrical, and the dimer sites are excited with a phase difference of π . This completely suppresses any tunneling of this dimer state to its environment. It can be easily proven that such dimer states are eigenstates of the underlying Hamiltonian, and due to their strictly limited spatial extent, they are known as *compact localized states* (CLS). In Fig. 7, for example, the CLS is given by $|\Psi_{\text{CLS}}\rangle = \frac{|1\rangle - |2\rangle}{\sqrt{2}}$, and one can easily show that it is an eigenstate of the underlying Hamiltonian \mathbf{H} with eigenvalue $\lambda = v - h$. Importantly, this is also an eigenvalue of the *isolated* Hamiltonian of the subsystem

$$\mathbf{H}_{SS} = \begin{pmatrix} v & h \\ h & v \end{pmatrix},$$

where v denotes the identical on-site potential of sites 1 and 2, and where $S = \{1, 2\}$. The fact that the eigenvalues of CLSs depend only on the subsystem on which they are localized is indeed a general property, and this is just one of the many intriguing features of these states. Not only do CLSs feature localization without disorder, as is the case for the well-known Anderson localization [43], but they are also strongly connected to the appearance of flat bands. These are, in turn, conjectured to play a role in the superconduction of cuprates [30,44–50]. We refer the reader interested in the exciting field of CLSs and flat bands to the review [30].

What makes compact localized states important in the context of this work is their unique combination of favorable properties. The fact that they are eigenstates allows for their perfect, i.e., unity fidelity, storage in idealized model systems, where imperfections can be ignored. If, on the other hand, such model systems are realized and imperfections are introduced, CLSs profit from the fact that they are localized only on a subdomain of the full system. This means that they are *immune* to any imperfections of the underlying Hamiltonian outside of this domain and its directly neighboring sites. Moreover, the fact that they are localized by means of

destructive interference means that they are even immune to certain perturbations inside or directly next to their domain of localization. For example, the coupling h' in Fig. 7 could be varying in time and, in particular, grow arbitrarily big, but $|\Psi_{\text{CLS}}\rangle$ would still remain a compactly localized eigenstate of $\mathbf{H}(t)$. This naturally changes if the symmetry of the couplings $h_{1,3}, h_{2,3}$ or the on-site potentials of sites 1 and 2 is broken. However, as has been demonstrated in [42], by tuning the CLSs eigenvalue $v - h$, the CLS can be energetically separated from the other states of the (unperturbed) system. It then follows from perturbation theory that, for weak perturbations, the CLS is only slightly affected.

The combination of all these properties clearly renders compact localized states ideal candidates for the storage of qubits. However, the fact that they are eigenstates of \mathbf{H} complicates their transfer, which is naturally impossible by simple time evolution if \mathbf{H} is time independent. In Ref. [42] a set of minimal changes to the setup have been demonstrated that allow for both perfect storage and perfect, i.e., unity fidelity, transfer of CLSs in specialized networks. Similar ideas—though not using the term of CLSs, and not focusing on the special properties of these states for storage—have been proposed earlier for the transport of qubits in Refs. [51,52]. In this section we use the underlying idea and show how a network capable of PGST of single-site excitations of sites u and v can be modified by a set of minimal changes such that (i) the network supports compact localized states and (ii) it is possible to perform pretty good transfer of these states. The only condition on the underlying network is that, during the transfer process, there are no direct links (edges) between u and v . The basic idea is sketched in Figs. 8(a) and 8(b). We start from a Hamiltonian \mathbf{H} —an example being depicted in Fig. 8(a)—which supports PGST from u to v , with time-dependent fidelity

$$F(t) = |\langle u | e^{i\mathbf{H}t} | v \rangle|^2. \quad (46)$$

We then create a modified version \mathbf{H}_m of \mathbf{H} by replacing u and v by dimers $u_{1,2}$ and $v_{1,2}$, and by replacing all couplings of u, v to their environment by symmetrized and renormalized couplings with the dimer. The modified Hamiltonian \mathbf{H}_m of \mathbf{H} of Fig. 8(a) is shown in Fig. 8(b). The fidelity

$$F'(t) = |\langle u_+ | e^{i\mathbf{H}_m t} | v_+ \rangle|^2 \quad (47)$$

for the transfer of symmetric excitations $|u_+\rangle = \frac{|u_1\rangle + |u_2\rangle}{\sqrt{2}}$ to $|v_+\rangle = \frac{|v_1\rangle + |v_2\rangle}{\sqrt{2}}$ by means of the modified Hamiltonian \mathbf{H}_m can then be shown (see Appendix E for details) to be *identical* to $F(t)$. In particular, while \mathbf{H} supports PGST of single site excitations u and v , its modified version \mathbf{H}_m supports PGST of *symmetric* dimer excitations $|u_+\rangle$ and $|v_+\rangle$.

On the other hand, \mathbf{H}_m supports also two compact localized states, $|u_-\rangle = \frac{|u_1\rangle - |u_2\rangle}{\sqrt{2}}$ and $|v_-\rangle = \frac{|v_1\rangle - |v_2\rangle}{\sqrt{2}}$. They are eigenstates of \mathbf{H}_m and can thus not be transferred by simple time evolution. However, $|u_-\rangle$ can be transferred to $|v_-\rangle$ by means of a time-dependent Hamiltonian $\mathbf{H}'_m(t)$. To this end, we constrain $\mathbf{H}'_m(t)$ such that

$$\mathbf{H}'_m(t < 0) = \mathbf{H}'_m(t \geq T_f) = \mathbf{H}_m \quad (48)$$

so that the transfer takes place between $t = 0$ and $t = T_f$. As a result, $|u_-\rangle$ and $|v_-\rangle$ are eigenstates before $t = 0$ and after

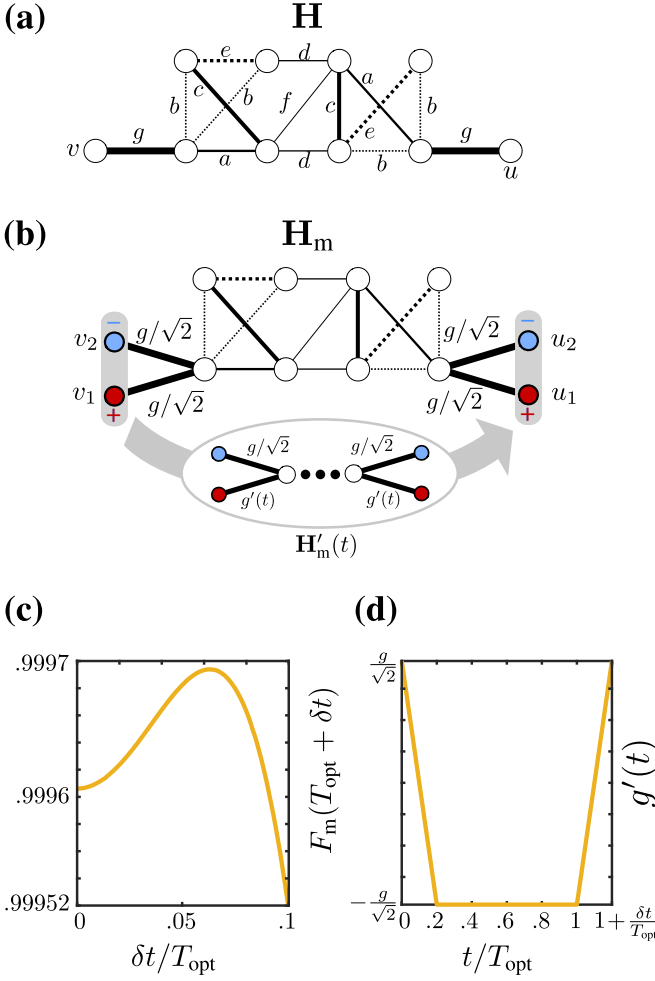


FIG. 8. (a) Original setup featuring PGST from u to v , described by \mathbf{H} . (b) Modified setup described by \mathbf{H}_m , featuring two CLS $|u_{-}\rangle = \frac{|u_1\rangle - |u_2\rangle}{\sqrt{2}}$ and $|v_{-}\rangle = \frac{|v_1\rangle - |v_2\rangle}{\sqrt{2}}$. By means of a time-dependent Hamiltonian $\mathbf{H}'_m(t)$ (as depicted in the inset), transfer of CLSs is possible. In the proposed protocol, $\mathbf{H}'_m(t)$ differs from \mathbf{H}_m in that only the couplings of one site of each dimer to the remainder of the setup are changed by linear ramps with ramp time δt . These ramps are depicted in (d). (c) The transfer fidelity over the ramp time δt for the setup (b), with all on-site potentials set to zero and coupling parameters $a-g$ given in Eq. (52). Here T_{opt} is the time for which, for $\delta t = 0$, a transfer fidelity of 0.996 has been reached (see text for more details).

$t = T_f$. We then construct $\mathbf{H}'_m(t)$ from \mathbf{H}_m by making all couplings h_{i,u_1} , h_{i,v_1} of u_1 , v_1 (but not of u_2 , v_2) time dependent. In the following we consider two different protocols.

In the simplest possible protocol, one instantaneously switches the sign of the couplings h_{i,u_1} and h_{i,v_1} at $t = 0$, and switches back at $t = T_f$. Due to this change, the initial state $|u_{-}\rangle$ is no longer an eigenstate of $\mathbf{H}'_m(t)$ for $t < 0 < T_f$, and thus spreads across the lattice. If we denote $\mathbf{H}'_m(0 < t < T_f) = \mathbf{H}'_m = \text{const.}$, then the transfer fidelity during this spreading is given by

$$F''(t) = |\langle u_{-} | e^{i\mathbf{H}'_m t} | v_{-} \rangle|^2 = F'(t) = F(t). \quad (49)$$

Once $F''(t)$ achieves a sufficiently high value $F''(T_f) = 1 - \epsilon$ for given ϵ , the second quench is performed, so that the

previously modified couplings are instantaneously switched back to their original value. At T_f , the state of the system is then given by

$$|\Psi(T_f)\rangle = e^{i\phi} \sqrt{1 - \epsilon} |v_{-}\rangle + \sum_v c_v |\psi^v\rangle, \quad (50)$$

where ϕ is a phase and the coefficients c_v must fulfill $|\langle \Psi(T_f) | \Psi(T_f) \rangle| = 1$. The states $|v_{-}\rangle$ and $|\psi^v\rangle \neq |v_{-}\rangle$ are eigenstates of the pre/post quench Hamiltonian \mathbf{H}_m . Since $\mathbf{H}(t) = \mathbf{H}_m$ for $t \geq T_f$, we have

$$|\langle v_{-} | \Psi(t \geq T_f) \rangle|^2 = F''(T_f) = \text{const.} \quad (51)$$

The CLS $|u_{-}\rangle$ is thus stored with the time-independent fidelity $F''(T_f)$ and, due to its properties, enjoys protection against a large number of imperfections of \mathbf{H}_m . As we wrote above, by connecting the two dimer sites hosting the CLS $|u_{-}\rangle$ by a coupling h , its energy can be tuned to be far away from all other states. As a consequence, the CLS becomes highly robust against perturbations, as has been shown in [42].

Our second protocol is motivated by the fact that, in practice, instantaneous coupling flips are rather unrealistic. Thus, they should be replaced by more realistic switching pulses. These will naturally change the transfer fidelity, and the strength of this change clearly depends both on the individual system and the realization of the flipping pulse. In Ref. [42], the impact of linear ramps (instead of instantaneous coupling flips) on linear chains that support perfect transfer of compact localized states has been investigated. As has been shown there for the case of chains of length $N = 5$, even extraordinary slow ramping times of nearly half of the total transfer time only leads to a decrease of the transfer fidelity from unity to 0.97. This being said, we now exemplarily investigate the impact of finite duration linear ramps of couplings on the transfer fidelity of the simple example setup shown in Fig. 8(a). Restricting all on-site potentials to be zero, the two sites u and v are cospectral for any choice of the seven parameters $\xi = \{a, b, c, d, e, f, g\} \in \mathbb{R}$. Before investigating the impact of finite-time ramps on the transfer of compact localized states, we first find the subspace $\xi'' \subseteq \xi$ in which the setup supports PGST of single site excitations. Within this subspace, we then look for realizations $\xi''' \subseteq \xi''$ for which the maximum transfer fidelity

$$F_{\text{max}}(T_f) = \max[F(t \leq T_f)]$$

from site u to v within a given time T_f and boundaries on the absolute values of parameters ξ'' is as large as possible. In other words, we optimize the system to (i) support PGST from u to v and (ii) reach an acceptable transfer fidelity in as little time as possible. In practical applications, such an optimization is always necessary. Since PGST by definition is an asymptotic property, the underlying network may reach a suitably high transfer fidelity only after prohibitively long transfer times. For the setup shown in Fig. 8(a), we restricted the optimization to the subspace where all on-site potentials vanish, and obtained a maximum transfer fidelity

$$F(T_{\text{opt}} = 10.8345) = 0.996$$

for

$$\begin{aligned} a &= 0.7975, & b &= 0.8103, & c &= 0.8880, & d &= 2.3473, \\ e &= 2.3005, & f &= 0.3061, & g &= 0.5489. \end{aligned} \quad (52)$$

In order to investigate the transfer of compact localized states, we first apply the above set of modifications to Fig. 8(a) and equip it with two compact localized states. The modified setup is shown in Fig. 8(b) and supports the two CLS $|u_{-}\rangle = \frac{|u_1\rangle - |u_2\rangle}{\sqrt{2}}$ and $|v_{-}\rangle = \frac{|v_1\rangle - |v_2\rangle}{\sqrt{2}}$. By performing instantaneous coupling flips at $t = 0$ and T_{opt} , we can transfer $|u_{-}\rangle$ to $|v_{-}\rangle$ (and vice versa) with the fidelity $F(T_{\text{opt}})$. We now slightly change the protocol and switch the couplings by performing linear *ramps* with a duration δt . The ramps are started at $t = 0$ and $t = T_{\text{opt}}$, so that the transfer process is finished at $t = T_{\text{opt}} + \delta t$. The process is sketched in Figs. 8(b)–8(d). At $t = 0$, the state of the system is given by $|\Psi(t = 0)\rangle = |u_{-}\rangle$, i.e., a single CLS is localized on the left dimer. The transfer process is then started [shown in the inset of Fig. 8(b)] by linearly ramping down $g'(t)$ such that $g'(t = \delta t) = -g/\sqrt{2}$. At $t = T_{\text{opt}}$, these are then linearly ramped up again, reaching their final value $g'(T_{\text{opt}} + \delta t) = g/\sqrt{2}$. The pulse $g'(t)$ is shown in Fig. 8(d) for $\delta t = T_{\text{opt}}/5$. In Fig. 8(c) the transfer fidelity is plotted against the pulse duration δt . Quite counterintuitively, the fidelity of transferring compact localized states *increases* first for increasing δt . Investigating the cause for this behavior would certainly be a worthwhile topic for further research. For larger δt , the fidelity falls off as expected, but overall remains quite high. Even for comparatively slow ramps of $\delta t = T_{\text{opt}}/10$, the transfer fidelity decreases only by roughly 10^{-4} . Notably, this high robustness against slow control pulses was also observed in Ref. [42] for the case of linear chains equipped with compact localized states.

V. BRIEF CONCLUSION

We presented a method to design Hamiltonians \mathbf{H} featuring pretty good state transfer (PGST) between two sites. A necessary condition for PGST is that these two sites are so-called strongly cospectral, which means that all eigenstates have parity ± 1 on these two sites. We showed how Hamiltonians featuring strongly cospectral sites can be designed. We then relied on so-called isospectral reductions of these Hamiltonians to yield a factoring of their characteristic polynomial in terms of smaller polynomials P_{\pm} , which are related to eigenvectors with parity ± 1 on u and v . The motivation for this factorization is the fact that PGST automatically arises in setups where the coefficients of P_{\pm} fulfill a set of relations, as has recently been shown by Eisenberg *et al.* [14]. Equipped with explicit knowledge of P_{\pm} , we show how they can be properly manipulated by changing couplings and on-site potentials while maintaining the strong cospectrality. Through these manipulations, PGST can therefore be achieved in certain setups, and we develop our method into an algorithm to design PGST Hamiltonians. We further show how Hamiltonians featuring PGST can be equipped with so-called compact localized states (CLS). Such states are eigenstates of \mathbf{H} and are strictly localized on a spatially finite (and usually very small) domain, which allows for robust storage of qubits encoded into such CLSs. We further present time-dependent protocols which allow for PGST of CLSs. Our work opens new routes towards flexible design of PGST networks and

broadens their scope to allow for robust storage as well. An important future task is to investigate how well the transfer fidelity of PGST Hamiltonians within a given maximal transfer time T_{max} can be optimized by parameter tuning. This task should be supported by the algorithm presented in this work, as it allows us to obtain rather small parameter spaces ξ in which a given parameter dependent Hamiltonian $H(\xi)$ features PGST.

ACKNOWLEDGMENTS

M.R. gratefully acknowledges financial support by the “Stiftung der deutschen Wirtschaft” in the framework of a scholarship. N.E.P. gratefully acknowledges financial support from the Hellenic Foundation for Research and Innovation (HFRI) and the General Secretariat for Research and Technology (GSRT) under the HFRI Ph.D. Fellowship Grant No. 868. I.B. acknowledges financial support by Greece and the European Union (European Social Fund – ESF) through the Operational Programme “Human Resources Development, Education and Lifelong Learning” in the context of the project “Reinforcement of Postdoctoral Researchers” (MIS-5001552), implemented by the State Scholarships Foundation (IKY). M.P. gratefully acknowledges financial support by the “Studienstiftung des deutschen Volkes” in the framework of a scholarship. We thank the anonymous referee for pointing out the alternative treatment shown in Sec. III B 5.

APPENDIX A: PROOF FOR AN ALTERNATIVE SET OF CONDITIONS FOR PGST

In the literature, two versions of the necessary and sufficient conditions for pretty good state transfer exist [14,34]. In the remainder of this Appendix, λ_i^+ , λ_j^- are the eigenvalues associated with eigenvectors $|\psi_i^+\rangle$, $|\psi_j^-\rangle$ of \mathbf{H} that fulfill

$$\langle \psi_i^+ | u \rangle = +\langle \psi_i^+ | v \rangle \neq 0, \quad \langle \psi_j^- | u \rangle = -\langle \psi_j^- | v \rangle \neq 0,$$

where $|u\rangle$, $|v\rangle$ describe single-site excitations of sites u and v , respectively. The first version of the necessary and sufficient conditions for PGST then reads as follows.

Theorem 1. There is PGST between sites u and v if and only if (i) u, v are strongly cospectral, and (ii) if all sets of integers $\{l_i, m_j\}$ which fulfill

$$\sum_i l_i \lambda_i^+ + \sum_j m_j \lambda_j^- = 0, \quad (\text{A1})$$

$$\sum_j m_j \text{ is odd}, \quad (\text{A2})$$

also fulfill

$$\sum_i l_i + \sum_j m_j \neq 0. \quad (\text{A3})$$

This version is explicitly proven in [34].

The second, and more commonly used, version is the one used in this work:

Theorem 2. There is PGST between sites u and v if and only if (i) u, v are strongly cospectral, and (ii) if all sets of integers $\{l_i, m_j\}$ which fulfill

$$\sum_i l_i \lambda_i^+ + \sum_j m_j \lambda_j^- = 0, \quad (\text{A4})$$

$$\sum_i l_i + \sum_j m_j = 0, \quad (\text{A5})$$

also fulfill

$$\sum_j m_j \text{ is even.} \quad (\text{A6})$$

Though Theorem 2 can easily be derived from Theorem 1, there seems to be no explicit derivation in the literature. We now give this derivation here for completeness and start from the proof of Theorem 1 in Sec. III of Ref. [34]. In the proof it is shown that pretty good state transfer between sites u and v occurs if and only if (i) u, v are strongly cospectral, and (ii) for any set of integers $\{l_i, m_j\}$ which fulfill

$$\sum_i l_i \lambda_i^+ + \sum_j m_j \lambda_j^- = 0 \quad (\text{A7})$$

there exists a $\delta \in \mathbb{R}$ such that

$$\delta \left(\sum_i l_i + \sum_j m_j \right) + \pi \left(\sum_j m_j \right) = 0 \pmod{2\pi}. \quad (\text{A8})$$

In [34] Theorem 1 is then deduced from Eqs. (A7) and (A8). To derive Theorem 2 which is used in this paper, we insert Eq. (A5), yielding

$$0\delta + \pi \left(\sum_j m_j \right) = 0 \pmod{2\pi}, \quad (\text{A9})$$

which is fulfilled for any $\delta \in \mathbb{R}$ if and only if $\sum_j m_j$ is even.

APPENDIX B: PROOF FOR THE INTERPRETATION OF MATRIX ENTRIES OF POWERS OF \mathbf{H}^k IN TERMS OF WALKS

We now prove Eq. (6) which states that

$$(\mathbf{H}^{k>0})_{a,b} = \sum_p w(p_{a,b}^{(k)}), \quad (\text{B1})$$

where $w(p_{a,b}^{(k)})$ denotes the weight of one possible walk of length k between vertices a and b , and the sum is over all such walks. To this end, we write $(\mathbf{H}^{k>0})_{a,b}$ as

$$(\mathbf{H}^{k>0})_{a,b} = \sum_{l_1, \dots, l_{k-1}} \mathbf{H}_{a,l_1} \mathbf{H}_{l_1,l_2} \cdots \mathbf{H}_{l_{k-2},l_{k-1}} \mathbf{H}_{l_{k-1},b}, \quad (\text{B2})$$

where each index l_i goes from 1 to N with $\mathbf{H} \in \mathbb{R}^{N \times N}$. We now interpret every term $\mathbf{H}_{i,j}$ occurring in Eq. (B2) as the weight of the edge connecting sites i and j . Each summand is, therefore, the weight of a walk of length k from site a to b via the sites l_1, l_2, \dots, l_{k-1} , where walks over physically nonexistent edges (i.e., those with vanishing weights $\mathbf{H}_{i,j} = 0$) naturally

have vanishing weights as well. As a consequence, we can write Eq. (B2) as Eq. (B1), and the value of the matrix element $(\mathbf{H}^k)_{a,b}$ is equal to the sum of weights of all walks of length k between vertices a and b .

APPENDIX C: PROOFS FOR COSPECTRALITY

We now prove the validity of the design mechanism presented in Sec. IID. In particular, we will prove that all changes shown in Fig. 4 applied onto an already cospectral network keep this cospectrality. To this end, we prove the following:

Theorem 3. Let

$$\mathbf{H}_i = \begin{pmatrix} \mathbf{H}_{SS} & \mathbf{H}_{S\bar{S}_i} \\ \mathbf{H}_{\bar{S}_i S} & \mathbf{H}_{\bar{S}_i \bar{S}_i} \end{pmatrix} \in \mathbb{R} \quad (\text{C1})$$

be symmetric matrices with $i = 1, 2$ and

$$\mathbf{H}_{SS} = \begin{pmatrix} E & h \\ h & E \end{pmatrix}$$

bisymmetric. Denote the two sites in \mathbf{H}_{SS} as $S = \{u, v\}$. If u, v are cospectral in \mathbf{H}_i , then they are also cospectral in

$$\mathbf{H}' = \begin{pmatrix} \mathbf{H}_{SS} & \mathbf{H}_{S\bar{S}_1} & \mathbf{H}_{S\bar{S}_2} \\ \mathbf{H}_{\bar{S}_1 S} & \mathbf{H}_{\bar{S}_1 \bar{S}_1} & \mathbf{0} \\ \mathbf{H}_{\bar{S}_2 S} & \mathbf{0} & \mathbf{H}_{\bar{S}_2 \bar{S}_2} \end{pmatrix}. \quad (\text{C2})$$

Proof. We use the fact [22] that the isospectral reduction $\mathbf{R}_{S=\{u,v\}}(\mathbf{H}, \lambda)$ is, for symmetric \mathbf{H} , bisymmetric if and only if the sites u and v are cospectral. Individually, we therefore have that

$$\mathbf{R}_S(\mathbf{H}_i, \lambda) = \mathbf{H}_{SS} - \mathbf{H}_{S\bar{S}_i}(\mathbf{H}_{\bar{S}_i \bar{S}_i} - \lambda \mathbf{I})^{-1} \mathbf{H}_{\bar{S}_i S}$$

is bisymmetric. We then evaluate the isospectral reduction of \mathbf{H}' , which can be written as

$$\mathbf{R}_S(\mathbf{H}', \lambda) = \mathbf{H}_{SS} - \mathbf{A} \mathbf{B}^{-1} \mathbf{A}^T, \quad (\text{C3})$$

where

$$\mathbf{A} = (\mathbf{H}_{S\bar{S}_1}, \mathbf{H}_{S\bar{S}_2}), \quad \mathbf{B} = \begin{pmatrix} \mathbf{H}_{\bar{S}_1 \bar{S}_1} - \lambda \mathbf{I} & \mathbf{0} \\ \mathbf{0} & \mathbf{H}_{\bar{S}_2 \bar{S}_2} - \lambda \mathbf{I} \end{pmatrix}.$$

Eq. (C3) then becomes

$$\mathbf{R}_S(\mathbf{H}', \lambda) = \mathbf{H}_{SS} - \sum_i \mathbf{H}_{S\bar{S}_i} (\mathbf{H}_{\bar{S}_i \bar{S}_i} - \lambda \mathbf{I})^{-1} \mathbf{H}_{\bar{S}_i S}.$$

This expression is bisymmetric, since \mathbf{H}_{SS} as well as each of the two summands are individually bisymmetric, and sums of bisymmetric matrices are bisymmetric again. Due to the connection between bisymmetry of $\mathbf{R}_{S=\{u,v\}}(\mathbf{H}, \lambda)$ and the cospectrality of sites u and v , we have therefore proven the above theorem. ■

To apply this theorem to Sec. IID, we divide the setups shown their into three parts, as shown in Fig. 9 for a slightly modified version of the graph depicted in Fig. 4(b3). We start by investigating only the subsystem \mathbf{H}_1 , i.e., we ignore the connections between \mathbf{H}_{SS} and $\mathbf{H}_{\bar{S}_2 \bar{S}_2}$. Since this subsystem \mathbf{H}_1 is, by construction, invariant under a permutation of the two red sites u and v , these two sites are automatically cospectral if \mathbf{H}_1 is decoupled from $\mathbf{H}_{\bar{S}_2 \bar{S}_2}$. We then separately investigate only the subsystem \mathbf{H}_2 , i.e., ignore the connections between \mathbf{H}_{SS} and $\mathbf{H}_{\bar{S}_1 \bar{S}_1}$. By computing the matrix powers \mathbf{H}_2 , it can be easily shown that u and v are cospectral in this subsystem as

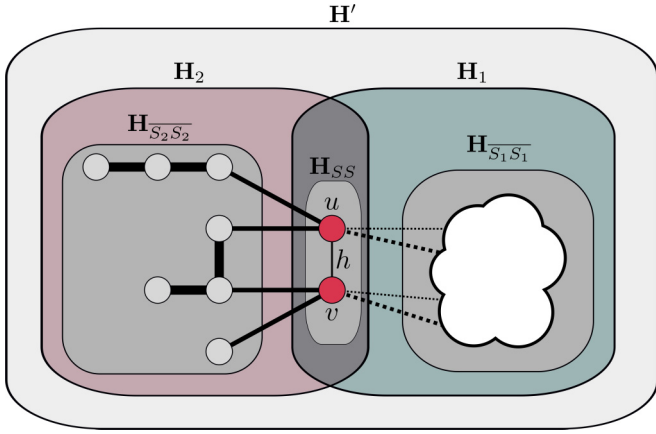


FIG. 9. Visualization of the decomposition of the graph \mathbf{H}' [which is a slightly modified version of the one depicted in Fig. 4(b3)] into subsystems \mathbf{H}_1 , \mathbf{H}_2 , \mathbf{H}_{SS} , $\mathbf{H}_{S_1S_1}$, and $\mathbf{H}_{S_2S_2}$.

well. Thus, the two sites u and v are cospectral in both \mathbf{H}_1 and \mathbf{H}_2 . It can then easily be shown that \mathbf{H}' of Fig. 9 has exactly the form of Eq. (C2). Thus, u and v are also cospectral in \mathbf{H}' .

By repeating this procedure for each graph presented in Fig. 4, it can be proven that u and v are cospectral in all of them. We have thus proven the validity of the design mechanism proposed in Sec. IID.

APPENDIX D: PROOF FOR THE FORM OF $P_{\mathbf{R}}^{\pm}$

We want to prove that, for bisymmetric

$$\mathbf{R}_S(\mathbf{H}, \lambda) = \begin{pmatrix} A(\lambda) & B(\lambda) \\ B(\lambda) & A(\lambda) \end{pmatrix}, \quad (\text{D1})$$

the characteristic polynomials $P_{\mathbf{R}}^{\pm}(\lambda)$ related to nonlinear eigenvectors of positive and negative parity, respectively, are given by $P_{\mathbf{R}}^{\pm}(\lambda) = A(\lambda) \pm B(\lambda) - \lambda$.

To prove this, we perform a similarity transform $\mathbf{R}'_S(\mathbf{H}, \lambda) = A^{-1}\mathbf{R}_S(\mathbf{H}, \lambda)A$, with

$$A = \begin{pmatrix} 1 & 1 \\ 1 & -1 \end{pmatrix}$$

so that

$$\mathbf{R}'_S(\mathbf{H}, \lambda) = \begin{pmatrix} A(\lambda) + B(\lambda) & 0 \\ 0 & A(\lambda) - B(\lambda) \end{pmatrix}$$

becomes block diagonal. Therefore, its nonlinear eigenvectors are obviously $(1, 0)^T$ (those of the first block) with eigenvalues $\{\lambda_i^1\}$ and $(0, 1)^T$ (those of the second block) with eigenvalues $\{\lambda_j^2\}$. Multiplying these nonlinear eigenvectors by A then yields the corresponding nonlinear eigenvectors of $\mathbf{R}_S(M, \lambda)$. Therefore, these are obviously $(1, 1)^T$ with eigenvalues $\{\lambda_i^1\}$ and $(1, -1)^T$ with eigenvalues $\{\lambda_j^2\}$. We remind the reader that, since $\mathbf{R}_S(M, \lambda)$ depends on λ , it can have *more* than two nonlinear eigenvectors, and these need not be linearly independent. The eigenvalues $\{\lambda_i^1\}$, $\{\lambda_j^2\}$ are therefore related to nonlinear eigenvectors of positive and negative parity, respectively, and are the solutions to the equations

$$\begin{aligned} \det[A(\lambda_i^1) + B(\lambda_i^1) - \lambda_i^1] &= 0, \\ \det[A(\lambda_j^2) - B(\lambda_j^2) - \lambda_j^2] &= 0. \end{aligned}$$

It is thus obvious that $P_{\mathbf{R}}^{\pm}(\lambda) = A(\lambda) \pm B(\lambda) - \lambda$ are the characteristic polynomials related to nonlinear eigenvectors of positive and negative parity, respectively, and that

$$P_{\mathbf{R}}^+ P_{\mathbf{R}}^- = \det[\mathbf{R}'_S(H)] = \det[\mathbf{R}_S(H)].$$

APPENDIX E: MATHEMATICAL DETAILS ON THE TRANSFER OF COMPACT LOCALIZED STATES

We now prove the statements made in Sec. IV. The proofs are similar to those done in [42], but are included here so that the current work is self-contained.

We assume that the original network is described by a Hamiltonian \mathbf{H} and supports PGST between sites $S = \{u, v\}$. We then partition the system such that

$$\mathbf{H} = \begin{pmatrix} \mathbf{H}_{\bar{S}\bar{S}} & \mathbf{H}_{\bar{S}S} \\ \mathbf{H}_{S\bar{S}} & \mathbf{H}_{SS} \end{pmatrix} \in \mathbb{R}^{(N+2) \times (N+2)}.$$

As stated in Sec. IV, we demand \mathbf{H} to have no direct coupling between u and v , so that

$$\mathbf{H}_{SS} = \begin{pmatrix} E & 0 \\ 0 & E \end{pmatrix} \in \mathbb{R}^{2 \times 2}$$

is diagonal. We denote the eigenvectors of \mathbf{H} as

$$|\phi^v\rangle = \begin{pmatrix} \mathbf{w}^v \\ x_u^v \\ x_v^v \end{pmatrix}, \quad \in \mathbb{R}^{(N+2) \times 1},$$

with $\mathbf{w}^v \in \mathbb{R}^{N \times 1}$. The fidelity for transfer from $|u\rangle$ to $|v\rangle$ is given as

$$|\langle u | e^{i\mathbf{H}t} | v \rangle|^2 = \left| \sum_v x_u^v (x_v^v)^* e^{i\lambda_v t} \right|^2.$$

We then modify the system as shown in Fig. 8(b), so that its Hamiltonian becomes

$$\mathbf{H}_m = \begin{pmatrix} \mathbf{H}_{\bar{S}\bar{S}} & \frac{1}{\sqrt{2}}\mathbf{H}_{\bar{S}\bar{S}} & \frac{1}{\sqrt{2}}\mathbf{H}_{\bar{S}\bar{S}} \\ \frac{1}{\sqrt{2}}\mathbf{H}_{\bar{S}\bar{S}} & \mathbf{H}_{SS} & \mathbf{0}_{2 \times 2} \\ \frac{1}{\sqrt{2}}\mathbf{H}_{\bar{S}\bar{S}} & \mathbf{0}_{2 \times 2} & \mathbf{H}_{SS} \end{pmatrix}.$$

By means of the *equitable partition theorem* [29,53–55] its $N + 4$ eigenstates can then be shown to be

$$|\phi^v\rangle = \begin{pmatrix} \mathbf{w}^v \\ \frac{1}{\sqrt{2}}x_u^v \\ \frac{1}{\sqrt{2}}x_v^v \\ \frac{1}{\sqrt{2}}x_u^v \\ \frac{1}{\sqrt{2}}x_v^v \end{pmatrix}, \quad |\phi^{N+2+r}\rangle = \begin{pmatrix} \mathbf{0}_{N \times 1} \\ \mathbf{z}^r \\ -\mathbf{z}^r \end{pmatrix},$$

with $v = 1, \dots, N + 2$ and $r = 1, 2$. The $\mathbf{z}^r \in \mathbb{C}^{2 \times 1}$ are the eigenvectors of the *isolated* \mathbf{H}_{SS} . We now denote the first N sites as \bar{S} , and the remaining four as u_1, v_1, u_2, v_2 . The fidelity

$$F'(t) = |\langle u_+ | e^{i\mathbf{H}_m t} | v_+ \rangle|^2 \quad (\text{E1})$$

[Eq. (47) from Sec. IV] for the transfer of symmetric excitations $|u_+\rangle = \frac{|u_1\rangle + |u_2\rangle}{\sqrt{2}}$ to $|v_+\rangle = \frac{|v_1\rangle + |v_2\rangle}{\sqrt{2}}$ can then be evaluated

as

$$\begin{aligned}
 F'(t) &= |\langle u_+ | e^{i\mathbf{H}_m t} | v_+ \rangle|^2 \\
 &= \left| \sum_{v=1}^{N+2} \langle u_+ | \phi^v \rangle \langle \phi^v | v_+ \rangle e^{i\lambda_v t} \right|^2 \\
 &= \left| \sum_{v=1}^{N+2} x_u^v (x_v^v)^* e^{i\lambda_v t} \right|^2 \\
 &= F(t)
 \end{aligned}$$

as claimed in Sec. IV, since the overlap of $|u_+\rangle, |v_+\rangle$ with $|\phi^{N+2+r}\rangle$ vanishes.

We now look at the compact localized states supported by \mathbf{H}_m . There are two of these, given by $|I'\rangle = \frac{|u_1\rangle - |u_2\rangle}{\sqrt{2}}$ (localized on sites u_1 and u_2) and $|F'\rangle = \frac{|v_1\rangle - |v_2\rangle}{\sqrt{2}}$ (localized on sites v_1 and v_2). To transfer $|I'\rangle$ to $|F'\rangle$, we perform an instantaneous flip of couplings at $t = 0$, so that

$$\mathbf{H}_m \rightarrow \mathbf{H}_m'' = \begin{pmatrix} \mathbf{H}_{SS} & \frac{1}{\sqrt{2}}\mathbf{H}_{S\bar{S}} & -\frac{1}{\sqrt{2}}\mathbf{H}_{S\bar{S}} \\ \frac{1}{\sqrt{2}}\mathbf{H}_{\bar{S}S} & \mathbf{H}_{SS} & \mathbf{0}_{2 \times 2} \\ -\frac{1}{\sqrt{2}}\mathbf{H}_{\bar{S}S} & \mathbf{0}_{2 \times 2} & \mathbf{H}_{SS} \end{pmatrix}$$

and $|I'\rangle, |F'\rangle$ are no longer eigenstates of \mathbf{H}_m'' . By means of the so-called *nonequitable partition theorem* [29,56] the $N + 4$

eigenstates of \mathbf{H}_m'' can then shown to be

$$|\phi^v\rangle = \begin{pmatrix} \mathbf{w}^v \\ \frac{1}{\sqrt{2}}x_u^v \\ \frac{1}{\sqrt{2}}x_v^v \\ -\frac{1}{\sqrt{2}}x_u^v \\ -\frac{1}{\sqrt{2}}x_v^v \end{pmatrix}, \quad |\phi^{N+2+r}\rangle = \begin{pmatrix} \mathbf{0}_{N \times 1} \\ \mathbf{z}^r \\ \mathbf{z}^r \end{pmatrix},$$

with $v = 1, \dots, N + 2$, $r = 1, 2$, and \mathbf{z}^r as above. We then yield

$$\begin{aligned}
 F''(t) &= |\langle u_- | e^{i\mathbf{H}_m'' t} | v_- \rangle|^2 \\
 &= \left| \sum_{v=1}^{N+2} \langle u_- | \phi^v \rangle \langle \phi^v | v_- \rangle e^{i\lambda_v t} \right|^2 \\
 &= \left| \sum_{v=1}^{N+2} x_u^v (x_v^v)^* e^{i\lambda_v t} \right|^2 \\
 &= F'(t) = F(t)
 \end{aligned}$$

as claimed in Sec. IV.

Thus, if \mathbf{H} supports PGST of single site excitations u and v , \mathbf{H}_m supports two compact localized states, and by switching $\mathbf{H}_m \xrightarrow{t=0} \mathbf{H}_m''$, these compact localized states can be pretty well transferred. As explained in Sec. IV, the compact localized states can also be stored with time-independent fidelity $F(t > T_f) = F(T_f)$ by instantaneously switching $\mathbf{H}_m'' \xrightarrow{t=T_f} \mathbf{H}_m$.

-
- [1] S. Bose, Quantum Communication Through an Unmodulated Spin Chain, *Phys. Rev. Lett.* **91**, 207901 (2003).
- [2] M. Christandl, N. Datta, A. Ekert, and A. J. Landahl, Perfect State Transfer in Quantum Spin Networks, *Phys. Rev. Lett.* **92**, 187902 (2004).
- [3] M. B. Plenio, J. Hartley, and J. Eisert, Dynamics and manipulation of entanglement in coupled harmonic systems with many degrees of freedom, *New J. Phys.* **6**, 36 (2004).
- [4] M. Christandl, N. Datta, T. C. Dorlas, A. Ekert, A. Kay, and A. J. Landahl, Perfect transfer of arbitrary states in quantum spin networks, *Phys. Rev. A* **71**, 032312 (2005).
- [5] C. Godsil, State transfer on graphs, *Discrete Math.* **312**, 129 (2012).
- [6] L. Vinet and A. Zhedanov, Almost perfect state transfer in quantum spin chains, *Phys. Rev. A* **86**, 052319 (2012).
- [7] G. Coutinho and K. Guo, Pretty good state transfer between internal nodes of paths, *Quantum Inf. Comput.* **17**, 0825 (2017).
- [8] X. Fan and C. Godsil, Pretty good state transfer on double stars, *Linear Algebra Appl.* **438**, 2346 (2013).
- [9] H. Pal and B. Bhattacharjya, Pretty good state transfer on circulant graphs, *Electron. J. Comb.* **24**, 2.23 (2017).
- [10] C. M. van Bommel, A complete characterization of pretty good state transfer on paths, *Quantum Inf. Comput.* **19**, 0601 (2019).
- [11] E. Ackelsberg, Z. Brehm, A. Chan, J. Munding, and C. Tamon, Laplacian state transfer in coronas, *Linear Algebra Appl.* **506**, 154 (2016).
- [12] C. Godsil, S. Kirkland, S. Severini, and J. Smith, Number-Theoretic Nature of Communication in Quantum Spin Systems, *Phys. Rev. Lett.* **109**, 050502 (2012).
- [13] A. Kay, Perfect and pretty good state transfer for field-free Heisenberg chains, [arXiv:1906.06223](https://arxiv.org/abs/1906.06223).
- [14] O. Eisenberg, M. Kempton, and G. Lippner, Pretty good quantum state transfer in asymmetric graphs via potential, *Discrete Math.* **342**, 2821 (2019).
- [15] M. Kempton, G. Lippner, and S.-T. Yau, Pretty good quantum state transfer in symmetric spin networks via magnetic field, *Quant. Info. Proc.* **16**, 210 (2017).
- [16] L. A. Bunimovich and B. Z. Webb, Isospectral graph transformations, spectral equivalence, and global stability of dynamical networks, *Nonlinearity* **25**, 211 (2011).
- [17] L. A. Bunimovich and B. Z. Webb, Isospectral compression and other useful isospectral transformations of dynamical networks, *Chaos* **22**, 033118 (2012).
- [18] L. Bunimovich and B. Webb, *Isospectral Transformations: A New Approach to Analyzing Multidimensional Systems and Networks* (Springer, New York, 2014).
- [19] F. G. Vasquez and B. Z. Webb, Pseudospectra of isospectrally reduced matrices, *Numer. Linear Algebra Appl.* **22**, 145 (2014).
- [20] P. Duarte and M. J. Torres, Eigenvectors of isospectral graph transformations, *Linear Algebra Appl.* **474**, 110 (2015).
- [21] D. Smith and B. Webb, Hidden symmetries in real and theoretical networks, *Physica A* **514**, 855 (2019).

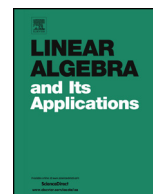
- [22] M. Kempton, J. Sinkovic, D. Smith, and B. Webb, Characterizing cospectral vertices via isospectral reduction, *Linear Algebra Appl.* **594**, 226 (2020).
- [23] P. A. Kalozoumis, C. Morfonios, N. Palaiodimopoulos, F. K. Diakonou, and P. Schmelcher, Local symmetries and perfect transmission in aperiodic photonic multilayers, *Phys. Rev. A* **88**, 033857 (2013).
- [24] P. A. Kalozoumis, C. Morfonios, F. K. Diakonou, and P. Schmelcher, Invariants of Broken Discrete Symmetries, *Phys. Rev. Lett.* **113**, 050403 (2014).
- [25] P. A. Kalozoumis, C. V. Morfonios, F. K. Diakonou, and P. Schmelcher, Invariant currents and scattering off locally symmetric potential landscapes, *Ann. Phys.* **362**, 684 (2015).
- [26] V. E. Zampetakis, M. K. Diakonou, C. V. Morfonios, P. A. Kalozoumis, F. K. Diakonou, and P. Schmelcher, Invariant current approach to wave propagation in locally symmetric structures, *J. Phys. A* **49**, 195304 (2016).
- [27] M. Röntgen, C. Morfonios, F. Diakonou, and P. Schmelcher, Non-local currents and the structure of eigenstates in planar discrete systems with local symmetries, *Ann. Phys.* **380**, 135 (2017).
- [28] C. V. Morfonios, P. A. Kalozoumis, F. K. Diakonou, and P. Schmelcher, Nonlocal discrete continuity and invariant currents in locally symmetric effective Schrödinger arrays, *Ann. Phys.* **385**, 623 (2017).
- [29] M. Röntgen, C. V. Morfonios, and P. Schmelcher, Compact localized states and flat bands from local symmetry partitioning, *Phys. Rev. B* **97**, 035161 (2018).
- [30] D. Leykam, A. Andreanov, and S. Flach, Artificial flat band systems: From lattice models to experiments, *Adv. Phys.* **3**, 1473052 (2018).
- [31] I. L. Garanovich, S. Longhi, A. A. Sukhorukov, and Y. S. Kivshar, Light propagation and localization in modulated photonic lattices and waveguides, *Phys. Rep.* **518**, 1 (2012).
- [32] A. Szameit, F. Dreisow, and S. Nolte, *Discrete Optics in Femtosecond Laser Written Waveguide Arrays*, Topics in Applied Physics (Springer, Berlin, 2012).
- [33] S. Bose, Quantum communication through spin chain dynamics: An introductory overview, *Contemp. Phys.* **48**, 13 (2007).
- [34] L. Banchi, G. Coutinho, C. Godsil, and S. Severini, Pretty good state transfer in qubit chains—The Heisenberg Hamiltonian, *J. Math. Phys.* **58**, 032202 (2017).
- [35] C. Godsil and J. Smith, Strongly cospectral vertices, [arXiv:1709.07975](https://arxiv.org/abs/1709.07975).
- [36] A. J. Schwenk, Almost all trees are cospectral, in *Proceedings of the Third Annual Arbor Conference* (Academic, New York, 1973), pp. 257–307.
- [37] B. D. McKay and A. Piperno, Practical graph isomorphism, II, *J. Symbol. Comput.* **60**, 94 (2014).
- [38] L. Bunimovich and L. Shu, Generalized eigenvectors of isospectral transformations, spectral equivalence and reconstruction of original networks, *Linear Algebra Appl.* **551**, 104 (2018).
- [39] It can be easily shown that if any eigenvector identically vanishes on both u and v , then its eigenvalue is contained in the spectrum of $\mathbf{H}_{\overline{SS}}$, which we excluded by assumption.
- [40] E. W. Weisstein, Resultant. From MathWorld—A Wolfram Web Resource, <http://mathworld.wolfram.com/Resultant.html>.
- [41] E. W. Weisstein, Polynomial Discriminant. From MathWorld—A Wolfram Web Resource, <http://mathworld.wolfram.com/PolynomialDiscriminant.html>.
- [42] M. Röntgen, C. V. Morfonios, I. Brouzos, F. K. Diakonou, and P. Schmelcher, Quantum Network Transfer and Storage with Compact Localized States Induced by Local Symmetries, *Phys. Rev. Lett.* **123**, 080504 (2019).
- [43] P. W. Anderson, Absence of diffusion in certain random lattices, *Phys. Rev.* **109**, 1492 (1958).
- [44] N. B. Kopnin, T. T. Heikkilä, and G. E. Volovik, High-temperature surface superconductivity in topological flat-band systems, *Phys. Rev. B* **83**, 220503(R) (2011).
- [45] V. I. Iglovikov, F. Hébert, B. Grémaud, G. G. Batrouni, and R. T. Scalettar, Superconducting transitions in flat-band systems, *Phys. Rev. B* **90**, 094506 (2014).
- [46] S. Peotta and P. Törmä, Superfluidity in topologically nontrivial flat bands, *Nat. Commun.* **6**, 8944 (2015).
- [47] A. Julku, S. Peotta, T. I. Vanhala, D.-H. Kim, and P. Törmä, Geometric Origin of Superfluidity in the Lieb-Lattice Flat Band, *Phys. Rev. Lett.* **117**, 045303 (2016).
- [48] K. Kobayashi, M. Okumura, S. Yamada, M. Machida, and H. Aoki, Superconductivity in repulsively interacting fermions on a diamond chain: Flat-band-induced pairing, *Phys. Rev. B* **94**, 214501 (2016).
- [49] M. Tovmasyan, S. Peotta, P. Törmä, and S. D. Huber, Effective theory and emergent SU(2) symmetry in the flat bands of attractive Hubbard models, *Phys. Rev. B* **94**, 245149 (2016).
- [50] L. Liang, T. I. Vanhala, S. Peotta, T. Siro, A. Harju, and P. Törmä, Band geometry, Berry curvature, and superfluid weight, *Phys. Rev. B* **95**, 024515 (2017).
- [51] A. Kay and M. Ericsson, Geometric effects and computation in spin networks, *New J. Phys.* **7**, 143 (2005).
- [52] P. J. Pemberton-Ross and A. Kay, Perfect Quantum Routing in Regular Spin Networks, *Phys. Rev. Lett.* **106**, 020503 (2011).
- [53] W. Barrett, A. Francis, and B. Webb, Equitable decompositions of graphs with symmetries, *Linear Algebra Appl.* **513**, 409 (2017).
- [54] A. Francis, D. Smith, D. Sorensen, and B. Webb, Extensions and applications of equitable decompositions for graphs with symmetries, *Linear Algebra Appl.* **532**, 432 (2017).
- [55] A. Francis, D. Smith, and B. Webb, General equitable decompositions for graphs with symmetries, *Linear Algebra Appl.* **577**, 287 (2019).
- [56] E. Fritscher and V. Trevisan, Exploring symmetries to decompose matrices and graphs preserving the spectrum, *SIAM J. Matrix Anal. Appl.* **37**, 260 (2016).



Contents lists available at ScienceDirect

Linear Algebra and its Applications

www.elsevier.com/locate/laa



Cospectrality preserving graph modifications and eigenvector properties via walk equivalence of vertices



C.V. Morfonios^{a,1}, M. Pyzh^{a,1}, M. Röntgen^{a,*,1}, P. Schmelcher^{a,b}

^a Zentrum für Optische Quantentechnologien, Fachbereich Physik, Universität Hamburg, Luruper Chaussee 149, 22761 Hamburg, Germany

^b The Hamburg Centre for Ultrafast Imaging, Universität Hamburg, Luruper Chaussee 149, 22761 Hamburg, Germany

ARTICLE INFO

Article history:

Received 15 July 2020

Accepted 5 April 2021

Available online 15 April 2021

Submitted by R. Brualdi

MSC:

05C50

15A18

05C22

81R40

81V55

Keywords:

Cospectrality

Symmetric matrices

Structure of eigenvectors

Matrix powers

Walk equivalence

ABSTRACT

Originating from spectral graph theory, cospectrality is a powerful generalization of exchange symmetry and can be applied to all real-valued symmetric matrices. Two vertices of an undirected graph with real edge weights are cospectral if and only if the underlying weighted adjacency matrix M fulfills $[M^k]_{u,u} = [M^k]_{v,v}$ for all non-negative integer k , and as a result any eigenvector ϕ of M has (or, in the presence of degeneracies, can be chosen to have) definite parity on u and v . We here show that the powers of a matrix with cospectral vertices induce further local relations on its eigenvectors, and also can be used to design cospectrality preserving modifications. To this end, we introduce the concept of *walk equivalence* of cospectral vertices with respect to *walk multipliers* which are special vertex subsets of a graph. Walk multipliers allow for systematic and flexible modifications of a graph with a given cospectral pair while preserving this cospectrality. The set of modifications includes the addition and removal of both vertices and edges, such that the underlying topology of the graph can be altered. In particular, we prove that any new vertex connected to a walk multiplier by suitable connection weights becomes a so-called unrestricted substitution point (USP), meaning that

* Corresponding author.

E-mail address: mroentge@physnet.uni-hamburg.de (M. Röntgen).

¹ These three authors contributed equally.

<https://doi.org/10.1016/j.laa.2021.04.004>

0024-3795/© 2021 Elsevier Inc. All rights reserved.

any arbitrary graph may be connected to it without breaking cospectrality. Also, suitable interconnections between walk multiplets within a graph are shown to preserve the associated cospectrality. Importantly, we demonstrate that the walk equivalence of cospectral vertices u, v imposes a local structure on every eigenvector ϕ obeying $\phi_u = \pm\phi_v \neq 0$ (in the case of degeneracies, a specific choice of the eigenvector basis is needed). Our work paves the way for flexibly exploiting hidden structural symmetries in the design of generic complex network-like systems.

© 2021 Elsevier Inc. All rights reserved.

1. Introduction

Eigenvalue problems of real symmetric matrices are ubiquitous in many fields of science. Special examples are graph theory in mathematics as well as properties of quantum systems in physics. A first step in dealing with such problems is often based on a symmetry analysis in terms of permutation matrices that commute with the matrix H at hand. Given a set of such permutation matrices, a symmetry-induced block-diagonalization of H is possible and powerful statements about the eigenvectors of H can be made [1,2]. The permutation symmetries of a matrix can be conveniently visualized in the framework of *graphs*. A graph representing a matrix $H \in \mathbb{R}^{N \times N}$ is a collection of N vertices connected by edges with weights $H_{i,j}$, like the one shown in Fig. 1. Due to this mapping between a matrix and the graph representing it we denote both the graph and the corresponding matrix with the same symbol H . In this graphical picture, the action of a permutation matrix P corresponds to permuting the vertices of the graph, along with the ends of the edges connected to them. H is then transformed to $H' = PHP^{-1}$, and if P and H commute, $PH = HP$, then the graph remains the same after the permutation, i.e. $H' = H$. In particular, if P exchanges two vertices u and v , while permuting the remaining vertices arbitrarily, its commutation with H means that the u -th and v -th row of H coincide, $H_{u,j} = H_{v,j}$ for all $j \in \llbracket 1, N \rrbracket \equiv \{1, 2, \dots, N\}$ (and the same for the

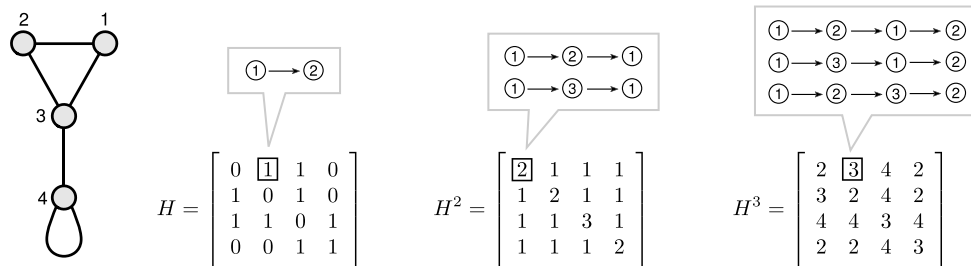


Fig. 1. An undirected, unweighted graph with four vertices represented by a 4×4 symmetric matrix H , and the interpretation of its powers H^k in terms of “walks”: The matrix element $[H^k]_{i,j}$ counts the number of distinct walks of length k from vertex i to j , as illustrated for $k = 1, 2, 3$.

u -th and v -th column, since H is symmetric). It can then be shown that the u -th and v -th diagonal elements of any non-negative integer power of H coincide,

$$[H^k]_{u,u} = [H^k]_{v,v} \quad \forall k \in \mathbb{N}, \quad (1)$$

and that any eigenvector ϕ of H has—or, if degenerate to another eigenvector, can be chosen to have—positive or negative parity on u and v [3], that is,

$$\phi_u = \pm \phi_v. \quad (2)$$

The eigenvector components on the remaining vertices, which are generally not pairwise exchanged by P , may have arbitrary components. Thus Eq. (2) constitutes a *local* parity of the eigenvectors. This property is intricately related to the interpretation of powers of H in terms of *walks* [4,3], which are sequences of vertices connected by edges, on the corresponding graph. For an unweighted graph (having $H_{i,j} \in \{0, 1\}$), the element $[H^k]_{i,j}$ counts all possible walks of length k from vertex i to j on the graph. This is illustrated in Fig. 1 for selected walks of length 1, 2, 3. With this interpretation, Eq. (1)—and thereby also Eq. (2)—hold if the graph has an equal number of “closed” walks starting and ending on u or v , for any walk length k . This is the case, e.g., for vertices 1 and 2 in the graph of Fig. 1. For weighted graphs (having $H_{i,j} \in \mathbb{R}$), the interpretation of matrix powers in terms of walks is modified by weighing the walks accordingly (see below), with all corresponding results staying valid.

Interestingly, and in many cases counterintuitively, the local parity of eigenvectors of a graph, Eq. (2), can be achieved even if H does not commute with any permutation matrix P , as long as Eq. (1) is fulfilled. Given this condition, the eigenvalue spectra of the two submatrices $H \setminus u$ and $H \setminus v$, obtained from H by deleting vertex u or v from the graph, respectively, coincide, and u and v are said to be *cospectral* [3]. Originating from spectral graph theory [5], the results of the study of cospectral vertices have so far been applied to the field of quantum information and quantum computing, but also—under the term *isospectral vertices*—to chemical graph theory [6–8]. In a very recent work [9], cospectral vertices have also been linked to so-called “isospectral reductions”, a concept which allows to transform a given matrix into a smaller version thereof which shares all (or, in special cases, a subset of) the eigenvalues with the original matrix.

Given a graph with cospectral vertices u and v , one may ask what kind of changes can be made to it without breaking the cospectrality. One particularly interesting feature that occurs for some graphs is the presence of so-called *unrestricted substitution points* (USPs), which were introduced in Ref. [8]. Given a graph H with two cospectral vertices u and v , a third vertex c is an USP if and only if one can attach an arbitrary subgraph to c without breaking the cospectrality of u and v . While it is a straightforward task to identify all USPs of a given graph, the origin of these special points has been elusive so far.

In this work we shed new light on this phenomenon by introducing the concept of *walk equivalence* of cospectral vertices u, v with respect to a vertex subset of a graph. In the

simplest case of an unweighted graph, two vertices u and v are walk equivalent relative to a vertex subset if the cumulative number of walks from u to this subset equals that from v to this subset, for any walk length. The vertex subset then corresponds to what we call a *walk multiplet* relative to the pair u, v . The smallest walk multiplets, which we call singlets, consist of a single vertex and are identified with the above mentioned USPs, and we here demonstrate how to create such points in a systematic way. Specifically, we show that a graph can be extended via any of its walk multiplets by connecting it to a new vertex while preserving the cospectrality of the associated vertex pair. This procedure can be repeated any number of times with different walk multiplets. All the newly added vertices turn out to be USPs, thus allowing us to connect arbitrary new graphs exclusively to them without breaking the cospectrality. Additionally, we show that one can also alter the topology of a graph *without extending it* by modifying the interconnections between two or more walk multiplets. This provides a systematic way to construct graphs with cospectral vertices but no permutation symmetry, based on breaking existing symmetries by walk multiplet-induced modifications. The concept of walk equivalence of vertices is further generalized to the case where walks to different subsets of a walk multiplet can be equipped with different weight parameters.

Apart from providing means to modify a graph without breaking the cospectrality, we show that walk multiplets can be used to obtain a substantial understanding of the structure of eigenvectors of general real symmetric matrices with cospectral pairs. In particular, for a suitably chosen eigenbasis, walk multiplets induce linear scaling relations between eigenvector components on the multiplet vertices, in dependence of the local parity—Eq. (2)—of the eigenvector on the cospectral vertex pair associated with the multiplet. As a special case, the eigenvector components vanish on any walk singlet and, by iteration, on any arbitrary new graph connected exclusively to walk singlets. We believe our work will provide valuable insights into the structure of eigenvectors of generic network-like systems and thereby aid in the design of desired properties.

The paper is structured as follows. In Section 2, we first motivate the concept of walk multiplets as a generalization of USPs, before we define them generally in terms of walks on graphs, and proceed discussing their properties. In Section 3, we show how walk multiplets allow for the modification of graphs without breaking vertex cospectrality. In Section 4, we apply the concept to derive relations between the components of eigenvectors on walk multiplet vertices, with vanishing components on walk singlets as a special case. In Section 5, we use walk multiplets to generate graphs that feature cospectral vertices without having any permutation symmetry. We conclude the work in Section 6. In the Appendix we provide the proofs of all theorems.

2. Walk multiplets

As the name suggests, the concept of “walk multiplets,” to be developed below, is based on walks along the vertices of a graph. In particular, as illustrated in Fig. 1, the entries of powers H^k can be interpreted in terms of walks [4] on the corresponding graph

with N vertices. Indexing the vertices of the graph by $v_i \in \llbracket 1, N \rrbracket$, a walk of length k from vertex v_1 to vertex v_{k+1} is a sequence

$$\alpha_k(v_1, v_{k+1}) = (v_1, v_2), (v_2, v_3), \dots, (v_k, v_{k+1}) \quad (3)$$

of k (possibly repeated) edges (v_i, v_{i+1}) corresponding to nonzero matrix elements $H_{v_i, v_{i+1}}$. Note that a diagonal element $H_{n, n}$ corresponds to a “loop” on vertex n , that is, an edge connecting n with itself. If the entries of H are either 0 or 1, that is, the graph is *unweighted*, then the element $[H^k]_{m, n}$ equals the number of walks from m to n on the graph. We leave it like this for now, but will consider walks on general weighted graphs further below. Throughout this work $H = H^\top \in \mathbb{R}^{N \times N}$ will denote a real symmetric matrix but also the corresponding graph itself, since there is a one-to-one mapping between them for our purposes.

2.1. Unrestricted substitution points: the simplest case of walk multiplets

Let us introduce the idea of walk multiplets, starting with some preliminary considerations by inspecting the example graph in Fig. 2(a), adapted from Ref. [8]. As is common in the field of chemical (or molecular) graph theory, this graph is used as a very simple representation of a molecule, with the vertices being atoms of some kind and the edges between them being atom-atom, i.e. molecular, bonds. For simplicity, we consider all bonds to be of the same unit strength, meaning that all edges have the same weight 1, and all atoms to have zero “onsite potential”, so there are no loops on vertices (like the one on vertex 4 in Fig. 1).

While seeming quite common, this graph has some interesting “hidden” properties. First of all, it has cospectral vertices labeled u and v . This cospectrality does not stem, though, from a corresponding exchange symmetry (permuting vertices u and v with each other). Indeed, without being symmetric under exchange, the cospectral vertices fulfill Eq. (1), that is, the number of closed walks from u back to u and from v back to v is the same, for any walk length k . Notably, cospectral vertices go under the name “isospectral points” in molecular graph theory.

A second interesting property of the graph in Fig. 2 is that it has some special vertices, labeled c and r , called “unrestricted substitution points” (USPs) [6,8], which were already mentioned in Section 1. Those are vertices to which new vertices or subgraphs may be attached, or which may even be removed completely, without breaking the cospectrality of u and v . This is done in Fig. 2(b). Now, let us approach this in terms of walks, and focus on the vertex c of the example for concreteness. Cospectrality of u, v is preserved when connecting c to the arbitrary new graph C , meaning that the number of closed walks from u and v is the same for any walk length also after this modification. All additionally created closed walks from u or v which visit the arbitrary subgraph C , however, necessarily traverse the USP c on the way. This suggests that the number of walks from u to c is the same as from v to c , for any walk length—because the possible

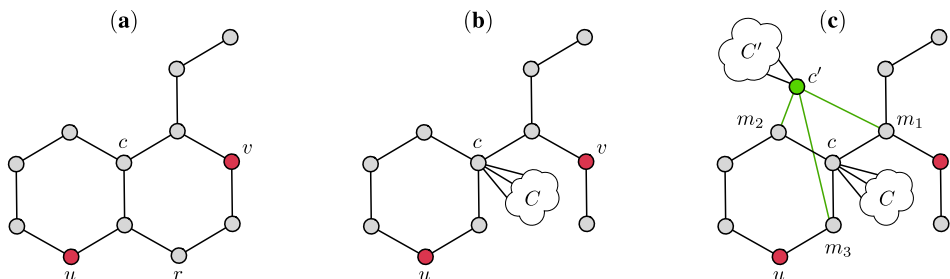


Fig. 2. (a) A molecular graph, taken from Ref. [8], which has two cospectral vertices u, v and two “unrestricted substitution points” (USPs) c, r . (b) The USPs are vertices which can be connected to any arbitrary graph C (as done with c) or also removed from the graph (as done with r), without breaking the cospectrality of u, v . (c) In the present work we generalize USPs to vertex subsets called “walk multiplets”, an example here being the subset $\mathbb{M} = \{m_1, m_2, m_3\}$. We can connect this subset to a new vertex c' , which we can in turn connect to an arbitrary graph C' , without breaking the cospectrality of u, v . The added vertex c' is a walk “singlet”, which is identified as an USP.

walk segments within C are evidently the same for walks from u and from v . Indeed, this turns out to be exactly the case: A vertex c of a graph H with cospectral vertices u, v is an USP if and only if it fulfills $[H^\ell]_{u,c} = [H^\ell]_{v,c}$ for any non-negative integer ℓ .

While already offering a great flexibility, USPs do not necessarily occur in all graphs with cospectral pairs. This leads to the question: Are there other possibilities of graph extensions, involving a *set of points* instead of just a single point to which one can connect an arbitrary graph? Imagine, for example, a subset \mathbb{M} of some graph’s vertex set to which some arbitrary new graph C' can be connected, by connecting an arbitrary single vertex c' of C' to all vertices in \mathbb{M} , without breaking the cospectrality between two vertices u, v of the original graph. Such a subset \mathbb{M} , associated in this way with a cospectral vertex pair, corresponds to what we will call a “walk multiplet” relative to u, v . An example is illustrated in Fig. 2(c). The key property, in analogy to USPs, is that the cumulative number of walks from u to all vertices in \mathbb{M} is the same as from v to \mathbb{M} . An USP is then just the simplest case of a walk multiplet consisting of a single vertex, a walk “singlet”.

Below, we will formalize the concept of walk multiplets and describe the various flavors they can assume in general undirected and real-weighted graphs, which correspond to real symmetric matrices. Their value in extending graphs with cospectral vertices will be shown subsequently in Section 3, and their significance for graph eigenvectors will be demonstrated in Section 4. First, we introduce some helpful key notions in the description of walks.

2.2. Weighted walks and walk matrices

Let us first extend the correspondence between walks on a graph, defined in Eq. (3), and powers of its matrix H to a weighted graph, where the entries of H are arbitrary real numbers. Any walk α_k from v_1 to v_{k+1} is then given a weight $w(\alpha_k)$ equal to

the product of the edge weights $w(v_i, v_{i+1}) = H_{v_i, v_{i+1}}$ of all edges traversed [10], that is,

$$w(\alpha_k(v_1, v_{k+1})) = w(v_1, v_2)w(v_2, v_3) \cdots w(v_k, v_{k+1}) = \prod_{i=1}^k [H]_{v_i, v_{i+1}}. \tag{4}$$

The entries $[H^k]_{m,n}$ are then given by the sum over weighted walks as [10]

$$[H^k]_{m,n} = \sum_{\alpha_k} w(\alpha_k(m, n)) \tag{5}$$

where the sum runs over all distinct walks of length k from m to n .

Consider, now, a subset $\mathbb{M} \subseteq \mathbb{V}$ of the set \mathbb{V} of the vertices of a graph H . The *walk matrix* of H relative to \mathbb{M} is the matrix [11] $W_{\mathbb{M}} = [e_{\mathbb{M}}, He_{\mathbb{M}}, \dots, H^{N-1}e_{\mathbb{M}}]$, whose k -th column equals the action of H^{k-1} on the so called *indicator* (or *characteristic*) vector $e_{\mathbb{M}}$ of \mathbb{M} with $[e_{\mathbb{M}}]_m = 1$ for $m \in \mathbb{M}$ and 0 otherwise. Thus, the element

$$[W_{\mathbb{M}}]_{s,\ell} = \sum_{m \in \mathbb{M}} [H^{\ell-1}]_{s,m} \tag{6}$$

equals the sum over weighted walks [in the sense of Eq. (5)] of length $\ell - 1 \in \llbracket 0, N - 1 \rrbracket$ from vertex s to all vertices of \mathbb{M} .

Below we will use this notion of collective walks to vertex subsets to identify structural properties of graphs and their eigenvectors. It will then be convenient, however, to account also for the case where the walks to different vertices $m \in \mathbb{M}$, represented by $[H^k]_{s,m}$, are multiplied by some (generally different) factors γ_m . Treating $W_{\mathbb{M}}$ as the Krylov matrix [12] of H generated by $e_{\mathbb{M}}$, we thus simply replace this generating vector with a *weighted indicator vector* $e_{\mathbb{M}}^{\gamma}$ having a tuple $\gamma = (\gamma_m)_{m \in \mathbb{M}}$ of general real values γ_m instead of 1's in its nonzero entries $m \in \mathbb{M}$. This extends the common walk matrix to a corresponding “weighted” version which we denote as $W_{\mathbb{M}}^{\gamma}$, that is

$$W_{\mathbb{M}}^{\gamma} = [e_{\mathbb{M}}^{\gamma}, He_{\mathbb{M}}^{\gamma}, \dots, H^{N-1}e_{\mathbb{M}}^{\gamma}], \quad \gamma = (\gamma_m)_{m \in \mathbb{M}}, \quad [e_{\mathbb{M}}^{\gamma}]_m = \begin{cases} \gamma_m, & m \in \mathbb{M}, \\ 0, & m \notin \mathbb{M}. \end{cases} \tag{7}$$

For this weighted walk matrix, Eq. (6) is accordingly modified to the more general form

$$[W_{\mathbb{M}}^{\gamma}]_{s,\ell} = \sum_{m \in \mathbb{M}} \gamma_m [H^{\ell-1}]_{s,m}, \quad \ell \in \llbracket 1, N \rrbracket, \tag{8}$$

so that the interpretation of matrix powers in terms of walks is further equipped with weights γ_m for the individual walk destinations m .

2.3. Walk equivalence of cospectral vertices

Combining the intuition of equal number of walks to vertex subsets in Section 2.1 with the notion of weighted walk matrices in Section 2.2, it now comes natural to define the general case of a walk multiplet. We will then discuss examples of walk multiplets before analyzing their consequences in the next sections.

Definition 1 (*Walk multiplet*). Let $H \in \mathbb{R}^{N \times N}$ be a matrix with vertex set \mathbb{V} and walk matrix $W_{\mathbb{M}}^\gamma$ relative to a subset $\mathbb{M} \subseteq \mathbb{V}$ with weighted indicator vector $e_{\mathbb{M}}^\gamma$ corresponding to the tuple $\gamma = (\gamma_m)_{m \in \mathbb{M}}$. If the u -th and v -th rows of $W_{\mathbb{M}}^\gamma$ fulfill

$$[W_{\mathbb{M}}^\gamma]_{u,*} = p[W_{\mathbb{M}}^\gamma]_{v,*} \tag{9}$$

(with $*$ denoting the range $\llbracket 1, N \rrbracket$, i.e. all matrix columns), then \mathbb{M} corresponds to an **even (odd) walk multiplet** with **parity** $p = +1$ (-1) relative to the two vertices u, v , denoted as $\mathbb{M}_{\gamma;u,v}^p$, and u, v are **walk equivalent (antiequivalent)** with respect to $\mathbb{M}_{\gamma;u,v}^p$.

A walk multiplet $\mathbb{M}_{\gamma;u,v}^p$ is thus not merely a subset \mathbb{M} , but this subset equipped with a $|\mathbb{M}|$ -tuple of weight parameters γ and a parity p , associated with a given vertex pair u, v . If all weights γ_m are equal, then $\mathbb{M}_{\gamma;u,v}^p$ is a *uniform* walk multiplet, and we will first discuss such multiplets. In this case the common weight is obviously a global scaling factor in Eq. (9) and can be set to unity without loss of generality, $\gamma_m = 1$ for all $m \in \mathbb{M}$. We will show cases of *nonuniform* walk multiplets (with unequal γ_m in general) afterwards. Although walk multiplets are generally defined above relative to any pair of vertices u, v , we will concentrate on multiplets relative to cospectral vertices u, v from now on. Also, for brevity, we will drop the indication of vertices u, v in the subscript of $\mathbb{M}_{\gamma;u,v}^p$ when they are clear from the context. According to their cardinality (the number $|\mathbb{M}|$ of vertices in \mathbb{M}) we call multiplets “singlets”, “doublets”, etc. Note that the same subset \mathbb{M} can in general correspond simultaneously to different walk multiplets relative to different cospectral vertex pairs or with different tuples γ . We should also point out that the notion of “walk equivalence” of two *graphs* as a whole has been used [13,14], and stress that we here introduce the notion of walk equivalence of two *vertices* with respect to a vertex subset.

Before showing examples of walk multiplets, we note that the condition (9) only incorporates walks of length $k \in \llbracket 0, N - 1 \rrbracket$ from u and from v to \mathbb{M} ; see Eq. (8). At first sight one might then wonder whether the sum over longer walks ($k \geq N$) to \mathbb{M} is also equal for u and v . This is indeed the case. Due to the Cayley-Hamilton theorem, we have that $H^N = \sum_{k=0}^{N-1} c_k H^k$ with constant coefficients c_k , meaning that higher powers $k > N - 1$ of H can be written as polynomials in H of order up to $N - 1$. Thus, if Eq. (9) holds, we have that

$$\sum_{m \in \mathbb{M}} \gamma_m [H^k]_{u,m} = p \sum_{m \in \mathbb{M}} \gamma_m [H^k]_{v,m} \quad \forall k \in \mathbb{N}. \tag{10}$$

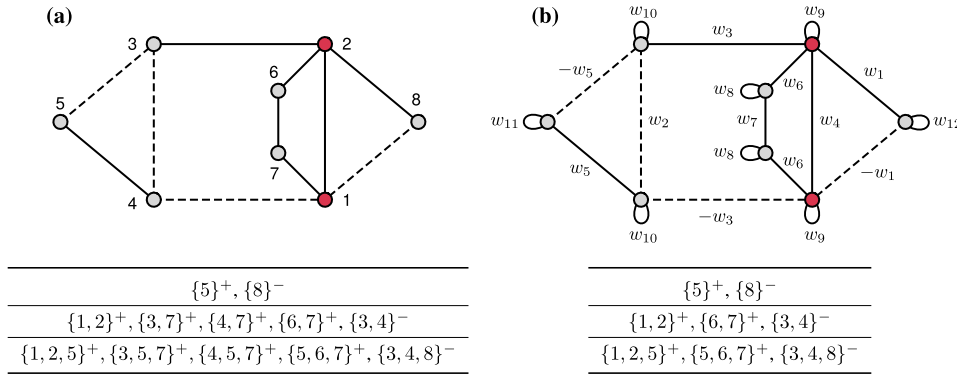


Fig. 3. (a) A graph with edge weights +1 (solid lines) and -1 (dashed lines) in which the two vertices 1 and 2 are cospectral (among other cospectral pairs) and (b) the same graph with edges weighted by 12 real parameters w_n as shown, preserving the cospectrality of $\{1, 2\}$. The tables below list all *uniform* walk singlets, doublets, and triplets (top to bottom) relative to $\{1, 2\}$, with superscripts indicating the parity p of each multiplet; see Example 1.

For an unweighted graph, the notion of walk equivalence of u and v with respect to \mathbb{M} then acquires a simple interpretation: An even uniform walk multiplet ($\gamma_m = 1$ for all $m \in \mathbb{M}$) corresponds to a vertex subset \mathbb{M} such that the number of walks from u to \mathbb{M} equals the number of walks from v to \mathbb{M} (that is, summed over all $m \in \mathbb{M}$) for any walk length k . Let us now have a look at some uniform walk multiplets in an example graph.

Example 1. In the graph depicted in Fig. 3(a), the two vertices $u = 1, v = 2$ are cospectral. All uniform walk singlets, doublets, and triplets of H with respect to $1, 2$ are given in the table below. We put a superscript $+(-)$ on each individual multiplet subset to indicate its even (odd) parity p . Importantly, the vertex cospectrality and multiplet structure of a graph are in general not strictly bound to a specific set of edge weight values. Indeed, one may generally “parametrize” the edge weights, by setting groups of them to the same but arbitrary real value, and still retain the graph’s vertex cospectrality as well as a subset of its walk multiplets. To demonstrate such a parametrization, in Fig. 3(b) the graph of Fig. 3(a) has been weighted by arbitrary real parameters w_n ($n = 1, 2, \dots, 12$) as shown. The uniform multiplets shown in the table below the graph are present for any choice of the weight parameters w_n , as does the cospectrality of $1, 2$. Note, however, that certain uniform multiplets of the original graph are removed in the parametrized one for arbitrary values w_n (that is, if there are no further constraints on these values); for example, $\{3, 7\}^+$ and $\{4, 7\}^+$. Other cospectrality-preserving edge weight parameterizations (not shown) may keep different sets of multiplets intact. We note here that the graphs in Fig. 3 were chosen to have a simple geometry to highlight the occurrence of even and odd walk multiplets. Indeed, in this particular case the graph’s matrix H (for both subfigures of Fig. 3) commutes with the *signed* permutation

$$H = \begin{bmatrix} 0 & 1 \\ 1 & 0 \end{bmatrix} \oplus \begin{bmatrix} 0 & -1 \\ -1 & 0 \end{bmatrix} \oplus 1 \oplus \begin{bmatrix} 0 & 1 \\ 1 & 0 \end{bmatrix} \oplus -1 \tag{11}$$

with $\Pi^2 = I$. This symmetry induces some of the present walk multiplets, e.g. the anti-doublet $\{3,4\}^-$ relative to $\{1,2\}$, since $[H^k]_{1,3} + [H^k]_{1,4} = [\Pi^2 H^k]_{1,3} + [\Pi^2 H^k]_{1,4} = [\Pi H^k \Pi]_{1,3} + [\Pi H^k \Pi]_{1,4} = -[H^k]_{2,4} - [H^k]_{2,3}$. In fact, all walk multiplets which are retained after the parametrization in Fig. 3(b) can be seen as a consequence of this symmetry. The remaining ones, that is, $\{3,7\}^+, \{4,7\}^+, \{3,5,7\}^+, \{4,5,7\}^+$ in Fig. 3(a), cannot be explained by this simple symmetry but rather by a symmetry of the graph’s walk structure—specifically, under row permutation on the graph’s walk matrix, see Eq. (9).

Surely, the graph in Example 1 also features a whole lot of nonuniform multiplets, but we do not show them for simplicity. We have another example dedicated to nonuniform multiplets right below. Apart from that, though, the reader might have noticed that the cospectral pair $\{1,2\}$ in Fig. 3 itself is included in the list of uniform walk multiplets. This is not a coincidence for this particular graph.

Remark 1. A cospectral vertex pair $\{u, v\}$ is a uniform even walk doublet relative to itself, since $[H^k]_{u,u} + [H^k]_{u,v} = [H^k]_{v,v} + [H^k]_{v,u}$, with $[H^k]_{u,u} = [H^k]_{v,v}$ by Eq. (1) and $[H^k]_{u,v} = [H^k]_{v,u}$ by the symmetry of $H = H^\top$. Thus Eq. (10) is fulfilled with $\mathbb{M} = \{u, v\}$ and $p = +1$.

In the next example, we will illustrate the occurrence of nonuniform walk multiplets, where the walks to different destinations m in the associated subset \mathbb{M} are *generally weighted differently* by weights γ_m . Usually, however, those weights γ_m are not *all* different from each other, but can be partitioned into groups of equal values. We call the vertex subset of a multiplet with such equal values in the tuple $\gamma = (\gamma_m)_{m \in \mathbb{M}}$ a *sublet* of the multiplet. In other words, given a nonuniform walk multiplet \mathbb{M}_γ^p , the subset \mathbb{M} is the union of $N_s = N_s(\gamma) \leq |\mathbb{M}|$ disjoint sublets \mathfrak{m}_μ , that is,

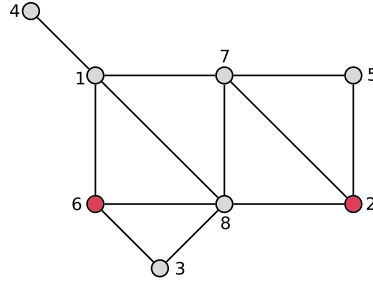
$$\mathbb{M} = \bigcup_{\mu=1}^{N_s} \mathfrak{m}_\mu, \quad \mathfrak{m}_\mu \cap \mathfrak{m}_\nu = \emptyset \quad \forall \mu \neq \nu, \quad \gamma_{m \in \mathfrak{m}_\mu} = \Gamma_\mu \tag{12}$$

such that all weights γ_m with $m \in \mathfrak{m}_\mu$ have equal value Γ_μ which we call the “coefficient” of the sublet \mathfrak{m}_μ . The expanded form of the multiplet condition, Eq. (10), then becomes

$$\sum_{\mu} \Gamma_\mu \sum_{m \in \mathfrak{m}_\mu} [H^k]_{u,m} = p \sum_{\mu} \Gamma_\mu \sum_{m \in \mathfrak{m}_\mu} [H^k]_{v,m} \quad \forall k \in \mathbb{N}. \tag{13}$$

We indicate the coefficients Γ_μ as subscripts of vertex sublets within a walk multiplet, as shown in the following example.

Example 2. The graph in Fig. 4 has two cospectral vertices $u = 2$ and $v = 6$, with walk multiplets shown in the table for a maximum number of 4 vertices (there are no singlets). As an example of notation, the even nonuniform walk triplet $\mathbb{M}_\gamma^p = \{(1,5)_a, (4)_{2a}\}^+$



$\{(2, 6)_a\}^+, \{(3, 7)_a\}^+, \{(4)_a, (8)_{-a}\}^+, \{(2)_{-a}, (6)_a\}^-$
$\{(1, 4)_a, (3)_{-a}\}^+, \{(1)_a, (3)_{-2a}, (5)_{-a}\}^+, \{(1, 8)_a, (3)_{-a}\}^+, \{(1, 5)_a, (4)_{2a}\}^+, \{(1, 4, 7)_a\}^+, \{(1)_a, (5)_{-a}, (7)_{2a}\}^+,$ $\{(1, 5)_a, (8)_{2a}\}^+, \{(1, 7, 8)_a\}^+, \{(3, 4, 5)_a\}^+, \{(3, 5, 8)_a\}^+, \{(4, 5)_a, (7)_{-a}\}^+, \{(5, 8)_a, (7)_{-a}\}^+$
$\{(1)_a, (3)_b, (4)_{2a+b}, (5)_{a+b}\}^+, \{(1, 4)_a, (3)_b, (7)_{a+b}\}^+, \{(1)_a, (3)_{-a}, (4)_b, (8)_{a-b}\}^+, \{(1)_a, (3)_b, (5)_{-a}, (7)_{2a+b}\}^+,$ $\{(1)_a, (3)_b, (5)_{a+b}, (8)_{2a+b}\}^+, \{(1, 8)_a, (3)_b, (7)_{a+b}\}^+, \{(1)_a, (4)_b, (5)_{-a+b}, (7)_{2a-b}\}^+, \{(1, 5)_a, (4)_b, (8)_{2a-b}\}^+,$ $\{(1, 7)_a, (4)_b, (8)_{a-b}\}^+, \{(1)_a, (5)_b, (7)_{a-b}, (8)_{a+b}\}^+, \{(2, 6)_a, (3, 7)_b\}^+, \{(2, 6)_a, (4)_b, (8)_{-b}\}^+,$ $\{(3)_a, (4, 5)_b, (7)_{a-b}\}^+, \{(3, 5)_a, (4)_b, (8)_{a-b}\}^+, \{(3, 7)_a, (4)_b, (8)_{-b}\}^+, \{(3)_a, (5, 8)_b, (7)_{a-b}\}^+,$ $\{(4)_a, (5)_b, (7)_{-b}, (8)_{-a+b}\}^+, \{(1, 3)_a, (5, 7)_{-a}\}^-, \{(1, 5)_a, (4, 8)_{-a}\}^-$

Fig. 4. An unweighted graph with two cospectral vertices 2, 6, with all existing walk multiplets up to maximal size of four vertices listed in the table below the graph (there are no walk singlets). Each walk multiplet $\{\dots\}^\pm$ is composed of sublets $(\dots)_{\Gamma_\mu}$ with coefficients $\Gamma_\mu \in \mathbb{R}$ which are *independent* among multiplets (although the same symbols a, b are used for brevity); see Example 2.

(with $\gamma = (\gamma_1, \gamma_4, \gamma_5) = (a, 2a, a)$) is composed of the sublets $m_1 = \{1, 5\}$ and $m_2 = \{4\}$ with coefficients $\Gamma_1 = a$ and $\Gamma_2 = 2a$, respectively, where the parameter a can take any nonzero value. Note that the values of sublet coefficients (like a, b in Fig. 4) in *different* multiplets are *unrelated*. For instance, $\{(4)_a, (8)_{-a}\}^+$ is an even doublet composed of sublets $\{4\}$ and $\{8\}$ with coefficients a and $-a$, independently of the values of a in the other multiplets in Fig. 4. Similarly, $\{(1)_a, (3)_b, (4)_{2a+b}, (5)_{a+b}\}^+$ is an even quadruplet composed of the four sublets $\{1\}, \{3\}, \{4\}, \{5\}$ with corresponding nonzero coefficients $a, b, 2a + b, a + b$. If, however, any $n > 0$ of these coefficients vanish, then the remaining $4 - n$ sublets with nonzero coefficients constitute a multiplet with $4 - n$ vertices. For example, if $b = -a$, the coefficient of $\{5\}$ vanishes, and the remaining three sublets form the triplet $\{(1, 4)_a, (3)_{-a}\}^+$. Finally, note that any uniform multiplet consists of a single sublet, like, e.g., $\{(1, 4, 7)_a\}^+$. As one can see, the number of nonuniform multiplets is much larger than the number of uniform ones in the present example.

Now, going back to Fig. 3, a closer look at the table there suggests that the union of multiplets of same parity p form a multiplet; for instance, $\{8\}^- \cup \{3, 4\}^- = \{3, 4, 8\}^-$. Indeed, the union of disjoint uniform multiplets of equal parity always forms a new uniform multiplet. In fact, different uniform multiplets may also overlap (that is, have common vertices), and their union is again a multiplet, though a *nonuniform* one. Take, e.g., the three uniform even multiplets $\{(3, 7)_a\}^+, \{(4, 7)_b\}^+, \{(5)_{a'}\}^+$, now written with

arbitrary uniform weights a, b, a' , respectively. Their union forms the nonuniform even multiplet $\{(3)_a, (4)_b, (5)_{a'}, (7)_{a+b}\}^+$ consisting of four sublets with coefficients $\Gamma_{1,2,3,4} = a, b, a', a+b$. Quite generally, any two walk multiplets of equal parity can be merged into a larger multiplet, as expressed by the following remark.

Remark 2. It is clear from Eq. (9) that, if \mathbb{A}_γ^p and \mathbb{B}_δ^p are two even (odd) walk multiplets with weighted indicator vectors $e_{\mathbb{A}}^\gamma$ and $e_{\mathbb{B}}^\delta$, respectively, then \mathbb{C}_ϵ^p with $\mathbb{C} = \mathbb{A} \cup \mathbb{B}$ is also an even (odd) multiplet with weighted indicator vector $e_{\mathbb{C}}^\epsilon = e_{\mathbb{A}}^\gamma + e_{\mathbb{B}}^\delta$.

Note, however, that not all nonuniform multiplets can be decomposed as a union of uniform multiplets. This is easily verified from the table of Fig. 4. For example, the even nonuniform walk quadruplet $\{(2, 6)_a, (3, 7)_b\}^+$ is the union of the two even uniform doublets $\{(2, 6)_a\}^+$ and $\{(3, 7)_b\}^+$, but none of the walk triplets can be decomposed into smaller multiplets (that is, a doublet and a singlet or two overlapping doublets). On the other hand, the nonuniform quadruplet $\{(1)_a, (3)_{-a}, (4)_b, (8)_{a-b}\}^+$ is composed of the nonuniform triplet $\{(1, 4)_a, (3)_{-a}\}$ and doublet $\{(4)_{a'}, (8)_{-a'}\}$ with $a' \equiv b - a$.

3. Preserving vertex cospectrality via walk multiplets

Walk multiplets are very valuable for the analysis and understanding of matrices with cospectral vertices u and v . As we will show, once (one or more of) the walk multiplets of H relative to u and v are known, one can use this knowledge to *extend* a graph H by connecting a new vertex (or even arbitrary graphs) to it whilst preserving the cospectrality of u and v . This naturally generalizes the notion of USPs to subsets of more than one vertex of a graph. We will also show how to *interconnect* walk multiplets, thereby changing the topology of a given graph, while preserving the associated vertex cospectrality.

In the literature [11], connecting a single vertex to a graph H via multiple edges of weight 1 results in a graph H' which is coined a “cone” of H . To treat general weighted graphs, we will here require cones with weighted edges:

Definition 2 (Weighted cone). Let $G \in \mathbb{R}^{N \times N}$ represent a graph with vertex set $\mathbb{V} = \{1, 2, \dots, N\}$. A **weighted cone** of G over a subset $\mathbb{M} \subseteq \mathbb{V}$ with weight tuple $\gamma = (\gamma_m)_{m \in \mathbb{M}}$ is the graph

$$H = \begin{bmatrix} G & e_{\mathbb{M}}^\gamma \\ e_{\mathbb{M}}^{\gamma^\top} & 0 \end{bmatrix}, \tag{14}$$

constructed by connecting a new vertex $c = N + 1$ (the **tip** of the cone) to \mathbb{M} with edges of weights $\gamma_m = H_{m,c} = H_{c,m}$ to the corresponding vertices $m \in \mathbb{M}$, where $e_{\mathbb{M}}^\gamma$ is the weighted indicator vector of Eq. (7) with nonzero entries γ_m .

For instance, the graph in Fig. 3(a) is the weighted cone H over the vertex subset $\{1, 2\}$ of the graph $H \setminus 8$ (H after removing vertex 8) with weight tuple $\gamma = (\gamma_1, \gamma_2) = (-1, 1)$. We can now state one of the main results of this work, which will allow for the systematic extension of graphs with cospectral pairs while keeping the cospectrality:

Theorem 1 (*Walk singlet extension*). *Let $G = G^T \in \mathbb{R}^{N \times N}$ represent an undirected graph with two cospectral vertices u, v , let \mathbb{M}_γ^p be an even (odd) walk multiplet of G relative to u, v , and let H be a weighted cone of G over the subset \mathbb{M} with real weight tuple $\gamma = (\gamma_m)_{m \in \mathbb{M}}$. Then*

- (i) *Vertices u, v are cospectral in H .*
- (ii) *The tip c of the cone H is an even (odd) walk singlet relative to u, v .*
- (iii) *Any even (odd) walk multiplet in G is an even (odd) walk multiplet in H .*

Point (i) of the theorem extends the notion of USPs to vertex subsets for the case of a single new connected vertex c : the vertex c is now connected to a subset \mathbb{M} instead of a single USP of a graph without breaking the associated vertex cospectrality. Further, by point (ii) of the theorem, another new vertex c' can be connected to c while preserving cospectrality, just as would be the case if c were a USP. Point (iii) finally allows *multiple* single new vertices to be connected to different walk multiplets, or to the same walk multiplet. In the case of a USP, however, cospectrality is preserved when connecting a new *arbitrary graph* to the USP, and not only a single new vertex. This is indeed also the case for a walk singlet.

Corollary 1. *Let the vertex c of a graph H be an even (odd) walk singlet relative to a cospectral pair u, v in H , and let C be a graph connected exclusively to c via any number of edges with arbitrary weights. Then all vertices of C are even (odd) walk singlets relative to u, v .*

We thus see that any walk singlet is a USP, and below (Corollary 3) we will also show that the reverse is true. Now, suppose we have connected some walk singlets to corresponding new subgraphs C, C', \dots , which then also consist purely of singlets. Those subgraphs may also be *interconnected* among each other in an arbitrary manner, by iteratively interconnecting pairs of singlets, leaving the associated cospectrality intact. In fact, vertex interconnections preserving cospectrality can be generalized to the suitable interconnection of *arbitrary walk multiplets of equal parity*, as ensured by the following theorem.

Theorem 2 (*Walk multiplet interconnection*). *Let $G \in \mathbb{R}^{N \times N}$ be a graph with a cospectral pair $\{u, v\}$ and $\mathbb{X}_\gamma^p, \mathbb{Y}_\delta^p$ be (in general non-uniform) walk multiplets relative to $\{u, v\}$ having same parity p and weight tuples γ, δ , respectively, with possible subset overlap $\mathbb{Z} = \mathbb{X} \cap \mathbb{Y} \neq \emptyset$. Then the cospectrality of $\{u, v\}$ and any walk multiplet relative to $\{u, v\}$ with parity p are preserved in the graph $H \in \mathbb{R}^{N \times N}$ with elements*

$$H_{x,y} = H_{y,x} = \begin{cases} G_{x,y} + \gamma_x \delta_y & \text{if } x \notin \mathbb{Z} \text{ or } y \notin \mathbb{Z} \\ G_{x,y} + \gamma_x \delta_y + \gamma_y \delta_x & \text{if } x, y \in \mathbb{Z} \end{cases} \quad \forall x \in \mathbb{X}, y \in \mathbb{Y}$$

and $H_{i,j} = G_{i,j}$ otherwise.

The above theorem, in contrast to the extension of a graph by external vertices in Theorem 1, allows for the internal modification of the graph itself while keeping the cospectrality of a given vertex pair. In particular, the *topology* of the graph may be changed by adding new edges or deleting existing ones. Before showing examples using Theorems 1 and 2, let us also note the following.

Remark 3. By Theorem 2, one can interconnect a cospectral pair $\{u, v\}$ (which corresponds to a walk doublet relative to itself) to itself by setting $\mathbb{X} = \mathbb{Y} = \{u, v\}$ and adding an edge between u, v as well as loops on u, v , all of equal arbitrary weight (added to possible existing edges), while keeping their cospectrality. Then, by Lemma 3.1 of Ref. [15], those loops can be removed, with u, v still remaining cospectral. In other words, two cospectral vertices u, v of a graph can be interconnected or disconnected without affecting their cospectrality.

To show Theorems 1 and 2 in action, we will now apply them to the example graphs in Fig. 3(a) and Fig. 4 of the previous section, whose walk multiplet structure has already been analyzed. With the first example, we showcase the cospectrality-preserving extension of a graph; via a uniform walk multiplet, via a combination of overlapping uniform multiplets, and finally by connecting another arbitrary graph to it.

Example 3. In Fig. 5(a) we have modified the graph of Fig. 3(a) by connecting a new vertex $c = 9$ to the even uniform walk doublet $\{3, 7\}^+$ relative to the cospectral pair $\{1, 2\}$ with weight a . In the terminology of Theorem 1, this new graph is the cone H of the graph in Fig. 3(a), G , over the subset $\mathbb{M} = \{3, 7\}$ with a weight tuple $\gamma = (\gamma_3, \gamma_7) = (a, a)$. By Theorem 1, vertex c then forms an even singlet and all even multiplets of the graph G in Fig. 3(a) are still present in the new graph of Fig. 5(a), as confirmed in the table at the bottom of the figure. Now, in Fig. 5(b) we further connect c to other vertices in H , without breaking the cospectrality of $\{1, 2\}$ or its walk equivalence to any even multiplet. Indeed, by Theorem 2, vertex c can be connected to the even singlet $\{5\}^+$ with some weight a' . We can—again by Theorem 2—additionally connect c , with weight b , to the even uniform doublet $\{4, 7\}^+$ which *overlaps* with the already connected one $\{3, 7\}^+$. As a result, the edge $(c, 7)$ now has weight $a + b$. Of course, these successive connections amount to the final graph simply being the weighted cone of the initial one with tip c over $\{3, 4, 5, 7\}$ with weight tuple $\gamma = (\gamma_3, \gamma_4, \gamma_5, \gamma_7) = (a, b, a', a + b)$. Thus, $\{(3)_a, (4)_b, (5)_{a'}, (7)_{a+b}\}^+$ is an even nonuniform walk quadruplet; see Remark 2. In Fig. 5(c) we make use of Corollary 1 and connect a whole graph C , represented by a cloud since it can be just any graph, to the even singlet c via any number of

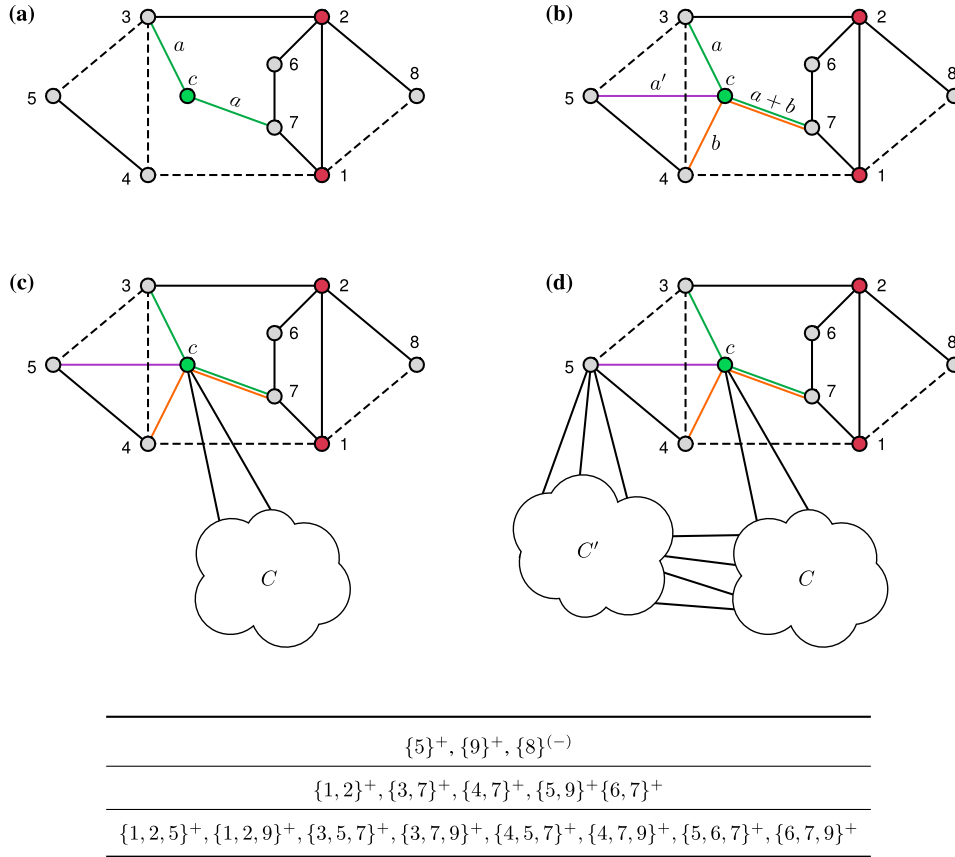


Fig. 5. Extension of a graph via walk multipliers, using Corollary 1 and Theorem 2; see Example 3 for details. The graph of Fig. 3(a) is successively extended by (a) connecting a new vertex $c = 9$ symmetrically to the even uniform walk doublet $\{3, 7\}^+$ relative to the cospectral pair $\{1, 2\}$ with weight a , (b) further connecting c to the even singlet $\{5\}^+$ with weight a' and to the even uniform doublet $\{4, 7\}^+$ with weight b , (c) connecting an arbitrary graph C (cloud) to the even walk singlet c via any number of edges with arbitrary weights, and (d) connecting another graph C' to the even walk singlet $\{5\}^+$ and then C' to C in an arbitrary manner, forming a larger arbitrary graph connected to vertices 5 and c . In all steps, the cospectrality of $\{1, 2\}$ as well as the uniform walk multipliers listed in the table below (for up to cardinality 3) are preserved. The graph in (b) is the “weighted cone” of the graph in Fig. 3(a) over subset $\{3, 4, 5, 7\}$ with weight tuple $\gamma = (\gamma_3, \gamma_4, \gamma_5, \gamma_7) = (a, b, a', a + b)$. Also, $\{(3)_a, (4)_b, (5)_{a'}, (7)_{a+b}\}^+$ is an even nonuniform walk quadruplet relative to $\{1, 2\}$ with the same weight tuple γ .

edges with arbitrary weights—again preserving cospectrality and walk equivalence of $\{1, 2\}$. In Fig. 5(d), we have connected another cloud graph C' to the walk singlet $\{5\}^+$. This latter cloud C' can finally be connected—by Theorem 2—in any arbitrary way to C into a larger cloud graph, since both $\{5\}^+$ and $\{c\}^+$ are even singlets (as are all cloud vertices connected to them). Note that point (iii) of Theorem 1 means that walk multipliers of the original graph G with parity *opposite* to that of \mathbb{M}_γ^p are *not* necessarily present in the new graph (cone) H . Indeed, in the present example with $p = +1$ all but one odd walk multiplier of Fig. 3(a) (the walk singlet $\{8\}^-$) disappeared in Fig. 5(a)–(d).

As we see, using Theorem 1 together with Corollary 1 and Theorem 2, given a graph H with cospectral vertices u, v one can: (1) generate walk singlets by connecting new vertices to existing walk multiplets, (2) connect an arbitrary new subgraph to such a singlet, and subsequently (3) even interconnect such subgraphs. In other words, we now see that, starting from a small graph with cospectral vertices u and v , one can construct *arbitrarily* complex graphs maintaining this cospectrality, using the concept and rules for the introduced walk multiplets.

Let us here also corroborate the necessity of equal parity of two walk multiplets for their combination to be a multiplet (see Remark 2), by a counterexample. In Fig. 5, $\{5\}^+, \{8\}^-$ are walk singlets of opposite parity relative to the cospectral pair $\{1, 2\}$. Assume, now, that these two singlets can be combined into a walk doublet \mathbb{C}_ϵ^p relative to $\{1, 2\}$ with subset $\mathbb{C} = \{5, 8\}$, weight tuple $\epsilon = (a, b)$ and parity $p = \pm 1$. Then, by Theorem 1, connecting a new vertex c' to \mathbb{C} via edges with weights a, b would not break the cospectrality. However, this is not the case. Indeed, in the extended graph we would get $[H^5]_{1,1} = [H^5]_{2,2} - 4ab$, violating Eq. (1) for $k = 5$ if $ab \neq 0$. This means that only one of the vertices $\{5\}^+$ and $\{8\}^-$ may be connected to c' ($a = 0$ or $b = 0$) to keep $\{1, 2\}$ cospectral. In other words, *either* even *or* odd walk multiplets can generally be simultaneously connected to a new vertex while keeping the cospectrality of the associated cospectral pair.

In the following example, we demonstrate how the topology of a graph itself can be modified, i.e. without extending it by new vertices, while preserving a cospectral pair.

Example 4. In Fig. 6, we apply Theorem 2 to the graph of Fig. 4, resulting in graphs with the same vertices as in the original graph but with some of them connected differently. Specifically, in Fig. 6(a), we interconnect the even uniform walk doublet $\{(3, 7)_a\}^+$ with the even nonuniform walk triplet $\{(1, 5)_b, (4)_{2b}\}^+$ (see list of walk multiplets in Fig. 4). According to Theorem 2, $\{u, v\} = \{2, 6\}$ remains cospectral if we add the product ab to the edge weights between each of the vertices 3, 7 of the doublet and vertices 1, 5 of the triplet, and $2ab$ to the edge weights between 3, 7 and 4, as shown in the figure. Thus, the *new* edges $(1, 3)$, $(3, 4)$, $(3, 5)$, and $(4, 7)$ are created in the resulting graph, so that the graph topology has been modified. Note, though, that the multiplet interconnection procedure comes with a partial restriction on the weights of the new graph. For instance, starting in Fig. 6(a) with an unweighted graph and setting also $a = b = 1$, the edges $(1, 7)$, $(3, 4)$, $(4, 7)$, $(5, 7)$ in the new graph have weight 2 (and the rest 1); that is, the new graph cannot be unweighted. In Fig. 6(b), we interconnect $\{(3, 7)_a\}^+$ with $\{(4)_b, (8)_{-b}\}^+$. Starting with the original graph unweighted and setting $a = b = 1$, the addition of edge weights according to Theorem 2 *removes* the edges $(3, 8)$ and $(7, 8)$, while adding $(3, 4)$ and $(4, 7)$, with $\{2, 6\}$ remaining cospectral. This demonstrates how walk multiplet interconnections can be used to disconnect vertices of a graph while preserving the associated cospectrality.

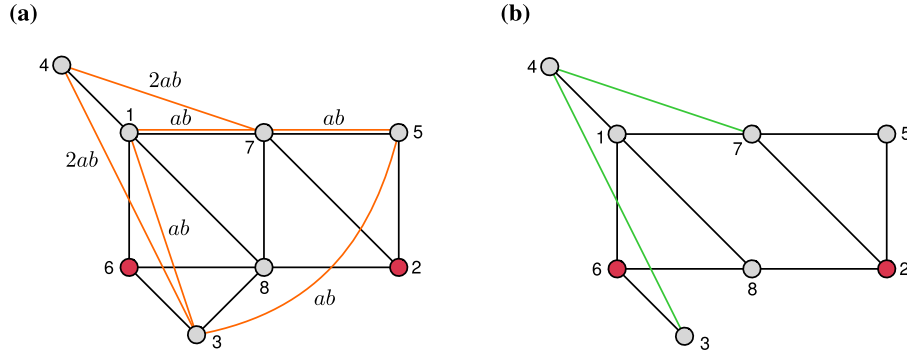


Fig. 6. Two modifications of the graph depicted in Fig. 4 which keep the cospectrality of the vertices 2 and 6 while changing the graph topology, using 2; see Example 4. In (a) we interconnect the walk multiplets $\{(3, 7)_a\}^+$ and $\{(1, 5)_b, (4)_{2b}\}^+$, with added edge weights as indicated, and in (b) we interconnect walk multiplets $\{(3, 7)_a\}^+$ with $\{(4)_a, (8)_{-a}\}^+$, starting from the original graph unweighted and setting $a = 1$.

By Theorem 1, the cospectrality of a vertex pair is preserved in the weighted cone over a walk multiplet of a graph with the same weight tuple γ , with the tip of the cone then being a walk singlet. We now ask for the reverse: When the cospectrality of u, v is preserved under a single-vertex addition, is that vertex *necessarily* a walk singlet relative to u, v ? The affirmative answer is given by the following theorem, which also makes a similar statement for the case of single vertex deletions.

Theorem 3 (*Preserved cospectrality under single vertex additions or deletions*). *Let G be a graph with vertex set \mathbb{V} and with two cospectral vertices $u, v \in \mathbb{V}$. Then*

- (i) *The cospectrality of u and v is preserved in the cone H of G over a subset $\mathbb{M} \subseteq \mathbb{V}$ with weight tuple $\gamma = (\gamma_m)_{m \in \mathbb{M}}$ if and only if \mathbb{M}_γ^p is a walk multiplet relative to u, v .*
- (ii) *The cospectrality of u and v is preserved in the graph $R = G \setminus c$ (obtained from G by removing the vertex $c \in \mathbb{V}$) if and only if c is a walk singlet in G relative to u, v .*

Recall that the tip of the cone in part (i) is a walk singlet relative to u, v (by Theorem 1). In part (ii), a walk singlet is removed, without breaking the cospectrality of $\{u, v\}$. Thus, the theorem implies that the only way to add a single vertex to a graph, or to remove a single vertex from it, without breaking the cospectrality of two vertices u, v , is if that vertex is a walk singlet relative to u, v .

A word of caution, though: Whereas walk *singlets* can safely be removed from a graph without destroying the associated cospectral pair, the same is not true for larger walk multiplets in general. An interesting special case where a multiplet can be removed is when (i) its vertices are pairwise cospectral and (ii) relative to each such cospectral pair its remaining vertices are singlets, as explained in the proof of Theorem 3 in the Appendix. An example of this is the walk anti-doublet $\{3, 4\}^-$ in Fig. 3(a), whose removal does preserve the cospectrality of the pair $\{1, 2\}$.

Combining Theorem 1 with Theorem 3 results in the following conclusion regarding walk singlets.

Corollary 2. *A vertex c of a graph is a walk singlet relative to cospectral vertices u, v if and only if it is exclusively connected via edges with weight tuple $\gamma = (\gamma_m)_{m \in \mathbb{M}}$ to a walk multiplet \mathbb{M}_γ^p relative to u, v .*

Let us now make the link to where we started (in Section 2.1), with the notion of USPs. Recall that an USP is a single vertex to which an arbitrary new graph can be connected, or which can also be removed, without breaking the cospectrality of a vertex pair. While it is clear from Theorem 1 that any walk singlet is an USP, one might ask if also the *reverse* is true, that is, whether any USP is a walk singlet. The removal of a walk singlet is covered by Theorem 3(ii). Regarding the connection of arbitrary graphs, we have the following.

Corollary 3 (*USPs are singlets*). *If the cospectrality of a vertex pair $\{u, v\}$ of a graph H is preserved when connecting an arbitrary graph C to a single vertex c of H , via edges of arbitrary weights, then c is a walk singlet relative to $\{u, v\}$.*

This statement can be easily understood from the above. Indeed, since C is an arbitrary graph, we can choose it to be a single vertex c' . If the cospectrality of u, v is preserved under this addition, then by Theorem 3(i), c' must then be a walk singlet. But by Corollary 2, c must be a walk singlet as well. Thus, we have that every USP is a walk singlet.

Before we proceed, let us review the above, starting with a recapitulation of the concept of cospectral vertices. Known in molecular graph theory as “isospectral points”, this concept can be seen as a *generalization* of exchange symmetry [6]. Indeed, any two vertices u and v that are exchange symmetric are also cospectral, but the reverse is not necessarily the case. Similar to the case of exchange symmetries, one can then draw powerful conclusions from the presence of cospectral vertices. For example, one can use the presence of cospectral vertices to express the characteristic polynomial of the underlying matrix H in terms of smaller polynomials [16]. In quantum physics it has been shown [3] that cospectrality of u and v is a necessary condition for so-called perfect state transfer between these two vertices, which is important in the realization of quantum computers. In general, if two vertices u and v are cospectral, then all eigenvectors have (in the case of degeneracies, can be chosen to have) definite parity on these two vertices [15]. The implications of such local parity depend, of course, on what the underlying matrix H represents, but can be quite impactful. In network theory [9,17], for example, the local parity of eigenvectors implies that two cospectral vertices have the same “eigenvector centrality”, which is a measure for their importance in the underlying network.

Irrespective of these powerful implications of cospectrality, however, one might object that fulfilling its defining Eq. (1) is rather difficult, especially in larger graphs comprising

thousands of vertices. What we have shown above is that fulfilling Eq. (1) is, on the contrary, *rather easy*: Given a small graph G with cospectral vertices u and v , one can easily embed G into a (much) larger graph G' by suitably connecting some vertices of G' to the walk multiplets of u and v . In other words, we have shown that cospectrality does not necessarily rely on *global* fine-tuning. This viewpoint-changing finding, however, is just the implication of a much more important insight. Namely, that the matrix powers of H —which are used to identify walk multiplets—are a source of detailed information about the underlying graph, as we will demonstrate in the following.

4. Eigenvector components on walk multiplets

Having seen how multiplets can be used to extend a graph whilst keeping the cospectrality of vertices, we now analyze their relation to the eigenvectors of H . To this end, we first choose the orthonormal eigenvector basis according to the following Lemma.

Lemma 1 (*Lemma 2.5 of [15]*). *Let H be a symmetric matrix, with u and v cospectral. Then the eigenvectors $\{\phi\}$ of H are (or, in the case of degenerate eigenvalues, can be chosen) as follows. For each eigenvalue λ there is at most one eigenvector ϕ with even local parity on u and v , i.e., $\phi_u = \phi_v \neq 0$, and at most one eigenvector ϕ with odd local parity on u and v , i.e., $\phi_u = -\phi_v \neq 0$. All remaining eigenvectors for λ fulfill $\phi_u = \phi_v = 0$. The even (odd) parity eigenvector can be found by projecting the vector $e_u \pm e_v$ onto the eigenspace associated with λ .*

Remark 4. If the projection of $e_u \pm e_v$ onto the eigenspace associated with λ yields the zero-vector, then the corresponding even (odd) parity eigenvector does not exist.

With this choice, the components of odd and even parity eigenvectors on a walk multiplet obey the following constraint.

Theorem 4 (*Eigenvector components on walk multiplets*). *Let $H = H^T \in \mathbb{R}^{N \times N}$ represent a graph with a pair of cospectral vertices u, v , and let its eigenvectors be chosen according to Lemma 1. Then any eigenvector ϕ of H with eigenvalue λ and nonzero components of odd (even) parity p on u, v ,*

$$\phi_u = p \phi_v \neq 0, \quad p \in \{+1, -1\}, \tag{15}$$

fulfills

$$\sum_{m \in \mathbb{M}} \gamma_m \phi_m = 0 \tag{16}$$

if and only if \mathbb{M}_γ^{-p} is a walk multiplet relative to u, v with even (odd) parity $-p$ and weight tuple $\gamma = (\gamma_m)_{m \in \mathbb{M}}$.

Remark 5. It is an interesting—and to the best of our present knowledge unanswered—question whether analogous general statements can be made regarding the eigenvector components on walk multiplets relative to a cospectral pair $\{u, v\}$ for eigenvectors with zero components on u, v .

Let us take a look at the impact of Theorem 4 in an example. We use a graph we are already familiar with and which has an interesting multiplet structure.

Example 5. The graph of Fig. 4 has three eigenvectors ϕ^ν (labeled by $\nu = 1, 2, 3$) with odd parity on the cospectral pair $\{2, 6\}$, given by the columns

$$\begin{bmatrix} -\frac{2}{\sqrt{10}} & \frac{1}{2\sqrt{5}} & -\frac{1}{2\sqrt{5}} \\ -\frac{1}{\sqrt{10}} & -\frac{1}{\sqrt{5}} & \frac{1}{\sqrt{5}} \\ -\frac{1}{\sqrt{10}} & \frac{1}{20}(5 + \sqrt{5}) & \frac{1}{20}(5 - \sqrt{5}) \\ \frac{1}{\sqrt{10}} & \frac{1}{20}(5 - \sqrt{5}) & \frac{1}{20}(5 + \sqrt{5}) \\ 0 & -\frac{1}{2} & -\frac{1}{2} \\ \frac{1}{\sqrt{10}} & \frac{1}{\sqrt{5}} & -\frac{1}{\sqrt{5}} \\ \frac{1}{\sqrt{10}} & \frac{1}{20}(-5 - \sqrt{5}) & \frac{1}{20}(\sqrt{5} - 5) \\ \frac{1}{\sqrt{10}} & \frac{1}{20}(5 - \sqrt{5}) & \frac{1}{20}(5 + \sqrt{5}) \end{bmatrix}.$$

As an example, we apply Theorem 4 for the even walk quadruplet $\{(1)_a, (3)_b, (4)_{2a+b}, (5)_{a+b}\}^+$ (shown in the table of Fig. 4) relative to $\{2, 6\}$. By Eq. (16), each of the above eigenvectors fulfills

$$a\phi_1^\nu + b\phi_3^\nu + (2a + b)\phi_4^\nu + (a + b)\phi_5^\nu = 0; \quad \phi_2^\nu = -\phi_6^\nu \neq 0, \quad \nu = 1, 2, 3, \quad (17)$$

for any values of the parameters a, b , as the reader may easily verify. Note that the above eigenvectors also have local odd parity on $\{3, 7\}$. This is again a result of Eq. (16), since $\{(3, 7)_a\}^+$ is an even walk doublet relative to the cospectral pair $\{2, 6\}$, so that $\phi_3^\nu + \phi_7^\nu = 0$ for $\nu = 1, 2, 3$.

For uniform walk multiplets, and especially singlets, Theorem 4 simplifies: If an even (odd) walk multiplet \mathbb{M}_γ^p relative to u, v is uniform ($\gamma_m = \text{const.}$), then $\sum_{m \in \mathbb{M}} \phi_m = 0$ for any eigenvector ϕ with odd (even) parity on u, v ; in particular, ϕ has zero component on any even (odd) walk singlet. The zero component of an eigenvector ϕ on a vertex c can be understood as a cancellation of weighted eigenvector components in the eigenvalue equation $H\phi = \lambda\phi$, written as $\sum_{m \neq c} H_{cm}\phi_m = (\lambda - H_{cc})\phi_c$. If $\phi_c = 0$, the sum over components ϕ_m on vertices m adjacent (i.e. connected by edges) to c , weighted by the corresponding edge weights, vanishes, i.e. $\sum_{m \neq c} H_{cm}\phi_m = 0$. This coincides, though, with Eq. (16) of Theorem 4 for $H_{cm} = \gamma_m$. Further, recall that the components of eigenvectors with parity p on cospectral vertices vanish on walk singlets with opposite parity $-p$. In the light of Theorem 1(ii) and Corollary 1, this suggests that walk multiplets may

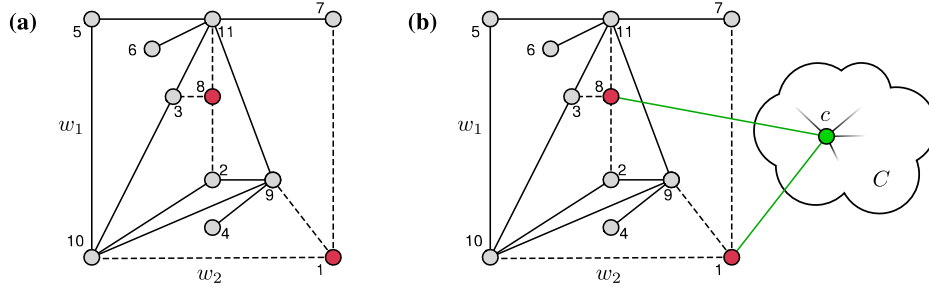


Fig. 7. (a) A graph with no walk singlets relative to the only cospectral pair $\{1, 8\}$ which remains cospectral for any nonzero edge weights w_1 (solid lines) and w_2 (dashed lines). The graph has seven eigenvectors with odd local parity (and nonzero components) on $\{1, 8\}$. (b) When connecting an arbitrary graph C symmetrically via a single vertex c to the cospectral pair $\{1, 8\}$, which is also a uniform even walk doublet $\{1, 8\}^+$, then by Corollary 1 all vertices within C are walk singlets relative to $\{1, 8\}$. The original odd parity eigenvectors vanish on all vertices of C .

be used to construct graphs having eigenvectors with multiple vanishing components, namely on graph extensions consisting only of walk singlets. We demonstrate this in the following example.

Example 6. We start with the graph in Fig. 7(a), which has no walk singlets (or any other walk multiplets up to size 5, for that matter) relative to its cospectral pair $\{1, 8\}$. The cospectrality of $\{1, 8\}$ is independent of the values of the weights w_1 and w_2 (indicated by solid and dashed lines), as long as they are nonzero. We can now easily create singlets by symmetrically connecting a new graph C , depicted by a cloud in Fig. 7(b), to the two cospectral vertices 1, 8 via a single vertex c of C . This is ensured by Corollary 1 and Theorem 2, with the cospectral pair here simultaneously representing a walk doublet (see Remark 1). The original graph in Fig. 7(a) has seven eigenvectors with odd parity on $\{1, 8\}$ for any choice of the edge weights $w_1, w_2 \neq 0$. We note that this number can be deduced by applying the methodology of Ref. [18], wherein the so-called “isospectral reduction” is used to split the graph’s characteristic polynomial into smaller pieces, the orders of which are linked to the number of positive and negative parity eigenvectors. Coming back to the example, we note that each of those seven odd parity eigenvectors has vanishing components on all vertices of C by Corollary 1 and Theorem 4. Of course, depending on the internal structure of the subgraph C , the total graph may now feature further eigenvectors (not those seven from above) which have zero components on different subgraphs (not C).

When the subgraph C is much larger than the original graph of Fig. 7(a), most of the eigenvector components of the seven odd parity eigenvectors vanish. Eigenvectors with such a property are known as “sparse eigenvectors” [19,20] in engineering or computer science. Such eigenvectors can also be characterized as “compact”, since they have nonzero components only on a strict subset of the vertex set of a graph H . Indeed, if H represents a Hamiltonian of a physical system composed of discrete sites (like the atoms

in molecular model of Fig. 2), then eigenstates of H which are strictly confined to a subset of sites are often referred to as “compact localized states” [21,22] or even “dark states” [23,24] depending on the context. We have here demonstrated how such compact eigenvectors can be generated for a graph featuring cospectral vertices, by extending the graph via walk multiplets. As a perspective for future work, this may be used to design discrete physical setups with compact localized states or, more generally, network systems with some eigenvectors vanishing on desired nodes.

5. Generating cospectral vertices without permutation symmetry from highly symmetric graphs

Until now, the existence of cospectral vertices has been assumed to be given, and we now come to the question of how to generate such graphs. One possible method is to start from two graphs G_1, G_2 with the same characteristic polynomial (such graphs can be constructed by means of the so-called “Godsil-McKay-switching” from Ref. [25]), and then search for a graph H such that $H \setminus u = G_1$ and $H \setminus v = G_2$. The two vertices u and v are then guaranteed to be cospectral in H .

The concept of walk multiplets, as introduced in this work, naturally suggests another scheme for generating graphs with cospectral vertices. Starting from a matrix H which commutes with a permutation matrix P which exchanges u and v (with arbitrary permutations of the remaining vertices, so that other vertices could be symmetry-related as well), one first identifies the walk multiplets of H relative to $\{u, v\}$. In a second step, H is changed by either (i) connecting one or more new vertices to (some of) the multiplets having common parity, following Theorem 1, or (ii) interconnecting multiplets by adding edge weights between them, following Theorem 2. Vertices u and v remain cospectral under these operations, but the resulting matrix H' may feature less permutation symmetries than H . Interestingly, H' could feature *no permutation symmetry at all*, as we demonstrate in the following examples.

Example 7. Fig. 8(a) shows a “ladder” graph with two legs and three rungs. As drawn here, it is symmetric both under a reflection about the horizontal and the vertical axis. As a result of the symmetry about the vertical axis, and among other cospectral pairs, the two central vertices u, v are cospectral. Moreover, as a result of the combined horizontal and vertical reflection symmetry, the two pairs $\{d_1, d_2\}$ and $\{d_1, d_3\}$ correspond to even uniform walk doublets relative to $\{u, v\}$. In Fig. 8(b), a new vertex c is connected to $\{d_1, d_2\}$ and another new vertex c' is connected to $\{d_1, d_3\}$, with some arbitrary but uniform weights a and b , respectively. The extension by c and c' breaks the previous reflection symmetries in the resulting graph, which in fact features no permutation symmetries at all. By Theorem 1, however, the vertices u, v remain cospectral. Note, in particular, that the occurrence of the walk doublet $\{d_1, d_3\}$ in Fig. 8(a) can be intuitively explained by the graph’s combined reflection symmetry about its vertical and horizontal axes. The symmetry about the horizontal axis is then broken when first adding ver-

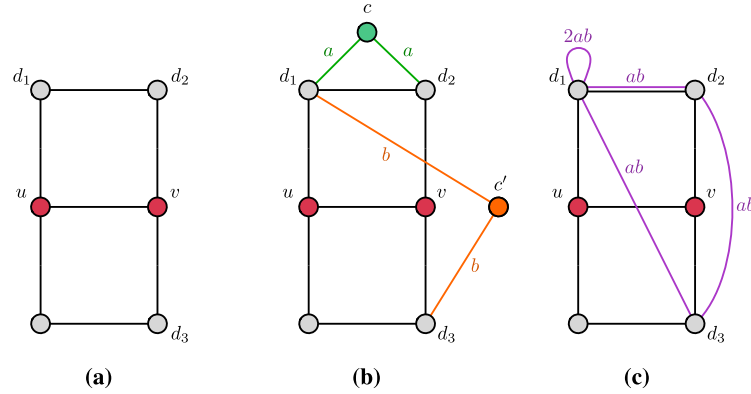


Fig. 8. Generation of a weighted graph with cospectral vertices and without any permutation symmetry; see Example 7. (a) A “ladder” graph, reflection symmetric about its vertical and horizontal axes, with cospectral vertices u and v , is modified by (b) connecting two new vertices c and c' to the uniform walk doublets $\{d_1, d_2\}^+$ and $\{d_1, d_3\}^+$ relative to $\{u, v\}$ with weights a and b , respectively, or (c) interconnecting those walk doublets by adding edge weights as shown. In both (a) and (b), the resulting graph has no permutation symmetries, while u, v remain cospectral, as ensured by Theorems 1 and 2, respectively.

tex c , so one might intuitively expect also the walk multiplet condition for $\{d_1, d_3\}$ to be violated. Nevertheless, Theorem 1 guarantees that $\{d_1, d_3\}$ remains a walk multiplet relative to $\{u, v\}$, and so c' can be further added without breaking cospectrality. An alternative way to generate a graph with cospectral vertices and no permutation symmetries is shown in Fig. 8(c). Here the same original graph is modified by applying Theorem 2: Instead of connecting the two walk doublets $\{d_1, d_2\}^+$ and $\{d_1, d_3\}^+$ to added vertices, they are now interconnected to each other. Specifically, the weights ab are added pairwise to the edges between d_1, d_2, d_3 , and a loop of weight $2ab$ is added to the overlap $d_1 = \{d_1, d_2\} \cap \{d_1, d_3\}$, with a and b being arbitrary parameters. Note that, while the vertex set of the graph remains the same, its topology has now changed by the added edges (d_1, d_3) and (d_2, d_3) . Again, the pair $\{u, v\}$ remains cospectral, while the resulting graph has no permutation symmetry.

Example 8. Fig. 9(a) shows again a graph which, as visualized, is vertically and horizontally reflection symmetric and has (among others) two cospectral vertices u, v and two uniform even walk doublets $\{d_1, d_2\}^+$ and $\{d_1, d_3\}^+$ relative to $\{u, v\}$. We now use Theorem 2 to change the topology of the original graph and subsequently Theorem 1 to further extend it by new vertices, with u, v remaining cospectral in the final graph where all permutation symmetries are broken. Specifically, in Fig. 9(b) we interconnect the walk doublet $\{d_1, d_3\}^+$ to the doublet $\{u, v\}^+$ by uniformly adding edge weights between their vertices (creating new edges if absent) according to Theorem 2. In Fig. 9(c) we proceed by connecting a new vertex c to the doublet $\{d_1, d_2\}^+$ and another new vertex c' first to $\{d_1, d_3\}^+$ and then to $\{u, v\}^+$ (equivalent to connecting c' directly to the walk quadruplet $\{(d_1, d_3)_a, (u, v)_b\}^+$), following Theorem 1. We finally also disconnect u from v , which leaves them cospectral according to Remark 3.

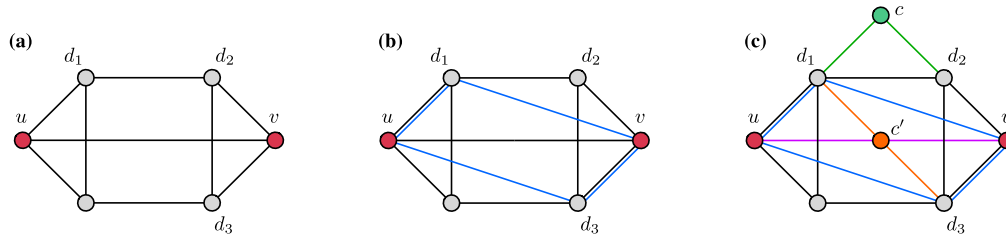


Fig. 9. The highly symmetric graph in (a) with (among other pairs) the cospectral vertex pair $\{u, v\}$ is modified by (b) interconnecting the walk doublets $\{u, v\}^+$ and $\{d_1, d_3\}^+$ (according to Theorem 2), and then (c) disconnecting the two cospectral vertices u, v from each other (Remark 3), connecting a new vertex c to the walk doublet $\{d_1, d_2\}^+$, and another new vertex c' to the walk quadruplet $\{(d_1, d_3)_a, (u, v)_b\}^+$ (Theorem 1), resulting in a graph with cospectral vertices u, v but no permutation symmetries; see Example 8.

The highly symmetric base graphs in Examples 7 and 8 were chosen unweighted and without loops for simplicity. Notably, they could easily be enriched by adding loops on their vertices and weighting the edges such that the indicated cospectral pairs $\{u, v\}$ are still present (that is, by respecting the reflection symmetries about the vertical and/or horizontal axes). Then, the extensions and interconnections described above could still be performed, creating weighted graphs featuring cospectral pairs without permutation symmetries.

6. Conclusions

Cospectral vertices offer the exciting possibility of eigenvectors of a matrix H having local parity on components corresponding to cospectral vertex pairs, even without the existence of corresponding permutation matrices commuting with H . Here, we introduced the notion of “walk equivalence” of two cospectral vertices with respect to a vertex subset of a graph represented by a matrix H . Such subsets, corresponding to what we call “walk multiplets”, provide a simple and generally applicable method of modifying a given graph with cospectral vertices such that the cospectrality is preserved. The definition of walk multiplets is based on the entries of the powers of H and can be expressed in terms of so-called walk matrices used in graph theory. As we demonstrate here, the concept of walk multiplets generalizes that of “unrestricted substitution points” (USPs), introduced for molecular graphs, to vertex subsets of arbitrary size: Any arbitrary new graph can be connected, via one of its vertices, to all vertices of a walk multiplet relative to a cospectral pair in an existing graph, without breaking the cospectrality. In fact, USPs turn out to coincide with walk “singlets”, that is, multiplets comprised of a single vertex. We further showed how walk multiplets can be used to derive sets of local relations between the components of an eigenvector with certain parity on a given associated cospectral pair. As a special case, the eigenvector components then vanish on any walk singlet as well as on any graph connected exclusively to walk singlets. This relates to the generation of so-called “compact localized states” in artificial physical setups, also known as “sparse eigenvectors” in other areas of science. We also presented a scheme in which we use

walk multipliers to construct a class of graphs having cospectral vertices without any permutation symmetries.

It is important to notice that the analysis performed here applies also to more than two cospectral vertices: For any subset \mathbb{S} of cospectral vertices, cospectrality is indeed defined *pairwise* for any two vertices $u, v \in \mathbb{S}$, and thus the walk multiplier framework applies to any such pair. Our results may thus offer a valuable resource in understanding and manipulating the structure of eigenvectors in an engineered network system via its walk multipliers—that is, by only utilizing the powers of the underlying matrix. In particular, the local eigenvector component relations derived here may be systematically exploited to deduce parametric forms of eigenvectors for generic graphs with cospectral pairs; an investigation left for future work.

Let us finally also hint at a possible connection to recent studies of local symmetries in discrete quantum models, which provide relations between the components of general states in the form of non-local continuity equations [26,27] and may offer advantages for state transfer on quantum networks [18]. In this context, it would be intriguing to explore the possible implications of walk multipliers for the dynamical evolution of wave excitations on general network-like systems.

Declaration of competing interest

The authors declare no conflict of interest.

Acknowledgements

M.R. is thankful to the Stiftung der Deutschen Wirtschaft and M.P. is thankful to the Studienstiftung des Deutschen Volkes for financial support in the framework of scholarships.

Appendix A. Proofs of theorems

We here restate Theorems 1 to 4 together with their proofs.

Theorem 1 (*Walk singlet extension*). *Let $G = G^T \in \mathbb{R}^{N \times N}$ represent an undirected graph with two cospectral vertices u, v , let \mathbb{M}_γ^p be an even (odd) walk multiplier of G relative to u, v , and let H be a weighted cone of G over the subset \mathbb{M} with real weight tuple $\gamma = (\gamma_m)_{m \in \mathbb{M}}$. Then*

- (i) *Vertices u, v are cospectral in H .*
- (ii) *The tip c of the cone H is an even (odd) walk singlet relative to u, v .*
- (iii) *Any even (odd) walk multiplier in G is an even (odd) walk multiplier in H .*

Proof. We partition any walk of length k in H into the walks restricted exclusively to G and the additionally generated walks in H visiting the new vertex c . Then we apply the multiplet condition, Eq. (10), which is valid in the old graph G . For convenience, we define

$$A_{s;\mathbb{M}}^{(\ell)} \equiv \sum_{m \in \mathbb{M}} \gamma_m [G^\ell]_{sm}, \quad B_{s;\mathbb{M}}^{(\ell)} \equiv \sum_{m \in \mathbb{M}} \gamma_m [H^\ell]_{sm}. \tag{A.1}$$

Then, since \mathbb{M}_γ^p is a walk multiplet relative to u, v in G , we have from Eq. (10) that

$$A_{u;\mathbb{M}}^{(k)} = p A_{v;\mathbb{M}}^{(k)} \quad \forall k \in \mathbb{N}, \quad p \in \{+1, -1\}. \tag{A.2}$$

To prove (i), we compute, with walk lengths fulfilling $\ell + n + r = k - 2$,

$$[H^k]_{u,u} = [G^k]_{u,u} + \sum_{\ell,n,r} \sum_{m,m' \in \mathbb{M}} [G^\ell]_{u,m} H_{m,c} [H^n]_{c,c} H_{c,m'} [G^r]_{m',u} \tag{A.3}$$

$$= [G^k]_{u,u} + \sum_{\ell,n,r} \sum_{m,m' \in \mathbb{M}} [G^\ell]_{u,m} \gamma_m [H^n]_{c,c} \gamma_{m'} [G^r]_{m',u} \tag{A.4}$$

$$= [G^k]_{u,u} + \sum_{\ell,n,r} A_{u;\mathbb{M}}^{(\ell)} [H^n]_{c,c} A_{u;\mathbb{M}}^{(r)} \tag{A.5}$$

$$= [G^k]_{v,v} + p^2 \sum_{\ell,n,r} A_{v;\mathbb{M}}^{(\ell)} [H^n]_{c,c} A_{v;\mathbb{M}}^{(r)} \tag{A.6}$$

$$= [H^k]_{v,v}, \tag{A.7}$$

where we used $p^2 = 1$, Eq. (A.2), and the cospectrality of u, v in G . To prove (ii), we compute, now with $\ell + n = k - 1$,

$$[H^k]_{u,c} = \sum_{\ell,n} \sum_{m \in \mathbb{M}} [G^\ell]_{u,m} H_{m,c} [H^n]_{c,c} = \sum_{\ell,n} \sum_{m \in \mathbb{M}} \gamma_m [G^\ell]_{u,m} [H^n]_{c,c} \tag{A.8}$$

$$= \sum_{\ell,n} A_{u;\mathbb{M}}^{(\ell)} [H^n]_{c,c} \tag{A.9}$$

$$= \sum_{\ell,n} p A_{v;\mathbb{M}}^{(\ell)} [H^n]_{c,c} = p [H^k]_{v,c} \tag{A.10}$$

To prove (iii), we compute, again with $\ell + n = k - 1$,

$$[H^k]_{u,m} = [G^k]_{u,m} + \sum_{\ell,n} \sum_{m' \in \mathbb{M}} [G^\ell]_{u,m'} H_{m',c} [H^n]_{c,m} \tag{A.11}$$

$$= [G^k]_{u,m} + \sum_{\ell,n} A_{u;\mathbb{M}}^{(\ell)} [H^n]_{c,m} \tag{A.12}$$

so that, multiplying by γ_m and summing over $m \in \mathbb{M}$, we have

$$B_{u;\mathbb{M}}^{(k)} = A_{u;\mathbb{M}}^{(k)} + \sum_{m \in \mathbb{M}} \gamma_m \sum_{\ell, n} A_{u;\mathbb{M}}^{(\ell)} [H^n]_{c,m} \tag{A.13}$$

$$= p A_{v;\mathbb{M}}^{(k)} + \sum_{m \in \mathbb{M}} \gamma_m \sum_{\ell, n} p A_{v;\mathbb{M}}^{(\ell)} [H^n]_{c,m} \tag{A.14}$$

$$= p \sum_{m \in \mathbb{M}} \gamma_m \left([G^k]_{v,m} + \sum_{\ell, n} A_{v;\mathbb{M}}^{(\ell)} [H^n]_{c,m} \right) = p \sum_{m \in \mathbb{M}} \gamma_m [H^k]_{v,m} = p B_{v;\mathbb{M}}^{(k)} \tag{A.15}$$

Note that, if any arbitrary graph C is connected exclusively to the added vertex c , then any vertex c' of C is also a walk singlet relative to $\{u, v\}$. Indeed, simply replacing $[H^n]_{cc}$ with $[H^n]_{cc'}$ in Eqs. (A.8) to (A.10) above leads to $[H^k]_{u,c'} = p [H^k]_{v,c'}$, which proves Corollary 1. \square

Theorem 2 (Walk multiplet interconnection). *Let $G \in \mathbb{R}^{N \times N}$ be a graph with a cospectral pair $\{u, v\}$ and $\mathbb{X}_\gamma^p, \mathbb{Y}_\delta^p$ be (in general non-uniform) walk multiplets relative to $\{u, v\}$ having same parity p and weight tuples γ, δ , respectively, with possible subset overlap $\mathbb{Z} = \mathbb{X} \cap \mathbb{Y} \neq \emptyset$. Then the cospectrality of $\{u, v\}$ and any walk multiplet relative to $\{u, v\}$ with parity p are preserved in the graph $H \in \mathbb{R}^{N \times N}$ with elements*

$$H_{x,y} = H_{y,x} = \begin{cases} G_{x,y} + \gamma_x \delta_y & \text{if } x \notin \mathbb{Z} \text{ or } y \notin \mathbb{Z} \\ G_{x,y} + \gamma_x \delta_y + \gamma_y \delta_x & \text{if } x, y \in \mathbb{Z} \end{cases} \quad \forall x \in \mathbb{X}, y \in \mathbb{Y}$$

and $H_{i,j} = G_{i,j}$ otherwise.

Proof. To prove that the vertices u, v remain cospectral in the modified graph H with added edge weights $H_{x,y} - G_{x,y}$ as described in the theorem, we will partition the walks in the new graph into walk segments such that the multiplet relations, Eq. (9), can be applied for the segments within the old graph G .

We first express the newly generated closed walks from u using (i) walks segments in the old graph G to reach a vertex of one of the multiplets \mathbb{X} (or \mathbb{Y}), (ii) the new edge (that is, the weight added if the edge already existed) to cross to the other multiplet \mathbb{Y} (or \mathbb{X}), and (iii) finally coming back to u using walks in the new graph H .

Defining $\mathbb{M} = \mathbb{X} \setminus \mathbb{Z}$, $\mathbb{W} = \mathbb{Y} \setminus \mathbb{Z}$, and with added edge weights $H_{ij} - G_{ij} = \gamma_i \delta_j$ (resp. $\gamma_i \delta_j + \gamma_j \delta_i$) if $i, j \in \mathbb{X} \cup \mathbb{Y} \wedge (i \notin \mathbb{Z} \vee j \notin \mathbb{Z})$ (resp. $i, j \in \mathbb{Z}$), we have

$$[H^k]_{u,u} = [G^k]_{u,u} + \sum_{l+n+1=k} \left\{ \sum_{m \in \mathbb{M}, w \in \mathbb{W}} [G^l]_{u,m} \gamma_m \delta_w [H^n]_{w,u} + \sum_{z \in \mathbb{Z}, w \in \mathbb{W}} [G^l]_{u,z} \gamma_z \delta_w [H^n]_{w,u} + \right. \tag{A.16}$$

$$\left. \sum_{w \in \mathbb{W}, m \in \mathbb{M}} [G^l]_{u,w} \delta_w \gamma_m [H^n]_{m,u} + \sum_{z \in \mathbb{Z}, m \in \mathbb{M}} [G^l]_{u,z} \delta_z \gamma_m [H^n]_{m,u} \right\} \tag{A.17}$$

$$\sum_{m \in \mathbb{M}, z \in \mathbb{Z}} [G^l]_{u,m} \gamma_m \delta_z [H^n]_{z,u} + \tag{A.18}$$

$$\sum_{w \in \mathbb{W}, z \in \mathbb{Z}} [G^l]_{u,w} \delta_w \gamma_z [H^n]_{z,u} + \tag{A.19}$$

$$\sum_{z' \in \mathbb{Z}, z \in \mathbb{Z}} [G^l]_{u,z'} (\gamma_{z'} \delta_z + \gamma_z \delta_{z'}) [H^n]_{z,u} \}. \tag{A.20}$$

We can now combine sums over subsets as follows: $\sum_{m \in \mathbb{M}} + \sum_{z \in \mathbb{Z}} = \sum_{x \in \mathbb{X}}$ in (A.16), and the same in (A.18) with the first term $(\gamma_{z'} \delta_z)$ in (A.20). Similarly, $\sum_{w \in \mathbb{W}} + \sum_{z \in \mathbb{Z}} = \sum_{y \in \mathbb{Y}}$ in (A.17), and the same in (A.19) with the second term $(\gamma_z \delta_{z'})$ in (A.20). This yields

$$\begin{aligned} [H^k]_{u,u} &= [G^k]_{u,u} + \sum_{l+n+1=k} \left\{ \sum_{x \in \mathbb{X}, w \in \mathbb{W}} [G^l]_{u,x} \gamma_x \delta_w [H^n]_{w,u} \right. \\ &\quad + \sum_{y \in \mathbb{Y}, m \in \mathbb{M}} [G^l]_{u,y} \delta_y \gamma_m [H^n]_{m,u} \\ &\quad + \sum_{x \in \mathbb{X}, z \in \mathbb{Z}} [G^l]_{u,x} \gamma_x \delta_z [H^n]_{z,u} + \sum_{y \in \mathbb{Y}, z \in \mathbb{Z}} [G^l]_{u,y} \delta_y \gamma_z [H^n]_{z,u} \} \\ &= [G^k]_{u,u} + \sum_{l+n+1=k} \left\{ \sum_{x \in \mathbb{X}, y \in \mathbb{Y}} [G^l]_{u,x} \gamma_x \delta_y [H^n]_{y,u} + \sum_{y \in \mathbb{Y}, x \in \mathbb{X}} [G^l]_{u,y} \delta_y \gamma_x [H^n]_{x,u} \right\}. \end{aligned} \tag{A.21}$$

Next, we account for the walk segments from vertex $i = x, y$ back to u , which have a similar form:

$$\begin{aligned} [H^n]_{i,u} &= [G^n]_{i,u} + \sum_{r+s+1=n} \left\{ \sum_{x' \in \mathbb{X}, y' \in \mathbb{Y}} [H^r]_{i,x'} \gamma_{x'} \delta_{y'} [G^s]_{y',u} \right. \\ &\quad + \sum_{y' \in \mathbb{Y}, x' \in \mathbb{X}} [H^r]_{i,y'} \delta_{y'} \gamma_{x'} [G^s]_{x',u} \}. \end{aligned} \tag{A.22}$$

Plugging this into (A.21), after some sorting and combining of terms we arrive at (with $x, x' \in \mathbb{X}$ and $y, y' \in \mathbb{Y}$)

$$\begin{aligned} [H^k]_{u,u} &= [G^k]_{u,u} + 2 \sum_{l+n+1=k} \sum_{x,y} [G^l]_{u,x} \gamma_x \delta_y [G^n]_{y,u} + \\ &\quad \sum_{l+r+s+2=k} \sum_{x,x',y,y'} \{ [G^l]_{u,x} \gamma_x \delta_y [H^r]_{y,y'} \delta_{y'} \gamma_{x'} [G^s]_{x',u} + \\ &\quad [G^l]_{u,y} \delta_y \gamma_x [H^r]_{x,x'} \gamma_{x'} \delta_{y'} [G^s]_{y',u} + \\ &\quad 2[G^l]_{u,x} \gamma_x \delta_y [H^r]_{y,x'} \gamma_{x'} \delta_{y'} [G^s]_{y',u} \} \end{aligned} \tag{A.23}$$

It is now evident that $[H^k]_{u,u}$ is equal to $[H^k]_{v,v}$ by applying cospectrality of u, v in G and multiplet conditions for $\mathbb{X}_\gamma^p, \mathbb{Y}_\delta^p$.

To prove that any general non-uniform walk multiplet \mathbb{Q}_ϵ^p (with weight tuple ϵ and of the same parity p as $\mathbb{X}_\gamma^p, \mathbb{Y}_\delta^p$) in G is preserved in H , we evaluate the following expression by using Eq. (A.22):

$$\begin{aligned} \sum_{q \in \mathbb{Q}} \epsilon_q [H^k]_{u,q} &= \sum_{q \in \mathbb{Q}} \epsilon_q \{ [G^k]_{u,q} + \sum_{r+s+1=k} \sum_{x \in \mathbb{X}, y \in \mathbb{Y}} [G^s]_{u,x} \gamma_x \delta_y [H^r]_{y,q} \\ &\quad + \sum_{r+s+1=k} \sum_{y \in \mathbb{Y}, x \in \mathbb{X}} [G^s]_{u,y} \delta_y \gamma_x [H^r]_{x,q} \} \end{aligned} \tag{A.24}$$

$$= p \sum_{q \in \mathbb{Q}} \epsilon_q [H^k]_{v,q}, \tag{A.25}$$

where in the last step we applied the multiplet conditions for $\mathbb{Q}_\epsilon^p, \mathbb{X}_\gamma^p, \mathbb{Y}_\delta^p$. \square

Theorem 3 (*Preserved cospectrality under single vertex additions or deletions*). *Let G be a graph with vertex set \mathbb{V} and with two cospectral vertices $u, v \in \mathbb{V}$. Then*

- (i) *The cospectrality of u and v is preserved in the cone H of G over a subset $\mathbb{M} \subseteq \mathbb{V}$ with weight tuple $\gamma = (\gamma_m)_{m \in \mathbb{M}}$ if and only if \mathbb{M}_γ^p is a walk multiplet relative to u, v .*
- (ii) *The cospectrality of u and v is preserved in the graph $R = G \setminus c$ (obtained from G by removing the vertex $c \in \mathbb{V}$) if and only if c is a walk singlet in G relative to u, v .*

Proof. We start with part (i) of the theorem. If \mathbb{M}_γ^p is a walk multiplet, then cospectrality of $\{u, v\}$ is preserved by Theorem 1. For the converse, we assume that $\{u, v\}$ remain cospectral, that is

$$[H^k]_{u,u} = [H^k]_{v,v} \quad \forall k \in \mathbb{N}, \tag{A.26}$$

where, with $A_{s;\mathbb{M}}^{(\ell)}$ defined as in Eq. (A.1),

$$[H^k]_{s,s} = [G^k]_{s,s} + \sum_n \sum_{\ell, \ell'} \sum_{m, m' \in \mathbb{M}} [G^\ell]_{s,m} \gamma_m [H^n]_{c,c} \gamma_{m'} [G^{\ell'}]_{m',s} \tag{A.27}$$

$$= [G^k]_{s,s} + \sum_n \sum_{\ell, \ell'} A_{s;\mathbb{M}}^{(\ell)} [H^n]_{c,c} A_{s;\mathbb{M}}^{(\ell')} \tag{A.28}$$

with $s \in \{u, v\}$, $\ell, \ell' \geq 0$, $n \geq 0$, and $\ell + \ell' = k - n - 2$. We further define

$$D_{\ell, \ell'} \equiv A_{u;\mathbb{M}}^{(\ell)} A_{u;\mathbb{M}}^{(\ell')} - A_{v;\mathbb{M}}^{(\ell)} A_{v;\mathbb{M}}^{(\ell')} = D_{\ell', \ell}, \quad a_n^{(k)} \equiv \sum_{\substack{\ell + \ell' = k - n - 2 \\ \ell, \ell' \geq 0}} D_{\ell, \ell'}. \tag{A.29}$$

Using $[G^k]_{u,u} = [G^k]_{v,v}$ and substituting the decomposition from Eq. (A.28) into Eq. (A.26) for $s = u, v$ we arrive at

$$[H^k]_{u,u} - [H^k]_{v,v} = \sum_{n=0}^{k-2} a_n^{(k)} [H^n]_{cc} = 0 \quad \forall k \in \mathbb{N}. \tag{A.30}$$

To prove that M_γ^p is a multiplet, we must show that (dropping the subscript M)

$$A_u^{(\ell)} = p A_v^{(\ell)} \quad \forall \ell \in \mathbb{N}, \quad p \in \{+1, -1\}. \tag{A.31}$$

We prove this by induction. For $k = 2$ (that is, $n = 0, \ell = \ell' = 0$), Eq. (A.30) yields $[A_u^{(0)}]^2 = [A_v^{(0)}]^2$ or

$$A_u^{(0)} = p A_v^{(0)}, \tag{A.32}$$

so that Eq. (A.31) is fulfilled in zeroth order $\ell = 0$. For the induction step, we assume that Eq. (A.31) is fulfilled up to some arbitrary order r , that is,

$$A_u^{(\ell)} = p A_v^{(\ell)} \quad \forall \ell \leq r, \tag{A.33}$$

and show that this equation also holds for $\ell = r + 1$. To this end, we evaluate Eq. (A.30) for $k = r + 3$. For this choice of k , all but two summands vanish, since the assumption Eq. (A.33) implies that $D_{\ell,\ell'} = 0$ if $\ell, \ell' \leq r$. We thus obtain $D_{0,r+1} + D_{r+1,0} = 0$, and since $D_{0,r+1} = D_{r+1,0}$, it follows that $A_u^{(0)} A_u^{(r+1)} = A_v^{(0)} A_v^{(r+1)}$. Thus, if $A_u^{(0)} \neq 0$, due to Eq. (A.32) we get $A_u^{(r+1)} = p A_v^{(r+1)}$, as desired.

If $A_u^{(0)} = 0$, it follows from Eq. (A.32) that also $A_v^{(0)} = 0$, and from Eq. (A.29) we obtain $D_{0,\ell} = D_{\ell,0} = 0$ for all ℓ . We exploit this fact by evaluating Eq. (A.30) for $k = r + 4$, yielding $D_{1,r+1} = D_{r+1,1} = 0$. Now, if $A_u^{(1)} \neq 0$ we again get $A_u^{(r+1)} = p A_v^{(r+1)}$, as desired. If $A_u^{(1)} = 0$, we proceed to the next higher order $k = r + 5$, and so on. In the limiting case where $A_u^{(\ell)} = 0$ for all $\ell \leq r$, we evaluate Eq. (A.30) for $k = 2(r + 2)$, which yields $D_{r+1,r+1} = 0$ and therefore $A_u^{(r+1)} = p A_v^{(r+1)}$. This completes the proof of the first part.

For part (ii), we first prove that, if c is a singlet in G , then its removal does not break the cospectrality of u and v . To this end, we use the fact that

$$[G^k]_{u,u} = [R^k]_{u,u} + \sum_{\ell+n=k} [G^\ell]_{u,c} [G^n]_{c,u} \tag{A.34}$$

$$= [R^k]_{u,u} + \sum_{\ell+n=k} [G^\ell]_{v,c} [G^n]_{c,v} \tag{A.35}$$

and

$$[G^k]_{v,v} = [R^k]_{v,v} + \sum_{\ell+n=k} [G^\ell]_{v,c} [G^n]_{c,v}. \tag{A.36}$$

Since u and v are cospectral in G , it follows that $[R^k]_{u,u} = [R^k]_{v,v}$ for all k , so that u, v are also cospectral in R if c is a singlet in G . For the reverse direction we need to prove that, if the cospectrality of u and v is preserved by the removal of a single vertex c , then this vertex must be a walk singlet. With G being a cone of R with tip c , and demanding u, v to be cospectral in both R and G , combining part (i) of this theorem with Theorem 1 immediately gives that c must be a singlet in G . \square

A.1. Comment: removal of a general multiplet

Consider removing a walk multiplet \mathbb{M}_γ^p instead of the singlet c . Then

$$[G^k]_{u,u} = [R^k]_{u,u} + \sum_{\ell+r+n=k} \sum_{m,m' \in \mathbb{M}} [G^\ell]_{u,m} [G^r]_{m,m'} [G^n]_{m',u} \tag{A.37}$$

and cospectrality is preserved in the resulting graph R only if

$$\sum_{\ell+r+n=k} \sum_{m,m' \in \mathbb{M}} [G^\ell]_{u,m} [G^r]_{m,m'} [G^n]_{m',u} = \sum_{\ell+r+n=k} \sum_{m,m' \in \mathbb{M}} [G^\ell]_{v,m} [G^r]_{m,m'} [G^n]_{m',v} \tag{A.38}$$

for all k . Thus, cospectrality of a vertex pair in a graph is generally not preserved when removing a multiplet, except if Eq. (A.38) is fulfilled. Assuming a uniform multiplet ($\gamma_m = 1$ for all $m \in \mathbb{M}$), a special case where this occurs is when all pairs $\{m, m'\}$ in \mathbb{M} are cospectral and, for each such pair, all remaining vertices $m'' \notin \{m, m'\}$ in \mathbb{M} are singlets relative to $\{m, m'\}$. Then $[G^r]_{m,m'}$ can be factored out of the sums in Eq. (A.38) (taken separately for $m = m'$ and $m \neq m'$) and equality follows from the multiplet condition Eq. (A.31), for both $p = \pm 1$. For a walk quadruplet, e.g., the elements $[G^r]_{m,m'}$ would have the form

$$[G^r]_{\mathbb{M},\mathbb{M}} = \begin{bmatrix} a_r & b_r & b_r & b_r \\ b_r & a_r & b_r & b_r \\ b_r & b_r & a_r & b_r \\ b_r & b_r & b_r & a_r \end{bmatrix}, \tag{A.39}$$

with the values a_r and b_r generally depending on the power r . For a uniform p -doublet, this reduces to $[G^r]_{m,m} = [G^r]_{m',m'}$ and $[G^r]_{m,m'} = [G^r]_{m',m}$. This is the case, e.g., for the walk anti-doublet $\{3, 4\}^-$ in Fig. 3(a) which can be removed without affecting the cospectrality of the pair $\{1, 2\}$.

Theorem 4 (*Eigenvector components on walk multiplets*). *Let $H = H^\top \in \mathbb{R}^{N \times N}$ represent a graph with a pair of cospectral vertices u, v , and let its eigenvectors be chosen according to Lemma 1. Then any eigenvector ϕ of H with eigenvalue λ and nonzero components of odd (even) parity p on u, v ,*

$$\phi_u = p \phi_v \neq 0, \quad p \in \{+1, -1\}, \tag{15}$$

fulfills

$$\sum_{m \in \mathbb{M}} \gamma_m \phi_m = 0 \tag{16}$$

if and only if \mathbb{M}_γ^{-p} is a walk multiplet relative to u, v with even (odd) parity $-p$ and weight tuple $\gamma = (\gamma_m)_{m \in \mathbb{M}}$.

Proof. Using the spectral decomposition

$$H = \sum_{\nu=1}^N \lambda_\nu \phi^\nu \phi^{\nu \top} \tag{A.40}$$

of H in the orthonormal eigenbasis $\{\phi^\nu\}$, chosen according to Lemma 1, we have, for $s \in \{u, v\}$,

$$[H^k]_{s,m} = \sum_{\nu=1}^N \lambda_\nu^k \phi_s^\nu \phi_m^\nu = \sum_{\nu \in \mathcal{N}^+} \lambda_\nu^k \phi_s^\nu \phi_m^\nu + \sum_{\nu \in \mathcal{N}^-} \lambda_\nu^k \phi_s^\nu \phi_m^\nu \quad \forall k \in \mathbb{N}, \tag{A.41}$$

where we have collected the labels ν of eigenvectors with parity ± 1 on $\{u, v\}$ into the set \mathcal{N}^\pm (the remaining eigenvectors with $\phi_u^\nu = \phi_v^\nu = 0$ do not appear in the sum). Note that Eq. (A.41) incorporates the spectral decomposition of the identity matrix, $I_{s,m} = \sum_{\nu=1}^N \phi_s^\nu \phi_m^\nu$ for $k = 0$, meaning that $\lambda_\nu^0 = 1$ even in the case of zero eigenvalues. Next we calculate:

$$[H^k]_{u,m} - p[H^k]_{v,m} = (1 - p) \sum_{\nu \in \mathcal{N}^+} \lambda_\nu^k \phi_u^\nu \phi_m^\nu + (1 + p) \sum_{\nu \in \mathcal{N}^-} \lambda_\nu^k \phi_u^\nu \phi_m^\nu \tag{A.42}$$

$$= 2 \sum_{\nu \in \mathcal{N}^{-p}} \lambda_\nu^k \phi_u^\nu \phi_m^\nu, \tag{A.43}$$

where we used the parity of eigenstates on $\{u, v\}$, i.e. $\phi_u^\nu = \pm \phi_v^\nu$ for $\nu \in \mathcal{N}^\pm$, so that the prefactor $(1 \mp p)$ of the sum over $\nu \in \mathcal{N}^\pm$ vanishes for $p = \pm 1$. Multiplying by γ_m and summing over $m \in \mathbb{M}$ we obtain

$$B_{u;\mathbb{M}}^{(k)} - p B_{v;\mathbb{M}}^{(k)} = 2 \sum_{\nu \in \mathcal{N}^{-p}} \lambda_\nu^k \phi_u^\nu \sum_{m \in \mathbb{M}} \gamma_m \phi_m^\nu, \tag{A.44}$$

with $B_{s;\mathbb{M}}^{(k)}$ defined as in Eq. (A.1). It follows that, if Eq. (16) is fulfilled with $\phi = \phi^\nu$, for all $\nu \in \mathcal{N}^{-p}$, then $B_{u;\mathbb{M}}^{(k)} = p B_{v;\mathbb{M}}^{(k)}$ for all k and thus \mathbb{M}_γ^p is a walk multiplet relative to $\{u, v\}$ with parity p . Conversely, if \mathbb{M}_γ^p is a multiplet, then the left side of Eq. (A.44)

vanishes for all $k \in \mathbb{N}$. For $k \in \llbracket 0, n_p - 1 \rrbracket$, where $n_p \equiv |\mathcal{N}^{-p}|$, we can write Eq. (A.44) in the matrix form

$$V\vec{c} \equiv \begin{bmatrix} 1 & 1 & \cdots & 1 \\ \lambda_1 & \lambda_2 & \cdots & \lambda_{n_p} \\ \lambda_1^2 & \lambda_2^2 & \cdots & \lambda_{n_p}^2 \\ \vdots & \vdots & \ddots & \vdots \\ \lambda_1^{n_p-1} & \lambda_2^{n_p-1} & \cdots & \lambda_{n_p}^{n_p-1} \end{bmatrix} \begin{bmatrix} c_1 \\ c_2 \\ \vdots \\ c_{n_p} \end{bmatrix} = \begin{bmatrix} 0 \\ 0 \\ \vdots \\ 0 \end{bmatrix}, \quad (\text{A.45})$$

with coefficients $c_\nu = 2\phi_u^\nu \sum_{m \in \mathbb{M}} \gamma_m \phi_m^\nu$, where V^\top is the (square) Vandermonde matrix with $[V^\top]_{i,j} = \lambda_i^{j-1}$, yielding

$$\det(V) = \det(V^\top) = \prod_{1 \leq \mu < \nu \leq n_p} (\lambda_\nu - \lambda_\mu). \quad (\text{A.46})$$

Now, our choice of eigenvectors ensures that $\lambda_\nu \neq \lambda_\mu$ for all $\nu \neq \mu$ with $\nu, \mu \in \mathcal{N}^{-p}$, so that $\det(V) \neq 0$. Thus V is invertible, so that Eq. (A.46) yields $c_\nu = 0$ for all $\nu \in \mathcal{N}^{-p}$, and since $\phi_u^\nu \neq 0$ we have that $\sum_{m \in \mathbb{M}} \gamma_m \phi_m^\nu = 0$ for all $\nu \in \mathcal{N}^{-p}$, completing the proof. \square

References

- [1] M.S. Dresselhaus, G. Dresselhaus, A. Jorio, *Group Theory: Application to the Physics of Condensed Matter*, Springer-Verlag, Berlin, Heidelberg, 2008.
- [2] A. Francis, D. Smith, B. Webb, General equitable decompositions for graphs with symmetries, *Linear Algebra Appl.* 577 (2019) 287–316, <https://doi.org/10.1016/j.laa.2019.04.035>.
- [3] C. Godsil, J. Smith, Strongly cospectral vertices, arXiv:1709.07975.
- [4] E. Estrada, P.A. Knight, *A First Course in Network Theory*, Oxford University Press, Oxford, New York, 2015.
- [5] A.J. Schwenk, Almost all trees are cospectral, in: *Proceedings of the Third Annual Arbor Conference*, Academic Press, New York, 1973, pp. 257–307.
- [6] C. Rücker, G. Rücker, Understanding the properties of isospectral points and pairs in graphs: the concept of orthogonal relation, *J. Math. Chem.* 9 (3) (1992) 207–238, <https://doi.org/10.1007/BF01165148>.
- [7] W.C. Herndon, The characteristic polynomial does not uniquely determine molecular topology, *J. Chem. Doc.* 14 (3) (1974) 150–151, <https://doi.org/10.1021/c160054a013>.
- [8] W.C. Herndon, M.L. Ellzey, Isospectral graphs and molecules, *Tetrahedron* 31 (2) (1975) 99–107, [https://doi.org/10.1016/0040-4020\(75\)85002-2](https://doi.org/10.1016/0040-4020(75)85002-2).
- [9] M. Kempton, J. Sinkovic, D. Smith, B. Webb, Characterizing cospectral vertices via isospectral reduction, *Linear Algebra Appl.* 594 (2020) 226–248, <https://doi.org/10.1016/j.laa.2020.02.020>.
- [10] R.A. Brualdi, D. Cvetkovic, *A Combinatorial Approach to Matrix Theory and Its Applications*, CRC Press, 2008.
- [11] C. Godsil, Controllable subsets in graphs, *Ann. Comb.* 16 (4) (2012) 733–744, <https://doi.org/10.1007/s00026-012-0156-3>.
- [12] C.D. Meyer, *Matrix Analysis and Applied Linear Algebra*, Society for Industrial and Applied Mathematics, USA, 2000.
- [13] B.L. Douglas, J.B. Wang, A classical approach to the graph isomorphism problem using quantum walks, *J. Phys. A, Math. Theor.* 41 (7) (2008) 075303, <https://doi.org/10.1088/1751-8113/41/7/075303>.
- [14] F. Liu, J. Siemons, Unlocking the walk matrix of a graph, arXiv:1911.00062.
- [15] O. Eisenberg, M. Kempton, G. Lippner, Pretty good quantum state transfer in asymmetric graphs via potential, *Discrete Math.* 342 (10) (2019) 2821–2833, <https://doi.org/10.1016/j.disc.2018.10.037>.

- [16] M. Röntgen, N.E. Palaiodimopoulos, C.V. Morfonios, I. Brouzos, M. Pyzh, F.K. Diakonos, P. Schmelcher, Designing pretty good state transfer via isospectral reductions, *Phys. Rev. A* 101 (4) (2020) 042304, <https://doi.org/10.1103/PhysRevA.101.042304>.
- [17] D. Smith, B. Webb, Hidden symmetries in real and theoretical networks, *Physica A* 514 (2019) 855–867, <https://doi.org/10.1016/j.physa.2018.09.131>.
- [18] M. Röntgen, N.E. Palaiodimopoulos, C.V. Morfonios, I. Brouzos, M. Pyzh, F.K. Diakonos, P. Schmelcher, Designing pretty good state transfer via isospectral reductions, *Phys. Rev. A* 101 (4) (2020) 042304, <https://doi.org/10.1103/PhysRevA.101.042304>.
- [19] K. Benidis, Y. Sun, P. Babu, D.P. Palomar, Orthogonal sparse PCA and covariance estimation via procrustes reformulation, *IEEE Trans. Signal Process.* 64 (23) (2016) 6211–6226, <https://doi.org/10.1109/TSP.2016.2605073>.
- [20] O. Teke, P.P. Vaidyanathan, Uncertainty principles and sparse eigenvectors of graphs, *IEEE Trans. Signal Process.* 65 (20) (2017) 5406–5420, <https://doi.org/10.1109/TSP.2017.2731299>.
- [21] M. Röntgen, C.V. Morfonios, P. Schmelcher, Compact localized states and flat bands from local symmetry partitioning, *Phys. Rev. B* 97 (3) (2018) 035161, <https://doi.org/10.1103/PhysRevB.97.035161>.
- [22] W. Maimaiti, S. Flach, A. Andreanov, Universal $d = 1$ flat band generator from compact localized states, *Phys. Rev. B* 99 (12) (2019) 125129, <https://doi.org/10.1103/PhysRevB.99.125129>.
- [23] P.J. Pemberton-Ross, A. Kay, S.G. Schirmer, Quantum control theory for state transformations: dark states and their enlightenment, *Phys. Rev. A* 82 (4) (2010) 042322, <https://doi.org/10.1103/PhysRevA.82.042322>.
- [24] T.P. Le, L. Donati, S. Severini, F. Caruso, How to suppress dark states in quantum networks and bio-engineered structures, *J. Phys. A, Math. Theor.* 51 (36) (2018) 365306, <https://doi.org/10.1088/1751-8121/aad3e6>.
- [25] C.D. Godsil, B.D. McKay, Constructing cospectral graphs, *Aequ. Math.* 25 (1) (1982) 257–268, <https://doi.org/10.1007/BF02189621>.
- [26] C.V. Morfonios, P.A. Kalozoumis, F.K. Diakonos, P. Schmelcher, Nonlocal discrete continuity and invariant currents in locally symmetric effective Schrödinger arrays, *Ann. Phys.* 385 (2017) 623–649, <https://doi.org/10.1016/j.aop.2017.07.019>.
- [27] M. Röntgen, C. Morfonios, F. Diakonos, P. Schmelcher, Non-local currents and the structure of eigenstates in planar discrete systems with local symmetries, *Ann. Phys.* 380 (2017) 135–153, <https://doi.org/10.1016/j.aop.2017.03.011>.

Flat bands by latent symmetryC. V. Morfonios¹, M. Röntgen¹, M. Pyzh¹ and P. Schmelcher^{1,2}¹Zentrum für Optische Quantentechnologien, Fachbereich Physik, Universität Hamburg, 22761 Hamburg, Germany²The Hamburg Centre for Ultrafast Imaging, Universität Hamburg, 22761 Hamburg, Germany

(Received 24 February 2021; revised 17 May 2021; accepted 15 June 2021; published 2 July 2021)

Flat energy bands of model lattice Hamiltonians provide a key ingredient in designing dispersionless wave excitations and have become a versatile platform to study various aspects of interacting many-body systems. Their essential merit lies in hosting compactly localized eigenstates which originate from destructive interference induced by the lattice geometry, in turn often based on symmetry principles. We here show that flat bands can be generated from a hidden symmetry of the lattice unit cell, revealed as a permutation symmetry upon reduction of the cell over two sites governed by an effective dimer Hamiltonian. This so-called latent symmetry is intimately connected to a symmetry between possible walks of a particle along the cell sites, starting and ending on each of the effective dimer sites. The summed amplitudes of any eigenstate with odd parity on the effective dimer sites vanish on special site subsets called walk multiplets. We exploit this to construct flat bands by using a latently symmetric unit cell coupled into a lattice via walk multiplet interconnections. We demonstrate that the resulting flat bands are tunable by different parametrizations of the lattice Hamiltonian matrix elements which preserve the latent symmetry. The developed framework may offer fruitful perspectives to analyze and design flat band structures.

DOI: [10.1103/PhysRevB.104.035105](https://doi.org/10.1103/PhysRevB.104.035105)**I. INTRODUCTION**

Wave excitations in a lattice system are governed by the form of its energy band structure and the corresponding eigenstates. Since the dawn of quantum mechanics, substantial efforts have been made to understand the response properties of crystals in terms of their energy bands. With the technological advances of the past decades, however, also artificial lattice systems have been realized with ever increasing accuracy. This has enabled an unprecedented engineering of bands with targeted properties. A most intriguing case is that of “flat” bands with vanishing curvature, which have become a subject of intense research for designed lattice setups [1]. Those range among various spatial scales and different technological platforms, such as photonic waveguide or resonator arrays [2–4], optical lattices for trapped atoms [5,6], superconducting wire networks [7], nanostructured electronic lattices [8], optomechanical setups [9], or electric circuit networks [10].

The remarkable features induced by flat bands essentially originate from the vanishing group velocity—or, equivalently, diverging effective mass—of the eigenstates residing in them. This allows for dispersionless wave excitations over the whole crystal-momentum range of the flat band [3], which may be exploited for their robust storage and transfer [11]. In turn, transport properties of flat band states can be manipulated by weak perturbations which set a dominant energy scale for them [1]. In particular, flat bands have been used, e.g., to model certain types of superfluidity [12–18] or topological phases of matter [19–23]. Flat bands have also been explored very recently to generate many-body localization [24–26] and “caging” [27,28] in the presence of interactions, or to control superradiance via synthetic gauge fields [29].

Flat bands of discrete lattice Hamiltonians rely on the occurrence of eigenstates which are strictly localized on a subset of sites, with vanishing amplitude in the remainder of the lattice [30]. Such “compact localized states” (CLSs) can be classified according to the number of unit cells they occupy [31]. Notably, they do not violate the translational invariance of the lattice since they can, due to their macroscopic degeneracy at the flat band energy, be linearly combined into extended Bloch states. A CLS originates from the destructive interference of its amplitudes on the neighboring lattice sites coupled to the site subset the CLS occupies. This mechanism may result directly from the geometric symmetry of the lattice unit cell under a site permutation operation [32,33]. It may also be caused by a bipartite (or chiral) symmetry of a lattice composed of sublattices [34], or induced “accidentally” by tuning the Bloch Hamiltonian matrix elements into the CLS condition. Various schemes for generating flat bands from CLSs have been proposed, based, e.g., on local permutation symmetries [33,35], “origami” rules [36], local basis transformations [32], solving inverse eigenvalue problems [31,37], and, as shown very recently, using the properties of Gram matrices [38] or combining lattice deformations with site additions [39]. Despite the great value of such approaches, the question remains whether flat bands may be systematically invoked by symmetry principles beyond the existing paradigms.

In the present work we propose a scheme to create flat bands which is based on a type of hidden symmetry in the unit cell Hamiltonian of a lattice. This so-called *latent symmetry*, introduced recently in graph theory [40], is revealed as a permutation symmetry once reducing the unit cell Hamiltonian over a particular subset of sites to an effective subsystem

Hamiltonian. Very recently, latent symmetries were proposed as a novel possibility to explain seemingly accidental spectral degeneracies of generic Hamiltonian matrices [41]. Reduction over a *pair* of latently exchange-symmetric sites—as we will focus on here—results in an effective two-site symmetric dimer, and the symmetry-induced parity of this dimer’s eigenstates is inherited in the original unit cell; that is, any of its eigenstates is locally even or odd on the latently symmetric sites. Latent symmetry of two sites can be intuitively interpreted as a collective symmetry of so-called *walks* [42] (i.e., sequential hoppings) along the coupled sites of the unit cell, starting and ending at each of those two sites. Equivalently, the latent symmetry is simply expressed in terms of powers of the Hamiltonian. We here combine latent symmetry with the occurrence of special subsets of sites called *walk multiplets*. On each such site subset, the amplitudes of any nondegenerate eigenvector with odd parity on the latently symmetric sites sum to zero. As we show, periodic lattices generated by interconnection of walk multiplets between latently symmetric unit cells host flat bands with corresponding CLSs which occupy single unit cells. Importantly, the underlying latent symmetry persists upon the simultaneous variation of certain parameters in the lattice Hamiltonian, making the generated flat bands systematically tunable. With our results applicable to arbitrary dimensions, we demonstrate the principle for one- and two-dimensional lattices with simple prototype cells possessing latent symmetries.

After introducing the concepts of latent symmetry and walk equivalence in Sec. II, we show how to combine them to generate flat band lattices in Sec. III, illustrating the principle with prototype examples. We discuss possible extensions in Sec. IV, while Sec. V concludes this work.

II. LATENT SYMMETRY, COSPECTRALITY, AND WALK MULTIPLETS

Consider the eigenvalue problem $H|\varphi\rangle = E|\varphi\rangle$ for a real symmetric $N \times N$ Hamiltonian matrix H represented in the orthonormal basis of single orbitals $|n\rangle$ on N coupled sites, $n \in \mathbb{H} \equiv \{1, \dots, N\}$. To introduce the notion of latent symmetry, let us partition the system into a selected subset $\mathbb{S} \subset \mathbb{H}$ with $N_{\mathbb{S}} = |\mathbb{S}|$ sites and its complement $\bar{\mathbb{S}} = \mathbb{H} \setminus \mathbb{S}$. The reduced $N_{\mathbb{S}} \times N_{\mathbb{S}}$ Hamiltonian $\tilde{H}_{\mathbb{S}}$ effectively describing subsystem \mathbb{S} under the influence of the rest of the system $\bar{\mathbb{S}}$ is then given by [43–45]

$$\tilde{H}_{\mathbb{S}}(E) = H_{\mathbb{S}} + \Gamma[E - H_{\bar{\mathbb{S}}}]^{-1} \Gamma^{\top} \equiv H_{\mathbb{S}} + \Sigma_{\bar{\mathbb{S}}}(E), \quad (1)$$

where the diagonal blocks $H_{\mathbb{X}} = H_{\mathbb{X}\mathbb{X}}$ of H are the Hamiltonians of the isolated subsystems $\mathbb{X} = \mathbb{S}, \bar{\mathbb{S}}$ and $\Gamma = H_{\mathbb{S}\bar{\mathbb{S}}}$ is the coupling from $\bar{\mathbb{S}}$ to \mathbb{S} . This is essentially Feshbach’s projection operator method [46] applied to the present discrete model, while the term $\Sigma_{\bar{\mathbb{S}}}(E)$ can be recognized as the “self-energy” [45,47] of \mathbb{S} induced by its coupling to $\bar{\mathbb{S}}$. It amounts to “renormalized” matrix elements in the resulting Hamiltonian $\tilde{H}_{\mathbb{S}}(E)$, in analogy to decimation procedures in real-space renormalization group theory [45], which has been applied to study, e.g., localization in disordered and quasiperiodic tight-binding structures [48–50]. The reduced eigenvalue problem now has a smaller dimension, but is nonlinear due

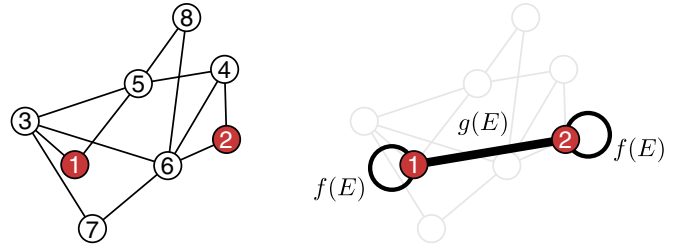


FIG. 1. *Left*: An unweighted graph, representing a Hamiltonian H with unit hopping (thin edge lines) and zero on-site elements, with two cospectral vertices $\mathbb{S} = \{u, v\} = \{1, 2\}$ forming a latently symmetric site pair. *Right*: H is reduced over \mathbb{S} to the effective Hamiltonian $\tilde{H}_{\mathbb{S}}$ describing a symmetric two-site dimer with on-site elements f (visualized as loop edges in the graph) and hopping g depending functionally on the eigenvalue E ; in this example $f(E) = (8 - 4E - 10E^2 + 2E^3 + 2E^4)/d(E)$ and $g(E) = (-6 + 6E^2 + 2E^3)/d(E)$, where $d(E) = 7E - 2E^2 - 8E^3 + E^5$.

to the E -dependence of $\tilde{H}_{\mathbb{S}}$. The spectrum $\sigma(\tilde{H}_{\mathbb{S}})$ of $\tilde{H}_{\mathbb{S}}$, given by $\det[E - \tilde{H}_{\mathbb{S}}(E)] = 0$, coincides with that of H after removing E values which happen to be eigenvalues of $H_{\bar{\mathbb{S}}}$ and for which $\tilde{H}_{\mathbb{S}}$ is not defined; symbolically, $\sigma(\tilde{H}_{\mathbb{S}}) = \sigma(H) - \sigma(H_{\bar{\mathbb{S}}})$ (note that σ is a multiset in the presence of repeated eigenvalues). Most importantly, any eigenvector $|\tilde{\varphi}\rangle$ of $\tilde{H}_{\mathbb{S}}$ equals the *restriction* of that of H , with the same eigenenergy, to the subsystem \mathbb{S} [51]: $\langle s|\tilde{\varphi}\rangle = \langle s|\varphi\rangle$ for $s \in \mathbb{S}$.

A *latent symmetry* is a permutation symmetry $\Pi_{\mathbb{S}}$ of the reduced Hamiltonian $\tilde{H}_{\mathbb{S}}$ such that any extended permutation $\Pi_{\mathbb{S}} \oplus \Pi_{\bar{\mathbb{S}}}$ (including the identity $\Pi_{\bar{\mathbb{S}}} = I_{\bar{\mathbb{S}}}$) is *not* a symmetry of the original Hamiltonian H . Throughout this work, \mathbb{S} will consist of two sites u and v , and by “latent symmetry” we will always mean symmetry under transposition (i.e., exchange) of u and v . Then $\tilde{H}_{\mathbb{S}}$ effectively behaves like a two-site dimer with E -dependent on-site potentials and coupling; see Fig. 1. If u and v are latently symmetric in H , this effective dimer is symmetric under exchange of u and v . If nondegenerate, its eigenstates $|\tilde{\varphi}\rangle$ accordingly have definite parity $\langle u|\tilde{\varphi}\rangle = \pm\langle v|\tilde{\varphi}\rangle$, and the same holds for the corresponding eigenstates, with the same eigenenergies, of H : $\langle u|\varphi\rangle = \pm\langle v|\varphi\rangle$. Such a parity of amplitudes on u and v in the original, extended system H , is usually traced back to an involutory site permutation symmetry. Remarkably, the global parity in $\tilde{H}_{\mathbb{S}}$ is here inherited to the eigenstates $|\varphi\rangle$ as a *local parity* in H , where there is *no permutation symmetry producing it*.

Latent symmetries were introduced very recently [40,52] in the context of isospectral graph reductions [53]. There, H is the (weighted) adjacency matrix of a connected graph with vertex set \mathbb{H} and edges with weights $H_{mn} = \langle m|H|n\rangle$ between vertices. For brevity we will refer to the graph itself simply as H . The *isospectral reduction* of the graph over a subset \mathbb{S} of its vertices is exactly the graph with adjacency matrix given in Eq. (1). An example graph is shown in Fig. 1, containing the two latently symmetric vertices $\mathbb{S} = \{u, v\} = \{1, 2\}$.

A crucial fact, promoting the treatment of latent symmetry with the tools of graph theory, is the following [42]: Two latently symmetric vertices u, v of a graph are *cospectral*, meaning that the spectra of the “vertex-deleted” graphs $H_{\bar{u}} = H - u$ and $H_{\bar{v}} = H - v$ (where vertices u and v , as well

as edges incident to them, have been deleted, respectively) coincide, $\sigma(H_{\bar{u}}) = \sigma(H_{\bar{v}})$. Alternatively, and of more use for our purposes here, cospectral vertices are defined by the property that their corresponding diagonal entries in any non-negative power r of H coincide [54],

$$[H^r]_{uu} = [H^r]_{vv} \quad \forall r \in \mathbb{N}. \quad (2)$$

In general, for an unweighted graph ($H_{mn} \in \{0, 1\}$) the element $[H^r]_{mn}$ gives the total number of all possible *walks* of length r from vertex m to n [55,56], that is, sequences

$$\alpha = (a_1 = m, b_1)(a_2, b_2) \cdots (a_r, b_r = n) \quad (3)$$

of r possibly repeated edges (a_i, b_i) with $a_{i+1} = b_i$. For example, the walk with steps $1 \rightarrow 3 \rightarrow 5 \rightarrow 8 \rightarrow 6 \rightarrow 2$ along the sites of Fig. 1 is denoted as the sequence of edges $(1, 3)(3, 5)(5, 8)(8, 6)(6, 2)$. Note that also *loops*, with $b_i = a_i$, may be included in a walk, representing on-site potentials $H_{a_i a_i}$. Equation (2) concerns the special case of closed walks ($n = m$) starting and ending at each cospectral vertex u or v . For instance, Eq. (2) can easily be verified in the unweighted graph of Fig. 1 for the first few powers r , by counting all closed walks of length r starting at $u = 1$ or $v = 2$. The closed walks of length $r = 3$, for example, are (in simplified step notation) $1 \rightarrow 3 \rightarrow 5 \rightarrow 1$ and $2 \rightarrow 4 \rightarrow 6 \rightarrow 2$, plus the same in opposite directions, in accordance with $[H^3]_{11} = [H^3]_{22} = 2$.

For a weighted graph, a weight $w(\alpha)$ is assigned to each walk, equal to the product of edge weights along it, $w(\alpha) = \prod_{i=1}^r w(a_i, b_i) = \prod_{i=1}^r H_{a_i b_i}$. The above interpretation of matrix powers in terms of walks is then generalized to a sum over walk weights [57],

$$[H^r]_{mn} = \sum_{\alpha \in \mathcal{A}_{mn}^{(r)}} w(\alpha), \quad r \in \mathbb{N}, \quad (4)$$

where $\mathcal{A}_{mn}^{(r)}$ is the set of all walks of length r from m to n .

Fortunately, there is no need to evaluate Eq. (2) beyond $k = N - 1$ since, by the Cayley-Hamilton theorem, any higher powers $H^{k \geq N}$ can be expressed as lower order polynomials in H . As a consequence, if Eq. (2) holds for $r = 0, \dots, N - 1$, it automatically holds for all r . This enables the use of the $N \times N$ *walk matrix* [58,59] $W_{\mathbb{M}}$ of a subset $\mathbb{M} \subseteq \mathbb{H}$ to encode walks ending in \mathbb{M} , constructed by the action of H^r on the indicator vector $|e_{\mathbb{M}}\rangle$ of \mathbb{M} (with $\langle m|e_{\mathbb{M}}\rangle = 1$ for $m \in \mathbb{M}$ and 0 otherwise):

$$W_{\mathbb{M}} = [|e_{\mathbb{M}}\rangle, H|e_{\mathbb{M}}\rangle, \dots, H^{N-1}|e_{\mathbb{M}}\rangle], \quad (5)$$

also known as the Krylov matrix of H generated by $|e_{\mathbb{M}}\rangle$ [60,61]. The r th column of $W_{\mathbb{M}}$ is given by $[W_{\mathbb{M}}]_{*r} = H^{r-1}|e_{\mathbb{M}}\rangle$ (* denoting all indices) and its element

$$[W_{\mathbb{M}}]_{sr} = \sum_{m \in \mathbb{M}} [H^{r-1}]_{sm} \quad (6)$$

yields the sum over weighted walks—in the sense of Eq. (4)—of length $r - 1$ from vertex s to all vertices in \mathbb{M} .

We call two vertices u, v *walk equivalent* [62] relative to \mathbb{M} if their summed walks to \mathbb{M} are equal for any walk length r , that is, if the corresponding rows of $W_{\mathbb{M}}$ are equal,

$$[W_{\mathbb{M}}]_{u*} = [W_{\mathbb{M}}]_{v*}. \quad (7)$$

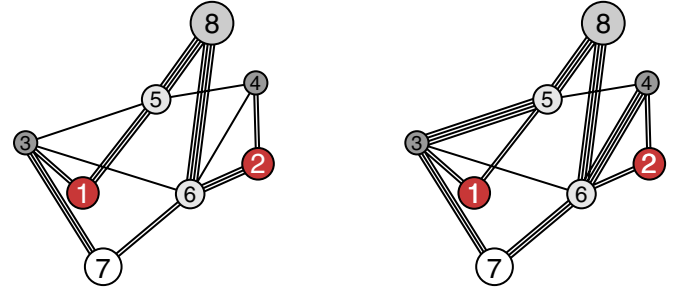


FIG. 2. The same graph as in Fig. 1, but now parametrically weighted in the two different ways which preserve the cospectrality of $\mathbb{S} = \{u, v\} = \{1, 2\}$. Different edges and loops (hopping and on-site elements in H) are visualized by different line numbers and vertex sizes, respectively. Subsets \mathbb{M}_μ ($\mu = 1, 2, \dots, 5$) of sites with same shading (also with same vertex size) are “walk multiplets” with respect to \mathbb{S} (with u, v being “walk equivalent” relative to any \mathbb{M}_μ , fulfilling Eq. (7)). Here the doublets are $\{1, 2\}$, $\{3, 4\}$, $\{5, 6\}$, and the singlets $\{7\}$, $\{8\}$.

Conversely, we say that \mathbb{M} then constitutes a *walk multiplet* with respect to $\{u, v\}$; specifically, a walk M -let of size $M = |\mathbb{M}|$ (singlet for $M = 1$, doublet for $M = 2$, etc.) [63].

Examples of walk singlets ($M = 1$) and doublets ($M = 2$) are shown in Fig. 2. There the weights of the graph in Fig. 1 have also been *parametrized* in two different ways such that the cospectral pair $\{1, 2\}$, and each shown walk multiplet relative to it, are preserved [64]. More specifically, the cospectrality of $\{1, 2\}$ and walk multiplets relative to it remain intact for any arbitrary value—a parameter of H —of edge weights (including loops) which are equal. For instance, in the right parametrization the equal weights $H_{13} = H_{15} = H_{24} = H_{26}$ can be varied together arbitrarily while retaining the cospectrality and walk multiplets of $\{1, 2\}$.

As we will see further below, this cospectrality- and multiplet-preserving parametrization will allow for a flexible tuning of flat bands. In the next section we will start by showing how the combination of walk equivalence with cospectrality for vertex pairs may be used to generate CLSs and corresponding flat band lattices.

Before continuing, let us note that, if two vertices u and v are related by a permutation symmetry of the graph, i.e., there is some permutation matrix Π commuting with H for which $\Pi|u\rangle = |v\rangle$, then Eq. (2) is automatically fulfilled. In this work we focus on cospectral pairs u, v for which Eq. (2) is *not* induced by permutation symmetry, but which correspond to *latent* symmetry as defined above. As will be discussed later on (see Sec. IV C), constructing such graphs is not a trivial task. We have here resorted to numerical validation of Eq. (2) for a fixed small graph size ($N = 8$), with a latently symmetric example provided in Fig. 1. It should thus be clear that the graphs we utilize as representative examples in this work are special cases whose structure supports latent symmetry. Modifying them *arbitrarily* (e.g., by adding or deleting edges) would in general invalidate Eq. (2) and thus break the latent symmetry between the selected vertices u, v in each case. Nevertheless, as shown in Ref. [62], there *exist* systematic graph modifications which do preserve the cospectrality of a given vertex pair. Those modifications are outlined below (in

Sec. III A) and will constitute the key ingredient in generating flat bands by combining latent symmetry with walk multiplets.

III. FLAT BANDS INDUCED BY WALK EQUIVALENT COSPECTRAL SITES

Let us now consider a graph H with cospectral vertices u, v which are walk equivalent relative to a multiplet \mathbb{M} , like in Fig. 2 (with \mathbb{M} chosen as one of the multiplets \mathbb{M}_μ). Due to cospectrality, any nondegenerate eigenvector $|\varphi_v\rangle$ has (or, if degenerate, can be chosen to have) local parity on $\{u, v\}$ [65],

$$\langle u|\varphi_v^\pm\rangle = \pm\langle v|\varphi_v^\pm\rangle, \quad (8)$$

with $+$ ($-$) denoting even (odd) parity. This local parity on the cospectral pair $\{u, v\}$ is equivalent to a symmetry Q of H with $Q^2 = I$ which exchanges u and v , that is, $Q|e_u\rangle = |e_v\rangle$, while acting as a general orthogonal transformation on the complement $\mathbb{H} \setminus \{u, v\}$ [41,54], as described in detail in Appendix A.

Now, by inserting the spectral decomposition $H = \sum_v E_v |\varphi_v\rangle\langle\varphi_v|$ into Eq. (7) and using Eq. (8), one can show [62] that the amplitude sum of any odd $\{u, v\}$ -parity eigenstate over any walk multiplet relative to $\{u, v\}$ vanishes, that is,

$$\sum_{m \in \mathbb{M}} \langle m|\varphi_v^- \rangle = \langle e_{\mathbb{M}}|\varphi_v^- \rangle = 0, \quad (9)$$

where, in the case of degenerate $|\varphi_v^- \rangle$, it has been chosen to be the only $\{u, v\}$ -odd eigenstate to its eigenvalue E_v , given by the projection of the vector $|u\rangle - |v\rangle$ onto that degenerate subspace [62]. In particular, $\langle m|\varphi_v^- \rangle$ vanishes on any walk *singlet* $\mathbb{M} = \{m\}$. We note that walk singlets are fixed (that is, each mapped onto itself) under the action of Q , as shown in Appendix A.

The generation of flat bands from a latently symmetric H will ultimately consist in converting it into a Bloch Hamiltonian by interconnecting any of its walk multiplets *within the same graph H itself* via edges with corresponding complex weights. To develop and demonstrate the principle step-by-step in the following subsections, we will first provide the necessary graph modification rules in Sec. III A; apply them to construct a periodic 1D lattice, or directly its Bloch Hamiltonian, hosting CLSs in Sec. III B; demonstrate how the corresponding flat bands can be parametrically tuned in Sec. III C; and combine the above in a 2D example in Sec. III D.

A. Graph modifications preserving walk multiplets

As shown in Ref. [62], certain modifications can be performed on a graph H such that the cospectrality of vertex pair $\{u, v\}$ together with the walk multiplets relative to it remain intact. For clarity, we here focus on their simplest form (see Sec. IV below for related generalizations).

The cospectrality of $\{u, v\}$, as well as any walk multiplet \mathbb{M} of H , are preserved in the new graph H' obtained by performing the following modifications:

(M1) Connection of an arbitrary graph exclusively to any walk singlet c of H via edges of arbitrary weights, whereby all vertices of the added graph become walk singlets in H' ;

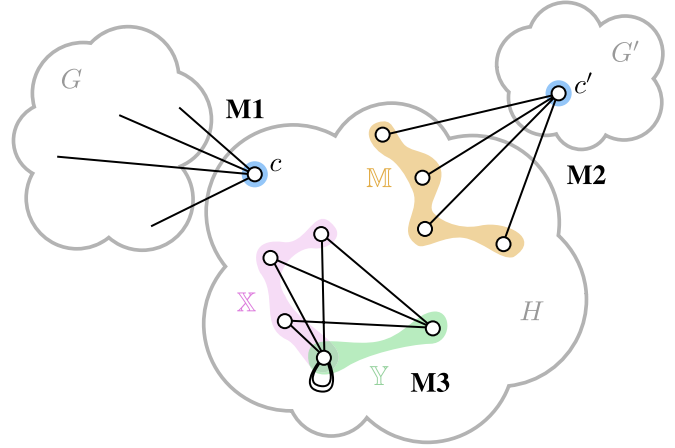


FIG. 3. Schematically depicted graph modifications addressed in Sec. III A and Appendix B: (M1) connection of an arbitrary graph G exclusively to a walk singlet c of H , (M2) connection of a walk multiplet \mathbb{M} of H to a single vertex c' of an arbitrary graph G' , and (M3) interconnection of two overlapping walk multiplets \mathbb{X} and \mathbb{Y} of H .

(M2) Connection of all vertices of any walk multiplet of H to a single vertex c' of an arbitrary graph via edges of uniform weight, whereby all vertices of the added graph become walk singlets in H' ;

(M3) Interconnection of any two walk multiplets of H via edges of uniform weight between all vertices of one multiplet and each vertex of the other (added to any already existing edge weights),

where any walk multiplet is implied relative to $\{u, v\}$. In Appendix B we provide brief proofs of the above properties in their general form. A generic schematic of the modifications is given in Fig. 3. Note that if the two multiplets in (M3) overlap (that is, have common vertices), then the vertices in the overlap are interconnected by double (additional) edges, like the double loop in Fig. 3; see Appendix B.

In the following we will employ the above modifications (M1)–(M3) for the construction of flat band lattices, illustrated in concrete examples.

B. Flat bands via walk multiplet interconnections

In the following principle for constructing flat band lattices, an original latently symmetric Hamiltonian H featuring walk multiplets will be used as a unit cell of a lattice with Hamiltonian H^\sharp . The unit cells are interconnected using the modifications described above in Sec. III A. In this way the latent symmetry in any copy of H is inherited by the whole lattice in the sense that it remains present after the interconnection. We stress that, in order to induce flat bands, the walk multiplets used in those interconnections are relative to a given cospectral site pair $\{u, v\}$, as described above, and not to any arbitrary site pair.

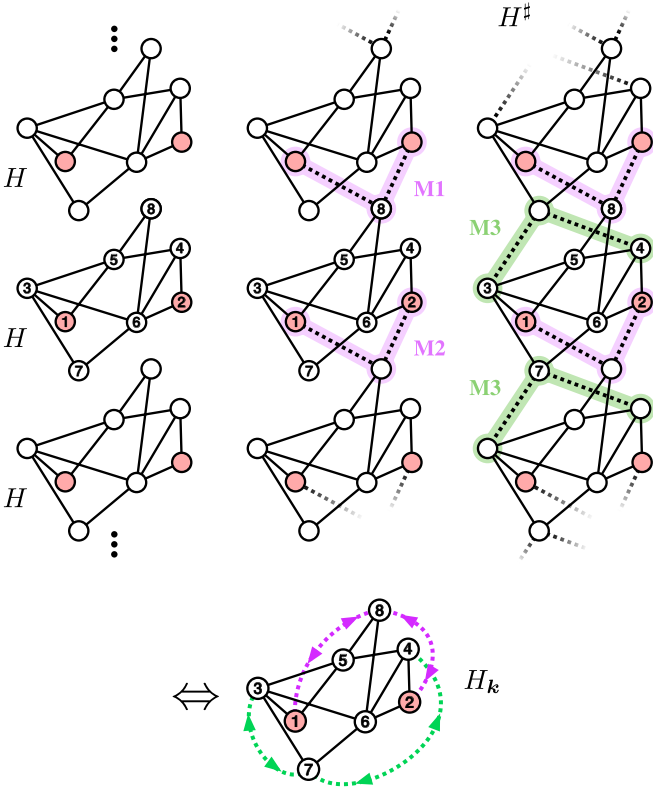


FIG. 4. *Top*: Construction of a lattice Hamiltonian H^\sharp using the Hamiltonian H of Fig. 1 as an isolated unit cell, via modifications (M1)–(M3) of Sec. III A with respect to its cospectral site pair $\{1, 2\}$: For each of the copies of H (left), setting the labeled graph as reference, first we connect the walk singlet $\{8\}$ to sites $1, 2$ of the cell above using (M1) and the walk doublet $\{1, 2\}$ to site 8 of the cell below using (M2) (middle), and then connect the walk multiplets $\{3, 4\}$ and $\{7\}$ to walk singlets of the resulting graph using (M3) (right), with intercell connections h indicated by dotted lines. *Bottom*: The Bloch Hamiltonian H_k corresponding to the lattice Hamiltonian H^\sharp can be constructed from H via (M3) by interconnecting the singlet $\{8\}$ ($\{7\}$) to the doublet $\{1, 2\}$ ($\{3, 4\}$), though with complex Hermitian couplings $h e^{\pm i k L}$ indicated by purple (green) double-headed dotted lines, with $k = |\mathbf{k}|$ and lattice constant L ; see Sec. III B.

In Fig. 4 (top) we illustrate the modifications (M1)–(M3) as applied to our example Hamiltonian H of Fig. 1 to create a periodic lattice H^\sharp with H as a unit cell. First, for a given reference cell H (the cell with labeled sites in Fig. 4; simply “cell” will mean “unit cell” from here on), we connect the walk singlet $\{8\}$ to sites $1, 2$ in the cell above and the doublet $\{1, 2\}$ to site 8 in the cell below. Thus, the cospectrality of the pair $\{1, 2\}$ and relative multiplets are preserved by simultaneous application of (M1) (connecting a singlet to the graph above) and (M2) (connecting a multiplet to the graph below). Note that, after this interconnection, all sites in the remainder of the lattice (outside the reference cell) are singlets relative to $\{1, 2\}$ in the reference cell. Second, in the resulting graph, we apply (M3) by interconnecting the doublet $\{3, 4\}$ with the site 7 of the cell above (a singlet relative to $\{1, 2\}$ in the reference cell) and the singlet $\{7\}$ to sites $3, 4$ of the cell below (both singlets relative to $\{1, 2\}$ in the reference cell).

Note that the same interconnections as for the reference cell to adjacent cells can be performed simultaneously for all periodically arranged copies of H , without affecting the cospectrality of $\{u, v\} = \{1, 2\}$ in the reference cell. Thus, since the reference cell is chosen arbitrarily, each unit cell in H^\sharp inherits the cospectral pair $\{u, v\}$ (in local labeling for that cell) and its relative walk multiplets from the isolated graph H . We also underline that the distinction between the different intercell connections in Fig. 4 by the labels M1, M2, M3 refers only to the way the lattice is constructed by sequential application of those graph modification rules. In the final lattice, those physical connections are qualitatively equivalent; in fact, the connections labeled M1 and M2 constitute the same intercell coupling, translated by one unit cell.

The intercell connection scheme previously outlined can be more compactly expressed directly at the level of the Bloch Hamiltonian H_k of the lattice. H_k is generally obtained by Fourier transformation of the lattice Hamiltonian elements [66] as

$$[H_k]_{mn} = \sum_{\ell} e^{i\mathbf{k}\cdot\ell} \langle m | H^\sharp | n_\ell \rangle, \quad (10)$$

where $|n_\ell\rangle$ is the orbital $|n\rangle$ in the cell at position ℓ , with $|n\rangle \equiv |n_{\ell=0}\rangle$ for the reference unit cell at $\ell = \mathbf{0}$. The eigenvalues $E_v(\mathbf{k})$ of H_k constitute the band structure of the lattice. Interconnections between *different* cells in the lattice graph H^\sharp (e.g., with some coupling $\langle m | H^\sharp | n_\ell \rangle = h \in \mathbb{R}$ between sites $m, n_{\ell \neq 0}$) are equivalent to the corresponding interconnections in the *single* cell graph H , though additionally weighted with conjugate Bloch phases (i.e., coupling $[H_k]_{mn} = [H_k]_{nm}^* = h e^{i\mathbf{k}\cdot\ell}$ between sites m, n). This is shown in Fig. 4 (bottom) for the example lattice. The resulting Bloch graph H_k is directed, with complex conjugate edge weights in opposite directions between any vertex pair being interconnected. In fact, H_k can be seen as resulting from the cospectrality-preserving modification (M3) (interconnection of two walk multiplets) on H , though with additional uniform prefactors $e^{\pm i\mathbf{k}\cdot\ell}$ in either direction of the connection (see Fig. 4). In Appendix C we explicate that site pair cospectrality and corresponding latent symmetry are preserved under walk multiplet interconnections (M3) with complex Hermitian coupling weights.

Let us now explain how the multiplet interconnection described above can induce CLSs and corresponding flat bands for the resulting lattice. Specifically, any $\{u, v\}$ -odd eigenstate $|\varphi_v^-\rangle$ of the initially isolated unit cell H constitutes a CLS in the lattice H^\sharp constructed via multiplet interconnection between unit cells. Indeed, consider the infinite-length column vector $|\varphi_{v;\ell}^-\rangle$ defined to have the components of $|\varphi_v^-\rangle$ on the cell at ℓ , padded with zeros on all other cells $\ell' \neq \ell$, that is, $\langle n_{\ell'} | \varphi_{v;\ell}^- \rangle = \langle n | \varphi_v^- \rangle \delta_{\ell\ell'}$. In other words, $|\varphi_{v;\ell}^- \rangle$ is a CLS occupying the cell at ℓ .

Notice now that $|\varphi_{v;\ell}^- \rangle$ is an eigenstate of the lattice Hamiltonian H^\sharp to the eigenenergy E_v (the eigenenergy of $|\varphi_v^- \rangle$ in the isolated cell H). To see this, let us write H^\sharp in the form

$$H^\sharp = \bigoplus_{\ell} H + \sum_{\ell \neq \ell', \mathbb{X}, \mathbb{Y}} (h_{\mathbb{X}\mathbb{Y}}^{\ell\ell'} |e_{\mathbb{X};\ell}\rangle \langle e_{\mathbb{Y};\ell'}| + \text{H.c.}), \quad (11)$$

where H is repeated on the block diagonal and $|e_{\mathbb{X};\ell}\rangle \langle e_{\mathbb{Y};\ell'}|$ contains the off-diagonal block coupling multiplet \mathbb{Y} in cell

ℓ' to multiplet \mathbb{X} in cell ℓ with uniform coupling strength $h_{\mathbb{X}\mathbb{Y}}^{\ell\ell'}$, and zeros otherwise ($|e_{\mathbb{X};\ell}\rangle$ being the infinite column with components $|e_{\mathbb{X}}\rangle$ on cell ℓ and zeros otherwise)—see, e.g., colored couplings in Fig. 4 (top right). Now, acting with H^\sharp on $|\varphi_{v;\ell}^-\rangle$ directly yields

$$H^\sharp|\varphi_{v;\ell}^-\rangle = E_v|\varphi_{v;\ell}^-\rangle, \quad (12)$$

since $H|\varphi_{v;\ell}^-\rangle = E_v|\varphi_{v;\ell}^-\rangle$ for block ℓ (corresponding to the only cell occupied by $|\varphi_{v;\ell}^-\rangle$), while $\langle e_{\mathbb{X};\ell}|\varphi_{v;\ell}^-\rangle = \langle e_{\mathbb{X}}|\varphi_{v;\ell}^-\rangle = 0$ by Eq. (9).

As an example, the lattice constructed in Fig. 4 features two different CLS types, which are illustrated in Fig. 5 (right panel) in two different unit cells of the lattice. The orange arrows indicate an example of how the CLS amplitudes cancel out (interfere destructively) on a neighboring cell site upon action of H^\sharp due to the multiplet condition, Eq. (9).

Analogously to the above, $|\varphi_{v;\ell}^-\rangle$ is an eigenvector of the Bloch Hamiltonian H_k constructed from H via multiplet interconnections. More specifically, H_k can be written as

$$H_k = H + \sum_{\ell, \mathbb{X}, \mathbb{Y}} (h_{\mathbb{X}\mathbb{Y}}^\ell e^{ik\cdot\ell} |e_{\mathbb{X}}\rangle\langle e_{\mathbb{Y}}| + \text{H.c.}), \quad (13)$$

summing over all interconnected multiplet pairs \mathbb{X}, \mathbb{Y} with \mathbb{Y} in cell ℓ and \mathbb{X} in the reference cell $\ell \equiv \mathbf{0}$ connected with uniform coupling weight $h_{\mathbb{X}\mathbb{Y}}^\ell$. Acting with H_k on $|\varphi_{v;\ell}^-\rangle$ immediately yields

$$H_k|\varphi_{v;\ell}^-\rangle = E_v|\varphi_{v;\ell}^-\rangle, \quad (14)$$

again due to Eq. (9). This holds for *any* k , so $|\varphi_{v;\ell}^-\rangle$ corresponds to a flat band at the k -independent eigenenergy E_v in the band structure of the lattice.

In Fig. 5 the band structure of the lattice constructed in Fig. 4 is shown [67]. As we see, there are two flat bands at $E = \pm\sqrt{2}$, corresponding to the two CLSs “CLS1” and “CLS2” depicted on the right, with odd parity on the cospectral sites $\{1, 2\}$.

We would like to underline here that the constructed flat bands are *independent* of the intercell coupling strength used in the walk multiplet interconnections. Indeed, as evidenced by Eq. (9), the hopping elements $h_{\mathbb{X}\mathbb{Y}}^\ell$ connecting the lattice cells do not enter the eigenvalue problem in Eq. (14). The corresponding flat band energy E_v is therefore unaffected by the value of the $h_{\mathbb{X}\mathbb{Y}}^\ell$, which however generally do affect the rest of the energy spectrum. Thus, the intercell coupling strengths used in the walk multiplet interconnections can be flexibly tuned to modify the dispersive part of the band structure around the constructed flat bands.

The above construction of CLSs and flat bands from latent symmetry and walk multiplets can be seen as a generalization of the construction from local permutation symmetries Π which are involutory ($\Pi^2 = I$) and leave certain sites of the unit cell fixed. If n is such a fixed site, i.e., $\Pi|n\rangle = |n\rangle$, then any eigenstate $|\varphi\rangle$ with odd parity under Π has $\langle n|\varphi\rangle = \langle n|\Pi^2\varphi\rangle = -\langle n|\varphi\rangle = 0$, that is, has a node (vanishing amplitude) on the fixed site. Interconnecting unit cells into a lattice by coupling such Π -fixed sites from cell to cell, any Π -odd eigenstate of the isolated unit cell yields a CLS and thus a corresponding flat band for the lattice. This scenario constitutes a special case of the construction described in

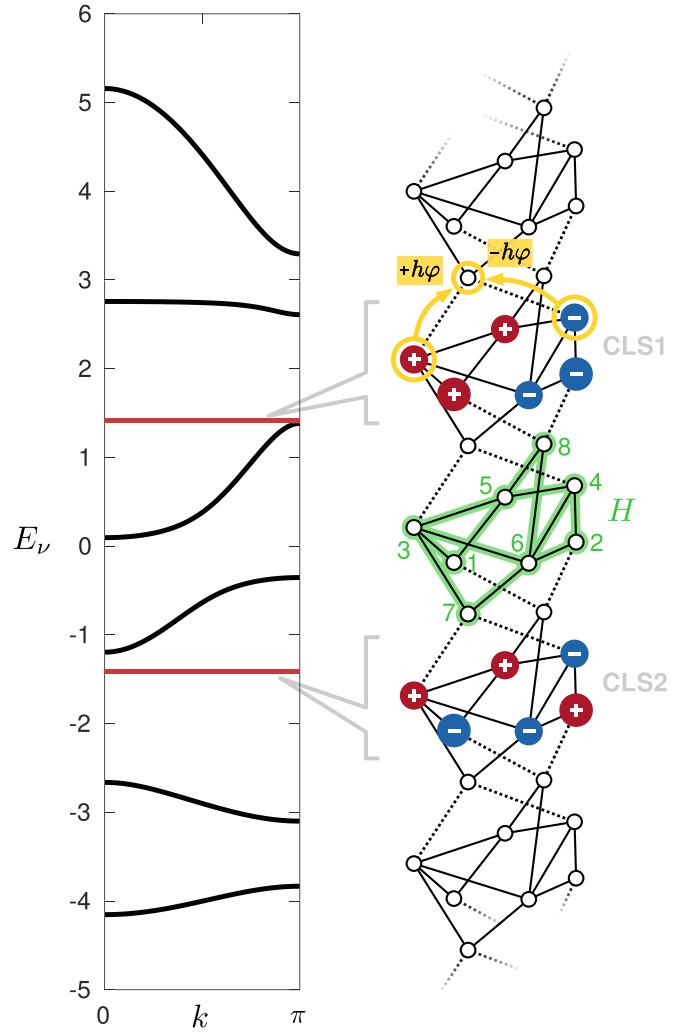


FIG. 5. Band structure (*left*) of the lattice H^\sharp in Fig. 4, with unit intracell couplings and intercell couplings $h = 2$. It features two flat bands at $E = \pm\sqrt{2}$ (red lines) corresponding to the two latent-symmetry induced CLSs “CLS1” and “CLS2” depicted (*right*). The amplitudes of each shown CLS are real with indicated relative sign + (red) and – (blue), with magnitudes proportional to the areas of the corresponding signed (red/blue) circles, and zero on all other sites. The isolated unit cell Hamiltonian H and site labeling are highlighted (green) in the middle. An example of destructive interference of one of CLS1’s amplitudes on the connected site of an adjacent cell is indicated by (orange) arrows, with $\pm\varphi$ denoting the amplitude on the walk doublet $\{3, 4\}$. Energies are in units of the uniform intracell site couplings, and lengths in units of the lattice constant $L = 1$ (quasimomentum k in units of $1/L$).

the present work (based on walk equivalent cospectral sites), where (a) the cospectral sites are related by a common permutation symmetry exchanging those sites and (b) the unit cells are interconnected via walk singlets relative to the pair of exchanged sites [68]. We note that such a local exchange symmetry is, in turn, a special case of general local permutation symmetries inducing CLSs, as addressed in Ref. [33] in terms of so-called *equitable partitions* of graphs. Relating that approach to latent symmetries involving site subsets \mathbb{S} of more than two sites is an interesting direction of further research.

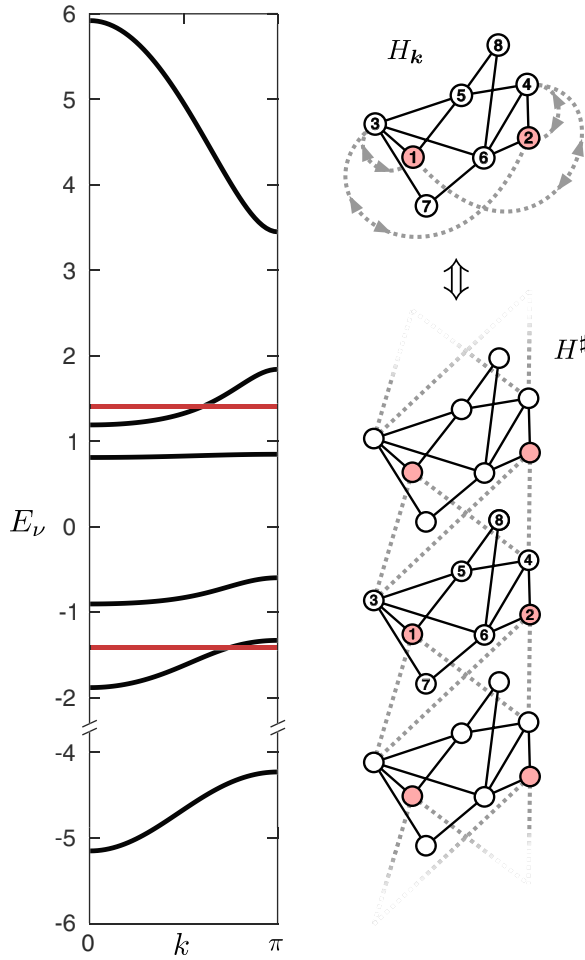


FIG. 6. Band structure (left) of a lattice constructed from H in Fig. 1 as a unit cell by interconnecting its walk doublets $\{1, 2\}$ and $\{3, 4\}$ as indicated by dotted edges in H_k and H^\sharp (right), with unit intracell couplings and intercell couplings $h = 2$. The two flat bands at $E = \pm\sqrt{2}$ (red lines) correspond to the same CLSs as in Fig. 5. Note that the band around $E \approx 0.8$ is dispersive and only looks rather flat at the used plotting scale of the E axis.

We stress that in the present case (Fig. 5), the zeros of the CLSs within the unit cell (on sites 7,8) are not induced by any permutation symmetry of the cell fixing those nodal sites, but rather by latent symmetry and walk equivalence (of the cospectral sites relative to walk singlets), as described above.

For simplicity we have applied walk singlet-to-doublet intercell connections in the above example (Figs. 4 and 5). It is clear from the above, however, that the procedure to generate flat bands applies naturally for any walk multiplet interconnection as intercell coupling; see Eqs. (13) and (14).

As an example, in Fig. 6 we start with the same graph H (as in Fig. 4) but now interconnect the walk doublets $\{1, 2\}$ and $\{3, 4\}$ in H_k , i.e., each site 1,2 to both 3,4 with complex Hermitian couplings (including Bloch phases), and corresponding real intercell couplings in H^\sharp , as explained above. This lattice maintains the same CLSs and flat bands as before (Fig. 5), though generally with modified dispersive bands.

In general, any Hermitian walk multiplet interconnection (M3) with complex Bloch phases, applied to a unit cell H , is

mapped to an intercell connection in the lattice Hamiltonian H^\sharp preserving the latent symmetry in each cell. This allows for great flexibility in generating flat bands with a given latently symmetric prototype cell.

To summarize, the proposed flat band construction principle consists in

- (i) starting with a Hamiltonian H in the form of a graph having two latently exchange-symmetric, cospectral vertices $\{u, v\}$,
- (ii) identifying walk multiplets of H relative to $\{u, v\}$, and
- (iii) using H as the unit cell of a lattice constructed by periodically interconnecting any walk multiplet of each cell to any walk multiplet of other cells (which can be neighboring cells but also more remote ones).

The resulting lattice H^\sharp then features a flat band for each eigenstate $|\varphi_v^-\rangle$ of H with odd parity on $\{u, v\}$, which becomes a macroscopically degenerate CLS in H^\sharp occupying one unit cell.

C. Parametric invariance of latent symmetry flat bands

It is important to notice that the generation of CLSs and resulting flat bands from latent symmetry and walk multiplets of a graph H is not restricted to a fixed set of edge weight values H_{mn} . Indeed, there is a certain freedom in changing H 's elements *parametrically* while still inducing flat bands from the same latent symmetry and walk multiplets. Specifically, this parametrization means that there exist groups of the elements H_{mn} which can be set to a common arbitrary real value per group, without breaking the given latent symmetry and selected walk multiplets. For example, the weight parametrizations shown in Fig. 2 preserve the cospectrality of $\{u, v\}$ as well as the multiplets interconnected to form the lattice in Fig. 4. Thus, when varying the weight parameters (that is, the common value of each group of elements H_{mn}), flat bands are still induced for the constructed lattice. Their energy positions, however, generally depend on the weight parameters, which allows for tuning the flat bands relative to the rest of the band structure.

We demonstrate this parametric invariance of the flat bands for our navigating example graph in Fig. 7, where the band edges for the lattice in Fig. 5 are plotted for a continuous variation of selected couplings in the unit cell. Specifically, using the cospectrality- and multiplet-preserving edge weight parametrization of Fig. 2 (right), a selected subset of couplings is set to a common varying value p (see Fig. 7 caption). As we see, while the dispersive band widths vary with p , the flat bands constructed by latent symmetry for $p = 1$ remain flat for any p (see red lines, whose vertical cross sections at any p are single points at the corresponding E_ν). This is in contrast to flat bands that may appear “accidentally” when varying p , as seen, e.g., for the second lowest band which becomes flat at a single point around $p \approx 0.4765$.

Furthermore, in this example the upper (lower) flat band energy increases (decreases) linearly with p across the dispersive bands and the gaps between them. This demonstrates the possibility to tune the flat band positions relative to dispersive bands without invoking any apparent symmetry of the unit cell.

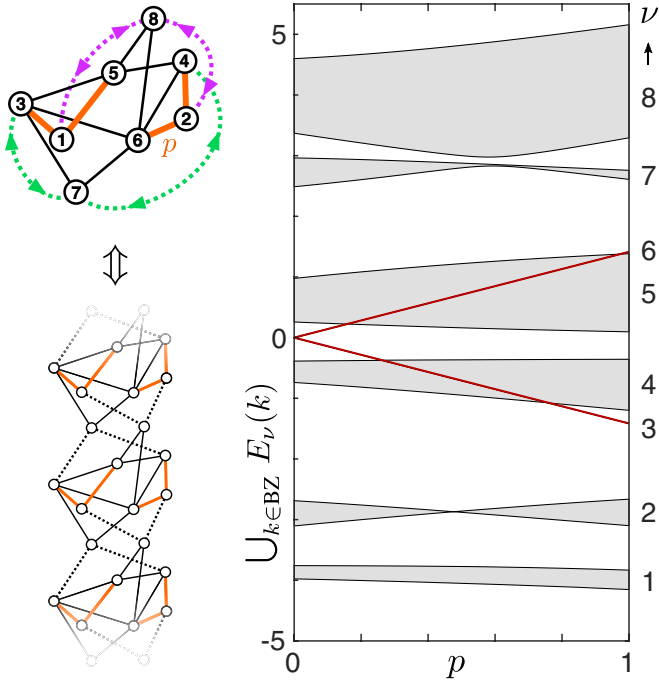


FIG. 7. Band edges (black lines) and band projections $\bigcup_{k \in \text{BZ}} E_\nu(k)$ (gray shades) of the bands $E_\nu(k)$ over the Brillouin zone (BZ) for the lattice in Fig. 5 with varying coupling parameter $H_{13} = H_{15} = H_{24} = H_{26} = p$ indicated (orange lines) in the schematic on the left; $p = 1$ corresponds to the band structure in Fig. 5. The two flat bands induced by latent symmetry of sites 1,2 occur at any p , with energies varying in p (thick red lines).

For clarity, let us here underline the qualitative difference of intercell and intracell variations regarding their influence on the constructed flat bands. The intercell couplings used in walk multiplet interconnections in the unit cell [the $h_{\mathbb{X}\mathbb{Y}}^\ell$ in Eq. (13) for each interconnected multiplet pair \mathbb{X}, \mathbb{Y}] can be varied at will leaving the flat bands intact in energy. In contrast, the intracell couplings must first be parametrized into groups of common values, as described above, whose variation then retains the occurrence of the flat bands but may generally alter their energy position. Combined, those inter- and intracell coupling variations constitute a flexible way to design the overall band structure featuring flat bands induced by latent symmetry.

D. Flat bands via walk singlet augmentation

Another variation of using the graph modifications in Sec. III A for flat band construction is to first modify a latently symmetric graph H itself, before interconnecting it into a lattice. In particular, using (M2) we can augment H by connecting new vertices to walk multiplets relative to a cospectral pair $\{u, v\}$. In the resulting graph H' , each such new vertex c' will be a walk singlet, which will in turn have vanishing amplitude in any nondegenerate eigenvector with odd parity on $\{u, v\}$; see Eq. (9). This “singlet augmentation” may be used, e.g., to bring a given unit cell into a more preferable shape for connection into a lattice.

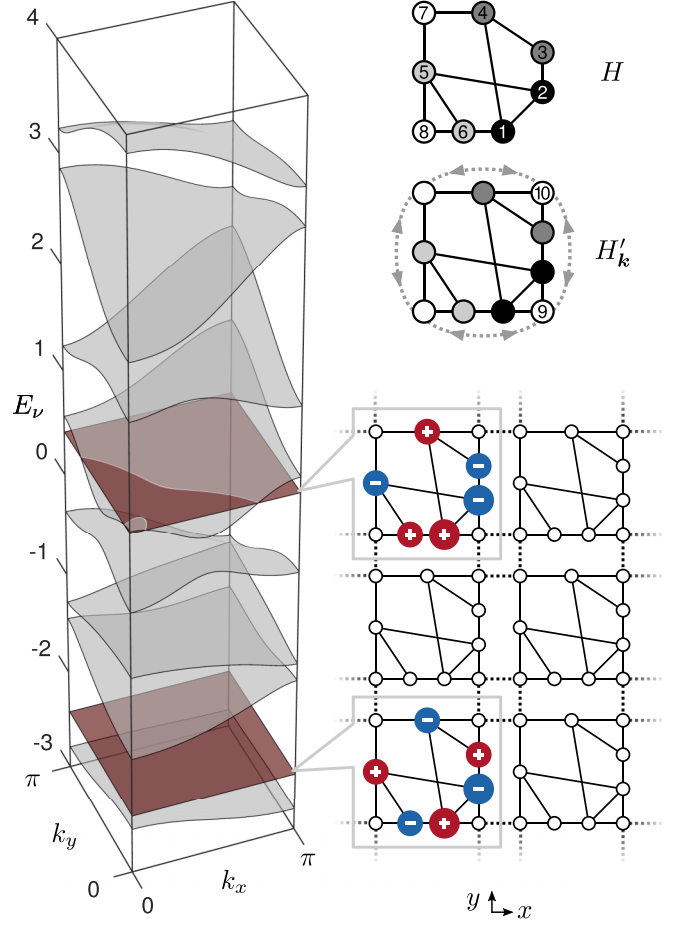


FIG. 8. Band structure (left) of a 2D lattice (bottom right) constructed by repetition of an unweighted 8-vertex graph H (with unit intracell couplings) augmented by two vertices 9 and 10 connected to the graph’s cospectral pair $\{1, 2\}$ and the walk doublet $\{3, 4\}$, respectively (top right), with dotted double-headed edges indicating complex couplings $he^{\pm ik_x(y)L}$ in $\pm x(y)$ direction in the Bloch Hamiltonian H'_k (see text). Intercell edges with unit weight $h = 1$ (dotted lines) connect the walk singlets $\{7, 8, 9, 10\}$ of the graph in x and y direction, preserving its two CLSs (depicted in the lattice; colormap as in Fig. 5) which correspond to two flat bands at $E = \pm\sqrt{2} - 1$.

We demonstrate this procedure by constructing a 2D flat band lattice in Fig. 8. The original 8-vertex graph H (upper right of figure) has four doublets relative to the cospectral pair $\{u, v\} = \{1, 2\}$, with one of them further consisting of the two singlets $\{7\}, \{8\}$. The graph has two eigenvectors with odd $\{u, v\}$ parity which vanish on those singlets. Note that, like the graph in Fig. 2, this one can also be parametrized in its edge weights while keeping its latent symmetry and corresponding compact eigenvectors, as we will see below. For simplicity we first keep its unweighted version. We now connect two new vertices 9 and 10 to two doublets using modification (M2), which thus yields two more singlets on which the previous compact eigenvectors also vanish. Then we connect the new graph H' into a 2D lattice—similarly to the procedure in Sec. III B—via its four corner singlet vertices, as shown, described by the corresponding Bloch Hamiltonian H'_k . The resulting band structure $E_\nu(\mathbf{k})$ features

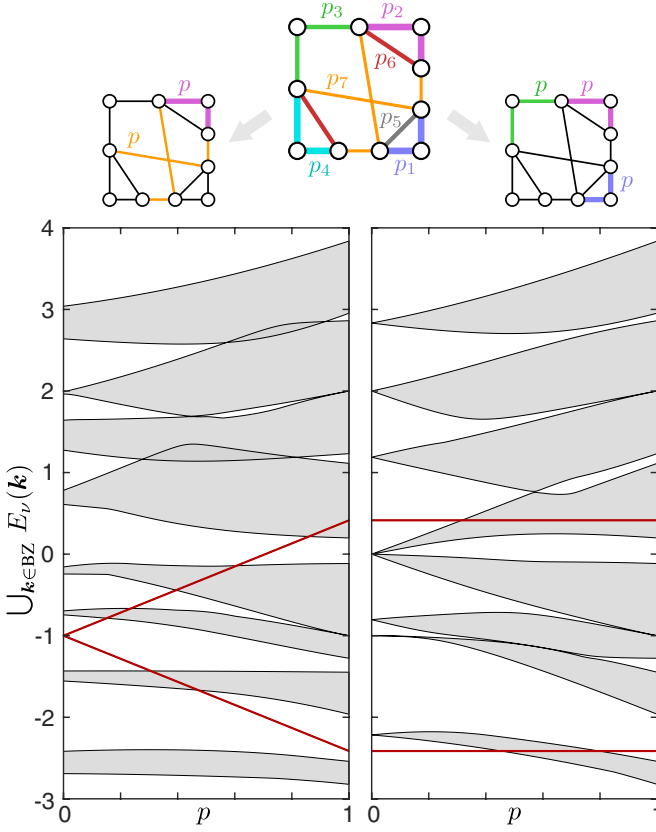


FIG. 9. Band edges and projections as in Fig. 7 but for the 2D bands of the lattice in Fig. 8 for varying parameter p in two different cases of the edge weight parametrization as shown at the top; $p = 1$ corresponds to the band structure in Fig. 8.

two flat bands at $E = \pm\sqrt{2} - 1$, with the corresponding CLSs depicted in two unit cells of the lattice.

We emphasize that the CLSs are induced by the latent symmetry of the site pair $\{1, 2\}$, and not by a permutation symmetry of the lattice cell. Specifically, the cell is indeed reflection symmetric about one diagonal (the line passing through sites 7 and 9), and the CLSs are odd under this reflection with nodes on this diagonal, as expected (recall discussion on permutation symmetry Π in Sec. III B). This symmetry does not explain, however, the other two CLS nodes at sites 8 and 10. Each of those are instead fixed under the latent symmetry operation Q (see Appendix A) induced by the cospectrality between u, v . In fact, a general weight parametrization preserving the walk multiplet structure violates the cell's reflection symmetry, though retains the compactness of the CLSs, that is, their nodes on the singlet sites, and the corresponding flat bands.

The latter is demonstrated in Fig. 9, where a cospectrality- and multiplet-preserving parametrization of the edge weights by real parameters $p_{i=1,2,\dots,7}$ is considered (top panel). Parametrization of the on-site elements, or loops, is also possible but not shown for simplicity. The band edge evolution for two parametrical variations is plotted. In the first case (left plot) we set $p_2 = p_7 = p$ (other intracell hoppings to unity) and vary p , whereby the flat bands (red lines) are preserved with linearly varying energy. In the second case (right

plot) we set $p_1 = p_2 = p_3 = p$ (other intracell hoppings again equal unity), whose variation modifies the dispersive bands but leaves the flat band energies fixed. We thus see that such parametrizations of the unit cell Hamiltonian preserving its latent symmetry, together with the chosen intercell couplings (whose variation, not shown here, evidently also preserves the latent symmetry), can be used to tune the induced flat bands flexibly in relation to the surrounding band structure.

Finally, we note that in this example we interconnected the unit cells via their corner walk singlets for simplicity. One could instead, or additionally, interconnect larger multiplets between the cells, still preserving the same CLSs and concomitant flat bands—though generally changing the dispersive bands. For example, the walk doublet $\{3, 4\}$ (see Fig. 8) of the cell at each ℓ could be connected diagonally in the lattice to the doublet $\{5, 6\}$ of the cell at $\ell + L\hat{x} + L\hat{y}$.

IV. DISCUSSION

Having demonstrated how latent symmetry, in combination with walk multiplets, may be employed to induce flat bands, let us now discuss some aspects and extensions of the presented framework.

A. Number and spatial extension of CLSs

In each of the above examples, Figs. 5 and 8, there were two CLSs per unit cell associated with a cospectral site pair $\{u, v\}$ in H . The number of such CLSs depends on the structure of the graph used as a cell. Specifically, the number of eigenstates of H with odd $\{u, v\}$ parity is given by the dimension of the Krylov subspace generated by the vector $|\rightarrow\rangle \equiv |u\rangle - |v\rangle$ [65], that is, the rank of the corresponding Krylov matrix $[|\rightarrow\rangle, H|\rightarrow\rangle, H^2|\rightarrow\rangle, \dots, H^{N-1}|\rightarrow\rangle]$. Also, there may be more than one cospectral pair in the graph H , each of which may induce different CLSs in a corresponding multiplet-interconnected lattice. Of course such latently symmetric cospectral pairs may further coexist with cospectral pairs corresponding to permutation symmetries swapping only two vertices u, v . Clearly for such pairs *all* other sites in H are walk singlets, with corresponding CLSs confined to $\{u, v\}$ in each lattice cell. In the examples shown here, we have chosen cell graphs having only latent symmetries for clarity.

Note, further, that in the above flat band construction scheme (see Sec. III B) we have explicitly considered the original graph H (or some augmented one, see Sec. III D) as the unit cell of the generated lattice H^\sharp . The induced CLSs then occupy $U = 1$ unit cell each, using the number of occupied unit cells U as a flat band classifier [31] (recently generalized accordingly for lattice dimensions $d > 1$ [69]). One could in principle, however, start with a supercell H' of a target lattice H^\sharp , consisting of $U > 1$ interconnected copies of H , and look for new cospectral pairs $\{u', v'\}$ which are not cospectral in H . Then, CLSs induced by $\{u', v'\}$ -odd eigenstates of H' will generally occupy $U > 1$ primitive unit cells within the supercell. The key challenge here would be to design inter- H connections which coincide with walk multiplet interconnections between supercells H' . We leave this endeavor for future work.

B. Generalizations of walk multiplets

The concept of walk multiplets can be generalized [62] by replacing the indicator vector of \mathbb{M} in Eq. (5) with a nonuniform version $|e_{\mathbb{M}}^{\gamma}\rangle$, with a tuple γ of generally different amplitudes

$$\gamma_m = \langle m | e_{\mathbb{M}}^{\gamma} \rangle \quad (15)$$

for $m \in \mathbb{M}$ and 0 otherwise. $\gamma_m = 1$, up to a global factor, corresponds to the uniform walk multiplets considered so far. If a new vertex c' is connected to \mathbb{M} via those weights γ_m , then the associated cospectrality is preserved and c becomes a walk singlet if Eq. (7) is fulfilled—now with the walk matrix generated by $|e_{\mathbb{M}}^{\gamma}\rangle$. In other words, the modification (M2) of Sec. III A is generalized to such nonuniform walk multiplets, as is, similarly, the multiplet-interconnection (M3); see Appendix B. A particular case is that of *overlapping* uniform multiplets \mathbb{M}_{μ} ($\mu = 1, 2, \dots$), whose union yields a nonuniform multiplet with indicator vector $|e_{\mathbb{M}}^{\gamma}\rangle = \sum_{\mu} |e_{\mathbb{M}_{\mu}}\rangle$, where $|e_{\mathbb{M}_{\mu}}\rangle$ is the usual indicator vector of multiplet \mathbb{M}_{μ} . An example is schematically shown as overlapping multiplets \mathbb{X} and \mathbb{Y} in Fig. 3.

Another variation is to consider walk *antieuivalence* by replacing Eq. (7) with $[W_{\mathbb{M}}]_{u*} = -[W_{\mathbb{M}}]_{v*}$. In this case, \mathbb{M} is a walk *antimultiplet* relative to $\{u, v\}$ and the role of parity is swapped: Now the eigenvectors $|\varphi_v^+\rangle$ with *even* parity on $\{u, v\}$ become CLSs, with vanishing amplitudes on anti-singlets [62]. These generalizations of the concept of walk multiplets offer an even larger flexibility in generating flat band lattices from graphs with latent symmetries.

C. Occurrence and construction of latently symmetric graphs

In all of the above we have assumed that the original graph H is latently exchange symmetric, that is, features some pair of vertices u and v which are cospectral but not exchange symmetric in H . We also assumed the given graph to feature some walk multiplets relative to $\{u, v\}$. The aim was to show how these properties, when given, can be used instead of common symmetries—that is, permutation operations commuting with H —to induce CLSs and corresponding flat bands for periodic lattice structures.

The systematic construction of latently symmetric graphs is far from trivial. To date, and to the best of our knowledge, there is indeed no general procedure for constructing undirected, latently symmetric graphs; it is rather a subject of ongoing research. One approach is based on “unpacking” the isospectrally reduced form of a graph [42], by applying partial fraction decomposition to its functional dependence on the eigenvalue E , and then accordingly constructing a generally directed graph with complex weights. Another recent, semiempirical approach [70], starts from a graph with trivially cospectral vertices—that is, induced by some permutation symmetry—which is then modified by adding vertices and edges such that the permutation symmetry is broken while the cospectrality is not.

In fact, the defining property of vertex cospectrality, Eq. (2) evaluated up to $r = N - 1$, makes it straightforward to resort to numerical iteration for verifying it. In this spirit, Ref. [70] reports on the occurrence of latently symmetric graphs out of all possible unweighted graphs of given small

size. Specifically, we have created a database of all unweighted graphs (adjacency matrices) of size up to $N = 11$ which have at least one cospectral vertex pair and *no* permutation symmetry. For $N \leq 7$ there is no such graph. For $N = 8, 9, 10, 11$ there are 78, 2 247, 78 489, 3 714 397 such graphs, respectively. Although this is, in each case, a small portion ($\approx 7.0, 8.6, 10.0, 4.7\%$) of all possible graphs, the analysis shows that there is a substantial number of latently symmetric unweighted graphs even for such small sizes. This means that latent symmetry would in principle not be hard to design in a targeted setup, consulting, e.g., the above database.

For larger graphs ($N \gg 1$) there is numerical evidence that the occurrence of latent symmetries is correlated to that of common permutation symmetries, in the sense that their percentage has been found to follow the same trend when varying a structural parameter for a class of randomly generated graphs, as stated in Ref. [52]. The exact reason for this behavior is an open question.

In the same manner as cospectral vertices, we identify walk multiplets relative to a cospectral pair $\{u, v\}$ of a given graph by scanning through all vertex subsets of all possible sizes for those that fulfill Eq. (7). For the graphs available in the above database, we have observed that, typically, the graphs have multiple walk multiplets [relative to the featured cospectral pair(s)] for each multiplet size—although there are, e.g., cases where walk singlets are absent—with the number of multiplets typically increasing with their size. Also, there is always at least one walk doublet, namely the cospectral pair itself. The walk multiplet structure is further enriched by considering their generalized version (nonuniform and antimultiplets, see Sec. IV B above), as described in detail in Ref. [62]. The relation of general walk multiplets to the structure of eigenvectors of graphs with cospectral vertices is an interesting topic to be pursued.

V. CONCLUSIONS

We have shown how flat bands can be induced by *latent symmetry* between a pair of sites in the unit cells of discrete lattices. This symmetry is revealed as an exchange permutation symmetry of the effective Hamiltonian upon reduction of the cell over the site pair subsystem, and imposes odd or even local parity of the original Hamiltonian eigenstates on those two sites. Using recent concepts and tools from graph theory, where latent symmetry takes the form of *cospectrality* between two vertices, we propose a framework for generating flat bands from the structural properties of graphs lacking permutation symmetries. The key ingredient is the occurrence of *walk equivalence* of cospectral vertices relative to vertex subsets called *walk multiplets*. This signifies a collective symmetry between possible walks along the edges of a graph from its cospectral vertices to a given walk multiplet, expressed in terms of corresponding *walk matrices*. Crucially, the amplitude sum on walk multiplets vanishes for any nondegenerate eigenvector with odd parity on cospectral vertices.

When connecting the graph as a unit cell into a lattice via its walk multiplets, those eigenvectors constitute compact localized states (CLSs) forming flat bands within an otherwise dispersive band structure. We illustrate the scheme for 1D and 2D lattices using simple graphs with cospectral sites. A

generalization to more complex cell geometries, possibly with multiple latent symmetries, and to higher-dimensional lattices is straightforward. As we demonstrate, the latent symmetry persists over flexible parametrizations of the lattice Hamiltonian elements, making the induced flat bands systematically tunable. This should allow for a feasible generation of flat bands from latent symmetries in various realization platforms such as, e.g., photonic waveguide arrays or electric circuit networks, with tailored intersite connections. We thus offer a fundamental insight into a class of CLSs originating from hidden Hamiltonian symmetries, which may also provide a valuable tool in designing flat band setups.

ACKNOWLEDGMENTS

We thank Jens Kwasniok for helpful discussions regarding Q matrices and walk multiplets. Funding by the Deutsche Forschungsgemeinschaft under Grant DFG Schm 885/29-1 is gratefully acknowledged. M.P. is thankful to the ‘‘Studienstiftung des deutschen Volkes’’ for financial support in the framework of a scholarship.

APPENDIX A: COSPECTRALITY FROM WALK MATRICES AND ORTHOGONAL SYMMETRY

Here we give a brief account on the orthogonal symmetry matrix Q describing vertex cospectrality. The purpose is to provide an insightful connection between the latent symmetry of a graph, upon reduction over two cospectral vertices, and the underlying symmetry operation exchanging those vertices in the original graph. The description is adapted from Ref. [58] to a graph with N vertices \mathbb{H} and symmetric weighted adjacency matrix H .

First, consider two arbitrary subsets $\mathbb{U}, \mathbb{V} \subseteq \mathbb{H}$ with walk matrices

$$W_{\mathbb{X}} = [|e_{\mathbb{X}}\rangle, H|e_{\mathbb{X}}\rangle, \dots, H^{N-1}|e_{\mathbb{X}}\rangle] \quad (\text{A1})$$

for the indicator vectors $|e_{\mathbb{X}}\rangle$, $\mathbb{X} = \mathbb{U}, \mathbb{V}$. If $W_{\mathbb{V}}$ is invertible (that is, has full rank N), then the matrix

$$Q_{\mathbb{U}\mathbb{V}} = W_{\mathbb{U}}W_{\mathbb{V}}^{-1} \quad (\text{A2})$$

commutes with H , thus representing a general symmetry transformation. To see this, recall that

$$H^N = \sum_{r=0}^{N-1} c_r H^r \quad (\text{A3})$$

by the Cayley-Hamilton theorem which states that H fulfills its own characteristic equation $\chi(x) = \sum_{r=0}^N a_r x^r = 0$, where $c_r = -a_r/a_N$. Therefore, we have that

$$HW_{\mathbb{X}} = W_{\mathbb{X}}C, \quad \mathbb{X} = \mathbb{U}, \mathbb{V}, \quad (\text{A4})$$

where

$$C = \begin{bmatrix} 0 & 0 & \dots & 0 & c_0 \\ 1 & 0 & \dots & 0 & c_1 \\ 0 & 1 & \dots & 0 & c_2 \\ \vdots & \vdots & \ddots & \vdots & \vdots \\ 0 & 0 & \dots & 1 & c_{N-1} \end{bmatrix} \quad (\text{A5})$$

is the companion matrix [60] for H . Thus,

$$\begin{aligned} HQ_{\mathbb{U}\mathbb{V}} &= W_{\mathbb{U}}CW_{\mathbb{V}}^{-1} \\ &= W_{\mathbb{U}}(W_{\mathbb{V}}^{-1}HW_{\mathbb{V}})W_{\mathbb{V}}^{-1} = Q_{\mathbb{U}\mathbb{V}}H. \end{aligned} \quad (\text{A6})$$

Furthermore, if both $W_{\mathbb{U}}$ and $W_{\mathbb{V}}$ are invertible and fulfill

$$W_{\mathbb{U}}^{\top}W_{\mathbb{U}} = W_{\mathbb{V}}^{\top}W_{\mathbb{V}}, \quad (\text{A7})$$

then $Q_{\mathbb{U}\mathbb{V}}$ is orthogonal:

$$\begin{aligned} Q_{\mathbb{U}\mathbb{V}}^{\top} &= [W_{\mathbb{V}}^{-1}]^{\top}W_{\mathbb{U}}^{\top} \\ &= [W_{\mathbb{V}}^{-1}]^{\top}W_{\mathbb{V}}^{\top}W_{\mathbb{V}}W_{\mathbb{U}}^{-1} = W_{\mathbb{V}}W_{\mathbb{U}}^{-1} = Q_{\mathbb{U}\mathbb{V}}^{-1}. \end{aligned} \quad (\text{A8})$$

With invertible $W_{\mathbb{X}}$ ($\mathbb{X} = \mathbb{U}$ or \mathbb{V}), H has simple eigenvalues [58] E_v (no degeneracies) and then, because $Q_{\mathbb{U}\mathbb{V}}$ commutes with H , it is a polynomial in H . Thus, if H is symmetric, so is $Q_{\mathbb{U}\mathbb{V}}$, and since it is also orthogonal, we obtain that

$$Q_{\mathbb{U}\mathbb{V}} = Q_{\mathbb{U}\mathbb{V}}^{\top} = Q_{\mathbb{U}\mathbb{V}}^{-1}. \quad (\text{A9})$$

Now, if $\mathbb{U} = \{u\}$ and $\mathbb{V} = \{v\}$ constitute two cospectral vertices, we have [54]

$$W_u^{\top}W_u = W_v^{\top}W_v. \quad (\text{A10})$$

Then, if both W_u and W_v are invertible, Eq. (A9) holds for $Q_{\{u\},\{v\}} \equiv Q$ of the main text, that is, $Q^2 = Q^{\top}Q = I$. In particular, since $QW_v = W_u$ and $QH = HQ$, we have that $Q|v\rangle = |u\rangle$ and $Q|u\rangle = |v\rangle$. Thus, being also orthogonal, Q is block diagonal with one block being the antidiagonal matrix

$$J_{\mathbb{S}} = \begin{bmatrix} 0 & 1 \\ 1 & 0 \end{bmatrix} \quad (\text{A11})$$

swapping u and v in $\mathbb{S} = \{u, v\}$.

Furthermore, for a walk multiplet \mathbb{M} the condition $[W_{\mathbb{M}}]_{u*} = [W_{\mathbb{M}}]_{v*}$ [Eq. (7)] yields $\langle u|H^r|e_{\mathbb{M}}\rangle = \langle v|H^r|e_{\mathbb{M}}\rangle = \langle v|H^rQ^{\top}Q|e_{\mathbb{M}}\rangle = \langle u|H^rQ|e_{\mathbb{M}}\rangle$ for $r = 0, \dots, N-1$, where we used $H = H^{\top}$, $QH = HQ$, and $Q|v\rangle = |u\rangle$. Since W_u has full rank, the N columns $H^r|u\rangle$ span an N -dimensional column space, meaning that $Q|e_{\mathbb{M}}\rangle = |e_{\mathbb{M}}\rangle$ (both vectors have equal projections in all N dimensions). Thus, if H has a vertex subset \mathbb{F} consisting of walk singlets, then $[W_s]_{u*} = [W_s]_{v*} \forall s \in \mathbb{F}$, so another block of Q is the $|\mathbb{F}| \times |\mathbb{F}|$ unit matrix $I_{\mathbb{F}}$ leaving the singlet vertices fixed (causing the odd- $\{u, v\}$ -parity eigenvectors to vanish on them).

The remaining orthogonal block $Q_{\mathbb{O}}$ operates on the remaining vertices within $\mathbb{O} = \mathbb{H} \setminus (\mathbb{S} \cup \mathbb{F})$, transforming the corresponding rows of W_v into those of W_u : $[W_u]_{\mathbb{O},*} = Q_{\mathbb{O}}[W_v]_{\mathbb{O},*}$. With vertices labeled accordingly, Q thus has the form

$$Q = J_{\mathbb{S}} \oplus I_{\mathbb{F}} \oplus Q_{\mathbb{O}}. \quad (\text{A12})$$

As an example, for the graph of Fig. 1 the $|\mathbb{O}| \times |\mathbb{O}|$ block is given by $Q_{\mathbb{O}} = \frac{1}{2} \begin{bmatrix} A & B \\ B & A \end{bmatrix}$, with $A = \begin{bmatrix} 1 & 1 \\ 1 & 1 \end{bmatrix}$ and $B = \begin{bmatrix} -1 & 1 \\ 1 & -1 \end{bmatrix}$, where $\mathbb{O} = \{3, 4, 5, 6\}$.

Notice here that, since Q commutes with H , its eigenvector matrix block-diagonalizes H accordingly under similarity transformation. Such a transformation can be seen as reminiscent of the ‘‘Fano detangling’’ procedure of Ref. [32], though here for a cospectral site pair $\{u, v\}$ (instead of a single site) and determined from the walk structure of H .

If the spectrum of H is degenerate or has any eigenvector with vanishing amplitudes on $\{u, v\}$, then W_u and W_v do not have full rank [54,59] and are thus not invertible. Hence, although a Q matrix still exists, which is unique under the convention of treating eigenvectors vanishing on $\{u, v\}$ as $\{u, v\}$ -even [54], it cannot be obtained directly from Eq. (A2) [71].

Alternatively, the following expression can be used for a Q matrix (obeying, $Q^2 = Q^\top Q = I$ and $Q|u\rangle = |v\rangle$) [41]:

$$Q = P_+ - P_- = I - 2P_-, \quad (\text{A13})$$

where $P_\pm = \sum_v |\varphi_v^\pm\rangle\langle\varphi_v^\pm|$ is the projector onto eigenvectors with \pm parity on $\{u, v\}$ (P_+ also including eigenvectors vanishing on $\{u, v\}$), chosen in case of degeneracy such that there is at most one eigenvector of each parity nonvanishing on $\{u, v\}$ for any given eigenvalue. This expression is not directly derived from the structure of the graph (specifically, its walk matrices W_u, W_v) but rather invokes the spectral properties of H —that is, one first needs to find its eigenvectors.

APPENDIX B: GENERAL COSPECTRALITY-PRESERVING GRAPH EXTENSIONS AND INTRACONNECTIONS

We show here that the cospectrality of a pair $\{u, v\}$ and the walk multiplets relative to it are preserved by the modifications (M1), (M2), and (M3) listed in Sec. III A. Like in Ref. [62], the modifications are now stated in a more general form for nonuniform walk multiplets with weighted indicator vector $|e_{\mathbb{M}}^\nu\rangle$ (see Sec. IV).

For an original weighted adjacency matrix of a graph H , the modified one H' will have the form of a sum

$$H' = A + B, \quad (\text{B1})$$

with

$$A = H \oplus G \quad (\text{B2})$$

generally being a block-diagonal matrix (including the case of absent or 0×0 block G) and

$$B = |b_1\rangle\langle b_2| + |b_2\rangle\langle b_1| \quad (\text{B3})$$

being a symmetric sum of rank-one coupling matrices. Setting the $|b_{1,2}\rangle$ to be site subset indicator vectors below, B will express the interconnection of those subsets in the modified graph H' .

The powers of H' , appearing in the corresponding modified walk matrices $W'_{\mathbb{M}}$, are given by

$$[A + B]^r = \sum_{p=0}^r \sum_{\pi(A,B)} \{A^{r-p} B^p\}, \quad (\text{B4})$$

where $\sum_{\pi(A,B)} \{A^{r-p} B^p\}$ denotes the sum of all distinct permutations of A 's and B 's in matrix products with $r-p$ A 's and p B 's; for instance, $AAB + ABA + BAA$ for $r=3, p=1$. H'^r is thus generally a weighted sum of products of the matrices $H^{r-p} \oplus G^{r-p}$, $[|b_1\rangle\langle b_1|]^{n_1}$, $[|b_2\rangle\langle b_2|]^{n_2}$, $[|b_1\rangle\langle b_2|]^{n_3}$, $[|b_2\rangle\langle b_1|]^{n_4}$ with $p \in \{0, 1, \dots, r\}$ and $n_i \in \{0, 1, \dots, p\}$.

In the following we briefly prove preservation of cospectrality and walk multiplets under modifications (M1), (M2), (M3), which are depicted schematically in Fig. 3.

1. Singlet extension (M1)

For a singlet c ($\neq u, v$) of H connected symmetrically—i.e., so that H' is symmetric—to an arbitrary graph G with vertices \mathbb{G} , we have $|b_1\rangle = |c\rangle$, which is the indicator vector of c in H' , and $|b_2\rangle = |e_{\mathbb{G}}^\nu\rangle$, which is the arbitrarily weighted indicator vector of \mathbb{G} , in Eq. (B3).

From Eqs. (B1) and (B4), elements $[H'^r]_{uu} = \langle u|H'^r|u\rangle$ thus only have contributions involving $|u\rangle$ in factors $[H^q]_{uu}$ and $[H^q]_{uc}, [H^q]_{cu}$ for different powers q . For instance, with $\langle c|e_{\mathbb{G}}^\nu\rangle = 0$, we have $A^2 B^2 A = A^2 (\langle e_{\mathbb{G}}^\nu | e_{\mathbb{G}}^\nu \rangle |c\rangle\langle c| + |e_{\mathbb{G}}^\nu\rangle\langle e_{\mathbb{G}}^\nu|) A$, whose uu element becomes $[A^2 B^2 A]_{uu} = [H^2]_{uc} \langle e_{\mathbb{G}}^\nu | e_{\mathbb{G}}^\nu \rangle H_{cu}$.

Since $\{u, v\}$ are cospectral in H and c is a walk singlet, those factors $[H^q]_{uu}, [H^q]_{uc}, [H^q]_{cu}$ remain equal under the replacement $u \rightarrow v$, as do, trivially, factors not containing the index u . This yields $[H'^r]_{uu} = [H'^r]_{vv}$, so $\{u, v\}$ remain cospectral in H' .

Similarly, walk matrix elements $[W'_{\mathbb{M}}]_{ur}$ for any walk multiplet \mathbb{M} of H only have contributions involving $|u\rangle$ in factors $[W_{\mathbb{M}}]_{uq}$ and $[H^q]_{uc}$. Thus, since $[W_{\mathbb{M}}]_{uq} = [W_{\mathbb{M}}]_{vq}$ (\mathbb{M} walk multiplet in H) and $[H^q]_{uc} = [H^q]_{vc}$ (c walk singlet in H), we have $[W'_{\mathbb{M}}]_{u*} = [W'_{\mathbb{M}}]_{v*}$, that is, \mathbb{M} is a walk multiplet also in H' .

2. Multiplet extension (M2)

For a walk multiplet \mathbb{M} of H connected symmetrically to a single vertex c' of an arbitrary graph G , we have $|b_1\rangle = |c'\rangle$, which is the indicator vector of c' in H' , and $|b_2\rangle = |e_{\mathbb{M}}\rangle$ in Eq. (B3). With similar arguments as in Appendix B 1 above, again we get $[H'^r]_{uu} = [H'^r]_{vv}$ and $[W'_{\mathbb{X}}]_{u*} = [W'_{\mathbb{X}}]_{v*}$ for any walk multiplet \mathbb{X} of H .

3. Multiplet interconnection (M3)

If two disjoint walk multiplets \mathbb{X} and \mathbb{Y} of H are symmetrically and fully interconnected—that is, each vertex of one is connected to all of the other, with weights added to any already existing connection—we have $A = H$ in Eq. (B2), with G now being absent, and $|b_1\rangle = |e_{\mathbb{X}}\rangle, |b_2\rangle = |e_{\mathbb{Y}}\rangle$ in Eq. (B3). With similar arguments as in Appendix B 1, cospectrality of the pair $\{u, v\}$ and any walk multiplet \mathbb{M} relative to it are preserved in H' . Using the same form of the interconnection matrix B , this also holds if \mathbb{X} and \mathbb{Y} overlap, that is, have common vertices.

APPENDIX C: SYMMETRY VERSUS HERMITICITY

In this Appendix we briefly comment on the relation between vertex cospectrality and latent symmetry when considering a complex Hermitian—as opposed to a real symmetric—Hamiltonian H . Note that, for complex Hermitian H , the cospectrality condition for a pair $\{u, v\}$ in terms of walk matrices, Eq. (A10), is replaced with

$$W_u^\dagger W_u = W_v^\dagger W_v, \quad (\text{C1})$$

with $(\)^\dagger = (\)^{\top*}$ denoting Hermitian conjugation.

It was recently shown [42] that cospectrality of a vertex pair $\{u, v\}$ of a graph H is equivalent to latent symmetry between u and v —that is, the 2×2 reduction $\tilde{H}_{\{u,v\}}$ of

H is bisymmetric—if H is symmetric, that is, its graph is undirected. Therefore, to relate vertex cospectrality to latent symmetry, we have assumed a symmetric unit cell Hamiltonian matrix H , which was also chosen real to generally possess a real eigenvalue spectrum.

Nevertheless, if H is modified into a Bloch Hamiltonian H_k exclusively by interconnecting walk multiplets with self-adjoint complex weights (a special case of a directed graph; see H_k in Fig. 4 with each dotted line indicating complex conjugate weights $he^{\pm ik \cdot \ell}$ in either direction), then vertex pair cospectrality does imply corresponding latent symmetry, and vice versa. Indeed, the multiplet interconnection in Appendix B above remains valid in the same form (with $\langle x | = |x \rangle^\dagger$ and “symmetric” replaced by “self-adjoint”) for walk multiplets with indicator vector $|e_{\mathbb{M}}^\gamma\rangle$ weighted by a complex tuple γ [see Eq. (15)]. For instance, in H_k in Fig. 4 the singlet $\{8\}$ is connected with complex weight $\gamma_8 = he^{ikL} = [H_k]_{8m} = [H_k]_{m8}^*$ ($m = 1, 2$) to the doublet $\{1, 2\}$ and the singlet $\{7\}$ is connected with complex weight $\gamma_7 = he^{-ikL} = [H_k]_{7m} = [H_k]_{m7}^*$ ($m = 3, 4$) to the doublet $\{3, 4\}$, for some real h .

Now, since such walk multiplet interconnections preserve $\{u, v\}$ -cospectrality and relative multiplets (as shown in Appendix B), in particular $\{u, v\}$ itself remains a walk doublet

in H_k :

$$[H_k^r]_{uu} + [H_k^r]_{uv} = [H_k^r]_{vv} + [H_k^r]_{vu} \quad (\text{C2})$$

for all powers $r \in \mathbb{N}$. As a consequence,

$$[H_k^r]_{uv} = [H_k^r]_{vu} \in \mathbb{R} \quad \forall r \in \mathbb{N}. \quad (\text{C3})$$

Thus, the restriction of each power H_k^r to the cospectral pair is bisymmetric, that is, commutes with the 2×2 exchange matrix $J_{\mathbb{S}=\{u,v\}}$, Eq. (A11).

As we showed very recently in Ref. [41], a necessary and sufficient condition for a latent symmetry transformation T upon reduction to a vertex subset \mathbb{S} is that all powers of H restricted to \mathbb{S} have the same symmetry:

$$T\tilde{H}_{\mathbb{S}} = \tilde{H}_{\mathbb{S}}T \iff T[H^r]_{\mathbb{S}} = [H^r]_{\mathbb{S}}T \quad \forall r \in \mathbb{N}. \quad (\text{C4})$$

In the present case $\mathbb{S} = \{u, v\}$ is a cospectral pair and $T = J_{\mathbb{S}}$, with $[H_k^r]_{\mathbb{S}}J_{\mathbb{S}} = J_{\mathbb{S}}[H_k^r]_{\mathbb{S}}$ implying $\tilde{H}_{k;\mathbb{S}}J_{\mathbb{S}} = J_{\mathbb{S}}\tilde{H}_{k;\mathbb{S}}$, meaning that H_k has a latent $J_{\mathbb{S}}$ symmetry in its reduction over $\{u, v\}$.

To summarize: For a general directed graph H , $\{u, v\}$ cospectrality is necessary but in general not sufficient for corresponding latent symmetry [42]; but for a complex self-adjoint H' (in our case the Bloch Hamiltonian H_k) constructed from an undirected H via Hermitian interconnection of walk multiplets relative to $\{u, v\}$, it is both necessary and sufficient.

-
- [1] D. Leykam, A. Andreanov, and S. Flach, Artificial flat band systems: From lattice models to experiments, *Adv. Phys.* **X 3**, 1473052 (2018).
- [2] D. Leykam and S. Flach, Perspective: Photonic flatbands, *APL Photonics* **3**, 070901 (2018).
- [3] S. Mukherjee, A. Spracklen, D. Choudhury, N. Goldman, P. Öhberg, E. Andersson, and R. R. Thomson, Observation of a Localized Flat-Band State in a Photonic Lieb Lattice, *Phys. Rev. Lett.* **114**, 245504 (2015).
- [4] R. A. Vicencio, C. Cantillano, L. Morales-Inostroza, B. Real, C. Mejía-Cortés, S. Weimann, A. Szameit, and M. I. Molina, Observation of Localized States in Lieb Photonic Lattices, *Phys. Rev. Lett.* **114**, 245503 (2015).
- [5] S. Taie, H. Ozawa, T. Ichinose, T. Nishio, S. Nakajima, and Y. Takahashi, Coherent driving and freezing of bosonic matter wave in an optical Lieb lattice, *Sci. Adv.* **1**, e1500854 (2015).
- [6] V. Apaja, M. Hyrkäs, and M. Manninen, Flat bands, Dirac cones, and atom dynamics in an optical lattice, *Phys. Rev. A* **82**, 041402(R) (2010).
- [7] C. C. Abilio, P. Butaud, T. Fournier, B. Pannetier, J. Vidal, S. Tedesco, and B. Dalzotto, Magnetic Field Induced Localization in a Two-Dimensional Superconducting Wire Network, *Phys. Rev. Lett.* **83**, 5102 (1999).
- [8] R. Drost, T. Ojanen, A. Harju, and P. Liljeroth, Topological states in engineered atomic lattices, *Nat. Phys.* **13**, 668 (2017).
- [9] L.-L. Wan, X.-Y. Lü, J.-H. Gao, and Y. Wu, Hybrid interference induced flat band localization in bipartite optomechanical lattices, *Sci. Rep.* **7**, 15188 (2017).
- [10] T. Helbig, T. Hofmann, C. H. Lee, R. Thomale, S. Imhof, L. W. Molenkamp, and T. Kiessling, Band structure engineering and reconstruction in electric circuit networks, *Phys. Rev. B* **99**, 161114(R) (2019).
- [11] M. Röntgen, C. V. Morfonios, I. Brouzos, F. K. Diakonov, and P. Schmelcher, Quantum Network Transfer and Storage with Compact Localized States Induced by Local Symmetries, *Phys. Rev. Lett.* **123**, 080504 (2019).
- [12] S. Peotta and P. Törmä, Superfluidity in topologically nontrivial flat bands, *Nat. Commun.* **6**, 8944 (2015).
- [13] A. Julku, S. Peotta, T. I. Vanhala, D.-H. Kim, and P. Törmä, Geometric Origin of Superfluidity in the Lieb-Lattice Flat Band, *Phys. Rev. Lett.* **117**, 045303 (2016).
- [14] N. B. Kopnin, T. T. Heikkilä, and G. E. Volovik, High-temperature surface superconductivity in topological flat-band systems, *Phys. Rev. B* **83**, 220503(R) (2011).
- [15] V. I. Iglovikov, F. Hébert, B. Grémaud, G. G. Batrouni, and R. T. Scalettar, Superconducting transitions in flat-band systems, *Phys. Rev. B* **90**, 094506 (2014).
- [16] K. Kobayashi, M. Okumura, S. Yamada, M. Machida, and H. Aoki, Superconductivity in repulsively interacting fermions on a diamond chain: Flat-band-induced pairing, *Phys. Rev. B* **94**, 214501 (2016).
- [17] M. Tovmasyan, S. Peotta, P. Törmä, and S. D. Huber, Effective theory and emergent SU(2) symmetry in the flat bands of attractive Hubbard models, *Phys. Rev. B* **94**, 245149 (2016).
- [18] L. Liang, T. I. Vanhala, S. Peotta, T. Siro, A. Harju, and P. Törmä, Band geometry, Berry curvature, and superfluid weight, *Phys. Rev. B* **95**, 024515 (2017).
- [19] E. Tang, J.-W. Mei, and X.-G. Wen, High-Temperature Fractional Quantum Hall States, *Phys. Rev. Lett.* **106**, 236802 (2011).

- [20] K. Sun, Z. Gu, H. Katsura, and S. Das Sarma, Nearly Flatbands with Nontrivial Topology, *Phys. Rev. Lett.* **106**, 236803 (2011).
- [21] T. Neupert, L. Santos, C. Chamon, and C. Mudry, Fractional Quantum Hall States at Zero Magnetic Field, *Phys. Rev. Lett.* **106**, 236804 (2011).
- [22] B. Pal, Nontrivial topological flat bands in a diamond-octagon lattice geometry, *Phys. Rev. B* **98**, 245116 (2018).
- [23] A. Bhattacharya and B. Pal, Flat bands and nontrivial topological properties in an extended Lieb lattice, *Phys. Rev. B* **100**, 235145 (2019).
- [24] C. Danieli, A. Andreanov, and S. Flach, Many-body flatband localization, *Phys. Rev. B* **102**, 041116(R) (2020).
- [25] Y. Kuno, T. Orito, and I. Ichinose, Flat-band many-body localization and ergodicity breaking in the Creutz ladder, *New J. Phys.* **22**, 013032 (2020).
- [26] T. Orito, Y. Kuno, and I. Ichinose, Nonthermalized dynamics of flat-band many-body localization, *Phys. Rev. B* **103**, L060301 (2021).
- [27] C. Danieli, A. Andreanov, T. Mithun, and S. Flach, Nonlinear caging in all-bands-flat lattices, [arXiv:2004.11871](https://arxiv.org/abs/2004.11871).
- [28] C. Danieli, A. Andreanov, T. Mithun, and S. Flach, Quantum caging in interacting many-body all-bands-flat lattices, [arXiv:2004.11880](https://arxiv.org/abs/2004.11880).
- [29] Y. He, R. Mao, H. Cai, J.-X. Zhang, Y. Li, L. Yuan, S.-Y. Zhu, and D.-W. Wang, Flat-Band Localization in Creutz Superradiance Lattices, *Phys. Rev. Lett.* **126**, 103601 (2021).
- [30] J.-W. Rhim and B.-J. Yang, Classification of flat bands according to the band-crossing singularity of Bloch wave functions, *Phys. Rev. B* **99**, 045107 (2019).
- [31] W. Maimaiti, S. Flach, and A. Andreanov, Universal $d = 1$ flat band generator from compact localized states, *Phys. Rev. B* **99**, 125129 (2019).
- [32] S. Flach, D. Leykam, J. D. Bodyfelt, P. Matthies, and A. S. Desyatnikov, Detangling flat bands into Fano lattices, *Europhys. Lett.* **105**, 30001 (2014).
- [33] M. Röntgen, C. V. Morfonios, and P. Schmelcher, Compact localized states and flat bands from local symmetry partitioning, *Phys. Rev. B* **97**, 035161 (2018).
- [34] A. Ramachandran, A. Andreanov, and S. Flach, Chiral flat bands: Existence, engineering, and stability, *Phys. Rev. B* **96**, 161104(R) (2017).
- [35] L. Morales-Inostroza and R. A. Vicencio, Simple method to construct flat-band lattices, *Phys. Rev. A* **94**, 043831 (2016).
- [36] R. G. Dias and J. D. Gouveia, Origami rules for the construction of localized eigenstates of the Hubbard model in decorated lattices, *Sci. Rep.* **5**, 16852 (2015).
- [37] W. Maimaiti, A. Andreanov, H. C. Park, O. Gendelman, and S. Flach, Compact localized states and flat-band generators in one dimension, *Phys. Rev. B* **95**, 115135 (2017).
- [38] Y. Xu and H. Pu, Building flat-band lattice models from Gram matrices, *Phys. Rev. A* **102**, 053305 (2020).
- [39] C.-C. Lee, A. Fleurence, Y. Yamada-Takamura, and T. Ozaki, Hidden mechanism for embedding the flat bands of Lieb, kagome, and checkerboard lattices in other structures, *Phys. Rev. B* **100**, 045150 (2019).
- [40] D. Smith and B. Webb, Hidden symmetries in real and theoretical networks, *Physica A* **514**, 855 (2019).
- [41] M. Röntgen, M. Pyzh, C. V. Morfonios, N. E. PalaioDIMopoulos, F. K. Diakonos, and P. Schmelcher, Latent Symmetry Induced Degeneracies, *Phys. Rev. Lett.* **126**, 180601 (2021).
- [42] M. Kempton, J. Sinkovic, D. Smith, and B. Webb, Characterizing cospectral vertices via isospectral reduction, *Linear Algebra Appl.* **594**, 226 (2020).
- [43] S. Priyadarshy, S. S. Skourtis, S. M. Risser, and D. N. Beratan, Bridge-mediated electronic interactions: Differences between Hamiltonian and Green function partitioning in a non-orthogonal basis, *J. Chem. Phys.* **104**, 9473 (1996).
- [44] L. Jin and Z. Song, Partitioning technique for discrete quantum systems, *Phys. Rev. A* **83**, 062118 (2011).
- [45] G. Grosso and G. P. Parravicini, *Solid State Physics* (Academic, New York, 2013).
- [46] H. Feshbach, A unified theory of nuclear reactions. II, *Ann. Phys. (NY)* **19**, 287 (1962).
- [47] S. Datta, *Electronic Transport in Mesoscopic Systems* (Cambridge University Press, Cambridge, UK, 1995).
- [48] B. Pal, S. K. Maiti, and A. Chakrabarti, Complete absence of localization in a family of disordered lattices, *Europhys. Lett.* **102**, 17004 (2013).
- [49] B. Pal and A. Chakrabarti, Absolutely continuous energy bands in the electronic spectrum of quasiperiodic ladder networks, *Physica E* **60**, 188 (2014).
- [50] B. Pal and A. Chakrabarti, Engineering bands of extended electronic states in a class of topologically disordered and quasiperiodic lattices, *Phys. Lett. A* **378**, 2782 (2014).
- [51] P. Duarte and M. J. Torres, Eigenvectors of isospectral graph transformations, *Linear Algebra Appl.* **474**, 110 (2015).
- [52] L. Bunimovich, D. Smith, and B. Webb, Finding hidden structures, hierarchies, and cores in networks via isospectral reduction, *Appl. Math. Nonlinear Sci.* **4**, 231 (2019).
- [53] L. Bunimovich and B. Webb, *Isospectral Transformations: A New Approach to Analyzing Multidimensional Systems and Networks*, Springer Monographs in Mathematics (Springer, New York, 2014).
- [54] C. Godsil and J. Smith, Strongly cospectral vertices, [arXiv:1709.07975](https://arxiv.org/abs/1709.07975).
- [55] E. Estrada and P. A. Knight, *A First Course in Network Theory* (Oxford University Press, New York, 2015).
- [56] Y. Tsuji and E. Estrada, Influence of long-range interactions on quantum interference in molecular conduction. A tight-binding (Hückel) approach, *J. Chem. Phys.* **150**, 204123 (2019).
- [57] R. A. Brualdi and D. Cvetkovic, *A Combinatorial Approach to Matrix Theory and Its Applications* (Chapman and Hall/CRC, Boca Raton, 2008).
- [58] C. Godsil, Controllable subsets in graphs, *Ann. Comb.* **16**, 733 (2012).
- [59] F. Liu and J. Siemons, Unlocking the walk matrix of a graph, [arXiv:1911.00062](https://arxiv.org/abs/1911.00062).
- [60] C. D. Meyer, *Matrix Analysis and Applied Linear Algebra* (Society for Industrial and Applied Mathematics, Philadelphia, PA, 2000).
- [61] H. Xu, Functions of a matrix and Krylov matrices, *Linear Algebra Appl.* **434**, 185 (2011).
- [62] C. V. Morfonios, M. Pyzh, M. Röntgen, and P. Schmelcher, Cospectrality preserving graph modifications and eigenvector properties via walk equivalence of vertices, *Linear Algebra Appl.* **624**, 53 (2021).

- [63] We note that the occurrence of a walk equivalent pair relative to some \mathbb{M} necessarily renders $W_{\mathbb{M}}$ noninvertible by reducing its rank. Incidentally, this lifts the so-called “controllability” [58,72,73] of \mathbb{M} relative to H , and as a consequence allows for local permutation symmetries in H mapping \mathbb{M} to itself [58].
- [64] We find such parametrizations numerically by starting with the unweighted graph and then (i) setting one weight to a random value (representing an independent parameter) and scanning through the graph for edges which can be set to that same value while preserving cospectrality, and (ii) repeating successively for unaltered edges until all edges are parametrized.
- [65] O. Eisenberg, M. Kempton, and G. Lippner, Pretty good quantum state transfer in asymmetric graphs via potential, *Discrete Math.* **342**, 2821 (2019).
- [66] D. Vanderbilt, *Berry Phases in Electronic Structure Theory: Electric Polarization, Orbital Magnetization and Topological Insulators* (Cambridge University Press, Cambridge, 2018).
- [67] For clarity we note that the bands were computed by standard numerical matrix diagonalization of the Bloch Hamiltonian $H_{\mathbf{k}}$ (in varying \mathbf{k}) and not from the corresponding nonlinear eigenvalue problem $\tilde{H}_{\mathbb{S},\mathbf{k}}(E)|\varphi\rangle = E|\varphi\rangle$ of the reduced $H_{\mathbf{k}}$ by finding the roots of $\det[E - \tilde{H}_{\mathbb{S},\mathbf{k}}(E)] = 0$ (which, as mentioned in Sec. II, would generally yield a subset of the full eigenvalue spectrum).
- [68] Note that two sites u, v related by an involutory permutation symmetry Π are automatically cospectral, since $\langle u|H^r|u\rangle = \langle u|H^r\Pi^2|u\rangle = \langle u|\Pi H^r \Pi|u\rangle = \langle v|H^r|v\rangle \forall r$ [see Eq. (2)], and any site c fixed by Π is a walk singlet relative to $\{u, v\}$, since $\langle u|H^r|c\rangle = \langle u|H^r\Pi|c\rangle = \langle u|\Pi H^r|c\rangle = \langle v|H^r|c\rangle \forall r$.
- [69] W. Maimaiti, A. Andreanov, and S. Flach, Flat-band generator in two dimensions, *Phys. Rev. B* **103**, 165116 (2021).
- [70] M. Röntgen, N. E. Palaiodimopoulos, C. V. Morfonios, I. Brouzos, M. Pyzh, F. K. Diakonov, and P. Schmelcher, Designing pretty good state transfer via isospectral reductions, *Phys. Rev. A* **101**, 042304 (2020).
- [71] One may then attempt to apply the modification (M3) (see Sec. III A) to lift the degeneracy and to remove the $\{u, v\}$ -vanishing eigenstate(s), without altering the graph’s multiplet structure (the simplest modification being an added loop of arbitrary weight to any walk singlet relative to $\{u, v\}$). The Q matrix can then be obtained from (A2). However, rigorously showing that this Q is the same as for the unmodified graph requires a more general account on walk multiplets, to be given elsewhere.
- [72] A. Farrugia and I. Sciriha, Controllability of undirected graphs, *Linear Algebra Appl.* **454**, 138 (2014).
- [73] C. O. Aguilar and B. Ghahesifard, Graph controllability classes for the Laplacian leader-follower dynamics, *IEEE Trans. Autom. Contr.* **60**, 1611 (2015).

Latent Symmetry Induced Degeneracies

M. Röntgen¹, M. Pyzh¹, C. V. Morfonios¹, N. E. Palaiodimopoulos², F. K. Diakonou², and P. Schmelcher^{1,3}

¹Zentrum für optische Quantentechnologien, Universität Hamburg, Luruper Chaussee 149, 22761 Hamburg, Germany

²Department of Physics, University of Athens, 15771 Athens, Greece

³The Hamburg Centre for Ultrafast Imaging, Universität Hamburg, Luruper Chaussee 149, 22761 Hamburg, Germany



(Received 26 November 2020; revised 11 February 2021; accepted 31 March 2021; published 3 May 2021)

Degeneracies in the energy spectra of physical systems are commonly considered to be either of accidental character or induced by symmetries of the Hamiltonian. We develop an approach to explain degeneracies by tracing them back to symmetries of an isospectral effective Hamiltonian derived by subsystem partitioning. We provide an intuitive interpretation of such latent symmetries by relating them to corresponding local symmetries in the powers of the underlying Hamiltonian matrix. As an application, we relate the degeneracies induced by the rotation symmetry of a real Hamiltonian to a non-Abelian latent symmetry group. It is demonstrated that the rotational symmetries can be broken in a controlled manner while maintaining the underlying more fundamental latent symmetry. This opens up the perspective of investigating accidental degeneracies in terms of latent symmetries.

DOI: [10.1103/PhysRevLett.126.180601](https://doi.org/10.1103/PhysRevLett.126.180601)

Introduction.—Identifying the origin of spectral degeneracies in quantum systems is of fundamental importance for the understanding and control of their structural and dynamical properties. Degenerate states are at the heart of spectacular phenomena like the Jahn-Teller effect [1] and the quantum Hall effect [2,3] as well as the electromagnetic response of, e.g., atoms or molecules [4,5] in general. In lattice systems designed macroscopic degeneracies can realize flat bands within a variety of setups including optical lattices, photonic waveguide arrays, and superconducting networks [6]. Further, degeneracies in the form of conical intersections of molecular potential energy surfaces play a central role for ultrafast dynamical decay processes [7,8] and are responsible, e.g., for molecular self-repair mechanisms in photobiology [9].

When degeneracies occur in the energy spectrum, the first place to seek their origin is commonly the group of geometrical symmetry operations commuting with the underlying Hamiltonian. Prominent examples for such symmetries are the molecular point group in chemistry or the space group in crystallography. If this group is non-Abelian—that is, if at least two symmetry operations do not commute with each other—it induces degeneracies of multiplicities determined by the dimensions of the group's irreducible representations. More challenging is the reverse question of assigning degeneracies to a symmetry group with a physical significance [10,11]. A famous example of a physically significant, yet not obvious, symmetry from the early days of quantum theory is the $SO(4)$ symmetry leading to the conservation of the Runge-Lenz vector in the hydrogen atom [12]. If no such physically meaningful symmetry group can be found, the degeneracy is traditionally called accidental [13]. This often occurs for

systems with several or many degrees of freedom where eigenenergies happen to coincide at some location in the corresponding parameter space, intersections of molecular potential energy surfaces being a typical example [14].

In this work, we promote a different viewpoint on assigning degeneracies to symmetries of the system. Instead of performing a symmetry analysis of the Hamiltonian itself, we do this for the effective Hamiltonian obtained from the original one by reducing it onto a subsystem while retaining the energy spectrum. We note that its core property—the preservation of the energy spectrum—clearly distinguishes this approach from those which analyze the symmetries of an effective model obtained by truncation or a mean-field ansatz. Focusing on generic discrete models, we here show how geometrical symmetries of the isospectrally reduced Hamiltonian induce spectral degeneracies for the original system. Such latent symmetries, as introduced recently in graph theory [15], are generally not apparent in the original system at hand. In fact, as we show here, they are directly linked to corresponding local symmetries, though in all powers of the original Hamiltonian. Navigating through the proposed concepts, visualized by minimalistic examples, we (i) show how non-Abelian latent symmetries are necessarily induced by rotation symmetries of a real Hamiltonian, and (ii) demonstrate that these latent symmetries, along with their induced degeneracies, can be preserved even when breaking the original rotational symmetry. Lastly, we link a special case of latent symmetry to what we call here a generalized exchange symmetry of the Hamiltonian.

Degeneracies from latent symmetries.—The concepts and results developed in this work are valid for generic setups described by a finite-dimensional matrix. This matrix can be drawn from a wide range of physical

platforms: It could represent a Bloch Hamiltonian of a tight-binding lattice [16], a molecular Hückel Hamiltonian [17,18], a multiport scattering matrix [19], or very generally the matrix H occurring in (linearized) dynamical problems [20], such as coupled oscillators [21]. To convey the main ideas in a transparent way, we will illustrate it by means of minimalistic prototypical setups.

In order to reveal the latent symmetries of a general complex matrix H , we will rely on a dimensional reduction of H which preserves the eigenvalue spectrum. This *isospectral* reduction is defined as [15,22]

$$\mathcal{R}_S(H, \lambda) = H_{SS} - H_{S\bar{S}}(H_{\bar{S}\bar{S}} - \lambda I)^{-1}H_{\bar{S}S}, \quad (1)$$

whereby S is a set sites and \bar{S} denotes the complement set of all other sites of the given setup. H_{SS} and $H_{\bar{S}\bar{S}}$ denote the respective Hamiltonians of the sub-systems consisting only of the sites in S or \bar{S} . $H_{\bar{S}S}$ and $H_{S\bar{S}}$ represent the coupling between the two sub-systems, and I is the identity matrix. The isospectral reduction $\mathcal{R}_S(H, \lambda)$ is equivalent to an effective Hamiltonian gained from a subsystem partitioning of H [23], and its entries are rational functions of the parameter λ .

A Hamiltonian H is *latently symmetric* if there exists an isospectral reduction $\mathcal{R}_S(H, \lambda)$ with a symmetry, that is, which commutes with a group of matrices $\{M\}$ independent of λ . We now demonstrate this concept by means of the simple 6-site Hamiltonian H depicted in fig. 1(a). This Hamiltonian illustrates the minimal prototype of a system with non-trivial latent symmetry. H is parametrized by three real coupling parameters $h_i \neq 0$, $i \in \{1, 2, 3\}$ and two on-site potentials v_1, v_2 . The eigenvalue spectrum of H contains two doubly degenerate eigenvalues for any choice of these parameters. To explain these degeneracies in terms of latent symmetries of H , we reduce it by means of Eq. (1) over $S = \{1, 2, 3\}$. This yields the symmetric matrix

$$\mathcal{R}_{S=\{1,2,3\}}(H, \lambda) = \begin{pmatrix} a & b & b \\ b & a & b \\ b & b & a \end{pmatrix}, \quad (2)$$

with $a = v_1 + (h_1^2 + h_2^2/\lambda - v_2)$, $b = (h_1 h_2/\lambda - v_2) + h_3$. A graphical representation of Eq. (2) is depicted in Fig. 1(b). The graph is highly symmetric and is invariant under six symmetry operations: three rotations and three reflections. These six operations form the so-called dihedral group D_3 , which is non-Abelian.

We now draw a general connection between non-Abelian latent symmetries of a given Hamiltonian H and its eigenvalue spectrum. To this end, we use the fact that *each* of the so-called ‘‘nonlinear’’ eigenvalues belonging to $\mathcal{R}_S(H, \lambda)$ in Eq. (2), defined as the solutions λ_j to the nonlinear eigenvalue problem

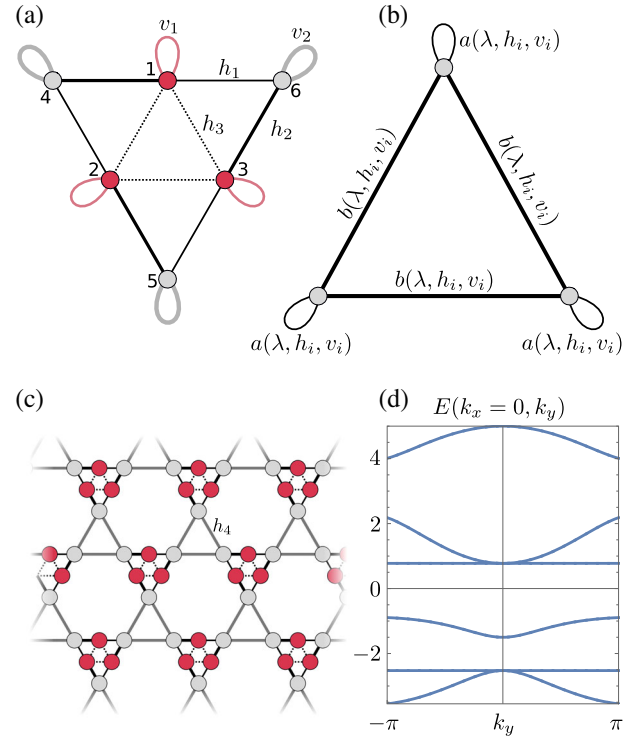


FIG. 1. (a) A six-site Hamiltonian H which features a non-Abelian D_3 permutation symmetry if $h_1 = h_2$, but only an Abelian C_3 permutation symmetry if $h_1 \neq h_2$. A line between two different sites i, j corresponds to a nonvanishing matrix element $H_{i,j}$, taking parametric values h_1, h_2 , or h_3 (indicated by different line styles). Loops connecting a site to itself correspond to diagonal matrix elements $H_{i,i}$ with parametric values v_1 or v_2 . (b) The result of the isospectral reduction of H over the three red sites $S = \{1, 2, 3\}$. The reduced Hamiltonian [Eq. (2)] features a D_3 permutation symmetry for any choice of λ, h_i , or v_i . (c) A modified kagome lattice with H as a unit cell. The band structure of this lattice for $k_x = 0$ is plotted in (d) for $h_1 = 4/3, h_2 = 5/3, h_3 = 0.7, h_4 = 3/2, v_i = 0$.

$$\text{Det}[\mathcal{R}_S(H, \lambda_j) - \lambda_j I] = 0 \quad (3)$$

is also an eigenvalue of H [22]. Moreover, whenever the eigenvalue spectra of H and of the subsystem $H_{\bar{S}\bar{S}}$ do not intersect, the eigenvalue spectra of $\mathcal{R}_S(H, \lambda)$ and H coincide [22]. This motivates calling $\mathcal{R}_S(H, \lambda)$ an ‘‘isospectral reduction.’’ From the above considerations, it is clear that degeneracies in the eigenvalue spectrum of $\mathcal{R}_S(H, \lambda)$ necessarily correspond to degeneracies in the eigenvalue spectrum of H . Moreover, and as we show in Sec. I. of the Supplemental Material [24], non-Abelian symmetries of the isospectral reduction $\mathcal{R}_S(H, \lambda)$ lead to degeneracies in the spectrum of its nonlinear eigenvalues. Thus, non-Abelian latent symmetries of H necessarily induce degeneracies onto the eigenvalue spectrum of H . Specifically, lower bounds on the multiplicity of H ’s eigenvalues are given by dimensions of the irreducible

representations of the underlying non-Abelian symmetry group of $\mathcal{R}_S(H, \lambda)$.

We emphasize that the above statements are completely general in the sense that they are valid for all kinds of latent symmetries (not just permutations), and for arbitrary (even non-Hermitian) diagonalizable matrices H . Irrespective of this applicability to general symmetries, we concentrate on the special case of permutation symmetries throughout this Letter. After all, permutation symmetries are among the easiest to detect—often by bare eye—and thus provide a convenient workhorse for depicting the main features of latent symmetries.

In the above, we have explained the spectral degeneracies of the prototype example Fig. 1(a) in terms of its latent symmetries. This system has been deliberately designed to be as simple as possible in order to convey the main ideas of latent symmetries. The underlying concept is, however, not limited to such basic examples, but can be applied to larger systems, as we demonstrate now. Figure 1(c) shows a lattice built by taking the prototype Hamiltonian H of Fig. 1(a) as a unit cell. The band structure of this lattice is depicted in Fig. 1(d). At the Γ point, that is, at $\mathbf{k} = 0$, the corresponding Bloch-Hamiltonian features the same latent symmetries as H in Fig. 1(a). This explains the two double degeneracies in the band structure [24]. Interestingly, the lattice further hosts two flat bands, which in general can also be designed through latent symmetries [30].

Latent D_n permutation symmetries.—Let us now examine the symmetries of the prototype example of Fig. 1 in more detail. This setup is invariant under permutations which cyclically permute sets of three sites, graphically represented by rotations of multiples of $2\pi/3$. These rotations form the abelian cyclic group of order 3, denoted by C_3 . As we have seen above, the setup also featured a latent D_3 permutation symmetry, and this is no coincidence. Indeed, as we show in the Supplemental Material, every C_n -permutation symmetric real Hamiltonian H features a latent D_n permutation symmetry [24]. As is well known, the dihedral group D_n is non-Abelian for $n \geq 3$, so that the underlying Hamiltonian automatically features degeneracies. This gives an alternative explanation to those degeneracies, which are classically understood in terms of the combination of the Abelian group $C_{n \geq 3}$ and the real valuedness of H which corresponds to a time-reversal symmetry of H [31].

Latent D_n symmetries without any permutation symmetries.—Above we have stated that a C_n permutation symmetry of a real Hamiltonian is a sufficient condition for a latent D_n permutation symmetry. However, it is not a necessary condition. Indeed, we demonstrate in the following the versatility of latent symmetries by showing that they can even exist when the underlying Hamiltonian H has no permutation symmetry at all. Figure 2(a) shows an example of such a Hamiltonian H , which can also be interpreted as

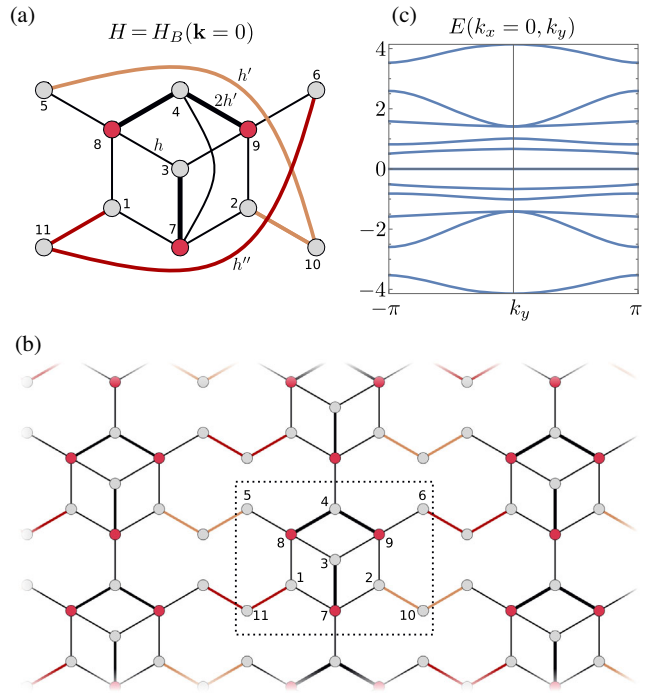


FIG. 2. (a) A Hamiltonian that features no permutation symmetry for $hh'h'' \neq 0$ and $h' \neq h''$. It does, however, feature a latent D_3 permutation symmetry that becomes visible when reducing over $S = \{7, 8, 9\}$. (b) A lattice whose Bloch-Hamiltonian H_B at $\mathbf{k} = 0$ equals H . The dotted box shows the lattice unit cell. (c) The band structure of this lattice for $k_x = 0, h = 1, h' = 1/2, h'' = 3/4$.

the Bloch Hamiltonian $H_B(\mathbf{k} = 0)$ of the lattice in Fig. 2(b) at crystal momentum $\mathbf{k} = 0$. A detailed derivation of this lattice is shown in Sec. V of the Supplemental Material [24]. For $hh'h'' \neq 0$ and $h' \neq h''$, H does not feature any permutation symmetry. However, for any choice of those three hopping parameters, it features a latent D_3 symmetry which becomes visible when reducing H over the three red sites $S = \{7, 8, 9\}$. As a result of this non-Abelian latent symmetry, H has at least one doubly degenerate eigenvalue pair for any choice of h' and h'' . We can now understand the two double degeneracies in the band structure [depicted in Fig. 2(c)] of the lattice of Fig. 2(b) at $k_x = k_y = 0$: At this point, the Bloch-Hamiltonian is given by H , so that it features a latent D_3 symmetry and therefore also degeneracies.

Interestingly, when setting $h' = h''$, H features a C_2 permutation symmetry, graphically corresponding to a reflection about the line connecting the sites 4 and 7. One can thus say that h' and h'' are control parameters for a symmetry breaking, and since H features a latent D_3 permutation symmetry for any choice of h, h', h'' , this opens the perspective of investigating and understanding symmetry breaking in terms of latent symmetries. In Sec. III. of the Supplemental Material, we show how latent symmetry preserving modifications (which may break permutation symmetries) can be derived [24].

Linking latent to local symmetries.—One might wonder if a latent symmetry leaves some recognizable traces in the original Hamiltonian. This is indeed the case: By expressing $\mathcal{R}_S(H, \lambda)$ as a power series in λ and subsequently analyzing it order by order, one can show [24] that

$$[\mathcal{R}_S(H, \lambda), M] = 0 \Leftrightarrow [(H^k)_{SS}, M] = 0 \quad \forall k, \quad (4)$$

where M denotes a symmetry operation. In other words, symmetries of $\mathcal{R}_S(H, \lambda)$ correspond to local symmetries [32,33] of H in all matrix powers. In particular, H itself has to be locally symmetric. Indeed, for our introductory example of Fig. 1(a) and $S = \{1, 2, 3\}$, we see that H_{SS} denotes the inner triangle, which obviously features the same symmetries as the corresponding isospectral reduction $\mathcal{R}_S(H, \lambda)$ depicted in Fig. 1(b).

Equation (4) can be used to facilitate the search for latent permutation symmetries. To this end, let us assume that we are given a (possibly large) Hamiltonian H and want to check if it features a latent permutation symmetry as the one depicted in Fig. 1(b). In other words, we look for a set of three sites $S = \{u, v, w\}$ such that $\mathcal{R}_S(H, \lambda)$ has the form of Eq. (2). Now, instead of computing and checking all possible isospectral reductions of H over three sites, we can use Eq. (4) to see that any candidate sites u, v, w necessarily have to fulfill $(H^k)_{u,u} = (H^k)_{v,v} = (H^k)_{w,w}$ for all k . This condition can be augmented by employing the Cayley-Hamilton theorem, which states that any matrix power $H^{k \geq N}$ (N being the dimension of H) is a polynomial in smaller powers. Thus, by computing the matrix powers H, H^2, \dots, H^{N-1} —the cost of which grows polynomially with N —and grouping the sites accordingly, the number of possible candidate sites $\{u, v, w\}$ can be drastically reduced. In particular, if there is any k such that H^k features no three sites with equal on-site potential $(H^k)_{i,i}$, a latent symmetry of the kind Eq. (2) is impossible.

Generalized exchange symmetries.—Having demonstrated the relation of latent symmetries to symmetries of the subsystem H_{SS} and to degeneracies of H , we finally relate a subclass of latent symmetries to symmetries of the original Hamiltonian H . This subclass consists of latent permutation symmetries of real Hamiltonians. Using graph-theoretical tools [34,35], such Hamiltonians can be shown to necessarily feature what we call here a *generalized exchange symmetry* (GES). A GES is an orthogonal symmetric matrix $Q^{(i,j)}$ fulfilling $[Q^{(i,j)}, H] = 0$ and $(Q^{(i,j)})^2 = I$ and which exchanges the two sites i, j while acting on the remaining sites as an orthogonal transformation. In the special case when this transformation is a pure permutation, $Q^{(i,j)}$ becomes a normal exchange symmetry, i.e., it acts on each site either as the identity or as an exchange operator. To provide an impression of the GESs, we explicitly computed—by solving the equations derived from its defining properties— $Q^{(1,2)}$ for the Hamiltonian of Fig. 1(a):

$$Q^{(1,2)} = \begin{pmatrix} 0 & 1 & 0 & 0 & 0 & 0 \\ 1 & 0 & 0 & 0 & 0 & 0 \\ 0 & 0 & 1 & 0 & 0 & 0 \\ 0 & 0 & 0 & \frac{h_1 h_2}{d} & 1 - \frac{h_1^2}{d} & \frac{h_1(h_1 - h_2)}{d} \\ 0 & 0 & 0 & 1 - \frac{h_1^2}{d} & \frac{h_1(h_1 - h_2)}{d} & \frac{h_1 h_2}{d} \\ 0 & 0 & 0 & \frac{h_1(h_1 - h_2)}{d} & \frac{h_1 h_2}{d} & 1 - \frac{h_1^2}{d} \end{pmatrix} \quad (5)$$

with $d = h_1^2 - h_2 h_1 + h_2^2$. Note that for the case of $h_1 = h_2$ the GES $Q^{(1,2)}$ becomes the ordinary exchange symmetry which permutes (1,2), (5,6), and leaves 3 and 4 invariant, and therefore describes the reflection about the line that connects sites 3 and 4 in Fig. 1. However, in the case where $h_1 \neq h_2$, this pure permutation symmetry is broken, whereas the more abstract GES persists. We note that, while the GESs as an abstract symmetry class persists, the *matrix entries* of $Q^{(1,2)}$ depend on h_1 and h_2 . This is an important difference to the latent D_3 permutation symmetry of H , whose matrix representation is independent of the values of h_i .

Finally, let us note that one can use the above insights to prove the existence of degeneracies for real latently $D_{n \geq 3}$ permutation symmetric Hamiltonians in yet another way [24]. Such Hamiltonians feature more than one GES, and by explicitly constructing them it can be shown that at least two of them do not commute with each other. Since the Hamiltonian H commutes with both of these GESs, it directly follows that H has to have at least one degenerate eigenvalue. It remains an open task to classify GESs using group-theoretical tools.

Conclusions.—We have provided a theoretical framework which connects non-Abelian latent symmetries of generic discrete models to their spectral degeneracies. For the important class of latent permutation symmetries, our results may allow for a geometrical explanation of apparently accidental degeneracies. Moreover, by identifying latent symmetries as local symmetries of all powers of the Hamiltonian, our results additionally suggest a convenient method for finding these latent symmetries. We further demonstrate that it is possible to break symmetries of an original Hamiltonian while preserving its latent symmetry. This may inspire techniques to modify—or probe—a given system asymmetrically without affecting its degeneracy.

Our considerations apply quite generally to physical systems possessing a discrete representation in terms of a finite-dimensional matrix. This includes, among others, tight-binding models, molecular Hamiltonians in truncated orbital bases, and multiport scattering setups. We therefore envision the applicability of our results in a broad variety of setups, contributing to the better understanding, design, and control of spectral degeneracies beyond conventional symmetries.

M. P. is thankful to the ‘Studienstiftung des deutschen Volkes’ for financial support in the framework of a scholarship. The authors thank G.M. Koutentakis and J. Schirmer for valuable comments on the manuscript.

M. R., M. P., and C. V. M. contributed equally to this work.

-
- [1] I. Bersuker, *The Jahn-Teller Effect* (Cambridge University Press, Cambridge, England, 2010).
- [2] Z. F. Ezawa, *Quantum Hall Effects: Recent Theoretical and Experimental Developments*, 3rd ed. (World Scientific, Singapore, 2013).
- [3] K. von Klitzing, Quantum Hall effect: Discovery and application, *Annu. Rev. Condens. Matter Phys.* **8**, 13 (2017).
- [4] W. D. Phillips, Nobel Lecture: Laser cooling and trapping of neutral atoms, *Rev. Mod. Phys.* **70**, 721 (1998).
- [5] *The Role of Degenerate States in Chemistry*, edited by M. Baer, G. D. Billing, I. Prigogine, and S. A. Rice, Advances in Chemical Physics Vol. 124 (Wiley-Interscience, New York, 2002).
- [6] D. Leykam, A. Andreanov, and S. Flach, Artificial flat band systems: From lattice models to experiments, *Adv. Phys.* **3**, 1473052 (2018).
- [7] W. Domcke, D. R. Yarkony, and H. Köppel, *Conical Intersections: Electronic Structure, Dynamics and Spectroscopy*, Advanced Series in Physical Chemistry, Vol. 15 (World Scientific, Singapore, 2004).
- [8] H. Köppel, W. Domcke, and L. S. Cederbaum, Multimode molecular dynamics beyond the Born-Oppenheimer approximation, in Advances in Chemical Physics (John Wiley & Sons, Ltd, New York, 1984), Vol. 57, pp. 59–246.
- [9] W. Domcke and D. R. Yarkony, Role of conical intersections in molecular spectroscopy and photoinduced chemical dynamics, *Annu. Rev. Phys. Chem.* **63**, 325 (2012).
- [10] H. V. McIntosh, On accidental degeneracy in classical and quantum mechanics, *Am. J. Phys.* **27**, 620 (1959).
- [11] H. McIntosh, Symmetry and degeneracy, in *Group Theory and Its Applications* (Academic Press, New York, 1971), Vol. 2.
- [12] V. Fock, Zur Theorie des Wasserstoffatoms, *Z. Phys.* **98**, 145 (1935).
- [13] J. von Neumann and E. Wigner, über das Verhalten von Eigenwerten bei adiabatischen Prozessen, *Phys. Z.* **30**, 467 (1929).
- [14] D. R. Yarkony, Diabolical conical intersections, *Rev. Mod. Phys.* **68**, 985 (1996).
- [15] D. Smith and B. Webb, Hidden symmetries in real and theoretical networks, *Physica (Amsterdam)* **514A**, 855 (2019).
- [16] F. Crasto de Lima and G. J. Ferreira, High-degeneracy points protected by site-permutation symmetries, *Phys. Rev. B* **101**, 041107(R) (2020).
- [17] W. C. Herndon and M. L. Ellzey, Isospectral graphs and molecules, *Tetrahedron* **31**, 99 (1975).
- [18] I. N. Levine, *Quantum Chemistry*, 5th ed. (Prentice Hall, New Jersey, NJ, 2000).
- [19] O. Richoux, V. Achilleos, G. Theocharis, I. Brouzos, and F. Diakonou, Multi-functional resonant acoustic wave router, *J. Phys. D* **53**, 235101 (2020).
- [20] O. Galor, *Discrete Dynamical Systems* (Springer-Verlag, Berlin, Heidelberg, 2007).
- [21] E. B. Wilson, J. C. Decius, and P. Cross, *Molecular Vibrations: The Theory of Infrared and Raman Vibrational Spectra*, revised edition ed. (Dover Publ Inc, New York, 1980).
- [22] L. Bunimovich and B. Webb, *Isospectral Transformations: A New Approach to Analyzing Multidimensional Systems and Networks* (Springer, New York, 2014).
- [23] G. Grosso and G. P. Parravicini, *Solid State Physics* (Academic Press, New York, 2013).
- [24] See Supplemental Material at <http://link.aps.org/supplemental/10.1103/PhysRevLett.126.180601> for mathematical details and proofs of the results presented here, which includes also Refs [25–29].
- [25] C. V. Morfonios, M. Pyzh, M. Röntgen, and P. Schmelcher, Cospectrality preserving graph modifications and eigenvector properties via walk equivalence of vertices, *Linear Algebra Appl.* **624**, 53 (2021).
- [26] A. Chan, G. Coutinho, W. Drazen, O. Eisenberg, C. Godsil, G. Lippner, M. Kempton, C. Tamon, and H. Zhan, Fundamentals of fractional revival in graphs, [arXiv:2004.01129](https://arxiv.org/abs/2004.01129).
- [27] O. Eisenberg, M. Kempton, and G. Lippner, Pretty good quantum state transfer in asymmetric graphs via potential, *Discrete Math.* **342**, 2821 (2019).
- [28] G. J. Tee, Eigenvectors of block circulant and alternating circulant matrices, *Res. Lett. Inf. Math. Sci.* **8**, 123 (2005).
- [29] D. Vanderbilt, *Berry Phases in Electronic Structure Theory: Electric Polarization, Orbital Magnetization and Topological Insulators* (Cambridge University Press, Cambridge, England, 2018).
- [30] C. V. Morfonios, M. Röntgen, M. Pyzh, and P. Schmelcher, Flat bands by latent symmetry, [arXiv:2102.12446](https://arxiv.org/abs/2102.12446).
- [31] L. D. Landau, E. M. Lifshitz, and J. Menzies, *Quantum Mechanics: Non-Relativistic Theory*, 3rd ed. (Elsevier Science & Technology, Jordan Hill, United Kingdom, 1981).
- [32] P. A. Kalozoumis, C. Morfonios, F. K. Diakonou, and P. Schmelcher, Invariants of Broken Discrete Symmetries, *Phys. Rev. Lett.* **113**, 050403 (2014).
- [33] P. A. Kalozoumis, C. Morfonios, F. K. Diakonou, and P. Schmelcher, Local symmetries in one-dimensional quantum scattering, *Phys. Rev. A* **87**, 032113 (2013).
- [34] M. Kempton, J. Sinkovic, D. Smith, and B. Webb, Characterizing cospectral vertices via isospectral reduction, *Linear Algebra Appl.* **594**, 226 (2020).
- [35] C. Godsil and J. Smith, Strongly cospectral vertices, [arXiv:1709.07975](https://arxiv.org/abs/1709.07975).

Supplemental Material

In this supplemental material, mathematical details of the proofs for the results presented in the main text as well as the Bloch-Hamiltonians for the lattices depicted in Figs. 1 and 2 of the main text are included. It is structured as follows. In section I we derive a connection between latent symmetries of H and degeneracies in its eigenvalue spectrum. Section II relates latent symmetries of H to local symmetries of H in all matrix powers. In section III we develop the concept of complement multiplets, which allow one to perturb a Hamiltonian featuring a latent permutation symmetry without breaking this symmetry. In section IV we provide details on the generalized exchange symmetries. Section V shows the derivation of the Bloch Hamiltonians for the lattices of Figs. 1 and 2 of the main text. Section VI contains auxiliary Lemmata used in proofs of Theorems in this Supplemental Material.

Throughout the following, \mathbb{L} denotes the set of values of λ for which the isospectral reduction $\mathcal{R}_S(H, \lambda)$ is defined.

I. THE RELATION BETWEEN THE SYMMETRIES OF THE ISOSPECTRAL REDUCTION AND DEGENERATE EIGENVALUES OF THE HAMILTONIAN

In the main part of this work, it was stated that non-abelian latent symmetries of a Hamiltonian necessarily induce degeneracies onto its eigenvalue spectrum. A key in proving this statement lies in the application of representation theoretical tools to the isospectral reduction, which we shall do in the following

Theorem 1: Symmetries of the isospectral reduction and degeneracies of H

Let $\mathcal{R}_S(H, \lambda)$ be the isospectral reduction of the Hamiltonian H over a set of sites S , and let G be a finite group with elements $\{g\}$ represented by matrices $\{\Gamma(g)\}$, and let $\mathcal{R}_S(H, \lambda)$ commute with all of them, i.e., $[\mathcal{R}_S(H, \lambda), \Gamma(g)] = 0 \forall \lambda \in \mathbb{L}, g \in G$.

Let Γ be decomposed into n pairwise non-equivalent irreducible representations $\tilde{\Gamma}_i$ of G with multiplicities $a_i \neq 0$ and with dimensions d_i , that is, there exists an invertible matrix A such that

$$\Gamma'(g) = A \Gamma(g) A^{-1} = \bigoplus_{i=1}^n \tilde{\Gamma}_i^{\oplus a_i}(g) \forall g \in G \quad (1)$$

where \oplus denotes the direct sum, and $M^{\oplus k} = \underbrace{M \oplus \dots \oplus M}_{k\text{-times}}$. Then for each a_i the eigenvalue spectrum of H contains *at least* a_i eigenvalues that are (individually) d_i -fold degenerate.

Proof. $\mathcal{R}_S(H, \lambda)$ represents a whole family of matrices parametric in λ . Each matrix in $\mathcal{R}_S(H, \lambda)$ commutes with the representation $\Gamma(g)$ of each group element g of the finite symmetry group G . Thus, employing Schur's lemma, it is easy to prove that for each $\lambda \in \mathbb{L}$, $\mathcal{R}_S(H, \lambda)$ is block-diagonalized by the same similarity transformation

$$\mathcal{R}'_S(H, \lambda) = A \mathcal{R}_S(H, \lambda) A^{-1} = \bigoplus_{i=1}^n B_i(\lambda) \quad (2)$$

with $B_i(\lambda)$ being a $(a_i d_i)$ -dimensional matrix. Moreover, due to Schur's lemma, each $B_i(\lambda)$ can be further block-diagonalized by permuting its rows and columns, thereby yielding

$$\mathcal{R}''_S(H, \lambda) = P \mathcal{R}'_S(H, \lambda) P^{-1} = \bigoplus_{i=1}^n b_i^{\oplus d_i}(\lambda) \quad (3)$$

with P denoting the corresponding permutation matrix, and $b_i(\lambda)$ a matrix of dimension a_i .

If we denote by \mathbb{W}_π the set of rational functions $p(\lambda)/q(\lambda)$ with the numerator degree being less than or equal to the denominator degree, then every matrix element $(\mathcal{R}_S)_{i,j} \in \mathbb{W}_\pi$ [1]. Moreover, since \mathbb{W}_π is closed under linear transformations, $(\mathcal{R}''_S)_{i,j} \in \mathbb{W}_\pi$. This means that every a_i -dimensional block $b_i(\lambda)$ of \mathcal{R}''_S , when being solved for its non-linear eigenvalues via $\det(\mathcal{R}''_S(H, \lambda) - \lambda I) = 0$, features *at least* a_i solutions [1]. Since \mathcal{R}''_S features d_i such blocks and since every eigenvalue of $\mathcal{R}_S(H, \lambda)$ is also an eigenvalue of H [1], it follows that for each irreducible representation $\tilde{\Gamma}_i$ of dimension d_i and multiplicity a_i the Hamiltonian H contains at least a_i eigenvalues that are (individually) d_i -fold degenerate. \square

II. THE CONNECTION BETWEEN SYMMETRIES OF THE ISOSPECTRAL REDUCTION AND LOCAL SYMMETRIES OF H^k

One of the main results of this work is the relation between latent symmetries of a matrix H and its local symmetries in every matrix power. This result was given without proof in the main part of this work, and is proven below.

Theorem 2

Let $\mathcal{R}_S(H, \lambda)$ denote the isospectral reduction of H over some set of sites S , and let $A \in \mathbb{C}^{|S| \times |S|}$, where $|S|$ denotes the number of sites in S . Then

$$[A, \mathcal{R}_S(H, \lambda)] = 0 \forall \lambda \in \mathbb{L} \Leftrightarrow [A, (H^k)_{S,S}] = 0 \forall k \geq 0, \quad (4)$$

where $(H^k)_{S,S}$ denotes the submatrix derived from H^k by taking the rows and columns corresponding to the set S .

Proof. “ \Rightarrow ” can be shown by induction. The initial case $k = 0$ is trivially fulfilled. The next step is to assume $[A, (H^k)_{S,S}] = 0$ holds for all $0 \leq k \leq k'$ and then to show it holds also for $0 \leq k \leq k' + 1$. By partitioning the matrix H into blocks over S and its complement \bar{S} the following identity can be shown to hold:

$$(H^k)_{S,S} = (H^{k-1})_{S,S} H_{S,S} + \sum_{m=0}^{k-2} (H^m)_{S,S} H_{S,\bar{S}} (H_{\bar{S},\bar{S}})^{k-2-m} H_{\bar{S},S}. \quad (5)$$

Evaluating the commutator of A with eq. (5) for $k = k' + 1$ and applying the induction assumption along with eq. (26) of lemma 3 we get $[A, (H^{k'+1})_{S,S}] = 0$, which completes the induction.

“ \Leftarrow ”: First, we evaluate the commutator of A with eq. (5) and apply the assumption $[A, (H^k)_{S,S}] = 0 \forall k \geq 0$. Next, again by induction we can show that $[A, H_{S,\bar{S}} (H_{\bar{S},\bar{S}})^l H_{\bar{S},S}] = 0 \forall l \geq 0$. To prove that $[A, \mathcal{R}_S(H, \lambda)] = 0$ for all $\lambda \in \mathbb{L}$ we use the identity eq. (28) for $\mathcal{R}_S(H, \lambda)$ from lemma 4. Since $[A, H_{S,S}] = 0$ by assumption and $[A, H_{S,\bar{S}} (H_{\bar{S},\bar{S}})^n H_{\bar{S},S}] = 0 \forall n \geq 0$ by induction, we have that $[A, \mathcal{R}_S(H, \lambda)] = 0$ for all $\lambda \in \mathbb{L}$. \square

III. MODIFICATIONS PRESERVING LATENT PERMUTATION SYMMETRIES

Given a Hamiltonian $H \in \mathbb{C}^{N \times N}$ with a latent permutation symmetry, it is often possible to modify H while keeping this symmetry. In particular, by analyzing the matrix powers of H , a large class of such latent-symmetry-preserving modifications can be found, as we derive in the following. We will start by defining what we call complement multiplets.

Definition 1: Complement multiplet

Let S be a set of sites of a hermitean Hamiltonian $H \in \mathbb{C}^{N \times N}$, that is, $S \subseteq \{1, \dots, N\}$, and \bar{S} denote its complement (i.e., all other sites of H). A set \mathbb{M} of sites of H with $\mathbb{M} \subseteq \bar{S}$ forms a complement multiplet with respect to S if

$$\sum_{m \in \mathbb{M}} (H \bar{H}^k)_{s,m} = c_k \in \mathbb{C} \forall s \in S, k \geq 0. \quad (6)$$

where \bar{H} is obtained from H by setting the couplings between S and \bar{S} to zero.

Once a (subset of) complement multiplets have been identified, they can be used to modify the Hamiltonian without breaking the underlying latent symmetry, with the procedure and its proof detailed in the following

Theorem 3

Let S be a set of sites of the hermitian Hamiltonian $\mathring{H} \in \mathbb{C}^{N \times N}$. If one modifies $\mathring{H} \rightarrow H \in \mathbb{C}^{(N+1) \times (N+1)}$ by adding a single site c (with arbitrary on-site potential) and subsequently coupling each complement multiplet \mathbb{M}_j of \mathring{H} to the site c with the coupling h_j , i.e.,

$$H_{x,c} = H_{c,x}^* = \sum_{x \in \mathbb{M}_j} h_j, \quad (7)$$

with the star denoting complex conjugate, then the isospectral reduction changes as

$$\mathcal{R}_S(H, \lambda) = \mathcal{R}_S(\mathring{H}, \lambda) + a(\lambda)J, \quad (8)$$

with $a(\lambda)$ being a rational function in λ , $J \in \mathbb{R}^{|\mathbb{S}| \times |\mathbb{S}|}$ is a matrix of ones, and where $|\mathbb{S}|$ denotes the number of sites in the set S . In particular, if S is latently permutation symmetric in \mathring{H} , it remains latently permutation symmetric in H .

Proof. In order to show eq. (8) holds, we evaluate the difference between $\mathcal{R}_S(H, \lambda)$ and $\mathcal{R}_S(\mathring{H}, \lambda)$. To this end, we define \tilde{H} as the matrix obtained from \mathring{H} by adding the site c *without connecting it*, and by lemma 2, $\mathcal{R}_S(\mathring{H}, \lambda) = \mathcal{R}_S(\tilde{H}, \lambda)$. Further, we denote $\tilde{S}_c = \tilde{S} \cup c$. Next, for a sufficiently large λ_0 and $|\lambda| > \lambda_0 > 0$, the matrix inverses occurring in $\mathcal{R}_S(H, \lambda)$ and $\mathcal{R}_S(\tilde{H}, \lambda)$ can be simultaneously formulated as convergent Neumann series. Finally, we note that $H_{S, \tilde{S}_c} = \tilde{H}_{S, \tilde{S}_c}$ and $H_{S,c} = \tilde{H}_{S,c} = 0$. We arrive at:

$$\mathcal{R}_S(H, \lambda) - \mathcal{R}_S(\mathring{H}, \lambda) = \sum_{k=1}^{\infty} H_{S, \tilde{S}_c} \left[\left(H_{\tilde{S}_c, \tilde{S}_c} \right)^{k-1} - \left(\tilde{H}_{\tilde{S}_c, \tilde{S}_c} \right)^{k-1} \right] H_{\tilde{S}_c, S} t^k \quad (9)$$

$$= \sum_{k=1}^{\infty} \mathring{H}_{S, \tilde{S}} \left[\left(H_{\tilde{S}, \tilde{S}} \right)^{k-1} - \left(\tilde{H}_{\tilde{S}, \tilde{S}} \right)^{k-1} \right] \mathring{H}_{\tilde{S}, S} t^k \quad (10)$$

where $t = 1/\lambda$. In the following, we abbreviate the terms in square brackets of eq. (10) by the matrix $\Delta_{\tilde{S}, \tilde{S}}^{(k-1)}$. We further denote by \overline{H} and $\mathring{\tilde{H}}$ the matrices obtained from H and \mathring{H} , respectively, by decoupling the set of sites S from the remaining sites.

Using a graph-theoretical interpretation (see Ref. [2]) the (i, j) -th matrix element of $\Delta_{\tilde{S}, \tilde{S}}^{(k)}$ can be expressed in terms of *walks* in a graph $\mathbb{G}(\overline{H})$ of length k starting at site \tilde{s}_i , that is, the i -th element of \tilde{S} , and ending at site \tilde{s}_j while necessarily visiting the new site c at least once. This yields

$$\Delta_{\tilde{S}, \tilde{S}}^{(k)} = \sum_{2+l+m+n=k} \left[\left(\sum_{x \in \cup_i \mathbb{M}_i} \left(\mathring{H}^l \right)_{\tilde{S}, x} H_{x,c} \right) \left(\overline{H}^m \right)_{c,c} \left(\sum_{x \in \cup_i \mathbb{M}_i} H_{c,x} \left(\mathring{H}^n \right)_{x, \tilde{S}} \right) \right] \quad (11)$$

Next, we replace $H_{x,c}$ by eq. (7) and multiply eq. (11) with $\mathring{H}_{S, \tilde{S}}$ on the left and its transpose on the right (compare with eq. (10)):

$$\sum_{2+l+m+n=k} \left[\left(\sum_i \sum_{x \in \mathbb{M}_i} \mathring{H}_{S, \tilde{S}} \left(\mathring{H}^l \right)_{\tilde{S}, x} h_i \right) \left(\overline{H}^m \right)_{c,c} \left(\sum_i \sum_{x \in \mathbb{M}_i} h_i^* \left(\mathring{H}^n \right)_{x, \tilde{S}} \mathring{H}_{\tilde{S}, S} \right) \right] \quad (12)$$

Using eq. (6), we recognize that $\sum_{x \in \mathbb{M}_i} \mathring{H}_{S, \tilde{S}} \left(\mathring{H}^l \right)_{\tilde{S}, x} = c_l^{(i)} \vec{1}_S$ with an all-constant $|\mathbb{S}|$ -dimensional vector $\vec{1}_S$. This means that the matrix in eq. (12) is proportional to all-one matrix J with a constant pre-factor $a^{(k)} = \sum_{2+l+m+n=k} \left[\left(\sum_i h_i c_l^{(i)} \right) \left(\overline{H}^m \right)_{c,c} \left(\sum_i h_i c_n^{(i)} \right)^* \right]$. Inserting this result in eq. (10), we obtain that $a(\lambda)$ from eq. (8) equals $\sum_{k=1}^{\infty} a^{(k-1)} \left(\frac{1}{\lambda} \right)^k$ for $|\lambda| > \lambda_0$.

Finally, we note that the left-hand side of eq. (10) is a rational function of λ . Since it equals $a(\lambda)J \forall |\lambda| > \lambda_0$, by the identity theorem for polynomials it must be equal to $a(\lambda)J$ also for $|\lambda| \leq \lambda_0$, $\lambda \in \mathbb{L}$. Now, since J commutes with any permutation matrix, each latent symmetry of \mathring{H} is preserved in H . \square

IV. THE CONNECTION BETWEEN (LATENT) $C_{n>2}$ SYMMETRIES AND DEGENERACIES FOR REAL-SYMMETRIC HAMILTONIANS

In the following, we will present more details on the concept of generalized exchange symmetry (GES). We will then use these to finally prove theorem 5, which states that, for real-valued Hamiltonians, a more than twofold rotational symmetry (that is, a symmetry $C_{n>2}$) necessarily leads to a non-abelian latent D_n symmetry.

As explained in the main part of this work, each generalized exchange symmetry (GES) is given by a symmetric orthogonal matrix $Q^{(u,v)}$ which permutes two sites u, v while acting as an orthogonal transformation on the others. The $Q^{(u,v)}$ were introduced in Ref. [3], where it has been shown that, for real Hamiltonians, $Q^{(u,v)}$ exists if and only if $(H^k)_{u,u} = (H^k)_{v,v}$ for all k . In this case, the eigenvalue spectra of $H \setminus u$ and $H \setminus v$ coincide, and the two sites u and v are said to be cospectral [3].

Similar to Ref. [4], we will now explicitly construct $Q^{(u,v)}$ by means of projectors. To this end, we first choose the eigenstates according to the following

Lemma 1: Lemma 2.5 of Ref. [5]

Let H be a real symmetric matrix, with u and v cospectral. Then the eigenstates $\{|\phi\rangle\}$ of H are (or, in the case of degenerate eigenvalues, can be chosen) as follows. For each eigenvalue λ there is at most one eigenstate $|\phi\rangle$ with even local parity on u and v , i. e., $\langle u|\phi_i^{(+)}\rangle = \langle v|\phi_i^{(+)}\rangle \neq 0$, and at most one eigenstate $|\phi\rangle$ with odd local parity on u and v , i. e., $\langle u|\phi_i^{(-)}\rangle = -\langle v|\phi_i^{(-)}\rangle \neq 0$. Here, $|x\rangle$ denotes a vector which possesses the value one at site x and zeros on all other sites. All remaining eigenstates for λ fulfill $\langle u|\phi_i^{(0)}\rangle = \langle v|\phi_i^{(0)}\rangle = 0$. The even (odd) parity eigenstate can be found by projecting the vector $|u\rangle \pm |v\rangle$ onto the eigenspace associated with λ .

With this choice of the eigenstate basis, we state the following

Theorem 4

Let the orthonormal eigenstates $\{|\phi\rangle\}$ of H be chosen according to lemma 1, and define the projectors

$$P_+^{(u,v)} = \sum_i |\phi_i^{(+)}\rangle \langle \phi_i^{(+)}|, \quad P_-^{(u,v)} = \sum_i |\phi_i^{(-)}\rangle \langle \phi_i^{(-)}|, \quad P_0^{(u,v)} = \sum_i |\phi_i^{(0)}\rangle \langle \phi_i^{(0)}| \quad (13)$$

Then $Q^{(u,v)} = P_+^{(u,v)} + P_0^{(u,v)} - P_-^{(u,v)}$ fulfills

$$(Q^{(u,v)})^{-1} = (Q^{(u,v)})^T = Q^{(u,v)}, \quad Q^{(u,v)}|u\rangle = |v\rangle. \quad (14)$$

Proof. The property $(Q^{(u,v)})^{-1} = Q^{(u,v)}$ follows simply from the fact that the projection matrices eq. (13) are idempotent. $(Q^{(u,v)})^T = Q^{(u,v)}$ follows from the fact that one can choose the eigenvectors of H to be real-valued, so that the projector onto the eigenspace associated to any eigenvalue is real, thereby rendering also the projection matrices eq. (13) real and therefore also symmetric.

In order to prove that $Q^{(u,v)}|u\rangle = |v\rangle$, we use lemma 1 and the orthonormality of eigenstates $|\phi_i\rangle$ to get $\langle v|Q^{(u,v)}|u\rangle = (Q^{(u,v)})_{u,v} = \sum_i \langle u|\phi_i\rangle \langle \phi_i|v\rangle = 1$. Additionally, since $\sum_i (Q_{u,i}^{(u,v)})^2 = \sum_i (Q_{v,i}^{(u,v)})^2 = 1$ due to the orthogonality of $Q^{(u,v)}$, it follows that $(Q^{(u,v)})_{u,i} = \delta_{i,v}$ and $(Q^{(u,v)})_{v,i} = \delta_{i,u}$. \square

With these prerequisites and a good understanding of the concept of GES, we are now finally able to prove the connection between C_n rotational symmetries of a real Hamiltonian and the necessary emergence of D_n latent permutation symmetries, explicated in the following

Theorem 5

Let $H \in \mathbb{R}^{N \times N}$ be a real symmetric Hamiltonian that features a latent or non-latent $C_{n>2}$ permutation symmetry. Then

- H necessarily also features a latent D_n permutation symmetry and features at least $\lfloor \frac{n-1}{2} \rfloor$ pairs of doubly degenerate eigenvalues, where $\lfloor x \rfloor$ rounds x down to the nearest integer.
- There exist two GESs of H which do not commute with each other.

Proof. • If H features a (latent or non-latent) $C_{n>2}$ permutation symmetry, then there is at least one set S of n sites and a $n \times n$ permutation matrix P fulfilling

$$P^k \neq I \forall 1 \leq k < n, \quad P^n = I, \quad [\mathcal{R}_S(H, \lambda), P] = 0 \forall \lambda \in \mathbb{L} \quad (15)$$

where I is the identity matrix. Together with the symmetry and real-valuedness of H , this property implies that the rows and column of $\mathcal{R}_S(H, \lambda)$ can be permuted such that it is a real symmetric circulant matrix. It is known that such matrices commute with the permutation matrix corresponding to the operation that performs a flip about the anti-diagonal. Together with the cyclic permutations of order n , this operation generates the dihedral group D_n , and H thus features a latent D_n permutation symmetry.

Next, we note that it is known that the eigenstates of real symmetric circulant matrices are independent of their entries [6], here in particular independent of λ . Using them to diagonalize $\mathcal{R}_S(H, \lambda)$ one obtains a diagonal $n \times n$ matrix with entries $f_j(\lambda) \in \mathbb{W}_\pi$, $j = 1, \dots, n$, that is, rational functions $p_j(\lambda)/q_j(\lambda)$ with the numerator degree being less than or equal to the degree of the denominator. The eigenvalues of $\mathcal{R}_S(H, \lambda)$ are thus given by the sum of the multisets denoting the solutions to $f_j(\lambda) - \lambda = 0$. Similar to the proof of theorem 1, it can be shown that each of these equations has at least one solution. Furthermore, $f_j(\lambda) = f_{n-j}(\lambda)$, because $\mathcal{R}_S(H, \lambda)$ is not only circulant but also real-symmetric. Finally, since every eigenvalue of $\mathcal{R}_S(H, \lambda)$ is contained in the spectrum of H [1], we conclude that H has at least $\lfloor \frac{n-1}{2} \rfloor$ pairs of doubly degenerate eigenvalues.

- From the above and from theorem 2 we have $[(H^k)_{S,S}, P] = 0$ for all $k \geq 0$, i.e. $(H^k)_{S,S}$ is a real symmetric circulant matrix. In each power k , the diagonal elements $(H^k)_{ii} = (H^k)_{jj} \forall i, j$ are pairwise equal, meaning that each pair of sites in S is cospectral. By Ref. [3], for each such pair there is a GES $Q^{(i,j)}$ which commutes with H and theorem 4 applies.

For the sake of simple notation let us now assume that the sites of H are labeled (if this is not the case, one can easily renumber the sites accordingly) such that $s_i \rightarrow i$, with P permuting the sites in $S = \{s_1, \dots, s_{|S|}\}$ such that the site $i < n$ is mapped onto the site $i + 1$, and n onto 1. The fact that $(H^k)_{S,S}$ is circulant symmetric then implies $(H^k)_{1,2} = (H^k)_{2,3} \forall k$. In the terminology of Ref. [2], site 2 is a walk-singlet w.r.t. the cospectral sites 1 and 3. Thus, by Theorem 4 from Ref. [2], the eigenstates of H [chosen according to lemma 1 for the cospectral pair 1 and 3] with negative parity on cospectral sites vanish on site 2. By combining the projector definition of $Q^{(1,3)}$ with the completeness relation of eigenstates one can show $(Q^{(1,3)})_{2,2} = 1$. Furthermore, since $Q^{(1,3)}$ is orthogonal, the matrix elements $(Q^{(1,3)})_{2,j} = \delta_{2,j}$. On the other hand, site 3 is not necessarily a singlet for the cospectral pair 1 and 2. Specifically, we have

$$Q^{(1,3)} = \left(\begin{array}{ccc|c} 0 & 0 & 1 & 0 \\ 0 & 1 & 0 & 0 \\ 1 & 0 & 0 & A \\ \hline 0 & & & \end{array} \right), \quad Q^{(1,2)} = \left(\begin{array}{cc|cc} 0 & 1 & 0 & 0 \\ 1 & 0 & a & b \\ \hline 0 & & b^T & B \end{array} \right) \quad (16)$$

where $A, B \in \mathbb{R}^{(N-3) \times (N-3)}$ and $b \in \mathbb{R}^{1 \times (N-3)}$. Since the upper left 3×3 block of the commutator of the above two matrices does not vanish, these two matrices do not commute. \square

V. BAND-STRUCTURE CALCULATIONS

To derive the Bloch-Hamiltonian $H_B(\mathbf{k}) = H_B(k_x, k_y)$, we follow the convention of Eq. (2.75) of Ref. [7]. To this end, let $|m_{\mathbf{R}}\rangle$ denote the state which is completely localized on site m of the unit cell located at position \mathbf{R} . For our two-dimensional lattices, the vectors $\mathbf{R} = A\vec{a}_1 + B\vec{a}_2$, where A, B are integers and $\vec{a}_{1,2}$ are the two primitive vectors describing the lattice. The Bloch-Hamiltonian can then be written as

$$(H_B(\mathbf{k}))_{nm} = \sum_{\mathbf{R}} e^{i\mathbf{k} \cdot \mathbf{R}} \langle m_{\mathbf{0}} | H_L | m_{\mathbf{R}} \rangle \quad (17)$$

where H_L denotes the Hamiltonian of the infinite lattice.

A. Bloch-Hamiltonian for the modified Kagome lattice

With $\vec{a}_1 = (1, 0)^T$, $\vec{a}_2 = (\frac{1}{2}, \frac{\sqrt{3}}{2})^T$, we obtain the Bloch-Hamiltonian of Fig. 1 (c) of the main text as

$$\begin{pmatrix} 0 & h_3 & h_3 & h_2 & 0 & h_1 \\ h_3 & 0 & h_3 & h_1 & h_2 & 0 \\ h_3 & h_3 & 0 & 0 & h_1 & h_2 \\ h_2 & h_1 & 0 & 0 & h_4 e^{i(\frac{\sqrt{3}k_y}{2} - \frac{k_x}{2})} & h_4 e^{-ik_x} \\ 0 & h_2 & h_1 & h_4 e^{-i(\frac{\sqrt{3}k_y}{2} - \frac{k_x}{2})} & 0 & h_4 e^{-i(\frac{k_x}{2} + \frac{\sqrt{3}k_y}{2})} \\ h_1 & 0 & h_2 & h_4 e^{ik_x} & h_4 e^{i(\frac{k_x}{2} + \frac{\sqrt{3}k_y}{2})} & 0 \end{pmatrix}. \quad (18)$$

At $k_x = k_y = 0$, the isospectral reduction of the Bloch-Hamiltonian over the sites $S = \{1, 2, 3\}$ then has the structure

$$\begin{pmatrix} a(\lambda) & b(\lambda) & b(\lambda) \\ b(\lambda) & a(\lambda) & b(\lambda) \\ b(\lambda) & b(\lambda) & a(\lambda) \end{pmatrix}. \quad (19)$$

Thus, the Bloch-Hamiltonian features a latent D_3 permutation symmetry at $\mathbf{k} = 0$.

B. Construction of the Bloch-Hamiltonian belonging to Fig. 2 (b)

Let us here briefly discuss how one could build a lattice from the Hamiltonian depicted in Fig. 2 (a) of the main text. The basic idea is to interpret H as the Bloch-Hamiltonian H_B of an extended lattice, evaluated at the Γ -point, that is, $H = H_B(\mathbf{k} = 0)$. Out of the many possible ways to achieve this, we here first remove the three curved couplings—the ones between sites (6, 11), (5, 10), and (4, 7)—from H , and use the resulting system H_{UC} as the unit cell of a lattice, as depicted in Fig. 2 (b). The corresponding Bloch-Hamiltonian $H_B(\mathbf{k}) = H_{UC} + H_{IC}(\mathbf{k})$ is the sum of the unit cell Hamiltonian H_{UC} and a \mathbf{k} -dependent inter-cell coupling $H_{IC}(\mathbf{k})$. The matrix elements of $H_{IC}(\mathbf{k})$ are obtained by taking an arbitrary reference unit cell, A . For each site i in A that is connected with coupling h_{ij} to a site j in an adjacent unit cell B , $(H_{IC}(\mathbf{k}))_{ij} = h_{ij} e^{i\mathbf{k} \cdot \mathbf{R}_{AB}}$ with \mathbf{R}_{AB} denoting the vector pointing from A to B , as one can show by means of eq. (17). At $\mathbf{k} = 0$, all complex exponentials in $H_{IC}(\mathbf{k})$ become unity, and one can design $H_B(\mathbf{k} = \mathbf{0}) = H$ by suitably connecting the initial unit cell to its neighbors. For the above choice and by choosing $\vec{a}_1 = (0, 1)^T$, $\vec{a}_2 = (\frac{5}{3} \cos(\pi/6), \frac{1}{2})^T$, we then obtain the Bloch-Hamiltonian of Fig. 2 (b) of the main text as

$$\begin{pmatrix} \mathbf{0}_{6 \times 6} & \mathbf{C} \\ \mathbf{C}^\dagger & \mathbf{0}_{5 \times 5} \end{pmatrix} \quad (20)$$

with $\mathbf{0}_{n \times n}$ denoting the $n \times n$ matrix of zeros, and

$$\mathbf{C} = \begin{pmatrix} h & h & 0 & 0 & h'' \\ h & 0 & h & h' & 0 \\ 2h & h & h & 0 & 0 \\ h e^{ik_y} & 2h & 2h & 0 & 0 \\ h & 0 & h' e^{i(\frac{k_y}{2} - \frac{5k_x}{2\sqrt{3}})} & 0 & 0 \\ 0 & 0 & h & 0 & h'' e^{i(\frac{5k_x}{2\sqrt{3}} + \frac{k_y}{2})} \end{pmatrix}. \quad (21)$$

For $k_x = k_y = 0$, this Hamiltonian equals the one depicted in Fig. 2 (a) of the main text, as intended.

VI. AUXILIARY LEMMATA

Lemma 2

Let S be a set of sites of \mathring{H} . If one extends

$$\mathring{H} \rightarrow H = \begin{pmatrix} \mathring{H} & 0 \\ 0 & H' \end{pmatrix} \quad (22)$$

then the isospectral reduction over S remains unchanged, i.e., $\mathcal{R}_S(H, \lambda) = \mathcal{R}_S(\mathring{H}, \lambda)$.

Proof. Follows straightforwardly from the fact that $(H_{\bar{S}, \bar{S}} - \lambda I)^{-1} = \begin{pmatrix} (H_{\bar{S}_1, \bar{S}_1} - \lambda I)^{-1} & 0 \\ 0 & (H_{\bar{S}_2, \bar{S}_2} - \lambda I)^{-1} \end{pmatrix}$ is block diagonal and $H_{S, \bar{S}_2} = 0$ with sites \bar{S}_1 from \mathring{H} , \bar{S}_2 from H' and $\bar{S}_1 \cup \bar{S}_2 = \bar{S}$. \square

Lemma 3

Let the isospectral reduction

$$\mathcal{R}_S(H, \lambda) = H_{S, S} - H_{S, \bar{S}} (H_{\bar{S}, \bar{S}} - \lambda I)^{-1} H_{\bar{S}, S} \quad (23)$$

over some set S of sites. If $\mathcal{R}_S(H, \lambda)$ commutes with a $|S| \times |S|$ matrix A , that is, $[A, \mathcal{R}_S(H, \lambda)] = 0 \forall \lambda \in \mathbb{L}$, then

$$[A, H_{S, S}] = 0 \quad (24)$$

$$\left[A, H_{S, \bar{S}} (H_{\bar{S}, \bar{S}} - \lambda I)^{-1} H_{\bar{S}, S} \right] = 0 \forall \lambda \in \mathbb{L}. \quad (25)$$

$$\left[A, H_{S, \bar{S}} (H_{\bar{S}, \bar{S}})^k H_{\bar{S}, S} \right] = 0 \forall k \geq 0. \quad (26)$$

Proof. First, eq. (24) follows from $[A, \mathcal{R}_S(H, \lambda)] = 0$ by evaluating the limit $\lambda \rightarrow \infty$. Second, eq. (25) follows from eq. (24) and $[A, \mathcal{R}_S(H, \lambda)] = 0$. Last, for a sufficiently large λ_0 and $|\lambda| > \lambda_0 > 0$, the left-hand side of eq. (25) can be formulated as a convergent power series in $x = \frac{1}{\lambda}$:

$$\frac{1}{\lambda_0} \sum_{k=1}^{\infty} c_k x^k = 0 \forall x : 0 < |x| < \frac{1}{\lambda_0} \quad (27)$$

where $c_k = \left[A, H_{S, \bar{S}} \left(\frac{H_{\bar{S}, \bar{S}}}{\lambda_0} \right)^{k-1} H_{\bar{S}, S} \right]$. By the identity theorem for power series it follows that all $c_k = 0$, thus proving eq. (26). \square

Lemma 4

Let $\mathcal{R}_S(H, \lambda) = H_{S, S} - H_{S, \bar{S}} (H_{\bar{S}, \bar{S}} - \lambda I)^{-1} H_{\bar{S}, S}$ be the isospectral reduction of H over a site set S . Then

$$\mathcal{R}_S(H, \lambda) = H_{S, S} + \sum_{k=1}^{|\bar{S}|} \frac{c_k}{c_0} \sum_{n=0}^{k-1} \binom{k-1}{n} (-\lambda)^{k-1-n} H_{S, \bar{S}} (H_{\bar{S}, \bar{S}})^n H_{\bar{S}, S} \forall \lambda \in \mathbb{L} \quad (28)$$

where $c_i = c_i(\lambda)$ are the coefficients of the characteristic polynomial of $H_{\bar{S}, \bar{S}} - \lambda I$.

Proof. For $\lambda \in \mathbb{L}$ the matrix $H_{\bar{S}, \bar{S}} - \lambda I := M$ is invertible, with characteristic polynomial $p_M(\lambda, x) = \sum_{k=0}^{|\bar{S}|} c_k(\lambda)x^k$ and $c_0 \neq 0$. From the Cayley-Hamilton theorem one obtains the identity relation $M^{-1} = -\sum_{k=1}^{|\bar{S}|} \frac{c_k}{c_0} M^{k-1}$. Inserting this relation into the definition of isospectral reduction and applying the binomial theorem for $\left(H_{\bar{S}, \bar{S}} - \lambda I\right)^{k-1}$ we arrive at eq. (28). \square

-
- [1] L. Bunimovich and B. Webb, *Isospectral Transformations: A New Approach to Analyzing Multidimensional Systems and Networks* (Springer, New York, NY, United State, 2014).
- [2] M. Röntgen, M. Pyzh, C. V. Morfonios, and P. Schmelcher, Cospectrality-preserving graph modifications and eigenvector properties via walk equivalence of vertices, (2020), [arXiv:2007.07609](#).
- [3] C. Godsil and J. Smith, Strongly Cospectral Vertices, (2017), [arXiv:1709.07975](#).
- [4] A. Chan, G. Coutinho, W. Drazen, O. Eisenberg, C. Godsil, G. Lippner, M. Kempton, C. Tamon, and H. Zhan, Fundamentals of fractional revival in graphs, (2020), [arXiv:2004.01129](#).
- [5] O. Eisenberg, M. Kempton, and G. Lippner, Pretty good quantum state transfer in asymmetric graphs via potential, *Discrete Math. Algebraic and Extremal Graph Theory*, **342**, 2821 (2019).
- [6] G. J. Tee, Eigenvectors of block circulant and alternating circulant matrices, *Res. Lett. Inf. Math. Sci.* **8**, 123 (2005).
- [7] D. Vanderbilt, *Berry Phases in Electronic Structure Theory: Electric Polarization, Orbital Magnetization and Topological Insulators* (Cambridge University Press, Cambridge, 2018).

IN this cumulative thesis, we investigated symmetries of physical systems described by a discrete model. Specifically, we investigated two different types of symmetries, the first one being local symmetries. *A local symmetry is a symmetry of a subsystem. That is, when isolating this subsystem from the remainder of the setup, it features a symmetry.* Or, phrased differently, a local symmetry is a symmetry that is, in general, valid only in a part of the system. The second symmetry type is that of a latent symmetry. When a Hamiltonian is latently symmetric, then a suitably chosen effective version of this Hamiltonian features a symmetry (more details will be given below). In the following, we will briefly motivate our works, summarize our main findings, link them together, and also give an outlook to interesting questions that arise from these findings.

Before we start, we apologize for repeating some introductory facts and figures that we already showed in Part [i](#) of this thesis. The reason is that we believe that summary, conclusions, and outlook should be comprehensible even without reading the main text of this work, and to this end, restating some material is necessary.

In the following, we will focus on tight-binding models to present our results in an intuitive manner. However, our results are applicable to general discrete models, and we will discuss this point in a concluding remark in Section [6.2.1](#).

6.1 LOCAL SYMMETRIES

What impact do local symmetries have on the eigenstates of a system? That is the main question driving the research presented in this section. Indeed, understanding the impact of local symmetries of a Hamiltonian on its eigenstates can be challenging: Contrary to the case of global symmetries, that is, symmetries *of the whole system*, the operators describing local symmetries usually do not commute with the underlying Hamiltonian. Without such a commuting operator, most instruments—group theory, for example—that are normally applied to the treatment of global symmetries cannot be used for their local counterparts. Nevertheless, and as was shown in a series of papers, the impact of local symmetries on the eigenstates of several wave physical setups can be quantified through a framework of current-like correlators, so-called non-local currents [[MR10](#), [30–32](#), [36](#)]. This framework represented the starting point for this entire thesis, and thus we will start by presenting our work [[MR1](#)] in which the non-local currents are measured in a photonic setup. Afterwards, we will move away from non-local currents, though stick with the topic of local symmetries and investigate its various aspects.

6.1.1 Local symmetries in one-dimensional systems

The measurement of non-local currents in a system of so-called evanescently coupled waveguides was the topic of our first work [MR1]. In such systems, neighboring waveguides are placed closely to each other so that their fundamental modes overlap. As a result, light propagating in such waveguides can “tunnel” to adjacent waveguides, and the propagation can be described by a discrete Schrödinger equation. As a consequence, and assuming equal waveguides, the system is mapped to a tight-binding model of sites that are coupled to each other via next-neighbor couplings $h_{i,j}$. In [MR1], we investigated the case where this tight-binding model is one-dimensional, that is, a chain. In such a chain, the spatial distribution of coupling strengths determines the symmetry of the setup, and in particular the chain may be either globally symmetric, locally symmetric, or completely asymmetric. Example waveguide setups for each of these classes were produced and the non-local currents were measured. We then showed that these currents can be used to distinguish between the three cases of global symmetry, local symmetry, or complete asymmetry.

Local symmetries in one-dimensional tight-binding chains were also the topic of our second work [MR2]. Specifically, we investigated tight-binding chains consisting of N sites with a constant next-neighbor coupling h and a variable on-site potential v_i , described by the Hamiltonian

$$\hat{H} = \sum_{i=1}^N v_i |i\rangle \langle i| + h \sum_{i=1}^{N-1} \left(|i\rangle \langle i+1| + |i+1\rangle \langle i| \right) \quad (6.1)$$

where $|n\rangle$ is a single-site excitation of the site n . The potential v_i was constrained to take only two different values, v_A and v_B . Such a binary chain features a large number of local symmetries for any possible arrangement of the A 's and B 's¹. Depending on the sequence of on-site potentials, the system then corresponds to different physical systems, such as a lattice (for a periodic sequence) or a completely disordered system (for a random sequence). We concentrated on the cases in-between these two extremes and analyzed different classes of so-called deterministic aperiodic systems, a popular example being quasicrystals. Specifically, we investigated three different sequences for the on-site potential values: the Fibonacci (corresponding to a quasicrystal), the Thue-Morse, and the Rudin-Shapiro sequence. For weak coupling h , the eigenstates of the investigated setups featured three properties: (i) They had low amplitude everywhere but on one or more identical substructures², and for most states the amplitude on these substructures was approximately locally symmetric. (ii) For most states, this substructure localization occurred simultaneously across the bulk of the chain, so that these states were rather extended within the bulk. Additionally, the eigenenergies of these states

¹ For example, already the simple sequence

$$\overbrace{AAA} \overbrace{BAB} \overbrace{BAB}$$

features a number of different local reflection symmetries, three of which are marked by brackets above and below this sequence.

² By “substructure” we mean a finite subsection of the chain comprising a small number of sites. In the previous footnote, some examples for substructures would be AAA , ABA , and BAB .

clustered to so-called quasi-bands. (iii) There were some states which were localized on a substructure on one of the edges of the finite chain, and whose eigenenergy lay in a gap between quasi bands; we thus called these states “gap-edge states”.

We were curious to see whether these three properties could be linked to each other and to the local symmetries of the chain itself. To this end, we developed a framework of local resonators. Backed by degenerate perturbation theory, this framework proposes that—at low coupling strength—certain substructures within the chain act as embedded resonators, that is, they are able to confine a wave at certain energies. In this picture, it is clear that any eigenstate Ψ of the chain that is (almost completely) localized on a single resonator has to locally (approximately) resemble one of the eigenmodes of this resonator. More specifically, if we denote the resonator by R , then up to a normalization factor the projection of Ψ onto R has to be approximately equal to an eigenmode³ ϕ of R . As a result, the energies of Ψ and ϕ are close to each other. Now, when a given resonator occurs more than once within the chain—as is the case in the systems that we investigated—it follows from the above argument that the eigenstate Ψ may simultaneously localize on some or even all of these resonators. Importantly, since most resonator structures in the three investigated chains were locally symmetric, their eigenmodes shared this symmetry. This is the reason why the localization patterns—that is, the distribution of high-amplitude values—of most eigenstates in these chains were found to be locally symmetric.

In general, there may be more than one eigenstate corresponding to the same resonator eigenmode. Since the energy of each of these states has to be approximately equal to that of this resonator mode, a quasi band emerges. In this picture, the presence of a gap-edge state can also be explained: A resonator lying on the edge of the chain differs from those in the bulk, and in general its eigenmodes energetically differ from those of other resonators. Thus, a state localized on such an edge-resonator is energetically separated from the other eigenstates of the chain, and since its energy matches none of the eigenmodes of other resonators in the chain, it is localized on the edge; in other words, this state corresponds to a gap-edge state.

In the above works [MR1, MR2], we showed that local symmetries are a versatile concept for the treatment of one-dimensional systems. Especially our second work [MR2] showed that local symmetries can have a drastic impact on the eigenstates of a system by causing them to localize on locally symmetric substructures. Local symmetry induced localization, though of a different kind, will also be the main topic of Section 6.1.2. Before we move there, however, let us give a brief outlook on potential topics of future research based on [MR1, MR2].

6.1.1.1 Outlook

Based on the above works, there are several routes for further research. The first would be the application of the theory of non-local currents to aperiodic chains. This is in particular appealing since, as we have written above, a locally symmetric setup usually *does not have* locally symmetric eigenstates. In this sense, the aperiodic chains with weak couplings are an exception, as their eigenstates indeed feature

³ To be precise, by “eigenmodes” of a resonator R we here mean the set of eigenstates that R would have if one would completely decouple it from the remainder of the chain.

(approximately) locally symmetric amplitude patterns on the resonators on which they localize. Thus, to analyze this phenomenon from another viewpoint, it would be interesting to analyze these chains in terms of non-local currents. Moreover, to complement the treatment, it would be interesting to combine the framework of non-local currents with degenerate perturbation theory that we used for the development of the local resonator framework.

The second pathway would be the generalization of the local resonator framework, for example, to higher-dimensional systems, or to *non-binary* chains, that is, to chains where the on-site potential is allowed to take more than just two different values. A first step in the latter direction would be to start with a binary chain, and then let some on-site potentials deviate from their binary value. In particular, this could be done to energetically control gap-edge states. In a preliminary study we found that by this method a gap-edge state could even be controllably moved in-between two bands. Moreover, the impact of *dynamically* changing the values of the non-binary potentials could be investigated, which, if suitably done, may allow the conversion of an extended state of the chain into a gap-edge state.

6.1.2 Compact localized states and flat bands through local symmetries

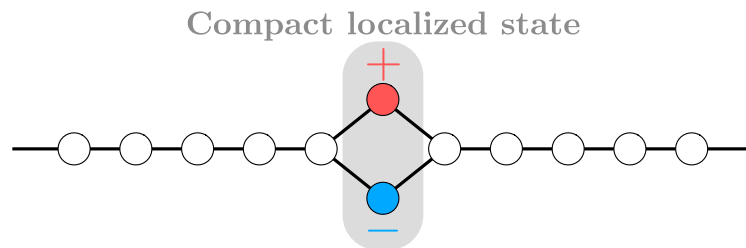


Figure 6.1: A simple tight-binding setup, with each solid line corresponding to a coupling of strength 1, with all on-site potentials set to zero. The symmetric dimer represents a defect in the infinitely extended chain and leads to compact localization in the form of an anti-symmetric excitation of the dimer.

Besides analyzing the impact of local symmetries on one-dimensional chains, a second focus of this thesis was the relation of local symmetries to so-called compact localized states (CLSs). A CLS is an eigenstate of a discrete model with compact support, that is, it vanishes outside of a (usually small) part of the system. We note that such a “discrete model” could describe many different setups such as interacting bosons or fermions on a lattice, and many more. To be specific, and to have an easily understandable setup, in the following we will concentrate on the tight-binding Hamiltonian

$$\hat{H} = \sum_i v_i |i\rangle \langle i| + \sum_{\langle i,j \rangle} h_{i,j} |i\rangle \langle j| \quad (6.2)$$

with the second sum going over neighboring sites, v_i being the on-site potential of site i , $h_{i,j}$ describing the coupling strength between the sites i and j , and with $|i\rangle$ denoting a single-site excitation of the i -th site. An example of a simple CLS in such a tight-binding model is depicted in Fig. 6.1.

The extreme localization of CLSs is caused by destructive interference, which is in turn allowed for by a suitable interplay of coupling strengths and the geometry

of the system. In lattices, such interplay may lead to macroscopically degenerate CLSs, and consequently to the emergence of a completely flat band.

CLSs and flat bands are interesting from many viewpoints—for example, they might play a role in high-temperature superconductivity—, but our personal motivation for entering this field was the fact that many systems that host CLSs feature local symmetries. In particular, we were curious whether these two phenomena are linked to each other.

In [MR3], we found—by applying recent insights from graph theory—that certain classes of local symmetries can indeed be systematically linked to compact localization. In particular, we derived a powerful construction principle that allows to equip tight-binding lattices with locally symmetric structures that host CLSs. Roughly speaking, this principle is based on replacing one or more sites of the lattice with highly symmetric structures that can host CLSs. In the simplest case, one chooses a unit cell of the lattice and replaces a single site of that cell with a reflection-symmetric dimer. Due to the resulting local reflection symmetry, the modified lattice then features one eigenstate that (i) is an anti-symmetric excitation of the two sites comprising the dimer and (ii) vanishes everywhere outside of this dimer. In other words, the modified lattice features a CLS localized on the dimer. The system depicted in Fig. 6.1 is an example where the above procedure has been applied to a one-dimensional chain whose unit cell comprises a single site.

Importantly, the parameters describing this dimer—such as its coupling strength to the remainder of the system—can be tuned such that the energy spectrum of the modified lattice equals that of the unmodified chain *plus* the single energy eigenvalue of the CLS. Additionally, the energy of this CLS may be tuned freely, and in particular may energetically lie within the energy continuum corresponding to one of the dispersive bands of the lattice. Since—as can easily be shown—this highly localized CLS is orthogonal to the extended eigenstates of this band, it corresponds to a bound state in the energy continuum⁴.

The above construction principle can be successively applied to an arbitrarily large number of unit cells. In particular, it may be applied to *each* unit cell in the same way. As a result, each unit cell is equipped with a CLS, and all of these CLSs have the same energy. These are thus macroscopically degenerate, and a flat band emerges. If, additionally, the procedure of adding each CLS is done in the minimally invasive way sketched above, that is, without changing the energy of any other eigenstate of the system, then the energetical position of this flat band can be tuned without modifying the energies of other bands of the lattice.

⁴ One might object that, due to the dimer defect, the Bloch states of the unperturbed lattice have been perturbed. However, this is not the case: Bloch’s theorem can be easily modified to describe this system provided that the dimerization is done in a suitable manner, that is, provided that the coupling parameters and on-site potentials are chosen appropriately. In this case, the band structure remains unchanged under the dimerization. Moreover, the nature of Bloch states is not changed. To be precise, if Ψ denotes an eigenstate of the unperturbed lattice, then after the dimerization this state becomes Ψ' , and we have

$$\Psi' = \begin{cases} \frac{\Psi}{\sqrt{2}} & \text{On each of the two dimer sites} \\ \Psi & \text{Everywhere else.} \end{cases} \quad (6.3)$$

Thus, the Bloch state Ψ is essentially unchanged, and in particular it is still extended throughout the lattice.

In [MR4], we moved away from tight-binding lattices, and applied the principle of local symmetry induced compact localization to systems of coupled dipolar nanoparticles. An important difference to tight-binding setups is the nature of the coupling, since the electromagnetic interactions between the dipoles are long ranged. Another difference is that the system is open and is now described not by a Hamiltonian, but by the so-called dyadic Green's matrix. Since each dipole scatterer has three degrees of freedom⁵, the Green's matrix of a setup with N scatterers is of dimension $3N$. To complete the description of the setup, we note that the spectral characteristics of this Green's matrix are linked to scattering properties of the system. That is, the eigenvalues correspond to the lifetime and frequency of scattering resonances, with the eigenvectors describing the electric field distribution of these resonances on the dipoles.

In this context of dipolar nanoparticles, a compact localized state corresponds to a scattering resonance whose electric field vanishes on most dipoles. And although the long range coupling makes it more difficult to achieve destructive interference that is necessary for this effect, we demonstrated that it is still possible. Specifically, we proposed a reflection symmetric setup that consists of $N + 2$ scatterers. All scatterers are placed on the xy -plane of the setup, with N scatterers additionally being arranged on a line, and with the remaining two scatterers being displaced from this line in a reflection symmetric manner. As a result of this reflection symmetry, the dyadic Green's matrix describing this setup becomes locally symmetric. That is, it is invariant under the operation which permutes the z -degrees of freedom of the two displaced masses, while acting as the identity on all other degrees of freedom. As a result of this local symmetry, a compact localized state is induced.

Concluding the above, we found that local symmetries play an important role for compact localization. In particular, local symmetries enable the systematic design of systems featuring such localization, both in tight-binding setups and in systems featuring long range coupling. In the following, we will discuss possibilities of further research in this exciting field of local symmetry induced compact localization.

6.1.2.1 Outlook

Overall, the study of compact localization and flat bands is a rapidly growing field, and there are many directions for further research building upon [MR3, MR4]. An especially interesting project would be the application of local symmetry principles not only to the tight-binding Hamiltonian of Eq. (6.2) or the dyadic Green's matrix, but also to Hamiltonians describing interacting particles⁶. Apart from such models, another route would be to apply the principle of local symmetry induced compact localization to other systems that can be described (in a suitable approximation) by discrete models, for example to networks of coupled optical waveguides. Here, a compact localized state would be an excitation in a subset of waveguides, with destructive interference preventing a spreading of this excitation to the remainder of the network. Moreover, since the results of [MR3] apply only to

⁵ Corresponding to electric field components in the x , y , and z -direction.

⁶ We note that the novelty in this proposal would not be the demonstration of compact localization in such systems, which has indeed already been proposed (see, e.g., [312, 313]), but the application of local symmetry concepts.

certain classes of local symmetries, the generalization of our ideas to other types of (local) symmetries would be another possible route for further research. In our work [MR8] that will be summarized below, we have already taken a first step into this direction by exploring *latent symmetry induced* compact localization.

With regard to [MR4], we saw that the proposed compact localization in systems of dipolar nanoparticles leads to scattering resonances whose electric field vanishes on a large number of dipoles. This is an unusual effect, and thus it would be interesting to explore technological applications of it. Another route for future research is a closer investigation of these systems: Since our model—in form of the dyadic Green’s matrix—operates in the dipole approximation, the investigation of the impact of higher-order-effects on the compact localization promises to yield interesting insights. Lastly, we note that the proposed setup is reflection symmetric, and an immediate generalization of the results would be the investigation of compact localization in asymmetric systems, one example of which we already discovered in our preliminary studies.

6.1.3 *Transfer of compact localized states*

Since a CLS is an eigenstate that is localized in a tiny volume of the system, it is completely unaffected by any perturbations that happen outside of this volume. It is thus ideally suited for the storage of information in a quantum computer. However, using CLSs in this manner would further require the ability of transferring them with high-fidelity in-between different quantum processing units. In [MR5, MR6], we explored means of achieving such transfer. To this end, we investigated networks of coupled spins described by the XX or the Heisenberg model. We restricted ourselves to the subspace where only one spin is excited, for which these models can be mapped to a tight-binding network described by the Hamiltonian of Eq. (6.2).

The core of [MR5] was the development of a specialized lattice supporting the simultaneous storage and transfer of a large number of CLSs. Since this lattice was obtained from the well-known Lieb lattice by replacing some sites by symmetric dimers, we called it the “decorated Lieb lattice”. Each unit cell of the decorated Lieb lattice is locally symmetric and possesses two symmetric dimers such as the one depicted in Fig. 6.1. As each of these dimers can host a CLS in the form of an anti-symmetric excitation, they can be used for the storage of these states. We further showed how a CLS can be transferred between different dimers. To this end, we explored two different methods.

The first method is based on optimal control techniques. That is, we achieved high-fidelity transfer of the CLS by modifying the underlying Hamiltonian in an optimized, time-dependent manner.

We further developed a second method for CLS transfer that is applicable not only to the decorated Lieb lattice, but to a broad range of setups. Apart from two control pulses initializing and finalizing the transfer, this method does not require a time-dependent control over the system’s parameter, and is thus much simpler. The method is based on the so-called perfect state transfer (PST) technique which was originally developed in the quantum information community for the transfer of qubits. More specifically, PST was developed in the context of a spin

network modeled by the XX or Heisenberg Hamiltonian, with the underlying idea being as follows. Initially, the network is prepared in a state where all spins point downwards. A qubit is then encoded into a single spin u , and the aim is to transfer this qubit across the network to another spin v by pure time-evolution of the underlying time-independent Hamiltonian. The fidelity of this process is demanded to be unity, for which the Hamiltonian has to be fine-tuned.

In the above sketched process, initially only the spin u is excited. As a result, it can be shown that the dynamics of this time-evolution take place in the subspace where only one spin is excited, and the system can be mapped to a tight-binding Hamiltonian. Here, the original qubit corresponds to a single-site excitation of u , with PST corresponding to the perfect transfer to a single-site excitation of v . For our method, we started with such a tight-binding PST Hamiltonian and modified it such that it allows for perfect transfer of dimer CLSs. Technically, this modification consisted of the dimerization of the sites u and v as well as the introduction of two local control pulses before and after the transfer process. This proposed method is completely general in that it can be used to equip a large class of PST Hamiltonians with dimer-CLSs, which can then be both stored and transferred with high fidelity.

In [MR6], we moved away from PST and instead investigated the related concept of so-called pretty good state transfer (PGST). Just as PST, this technique has been developed for the transfer of qubits (or, equivalently, of single-site excitations), but in general only achieves near-unity fidelities. Among others, the motivation for using such a non-optimal transfer technique is that (i) the requirements that a Hamiltonian must fulfill to feature PST are rather demanding, thereby limiting the number of potential networks capable of such transfer, and (ii) in an experiment, a fidelity of unity will anyway not be reached due to imperfections. In our work on PGST, we achieved two things. Firstly, we developed a novel algorithm for the design of tight-binding Hamiltonians featuring PGST. Secondly, and in complete similarity to the above procedure for PST setups, we showed that large classes of systems featuring pretty good transfer of single site excitations can easily be modified such that they feature both pretty good transfer of CLSs as well as the ability to store these states.

In summary, in the works [MR5, MR6] we developed different methods for the combined high-fidelity transfer and storage of CLSs. Interestingly, these methods turned out to be remarkably robust against imperfections and perturbations, which became apparent in the context of detailed robustness studies in both [MR5] and [MR6].

6.1.3.1 Outlook

When thinking about future pathways, there are three important points to bear in mind: Firstly, the fact that even a single symmetric dimer can host a CLSs. Secondly, the fact that the *compact* localization of CLSs enormously simplified our works [MR5, MR6]. For example, the modification of the established transfer mechanisms of single-site excitations to dimer-CLSs was remarkably simple, consisting only of a dimerization of two sites and two local control pulses. Thirdly, the fact that their compact localization also makes CLSs highly robust against imperfections and perturbations.

Thus, we can see that CLSs are a highly versatile tool, and given this versatility, there are many open routes that one could go. Among others, one might implement logical or quantum gates with CLSs, promote the dimer-CLSs to polymer-CLSs, or find mechanisms to “catch” an extended excitation of a setup by converting it into a CLS.

As written above, the results of [MR5, MR6] can be applied to spin systems described by a Heisenberg or XX model provided that one works in the subspace where only one spin is excited. Moving away from this regime is a promising direction, and also connects to our proposal in Section 6.1.2.1 of analyzing the impact of local symmetries on compact localization in many-body systems.

6.2 LATENT SYMMETRIES

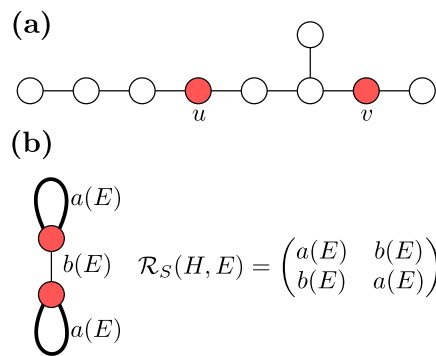


Figure 6.2: **(a)** A simple 9-site tight-binding system in which the two red sites u and v are latently symmetric (see text for details). All solid lines correspond to couplings of strength 1, and all on-site potentials are equal to zero. **(b)** The isospectral reduction of the setup in (a) over $S = \{u, v\}$, depicted as a graph (left) and as a matrix (right).

In the last part of this thesis, we focused on a concept which is—at first glance—unrelated to the concept of local symmetries. This concept is called “latent symmetries”, and was introduced in 2019 in the context of graph theory [306]. Latent symmetries can be defined for a large number of discrete models, but, just as for CLSs, it is easiest to discuss them in the context of the tight-binding Hamiltonian of Eq. (6.2). In Section 6.2.1, we shall discuss the wide applicability of latent symmetries in more detail.

Figure 6.2 (a) shows a latently symmetric tight-binding model comprising nine sites. At first glance, the system features no symmetry, that is, it is not invariant under any reflection, rotation, or combination thereof. However, and irrespective of this apparent asymmetry, the two sites u and v are latently symmetric. A latent symmetry is defined via the so-called isospectral reduction

$$\mathcal{R}_S(H, E) = H_{SS} + H_{S\bar{S}} (E - H_{\bar{S}\bar{S}})^{-1} H_{\bar{S}S} \quad (6.4)$$

which is equivalent to an effective Hamiltonian obtained through subsystem partitioning. In Eq. (6.4), E denotes the energy, S is the set of sites over which the original Hamiltonian is reduced, and \bar{S} denotes its complement, that is, all other sites of the system. The matrices H_{SS} and $H_{\bar{S}\bar{S}}$ denote the sub-Hamiltonians describing

only the subsystem S or \bar{S} , with $H_{S\bar{S}}$ and $H_{\bar{S}S}$ denoting the coupling between these two subsystems. We remark that the quantities H_{SS} , $H_{\bar{S}\bar{S}}$, $H_{S\bar{S}}$, and $H_{\bar{S}S}$ denote submatrices of the Hamiltonian matrix H , while so far we have talked—for example, in Eq. (6.2)—on the level of the Hamiltonian operator \hat{H} . While we will discuss this issue in more detail in Section 6.2.1, for simplicity we here concentrate on our tight-binding Hamiltonian of Eq. (6.2). If this Hamiltonian operator \hat{H} describes a setup of N sites, then we can write it as the $N \times N$ matrix H by choosing the basis of single site-excitations. In this basis, the matrix element H_{ij} of H is given by v_i if $i = j$, h_{ij} if $i \neq j$ and i, j are coupled, and zero otherwise. Since it is thus clear how the Hamiltonian \hat{H} and the corresponding Hamiltonian matrix H are related to each other, in the following we will use these two terms interchangeably.

After this small, but necessary excursion on matrices, let us come back to the topic of latent symmetries. The simplest kind of latent symmetry occurs when the original Hamiltonian is reduced over a set of just two sites $S = \{u, v\}$ such that this reduction is reflection symmetric [an example is shown in Fig. 6.2 (b)]. This has a profound impact on the system: In the simplest case where all eigenvalues are non-degenerate, the eigenstates of the Hamiltonian have definite parity on u and v .

Initially, our motivation to study latent symmetries stemmed solely from the observation of this rather counter-intuitive parity. However, we soon realized that latent symmetries are related to a much more profound fact. Namely, that the powers of a Hamiltonian H are a valuable source of knowledge. For example, if the Hamiltonian $H = H^T$ is real-symmetric, then a latent symmetry of two sites u and v is equivalent to the statement that

$$\left(H^k\right)_{u,u} = \left(H^k\right)_{v,v} \quad (6.5)$$

for all positive integer k . That is, the diagonal entries of u and v are equal in all matrix powers of H .

In [MR7], we were interested in a simple question: Given a tight-binding Hamiltonian H with two latently symmetric sites u and v , which modifications are allowed without breaking this latent symmetry? The answer—and this should not be surprising after our above emphasis—can be found through a thorough analysis of the matrix powers of H . Indeed, we found that such an analysis can be used to derive a broad range of latent symmetry preserving modifications. For example, if we pick a single site c of our latently symmetric Hamiltonian H , and connect this site to another system H' , then this extension does not break latent symmetry if and only if

$$\left(H^k\right)_{u,c} = p \left(H^k\right)_{v,c} \quad (6.6)$$

for all positive integer powers k , and with $p \in \{\pm 1\}$. Moreover, we showed that the analysis of the Hamiltonian's matrix powers gives deep insights about the system's eigenstates. For example, any eigenstate with negative parity on u and v necessarily vanishes on each site c fulfilling Eq. (6.6) with $p = 1$.

In [MR8], we applied the derived principles of latent symmetry preserving modifications to the design of tight-binding setups with latent symmetry induced flat bands. We devised several design strategies. In the simplest strategy, we start with a latently symmetric Hamiltonian H that features one or more sites $\{c_i\}$ that fulfill Eq. (6.6). We then build a lattice by using H as a unit cell and connecting

it to other unit cells—that is, other copies of H —via one or more of the sites $\{c_i\}$. Each unit cell is then guaranteed to keep its latent symmetry, and if we label the latently symmetric sites in a given unit cell by u and v , we see that each eigenstate with negative parity⁷ on these two sites vanishes outside of this unit cell. Thus, it corresponds to a compact localized state. Relying on our results from [MR7], we demonstrated that the lattice Hamiltonian parameters—that is, couplings and on-site potentials—can be parametrized in a high-dimensional manifold without breaking the latent symmetry or the condition Eq. (6.6) for the sites $\{c_i\}$. In particular, such a parametrization allows to change the overall band structure of the setup without losing the latent symmetry induced flat bands.

So far, we have only discussed the special case of a latent symmetry of two sites u and v . That is, we discussed the case where the isospectral reduction Eq. (6.4) of the original Hamiltonian over $S = \{u, v\}$ has a symmetry. The concept of latent symmetry can also be generalized, that is, the reduction of the Hamiltonian over a larger set of $n > 2$ sites can have a symmetry as well. An especially interesting case arises when such a reduction features several symmetries such that the group formed by them is non-abelian. In this case, we say that the underlying Hamiltonian features a non-abelian latent symmetry (group).

In [MR9], we investigated such non-abelian latent symmetries in more detail. This investigation led to two important insights. Firstly, we found that non-abelian latent symmetries necessarily induce degeneracies in the eigenvalue spectrum of the underlying Hamiltonian. In this respect, latent symmetries thus behave analogously to “conventional” non-abelian symmetries of the Hamiltonian itself, for which the induction of degeneracies is well-known. An important consequence of this finding is the classification of spectral degeneracies: While these can often be related to symmetries of the underlying Hamiltonian, there are cases where no suitable symmetry can be found, and the degeneracies are then usually said to be “accidental”. Now, given that (i) latent symmetries are usually hidden from direct observation, but become visible only after performing the isospectral reduction, and that (ii) non-abelian latent symmetries induce degeneracies, it could be that several so-called accidental degeneracies are in fact caused by non-abelian latent symmetries.

Secondly, we found that there is a profound connection between the two main topics of this thesis, namely, local and latent symmetries. Specifically, we found that

$$[\mathcal{R}_S(H, E), M] = 0 \quad \Leftrightarrow \quad \left[\left(H^k \right)_{SS}, M \right] = 0 \quad \forall k. \quad (6.7)$$

Here, M is a matrix describing the symmetry of the isospectral reduction; in the simplest case, it would be a 2×2 matrix describing a reflection symmetry of two sites u, v . This equation states that a latent symmetry M of the isospectral reduction over S is equivalent to a local symmetry M of the Hamiltonian *in all matrix powers*⁸. Once again, this result shows that the matrix powers of the Hamiltonian are an important and valuable source of knowledge.

⁷ Due to the latent symmetry of u and v , there is at least one such state

⁸ We remark that, to see whether a Hamiltonian features a latent symmetry, one might thus either (i) look for local symmetries in H itself and *in all matrix powers* H^k , or (ii) investigate the isospectral reduction of H . In both cases, whether a given Hamiltonian H features a latent symmetry or not is usually not clear when investigating only H .

Overall, in our above works and also in several other preliminary studies, we found that latent symmetries are an exciting and very rich concept allowing to see a physical system from a completely new viewpoint. Applying this concept to a variety of physical setups is a logical next step, and in the following we shall discuss some potential pathways for this application.

6.2.1 Outlook

In our above studies of latent symmetries, we focused on tight-binding setups. However, and as we also noted above, latent symmetries are applicable to a much broader class of systems. The reason for this broad applicability is that the isospectral reduction Eq. (6.4) is defined in terms of a general square and diagonalizable matrix H , which in particular even does not need to be hermitian. Thus, the concept of latent symmetry can be applied to any physical system that is described by the matrix eigenvalue problem

$$H\vec{\Psi} = \lambda\vec{\Psi}. \quad (6.8)$$

This includes, in particular, tight-binding setups and the Green's matrix that we discussed in Section 6.1.2, systems of coupled oscillators (in the harmonic approximation), or multi-port systems described by the scattering matrix. Moreover, many-body systems described by, e.g., the Bose-Hubbard model or the Heisenberg model can be related to Eq. (6.8) by writing the corresponding Hamiltonian as a matrix. To perform this step, one needs to go into a specific basis, for which often a "natural choice" exists. For example, for a system of interacting fermions or bosons, one would typically work with Fock states.

So far our investigation of latent symmetries did not focus on a specific physical system, but rather on the generic discrete model of Eq. (6.2). In particular, we assumed complete control over all on-site and coupling elements, without taking into account conditions on these that might be induced by the specific underlying physical system. This was necessary, since the phenomenon of latent symmetries has been barely investigated so far, and we first needed to build a solid foundation of insights before we could start a search for latent symmetries in specific physical systems. With the above works [MR7–MR9], this foundation is now built, and we have already started several projects that focus on latent symmetries in specific systems, such as multi-port scattering systems, systems of coupled acoustic waveguides, chemical molecules, and coupled oscillators.

A recurring theme in our studies of latent symmetries is that the powers of the matrix H occurring in the above matrix eigenvalue problem Eq. (6.8) are a very valuable source of knowledge. In view of this, further research in this direction promises to yield interesting results.

REFERENCES

- ¹E. Noether, "Invariante Variationsprobleme," *Nachrichten Von Ges. Wiss. Zu Gött. Math.-Phys. Kl.* **1918**, 235 (1918).
- ²C. Cohen-Tannoudji, B. Diu, and L. Franck, *Quantum mechanics, volume 2: angular momentum, spin, and approximation methods*, Hardcover, Vol. 2, 3 vols. (Wiley-VCH, 4), 688 pp.
- ³E. B. Wilson, J. C. Decius, and P. Cross, *Molecular vibrations: the theory of infrared and raman vibrational spectra*, Revised Edition (Dover Publications, New York, Mar. 1, 1980), 416 pp.
- ⁴D. C. Harris and M. D. Bertolucci, *Symmetry and spectroscopy: an introduction to vibrational and electronic spectroscopy*, 1st ed. (Dover Publications, New York, 1989), 550 pp.
- ⁵F. A. Cotton, *Chemical applications of group theory*, 3rd ed. (Wiley-Interscience, New York, Mar. 2, 1990), 480 pp.
- ⁶M. S. Dresselhaus, G. Dresselhaus, and A. Jorio, *Group theory: application to the physics of condensed matter*, 1st ed. (Springer-Verlag, Berlin Heidelberg, 2008), 582 pp.
- ⁷H. McIntosh, "Symmetry and degeneracy," in *Group Theory and its Applications*, Vol. 2 (Academic Press, New York, NY, USA, 1971), pp. 75–144.
- ⁸P. Wochner, C. Gutt, T. Autenrieth, T. Demmer, V. Bugaev, A. D. Ortiz, A. Duri, F. Zontone, G. Grübel, and H. Dosch, "X-ray cross correlation analysis uncovers hidden local symmetries in disordered matter," *Proc. Natl. Acad. Sci. U.S.A.* **106**, 11511 (2009).
- ⁹K. Fichtner, "Order-disorder structures," *Comput. Math. with Appl.* **16**, 469 (1988).
- ¹⁰A. P. Dudka and N. E. Novikova, "Description of the atomic disorder (local order) in crystals by the mixed-symmetry method," *Crystallogr. Rep.* **62**, 1009 (2017).
- ¹¹E. Belokoneva, A. Topnikova, and S. Aksenov, "Topology-symmetry law of structure of natural titanosilicate micas and related heterophyllosilicates based on the extended OD theory: structure prediction," *Crystallogr. Rep.* **60**, 5 (2015).
- ¹²E. Maciá, "The role of aperiodic order in science and technology," *Rep. Prog. Phys.* **69**, 397 (2006).
- ¹³S. V. Zhukovsky, "Perfect transmission and highly asymmetric light localization in photonic multilayers," *Phys. Rev. A* **81**, 053808 (2010).
- ¹⁴R. W. Peng, X. Q. Huang, F. Qiu, M. Wang, A. Hu, S. S. Jiang, and M. Mazzer, "Symmetry-induced perfect transmission of light waves in quasiperiodic dielectric multilayers," *Appl. Phys. Lett.* **80**, 3063 (2002).

- ¹⁵R. W. Peng, Y. M. Liu, X. Q. Huang, F. Qiu, M. Wang, A. Hu, S. S. Jiang, D. Feng, L. Z. Ouyang, and J. Zou, "Dimerlike positional correlation and resonant transmission of electromagnetic waves in aperiodic dielectric multilayers," *Phys. Rev. B* **69**, 165109 (2004).
- ¹⁶W. J. Hsueh, S. J. Wun, Z. J. Lin, and Y. H. Cheng, "Features of the perfect transmission in Thue-Morse dielectric multilayers," *J. Opt. Soc. Am. B* **28**, 2584 (2011).
- ¹⁷Z. V. Vardeny, A. Nahata, and A. Agrawal, "Optics of photonic quasicrystals," *Nat. Photon.* **7**, 177 (2013).
- ¹⁸H. Liu, M. S. Ukhtary, and R. Saito, "Hidden symmetries in N-layer dielectric stacks," *J. Phys.: Condens. Matter* **29**, 455303 (2017).
- ¹⁹J. Blumberg, M. S. Ukhtary, and R. Saito, "Enhancement of the electric field and diminishment of the group velocity of light in dielectric multilayer systems: a general description," *Phys. Rev. Applied* **10**, 064015 (2018).
- ²⁰D. K. Ferry, S. M. Goodnick, and J. Bird, *Transport in nanostructures*, 2nd ed. (Cambridge University Press, Cambridge, 2009).
- ²¹A. C. Hladky-Hennion, J. O. Vasseur, S. Degraeve, C. Granger, and M. de Billy, "Acoustic wave localization in one-dimensional Fibonacci phononic structures with mirror symmetry," *J. Appl. Phys.* **113**, 154901 (2013).
- ²²W. J. Hsueh, C. H. Chen, and R. Z. Qiu, "Perfect transmission of spin waves in a one-dimensional magnonic quasicrystal," *Phys. Lett. A* **377**, 1378 (2013).
- ²³A. D. Liehr, "On the use of local symmetry in analyzing the infrared spectra of complex molecules," *J. Chem. Phys.* **24**, 162 (1956).
- ²⁴E. Ortoleva, G. Castiglione, and E. Clementi, "A program to introduce local symmetry in ab-initio computations of molecules: IBMOL-7," *Comput. Phys. Commun.* **19**, 337 (1980).
- ²⁵J. Echeverría, A. Carreras, D. Casanova, P. Alemany, and S. Alvarez, "Concurrent symmetries: the interplay between local and global molecular symmetries," *Chem. Eur. J.* **17**, 359 (2011).
- ²⁶D. Casanova and P. Alemany, "Revisiting the foundations of symmetry operation measures for electronic wavefunctions," *Chem. Phys. Lett.* **511**, 486 (2011).
- ²⁷M. Altarelli, R. P. Kurta, and I. A. Vartanyants, "X-ray cross-correlation analysis and local symmetries of disordered systems: general theory," *Phys. Rev. B* **82**, 104207 (2010).
- ²⁸R. P. Kurta, M. Altarelli, E. Weckert, and I. A. Vartanyants, "X-ray cross-correlation analysis applied to disordered two-dimensional systems," *Phys. Rev. B* **85**, 184204 (2012).
- ²⁹R. P. Kurta, R. Dronyak, M. Altarelli, E. Weckert, and I. A. Vartanyants, "Solution of the phase problem for coherent scattering from a disordered system of identical particles," *New J. Phys.* **15**, 013059 (2013).

- ³⁰P. A. Kalozoumis, C. Morfonios, F. K. Diakonou, and P. Schmelcher, “Local symmetries in one-dimensional quantum scattering,” *Phys. Rev. A* **87**, 032113 (2013).
- ³¹P. A. Kalozoumis, C. Morfonios, F. K. Diakonou, and P. Schmelcher, “Invariants of broken discrete symmetries,” *Phys. Rev. Lett.* **113**, 050403 (2014).
- ³²P. A. Kalozoumis, C. Morfonios, N. Palaiodimopoulos, F. K. Diakonou, and P. Schmelcher, “Local symmetries and perfect transmission in aperiodic photonic multilayers,” *Phys. Rev. A* **88**, 033857 (2013).
- ³³P. A. Kalozoumis, C. V. Morfonios, F. K. Diakonou, and P. Schmelcher, “Invariant currents and scattering off locally symmetric potential landscapes,” *Ann. Phys.* **362**, 684 (2015).
- ³⁴M. A. Metaxas, P. Schmelcher, and F. K. Diakonou, “Symmetry-induced non-local divergence-free currents in two-dimensional quantum scattering,” *Phys. Rev. A* **103**, 032203 (2021).
- ³⁵T. Wulf, C. V. Morfonios, F. K. Diakonou, and P. Schmelcher, “Exposing local symmetries in distorted driven lattices via time-averaged invariants,” *Phys. Rev. E* **93**, 052215 (2016).
- ³⁶C. V. Morfonios, P. A. Kalozoumis, F. K. Diakonou, and P. Schmelcher, “Non-local discrete continuity and invariant currents in locally symmetric effective Schrödinger arrays,” *Ann. Phys.* **385**, 623 (2017).
- ³⁷P. Schmelcher, S. Krönke, and F. K. Diakonou, “Dynamics of local symmetry correlators for interacting many-particle systems,” *J. Chem. Phys.* **146**, 044116 (2017).
- ³⁸M. Born and H. S. Green, “A general kinetic theory of liquids. IV. quantum mechanics of fluids,” *Proc. R. Soc. Lond. Ser. Math. Phys. Sci.* **191**, 168 (1947).
- ³⁹N. N. Bogoliubov, *The dynamical theory in statistical physics* (Hindustan Publishing Corporation, Delhi, India, 1965).
- ⁴⁰J. G. Kirkwood, “The statistical mechanical theory of transport processes I. general theory,” *J. Chem. Phys.* **14**, 180 (1946).
- ⁴¹J. Yvon, “Une méthode d’étude des corrélations dans les fluides quantiques en équilibre,” *Nucl. Phys.* **4**, 1 (1957).
- ⁴²M. Bonitz, *Quantum kinetic theory*, 2nd ed. (Springer International Publishing, 2016), 424 pp.
- ⁴³A. Akbari, M. J. Hashemi, A. Rubio, R. M. Nieminen, and R. van Leeuwen, “Challenges in truncating the hierarchy of time-dependent reduced density matrices equations,” *Phys. Rev. B* **85**, 235121 (2012).
- ⁴⁴F. K. Diakonou and P. Schmelcher, “Super-lagrangian and variational principle for generalized continuity equations,” *J. Phys. A: Math. Theor.* **52**, 155203 (2019).
- ⁴⁵P. A. Kalozoumis, G. Pappas, F. K. Diakonou, and P. Schmelcher, “Systematic pathway to PT-symmetry breaking in scattering systems,” *Phys. Rev. A* **90**, 043809 (2014).

- ⁴⁶P. A. Kalozoumis, C. V. Morfonios, F. K. Diakonov, and P. Schmelcher, "PT-symmetry breaking in waveguides with competing loss-gain pairs," *Phys. Rev. A* **93**, 063831 (2016).
- ⁴⁷C. M. Bender and S. Boettcher, "Real spectra in non-hermitian Hamiltonians having PT symmetry," *Phys. Rev. Lett.* **80**, 5243 (1998).
- ⁴⁸C. M. Bender, D. C. Brody, and H. F. Jones, "Complex extension of quantum mechanics," *Phys. Rev. Lett.* **89**, 270401 (2002).
- ⁴⁹R. El-Ganainy, K. G. Makris, M. Khajavikhan, Z. H. Musslimani, S. Rotter, and D. N. Christodoulides, "Non-hermitian physics and PT symmetry," *Nat. Phys.* **14**, 11 (2018).
- ⁵⁰H. Zhao and L. Feng, "Parity–time symmetric photonics," *Natl. Sci. Rev.* **5**, 183 (2018).
- ⁵¹P. A. Kalozoumis, O. Richoux, F. K. Diakonov, G. Theocharis, and P. Schmelcher, "Invariant currents in lossy acoustic waveguides with complete local symmetry," *Phys. Rev. B* **92**, 014303 (2015).
- ⁵²A. Szameit, J. Burghoff, T. Pertsch, S. Nolte, A. Tünnermann, and F. Lederer, "Two-dimensional soliton in cubic fs laser written waveguide arrays in fused silica," *Opt. Express* **14**, 6055 (2006).
- ⁵³D. N. Christodoulides, F. Lederer, and Y. Silberberg, "Discretizing light behaviour in linear and nonlinear waveguide lattices," *Nature* **424**, 817 (2003).
- ⁵⁴I. L. Garanovich, S. Longhi, A. A. Sukhorukov, and Y. S. Kivshar, "Light propagation and localization in modulated photonic lattices and waveguides," *Physics Reports, Light Propagation and Localization in Modulated Photonic Lattices and Waveguides* **518**, 1 (2012).
- ⁵⁵P. Millar, J. S. Aitchison, J. U. Kang, G. I. Stegeman, A. Villeneuve, G. T. Kennedy, and W. Sibbett, "Nonlinear waveguide arrays in AlGaAs," *J. Opt. Soc. Am. B, JOSAB* **14**, 3224 (1997).
- ⁵⁶J. W. Fleischer, M. Segev, N. K. Efremidis, and D. N. Christodoulides, "Observation of two-dimensional discrete solitons in optically induced nonlinear photonic lattices," *Nature* **422**, 147 (2003).
- ⁵⁷T. Pertsch, U. Peschel, J. Kobelke, K. Schuster, H. Bartelt, S. Nolte, A. Tünnermann, and F. Lederer, "Nonlinearity and disorder in fiber arrays," *Phys. Rev. Lett.* **93**, 053901 (2004).
- ⁵⁸A. Szameit and S. Nolte, "Discrete optics in femtosecond-laser-written photonic structures," *J. Phys. B: At. Mol. Opt. Phys.* **43**, 163001 (2010).
- ⁵⁹R. Keil, A. Szameit, F. Dreisow, M. Heinrich, S. Nolte, and A. Tünnermann, "All-optical routing and switching in two-dimensional waveguide arrays," in *Integrated Photonics Research, Silicon and Nanophotonics and Photonics in Switching (2010)*, paper PWA5 (July 25, 2010), PWA5.
- ⁶⁰R. Keil, M. Heinrich, F. Dreisow, T. Pertsch, A. Tünnermann, S. Nolte, D. N. Christodoulides, and A. Szameit, "All-optical routing and switching for three-dimensional photonic circuitry," *Sci. Rep.* **1**, 94 (2011).

- ⁶¹R. A. Vicencio and C. Mejía-Cortés, “Diffraction-free image transmission in kagome photonic lattices,” *J. Opt.* **16**, 015706 (2013).
- ⁶²S. Rojas-Rojas, L. Morales-Inostroza, R. A. Vicencio, and A. Delgado, “Quantum localized states in photonic flat-band lattices,” *Phys. Rev. A* **96**, 043803 (2017).
- ⁶³S. Xia, Y. Hu, D. Song, Y. Zong, L. Tang, and Z. Chen, “Demonstration of flat-band image transmission in optically induced Lieb photonic lattices,” *Opt. Lett.* **41**, 1435 (2016).
- ⁶⁴R. A. Vicencio, C. Cantillano, L. Morales-Inostroza, B. Real, C. Mejía-Cortés, S. Weimann, A. Szameit, and M. I. Molina, “Observation of localized states in lieb photonic lattices,” *Phys. Rev. Lett.* **114**, 245503 (2015).
- ⁶⁵A. Szameit, F. Dreisow, and S. Nolte, “Discrete optics in femtosecond laser written waveguide arrays,” in *Femtosecond laser micromachining: photonic and microfluidic devices in transparent materials*, Topics in Applied Physics 123 (Springer, Berlin, Heidelberg, 2012), pp. 351–388.
- ⁶⁶B. Real, C. Cantillano, D. López-González, A. Szameit, M. Aono, M. Naruse, S.-J. Kim, K. Wang, and R. A. Vicencio, “Flat-band light dynamics in stub photonic lattices,” *Sci. Rep.* **7**, 15085 (2017).
- ⁶⁷A. Szameit, T. Pertsch, S. Nolte, A. Tünnermann, and F. Lederer, “Long-range interaction in waveguide lattices,” *Phys. Rev. A* **77**, 043804 (2008).
- ⁶⁸R. Morandotti, U. Peschel, J. S. Aitchison, H. S. Eisenberg, and Y. Silberberg, “Experimental observation of linear and nonlinear optical bloch oscillations,” *Phys. Rev. Lett.* **83**, 4756 (1999).
- ⁶⁹T. Pertsch, P. Dannberg, W. Elflein, A. Bräuer, and F. Lederer, “Optical bloch oscillations in temperature tuned waveguide arrays,” *Phys. Rev. Lett.* **83**, 4752 (1999).
- ⁷⁰F. Bloch, “Über die Quantenmechanik der Elektronen in Kristallgittern,” *Z. Physik* **52**, 555 (1929).
- ⁷¹L. Martin, G. D. Giuseppe, A. Perez-Leija, R. Keil, F. Dreisow, M. Heinrich, S. Nolte, A. Szameit, A. F. Abouraddy, D. N. Christodoulides, and B. E. A. Saleh, “Anderson localization in optical waveguide arrays with off-diagonal coupling disorder,” *Opt. Express* **19**, 13636 (2011).
- ⁷²P. W. Anderson, “Absence of diffusion in certain random lattices,” *Phys. Rev.* **109**, 1492 (1958).
- ⁷³M. C. Rechtsman, J. M. Zeuner, Y. Plotnik, Y. Lumer, D. Podolsky, F. Dreisow, S. Nolte, M. Segev, and A. Szameit, “Photonic floquet topological insulators,” *Nature* **496**, 196 (2013).
- ⁷⁴M. Segev and M. A. Bandres, “Topological photonics: where do we go from here?” *Nanophotonics* **10**, 425 (2021).
- ⁷⁵T. Ozawa, H. M. Price, A. Amo, N. Goldman, M. Hafezi, L. Lu, M. C. Rechtsman, D. Schuster, J. Simon, O. Zilberberg, and I. Carusotto, “Topological photonics,” *Rev. Mod. Phys.* **91**, 015006 (2019).

- ⁷⁶J. K. Asbóth, L. Oroszlány, and A. Pályi, *A short course on topological insulators: band structure and edge states in one and two dimension*, 1st ed., Lecture Notes in Physics 919 (Springer International Publishing, Basel, Switzerland, 2016), 180 pp.
- ⁷⁷M. Z. Hasan and C. L. Kane, “Colloquium: topological insulators,” *Rev. Mod. Phys.* **82**, 3045 (2010).
- ⁷⁸M. A. Bandres, M. C. Rechtsman, and M. Segev, “Topological photonic quasicrystals: fractal topological spectrum and protected transport,” *Phys. Rev. X* **6**, 011016 (2016).
- ⁷⁹J.-B. Suck, M. Schreiber, and P. Häussler, eds., *Quasicrystals: an introduction to structure, physical properties and applications*, Springer Series in Materials Science (Springer-Verlag, Berlin Heidelberg, 2002).
- ⁸⁰M. Heinrich, M.-A. Miri, S. Stützer, S. Nolte, D. N. Christodoulides, and A. Szameit, “Observation of supersymmetric scattering in photonic lattices,” *Opt. Lett.* **39**, 6130 (2014).
- ⁸¹D. Leykam, A. Andreanov, and S. Flach, “Artificial flat band systems: from lattice models to experiments,” *Adv. Phys.* **3**, 1473052 (2018).
- ⁸²Y. Lumer, M. A. Bandres, M. Heinrich, L. J. Maczewsky, H. Herzig-Sheinfux, A. Szameit, and M. Segev, “Light guiding by artificial gauge fields,” *Nat. Photon.* **13**, 339 (2019).
- ⁸³F. Dreisow, M. C. Rechtsman, J. M. Zeuner, Y. Plotnik, R. Keil, S. Nolte, M. Segev, and A. Szameit, “Dirac dynamics in waveguide arrays: from zitterbewegung to photonic topological insulators,” in *Quantum Simulations with Photons and Polaritons: merging Quantum Optics with Condensed Matter Physics*, edited by D. G. Angelakis, Quantum Science and Technology (Springer International Publishing, Cham, 2017), pp. 181–214.
- ⁸⁴F. Klauck, L. Teuber, M. Ornigotti, M. Heinrich, S. Scheel, and A. Szameit, “Observation of PT-symmetric quantum interference,” *Nat. Photon.* **13**, 883 (2019).
- ⁸⁵C. M. Bender, “PT symmetry in quantum physics: from a mathematical curiosity to optical experiments,” *Europhys. News* **47**, 17 (2016).
- ⁸⁶Y. N. Joglekar, C. Thompson, D. D. Scott, and G. Vemuri, “Optical waveguide arrays: quantum effects and PT symmetry breaking,” *Eur. Phys. J. Appl. Phys.* **63**, 30001 (2013).
- ⁸⁷S. Longhi, “Quantum-optical analogies using photonic structures,” *Laser Photonics Rev.* **3**, 243 (2009).
- ⁸⁸Inductiveload, *Penrose tiling (p3)*, (Feb. 1, 2009) [https://commons.wikimedia.org/wiki/File:Penrose_Tiling_\(Rhombi\).svg](https://commons.wikimedia.org/wiki/File:Penrose_Tiling_(Rhombi).svg).
- ⁸⁹P. J. Steinhardt, “Quasicrystals: a brief history of the impossible,” *Rend. Fis. Acc. Lincei* **24**, 85 (2013).
- ⁹⁰D. Shechtman, I. Blech, D. Gratias, and J. W. Cahn, “Metallic phase with long-range orientational order and no translational symmetry,” *Phys. Rev. Lett.* **53**, 1951 (1984).

- ⁹¹L. Pauling, "Apparent icosahedral symmetry is due to directed multiple twinning of cubic crystals," *Nature* **317**, 512 (1985).
- ⁹²L. Pauling, "Interpretation of so-called icosahedral and decagonal quasicrystals of alloys showing apparent icosahedral symmetry elements as twins of an 820-atom cubic crystal," *Comput. Math. with Appl.* **17**, 337 (1989).
- ⁹³E. Maciá Barber, *Aperiodic structures in condensed matter: fundamentals and applications*, 1st ed. (Taylor & Francis Inc, Boca Raton, Nov. 3, 2008), 443 pp.
- ⁹⁴E. Maciá Barber, "Chemical bonding and physical properties in quasicrystals and their related approximant phases: known facts and current perspectives," *Appl. Sci.* **9**, 2132 (2019).
- ⁹⁵M. Yoshimura and A. P. Tsai, "Quasicrystal application on catalyst," *J. Alloy. Comp., Proceedings from the 'Quasicrystals 2001' Conference* **342**, 451 (2002).
- ⁹⁶J.-M. Dubois, "Properties- and applications of quasicrystals and complex metallic alloys," *Chem. Soc. Rev.* **41**, 6760 (2012).
- ⁹⁷W. Steurer and S. Deloudi, "Fascinating quasicrystals," *Acta Cryst A* **64**, 1 (2008).
- ⁹⁸A. M. Selvam, "Quasicrystalline pattern formation in fluid substrates and phyllotaxis," in *Symmetry in Plants*, Series in Mathematical Biology and Medicine 4 (World Scientific Publishing Co Pte Ltd, Singapore, Mar. 1, 1998), pp. 795–809.
- ⁹⁹R. Lifshitz and H. Diamant, "Soft quasicrystals—Why are they stable?" *Philos. Mag.* **87**, 3021 (2007).
- ¹⁰⁰K. Hayashida, T. Dotera, A. Takano, and Y. Matsushita, "Polymeric quasicrystal: mesoscopic quasicrystalline tiling in ABC star polymers," *Phys. Rev. Lett.* **98**, 195502 (2007).
- ¹⁰¹L. Guidoni, C. Triché, P. Verkerk, and G. Grynberg, "Quasiperiodic optical lattices," *Phys. Rev. Lett.* **79**, 3363 (1997).
- ¹⁰²N. Macé, A. Jagannathan, and M. Duneau, "Quantum simulation of a 2D quasicrystal with cold atoms," *Crystals* **6**, 124 (2016).
- ¹⁰³T. A. Corcovilos and J. Mittal, "Two-dimensional optical quasicrystal potentials for ultracold atom experiments," *Appl. Opt.* **58**, 2256 (2019).
- ¹⁰⁴R. Gautier, H. Yao, and L. Sanchez-Palencia, "Strongly interacting bosons in a two-dimensional quasicrystal lattice," *Phys. Rev. Lett.* **126**, 110401 (2021).
- ¹⁰⁵J. Bellissard, A. Bovier, and J.-M. Ghez, "Gap labelling theorems for one dimensional discrete Schrödinger operators," *Rev. Math. Phys.* **04**, 1 (1992).
- ¹⁰⁶E. Akkermans, Y. Don, J. Rosenberg, and C. L. Schochet, "Relating diffraction and spectral data of aperiodic tilings: towards a Bloch theorem," *Journal of Geometry and Physics* **165**, 104217 (2021).
- ¹⁰⁷L. Dal Negro, R. Wang, and F. Pinheiro, "Structural and spectral properties of deterministic aperiodic optical structures," *Crystals* **6**, 161 (2016).
- ¹⁰⁸A. Jagannathan, *The Fibonacci quasicrystal: case study of hidden dimensions and multifractality*, (Apr. 30, 2021) <http://arxiv.org/abs/2012.14744>.

- ¹⁰⁹D. Damanik, A. Gorodetski, and W. Yessen, "The Fibonacci Hamiltonian," *Invent. math.* **206**, 629 (2016).
- ¹¹⁰E. Maciá, "On the nature of electronic wave functions in one-dimensional self-similar and quasiperiodic systems," *ISRN Condensed Matter Physics* **2014**, 165943 (2014).
- ¹¹¹Q. Niu and F. Nori, "Renormalization-group study of one-dimensional quasiperiodic systems," *Phys. Rev. Lett.* **57**, 2057 (1986).
- ¹¹²B. A. Van Tiggelen, "Localization of waves," in *Diffuse Waves in Complex Media*, edited by J.-P. Fouque, NATO Science Series (Springer Netherlands, Dordrecht, 1999), pp. 1–60.
- ¹¹³A. Lagendijk, B. van Tiggelen, and D. S. Wiersma, "Fifty years of Anderson localization," *Phys. Today* **62**, 24 (2009).
- ¹¹⁴E. Abrahams, ed., *50 years of anderson localization*, 1st ed. (World Scientific Publishing Co. Pte. Ltd., Singapore, 2010), 612 pp.
- ¹¹⁵P. Sheng, *Introduction to wave scattering, localization and mesoscopic phenomena*, 2nd ed., Springer Series in Materials Science 88 (Springer-Verlag, Berlin Heidelberg, 2006).
- ¹¹⁶T. Brandes and S. Kettemann, eds., *Anderson localization and its ramifications: disorder, phase coherence, and electron correlations*, 1st ed., Lecture Notes in Physics 630 (Springer, 2003), 327 pp.
- ¹¹⁷D. J. Thouless, "Anderson's theory of localized states," *J. Phys. C: Solid State Phys.* **3**, 1559 (1970).
- ¹¹⁸L. Dal Negro, *Optics of aperiodic structures: fundamentals and device applications* (Pan Stanford Publishing Pte Ltd, Singapore, Dec. 21, 2013), 509 pp.
- ¹¹⁹E. Maciá, "Exploiting aperiodic designs in nanophotonic devices," *Rep. Prog. Phys.* **75**, 036502 (2012).
- ¹²⁰L. Dal Negro and S. Inampudi, "Fractional transport of photons in deterministic aperiodic structures," *Sci. Rep.* **7**, 2259 (2017).
- ¹²¹W. Gellermann, M. Kohmoto, B. Sutherland, and P. C. Taylor, "Localization of light waves in Fibonacci dielectric multilayers," *Phys. Rev. Lett.* **72**, 633 (1994).
- ¹²²R. Merlin, K. Bajema, R. Clarke, F. -Y. Juang, and P. K. Bhattacharya, "Quasiperiodic GaAs-AlAs heterostructures," *Phys. Rev. Lett.* **55**, 1768 (1985).
- ¹²³F. Axel and H. Terauchi, "High-resolution X-ray-diffraction spectra of Thue-Morse GaAs-AlAs heterostructures: towards a novel description of disorder," *Phys. Rev. Lett.* **66**, 2223 (1991).
- ¹²⁴E. Diez, F. Domínguez-Adame, E. Maciá, and A. Sánchez, "Dynamical phenomena in Fibonacci semiconductor superlattices," *Phys. Rev. B* **54**, 16792 (1996).
- ¹²⁵P. Panchadhyayee, R. Biswas, A. Khan, and P. K. Mahapatra, "Current density in generalized Fibonacci superlattices under a uniform electric field," *J. Phys.: Condens. Matter* **20**, 275243 (2008).
- ¹²⁶P. Panchadhyayee, "Efficient band-pass and stop-band filtering by GaAs–Al_cGa_{1-c}As generalized Thue–Morse multibarrier systems," *Philos. Mag.* **93**, 2654 (2013).

- ¹²⁷E. J. Guzmán, S. Molina-Valdovinos, O. Oubram, and I. Rodríguez-Vargas, “Enhancement of the seebeck coefficient and power factor in gated silicene superlattices induced by aperiodicity,” *Journal of Applied Physics* **128**, 224302 (2020).
- ¹²⁸A. Ghosh and S. N. Karmakar, “Existence of only delocalized eigenstates in the electronic spectrum of the Thue–Morse lattice,” *Physica A: Statistical Mechanics and its Applications* **274**, 555 (1999).
- ¹²⁹R. Riklund, M. Severin, and Y. Liu, “The Thue-Morse aperiodic crystal, a link between the Fibonacci quasicrystal and the periodic crystal,” *Int. J. Mod. Phys. B* **01**, 121 (1987).
- ¹³⁰S. G. Davison and M. Steslicka, *Basic theory of surface states*, Monographs on the Physics and Chemistry of Materials (Oxford University Press, Oxford, New York, May 30, 1996), 238 pp.
- ¹³¹J. Zak, “Symmetry criterion for surface states in solids,” *Phys. Rev. B* **32**, 2218 (1985).
- ¹³²C. Morfonios, P. Schmelcher, P. A. Kalozoumis, and F. K. Diakonov, “Local symmetry dynamics in one-dimensional aperiodic lattices: a numerical study,” *Nonlinear Dyn.* **78**, 71 (2014).
- ¹³³M. Filoche and S. Mayboroda, “Universal mechanism for anderson and weak localization,” *Proc. Natl. Acad. Sci. U.S.A* **109**, 14761 (2012).
- ¹³⁴J. O. Hirschfelder and P. R. Certain, “Degenerate RS perturbation theory,” *J. Chem. Phys.* **60**, 1118 (1974).
- ¹³⁵L. Kroon and R. Riklund, “Absence of localization in a model with correlation measure as a random lattice,” *Phys. Rev. B* **69**, 094204 (2004).
- ¹³⁶Y. Zong, S. Xia, L. Tang, D. Song, Y. Hu, Y. Pei, J. Su, Y. Li, and Z. Chen, “Observation of localized flat-band states in kagome photonic lattices,” *Opt. Express* **24**, 8877 (2016).
- ¹³⁷S. Mukherjee and R. R. Thomson, “Observation of localized flat-band modes in a quasi-one-dimensional photonic rhombic lattice,” *Opt. Lett.* **40**, 5443 (2015).
- ¹³⁸Y. Nakata, T. Okada, T. Nakanishi, and M. Kitano, “Observation of flat band for terahertz spoof plasmons in a metallic kagome lattice,” *Phys. Rev. B* **85**, 205128 (2012).
- ¹³⁹S. Kajiwarra, Y. Urade, Y. Nakata, T. Nakanishi, and M. Kitano, “Observation of a nonradiative flat band for spoof surface plasmons in a metallic lieb lattice,” *Phys. Rev. B* **93**, 075126 (2016).
- ¹⁴⁰M. R. Slot, T. S. Gardenier, P. H. Jacobse, G. C. P. van Miert, S. N. Kempkes, S. J. M. Zevenhuizen, C. M. Smith, D. Vanmaekelbergh, and I. Swart, “Experimental realization and characterization of an electronic Lieb lattice,” *Nat. Phys.* **13**, 672 (2017).
- ¹⁴¹R. Drost, T. Ojanen, A. Harju, and P. Liljeroth, “Topological states in engineered atomic lattices,” *Nat. Phys.* **13**, 668 (2017).

- ¹⁴²G.-B. Jo, J. Guzman, C. K. Thomas, P. Hosur, A. Vishwanath, and D. M. Stamper-Kurn, "Ultracold atoms in a tunable optical kagome lattice," *Phys. Rev. Lett.* **108**, 045305 (2012).
- ¹⁴³J. H. Kang, J. H. Han, and Y. Shin, "Creutz ladder in a resonantly shaken 1D optical lattice," *New J. Phys.* **22**, 013023 (2020).
- ¹⁴⁴S. Taie, T. Ichinose, H. Ozawa, and Y. Takahashi, "Spatial adiabatic passage of massive quantum particles in an optical Lieb lattice," *Nat. Commun.* **11**, 257 (2020).
- ¹⁴⁵S. Taie, H. Ozawa, T. Ichinose, T. Nishio, S. Nakajima, and Y. Takahashi, "Coherent driving and freezing of bosonic matter wave in an optical Lieb lattice," *Sci. Adv.* **1**, e1500854 (2015).
- ¹⁴⁶N. Lazarides and G. P. Tsironis, "Compact localized states in engineered flat-band PT metamaterials," *Sci. Rep.* **9**, 1 (2019).
- ¹⁴⁷L.-L. Wan, X.-Y. Lü, J.-H. Gao, and Y. Wu, "Hybrid interference induced flat band localization in bipartite optomechanical lattices," *Sci. Rep.* **7**, 15188 (2017).
- ¹⁴⁸N. Myoung, H. C. Park, A. Ramachandran, E. Lidorikis, and J.-W. Ryu, "Flat-band localization and self-collimation of light in photonic crystals," *Sci. Rep.* **9**, 2862 (2019).
- ¹⁴⁹W. Zhu, S. Hou, Y. Long, H. Chen, and J. Ren, "Simulating quantum spin hall effect in the topological Lieb lattice of a linear circuit network," *Phys. Rev. B* **97**, 075310 (2018).
- ¹⁵⁰T. Helbig, T. Hofmann, C. H. Lee, R. Thomale, S. Imhof, L. W. Molenkamp, and T. Kiessling, "Band structure engineering and reconstruction in electric circuit networks," *Phys. Rev. B* **99**, 161114 (2019).
- ¹⁵¹M. Ostmann, M. Marcuzzi, J. Minář, and I. Lesanovsky, "Synthetic lattices, flat bands and localization in Rydberg quantum simulators," *Quantum Sci. Technol.* **4**, 02LT01 (2019).
- ¹⁵²F. Liu, Z.-C. Yang, P. Bienias, T. Iadecola, and A. V. Gorshkov, *Localization and criticality in antiblockaded 2D Rydberg atom arrays*, (Dec. 7, 2020) <http://arxiv.org/abs/2012.03946>.
- ¹⁵³J. von Neumann and E. Wigner, "Über merkwürdige diskrete Eigenwerte," *Phys. Z.* **30**, 465 (1929).
- ¹⁵⁴C. W. Hsu, B. Zhen, A. D. Stone, J. D. Joannopoulos, and M. Soljačić, "Bound states in the continuum," *Nat. Rev. Mater.* **1**, 16048 (2016).
- ¹⁵⁵Y. Plotnik, O. Peleg, F. Dreisow, M. Heinrich, S. Nolte, A. Szameit, and M. Segev, "Experimental observation of optical bound states in the continuum," *Phys. Rev. Lett.* **107**, 183901 (2011).
- ¹⁵⁶J.-W. Rhim and B.-J. Yang, "Classification of flat bands according to the band-crossing singularity of Bloch wave functions," *Phys. Rev. B* **99**, 045107 (2019).
- ¹⁵⁷D. Leykam, J. D. Bodyfelt, A. S. Desyatnikov, and S. Flach, "Localization of weakly disordered flat band states," *Eur. Phys. J. B* **90**, 10.1140/epjb/e2016-70551-2 (2017).

- ¹⁵⁸H. Tasaki, "From Nagaoka's ferromagnetism to flat-band ferromagnetism and beyond: an introduction to ferromagnetism in the Hubbard model," *Progress of Theoretical Physics* **99**, 489 (1998).
- ¹⁵⁹H. Tasaki, "Hubbard model and the origin of ferromagnetism," *Eur. Phys. J. B* **64**, 365 (2008).
- ¹⁶⁰O. Derzhko, J. Richter, and M. Maksymenko, "Strongly correlated flat-band systems: the route from Heisenberg spins to Hubbard electrons," *Int. J. Mod. Phys. B* **29**, 1530007 (2015).
- ¹⁶¹A. Mielke, "Pair formation of hard core bosons in flat band systems," *J Stat Phys* **171**, 679 (2018).
- ¹⁶²P. Puderliner and A. Mielke, "Interacting bosons in two-dimensional flat band systems," *Eur. Phys. J. B* **88**, 207 (2015).
- ¹⁶³S. Takayoshi, H. Katsura, N. Watanabe, and H. Aoki, "Phase diagram and pair Tomonaga-Luttinger liquid in a Bose-Hubbard model with flat bands," *Phys. Rev. A* **88**, 063613 (2013).
- ¹⁶⁴B. Grémaud and G. G. Batrouni, "Haldane phase on the sawtooth lattice: edge states, entanglement spectrum, and the flat band," *Phys. Rev. B* **95**, 165131 (2017).
- ¹⁶⁵M. Tovmasyan, "Strongly correlated phases in flatband lattices" (ETH Zurich, 2018), 148 p.
- ¹⁶⁶Z. Gulácsi, "Interaction-created effective flat bands in conducting polymers," *Eur. Phys. J. B* **87**, 143 (2014).
- ¹⁶⁷B. Sutherland, "Localization of electronic wave functions due to local topology," *Phys. Rev. B* **34**, 5208 (1986).
- ¹⁶⁸A. Mielke, "Ferromagnetic ground states for the Hubbard model on line graphs," *J. Phys. A: Math. Gen.* **24**, L73 (1991).
- ¹⁶⁹A. Mielke, "Ferromagnetism in the Hubbard model on line graphs and further considerations," *J. Phys. Math. Gen.* **24**, 3311 (1991).
- ¹⁷⁰H. Tasaki, "Ferromagnetism in the Hubbard models with degenerate single-electron ground states," *Phys. Rev. Lett.* **69**, 1608 (1992).
- ¹⁷¹E. H. Lieb, "Two theorems on the Hubbard model," *Phys. Rev. Lett.* **62**, 1201 (1989).
- ¹⁷²T. Wehling, A. Black-Schaffer, and A. Balatsky, "Dirac materials," *Adv. Phys.* **63**, 1 (2014).
- ¹⁷³S. Mukherjee, A. Spracklen, D. Choudhury, N. Goldman, P. Öhberg, E. Andersson, and R. R. Thomson, "Observation of a localized flat-band state in a photonic Lieb lattice," *Phys. Rev. Lett.* **114**, 245504 (2015).
- ¹⁷⁴S. Peotta and P. Törmä, "Superfluidity in topologically nontrivial flat bands," *Nat. Commun.* **6**, 8944 (2015).
- ¹⁷⁵A. Julku, S. Peotta, T. I. Vanhala, D.-H. Kim, and P. Törmä, "Geometric origin of superfluidity in the Lieb-lattice flat band," *Phys. Rev. Lett.* **117**, 045303 (2016).

- ¹⁷⁶K. Kobayashi, M. Okumura, S. Yamada, M. Machida, and H. Aoki, "Superconductivity in repulsively interacting fermions on a diamond chain: flat-band-induced pairing," *Phys. Rev. B* **94**, 214501 (2016).
- ¹⁷⁷M. Tovmasyan, S. Peotta, P. Törmä, and S. D. Huber, "Effective theory and emergent SU(2) symmetry in the flat bands of attractive Hubbard models," *Phys. Rev. B* **94**, 245149 (2016).
- ¹⁷⁸L. Liang, T. I. Vanhala, S. Peotta, T. Siro, A. Harju, and P. Törmä, "Band geometry, Berry curvature, and superfluid weight," *Phys. Rev. B* **95**, 024515 (2017).
- ¹⁷⁹A. Ramachandran, A. Andreanov, and S. Flach, "Chiral flat bands: existence, engineering, and stability," *Phys. Rev. B* **96**, 161104(R) (2017).
- ¹⁸⁰A. Nandy and A. Chakrabarti, "Engineering flat electronic bands in quasiperiodic and fractal loop geometries," *Phys. Lett. A* **379**, 2876 (2015).
- ¹⁸¹B. Pal and K. Saha, "Flat bands in fractal-like geometry," *Phys. Rev. B* **97**, 195101 (2018).
- ¹⁸²S. Weimann, L. Morales-Inostroza, B. Real, C. Cantillano, A. Szameit, and R. A. Vicencio, "Transport in sawtooth photonic lattices," *Opt. Lett.* **41**, 2414 (2016).
- ¹⁸³L. Morales-Inostroza and R. A. Vicencio, "Simple method to construct flat-band lattices," *Phys. Rev. A* **94**, 043831 (2016).
- ¹⁸⁴S. Flach, D. Leykam, J. D. Bodyfelt, P. Matthies, and A. S. Desyatnikov, "Detangling flat bands into Fano lattices," *Europhys. Lett.* **105**, 30001 (2014).
- ¹⁸⁵R. G. Dias and J. D. Gouveia, "Origami rules for the construction of localized eigenstates of the Hubbard model in decorated lattices," *Sci. Rep.* **5**, 16852 (2015).
- ¹⁸⁶W. Maimaiti, S. Flach, and A. Andreanov, "Universal $d=1$ flat band generator from compact localized states," *Phys. Rev. B* **99**, 125129 (2019).
- ¹⁸⁷W. Maimaiti, A. Andreanov, H. C. Park, O. Gendelman, and S. Flach, "Compact localized states and flat-band generators in one dimension," *Phys. Rev. B* **95**, 115135 (2017).
- ¹⁸⁸W. Maimaiti, A. Andreanov, and S. Flach, "Flat-band generator in two dimensions," *Phys. Rev. B* **103**, 165116 (2021).
- ¹⁸⁹W. Maimaiti and A. Andreanov, "Non-hermitian flat-band generator in one dimension," *Phys. Rev. B* **104**, 035115 (2021).
- ¹⁹⁰W. Barrett, A. Francis, and B. Webb, "Equitable decompositions of graphs with symmetries," *Linear Algebra Its Appl.* **513**, 409 (2017).
- ¹⁹¹A. Francis, D. Smith, D. Sorensen, and B. Webb, "Extensions and applications of equitable decompositions for graphs with symmetries," *Linear Algebra Its Appl.* **532**, 432 (2017).
- ¹⁹²A. Francis, D. Smith, and B. Webb, "General equitable decompositions for graphs with symmetries," *Linear Algebra Its Appl.* **577**, 287 (2019).
- ¹⁹³E. Fritscher and V. Trevisan, "Exploring symmetries to decompose matrices and graphs preserving the spectrum," *SIAM J. Matrix Anal. Appl.* **37**, 260 (2016).

- ¹⁹⁴S. I. Azzam and A. V. Kildishev, “Photonic bound states in the continuum: from basics to applications,” *Adv. Opt. Mater.* **9**, 2001469 (2021).
- ¹⁹⁵M. Prado, F. Sgrignuoli, Y. Chen, L. D. Negro, and F. A. Pinheiro, *Structural entropy and spatial decay of quasimodes in Vogel spirals*, (Aug. 19, 2021) <http://arxiv.org/abs/2106.06116>.
- ¹⁹⁶S. Zhang and A. Z. Genack, “Wave Interference and Modes in Random Media,” in *Tutorials in Complex Photonic Media* (SPIE, Bellingham, Washington, USA, Dec. 29, 2009), pp. 229–277.
- ¹⁹⁷S. B. Hasan, A. P. Mosk, W. L. Vos, and A. Lagendijk, “Finite-size scaling of the density of states in photonic band gap crystals,” *Phys. Rev. Lett.* **120**, 237402 (2018).
- ¹⁹⁸F. Sgrignuoli and L. Dal Negro, “Subdiffusive light transport in three-dimensional subrandom arrays,” *Phys. Rev. B* **101**, 214204 (2020).
- ¹⁹⁹A. Christofi, F. A. Pinheiro, and L. D. Negro, “Probing scattering resonances of Bogel spirals with the Green’s matrix spectral method,” *Opt. Lett.* **41**, 1933 (2016).
- ²⁰⁰R. Wang, F. A. Pinheiro, and L. Dal Negro, “Spectral statistics and scattering resonances of complex primes arrays,” *Phys. Rev. B* **97**, 024202 (2018).
- ²⁰¹F. Sgrignuoli, R. Wang, F. A. Pinheiro, and L. Dal Negro, “Localization of scattering resonances in aperiodic Vogel spirals,” *Phys. Rev. B* **99**, 104202 (2019).
- ²⁰²A. Goetschy and S. E. Skipetrov, “Non-hermitian euclidean random matrix theory,” *Phys. Rev. E* **84**, 011150 (2011).
- ²⁰³S. E. Skipetrov and I. M. Sokolov, “Absence of Anderson localization of light in a random ensemble of point scatterers,” *Phys. Rev. Lett.* **112**, 023905 (2014).
- ²⁰⁴S. E. Skipetrov, “Localization of light in a three-dimensional disordered crystal of atoms,” *Phys. Rev. B* **102**, 134206 (2020).
- ²⁰⁵S. E. Skipetrov, “Finite-size scaling of the density of states inside band gaps of ideal and disordered photonic crystals,” *Eur. Phys. J. B* **93**, 70 (2020).
- ²⁰⁶M. Antezza and Y. Castin, “Photonic band gap in an imperfect atomic diamond lattice: penetration depth and effects of finite size and vacancies,” *Phys. Rev. A* **88**, 033844 (2013).
- ²⁰⁷S. E. Skipetrov and I. M. Sokolov, “Search for Anderson localization of light by cold atoms in a static electric field,” *Phys. Rev. B* **99**, 134201 (2019).
- ²⁰⁸S. E. Skipetrov and I. M. Sokolov, “Magnetic-field-driven localization of light in a cold-atom gas,” *Phys. Rev. Lett.* **114**, 053902 (2015).
- ²⁰⁹L. Dal Negro, Y. Chen, and F. Sgrignuoli, “Aperiodic photonics of elliptic curves,” *Crystals* **9**, 482 (2019).
- ²¹⁰G. W. Mulholland, C. F. Bohren, and K. A. Fuller, “Light scattering by agglomerates: coupled electric and magnetic dipole method,” *Langmuir* **10**, 2533 (1994).

- ²¹¹B. García-Cámara, F. Moreno, F. González, and O. J. F. Martin, “Light scattering by an array of electric and magnetic nanoparticles,” *Opt. Express* **18**, 10001 (2010).
- ²¹²A. Legendijk and B. A. van Tiggelen, “Resonant multiple scattering of light,” *Physics Reports* **270**, 143 (1996).
- ²¹³S. Bose, “Quantum communication through an unmodulated spin chain,” *Phys. Rev. Lett.* **91**, 207901 (2003).
- ²¹⁴M. Christandl, N. Datta, A. Ekert, and A. J. Landahl, “Perfect state transfer in quantum spin networks,” *Phys. Rev. Lett.* **92**, 187902 (2004).
- ²¹⁵M. B. Plenio, J. Hartley, and J. Eisert, “Dynamics and manipulation of entanglement in coupled harmonic systems with many degrees of freedom,” *New J. Phys.* **6**, 36 (2004).
- ²¹⁶G. M. Nikolopoulos and I. Jex, eds., *Quantum state transfer and network engineering*, 1st ed., Quantum Science and Technology (Springer-Verlag, Berlin Heidelberg, 2014), 258 pp.
- ²¹⁷J. Zhang, G. L. Long, W. Zhang, Z. Deng, W. Liu, and Z. Lu, “Simulation of Heisenberg XY interactions and realization of a perfect state transfer in spin chains using liquid nuclear magnetic resonance,” *Phys. Rev. A* **72**, 012331 (2005).
- ²¹⁸X. Li, Y. Ma, J. Han, T. Chen, Y. Xu, W. Cai, H. Wang, Y. Song, Z.-Y. Xue, Z.-q. Yin, and L. Sun, “Perfect quantum state transfer in a superconducting qubit chain with parametrically tunable couplings,” *Phys. Rev. Applied* **10**, 054009 (2018).
- ²¹⁹A. Perez-Leija, R. Keil, A. Kay, H. Moya-Cessa, S. Nolte, L.-C. Kwek, B. M. Rodríguez-Lara, A. Szameit, and D. N. Christodoulides, “Coherent quantum transport in photonic lattices,” *Phys. Rev. A* **87**, 012309 (2013).
- ²²⁰R. J. Chapman, M. Santandrea, Z. Huang, G. Corrielli, A. Crespi, M.-H. Yung, R. Osellame, and A. Peruzzo, “Experimental perfect state transfer of an entangled photonic qubit,” *Nat. Commun.* **7**, 11339 (2016).
- ²²¹M. Christandl, N. Datta, T. C. Dorlas, A. Ekert, A. Kay, and A. J. Landahl, “Perfect transfer of arbitrary states in quantum spin networks,” *Phys. Rev. A* **71**, 032312 (2005).
- ²²²A. Kay, “Perfect, efficient, state transfer and its application as a constructive tool,” *Int. J. Quantum Inform.* **08**, 641 (2010).
- ²²³V. M. Kendon and C. Tamon, “Perfect state transfer in quantum walks on graphs,” *J. Comput. Theor. Nanosci.* **8**, 422 (2011).
- ²²⁴D. M. Cvetković, “Applications of graph spectra in quantum physics,” in *Selected Topics on Applications of Graph Spectra*, Zbornik Radova / Matematički Institut SANU (Matematički institut SANU, Beograd, 2011).
- ²²⁵R. Ronke, T. P. Spiller, and I. D’Amico, “Effect of perturbations on information transfer in spin chains,” *Phys. Rev. A* **83**, 012325 (2011).

- ²²⁶M. Christandl, L. Vinet, and A. Zhedanov, "Analytic next-to-nearest-neighbor XX models with perfect state transfer and fractional revival," *Phys. Rev. A* **96**, 032335 (2017).
- ²²⁷A. Kay, "Perfect state transfer: beyond nearest-neighbor couplings," *Phys. Rev. A* **73**, 032306 (2006).
- ²²⁸V. Kostak, G. M. Nikolopoulos, and I. Jex, "Perfect state transfer in networks of arbitrary topology and coupling configuration," *Phys. Rev. A* **75**, 042319 (2007).
- ²²⁹A. Wójcik, T. Łuczak, P. Kurzyński, A. Grudka, T. Gdala, and M. Bednarska, "Unmodulated spin chains as universal quantum wires," *Phys. Rev. A* **72**, 034303 (2005).
- ²³⁰T. J. G. Apollaro and F. Plastina, "Quantum information storage in the localized state of a spin chain," *Open Syst. Inf. Dyn.* **14**, 41 (2007).
- ²³¹A. O. Lyakhov and C. Bruder, "Use of dynamical coupling for improved quantum state transfer," *Phys. Rev. B* **74**, 235303 (2006).
- ²³²M. Kempton, G. Lippner, and S.-T. Yau, "Perfect state transfer on graphs with a potential," *Quantum Inf. Comput.* **17**, 303 (2017).
- ²³³L. Vinet and A. Zhedanov, "Almost perfect state transfer in quantum spin chains," *Phys. Rev. A* **86**, 052319 (2012).
- ²³⁴C. Godsil, "State transfer on graphs," *Discrete Math.* **312**, 129 (2012).
- ²³⁵C. Godsil, S. Kirkland, S. Severini, and J. Smith, "Number-theoretic nature of communication in quantum spin systems," *Phys. Rev. Lett.* **109**, 050502 (2012).
- ²³⁶X. Fan and C. Godsil, "Pretty good state transfer on double stars," *Linear Algebra Its Appl.* **438**, 2346 (2013).
- ²³⁷G. Coutinho and K. Guo, "Pretty good state transfer between internal nodes of paths," *Quantum Inf. Comput.* **17**, 0825 (2017).
- ²³⁸H. Pal and B. Bhattacharjya, "Pretty good state transfer on circulant graphs," *Electron. J. Comb.* **24** (2017).
- ²³⁹C. M. van Bommel, "A complete characterization of pretty good state transfer on paths," *Quantum Inf. Comput.* **19**, 0601 (2019).
- ²⁴⁰E. Ackelsberg, Z. Brehm, A. Chan, J. Munding, and C. Tamon, "Laplacian state transfer in coronas," *Linear Algebra Its Appl.* **506**, 154 (2016).
- ²⁴¹K. Heshami, D. G. England, P. C. Humphreys, P. J. Bustard, V. M. Acosta, J. Nunn, and B. J. Sussman, "Quantum memories: emerging applications and recent advances," *J. Mod. Opt.* **63**, 2005 (2016).
- ²⁴²C. Simon, M. Afzelius, J. Appel, A. Boyer de la Giroday, S. J. Dewhurst, N. Gisin, C. Y. Hu, F. Jelezko, S. Kröll, J. H. Müller, J. Nunn, E. S. Polzik, J. G. Rarity, H. De Riedmatten, W. Rosenfeld, A. J. Shields, N. Sköld, R. M. Stevenson, R. Thew, I. A. Walmsley, M. C. Weber, H. Weinfurter, J. Wrachtrup, and R. J. Young, "Quantum memories," *Eur. Phys. J. D* **58**, 1 (2010).
- ²⁴³D. A. Lidar, "Review of decoherence-free subspaces, noiseless subsystems, and dynamical decoupling," in *Quantum Information and Computation for Chemistry*, Advances in Chemical Physics 154 (John Wiley & Sons, Ltd, 2014), pp. 295–354.

- ²⁴⁴C. Grèzes, *Towards a spin-ensemble quantum memory for superconducting qubits: design and implementation of the write, read and reset steps*, 1st ed., Springer Theses (Springer International Publishing, 2016).
- ²⁴⁵C. Dłaska, B. Vermersch, and P. Zoller, “Robust quantum state transfer via topologically protected edge channels in dipolar arrays,” *Quantum Sci. Technol.* **2**, 015001 (2017).
- ²⁴⁶F. Mei, G. Chen, L. Tian, S.-L. Zhu, and S. Jia, “Robust quantum state transfer via topological edge states in superconducting qubit chains,” *Phys. Rev. A* **98**, 012331 (2018).
- ²⁴⁷J. I. Cirac, P. Zoller, H. J. Kimble, and H. Mabuchi, “Quantum state transfer and entanglement distribution among distant nodes in a quantum network,” *Phys. Rev. Lett.* **78**, 3221 (1997).
- ²⁴⁸X.-P. Zhang, B. Shao, S. Hu, J. Zou, and L.-A. Wu, “Optimal control of fast and high-fidelity quantum state transfer in spin-1/2 chains,” *Ann. Physics* **375**, 435 (2016).
- ²⁴⁹M. Murphy, S. Montangero, V. Giovannetti, and T. Calarco, “Communication at the quantum speed limit along a spin chain,” *Phys. Rev. A* **82**, 022318 (2010).
- ²⁵⁰H. Nakao and N. Yamamoto, “Optimal control for perfect state transfer in linear quantum memory,” *J. Phys. B: At. Mol. Opt. Phys.* **50**, 065501 (2017).
- ²⁵¹C. Brif, R. Chakrabarti, and H. Rabitz, “Control of quantum phenomena: past, present and future,” *New J. Phys.* **12**, 075008 (2010).
- ²⁵²S. J. Glaser, U. Boscain, T. Calarco, C. P. Koch, W. Köckenberger, R. Kosloff, I. Kuprov, B. Luy, S. Schirmer, T. Schulte-Herbrüggen, D. Sugny, and F. K. Wilhelm, “Training Schrödinger’s cat: quantum optimal control,” *Eur. Phys. J. D* **69**, 279 (2015).
- ²⁵³P. Doria, T. Calarco, and S. Montangero, “Optimal control technique for many-body quantum dynamics,” *Phys. Rev. Lett.* **106**, 190501 (2011).
- ²⁵⁴T. Caneva, T. Calarco, and S. Montangero, “Chopped random-basis quantum optimization,” *Phys. Rev. A* **84**, 022326 (2011).
- ²⁵⁵R. L. Breiger and P. E. Pattison, “Cumulated social roles: the duality of persons and their algebras,” *Soc. Netw.* **8**, 215 (1986).
- ²⁵⁶J. W. Higdon and S. H. Ferguson, “Past, present, and future for bowhead whales (*balaena mysticetus*) in northwest Hudson bay,” in *A Little Less Arctic: top Predators in the World’s Largest Northern Inland Sea, Hudson Bay*, edited by S. H. Ferguson, L. L. Loseto, and M. L. Mallory (Springer Netherlands, Dordrecht, 2010), pp. 159–177.
- ²⁵⁷S. Boccaletti, V. Latora, Y. Moreno, M. Chavez, and D. -U. Hwang, “Complex networks: structure and dynamics,” *Physics Reports* **424**, 175 (2006).
- ²⁵⁸M. E. J. Newman, “The structure and function of complex networks,” *SIAM Rev.* **45**, 167 (2003).
- ²⁵⁹R. Albert and A.-L. Barabási, “Statistical mechanics of complex networks,” *Rev. Mod. Phys.* **74**, 47 (2002).

- ²⁶⁰E. Estrada and P. A. Knight, *A first course in network theory*, 1st ed. (Oxford University Press, Oxford, New York, Mar. 26, 2015), 272 pp.
- ²⁶¹P. Van Mieghem, *Graph spectra for complex networks* (Cambridge University Press, Cambridge, UK ; New York, 2011), 346 pp.
- ²⁶²M. Newman, *Networks: an introduction*, 2nd ed. (Oxford University Press, Oxford, 2018), 800 pp.
- ²⁶³Albert-László Barabási, *Network science*, Hardcover (Cambridge University Press, 2016), 475 pp.
- ²⁶⁴P. Bonacich, "Factoring and weighting approaches to status scores and clique identification," *J. Math. Sociol.* **2**, 113 (1972).
- ²⁶⁵R. B. Mallion, N. Trinajstić, and A. J. Schwenk, "Graph theory in chemistry — generalisation of Sachs' formula," *Z. Für Naturforschung A* **29**, 1481 (1974).
- ²⁶⁶R. Milo, S. Shen-Orr, S. Itzkovitz, N. Kashtan, D. Chklovskii, and U. Alon, "Network motifs: simple building blocks of complex networks," *Science* **298**, 824 (2002).
- ²⁶⁷E. W. Dijkstra, "A note on two problems in connexion with graphs," *Numer. Math.* **1**, 269 (1959).
- ²⁶⁸S. N. Dorogovtsev and J. F. F. Mendes, "Evolution of networks," *Adv. Phys.* **51**, 1079 (2002).
- ²⁶⁹A. Lucas, "Ising formulations of many NP problems," *Front. Phys.* **2**, 5 (2014).
- ²⁷⁰B. D. MacArthur, R. J. Sánchez-García, and J. W. Anderson, "Symmetry in complex networks," *Discrete Appl. Math.* **156**, 3525 (2008).
- ²⁷¹B. D. MacArthur and R. J. Sánchez-García, "Spectral characteristics of network redundancy," *Phys. Rev. E* **80**, 026117 (2009).
- ²⁷²F. N. Silva, C. H. Comin, T. K. D. Peron, F. A. Rodrigues, C. Ye, R. C. Wilson, E. R. Hancock, and L. da F. Costa, "Concentric network symmetry," *Inf. Sci.* **333**, 61 (2016).
- ²⁷³C. P. Dettmann and G. Knight, "Symmetric motifs in random geometric graphs," *J. Complex Netw.* **6**, 95 (2018).
- ²⁷⁴J. E. Simões, D. R. Figueiredo, and V. C. Barbosa, "Local symmetry in random graphs," *IEEE Trans. Netw. Sci. Eng.* **7**, 1913 (2020).
- ²⁷⁵R. J. Sánchez-García, "Exploiting symmetry in network analysis," *Commun. Phys.* **3**, 1 (2020).
- ²⁷⁶M. Marcuzzi, J. Minář, D. Barredo, S. de Léséleuc, H. Labuhn, T. Lahaye, A. Browaeys, E. Levi, and I. Lesanovsky, "Facilitation dynamics and localization phenomena in Rydberg lattice gases with position disorder," *Phys. Rev. Lett.* **118**, 063606 (2017).
- ²⁷⁷E. R. van Dam and W. H. Haemers, "Which graphs are determined by their spectrum?" *Linear Algebra Its Appl., Combinatorial Matrix Theory Conference (Pohang, 2002)* **373**, 241 (2003).
- ²⁷⁸L. Katz, "A new status index derived from sociometric analysis," *Psychometrika* **18**, 39 (1953).

- ²⁷⁹S. Brin and L. Page, "The anatomy of a large-scale hypertextual web search engine," *Computer Networks and ISDN Systems, Proceedings of the Seventh International World Wide Web Conference* **30**, 107 (1998).
- ²⁸⁰Amy N. Langville and Carl D. Meyer, *Google's PageRank and beyond: the science of search engine rankings* (Princeton University Press, 2012).
- ²⁸¹A. E. Brouwer and W. H. Haemers, *Spectra of graphs*, 1st ed., Universitext (Springer New York, New York, NY, 2012).
- ²⁸²D. M. Cvetković, P. Rowlinson, and S. Simić, *Eigenspaces of graphs*, Encyclopedia of Mathematics and Its Applications v. 66 (Cambridge University Press, Cambridge ; New York, 1997), 258 pp.
- ²⁸³A. J. Schwenk, "Almost all trees are cospectral," in Proceedings of the Third Annual Arbor Conference (1973), pp. 257–307.
- ²⁸⁴C. D. Godsil and B. D. McKay, "Constructing cospectral graphs," *Aeq. Math.* **25**, 257 (1982).
- ²⁸⁵C. Godsil and J. Smith, *Strongly cospectral vertices*, (Sept. 22, 2017) <http://arxiv.org/abs/1709.07975>.
- ²⁸⁶O. Eisenberg, M. Kempton, and G. Lippner, "Pretty good quantum state transfer in asymmetric graphs via potential," *Discrete Math., Algebraic and Extremal Graph Theory* **342**, 2821 (2019).
- ²⁸⁷M. Langberg and D. Vilenchik, "Constructing cospectral graphs via a new form of graph product," *Linear Multilinear Algebra* **66**, 1838 (2018).
- ²⁸⁸K. Lorenzen, "Cospectral constructions and spectral properties of variations of the distance matrix," Doctor of Philosophy (Iowa State University, 2021).
- ²⁸⁹C. Rücker and G. Rücker, "Understanding the properties of isospectral points and pairs in graphs: the concept of orthogonal relation," *J. Math. Chem.* **9**, 207 (1992).
- ²⁹⁰W. C. Herndon, "The characteristic polynomial does not uniquely determine molecular topology," *J. Chem. Doc.* **14**, 150 (1974).
- ²⁹¹W. C. Herndon and M. L. Ellzey, "Isospectral graphs and molecules," *Tetrahedron* **31**, 99 (1975).
- ²⁹²C. Godsil, "Controllable subsets in graphs," *Ann. Comb.* **16**, 733 (2012).
- ²⁹³C. Godsil and S. Severini, "Control by quantum dynamics on graphs," *Phys. Rev. A* **81**, 052316 (2010).
- ²⁹⁴D. D'Alessandro, *Introduction to quantum control and dynamics*, 1st ed. (Chapman and Hall/CRC, New York, NY, USA, Aug. 3, 2007), 360 pp.
- ²⁹⁵G. Frobenius, "Ueber lineare Substitutionen und bilineare Formen," *J. Für Reine Angew. Math.* **84**, 1 (1877).
- ²⁹⁶S. Axler, *Linear algebra done right*, 3rd ed., Undergraduate Texts in Mathematics (Springer International Publishing, Cham, Switzerland, 2015), 352 pp.
- ²⁹⁷Y. Tsuji, E. Estrada, R. Movassagh, and R. Hoffmann, "Quantum Interference, Graphs, Walks, and Polynomials," *Chem. Rev.* **118**, 4887 (2018).

- ²⁹⁸L. A. Bunimovich and B. Z. Webb, “Isospectral graph transformations, spectral equivalence, and global stability of dynamical networks,” *Nonlinearity* **25**, 211 (2011).
- ²⁹⁹L. Bunimovich and B. Webb, *Isospectral transformations: a new approach to analyzing multidimensional systems and networks*, 1st ed., Springer Monographs in Mathematics (Springer, New York, NY, United States, 2014), 191 pp.
- ³⁰⁰L. A. Bunimovich and B. Z. Webb, “Isospectral graph reductions and improved estimates of matrices’ spectra,” *Linear Algebra Its Appl.* **437**, 1429 (2012).
- ³⁰¹L. A. Bunimovich and B. Z. Webb, “Restrictions and stability of time-delayed dynamical networks,” *Nonlinearity* **26**, 2131 (2013).
- ³⁰²D. Reber and B. Webb, “Intrinsic stability: stability of dynamical networks and switched systems with any type of time-delays,” *Nonlinearity* **33**, 2660 (2020).
- ³⁰³Vasquez Fernando Guevara and Webb Benjamin Z., “Pseudospectra of isospectrally reduced matrices,” *Numer. Linear Algebra Appl.* **22**, 145 (2014).
- ³⁰⁴L. A. Bunimovich and B. Z. Webb, “Improved estimates of survival probabilities via isospectral transformations,” in *Ergodic Theory, Open Dynamics, and Coherent Structures*, edited by W. Bahoun, C. Bose, and G. Froyland, Springer Proceedings in Mathematics & Statistics (2014), pp. 119–135.
- ³⁰⁵G. Grosso and G. P. Parravicini, *Solid state physics* (Academic Press, Oct. 2013).
- ³⁰⁶D. Smith and B. Webb, “Hidden symmetries in real and theoretical networks,” *Physica A* **514**, 855 (2019).
- ³⁰⁷M. Kempton, J. Sinkovic, D. Smith, and B. Webb, “Characterizing cospectral vertices via isospectral reduction,” *Linear Algebra Its Appl.* **594**, 226 (2020).
- ³⁰⁸L. Banchi, G. Coutinho, C. Godsil, and S. Severini, “Pretty good state transfer in qubit chains—The Heisenberg Hamiltonian,” *J. Math. Phys.* **58**, 032202 (2017).
- ³⁰⁹L. Bunimovich, D. Smith, and B. Webb, “Finding hidden structures, hierarchies, and cores in networks via isospectral reduction,” *Appl. Math. Nonlinear Sci.* **4**, 231 (2019).
- ³¹⁰L. D. Landau, E. M. Lifshitz, and J. Menzies, *Quantum mechanics: non-relativistic theory*, 3rd ed. (Elsevier Science & Technology, Jordan Hill, United Kingdom, 1981).
- ³¹¹H. V. McIntosh, “On accidental degeneracy in classical and quantum mechanics,” *Am. J. Phys.* **27**, 620 (1959).
- ³¹²Y. Kuno, T. Orito, and I. Ichinose, “Flat-band many-body localization and ergodicity breaking in the Creutz ladder,” *New J. Phys.* **22**, 013032 (2020).
- ³¹³F. D. R. Santos and R. G. Dias, “Methods for the construction of interacting many-body Hamiltonians with compact localized states in geometrically frustrated clusters,” *Sci. Rep.* **10**, 4532 (2020).

EIDESSTATTLICHE VERSICHERUNG / DECLARATION ON
OATH

Hiermit versichere ich an Eides statt, die vorliegende Dissertationsschrift selbst verfasst und keine anderen als die angegebenen Hilfsmittel und Quellen benutzt zu haben.

Die eingereichte schriftliche Fassung entspricht der auf dem elektronischen Speichermedium.

Die Dissertation wurde in der vorgelegten oder einer ähnlichen Form nicht schon einmal in einem früheren Promotionsverfahren angenommen oder als ungenügend beurteilt.

Hamburg, den

Malte Röntgen

EPILOGUE AND ACKNOWLEDGEMENTS

During the last years, I had the exciting opportunity to dive into many different topics, and for this reason I personally consider my Ph.D. as a journey into the unknown. And as with all such journeys, by far the most beautiful and fascinating parts were not those which were planned for, but rather those that happened unexpectedly. When I began with my endeavour, both the starting point and main motivation was to better understand the concept of non-local currents. But as the journey proceeded, I began to discover new aspects of local symmetries, which lead me to new shores. The work on local resonator theory and the one on compact localized states opened my eyes to the realm of photonic systems and graph theory. The question of how one might transfer such a compact localized state then lead me to the field of perfect and pretty good state transfer, and I stumbled upon the concept of cospectrality. I learned that relations on the matrix powers of a Hamiltonian can have great impact on its eigenvectors, an idea that should completely change my viewpoint of discrete systems. Soon after, the isospectral reduction came aboard, and with it the whole field of latent symmetries. Very recently, the two concepts of latent symmetries and cospectrality have been unified, and as the journey proceeds, we soon shall see more and more applications of latent symmetries: The explanation of accidental degeneracies, hidden symmetries in acoustic systems, chemical molecules, coupled oscillators, and many more. Clearly, this journey has just begun!

There are countless people without whom this endeavor would not have been possible. First of all, I would like to thank Prof. Dr. Peter Schmelcher for introducing me to the beautiful topic of local symmetries and for supervising both my Master and my Ph.D. thesis. I profited enormously from both his advice and enthusiasm. I am further very grateful to the German state for supporting my Bachelor and Master studies through BAföG, and for the "Stiftung der deutschen Wirtschaft" for granting me a Ph.D. scholarship.

The works presented in this thesis as well as those works that are still in progress have been done in collaboration with many brilliant scientist from around the world, and I would like to thank all of them for giving me the opportunity to broaden my knowledge by learning from them. In particular, I would like to thank Prof. Dr. Vincent Pagneux, Prof. Dr. Olivier Richoux, Prof. Dr. Georgios Theocharis, and Prof. Dr. Vassos Achilleos for showing me the beautiful world of acoustics; Prof. Dr. Luca Dal Negro for introducing me to photonics, and Prof. Dr. Fotios Diakonou for his hospitality as well as many very fruitful discussions on local and latent symmetries. I also had countless stimulating discussions with the student assistant B.Sc. Jens Kwasniok and with my office mates and collaborators M.Sc. Maxim Pyzh and Dr. Christian Morfonios, which I enjoyed very much. The (adjacency) matrix has you! Furthermore, I had the pleasure to co-supervise several bachelor students, namely, B.Sc. Friederike Horn, B.Sc. Lasse Blana, and B.Sc. Lasse Wendland. I really enjoyed working with you! I further would like to thank all members of Peter's

group for the stimulating atmosphere and the countless and memorable lunch times.

Besides these professional acknowledgments, I also would like to take this opportunity to thank my wife and best friend Sarah for always being there for me. I love you!

Sarah, my family, my deceased father, and all my friends, thank you so much for always supporting me. Without you, none of these works would have been possible!

Lastly, I want to thank the following people for helping me to come down from work during my free time, and for teaching important life lessons:

- Aritra, for giving me the opportunity to get insights into the Indian culture (especially Diwali!), for helping to plan our trip to India, and of course for recommending me all the nice indian restaurants in Hamburg.
- Tawete and his family, for reminding me to never forget Swahili or my time in Tanzania, and for hosting us on our trips to Njombe. Asanteni sana!
- Lasse, for being such a good friend and best man, and for introducing me to the high art of taking a regular Sauna.
- Marcel, for introducing me to the fascinating field of galactic warfare, trade and diplomacy.
- Maxim, Martin, Alejandro, and all the other members of our regular Twilight Imperium group, for our (literally) endless days of playing and for showing me the true meaning of “non-binding” agreements.
- My 96-year old neighbor Gisela, for showing me that learning new things is possible at any age, that smartphones, tablets, and e-book readers are not just for youngsters, and that Internet shops can make life easier, especially for the elder people.